A NON-CONTACT GEOMATICS TECHNIQUE FOR MONITORING MEMBRANE ROOF STRUCTURES

SHIH-YUAN LIN

Thesis submitted for the Degree of
Doctor of Philosophy

NEWCASTLE UNIVERSITY LIBRARY
206 53302 1
Thesis L8608



School of Civil Engineering and Geosciences
Newcastle University

September 2007

ABSTRACT

This thesis presents research carried out to monitor the behaviour of membrane structures, using the non-contact geomatics techniques of terrestrial laser scanning and videogrammetry. Membrane structures are covers or enclosures in which fabric surface is pre-tensioned to provide a stable shape under environmental loads. It is most often adopted by structural engineers as the solution to the roof of a building. Membrane structures resist externally-imposed loads by a combination of curvature and tension of the highly flexible fabric membrane. However, collapse may occur if the real deflections exceed the designed tolerances. In order to avoid such failures in the future, a generic monitoring system, incorporating in-house software for observing and analysing the behaviour of existing membrane structures, was developed. This system has been applied to observe three different types of as-built membrane structures, with two primary issues investigated and resolved.

The first aspect of the research was devoted to determining differences which exist between the designed model and the finished structure. To address this issue, terrestrial laser scanning was applied to generate the as-built model of the membrane structure. Statistical comparisons were then performed between the resultant scanned model and the designed mathematical model. The disparities were determined, allowing the factors causing these differences to be further explored. The second research issue investigated the effects of loading on the displacement of the membrane roof. A videogrammetric monitoring system employing stereo CCD video cameras was used to observe the movements of the membrane roofs. In order to accommodate constraints at the test site, a non-contact control method and structured light targeting were adopted in the monitoring scheme. Once the processing was completed, displacements occurring over time were determined.

Investigations on the three types of finished membrane structures have been successfully achieved, proving the system to be a viable metrology tool for structural engineers involved in monitoring real-world membrane structures. The system effectively fulfilled the requirements for understanding the interaction of membrane surface geometry, applied loads and structural response. The information acquired by the system offers great potential to collaborating engineers who are involved in the design and refinement of such structures.

ACKNOWLEDGEMENTS

Pursuing a PhD at Newcastle University has been absolutely fantastic. It is with pleasure that I offer my sincere gratitude to following people who have made this come true.

Firstly, I would like to thank my supervisor, Prof. Jon Mills. With his instruction and knowledge, he helped me to conduct this project in a complete and effective manner. Throughout my thesis-writing period, he provided encouragement, sound advice and good teaching. This work would not have been possible without his assistance. Also, I would like to thank my co-supervisor, Prof. Peter Gosling, for providing the opportunity to apply my knowledge and skills to the field of structural engineering. This has been a great experience.

I wish to thank Arup for providing the designed model of the Dalton Park membrane structure as well as enabling access to the study area used in this project. In addition, I am particularly indebted to my colleagues from Geomatics for preparing the surveying equipment and helping with the fieldwork. Thanks go to Martin Robertson, Pauline Miller, Henny Mills, David Barber, Mat Md Wazir and Jon. I am also grateful to Michael Lim, David, Gobe Hobona, Iain Wood and Pierre De Leusse for reading the draft of my thesis and giving me many valuable suggestions.

I am really lucky to have made many good friends during the last four years: Pauline, Henny, Mat, Ali, Gobe, Anh, Hamlan, Yu-Ching, Ming and Kou. Thanks for your assistance and company, no matter the aspects of academic research or relaxation time, this all makes my life in Newcastle more meaningful.

Lastly, and most importantly, I wish to thank my dad, mom, sisters and brother for their support. I am particularly grateful to Pei-Chi, without your complete back-up and constant encouragement I would never have finished my thesis. It is to them that I dedicate this work.

TABLE OF CONTENTS

ABSTRACT.....i

ACKNOWLEDGEMENTS.....ii

TABLE OF CONTENTS.....iii

LIST OF FIGURES.....vii

LIST OF TABLES.....xix

LIST OF ABBREVIATIONS.....xxi

CHAPTER 1 INTRODUCTION **1**

1.1 Overview 1

1.2 Membrane Structures 2

1.2.1 Definition and Classification 2

1.2.2 Design Process 6

1.2.3 Design Principles 9

1.2.4 Installation 10

1.2.5 Potential Issues 12

1.2.6 Test Site 14

1.3 Aims and Objectives 15

1.4 Research Methodology 15

1.5 Thesis Structure 16

CHAPTER 2 GEOMATICS TECHNIQUES FOR CLOSE RANGE MEASUREMENT AND MONITORING **18**

2.1 Introduction 18

2.2 Terrestrial Surveying with Total Station Instruments 18

2.2.1 Background 18

2.2.2 Coordinate Measurement with a Total Station 20

2.2.3 Applications in Structural Measurement and Monitoring 21

2.2.4 Other Applications with Total Stations 25

2.2.5 Suitability for Membrane Structure Measurement and Monitoring 26

2.3 Terrestrial Surveying with Terrestrial Laser Scanning (TLS) 27

2.3.1 Introduction 27

2.3.2 Instrumentation 28

2.3.3 Laser Scanned Data Processing 30

2.3.4 Applications in Structural Measurement and Monitoring 34
2.3.5 Other Applications with TLS 39
2.3.6 Suitability for Membrane Structure Measurement and Monitoring 40
2.4 Image-based Measurement Methods 41
2.4.1 Digital Photogrammetry and Computer Vision 42
2.4.2 Principles of Digital Photogrammetry 44
2.4.3 Instrumentation for Data Acquisition 56
2.4.4 Suitability for Membrane Structure Measurement and Monitoring 67
2.5 Additional Technologies 69
2.5.1 Laser Tracking 69
2.5.2 Laser Vibrometry 70
2.5.3 Suitability for Membrane Structure Measurement and Monitoring 72
2.6 Chapter Summary 73

CHAPTER 3 METHODOLOGIES FOR MEMBRANE STRUCTURE MONITORING 75
3.1 Introduction 75
3.2 Static Surface Modelling 75
3.2.1 Terrestrial Laser Scanning 76
3.2.2 Surface Model Comparison – Surface Matching 79
3.2.3 Surface Model Comparison – 3D Conformal Transformation 81
3.3 Dynamic Surface Modelling 82
3.3.1 Videogrammetric Instrumentation 82
3.3.2 Non-contact Control Method 88
3.3.3 Projected-dot Videogrammetry 91
3.3.4 Workflow 92
3.4 Laboratory Experiments 93
3.4.1 Overview 93
3.4.2 Test 1 – Spectral Reflectance Analysis 93
3.4.3 Test 2 – Reliability Test of Using Laser Footprint as Control 96
3.4.4 Test 3 – Static Ceiling Surface Modelling 102
3.4.5 Test 4 – Simulated Dynamic Membrane Modelling I 105
3.4.6 Test 5 – Simulated Dynamic Membrane Modelling II 110
3.5 Chapter Summary 114
3.5.1 Summary of Findings 114
3.5.2 Concluding Remarks 116

CHAPTER 4 MEMBRANE STRUCTURE MONITORING SYSTEM (MS^2) 117
4.1 Introduction 117

4.2 Required Software 117
4.3 System Structure 118
4.3.1 Main Menu 118
4.3.2 Static Surface Comparison 119
4.3.3 Dynamic Surface Modelling 123
4.4 Assessment of MS^2 Performance 138
4.4.1 Introduction 138
4.4.2 Static Monitoring Performance 138
4.4.3 Dynamic Monitoring Performance 145
4.4.4 Discussion 153
4.5 Chapter Summary 154

CHAPTER 5 DALTON PARK MONITORING SCHEME – SITE ASSESSMENT 155
5.1 Introduction 155
5.2 The Observed Membrane Structure 155
5.3 Static Surface Modelling 157
5.3.1 Mathematical Model 157
5.3.2 TLS Model 157
5.3.3 Static Surface Comparison 164
5.3.4 Discussion 177
5.3.5 Summary: Static Surface Modelling 179
5.4 Dynamic Surface Modelling 179
5.4.1 On-site Methodology 179
5.4.2 Data Processing – MS^2 181
5.4.3 Results 186
5.4.4 Discussion 188
5.4.5 Summary: Dynamic Surface Modelling 189
5.5 Chapter Summary 190
5.5.1 Summary of Findings 190
5.5.2 Concluding Remarks 191

CHAPTER 6 DALTON PARK MONITORING SCHEME – TRANSFERABILITY ASSESSMENT 192
6.1 Introduction 192
6.2 Type 2 Membrane Structure 192
6.2.1 Background 192
6.2.2 Static Surface Modelling 194
6.2.3 Dynamic Surface Modelling 201

6.2.4 Summary: Monitoring of Type 2 Membrane Structure 224
6.3 Type 3 Membrane Structure 225
6.3.1 Background 225
6.3.2 Static Surface Modelling 227
6.3.3 Dynamic Surface Modelling 234
6.3.4 Summary: Monitoring of Type 3 Membrane Structure 238
6.4 Chapter Summary 239

CHAPTER 7 CONCLUDING REMARKS 240
7.1 Conclusions 240
7.1.1 Applied Geomatics Techniques 240
7.1.2 Hardware and Software Aspects of the Monitoring System 241
7.1.3 On-site Observation using the Monitoring System 242
7.1.4 Transferability of the Monitoring System 243
7.1.5 Investigations into Membrane Structure Behaviour 244
7.1.6 Summary 245
7.2 Suggestions for Future Work 246

APPENDIX ONE MATLAB CODES FOR MS^2 IMPLEMENTATION 249
A1.1 Static Surface Modelling 249
A1.1.1 Read Math Model 249
A1.1.2 Locate Control Points 250
A1.1.3 Surface Comparison 251
A1.2 Dynamic Surface Modelling 253
A1.2.1 Camera Orientation Module 253
A1.2.2 Target Referencing Module 254
A1.2.3 Target Tracking Module 256
A1.2.4 Target Calculation Module 257

LIST OF REFERENCES 260

LIST OF FIGURES

Figure 1-1: The family of tensile structures (Scheuermann and Boxer, 1996). 3

Figure 1-2: Examples of the basic type of membrane structure. Left: Priestfield football stadium in Kent, U.K., completed in 2001; right: Ford showroom in Stevenage, U.K., completed in 2004 (photo by Architen Landrell).....4

Figure 1-3: Examples of boundary tensioned membrane structures. Left: a series of tensile canopy for Stratford bus interchange in London, completed in 1994 (photo by Architen Landrell); right: the Starwave tent in Cologne, Germany, rebuilt in 2000 (photo by SL-Rasch GMBH). 4

Figure 1-4: Examples of prestressed cable net structures. Left: Munich Olympic Stadium (photo by Aviewoncities); right: "Le Nuage" at La Défense near Paris, where a cable net structure is externally suspended from the "Grand Arche" by steel cables (photo by Arup). 5

Figure 1-5: Example of pneumatic structure: exterior and interior views of Total Soccer stadium in Michigan, U.S.A. (photo by The Farley Group).....5

Figure 1-6: Classification of styles of tensile structures (Bradatsch et al., 2004). 6

Figure 1-7: Mathematical model of a saddle structure (left) and the membrane roof surface at Chavasse Park, Liverpool, U.K. (right). 7

Figure 1-8: Digital cutting patterns layout (a), stripes (b) and cutting patterns (c) (after Bradatsch et al., 2004).....8

Figure 1-9: Left: small-scale model for wind tunnel test; right: graphical display of wind pressure distribution (photo by SL-Rasch GMBH).....8

Figure 1-10: Flowchart of the general approach to tensile membrane structure design and construction (after Campbell, 1991).....9

Figure 1-11: Situations during installation (Bridgens et al., 2004). 11

Figure 1-12: The failure of the membrane roof at Olympic Stadium in Montreal (Nightly.Net, 2006).....13

Figure 1-13: The failure of the membrane roof at Waldstadiom in Frankfurt (Associated Press, 2005). 13

Figure 1-14: Dalton Park plan (Bridgens et al., 2004). 14

Figure 2-1: The 3D coordinates of a point determined by a total station within a local coordinate system (after Feng et al., 2003). 20

Figure 2-2: The Leica TCA 2003 (left), prism (top right) and reference point (bottom right) set up for load testing (after Merkle and Myers, 2004). 22

Figure 2-3: Robotic total station observation scheme (left); the RTS is mounted on a pillar in an observation shelter (right) (after Lutes, 2002). 23

Figure 2-4: Part of the valley pit plan, showing prisms (blue dots), selected instability areas and RTS locations (Newcomen et al., 2003). 24

Figure 2-5: The scissors arches of Wells Cathedral (left) and the point cloud measured by robotic total station (right). 25

Figure 2-6: The principle of laser scanning (Staiger, 2003). 28

Figure 2-7: An example point cloud (left) and its TIN model (right). 32

Figure 2-8: Left: downstream face of the Cancano Lake dam. Right: deformation map acquired from scans recorded at two epochs (after Alba et al., 2006a). 35

Figure 2-9: Raw point clouds with irregular and non-uniform sampling (left) and the interpolated grid (right), identical for every point cloud. The deformation is derived by computing the difference in y-direction (Schafer et al., 2004). 36

Figure 2-10: The tunnel (left) and its resultant laser scanned model (right) (Gosliga et al., 2006). 37

Figure 2-11: Left: residuals after fitting a cylindrical model to the tunnel data. Right: changes between the two measurement epochs (Gosliga et al., 2006). 37

Figure 2-12: Schematic diagram for deformation of a beam (Gordon et al., 2004). 38

Figure 2-13: The interrelation of various image-based measurement methods. 44

Figure 2-14: The effect on triangulation precision of changes in network geometry (Fraser, 2001). 45

Figure 2-15: The symmetrical camera network. 46

Figure 2-16: The collinearity condition (after Fraser, 2006). 47

Figure 2-17: Network of photogrammetric bundles (Kraus, 1993). 48

Figure 2-18: Images of a calibration planar checkerboard (top) and the solved 3D

positions of the grids with respect to the camera (bottom) (Strobl et al., 2007).....51

Figure 2-19: Calibrating the video cameras ((a), (b) and (c)) with a moved reference bar (d) (Maas, 1998a). 52

Figure 2-20: Cross section of retro-reflective target (Zumbrunn, 1995).....55

Figure 2-21: CCD analogue video camera and frame grabber (National Instruments, 2007).....57

Figure 2-22: Progressive and interlaced frames (Ghanbari, 1999).....57

Figure 2-23: The observed bridge of the Franckestraße over the Flutgraben in Erfurt, Germany (left); the adopted CCD video camera (right) (Albert et al., 2002). 58

Figure 2-24: Experimental setup for the vibrating wing structure (top); the mode of vibration of the wing structure (bottom) (Ryall and Fraser, 2002).....59

Figure 2-25: Example of motion measured for part of a wheat plant over a period of one minute (top); various projections of trajectories measured for two bubbles inside a low-speed vertical vortex (bottom) (Hobbs, 2003).....61

Figure 2-26: The underwater stereo-video system based on DV camcorders in acrylic housings (Shortis et al., 2007). 62

Figure 2-27: The software interface showing length measurements of a Southern Bluefin Tuna (Harvey et al., 2001).....62

Figure 2-28: The reconstruction of a flight path (the red curve) of Eptesicus bottae (after Holderied et al., 2005). 63

Figure 2-29: An imaging system consisting of five IEEE-1394 video cameras (D'Apuzzo and Kochi, 2003). 64

Figure 2-30: Different configurations of camera array (Wilburn et al., 2005).....64

Figure 2-31: The panoramic camera system for the capture of 360° images (top); the panoramic browser interface (bottom) (As-Built Solutions Ltd., 2007). ...66

Figure 2-32: Typical frame recording moving golf club (after Smith et al., 1998).....67

Figure 2-33: Kits for synchronising cameras: (a) synchronisation cable release; (b) wired controller; (c) wireless controller and receivers. 67

Figure 2-34: Schema of laser tracking technique (Lau, 2003). 69

Figure 2-35: Monitoring system for measuring vibration of ventilated walls (Esposito et al., 2004).....71

Figure 2-36: Experimental setup of the monitoring system (left); map of the resulting vibrations (right) (after Esposito et al., 2004). 71

Figure 2-37: The observed solar sail model (left); shaker with attachment to sail model (right) (Blandino et al., 2003).....72

Figure 2-38: Vibration map of the observed surface (Blandino et al., 2003). 72

Figure 3-1: Terrestrial laser scanners employed (left: Leica HDS2500; right: Leica HDS3000).....76

Figure 3-2: The strategy of extracting corner points from a dense point cloud. 78

Figure 3-3: Surface matching procedure in the 3D Surf program (Buckley, 2003). 80

Figure 3-4: Employed DV camcorders (top left: JVC GR-D30U; top right: Sony DCR-PC101; bottom right: Sharp VL-Z1).....83

Figure 3-5: The CCD video camera employed, Oscar OF-810C and the rear of the camera ((a): IEEE- 1394 plug; (b): HiRose plug). 85

Figure 3-6: The pulse generator employed (Thurlby Thandar Instruments (TTi) TG 215), the frequency was adjustable and displayed in the window. 86

Figure 3-7: The close range calibration field.....86

Figure 3-8: The camera network in the close range calibration field. 87

Figure 3-9: Hardware configuration of the videogrammetric monitoring system. 88

Figure 3-10: Generation of the image of all laser footprints. 90

Figure 3-11: Spectral reflectance test by using the contact reflectance probe. 94

Figure 3-12: Spectral reflectance of the PVC-coated polyester fabric. 95

Figure 3-13: Spectral reflectance of PVC fabric obtained by Navin (2005). 95

Figure 3-14: Setup of reliability test of non-contact control method. 96

Figure 3-15: Images of complete control footprints and attached targets. Top to bottom are images taken from left (Sony DCR-PC101), middle (Sharp VL-Z1) and

right (JVC GR-D30U) camera stations. 98

Figure 3-16: Images of complete control footprints, single zoom-in footprint and attached targets, taken by the two Oscar cameras. 100

Figure 3-17: Setup of the Test 3: Sharp VL-Z1 camcorder (a); Sony DCR-PC101 camcorder (b); data projector (c); total station (d); projected pattern (e). 102

Figure 3-18: Images of the complete laser footprints.....103

Figure 3-19: Stereopair of the projected-dots.....103

Figure 3-20: The point model (top) and meshed model (bottom) of the ceiling. 104

Figure 3-21: Close up views of sequential frames (frame 593 to 595) recorded laser footprints (Sony DCR-PC101), showing three consecutive sections of scan line 4. 106

Figure 3-22: Close up views of interpolated laser footprints. From left to right: even and odd field of 593rd frame, even and odd field of 594th frame, even and odd field of 595th frame. 106

Figure 3-23: Complete control image (shot by Sony DCR-PC101) and the selected control footprints in Test 4 (outlined by black circles).....107

Figure 3-24: Example of synchronous frames set and the monitored dynamic surface was outlined by dotted lines. From top to bottom are images of projected-dots taken from left camera station (Sony DCR-PC101), middle camera station (Sharp VL-Z1) and right camera station (JVC GR-D30U).108

Figure 3-25: Dynamic surface movement (up: the movement occurring between t1 to t5; bottom: the movement occurring between t6 to t10).....109

Figure 3-26: Configuration in Test 5: Oscar camera (right exposure station) (a); Leica TCRA1103 total station (b); data projector (c); pulse generator (d); host laptop computer (e); moving projector screen (f).....111

Figure 3-27: Extracted laser footprints (outlined by red triangles) and projected-dots (outlined by white crosses).....112

Figure 3-28: Example sequential point model of the dynamic surface in Test 5. 113

Figure 4-1: User interface of the Main Menu.....118

Figure 4-2: User interface of the Locate Control Points Module.....120

Figure 4-3: User interface of the Surface Comparison Module. 122

Figure 4-4: Meshed model generated by different interpolation methods. Top to bottom: nearest neighbour, linear and cubic interpolation.....123

Figure 4-5: Computation sequence of the dynamic surface modelling in MS^2.....124

Figure 4-6: User interface of the control footprints extraction in Camera Orientation Module.....125

Figure 4-7: User interface of the control footprints matching in Camera Orientation Module.....126

Figure 4-8: User interface of Target Extraction Module. 127

Figure 4-9: Saved data structure of the projected targets extracted from left and right cameras at each epoch. 127

Figure 4-10: Ambiguities of applying epipolar geometry in the dynamic monitoring scheme. 128

Figure 4-11: Schema of target referencing: top, ideal target extraction; middle, results after real-life extraction; bottom, results after target reconstruction. 130

Figure 4-12: User interface of Target Referencing Module. 131

Figure 4-13: Data structure of the corresponding targets at first epoch. 131

Figure 4-14: Workflow of the Target Referencing Module. 132

Figure 4-15: User interface of Target Tracking Module.....133

Figure 4-16: Workflow of Target Tracking Module. 134

Figure 4-17: Data structure of the tracked target, based on the structure saved in Target Referencing Module. 134

Figure 4-18: User interface of Target Calculation Module – Intersection (left) and Bundle Adjustment (right).....135

Figure 4-19: Saved data structure of the determined 3D positions of projected targets at each epoch. 135

Figure 4-20: User interface of Target Modelling Module – Overall Query.....137

Figure 4-21: User interface of Target Modelling Module – Advanced Query. 137

Figure 4-22: Dot pattern projected onto the static wall, observed by the left camera...139

Figure 4-23: Videogrammetric network comprising two camera stations and the projected-dot pattern.....139

Figure 4-24: Image of extracted control footprints from left and right exposure stations.140

Figure 4-25: 3D map of the control footprints observed by the total station. 141

Figure 4-26: The resulting match of control footprints. 141

Figure 4-27: Image of extracted projected targets from left and right exposure stations.142

Figure 4-28: Resulting displacement for the static surface monitoring test. 144

Figure 4-29: Images of extracted control footprints from left and right exposure stations, produced by MS^2. 146

Figure 4-30: Example sequential stereopairs of extracted projected targets. 147

Figure 4-31: The example sequential meshed model of the dynamic surface (from epoch 43 to epoch 50). 148

Figure 4-32: Average and maximum movement occurred at each epoch.....149

Figure 4-33: The displacement of the observed surface. The surface model of the 1st epoch was set as the base, the vectors represent the differences occurred at the 44th (top) and the 120th (bottom) epoch. 150

Figure 4-34: Differences in profiles between the base and the selected six surface models. Left: the profile along Z-axis where X=105.1 m; right: the profile along X-axis where Z=10.9 m. 151

Figure 4-35: The moving trajectory along the range direction of the specific points (105.1 m, 12.3 m) (left) and (103.95 m, 10.8 m) (right) occurred during the monitoring. 151

Figure 4-36: The resulting interfaces of the overall and advanced queries of the surface movement. 152

Figure 5-1: Design plan of Dalton Park, the observed membrane structure of Tent Type 1 is outlined by dashed line. 156

Figure 5-2: Components of the observed membrane structure: beams (a); flying mast (b); cables (c); fabric membranes (d) and top ring (e). 156

Figure 5-3: Mathematical model of the observed membrane structure.....157

Figure 5-4: Point model of the observed membrane structure. 157

Figure 5-5: The Leica HDS2500 in operation and the resulting scanned model. Two control points (CP5 and CP6) are indicated by blue triangles. 158

Figure 5-6: Control network for the registration of the laser scanned models.....158

Figure 5-7: Scanning from the raised platform. 159

Figure 5-8: Scanner network using a Leica HDS2500 for the membrane structure observation; including four ground scanning stations (Ground 1 – 4) and four platform-mounted scan stations (Tower 1 – 4). 159

Figure 5-9: Scanner network of using Leica HDS3000 (Tower 1-3) in the membrane structure observation. 160

Figure 5-10: Amalgamated laser scanned model of the membrane structure generated by Leica HDS2500 (top) and HDS3000 (bottom) laser scanners. 161

Figure 5-11: Fabric membrane roof extracted from the HDS3000 laser scanned model for surface comparison. 161

Figure 5-12: The scanned supporting steelworks and the resulting cylinder models (grey pipes) and centre lines (blue lines). 162

Figure 5-13: The beam (Beam 4) used in the estimation of the accuracy of the laser scanned model. 163

Figure 5-14: The example section of Beam 4 showing discrepancies between the check points (blue points) and the centre line of the beam (red line).....163

Figure 5-15: Discrepancy map derived from surface matching. 166

Figure 5-16: Resultant meshed models after surface matching (green mesh: laser scanned model; red mesh: transformed mathematical model). 167

Figure 5-17: Differences in profiles between the two surface models (top: profiles along the Y-axis; bottom: profiles along the X-axis).....168

Figure 5-18: Four common control points in the mathematical model and laser scanned model. 169

Figure 5-19: Control point (outlined by the circle) in laser scanned model (left),

modelled beams (centre), and mathematical model (right). 169

Figure 5-20: Discrepancy map derived from 3D conformal transformation.....171

Figure 5-21: Differences in profiles between the two surface models. Top: profile along the Y-axis; bottom: profile along the X-axis (the green profile line was derived from the laser scanned model, and the magenta line represented the profile of the transformed mathematical model). 172

Figure 5-22: Differences in profile between the surface matched and 3D conformal transformed models (red: transformed mathematical model from surface matching; magenta: transformed math model from conformal transformation). 174

Figure 5-23: Differences in profile along the Y-axis between the transformed mathematical model (magenta curve) and the laser scanned model (green curve). 175

Figure 5-24: Differences in profile along the X-axis between the transformed mathematical model (magenta curve) and the laser scanned model (green curve). 176

Figure 5-25: The reference steelwork (gray frame), arch steelwork and top ring extracted from the TLS model (top), transformed mathematical model (middle), and the resulting discrepancies between them (bottom).....177

Figure 5-26: Workflow of on-site image acquisition.....180

Figure 5-27: Laser scanned model (green points) and videogrammetric monitoring area (red points) on the observed membrane roof structure.....181

Figure 5-28: Stereopair of the complete control footprints (images being enhanced). .182

Figure 5-29: Stereopair of extracted control footprints. 183

Figure 5-30: Stereopair of original projected targets at epoch 1. 184

Figure 5-31: Stereopair of extracted projected targets at epoch 1. 185

Figure 5-32: Point (top) and meshed (bottom) model of the observed surface. 187

Figure 5-33: Resulting displacement for the observations on the fabric membrane. 188

Figure 6-1: Design plan of Dalton Park, the observed Tent Type 2 membrane structure is outlined by the dashed line. 193

Figure 6-2: The Type 2 membrane structure. 193

Figure 6-3: Mathematical model of the Type 2 membrane structure. 194

Figure 6-4: Point model of the Type 2 membrane structure. 194

Figure 6-5: Control points (CP1 – CP8) for model registration. 195

Figure 6-6: Scanner network and the resultant scanned model of the Type 2 membrane structure, the network includes four ground scanning stations (Ground 1 – 4) and two scan station on the platform (Tower 1 – 2). 195

Figure 6-7: Fabric membrane roof extracted from laser scanned model for surface comparison. 196

Figure 6-8: The modelled supporting steelwork and derived centre lines. 196

Figure 6-9: Four corresponding control points in the mathematical model and laser scanned model. 197

Figure 6-10: Discrepancy map derived from 3D conformal transformation. 198

Figure 6-11: Differences in profiles along the Y axis between the two surface models (the green profile line is derived from the laser scanned model, and the red line represents the profile of the transformed mathematical model). 199

Figure 6-12: Differences in profiles along the X axis between the two surface models (the green profile line is derived from the laser scanned model, and the red line represents the profile of the transformed mathematical model). 200

Figure 6-13: Hardware configuration for Type 2 membrane structure monitoring. 202

Figure 6-14: Laser scanned model and videogrammetric monitoring area (red points) of the Type 2 membrane structure. 202

Figure 6-15: Stereopair of extracted control footprints. 204

Figure 6-16: Stereopair of extracted projected-dots at epoch 1 205

Figure 6-17: Resulting displacement for the observations on the Type 2 membrane structure. 206

Figure 6-18: The displacement map of the observed surface. The base is the surface model of the 1st epoch, the vectors (which are three times magnified) represent the differences to the specific epoch. 208

Figure 6-19: Differences in profile (X=99.4 m) amongst the six temporal epochs.....209

Figure 6-20: Differences in profile (Y=107.1 m) amongst the six temporal epochs. ...210

Figure 6-21: Indication of profiles investigated over the observed surface. 211

Figure 6-22: Movements that occurred along the Y axis across the surface. 212

Figure 6-23: Movements that occurred along the X axis across the surface. 213

Figure 6-24: The sequential displacement map. The base is the surface model of the 1st epoch and the vectors (which are three times magnified) represent the differences to the specific epoch. 215

Figure 6-25: Movements that occurred along the Y axis across the surface. 217

Figure 6-26: Movements that occurred along the X axis across the surface. 218

Figure 6-27: The displacement maps of epoch of maximum mean of positive (top, epoch 1371) and negative (bottom, epoch 1085) displacements. 219

Figure 6-28: The displacement maps of epochs of maximum (top) and minimum (bottom) instantaneous movements. The base is the surface model of the epoch 983 and 3503 respectively, and the blue vectors (which are three times magnified) represent the displacements at epochs 984 and 3504...220

Figure 6-29: The 25 points observed across the surface. 221

Figure 6-30: The videogrammetric monitored area on the membrane roof; points measured with obvious displacements are marked by red points. 222

Figure 6-31: RMS error values vs. diverse number of adopted control points. 223

Figure 6-32: The superimposed map of displacements and discrepancy map. 224

Figure 6-33: Design plan of Dalton Park, the observed membrane structure of Tent Type 3 is outlined by the dashed line. 226

Figure 6-34: The Tent Type 3membrane structure. 226

Figure 6-35: Mathematical model of the Type 3 membrane structure. 227

Figure 6-36: Point model of the Type 3 membrane structure. 227

Figure 6-37: Scanner network and the resultant scanned model of the Type 3 membrane structure, the network includes three ground scanning stations (Ground

S1 – S3) and three scan stations on the platform (Tower 1 – 2).....228

Figure 6-38: Control points for the scanned model registration (CP1 – CP12).....228

Figure 6-39: Fabric membrane roof extracted from laser scanned model.....228

Figure 6-40: The modelled supporting steelwork and derived centre lines. 229

Figure 6-41: Five corresponding control points in the mathematical model and laser scanned model. 230

Figure 6-42: Discrepancy map derived from 3D conformal transformation.....231

Figure 6-43: Differences in profiles along Y axis between the two surface models (the green profile line is derived from the laser scanned model, and the red line represents the profile of the transformed mathematical model).....232

Figure 6-44: Differences in profiles along X axis between the two surface models (the green profile line is derived from the laser scanned model, and the red line represents the profile of the transformed mathematical model).....233

Figure 6-45: The reference steelwork (gray frame) and top ring extracted from the TLS model (green) and transformed mathematical model (red). 234

Figure 6-46: Laser scanned model and videogrammetric monitoring area (red points) of Type 3 membrane structure. 235

Figure 6-47: Stereo pair of extracted control footprints. 236

Figure 6-48: Stereo pair of extracted projected-dots of epoch 1. 237

Figure 6-49: Resulting displacement for the observations on the Type 3 membrane structure. 238

LIST OF TABLES

Table 2-1: Classification of laser scanners (after Frohlich and Mettenleiter, 2004; Schulz and Ingensand, 2004b).....30

Table 3-1: Specifications of HDS2500 and HDS3000 terrestrial laser scanners. 77

Table 3-2: Specifications of the DV camcorders employed. 83

Table 3-3: Example interior orientation parameters of the three DV camcorders (the coefficients are pre-defined in Section 2.4.2.3).....84

Table 3-4: Specifications of the Oscar camera (Allied Vision Technologies, 2005).....87

Table 3-5: Example interior orientation parameters determined in camera calibration. .88

Table 3-6: Check point quality from the two control methods.....99

Table 3-7: Check point quality from the two control methods – Oscar cameras. 100

Table 3-8: A comparison of the DV camcorder and the Oscar camera. 115

Table 4-1: Orientation results for the static surface monitoring test. 141

Table 4-2: Input parameters for MS^2 implementation.....143

Table 4-3: Input parameters for MS^2 implementation. 145

Table 4-4: Orientation results for the dynamic surface monitoring test. 146

Table 5-1: Diameter differences between the physical and the modelled beams. 164

Table 5-2: Parameters for transformation before running 3D Surf. 165

Table 5-3: Solved transformation parameters and surface comparison results. 165

Table 5-4: 3D coordinates of corresponding control points in mathematical and TLS model. 170

Table 5-5: Solved transformation parameters and surface comparison results. 171

Table 5-6: Input parameters for Camera Orientation Module. 182

Table 5-7: Orientation results for the static surface monitoring test. 183

Table 5-8: Input parameters for Target Extraction Module. 185

Table 5-9: Input parameters for Target Referencing and Tracking Modules.....186

Table 5-10: Results of the point measurement for the Type 1 membrane structure monitoring. 186

Table 5-11: Solved displacement for the membrane structure monitoring.....188

Table 6-1: 3D coordinates of corresponding control points in the mathematical and TLS model. 197

Table 6-2: Solved transformation parameters and surface comparison results. 197

Table 6-3: Measured (from the TLS model) and designed (from the transformed mathematical model) positions of the centres of the top ring steelworks at two Tent Type 2 canopies. 201

Table 6-4: Input parameters for MS^2 implementation. 203

Table 6-5: Orientation results for the Type 2 membrane structure monitoring. 204

Table 6-6: Results of the point measurement for the Type 2 membrane structure monitoring. 205

Table 6-7: Range of displacement that occurred along the Y axis. 212

Table 6-8: Range of displacement that occurred along the X axis. 213

Table 6-9: Range of displacements that occurred along the Y axis.....217

Table 6-10: Range of displacements that occurred along the X axis.....218

Table 6-11: Statistics of the Z-values of the 25 points occurring over 3600 epochs.....222

Table 6-12: 3D coordinates of corresponding control points in mathematical and TLS model. 230

Table 6-13: Solved transformation parameters and surface comparison results. 231

Table 6-14: Input parameters for MS^2 implementation. 235

Table 6-15: Orientation results for the Type 3 membrane structure monitoring. 236

Table 6-16: Results of the point measurement for the Type 3 membrane structure monitoring. 237

Table 6-17: Solved displacement for the Type 3 membrane structure monitoring.....238

Table 7-1: Comparison of camera buses (summarised from National Instruments (2007)). 247

LIST OF ABBREVIATIONS

2D	Two-dimensional
3D	Three-dimensional
AC	Alternating Current
A/D	Analogue / Digital
ASCII	American Standard Code for Information Interchange
ASD	Analytical Spectral Devices
AVI	Audio Video Interleave
CAD	Computer Aided Design
CCD	Charge Coupled Device
cm	Centimetre
CMOS	Complementary Metal-Oxide-Semiconductor
CUBA	City University Bundle Adjustment
DDE	Dynamic Data Exchange
DEM	Digital Elevation Model
DLT	Direct Linear Transformation
DN	Digital Number
DV	Digital Video
EDM	Electromagnetic Distance Measurement
EO	Exterior Orientation
FOV	Field of View
fps	Frame per Second
g	Gram
GigE	Gigabit Ethernet
GPS	Global Positioning System

GUI	Graphical User Interface
Hz	Hertz
IEEE	Institute of Electrical and Electronics Engineers
IO	Interior Orientation
LCD	Liquid Crystal Display
LED	Light Emitting Diode
LP	Long Play
m	Metre
max	maximum
MB	Megabyte
mm	Millimetre (10^{-3} m)
µm	Micrometre (10^{-6} m)
MPEG	Moving Picture Experts Group
MS^2	Membrane Structure Monitoring System
nm	Nanometre (10^{-9} m)
NSSS	National Structural Steelwork Specification
NTSC	National Television Standards Committee
PMV	PhotoModeler Video
ppm	Parts per Million
PTFE	Polytetrafluoroethylene
PVC	Polyvinyl Chloride
RMS	Root Mean Square
RTC	Robotic Total Station
Sec	Second
Std. dev.	Standard Deviation

SP	Standard Play
TIN	Triangular Irregular Networks
TLS	Terrestrial Laser Scanning
ω	Omega rotation
ϕ	Phi rotation
κ	Kappa rotation

CHAPTER ONE

INTRODUCTION

1.1 Overview

Membrane structures are covers or enclosures in which a fabric surface is pre-shaped and pre-tensioned to provide a shape that is stable under environmental loads (Huntington, 2004). It is most often adopted by structural engineers as the solution to the roof of a building. Due to the advantages of rapid construction speeds with extremely competitive unit costs, as well as the fact that membrane structures provide good durability with low maintenance, the number of such structures has increased significantly worldwide over the last decade and a half (Gosling, 2001). Different from conventional structural forms, membrane structures allow sufficient deflections to occur under imposed loads (e.g. self-weight, wind, snow, etc.) (Lewis, 2003). When external loads are applied, the structure resists them by a combination of curvature and tension of the highly flexible fabric membrane. It is therefore important, at the design stage, to calculate the strength and displacement which the fabric membrane requires in order to withstand the forces which are likely to be subsequently applied. Once the structure is built, collapse may occur if the real curvature and tension exceed the tolerances of the original design. In order to avoid such failures in future, further research into understanding the behaviour of existing membrane structures is necessary. To this end, this thesis reports on the development of a generic monitoring system that is capable of inspecting all manner of membrane structures. By using the system, measurement and monitoring has been carried out on three types of finished "as-built" membrane structures. In each case study, two schemes were undertaken to investigate the behaviour of the membrane structure.

Firstly, the disparity between the designed mathematical model and the finished as-built membrane structure were determined. To achieve this, the technique of terrestrial laser scanning (TLS) was applied to generate a model of the membrane structure under a reference coordinate system. The mathematical model was then transformed into the same reference frame. The parts of the models that represented the membrane roof were extracted and compared statistically. As a result, the magnitude and distribution of the disparities across the roof surface were realised, and any differences that existed could be measured.

Secondly, the issue of displacement occurring in the membrane roof has also been addressed. A videogrammetric monitoring system employing stereo machine vision type CCD video cameras was used to observe the membrane roof. To accommodate constraints in the working environment (such as a uniform surface texture and unreachable height), a non-contact control and structured light targeting method were adopted in the monitoring scheme. Once the image processing and measurement are complete, the displacements occurring over time were determined.

The development of an in-house software suite, the Membrane Structure Monitoring System (MS^2), is one of the highlights of this thesis. For computing the disparities between the mathematical and TLS models of the membrane structures and also estimating the displacements of the membrane roof, the "Static Surface Comparison" and "Dynamic Surface Modelling" panels in MS^2 were utilised respectively. The capability of the system has been proved to produce high quality measurements in laboratory testing and was subsequently employed in the real world monitoring scheme.

1.2 Membrane Structures

1.2.1 Definition and Classification

The term tensile structure covers a broad category of structures, which includes membrane structures, prestressed cable net structures and pneumatic structures (Lewis, 2003). For detailed classification, Scheuermann and Boxer (1996) outline the family of the tensile structures (Figure 1-1). Lewis (2003) notes that tensile structures are currently being used either as roofing forms, bridge structures, or as permanent features of modern architecture, showing their potential for exploitation as efficient structures and aesthetically pleasing art forms.

In the category of membrane structures, the essential elements include (Lewis, 2003):

(i) a flexible fabric held under tension in order to generate stiffness in the surface;

(ii) one-dimensional flexible elements, such as ties or cables, to create ridges, valleys and edge boundaries;

(iii) rigid support members sustaining compression and bending.

The fabric membrane (materials most commonly used are polyvinyl chloride-coated (PVC) polyester, polytetrafluoroethylene-coated (PTFE) glass fibre and silicone-coated glass (Happold et al., 1987)) needs to be supported and tensioned along its boundaries. In addition, the supporting system has to be strong enough to collect all the reaction forces of the tensioned membrane and further counterbalance the membranes surface tensions safely for all deformed membrane states (Bradatsch et al., 2004). The basic roof type, with a central mast and a conical membrane surrounding (Otto, 1969), as well as various other types of membrane structure can be found in Figure 1-2 and Figure 1-3 respectively.

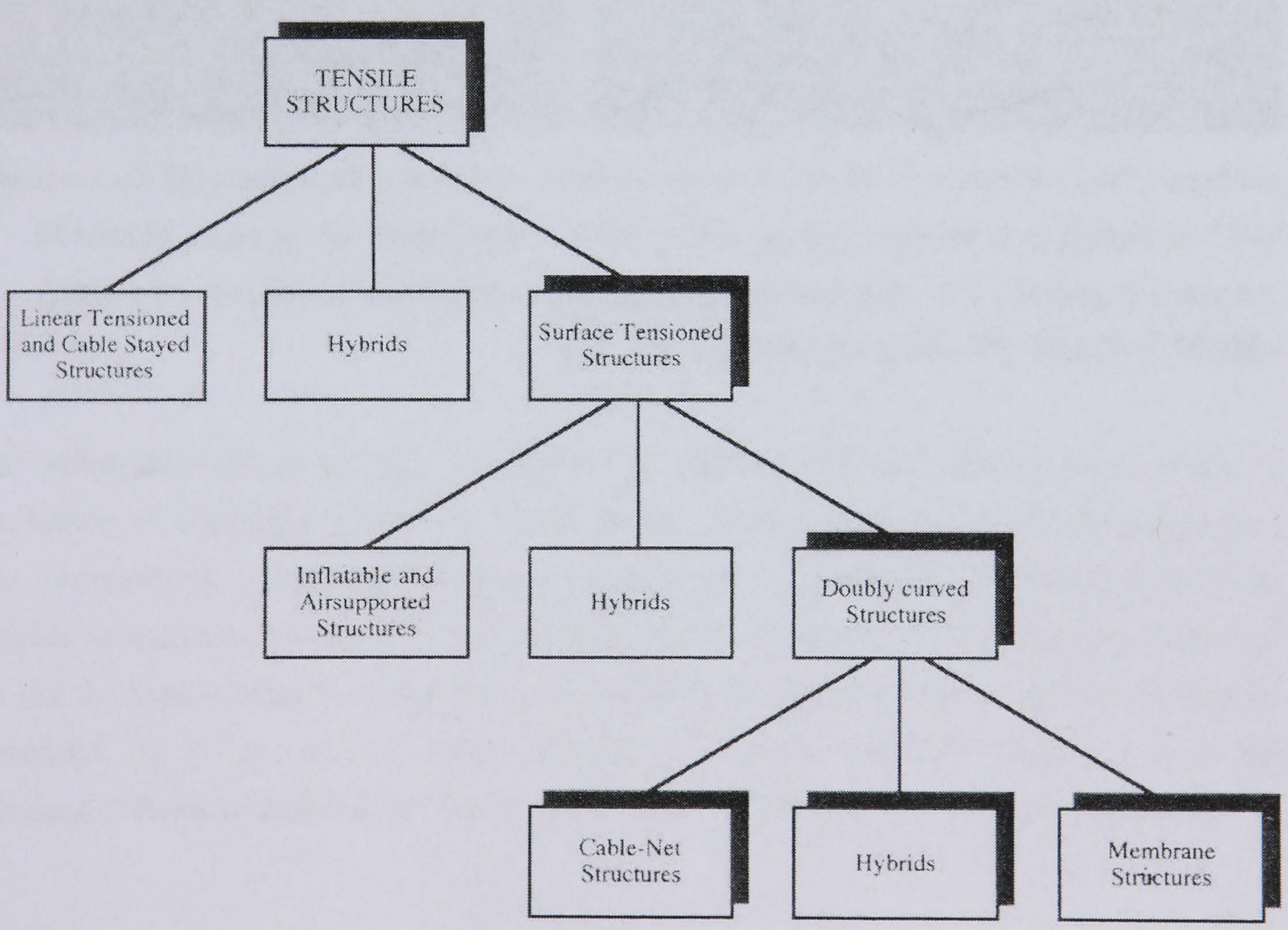


Figure 1-1: The family of tensile structures (Scheuermann and Boxer, 1996).

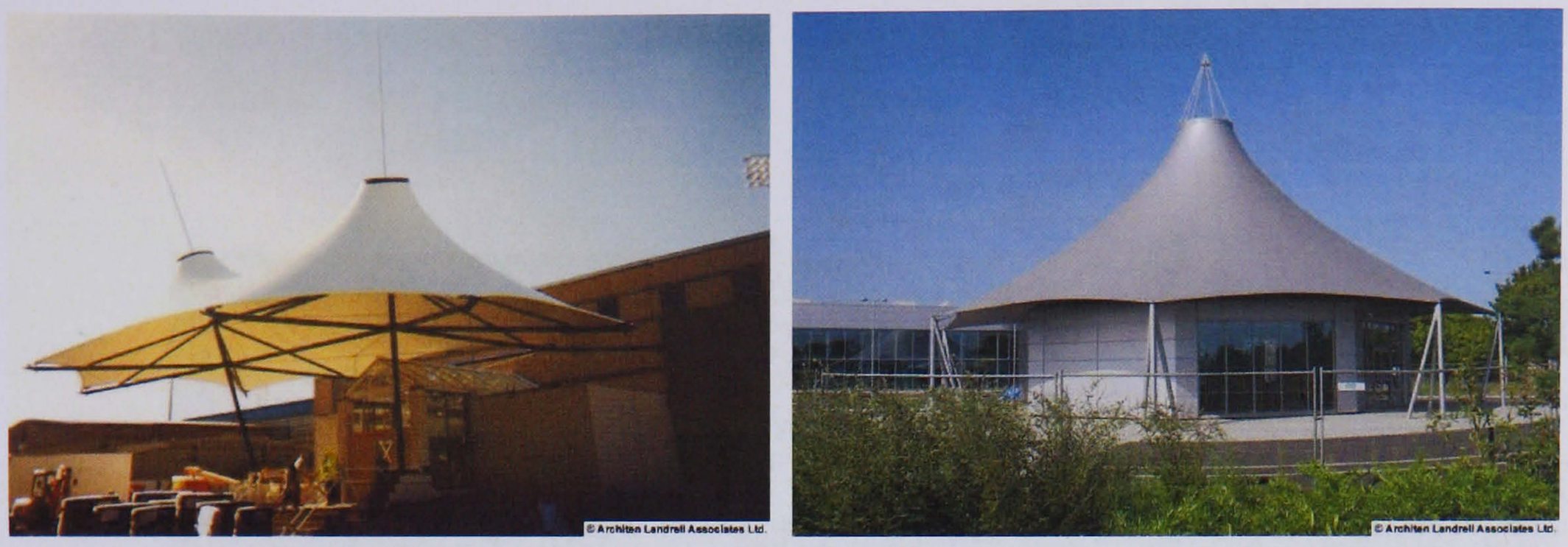


Figure 1-2: Examples of the basic type of membrane structure. Left: Priestfield football stadium in Kent, U.K., completed in 2001; right: Ford showroom in Stevenage, U.K., completed in 2004 (photo by Architen Landrell).



Figure 1-3: Examples of boundary tensioned membrane structures. Left: a series of tensile canopy for Stratford bus interchange in London, completed in 1994 (photo by Architen Landrell); right: the Starwave tent in Cologne, Germany, rebuilt in 2000 (photo by SL-Rasch GMBH).

Cable structures (such as the examples in Figure 1-4) are constructed using a combination of elements (i) and (ii) listed above. As similar components are employed in the construction, strong similarities of behaviour are identified between membrane and cable structures (Lewis, 2003). Therefore for the purpose of analysis, a prestressed cable net is often treated as a discrete type membrane. Alternatively, a membrane can be represented by a system of cable elements. Munich Olympic Stadium and the Millennium Dome in London are two representative examples of such structures.



Figure 1-4: Examples of prestressed cable net structures. Left: Munich Olympic Stadium (photo by Aviewoncities); right: "Le Nuage" at La Défense near Paris, where a cable net structure is externally suspended from the "Grand Arche" by steel cables (photo by Arup).

Pneumatic structures (Figure 1-5), or air supported structures, are tensioned membranes stabilised wholly or mainly by pressure differences across their surface (Otto, 1967; Forster, 1994). The pressure difference is generated by fans that supply air into an airtight membrane cover. There is no need for rigid supporting elements like columns, walls, arches, etc, and this characteristic makes air supported structures the most minimal and lightest of man-made constructions (Bradatsch et al., 2004). However, this same feature means that the shape of the membrane is strongly affected by the difference between the internal and external pressures, which changes continually as a result of temperature variations, wind and snow loading conditions (Lewis, 2003).

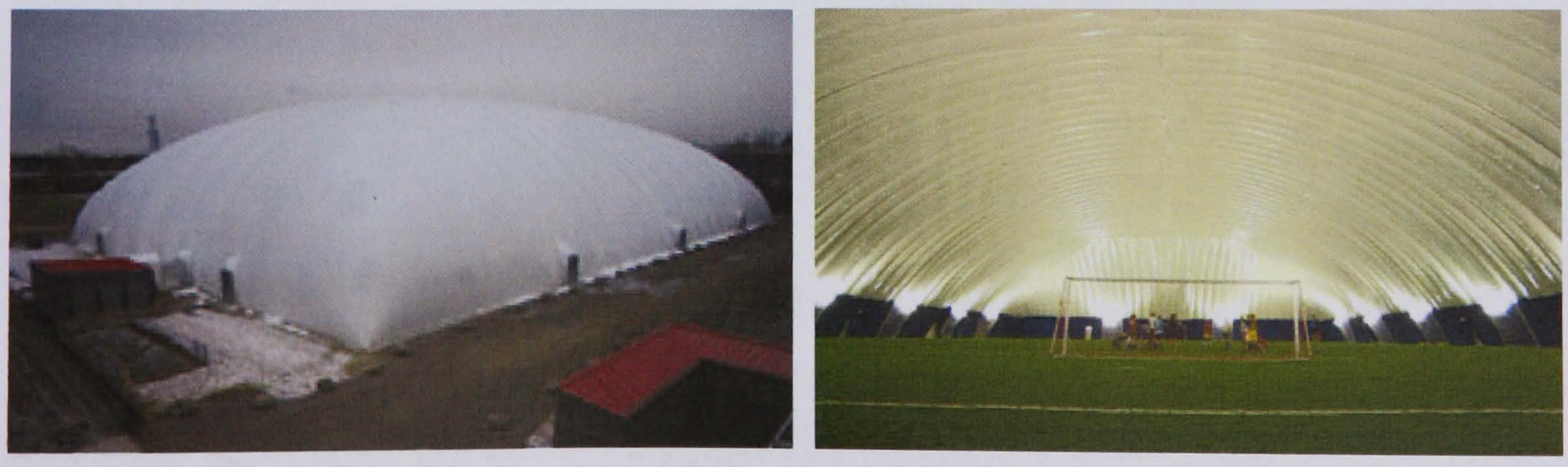


Figure 1-5: Example of pneumatic structure: exterior and interior views of Total Soccer stadium in Wixom, Michigan, U.S.A. (photo by The Farley Group).

Nowadays tensile structures are already in use in different styles for a wide range of buildings serving a variety of purposes. A schematic classification is illustrated by Bradatsch et al. (2004) to demonstrate the applicable styles (Figure 1-6), in which the columns from left to right show "open constructions", "enclosed" and "convertible" envelopes. Different uses of the fabric membranes including envelopes, internal applications or constructions attached to a building are presented in the three rows.

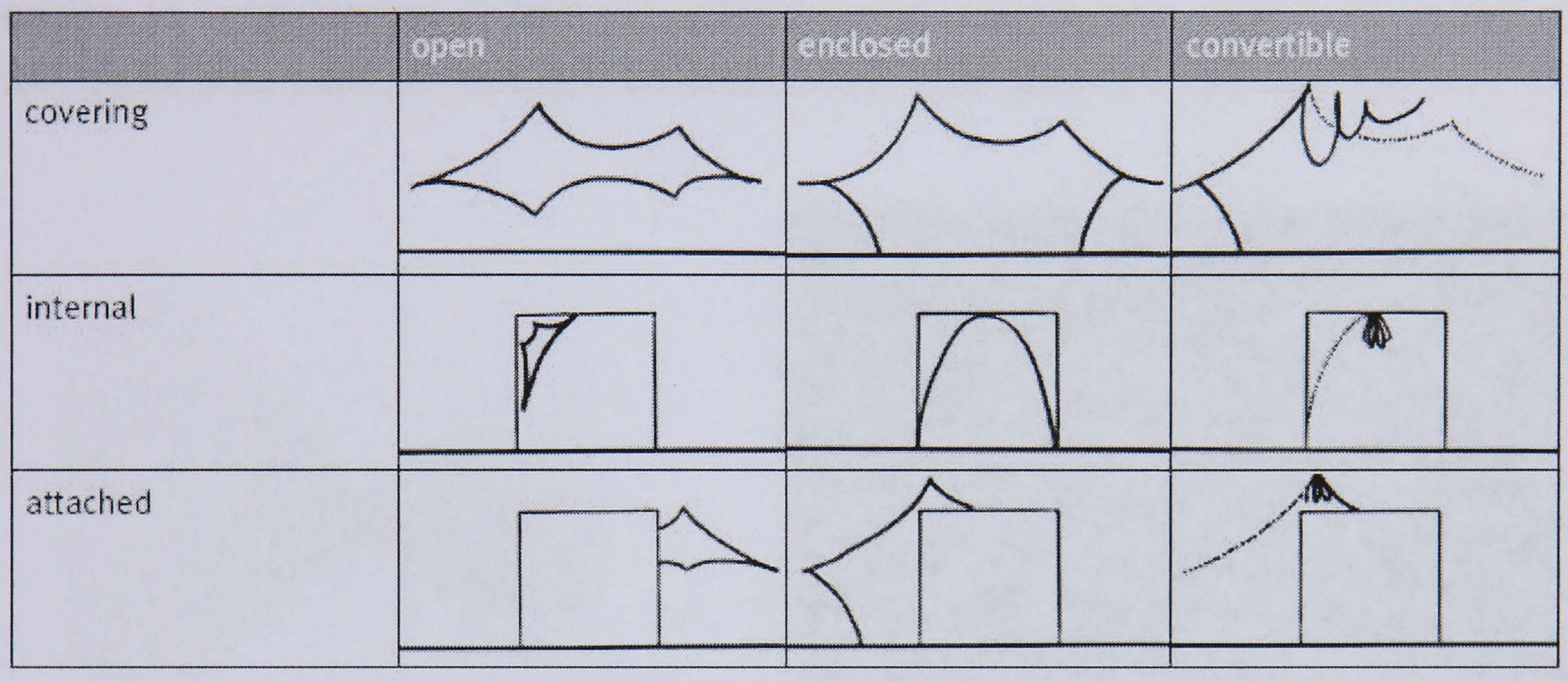


Figure 1-6: Classification of styles of tensile structures (Bradatsch et al., 2004).

1.2.2 Design Process

The special characteristics of tensile structures have made themselves not applicable to the design and analysis of typical structures. For example, their stiffness is achieved by virtue of initial prestress in the membranes and their supporting components, and this prestress, which is an internal stress condition, is usually prescribed by the designer to realise the desired performance of the structure (Campbell, 1991). In general, the design of boundary tensioned membrane structures and prestressed cable net structures follows a three-stage procedure (Lewis, 2003):

(i) form-finding;

(ii) patterning;

(iii) static and dynamic analysis.

At the stage of form-finding, the goal is to define the basic static shape of the tension structures, addressing the surface geometry of the tension membrane spanning a given boundary configuration (Lewis, 2003). To this end, physical models can be used to determine a wide variety of complex forms, however, the prestress and surface geometry information required for fabricating and stressing the membrane shape can not

be described and measured accurately through these models. For more robust form-finding process, iterative computations are carried out until the equilibrium surface geometry is resolved (Campbell, 1991). Currently a number of form-finding algorithms are in use. The most common methods are the transient stiffness method, the force density method and the dynamic relaxation method. The details are provided in Lewis (2003). Once the form is determined, the mathematical model of the tension structure is generated (Figure 1-7). One of the main advantages of using such a computational approach to form-finding is that the subsequent prediction and analysis of member forces under both prestress and applied load is facilitated (Barnes et al., 2004b).

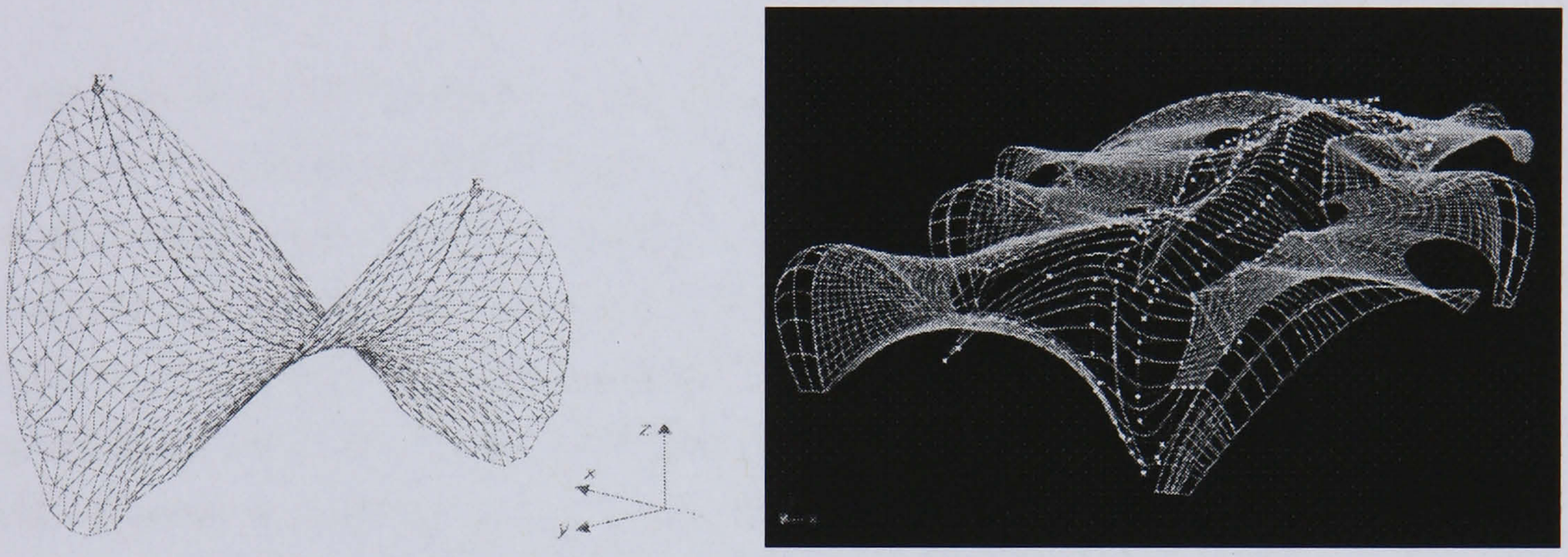


Figure 1-7: Mathematical model of a saddle structure (left) and the membrane roof surface at Chavasse Park, Liverpool, U.K. (right).

The patterning stage allows a 3D shape of a tensioned surface to be translated and relaxed into a 2D cutting pattern, enabling the manufacture of the membrane (Lewis, 2003). To provide useful information, the physical models may be employed, but owing to the limitations indicated above, their exploitation is insufficient. Due to the ability to generate shapes within a prescribed boundary with a prescribed prestress, automated computation on computers is carried out to determine the shapes of cutting patterns, improving the performance of patterning (Campbell, 1991). Normally the membranes lead to characteristic cutting patterns layouts, such as a radial layout for conical shapes and a parallel one for saddle shapes. The cutting patterns are made out of strips of fabric of 2 – 3 metres wide, with minimum waste of material and distortions of the fabric (Figure 1-8) (Lewis, 2003; Bradatsch et al., 2004).

Although the tasks of form-finding and patterning can be accomplished by automated computations, Lewis (2003) suggests that the physical models are still advantageous for visualisation purposes, therefore an analysis through computation and physical modelling used interactively is the most effective approach to both procedures.

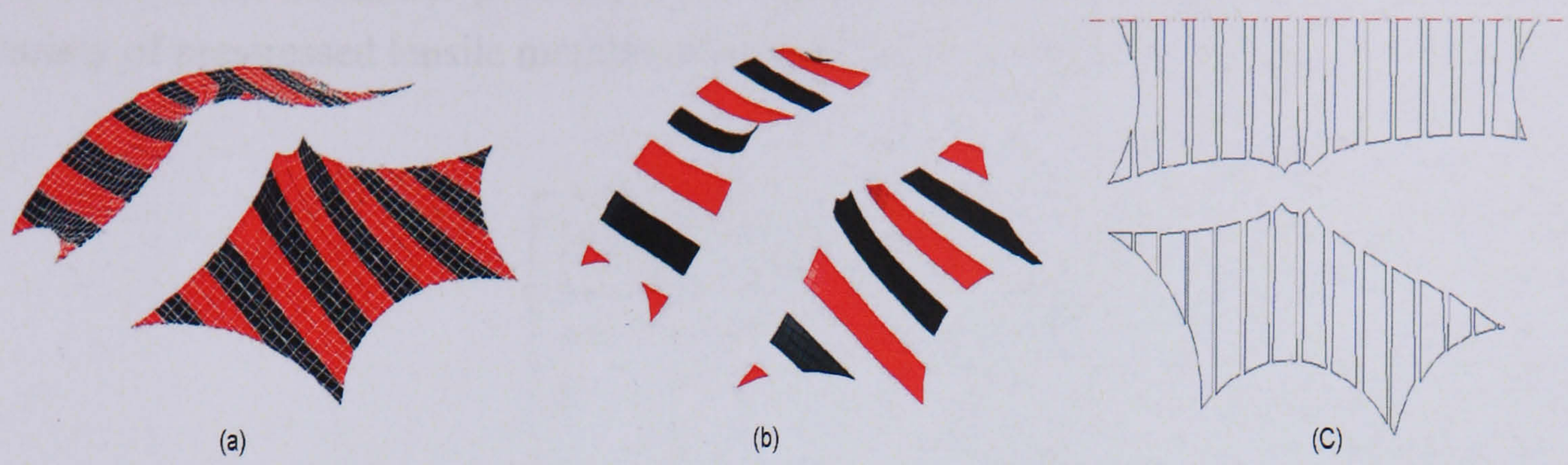


Figure 1-8: Digital cutting patterns layout (a), stripes (b) and cutting patterns (c) (after Bradatsch et al., 2004).

Static analysis is a continuation of the form-finding process, in which stresses and deformations are calculated under imposed external loads. The process begins with the form-found shape of the structure, whose surface stress distribution is known and in initial equilibrium. Static loads are subsequently applied on the surface, and a new state of equilibrium is reached. The displacements of the structure and stresses resulting from the applied loads are finally determined through an iterative computation (Lewis, 2003). Dynamic analysis is typically based on the data derived from wind tunnel experiments involving small-scaled physical models. The local pressure coefficients can be determined from such tests and the reliability of the design loading is improved in the end (Balz and Dencher, 2004). In Figure 1-9, an example implementation of the wind tunnel test is shown and one of the results is illustrated as well.

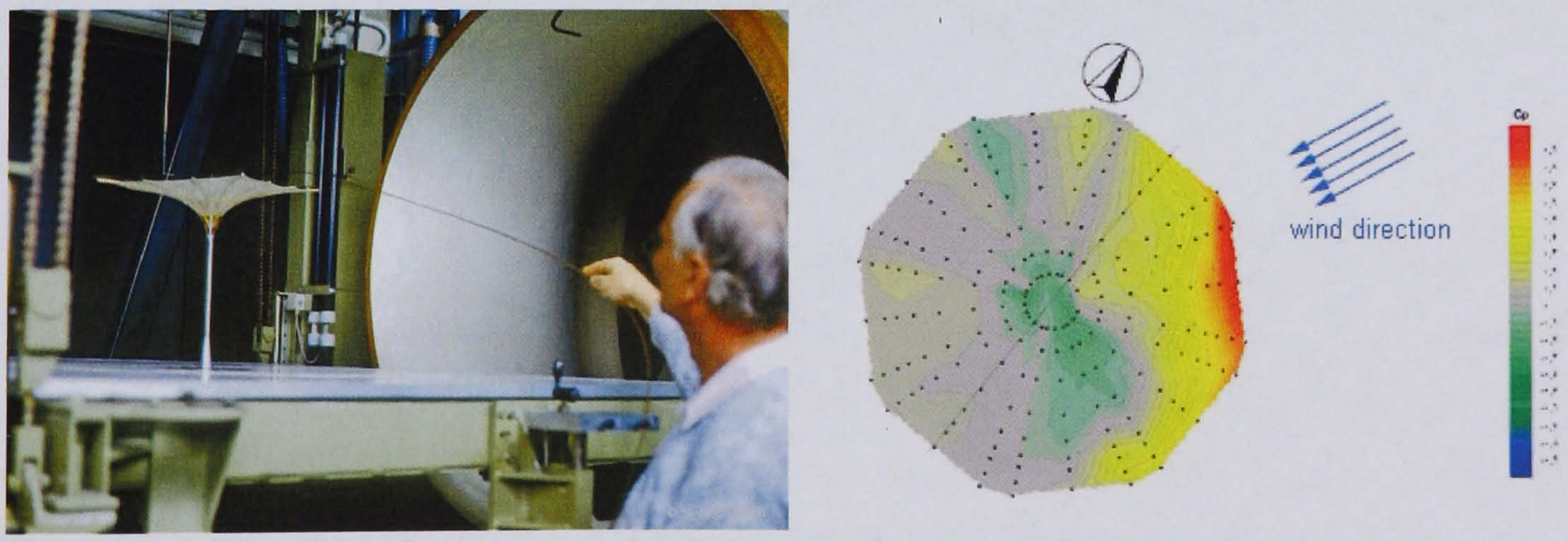


Figure 1-9: Left: small-scale model for wind tunnel test; right: graphical display of wind pressure distribution (photo by SL-Rasch GMBH).

In addition to the processes above, a more detailed method performed in the design and construction of a tensile membrane structure is illustrated in Figure 1-10, in which the automated processes are highlighted. As a number of successful algorithms are available

for each of the computer processes, the approach illustrated is appropriate for a wide variety of prestressed tensile membrane structures (Campbell, 1991).

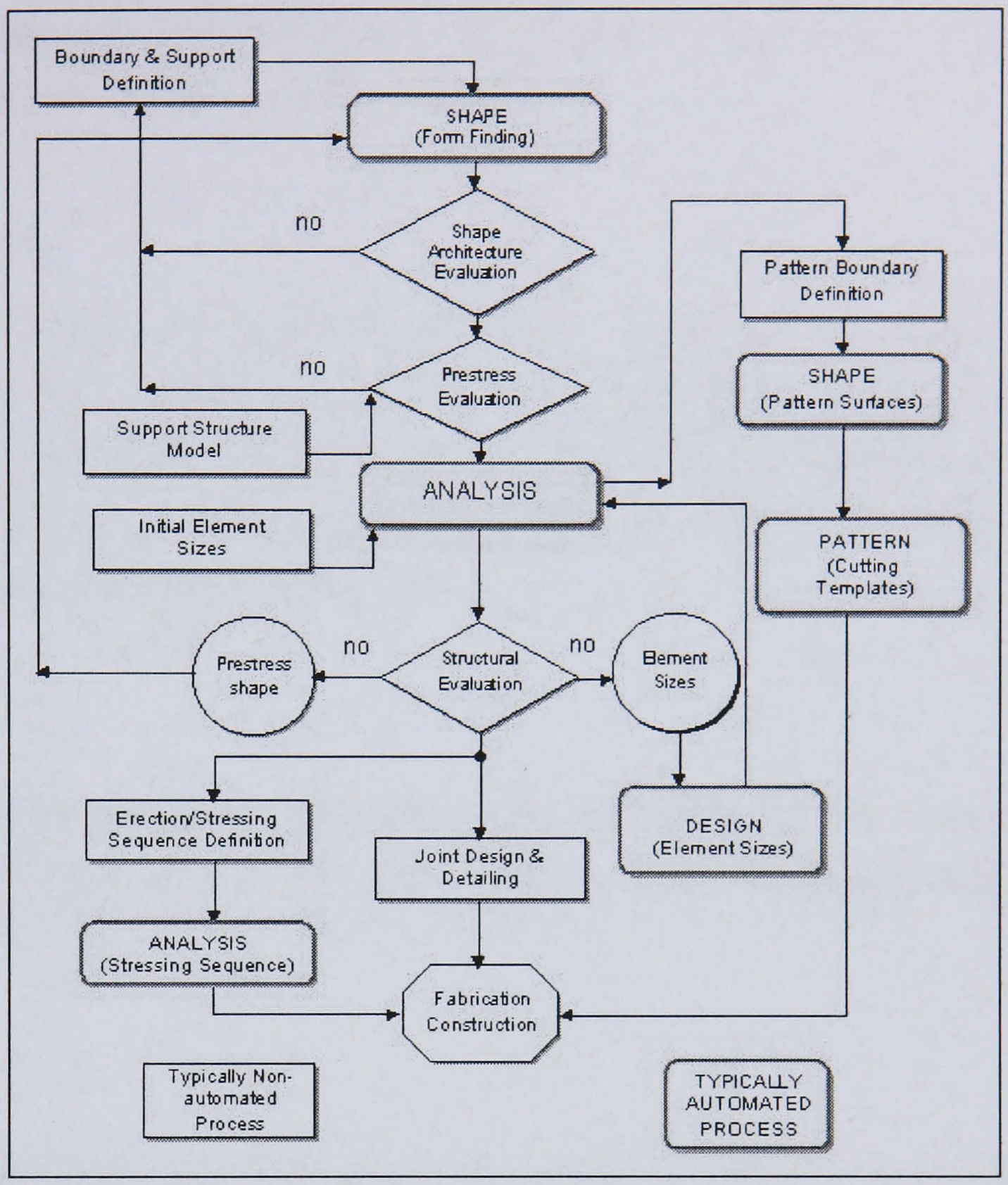


Figure 1-10: Flowchart of the general approach to tensile membrane structure design and construction (after Campbell, 1991).

1.2.3 Design Principles

The strength of a membrane material and its seams or joints relies on factors such as age, handling degradation, creasing, fatigue, creep, temperature and other environmental conditions, as well as unevenness of the material made during manufacture. Most of these factors are affected by the type of material used, the method of jointing, the scale of the structure, and the intended service life of the structural fabric (Barnes et al., 2004a). In order to construct a safe and proper functioning tensile structure considering these elements, a number of guides and requirements have been developed and should be taken into account at the design stage. Although there are currently still no standard British or European codes for the design of membrane structures, the main requirements for an appropriate design are collated from good practice and recommendations, they are summarised below (Balz and Dencher, 2004; Haase et al., 2006):

- Strength and stability

When external loads are imposed on the membrane structure, they are transferred from the membrane, through the connections into the primary structure and finally into the foundations. To assure the strength and stability of the structure, the design of the connection parts should be provided in the mathematical model.

- Flexibility for displacements

Compared to conventional buildings, the displacements of the membrane structure are relatively large. The range of the displacements under loading should be investigated with the mathematical model. Moreover, it is important that the resulting displacements of a load combination are found by adding loads and then analysing, rather than analysing each load separately and then adding the results.

- Adjustability

It is advised that re-tension of the membrane should be performed during the lifetime of the structure. The facilities employed and the final situation after installation and tensioning should be provided.

- Redundancy

Redundancy indicates the redundant structural components added deliberately to avoid chain collapse. As the membrane functions as a structural element transferring loads to the supporting structure, this will be the first part to fail when collapses occur. In this occasion if secondary structures (e.g. cable-net and catch cables) are attached to the membrane roof, total collapse of the structure will be avoided.

- Effect of scale

Because the forces in a membrane structure do not grow linearly as the span of the structures increases, it is therefore dangerous to scale the structural systems. That is a design suitable for small structures will not automatically work properly for large scale structures. An appropriate design should be provided for a specific structure.

1.2.4 Installation

Prior to installation of the membrane structure, the strips cut at the patterning stage are welded together in a controlled environment to produce the complete canopy ready for

delivery to site for installation. Furthermore, prestress contributes significantly to the stiffness of a membrane. The level of prestress in a membrane surface will affect all the elements within the supporting structure (masts, frames, cables etc.). The prestress level is chosen as a result of the "form finding" process, and has to be achieved and sustained during the erection and life of the structure (Balz and Dencher, 2004). During installation, Bridgens et al. (2004) point out that the rate of application of the prestress load is very important, however this is usually only informed by experience and the "observational method", whereby the extension of the fabric is observed during installation, with tensioning applied as and when required. Bridgens et al. (2004) also indicate that the time required for installation varies substantially depending on environmental factors such as the temperature and wind loading during installation, the type of fabric material, the shape of the structure and the method of installation. For example, PTFE glass fibre fabric becomes very stiff at temperature below 5°C, and can fail during installation unless the load is applied very slowly, over a period of weeks rather than days. Some example situations during installation are shown in Figure 1-11.

In addition to the above indications, Gipperich et al. (2004) address some other noteworthy points during installation. For example, appropriate and continuous checks have to be made to ensure that the target dimensions are being approached, and proper connection to the anchor points occurs. Technical design specifications such as the tightening of bolts to a defined torque, securing of nuts and bolts, sealing of joints, alignment of cable heads are to be strictly adhered to and are to be checked. Moreover, as the fabric membrane is not under tension during installation, it is usually in an unstable state and is subject to external influences such as wind and rain. Therefore to avoid the damage or rupture to the material, the membrane should be kept free from any debris at all times (Essrich, 2005).

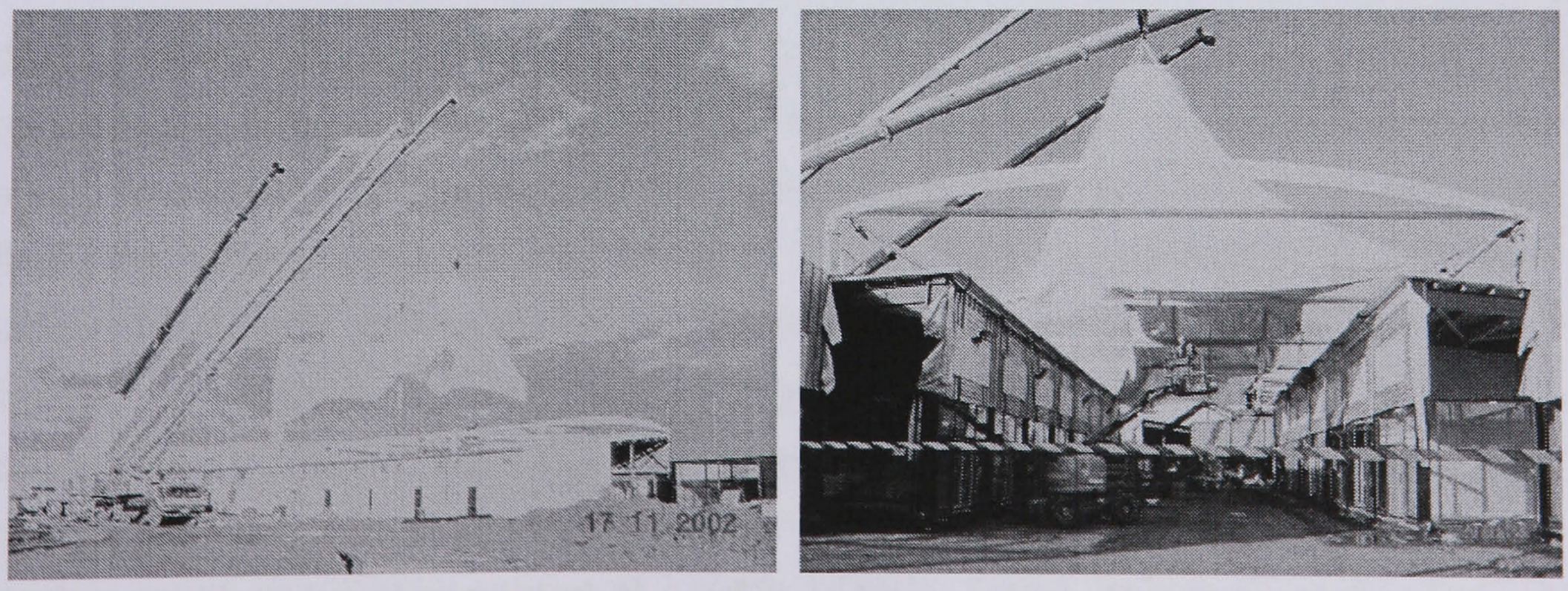


Figure 1-11: Situations during installation (Bridgens et al., 2004).

1.2.5 Potential Issues

As the membrane structure resists external loads by a combination of curvature and tension of the flexible fabric membrane, it is important at the design stage to calculate the strength and displacement which the fabric membrane requires in order to withstand the forces which are likely to be applied (Section 1.2.2). Once the structure is built, collapse may occur if the real curvature and tension exceeds the tolerances of the original design. In January 1999, for example, the new membrane roof over Montreal's Olympic Stadium failed (Figure 1-12). The cause of failure was identified as a design fault, not an accident (Parker, 1999a; 1999b). Another recent example of a failure occurred at the Waldstadiom in Frankfurt, during the final of the Confederation Cup in June 2005 (Figure 1-13). To avoid such failures in future, further research into realising the surface geometry and dynamic behaviour of existing membrane structures is necessary, and is the motivation behind this research.

When considering the development of a membrane roof monitoring system there are two fundamental issues that structural engineers engaged in designing such structures require the scheme to address. The first issue relates to any differences that exist between the designed model and the finished structure. As Scheuermann and Boxer (1996) point out, once the arrangement of supports for a membrane structure has been established, any change of position, length or angle of the compression elements (e.g. masts) results in an immediate variation of volume, form and structural behaviour. That is unexpected structural response or even failure may occur if such change deviates largely from the original designed specifications. To solve this problem, the inspections will start with the disparities at the membrane roofs, and continue to the steelworks employed in the membrane structure if differences greater than the required tolerances are detected.

Although membrane structures allow sufficient displacements to occur under imposed applied loads, failures will still occur if the movements exceed the designed tolerance values. To avoid this, the other fundamental issue is the displacement that occurs on the membrane surface under loading (Essrich, 2005). With regard to the applied wind loading, wind tunnel testing is normally performed using a small-scale physical model. However, as the model is usually made of rigid material, it is incapable of giving a true representation of the pressures that may develop on the surface of a flexible membrane. To accommodate this, conservative values of "equivalent static loads" are used to simulate wind action (Happold et al., 1987; Liddell, 1994). This method can also be

adopted in the tests of snow loading (Dakov and Tanev, 2005). Although the approximation has proved to err on the safe side, Lewis (2003) still emphasizes that the need for further research into the interaction of surface geometry, applied loads and structural response is necessary. To this end, a monitoring system has been developed and used to observe membrane roofs and determine the dynamic behaviour. Moreover, the results of a load combination (e.g. snow downward plus wind uplift) can be identified by utilising the proposed monitoring system.

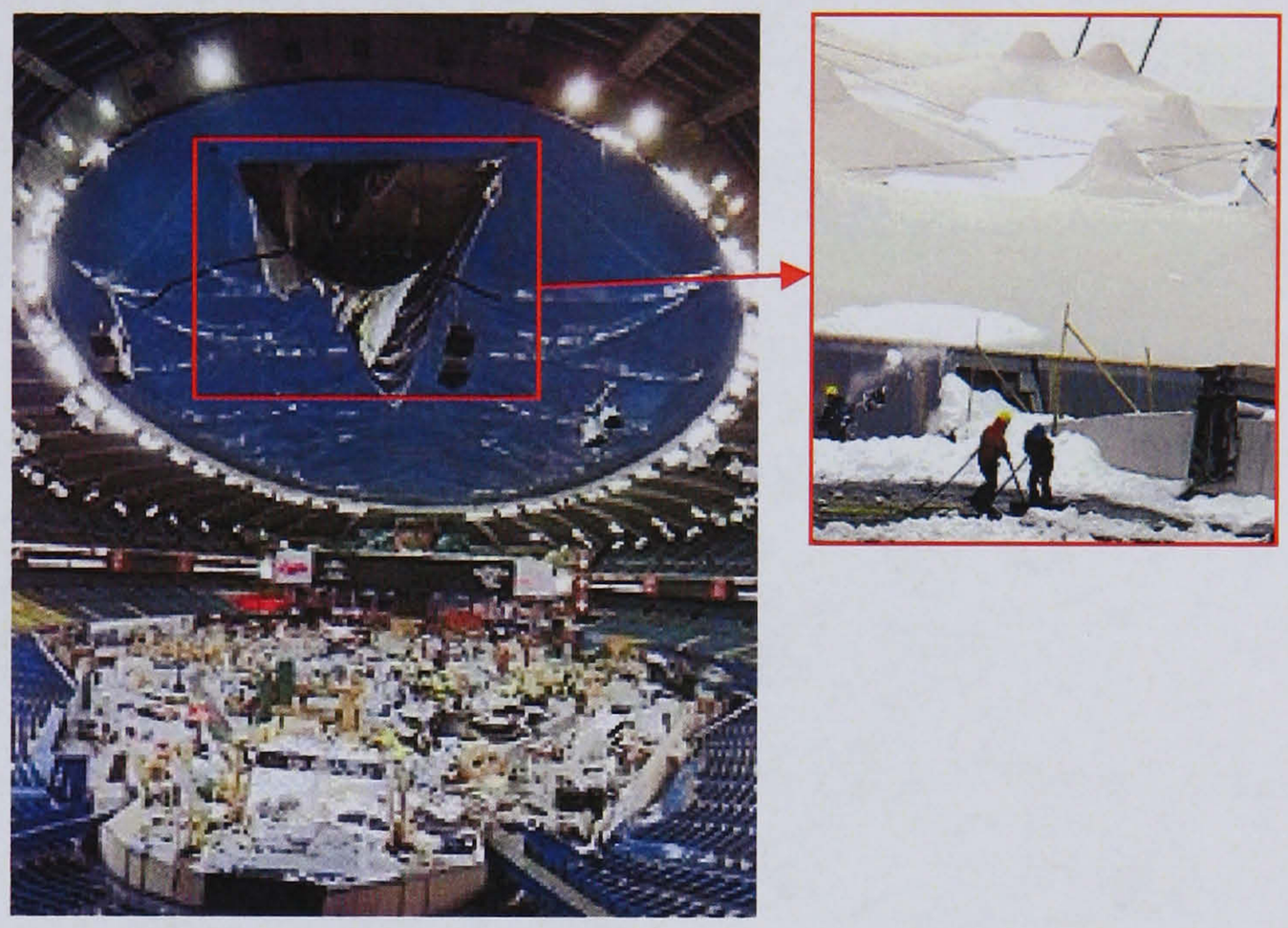


Figure 1-12: The failure of the membrane roof at Olympic Stadium in Montreal (Nightly.Net, 2006).



Figure 1-13: The failure of the membrane roof at Waldstadiom in Frankfurt (Associated Press, 2005).

1.2.6 Test Site

Dalton Park is a retail outlet centre in the north east of England. It features a variety of fabric membrane canopies, and is used in the research as the study area for membrane structure measurement and monitoring. Two lines of single shop units are arranged on either side of a central street. The street is partially covered by seven fabric canopies based on single and multiple conic forms (Figure 1-14). They are all categorised as boundary tensioned membrane structures and are designed to provide shelter from the wind and rain, and shade from the sun, whilst providing a light, airy outdoor environment (Bridgens et al., 2004). In the project, the membrane structures of Tent Type 1, 2 and 3 are measured and monitored. The detailed introduction of the membrane structures observed will be further described in Chapters Five and Six.

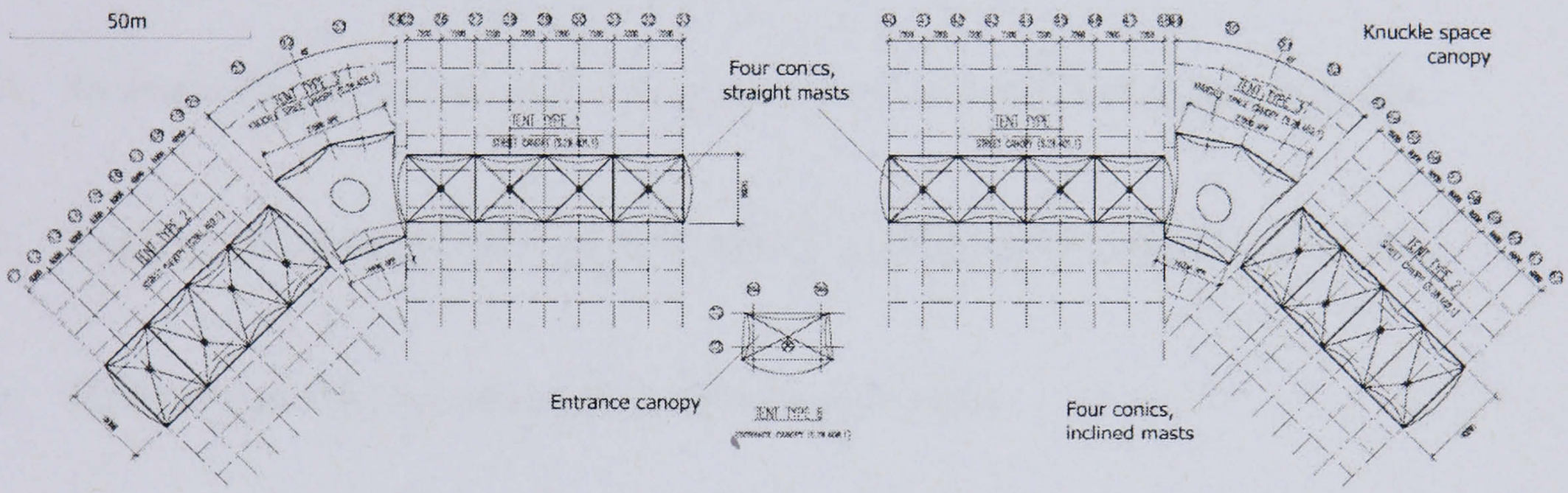


Figure 1-14: Dalton Park plan (Bridgens et al., 2004).

The steelwork at Dalton Park is constructed to comply with the National Structural Steelwork Specification (NSSS), in which the permitted deviation of the position of steelwork is 10 mm and tolerant deviation in length or width is 20 mm (when overall dimension is less than 30 metres) (The British Constructional Steelwork Association Limited, 2002). With regard to the displacements of the membrane roof, the fabric membrane itself deflects significantly under extreme external loading. According to the design specification, the predicted displacements in the middle of the panels are occasionally in excess of +/- 250 mm, however, this is due to 50 year wind or snow loading (i.e. the wind/snow loading which has an annual probability of being exceeded of 0.02) (Bridgens et al., 2004). Thereby in order to monitor the membrane structures at Dalton Park efficiently, the system developed should be capable of measuring the structures within these tolerances.

1.3 Aims and Objectives

To assist structural engineers to better understand membrane structure behaviour, this geomatics engineering research programme aims to utilise suitable geomatics tools to provide an optimum measurement and analysis solution for determining the disparities between the designed and finished structure and modelling the dynamic behaviour of the membrane surface. Specific research objectives to achieve the aims are:

- To identify potential geomatics tools for use in a membrane structure monitoring system.
- To propose a monitoring system and examine its feasibility.
- To assess the performance of the system on a real world membrane structure.
- To prove the transferability of the system by repeating on different structures.
- To investigate the behaviour of membrane structures.

1.4 Research Methodology

To achieve the aims and objectives set out in Section 1.3, the following methodology was carried out:

- Preliminary investigation began by conducting a literature review into the possible geomatics solutions and their relevant applications in structural measurement and monitoring. Simultaneously, the constraints of the working environment were considered, and proof-of-concept experiments were conducted to verify the modifications proposed and also enable familiarisation with equipment.
- An in-house software suite, the Membrane Structure Monitoring System (MS^2), was continuously developed during the period of research. The essential requirement for the development of the system was that it should be robust and user friendly. The system performance was proved by using two laboratory tests simulating the configuration that would be adopted in the field.

- The proposed methodology and MS^2 software have been thoroughly applied to three different types of as-built membrane structures. The results of the monitoring were examined and discussed with structural engineers. Further suggestions for possible occasions suitable for the implementation of this system were also provided. In this manner, the developed monitoring system has been proven as a metrology tool for structural engineering.

1.5 Thesis Structure

The thesis is composed of seven chapters, including this introduction, and a list of references. Chapters Two and Three are literature-based, proposing the potential solutions for the problems involved in monitoring membrane structures. The remainder of the thesis provides a description and analysis of the development of the monitoring system and practical work that has been undertaken.

- Chapter Two consists of a review of the potential geomatics solutions for structural measurement and monitoring. The background, principles and relevant applications of the techniques proposed are discussed and appraised. As a result, the most appropriate methods being applied in the membrane structure monitoring scheme are determined.

- Chapter Three proposes a generic monitoring system using terrestrial laser scanning and videogrammetry for observing the fabric roof of the membrane structures. The methodology for performing static surface comparison and dynamic surface modelling is introduced, and the feasibility of the proposed methods is further evaluated by conducting proof-of-concept experiments.

- Chapter Four focuses on the development of the in-house software package called Membrane Structure Monitoring System (MS^2). The tools and algorithms for static surface comparison and dynamic surface modelling are reported. By processing the data derived from two simulated experiments using MS^2, the performance of the system is also evaluated.

- Chapter Five presents the application of the developed methodology to a real world test site, at which a membrane structure of Tent Type 1 is measured. Conclusive on-site workflows of static surface comparison and dynamic surface modelling are

determined and the results of the monitoring are reported.

- Chapter Six proves the transferability of the monitoring system by observing the membrane structures of Tent Type 2 and Type 3. The differences between the designed model and the as-built structure, and the displacements of the fabric membrane roof are determined.
- Chapter Seven concludes the thesis, evaluating the success of the methodology with respect to the research objectives. Some suggestions for future work are provided at the end.

CHAPTER TWO

GEOMATICS TECHNIQUES FOR CLOSE RANGE MEASUREMENT AND MONITORING

2.1 Introduction

In order to investigate solutions for the issues involved in measuring the membrane structures, geomatics techniques currently used for measurement and monitoring were reviewed. The review included terrestrial surveying methods adopting total station instruments as well as terrestrial laser scanners, and image-based methods comprising photogrammetry and videogrammetry. Through the review of the techniques and discussion of the related applications, the most appropriate methods to be applied in the membrane structure monitoring scheme could be determined.

2.2 Terrestrial Surveying with Total Station Instruments

2.2.1 Background

The essential task of structural measurement and monitoring is to determine the 3D coordinates of points of interest. This is achieved by the measurement of angles and distances to the specific points (Bannister et al., 1998; Uren and Price, 2006) when using terrestrial surveying methods. In order to investigate the feasibility of automated measurement, total station instruments are selected from surveying instrumentation and are introduced in this section.

The total station first appeared in the late 1980s as a result of the development of

electronics and computerisation of surveying instrumentations (Kavanagh and Bird, 1992; Sakimura and Maruyama, 2007). With the rapid development of electronics and computer technology in the 1990s, the total station underwent a rapid refinement in its functionality, precision and lowering of the cost. Total stations are precision electronic instruments, which incorporate a theodolite with an Electromagnetic Distance Measurement (EDM) unit, an electronic angle measuring component, data storage and a computer or microprocessor (Wolf and Ghilani, 2002). With EDM equipment, either phase shift or time pulsed methods are used to measure distance. The phase shift (or phase comparison) method utilises continuous electromagnetic waves. Here the distance is measured as a phase difference with ambiguity resolution. The pulsed method uses the pulses of laser radiation to derive the distance from computing transit times. This technique is also known as the time-of-flight method. It is noticeable that the accuracy obtained with a phase shift method is typically higher than with time pulsed instruments, but the instruments using pulsed laser technology can measure longer distance than the ones using the phase shift method (Uren and Price, 2006).

A return or reflected signal is required for measuring distance when using both methods. This can be obtained using a special reflector (corner cube reflector / prism) or directly from an existing identifiable target. Currently, most total station instruments can switch between reflector and non-reflector (reflectorless) modes for distance measurement. Total stations equipped with reflectorless EDM can efficiently increase the speed in many construction and terrestrial surveying projects. This is particularly evident when measuring to targets (prisms) is inaccessible (Wolf and Ghilani, 2002). If automatic reflectorless measurement is possible with a total station, the total station can be treated as a point-sensor laser scanner to scan a selected surface of interest.

The function of automatic target tracking is another sophisticated feature offered in modern total station instruments. It was first realised in the late 1990s when Geodimeter introduced the "robotic total station (RTS)" (Savvaidis et al., 2005). RTSs are equipped with servo drive mechanisms that enable the instrument to aim automatically at a point. With a RTS instrument, it is only necessary to identify the points (prisms) at the beginning of the survey. The computer then retrieves or computes the directions to the predefined points and activates a servomotor to turn the telescope to those directions in order to make the measurements. The measurements can be repeated at any predefined interval (Wolf and Ghilani, 2002). The RTS therefore permits automated operation for many surveying projects. These characteristics make it possible to employ a RTS in automatic movement monitoring applications.

2.2.2 Coordinate Measurement with a Total Station

For the majority of surveying and engineering work, the 3D coordinates of points of interest are specified in a rectangular coordinate system (Wirth and Moritz, 1995; Uren and Price, 2006). In the applications where relative positions of points are desired, the polar method is used to involve the total station measurements in determining the points' 3D coordinates. In surveying the term polar is used to mean that a vector originates from the centre of a surveying instrument and ends at the defined centre of a target (Wunderlich, 2004). In the object space where a total station is applied, this is achieved by using the following procedure. Firstly, the total station is set on a control station with a backsight to another reference point. The horizontal angle can then be set to zero or any azimuth value. Once the total station has been oriented in this manner, the survey can commence by observing the horizontal angle, the vertical angle and the slope distance of any specific point. The elevation is determined later by considering the height of the instrument station and appropriate instrument and reflector heights (Kavanagh, 2003; Uren and Price, 2006). Figure 2-1 schematically shows the measuring principle of a total station.

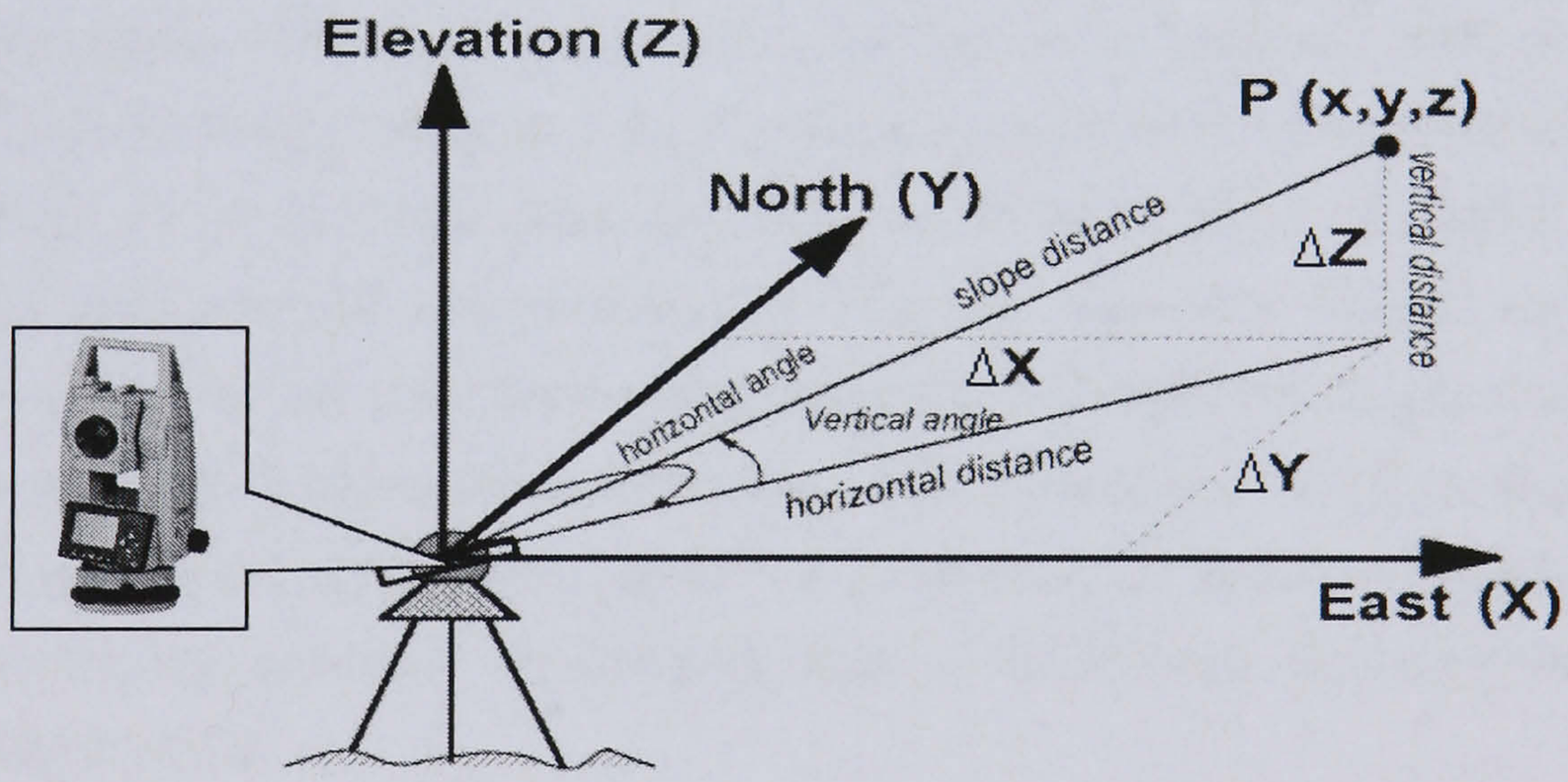


Figure 2-1: The 3D coordinates of a point determined by a total station within a local coordinate system (after Feng et al., 2003).

From the measurements of angles and distances, the 3D coordinates of the target point are calculated with Equation 2-1 by the on-board microprocessor (Feng et al., 2003).

$$\Delta X = S \times \cos(VA) \times \sin(HA)$$

$$\Delta Y = S \times \cos(VA) \times \cos(HA) \qquad \textbf{Equation 2-1}$$

$$\Delta Z = S \times \sin(VA)$$

In Equation 2-1, S is slope distance; VA is vertical angle and HA is horizontal angle. The results are stored in the data storage and can be transferred to a computer for various surveying applications.

2.2.3 Applications in Structural Measurement and Monitoring

The total station instrument is usually used for measuring the 3D coordinates of control points in space (Moffitt and Bossler, 1998). Moreover, it has also been broadly applied in various structural measurement and monitoring projects. Serviceability, or deflection, is very important in monitoring the health of a structural system. Merkle and Myers (2004) employed a robotic total station and Linear Variable Displacement Transducers (LVDTs) to perform a serviceability monitoring project. This monitoring was undertaken through a series of load tests for several retrofitted bridges. LVDTs are the traditional equipment used to measure deflection in many load tests. However, access to the field, long setup times and intensive manpower for both preparation and testing become an issue with this instrumentation system. Therefore a total station instrument was introduced to test the performance. As a result it was found that by using a total station, the testing took advantage of more efficient setup and operation, reducing labour and time requirements. The total station was set up at a location with an unobstructed view of the field targets (Figure 2-2). A reference point was set in place to transfer a horizontal angle or an elevation from the reference point to the total station, and then from the total station to the targets (prisms). The user manually located the targets at the start of testing, and the total station automatically relocated the target and measured deformation once the monitoring commenced. The results derived from the total station revealed that the total station was capable of measuring deflection accurate to 0.2 millimetres, having an accuracy challenging that of traditional deformation monitoring systems using LVDTs.

The deployment of total station instruments for bridge health monitoring can also be seen in Kuhlmann and Glaser (2002), Roberts et al. (2004), James (2005), Hernandez et al. (2006) and Palazzo et al. (2006). Through these experiments, the feasibility and accuracy of terrestrial survey methods using total stations is proven. However, it is also stated that rapid load testing is not practicable with the total station owing to the time required for measuring every point. This major drawback will continue to mean that terrestrial surveying equipment cannot be used to monitor serviceability during a dynamic load test.

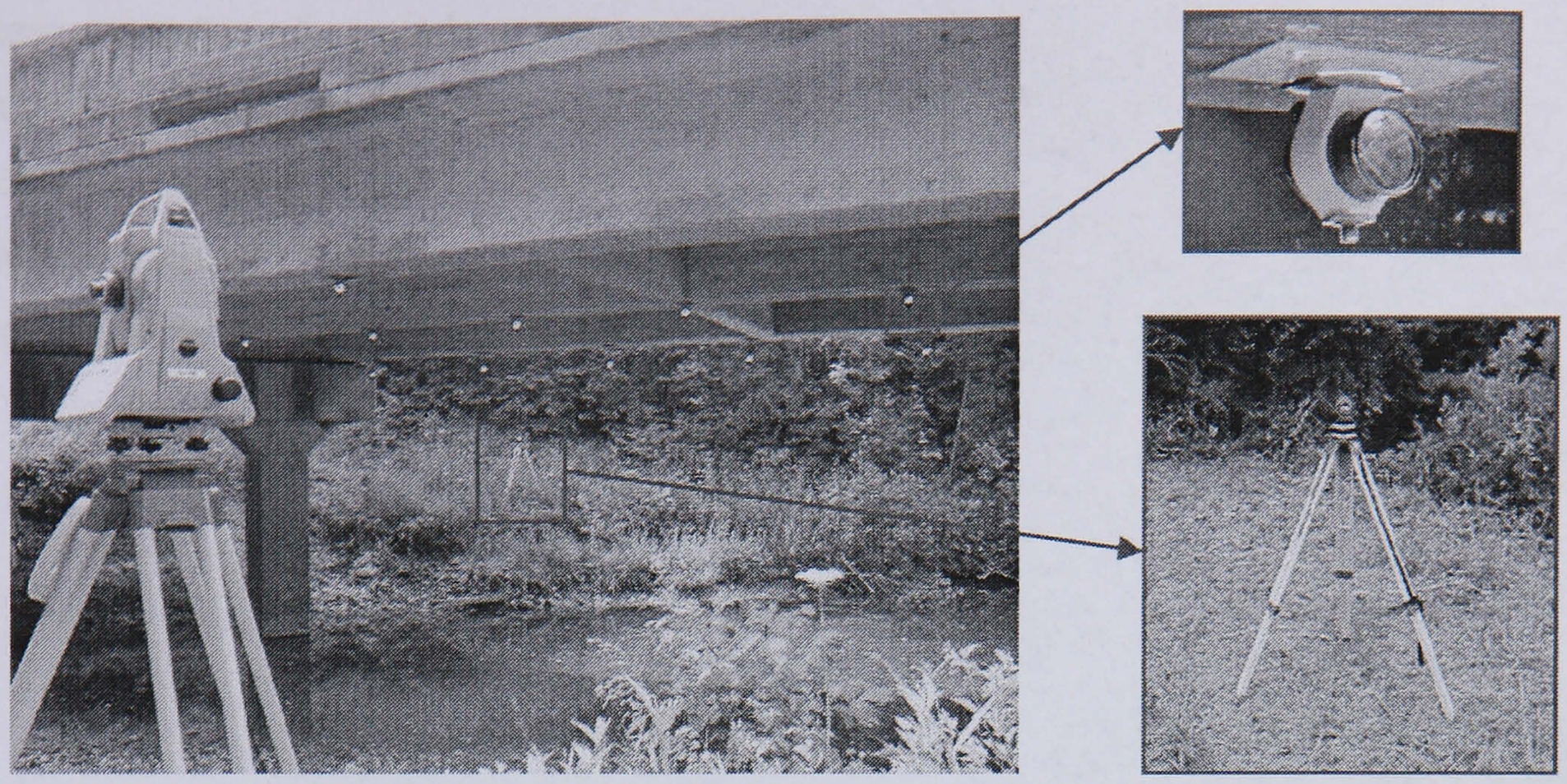


Figure 2-2: The Leica TCA 2003 (left), prism (top right) and reference point (bottom right) set up for load testing (after Merkle and Myers, 2004).

In other applications terrestrial survey methods have been used to acquire structural response data during earthquakes, and assist in analysing, designing, repairing and retrofitting earthquake resistant structural systems. Accelerometers are most commonly used to monitor structural systems during earthquakes, however they do not directly measure structural displacements. Therefore a robotic total station capable of providing direct displacement information in real-time was adopted by Tsakiri et al. (2003). Tsakiri et al. reported sets of experiments designed to examine the suitability of using a total station for monitoring the dynamic response of control points on the deck of the Evripos cable-stayed bridge in Greece. Results from a robotic total station were presented in conjunction with respective displacements derived from the permanent accelerometer network installed on the bridge. The total station measurements were found to offer additional information to accelerometer data for the structural analysis, and obtained more precise characteristics of the signal vibration. The use of terrestrial surveying techniques demonstrated the advantage of augmenting existing monitoring campaigns for relatively straightforward recovery of absolute displacements in a pre-orientated reference frame.

Lutes (2002) designed an automated data collection and processing system for monitoring of point displacements at a large earth fill dam project in southern California. Because of the large size of this facility, the monitoring was implemented using a network of permanently installed robotic total stations (Figure 2-3) to carry out the measurements and data processing in a fully automatic fashion. The acquired data was processed using in-house software and the updated point coordinates were delivered to

the system operator after each measurement cycle. The automated monitoring system was first activated in October 2000 and successfully collected displacement measurements for more than a year. Measurements were collected at different times of day to allow the system to meet its design goal of detecting displacements larger than 10 mm at the 95% confidence level.

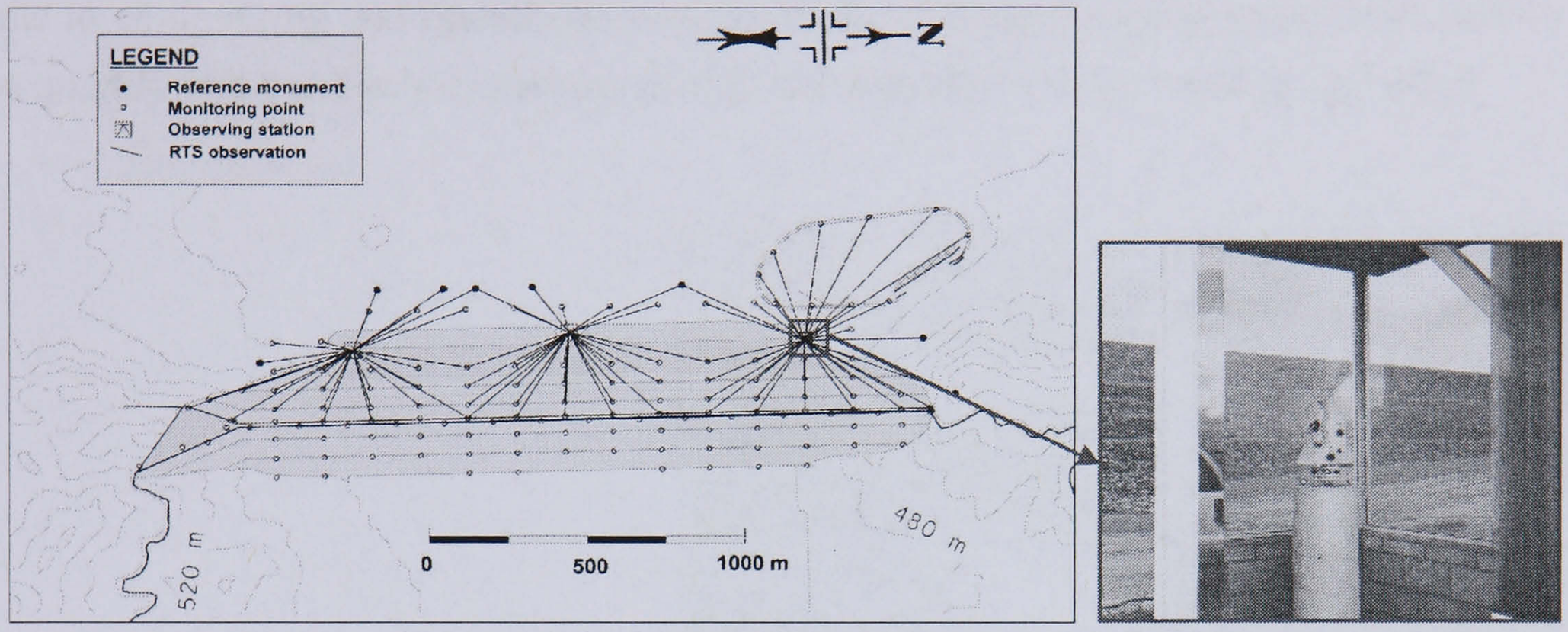


Figure 2-3: Robotic total station observation scheme (left); the RTS is mounted on a pillar in an observation shelter (right) (after Lutes, 2002).

An automatic tunnel displacement monitoring system, consisting of a motorised total station, was developed to monitor the tunnel deformations during excavation (Sharma et al., 2001; Bhalla et al., 2005). A robotic total station was installed at a permanent location inside the Mass Rapid Transit (MRT) tunnels to monitor their displacements and to ensure that the stringent requirements for safeguarding the tunnels were not violated during any part of the excavation works. The monitoring target prisms were mounted onto the brackets on the inside of the tunnel lining. In order not to be affected by the excavation, the system measured the tunnel displacements with respect to a few stable reference points located sufficiently far away from the excavation site. As a result, the automatic tunnel monitoring system was accurate to within +/- 1 mm. With these systems, the displacements of the tunnel lining were continuously monitored during excavation and construction.

Pit monitoring is imperative in mining as pit wall displacements seriously affect the safety of mining operations. The success of the monitoring approach is highly dependent on the application of a reliable and accurate automated monitoring system. This must be put in place in order to inform mine operations and engineering personnel of up-to-date slope movement trends. To achieve this, Newcomen et al. (2003) adopted robotic total stations to measure 500 slope monitoring points located strategically

throughout the pits in Highland Valley Copper, Canada (Figure 2-4). Surveys of these points were repeated at defined intervals to optimise operational efficiency. The system's accuracy and reliability were consistently improved by reducing the effects of systematic errors due to atmospheric refraction, long shot distances, unstable instrument, possible movement of the reference point positions and other constraints due to mining activity. The development of software for processing the survey data and providing the results to engineering and operations personnel allowed slope displacement information to be quickly and concisely communicated to the front lines of the mining operation.

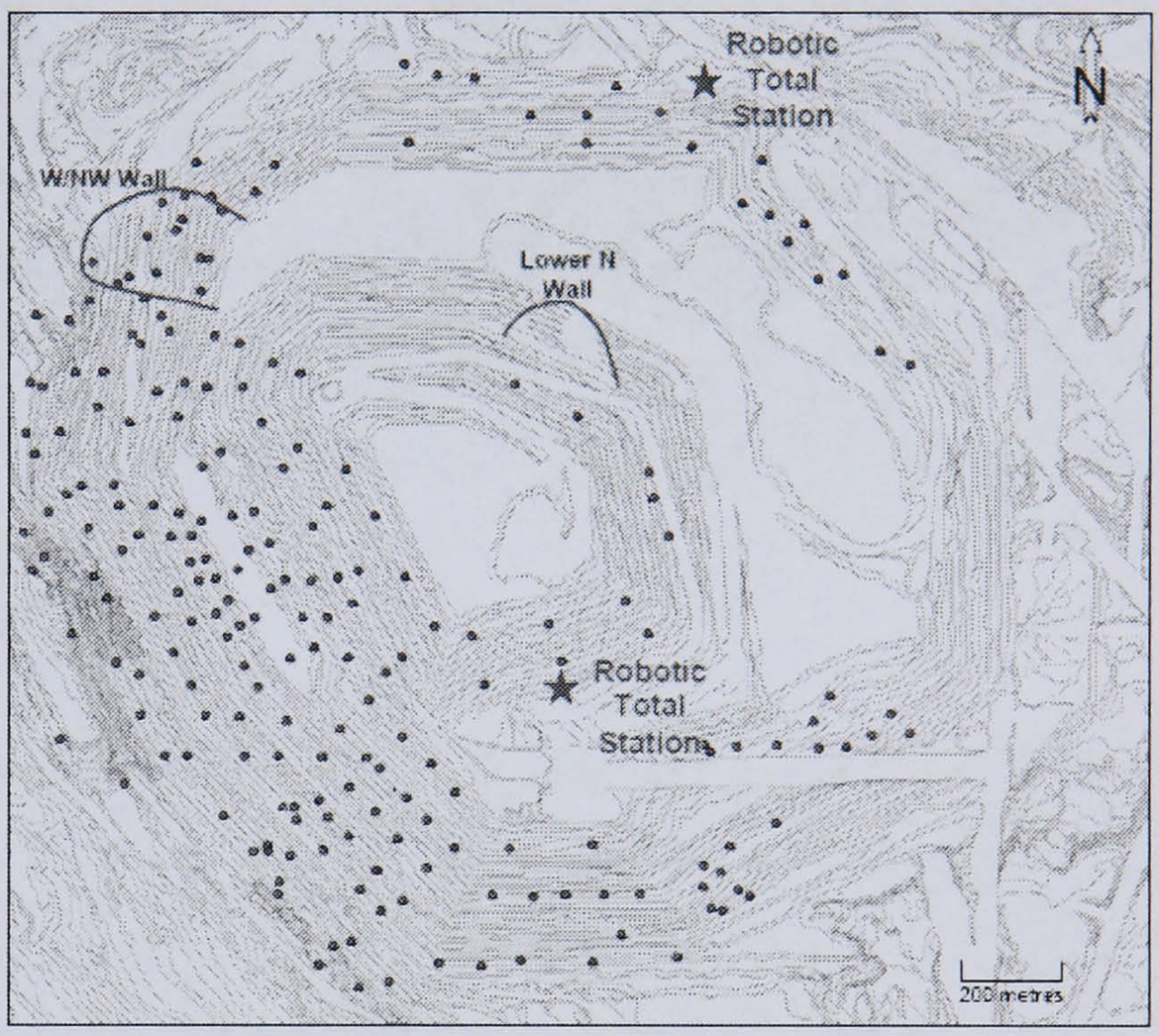


Figure 2-4: Part of the valley pit plan, showing prisms (blue dots), selected instability areas and RTS locations (Newcomen et al., 2003).

In another structural documentation and analysis project, a modelling system was designed to survey the scissors arches of Wells Cathedral in the U.K. (D'Ayala and Smars, 2003). Considering the on-site accessibility problems, non-contact techniques were favourable in the project. A solution was therefore identified in the form of a hybrid approach, combining elements of terrestrial survey using a robotic total station and digital photogrammetry. To construct models of the different elements (e.g. columns and arches), the RTS was firstly used to measure points on the specific structural components. The example point cloud is shown in Figure 2-5. In order to give a smooth surface representation, the point cloud was then meshed using Delaunay triangulation. It is noteworthy that no prisms were attached on the structure for RTS surveying; instead the measurement was accomplished using the reflectorless observation mode.

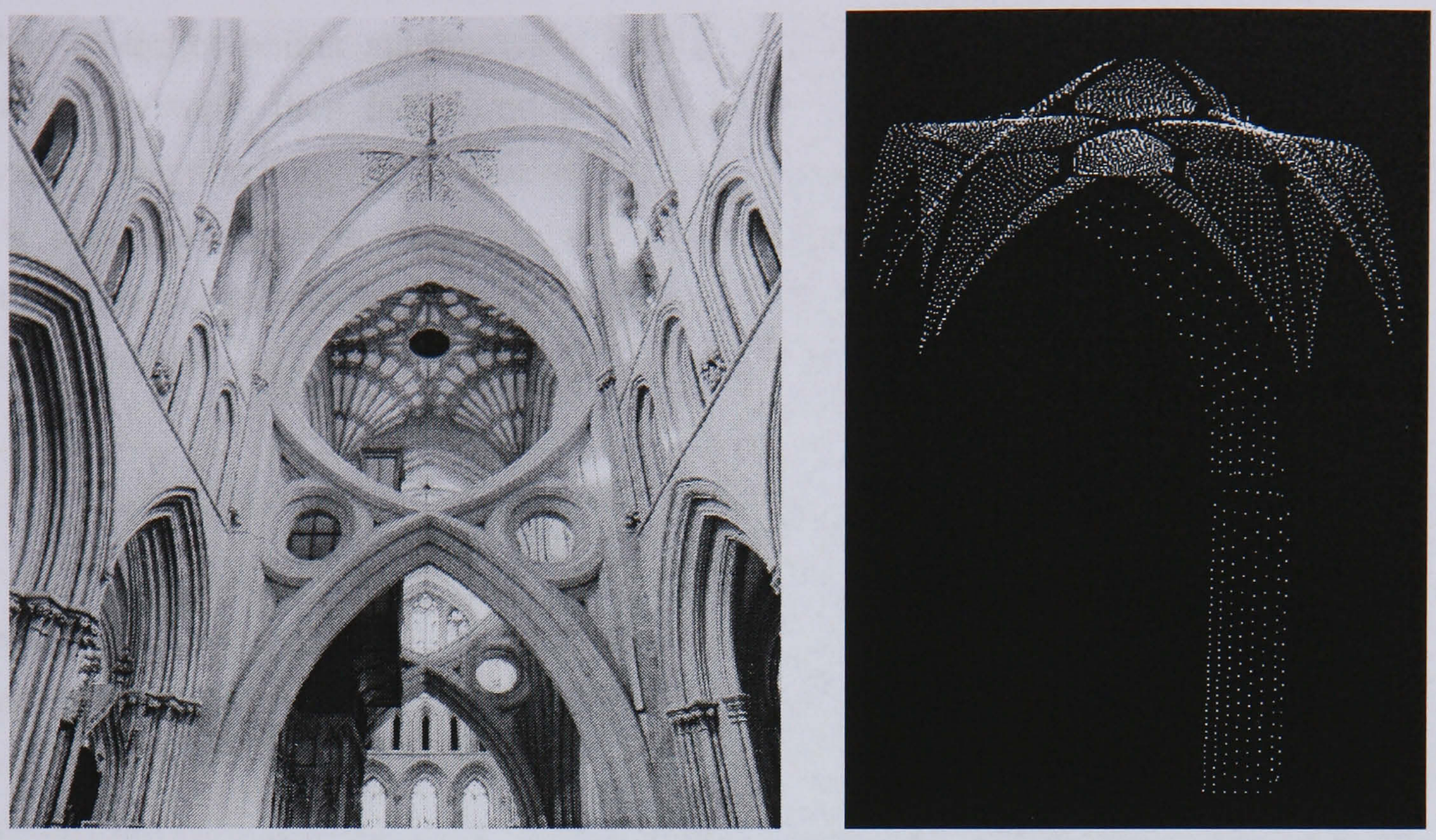


Figure 2-5: The scissors arches of Wells Cathedral (left) and the point cloud measured by robotic total station (right) (D'Ayala and Smars, 2003).

2.2.4 Other Applications with Total Stations

In addition to structural measurement and monitoring, terrestrial surveying using total station instruments has also been widely adopted in geotechnical engineering applications. In order to estimate cliff erosion rate, Gulyaev and Buckeridge (2004) used a total station to manually measure 50-100 points in reflectorless mode across a cliff face. The erosion rate was determined on the basis of repeat surveys. Another example of geotechnical surveying is the investigation of the landslide motion. In the experiment conducted by Savvaidis et al. (2005), a robotic total station was employed to identify possible landslides at the site under investigation. Moreover, an alert system integrating a total station, geodetic levelling and Global Positioning System (GPS) technology was designed for landslide detection. In general, the results of the survey showed that large parts of the investigated area were affected by slow, continuous deformations. A permanent monitoring system integrating GPS and total station technology was therefore developed for landslide investigation.

Projects using reflectorless total stations have also been undertaken to determine the fracture traces and estimate the dip angle and dip direction of fractures (Bulut and Tudes, 1996; Feng et al., 2001). In research measuring the roughness of large rock fracture surfaces (Feng et al., 2003), reflectorless EDM could record data without placing any reflector on the target, as the target itself reflected back the signal. The total station was treated as a point-sensor laser scanner to capture 3D coordinates of a large

number of target points automatically within a defined area of the fracture surface. These points were then input into the special software for quantitative and spatial analysis of fracture roughness. The method was implemented for various rock surfaces and it revealed that the primary roughness of fracture surfaces can be measured accurately, however in some cases, roughness of fracture surfaces could not be detected due to the low resolution of points measured by the total station.

Due to the valuable potential of applying total stations for monitoring various events, such instruments have been introduced in versatile automated commercial monitoring systems, such as Sol Data (1993) and eMs (1999). These systems comprised four basic components, including the total station(s), a computer, a cable network or wireless technologies to connect the station(s) with the computer, and proprietary software for processing the derived observations. Data can be made continuously available for rapid interpretation and an alert sent to the service personnel if any monitoring status falls out of its expected limit. This category of monitoring system has been successfully adopted for tunnel monitoring, structural deformation monitoring, and slope stability monitoring.

2.2.5 Suitability for Membrane Structure Measurement and Monitoring

From the previous examples, it is clear that terrestrial survey methods applying total station instrumentation have become some of the most utilised techniques in structural measurement and monitoring schemes. This is primarily due to the highly improved features of the surveying equipment, such as EDM units, reflectorless measurement mode, and automatic target tracking techniques, making automated surveying feasible. These kinds of non-contact measurement methods also meet the requirements of membrane structure monitoring. However, as the characteristics of the membrane structures are different from the traditional structures, the suitability of employing total stations in observing such structures may be limited.

For the scheme of deriving the as-built static model of the fabric roof, the adoption of total stations capable of reflectorless measurement is possible (Bulut and Tudes, 1996; D'Ayala and Smars, 2003;). However, the measurement speed of the employed total station should be considered as it will affect the efficiency of data collection. From the experiments reported in Gulyaev and Buckeridge (2004) with a Leica TC 307 total station, it took two hours for a trained technician to measure a set of 70 points on a cliff face. For a membrane structure, in order to represent the complete fabric membrane 70

points are obviously insufficient, therefore the time for full measurement would be considerably longer. This limitation is also pointed out in Feng et al. (2003): although a total station provides the possibility to scan the surface geometry of rock fractures, it is difficult to scan a large area with many data points.

As the function of automatic tracking is supplied in robotic total stations, the feasibility of deformation monitoring is demonstrated by using this type of instrument (Moffitt and Bossler, 1998; Sharma et al., 2001; Lutes, 2002; Newcomen et al., 2003; Savvaidis et al., 2005). To accomplish this, however, target prisms must be attached to the observed object, which does not fit with the non-contact requirement of the membrane structure monitoring scheme. Moreover, the displacement monitored by a total station is performed on point by point basis. It indicates the comparison can only be performed at each single point, and the sequential displacement analysis of the overall surface is unachievable. Even though the measurement could be accomplished with reflectorless operation, the surface-based comparison still remains unavailable due to the long measurement time per point (for example in Leica series total stations, it typically takes 3-6 seconds to measure a single point).

Conclusively, although it possesses the advantages of easy setup and accurate measurement, a total station is not suitable and will not be used directly in the membrane structure monitoring scheme for measuring and monitoring the fabric membrane roof. Nevertheless, a total station will still be introduced in the monitoring scheme to measure the 3D coordinates of the necessary control points.

2.3 Terrestrial Surveying with Terrestrial Laser Scanning (TLS)

2.3.1 Introduction

As defined by Boehler and Marbs (2002), terrestrial laser scanning (TLS) is a technique which allows the collection of high-density point clouds distributed over a given region of an object's surface by measuring their three-dimensional coordinates automatically in near real-time. Since the early 1990s, terrestrial laser scanning has been increasingly adopted in the surveying market as an efficient alternative 3D measurement system with respect to photogrammetry or geodetic methods (Guarnieri et al., 2005). Due to the capability of measuring an enormous amount of points at a high rate in near real-time, complete and detailed 3D models of objects can be efficiently and easily created from acquired point clouds. These features have allowed laser scanning technologies to be

widely applied in industrial metrology, deformation analysis, civil engineering, cultural heritage, topographic surveying, and engineering geodesy (Tucker, 2002; Barber, 2003; Schulz and Ingensand, 2004a). To investigate the feasibility of applying TLS in the membrane structure measuring and monitoring scheme, the technical background and the related applications of this technique are reviewed and discussed.

2.3.2 Instrumentation

Most terrestrial laser scanning systems are a combination of a one dimensional distance measurement system with a mechanical deflection system, directing the laser beam into different directions and measuring the distance to the closest object for each direction (Frohlich and Mettenleiter, 2004). The principle of laser scanning is demonstrated in Figure 2-6, where one slope distance (s') and two orthogonal angles (w_1 and w_2) are measured for each point (Staiger, 2003). According to the derived distances and angles, the space polar method is applied using Equation 2-1 to determine the 3D coordinates of detailed points.

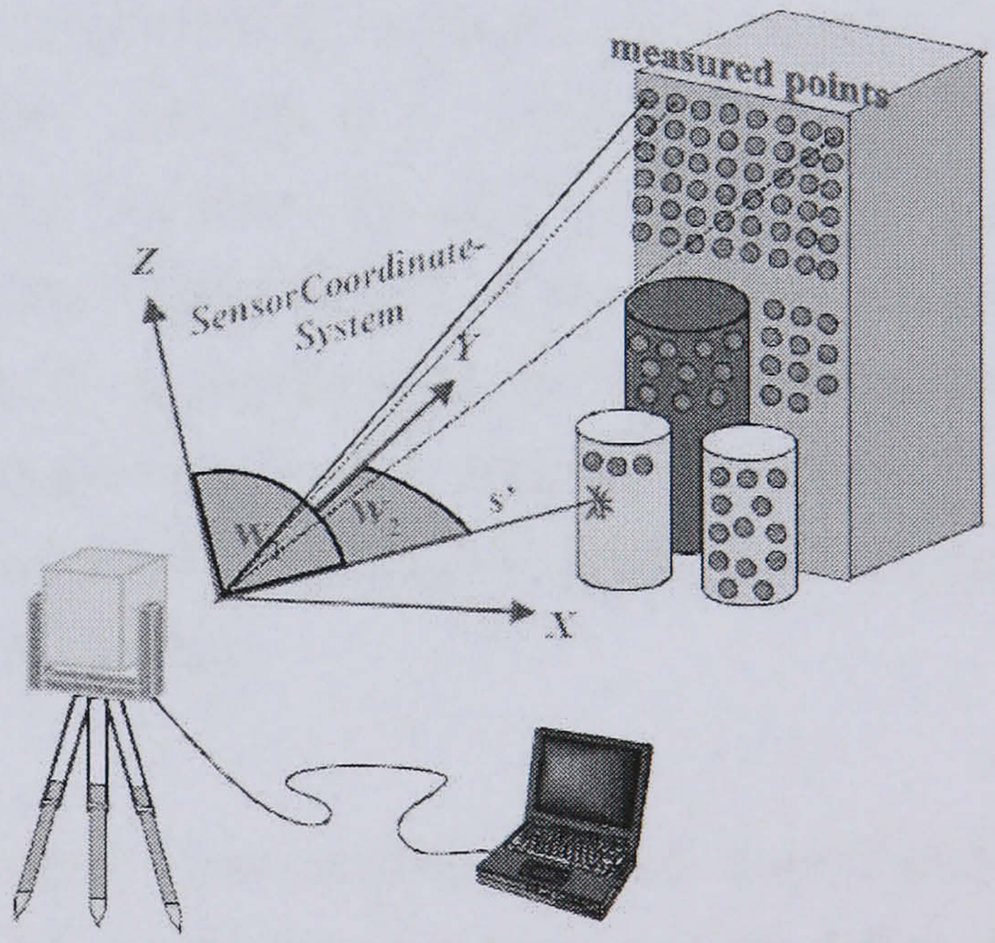


Figure 2-6: The principle of laser scanning (Staiger, 2003).

Terrestrial laser scanners can be categorised into time-of-flight, phase comparison and triangulation systems, according to the principle of distance measurement adopted by the instrument (Boehler and Marbs, 2002). Basically the first two methods operate on the same principles employed by an EDM unit, as described in Section 2.2.1. Most commercial laser scanners are currently based on the time-of-flight principle, where the technology is based on sending out a laser pulse and observing the time taken to reflect from an object and return to the instrument. Advanced electronics are used to compute

the range to the target. These scanners typically allow measurements of distances up to several hundred metres, with ranges beyond one kilometre achievable in some scanners (Frohlich and Mettenleiter, 2004; Lemmon and Biddiscombe, 2006). Phase comparison technology works by sending a laser beam with a sinusoidal wave into the centre of a rotating mirror, which deflects the laser around the environment being scanned. The beam is then reflected back into the scanner and the "phase shift" of the laser is measured, giving the distance of the laser from the object. Phase comparison scanners are limited to shorter distances, typically up to about 100 metres for optimal use (Schulz and Ingensand, 2004b; Lemmon and Biddiscombe, 2006). For detailed scanning, laser scanners applying the triangulation method with typical ranges up to few metres are available. In triangulation laser scanners, a laser is emitted onto the subject and a camera is exploited to capture the location of the laser dot. The centre of the dot is extracted from the image. The relative positions of the laser emitter and the camera are used to find the 3D coordinates of the laser dot by triangulation (Curless and Levoy, 1995; Kil et al., 2006).

When scanning with a one dimensional distance measurement system, a profile of points can be collected no matter what range measurement method is used. In order to produce a point cloud over the complete object surface, it is necessary to alter the direction of the profile and record a new profile of points. To achieve this, the scan is repeated with the direction of the laser being physically altered, or the direction of the laser beam diverted using a mirror or prism, or a combination of these approaches (Barber, 2003). During laser scanning, encoders are employed to measure and record the angles determined from the position of the plane oscillating mirrors, prisms or from the rotation of the head of the scanner (Kremen et al., 2006).

It is worthy of note that there is no universal laser scanner for all conceivable applications (Frohlich and Mettenleiter, 2004). Terrestrial laser scanners with different distance measurement systems contain different characteristics. Normally, the advantage of long ranges implies less accurate distance measurement. Based on the three main measurement principles, the laser scanners currently available on the market are classified in Table 2-1, which shows the maximum measuring range and precision. The appropriate laser scanner has to be selected depending on the requirements of the applications.

	Typical Range (m)	*Typical Precision (mm)*	*Manufacturers*
Time-of-flight	< 100	< 10	Callidus, Faro UK, Leica, Mensi, Optech, Riegl
	< 1000	< 20	MDL, Optech, Riegl, Trimble
Phase comparison	< 100	< 10	IQSun, Leica, VisImage, Zoller and Froelich
Triangulation	< 5	< 1	Mensi, Minolta

Table 2-1: Classification of laser scanners (after Frohlich and Mettenleiter, 2004; Schulz and Ingensand, 2004b).

2.3.3 Laser Scanned Data Processing

2.3.3.1 Point Cloud Registration

In measurement schemes using TLS, more than one scan performed from different positions are normally necessary for covering multi-faceted objects. The point cloud derived from each scan is located in an arbitrary coordinate system with respect to the scanner centre (the original point). In order to combine these point clouds for further applications, the task of point cloud registration is performed, transforming all of the point clouds into a common reference frame (Staiger, 2003). As stated by Barber (2003), the fusion of the point clouds can be accomplished by point-to-point or cloud-to-cloud registration. In the former approach, if at least three retro-reflective targets or identifiable features in the point cloud can be found in the overlapping area of the adjacent scans, they are treated as tie points. A 3D conformal transformation is then carried out to align the two point clouds into a unique object reference system (Scaioni and Forlani, 2003; Gordon and Lichti, 2004). Kremen et al. (2006) point out the point-to-point registration method is more accurate if the employed targets for relating different scans are suitably located in the overlapping area. Moreover, while defining the minimum overlapping area between two adjacent scans, Bornaz et al. (2003) report that at least 30% overlap must be provided in order to get a registration of two adjacent scans without a loss in the precision of the laser scanner instrument used. Compared to the pairwise registration, if the 3D coordinates of retro-reflective targets or features have been determined in a global coordinate system, the point clouds encompassing at least three known targets can be transformed directly into the global frame (Staiger, 2003).

The method of cloud-to-cloud registration is carried out by matching point clouds using techniques such as the iterative closest point (ICP) algorithm (Besl and McKay, 1992). With only approximations for rotation and translation parameters, two or more sets of scan data with overlapping coverage are mathematically compared to obtain the transformation parameters. Cloud-to-cloud registration is advantageous in registrations where control points are not available. Based on the ICP algorithm, several variations have been made (Masuda and Yokoya, 1995; Bergevin et al., 1996; Godin et al., 2001). On the other hand, there are also many approaches adopting various strategies being proposed by Johnson and Hebert (1999), Williams and Bennamoun (2001), Balzani et al. (2002), Gruen and Akca (2004), and Guarnieri et al. (2005), to solve the point cloud and surface global registration problems.

2.3.3.2 Point Cloud Modelling

TLS has been widely accepted for diverse applications, in which the resultant point clouds are frequently coloured using additional image data for visualisation purposes (Briese, 2006). However, as this form of representation is not suitable for mathematical analysis, the point cloud is generally not yet considered as an appropriate deliverable. Instead, point cloud modelling is often performed to convert the scanned data into a more acceptable deliverable format. Modelling techniques, including surface reconstruction and primitive fitting, are therefore introduced.

Polygons are usually the most flexible way to accurately represent the results of 3D measurements as they provide an optimal surface description (Remondino and El-Hakim, 2006). To this end, surface reconstruction (or mesh generation) is often performed to create a surface model which approximates an unknown surface that a given set of points are assumed to lie on or near (Hoppe, 1994). For representing the measured points, regular grid and triangulated irregular network (TIN) are two commonly adopted forms of mesh (Wolf and Dewitt, 2000). The TIN is preferable in the processing of laser scanned data since it can better follow discontinuities and model concave or convex surfaces (Visintini et al., 2006). To construct the triangular meshes, the method of Delaunay triangulation is generally used. The triangles are generated by drawing the lines between points in closest proximity to each other, without any lines intersecting. The polygon composed of the resulting set of triangles is used to represent the measured points (Figure 2-7). According to the geometry of the input data, triangulation can be performed in two or three dimensions. The full methods are described in Remondino and El-Hakim (2006).

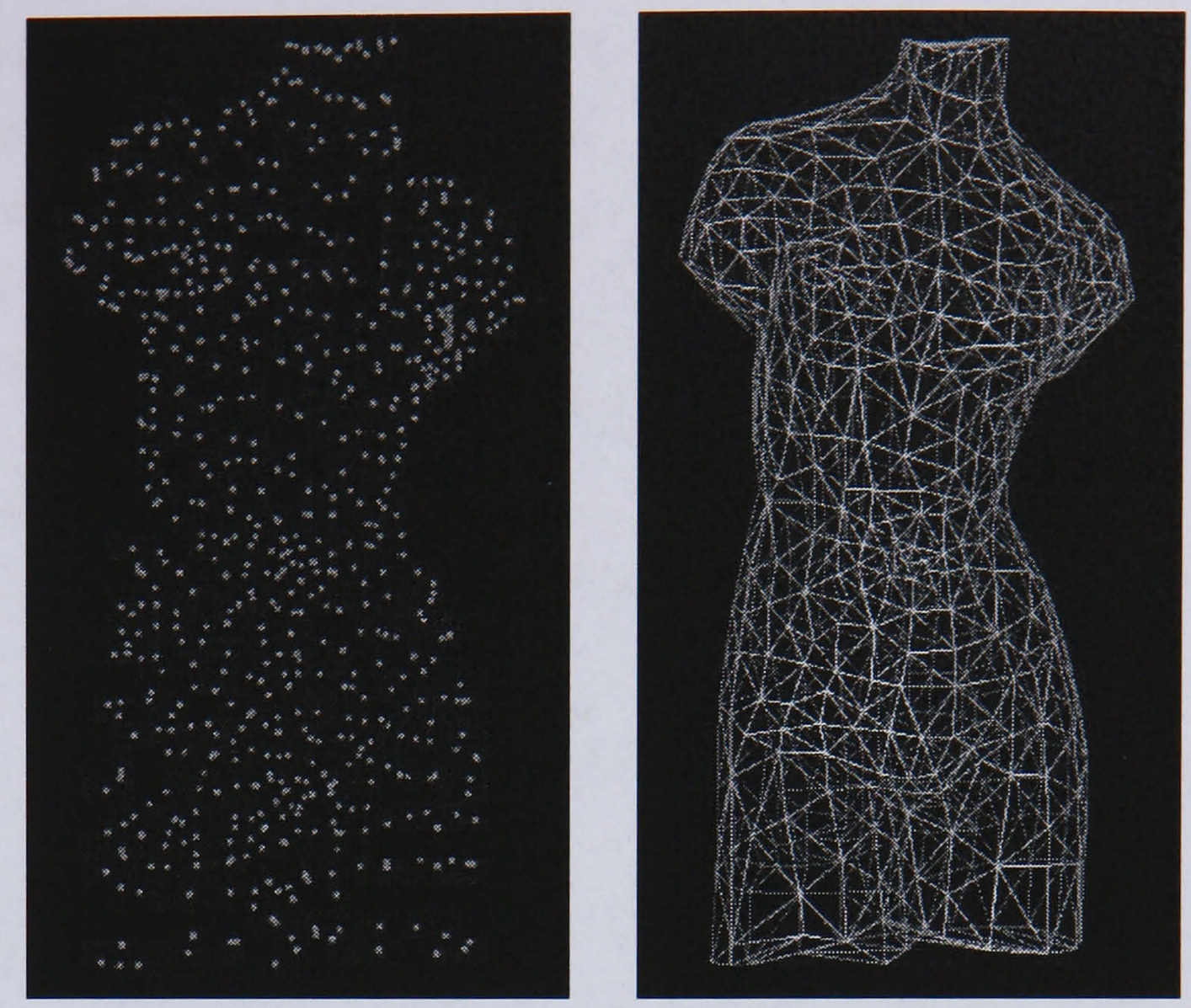


Figure 2-7: An example point cloud (left) and its TIN model (right).

Normally the correctness of the resolved surface relates to the complexity of the observed surface and the number of measured points representing the observed surface. For example if a smooth surface is observed, merely a small number of points are required and the surface reconstruction is achieved with only a few triangular meshes fitting to the data. In complex modelling applications, denser point clouds are necessary for successful surface reconstruction. In order to get an optimal result from surface reconstruction, therefore, mesh simplification is performed to retain triangles of high density in geometrically complicated areas and reduce the number of triangles in uncomplicated (flatter) regions (Hoppe, 1993; Barber, 2003).

With the same goal of surface reconstruction, primitive fitting is performed to employ simple CAD primitives for representing the results of 3D measurements. Basic CAD objects, including lines, planes, spheres, cones and cylinders, are used to describe the elementary parts of the scanned objects. The process of primitive fitting is to estimate the size and orientation of a primitive by minimising the distance between the scan points and the object model (Barber, 2003). When the modelling is finished, some items such as fitting tolerance (e.g. the standard deviation value from the modelling) and fitting constraints (e.g. the known diameter of a cylinder or known centre of a sphere) are examined to assure the modelling is performed correctly.

Currently the function of primitive fitting is largely supported in most proprietary laser scanner software. There are also a lot of CAD packages available with direct import of

point clouds from laser scanners which enable direct modelling in the CAD software (Frohlich and Mettenleiter, 2004). In both cases, primitive fitting is undertaken easily by setting the parameters required in different primitives. Once the modelling of the scanned data is complete, the dimensions and measurements of the modelled objects are available. Also, data compression is realised and the display speed can be improved. Moreover, since large numbers of repeat observations are made and the noise is partially filtered during modelling, improved measurement accuracy is achievable (Barber, 2003; Lindenbergh and Pfeifer, 2005).

2.3.3.3 Workflow

In general, the laser scanning workflow involves placing the laser scanner at locations about the survey site and measuring to a number of control points (e.g. retro-reflective targets or identifiable features) and the actual object of interest. The scanner is then moved to the second location and at least three common control points from the first scanner location are measured. The common measurements to the control points are then used to relate the scans together by registration (Lemmon and Biddiscombe, 2006). At the last stage, the modelling of the whole combined point cloud or specific components is performed depending on the requirements of the application. In addition to the general workflow, specific details noteworthy during the scanning procedure are introduced below.

Prior to the implementation of scanning, laser scanning network design is essential if multiple scans are required. To achieve this, Lahoz et al. (2006) emphasise that the optimal station number is decided by considering the efficiency of the multi-station orientation procedures and the assurance of a global coverage of all desired surfaces. In addition, the positions of the scanner are arranged considering the incidence ray angle at the facade and the maximum scanning distance. Once the network of the scanner has been resolved, the network of the control points is designed and arranged accordingly.

At the data acquisition stage, scanning density is one of the parameters required in the laser scanning settings. With the Leica HDS3000 scanning system for example, the scanning density is defined as horizontal and vertical spatial resolutions of the adjacent points at a certain distance from the scanner (at which the object is measured). When the scanning density is input, the given length intervals for horizontal and vertical direction will be maintained at the set distance. The scanner transfers the length intervals into angle intervals then it measures the sequential points by increasing the computed angles

of the scanning mirrors or prisms. The vertical interval of the scanned points at the set distance therefore complies with the given value. The scanned points nearer to the scanner will be measured much more densely while the number of points decreases rapidly with increasing distance away from laser scanner (Lindenbergh et al., 2005). The volume of acquired data and the time of measurement will grow as a result of increased resolution, and in order to choose appropriate interval values this fact should be taken into account (Kremen et al., 2006). However, with the intention of meeting required accuracy, Hoffman (2005) suggests that the spatial resolution should be equal to half of the measurement accuracy, ensuring the project receives the amount of data required.

Once data collection is complete, data are imported into proprietary software for further processing. The noise included in the TLS data may alter the mesh generation and mathematical analysis performed later (Briese, 2006), therefore, the disturbing points in the individual scans are firstly removed until there are only points on the determined surface left. This procedure can be accomplished manually (Suwannakanthi et al., 2006) or automatically (Lerma and Biosca, 2005; Lichti, 2005). Consequently a registration transforming individual scans into one final point cloud under the required coordinates system and further processing or analysis follows.

2.3.4 Applications in Structural Measurement and Monitoring

For applications in structural measurement and monitoring, a common problem in using total stations is the small number of points that can be measured on the object of interest. The amount of points is generally insufficient for representing the surface and further analysing the overall behaviour of the object. Terrestrial laser scanners, however, are capable of obtaining huge numbers of points so that the measurements are extended to the whole structure instead of being limited to a few points. Hence they are of more practical use for structural measurement and monitoring.

In the project conducted by Alba et al. (2006), it was noted that the monitoring of the static behaviour of large dams has always been a topic of great importance. To achieve this, many instruments and surveying methods (e.g. opto-electronic collimators, robotic total stations) have been applied to continuously assess the safety of this kind of large structure. However, it is inefficient to observe sufficient points for representing the large surface of the dam. To obtain a better solution, TLS was adopted and two laser scanners, including a long range Riegl LMS-Z420i and a medium range Leica HDS3000, were

employed in observation campaigns at the Cancano Lake dam (Valtellina, Italy), whose dimensions are 136 m in height by 381 m in length at the crest (Figure 2-8, left). By adopting the two laser scanners, data acquisition was carried out at three epochs to collect dense point clouds of the dam. When the model registration was finished, the complete surface of the dam was generated and the deformation analysis was performed.

For determining deformation using TLS, it is not possible to point at identical points in different scan epochs since there is no opportunity to set the mirror positions to defined angles (Schafer et al., 2004). Therefore, raw point clouds have to be post-processed in order to derive the deformation information. To determine the deformation of the Cancano Lake dam an area-based method was used, in which a comparison was made between data acquired at different times by considering mathematical surfaces fitted to the measured points. To accomplish this, the surface of the dam was divided into small homogeneous areas and for each of these an interpolated surface with a uniform and regular grid was estimated. Because multi-temporal point clouds were geo-referenced into the same reference system, the comparison between interpolated surfaces allowed evaluation of the displacements (Figure 2-9). As a result, a map of deformations, evaluated by comparing the meshed surfaces derived from the scan acquired in October 2005 and May 2006, could be determined (Figure 2-8 (right)).

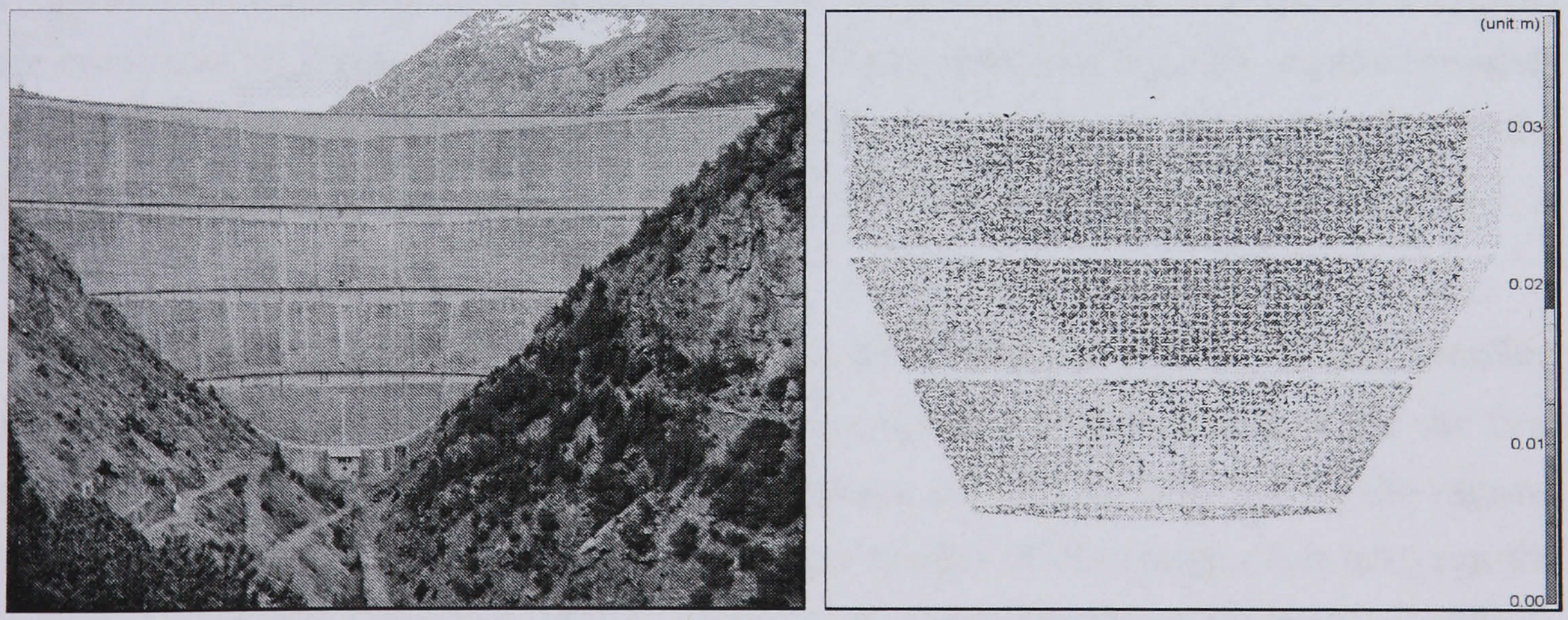


Figure 2-8: Left: downstream face of the Cancano Lake dam. Right: deformation map acquired from scans recorded at two epochs (after Alba et al., 2006).

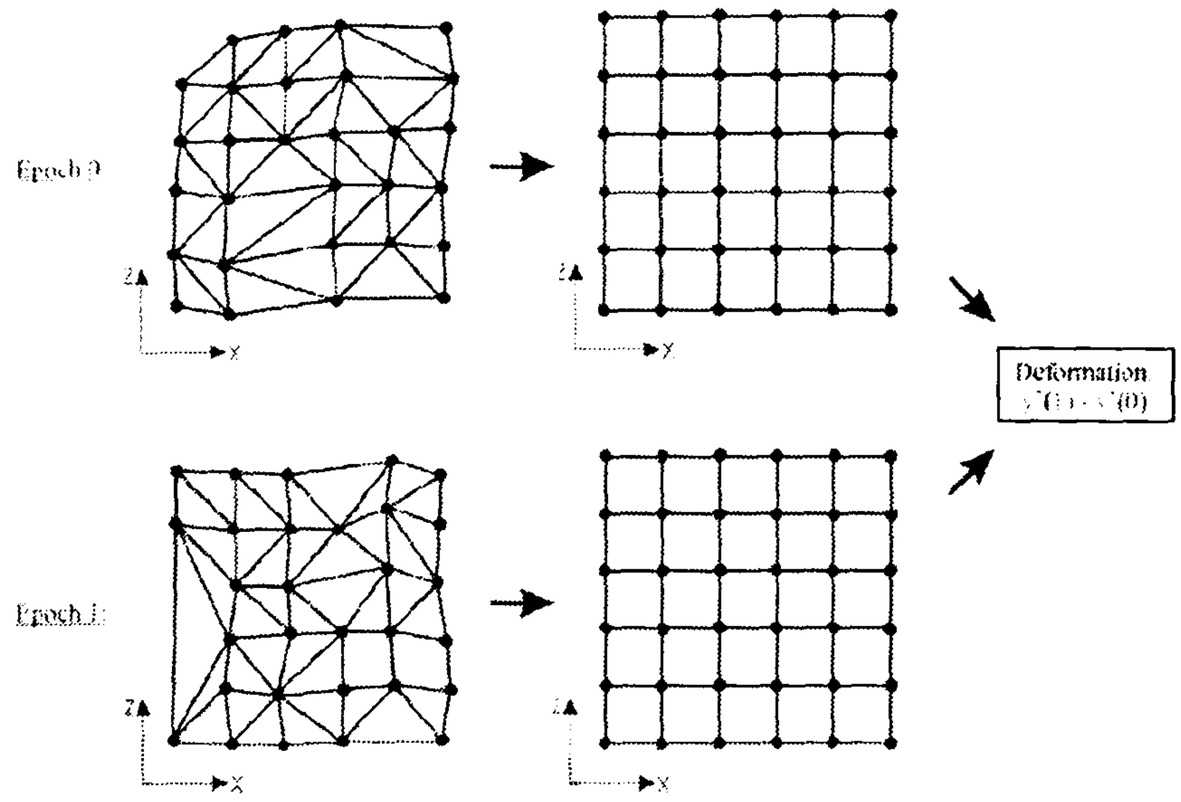


Figure 2-9: Raw point clouds with irregular and non-uniform sampling (left) and the interpolated grid (right), identical for every point cloud. The deformation is derived by computing the difference in y-direction (Schafer et al., 2004).

van Gosliga et al. (2006) used TLS to support the detection of deformations in a bored tunnel. In this project, the deformations of the completed tunnel with respect to the design model, and also the deformations occurring after construction was finished (between any two measurement epochs) were both considered. To this end, a cylinder primitive was firstly fitted to the resultant scanned model of the tunnel using a linearised iterative least squares approach, and the output cylinder was treated as the optimal tunnel model. To compare the actual tunnel data to the idealised tunnel model, the data was fitted to the model and the resulting residuals indicated the disparities from the optimal construction. In addition, the scan data collected at two different epochs were compared to show the changes over time. To accomplish this, the scanned models of the tunnels at both epochs were interpolated to a regular grid. The differences in the range ordinates at a grid point demonstrated the differences between the two epochs.

In the observation campaign, a length of 100m of the Heinenoordtunnel in Rotterdam was scanned twice using a Leica HDS4500 laser scanner (Figure 2-10). After the first scan, some artificial deformations were put against the tunnel wall before the second scan was performed. Figure 2-11 (left) shows the results of the comparison between the first scan data and the idealised tunnel model: a strongly deviating segment is visible on the bottom left of the scanned tunnel and it was suspected that the segment was placed in a bad way during construction of the tunnel. In order to determine the changes between the two measurement periods, the data from both epochs was interpolated to a regular grid of 15 cm by 15cm along the tunnel wall. The deformations are shown in Figure 2-11 (right), in which clear deformations can be found at locations A, B and C, where the artificial deformations were arranged. However, the artificial deformations

were only partly detected due to the large interpolated grid size in comparison to the small deformations.

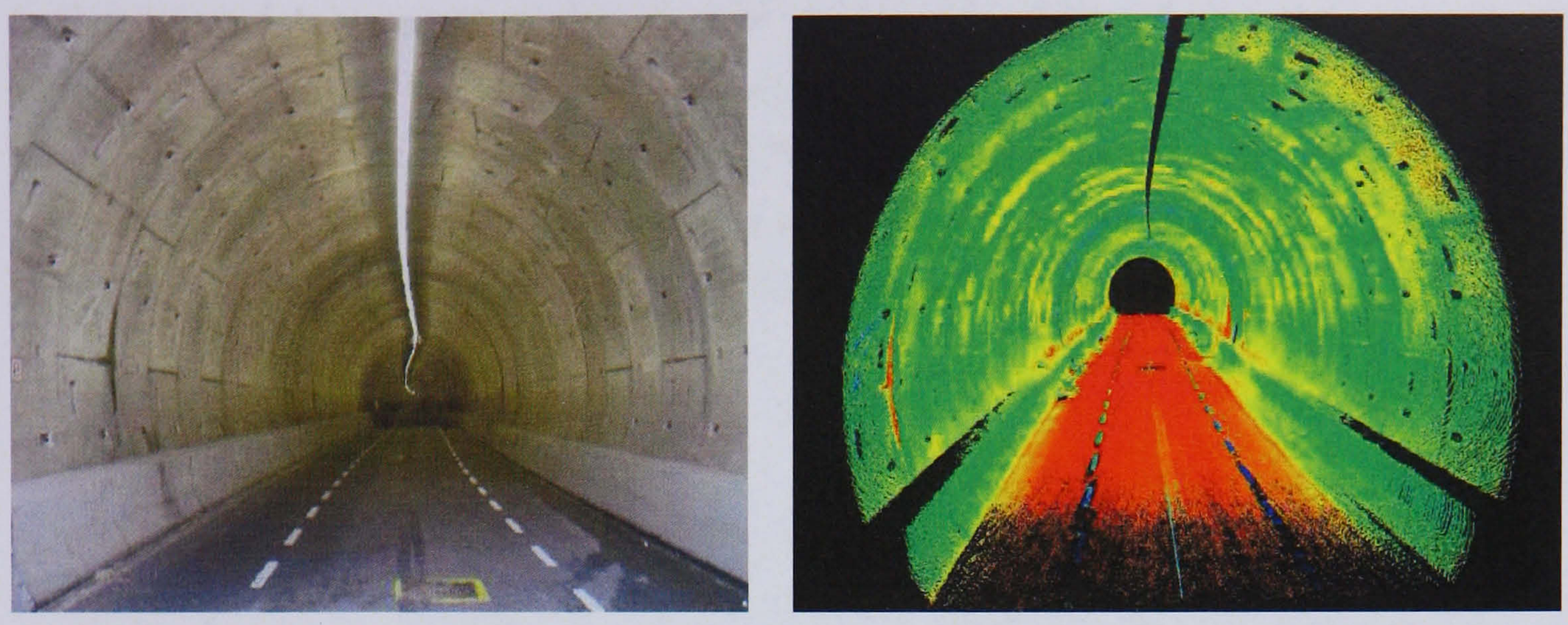


Figure 2-10: The tunnel (left) and its resultant laser scanned model (right) (Gosliga et al., 2006).

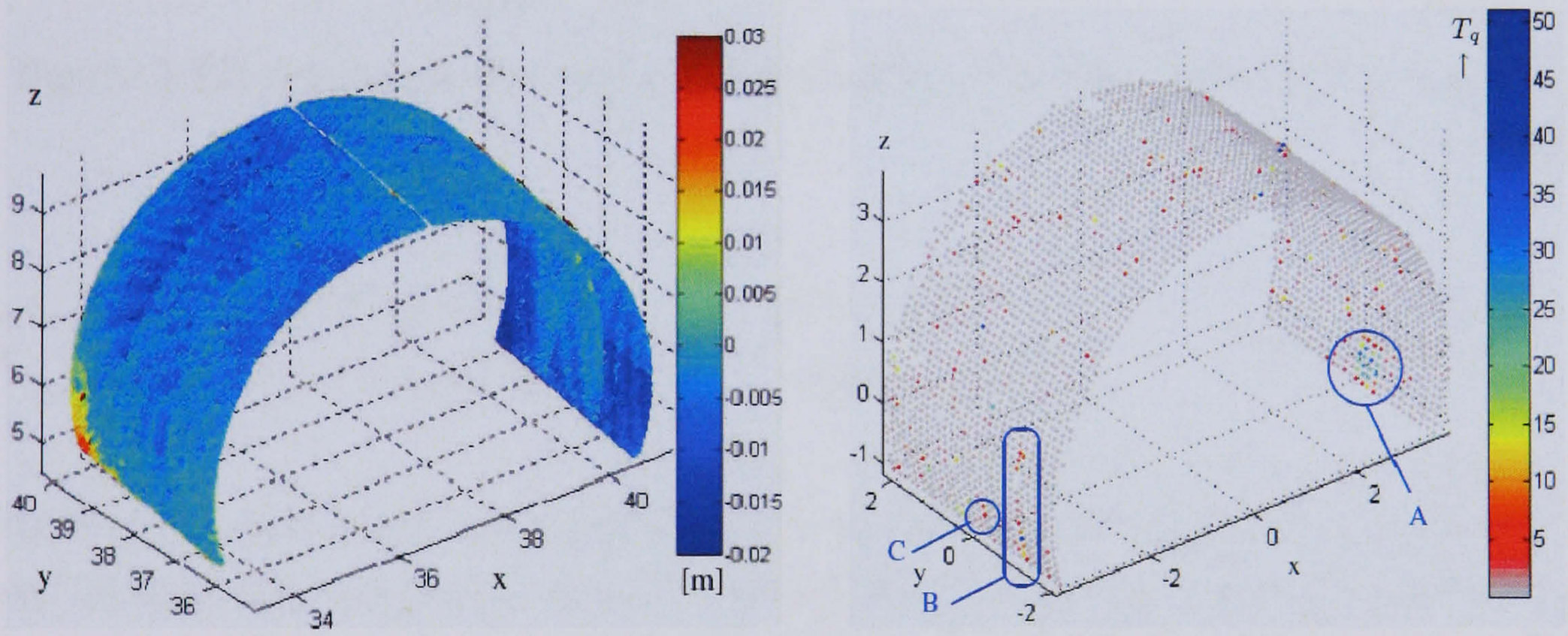


Figure 2-11: Left: residuals after fitting a cylindrical model to the tunnel data. Right: changes between the two measurement epochs (van Gosliga et al., 2006).

In addition to the tunnel deformation analysis introduced above, CAD primitive modelling has been introduced in other structural applications, including the reconstruction of traffic facilities such as highway bridges (Kretschmer et al., 2004), and also a renovation plan of an abandoned theatre (Klimoski, 2006).

Two structural deformation measurement experiments, involving beams (both concrete and timber) being control loaded in a load-testing frame, were conducted by Gordon et al. (2004). As a modelled surface is a more precise representation of the object than the raw point cloud, the change of shape of a structure is effectively detected in the

modelled data. In this research, different from the widely used modelling applications such as a triangulated irregular network (TIN) and regular gridding algorithm, the method chosen to determine the vertical deflections of the beam was based on forming analytical models to represent the physical bending. The timber beam, for example, was supported at each of its ends and the loading applied at point P (Figure 2-12). The bending moment was represented by two functions (one each side of point P), the generalised form of which is given in Equation 2-2 (Gordon et al., 2003). This was used to fit the curve describing the bending of the beam as shown in Figure 2-12.

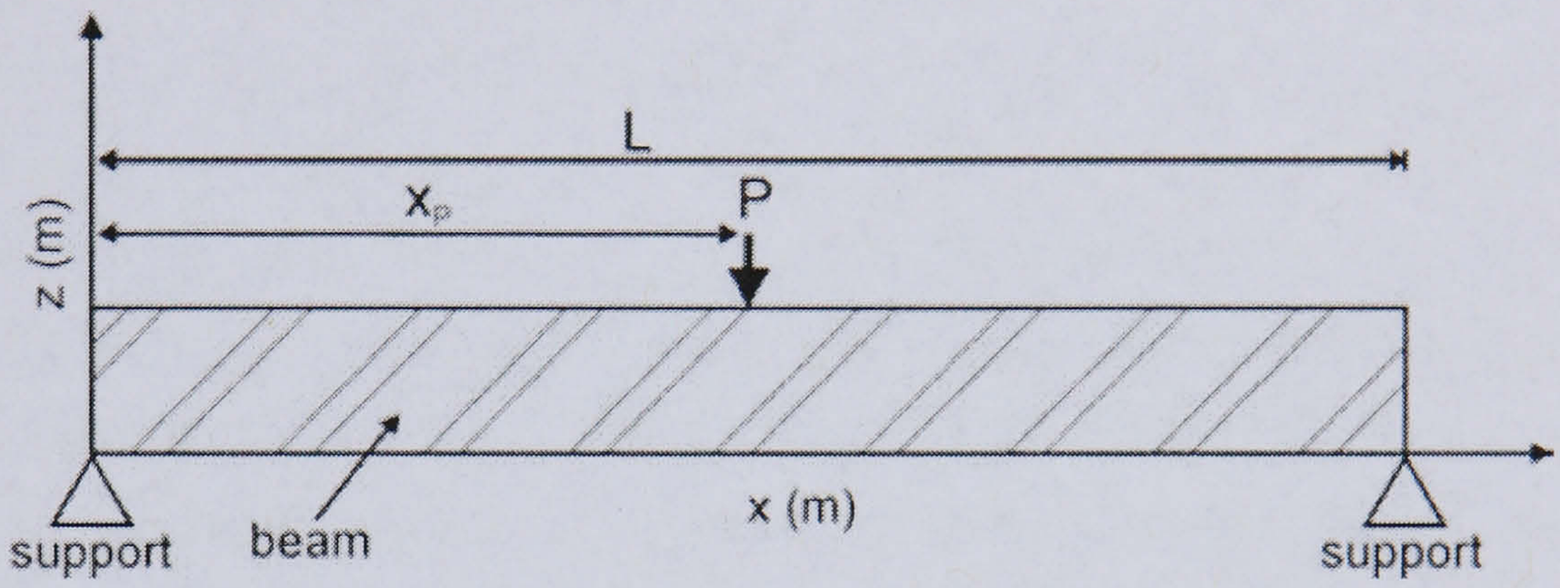


Figure 2-12: Schematic diagram for deformation of a timber beam (Gordon et al., 2004).

$$\begin{cases} z_1 = a_{30}x^3 + a_{10}x + a_{00} + a_{01}y & when \quad 0 \le x \le x_p \\ z_2 = b_{30}x^3 + b_{20}x^2 + b_{10}x + b_{00} + a_{01}y & when \quad x_p \le x \le L \end{cases} \qquad \textbf{Equation 2-2}$$

where x, y, z_1 and z_2 are 3D coordinates of the scanned point. During the experiment, a total of eight load increments were sequentially applied at point P. At each epoch, laser scanning was performed to collect a point cloud of the beam. Once finished, all TLS data for a single epoch was input into Equation 2-2 and processed by a least squares adjustment, thus the coefficients were solved and the left (z_1) and right (z_2) models of the beam derived. For determining the vertical deflections of the beam, the estimated models for each of the eight load epochs were used. The x- and y-ordinates of the 13 targets attached on the beam were passed into the estimated models to compute the correspondent z-ordinates. The z-ordinates were then used to determine vertical deflections between epochs.

Since the targets were also measured by photogrammetry, the vertical deflections solved by TLS were compared to the photogrammetric results, revealing both methods were in the same sub-millimetre accuracy level. These results highlighted the potential

application of TLS for precision metrology, given that the accuracy can be greatly improved by exploiting the 3D point clouds with simple modelling techniques.

2.3.5 Other Applications with TLS

There have been many research projects involving the scanning of historical structures for cultural heritage documentations. For example Levoy et al. (2000) used a custom laser triangulation scanner built by Cyberware to scan 10 statues by Michelangelo. The images of the statues shot by a still video camera were mapped onto the resultant meshed model, rendering full-resolution and full-colour 3D models of the statues. A project sponsored by English Heritage Archaeology Commissions Team employed various terrestrial laser scanners, including a Leica HDS2500, a Zoller and Froelich Imager 5003 system and a Riegl LMS Z320 system, to measure Tynemouth Priory and Clifford's Tower in the UK (Barber et al., 2003; Bryan et al., 2004), for cultural heritage recording. Bonora et al. (2005) used a Leica HDS2500 scanner to create a 3D scanned model describing the dome intrados of the Colleoni Chapel in Italy. In addition to the 3D scanned models, 2D cross-sections were also extracted for architectural describing and investigating historical buildings in the Meldorf Cathedral in Germany, a measurement was performed with a Zoller and Froelich Imager 5003 system (Sternberg, 2006). After long-term observations, deformations were determined by comparing the grid points, linear structures and surfaces acquired at different epochs.

TLS has also been applied in natural environmental measurement and monitoring. For the purpose of coastal erosion monitoring, Lim et al. (2005) and Miller et al. (2006) adopted a MDL LaserAce 600 and a Leica HDS3000 terrestrial laser scanner respectively to record the detailed surface of coastal cliffs at different epochs. Integrated with photogrammetry, the volumetric losses and erosion magnitude of the costal cliffs were determined. Hunter et al. (2003) used a long-range laser scanner for monitoring volcanic activity. Although the equipment could not penetrate through mist and volcanic gas, the portable system still showed the feasibility of deriving sufficient data for the creation of a digital terrain model, which was useful in volcano monitoring. Due to ecological and economical reasons, the investigation of single trees in a forest was undertaken by Pfeifer et al. (2004). A tree was firstly scanned and the branches were intended to be modelled by cylinder primitives. To achieve this, a set of algorithms was developed for automatically fitting and further tracking cylinders along branches and reconstructing the entire tree. The cylinder models of the individual tree stems were used for determining important parameters describing timber quality like taper, sweep

and lean which are closely related to the proportion of reaction wood. Other research addressing quantitative tree measurements using TLS are addressed in Thies and Spiecker (2004) and Watt and Donoghue (2005).

2.3.6 Suitability for Membrane Structure Measurement and Monitoring

Similar to the employment of total station instruments, terrestrial laser scanning has been widely applied and offers a range of benefits in structural measurement and modelling projects, due to their capability to automatically measure 3D coordinates. However, there are many differences between total stations and laser scanners, such as measurement time, maximum measuring range, additional hardware and software required, etc. Amongst these factors, the major factor affecting the performance of structural measurement is the measurement speed. The time for reflectorless measurement taken by a total station varies from 1 point per 2.2 to 7.0 seconds (in Leica TPS800 series; Nikon NPL-821 series; Pentax R-300X series; Sokkia Set030R series; Topcon GPT-7000 series; Trimble 5600 series), while the scan rate of time-of-flight laser scanners ranges from 1 750 to 12 000 points per second (in Callidus CP3200; Leica HDS3000; Riegl UK LMS-Z360i; Trimble GS200) and it is at least 500 000 Hz for phase comparison scanners (Leica HDS4500; Z+F UK Ltd LARA 25200). The fast sampling speed of TLS allows a more complete and detailed point model of the object surface to be derived efficiently (Alba et al., 2006; Ioannides et al., 2006), rather than only measuring limited points using total stations (Merkle and Myers, 2004; D'Ayala and Smars, 2003). Therefore it is proposed to introduce the technique of TLS into the membrane structure monitoring scheme for generating the surface model of the fabric roof. The resultant as-built model is consequently used in comparison with the mathematical model, determining the disparities between the finished structure and the designed drawing.

According to the range measurement principle, attainable measurement distance and accuracy, terrestrial laser scanners are classified into four categories (Table 2-1). Considering the required accuracy and the measuring distance at the test site, the phase comparison and median-range time-of-flight laser scanners are more appropriate instruments. Once the scanned models of the membrane structures are derived, their accuracy will be evaluated, thus validating the reliability of the following surface comparison and analysis.

From the projects discussed in Section 2.3.4, it is found that TLS is capable of

undertaking structural monitoring tasks. Unlike the low-density observations made by total station instruments, a much more complete object surface is measured using TLS. The deformation occurring at different epochs can be investigated based on measurements taken across the whole surface. However, as an irregular point cloud is derived each epoch, the deformation analysis can not be undertaken directly. To achieve this, data modelling is performed to convert the scanned data into a regular form and partial filtering of measurement noise is accomplished (Lindenbergh and Pfeifer, 2005). A more precise representation of the scanned object is therefore generated. The deformation analysis is subsequently carried out based on these modelled surfaces. As stated by Gordon et al. (2004), the appropriate modelling method should be selected by the degree to which it permits accurate computation of the deformation. Considering the efficiency, the area-based method adopted by Schafer et al. (2004) is introduced in the membrane structure monitoring scheme in order to determine the disparities between the designed and finished structure. The implementation is explained in Figure 2-9, in which the data of epoch 0 and epoch 1 are replaced by the mathematical model and the scanned model. This process allows resolution of the differences between the two surfaces. When using this method, van Gosliga et al. (2006) highlight that a proper interpolated grid size should be given in accordance with the required level of deformation detail. Small deformations may not be determined if a large interpolated grid size is used.

The feasibility of using TLS to determine the dynamic behaviour of the membrane roof is further discussed. For capturing fast-moving and unpredictable displacements occurring across the surface, a sequential surface model with short temporal interval is required. However, from the implementation of laser scanning, it is found that although the object is rapidly scanned point by point, it still takes some time to finish scanning the surface of interest. As the surface model is not generated at a specific instant, the result derived from the comparison between any two scanned surface models doesn't indicate the differences occurring at any two specific epochs. Due to the rationale of deriving the surface model, the TLS technique is only capable of monitoring objects with predictable or occasional movements (such as the projects demonstrated in Section 2.3.4). For the purpose of determining the dynamic behaviour of a membrane roof in the monitoring scheme, other techniques will be employed.

2.4 Image-based Measurement Methods

As discussed in Section 2.3, although TLS is potentially practical to solve structural

deformation problems, the nature of data collection constrains its application in determining rapid and unpredictable displacements occurring on the membrane roof. In order to solve this problem, image-based measurement methods are considered and their feasibilities are reviewed below.

2.4.1 Digital Photogrammetry and Computer Vision

Amongst image-based measurement methods, photogrammetry is the most recognised technique in the field of geomatics. Fryer (2001b) defines photogrammetry as "the science and art of determining the size and shape of objects through image analysis". The 3D coordinates of a specific object in space can be computed from the corresponding 2D information extracted from recorded photos through photogrammetric processing. Thompson (1962) further stated that photogrammetric methods of measurement are especially useful in conditions where the object to be measured is inaccessible, or when the object is not rigid and its instantaneous dimensions are required. Due to the features of rapid data acquisition, non-contact measurement, permanent recording, and capabilities of measuring deformation and movement, photogrammetry demonstrates its capacity to be used in many applications involving measurement (Torlegard, 1980; Waldhausl, 1992). Along with the developments in micro-electronics and semiconductor technology since the 1990s, digital photogrammetry has been driven by the development of new sensors (such as solid state cameras) and more powerful computers. The improving efficiency in image processing and automated measurement have resulted in an increasing number of fully automated systems and diversity of photogrammetric applications (Mills, 1996; Wolf and Dewitt, 2000; Fryer, 2001b; Gruen, 2001). Thereby the subsequent discussions will focus on digital photogrammetry.

In the early days of photogrammetry, the science was treated as a tool for topographic mapping, and applications outside the realm of topography were therefore encompassed by the term "non-topographic photogrammetry" (Karara, 1989). In addition, a number of terms were used to describe more specific photogrammetric applications. For example, when the extent of the object to be measured is less than approximately 100 metres, and when the cameras are positioned close to it, the term "close range photogrammetry" is used to indicate the operation (Cooper and Robson, 2001). For measuring dynamic objects and tracking a moving trajectory with high temporal resolution requirements, "videogrammetry" offers a practical method (Gruen, 1997; Ryall and Fraser, 2002). Black and Pappa (2003) further define videogrammetry as "the

science of calculating 3D object coordinates as a function of time from image sequences captured by video cameras, enabling the observed object to be defined dynamically".

Meanwhile another image-based method, computer vision, is also commonly studied and exploited by the communities of computer science and electrical engineering. As defined by Haralick and Shapiro (1992), computer vision is "the science that develops the theoretical and algorithmic basis by which useful information about the world can be automatically extracted and analysed from an observed image, image set, or image sequence from computations made by special-purpose or general-purpose computers". Similar to photogrammetry, computer vision aims to relate 2D information extracted from images to a 3D description of any unknown object in the real world. However, computer vision research focuses more on questions such as how to automatically recognise objects in digital images, how to represent those objects in a computer, how to determine the shapes of objects from imagery, and how to reconstruct the position and orientation of the recorded images or imaged objects (Ballard and Brown, 1982; Haralick and Shapiro, 1992; Vosselman et al., 2004). Based on these objectives, computer vision can be divided into two broad categories: machine vision and image understanding (Vernon, 1991).

In machine vision, imaging conditions (e.g. lighting and camera positioning) are typically close range and highly controlled. Objects in the scene are relatively well defined for specific extraction tasks (Agouris et al., 2004). Rather than true 3D measurement, most applications are used in the manufacturing industry for inspection of machine parts, optical character recognition, and feature extraction from scanned images. Machine vision algorithms tend to be simple, fast, and provide precise dimensional or orientation measurements (Sleigh, 1991). Moreover, robot vision is a subclass of machine vision in the sense it uses the machine vision principles strictly for time-constrained solutions (Vernon, 1991; Gruen, 2001). The requirement of direct feedback for guiding the robot demands fast image processing to obtain the analysis and 3D description of the robot environment. In image understanding, problems that are often met involve features in the scene being ambiguous, and the existence of background clutter and noise. In addition, images may consist of several multispectral bands, which is rarely the case in machine vision (Agouris et al., 2004). The goal of image understanding is to model the scene for facilitating some form of feature extraction. Typical image understanding applications in Geomatics involve object detection and extraction from remotely sensed imagery from space, aerial and terrestrial sensors.

To summarise, image-based measurement methods can be broadly divided into two groups, digital photogrammetry and computer vision. The subclasses and interrelations between the techniques introduced above are illustrated in Figure 2-13. As numerous theories and algorithms in image processing, object representations, feature extraction and image matching have been developed in computer vision research over the past few decades, these techniques have increasingly been incorporated into modern digital photogrammetry systems in the form of automated tools that improve robustness and increase efficiency (Mikhail et al., 2001; Agouris et al., 2004; Vosselman et al., 2004). These developments have provided overlap between the two techniques.

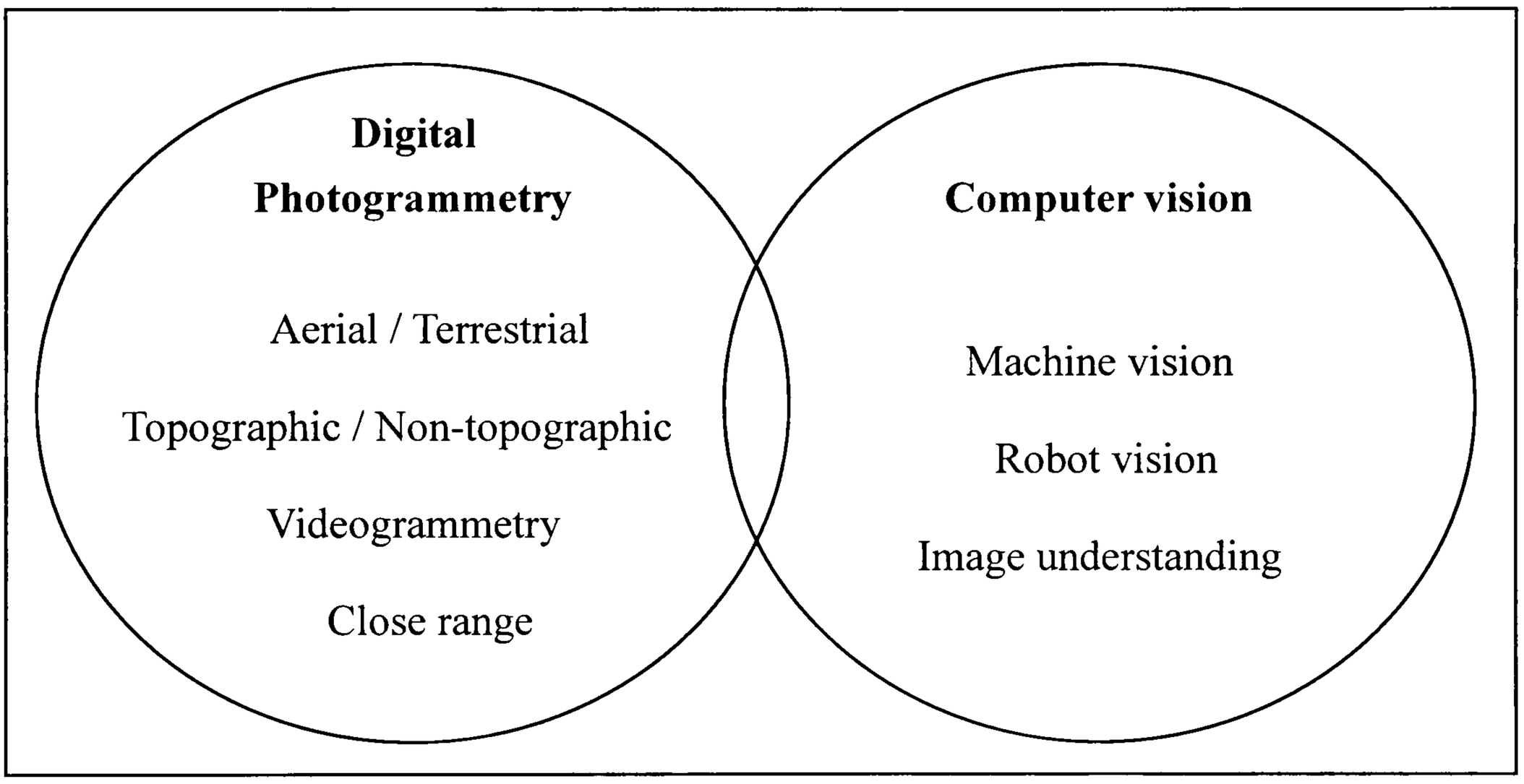


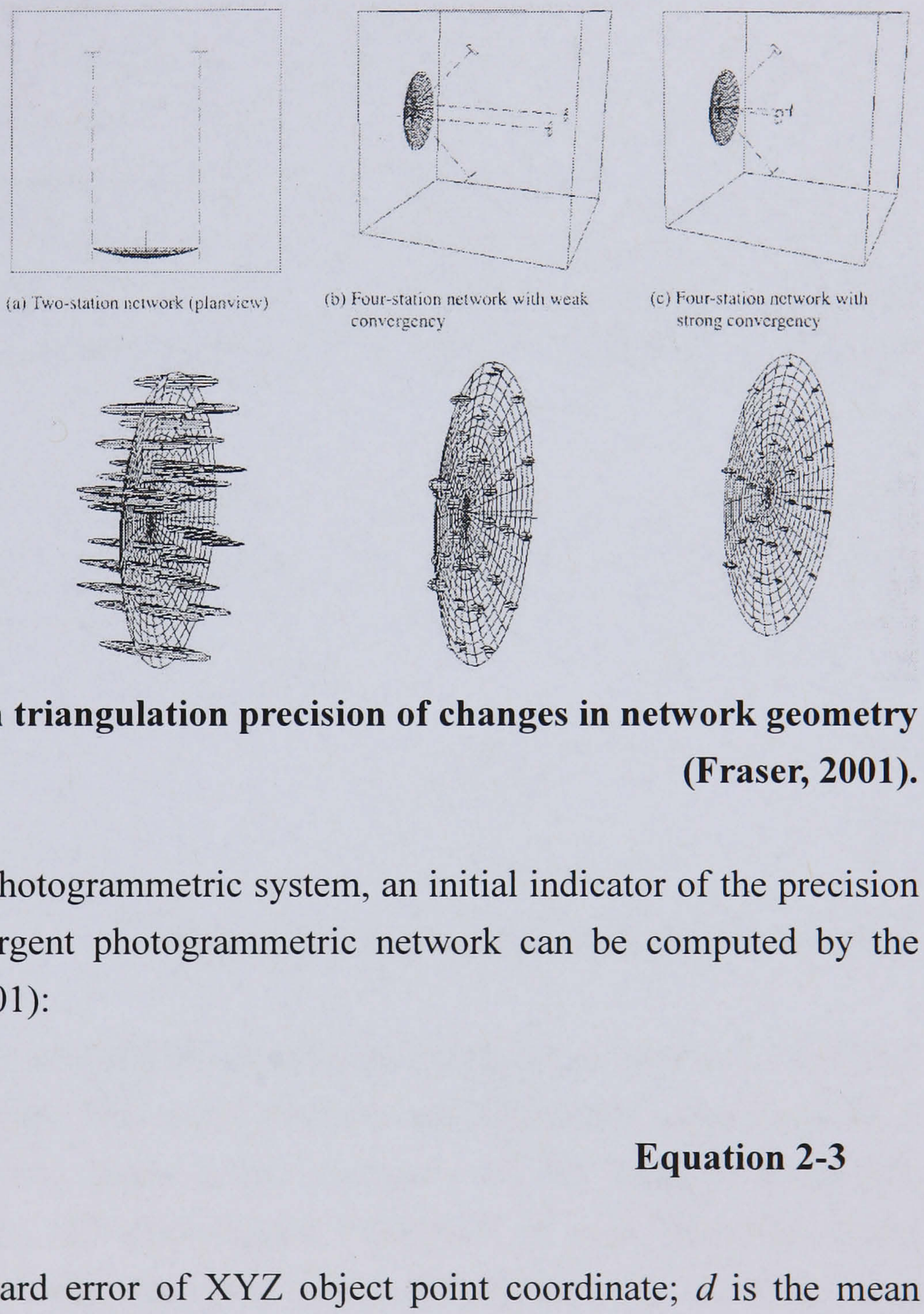
Figure 2-13: The interrelation of various image-based measurement methods.

2.4.2 Principles of Digital Photogrammetry

2.4.2.1 Network Design

Within the applications of close range photogrammetry, network design plays an important role in the optimisation of measurement performance in terms of both accuracy and economy. Various factors including the selection of image scale, the number of camera stations and their relative geometry should be considered at the stage of network design (Fraser, 2001). Network geometry is the principal design parameter. It is established with a variable number of cameras in different positions, and a higher triangulation precision will be derived from measurements made with a strong network geometry. In Figure 2-14, three different photogrammetric networks were used to measure the same target array and the error ellipses of the measured points illustrated (Fraser, 2001). For the two-station stereoscopic configuration (Figure 2-14 (a)), the

measurement precision in depth was found to be relatively poor. However in the next network, the precision was improved due to the addition of convergent imagery. The most optimal solution was found in the third network, a convergent configuration of four images, considered a "strong" network geometry. High precision measurement usually requires multi-image, convergent networks, whereas stereo solutions can be expected to be two to five times less accurate (Fraser, 2006).



(a) Two-station network (planview)

(b) Four-station network with weak convergency

(c) Four-station network with strong convergency

Figure 2-14: The effect on triangulation precision of changes in network geometry (Fraser, 2001).

For developing an optimal photogrammetric system, an initial indicator of the precision of triangulation in a convergent photogrammetric network can be computed by the formula given by Fraser (2001):

$$\sigma_c = \frac{q}{\sqrt{k}} \frac{d}{c} \sigma \qquad \textbf{Equation 2-3}$$

where σ_c is the mean standard error of XYZ object point coordinate; d is the mean camera-object distance; c is the camera principal distance (thus d/c is the given scale number); σ is the image coordinate standard error; q is design factor expressing the strength of the camera station configuration (stronger network geometry is represented by a smaller q value); and k is the average number of exposures at each station. From Equation 2-3, it is clear that in addition to the strong camera network, the measurement precision will improve with the increasing number of exposures recorded at each station, more accurate image mensuration, and smaller scale number.

In some applications where only two cameras are available and their positions are fixed (for example in a dynamic object observation), the expected standard deviations of the space coordinates (m_T) are estimated by the formula (Marzan and Karara, 1976):

$$m_T = \frac{D}{2} m \sqrt{(\frac{1}{2}\sec^2\phi + \frac{1}{2} + \frac{1}{2}\cos^2\phi)} \qquad \textbf{Equation 2-4}$$

where m is the accuracy of the image coordinates and D is the object distance. Since this formula is developed under the assumption of symmetrical situation, ϕ is equal to half of the value of the convergence angle, θ (Figure 2-15). From Equation 2-4, it is found the angular orientation of the camera is also an important consideration in the network design. To achieve highest overall accuracy, Fraser (2006) stated that the desirable operating field of view is typically 35° to 80°. Wolf and Dewitt (2000) identified the ideal convergent angle as close to 90°, while small convergent angles should be avoided.

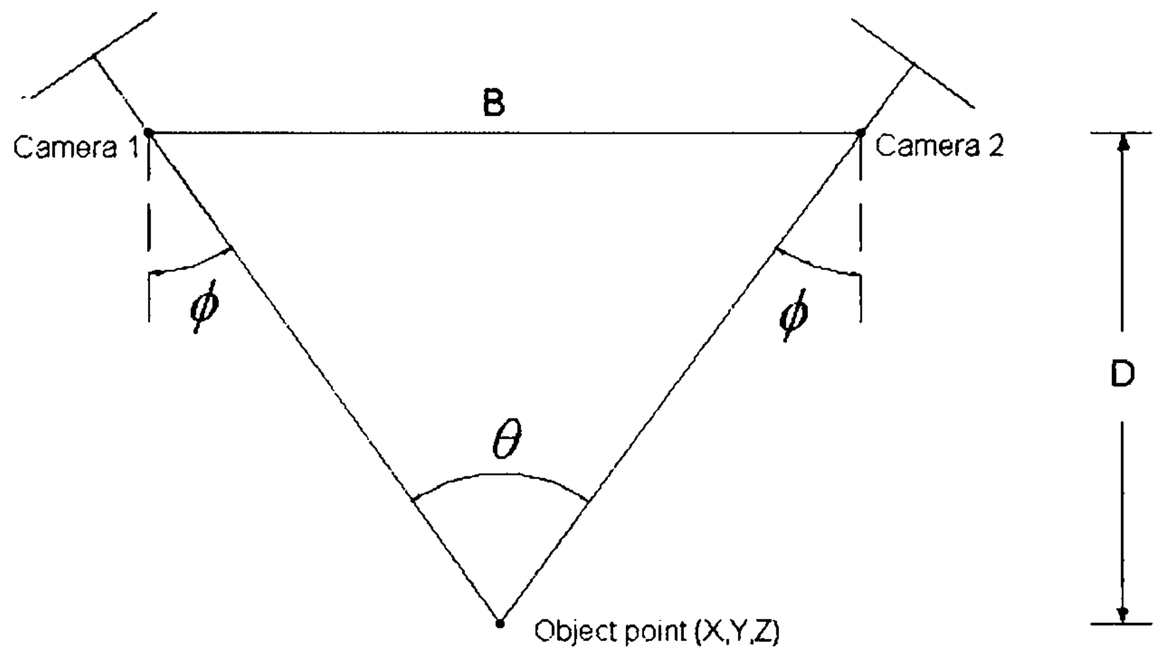


Figure 2-15: The symmetrical camera network.

From the above discussion, the factors involved in the design of a network are realised. However, it is noteworthy that these considerations are frequently constrained by a number of physical conditions, such as the capability of the cameras employed, visibility of the object points, and the confined workspace or short allowable object distance (Mason, 1995). Therefore for optimising a photogrammetric network, these constraints must also be taken into account.

2.4.2.2 Bundle Adjustment

Collinearity, a fundamental principle of photogrammetry, is the condition in which the object point (A), exposure station (O) and image point (a) all lie on a straight line (Figure 2-16). To represent the relation between point "a" within the image space and

point "A" of the object space as a mathematical form, the collinearity equations are developed:

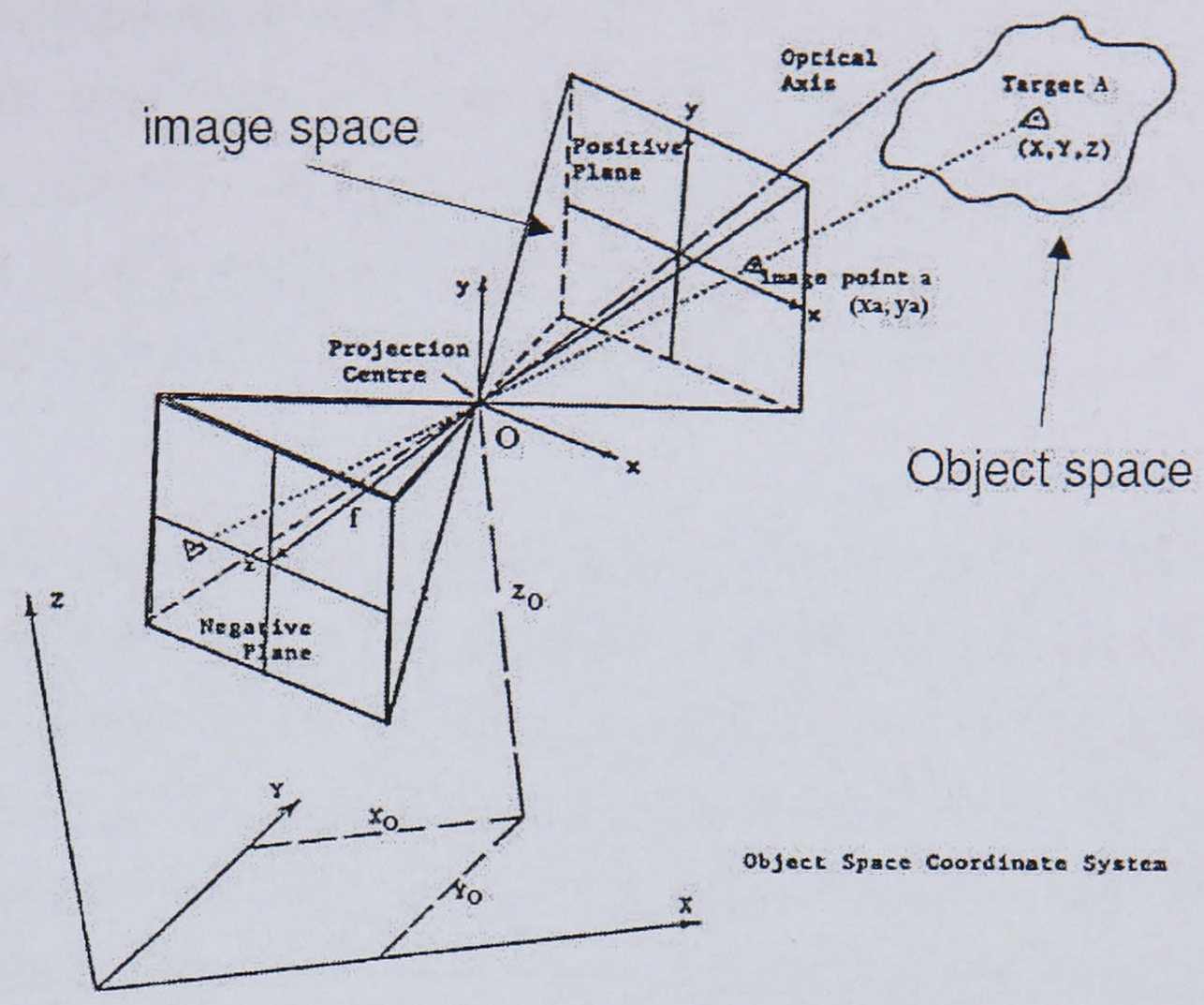


Figure 2-16: The collinearity condition (after Fraser, 2006).

$$x_a = -f\left[\frac{m_{11}(X_A - X_O) + m_{12}(Y_A - Y_O) + m_{13}(Z_A - Z_O)}{m_{31}(X_A - X_O) + m_{32}(Y_A - Y_O) + m_{33}(Z_A - Z_O)}\right] \qquad \textbf{Equation 2-5}$$

$$y_a = -f\left[\frac{m_{21}(X_A - X_O) + m_{22}(Y_A - Y_O) + m_{23}(Z_A - Z_O)}{m_{31}(X_A - X_O) + m_{32}(Y_A - Y_O) + m_{33}(Z_A - Z_O)}\right] \qquad \textbf{Equation 2-6}$$

where $m_{11} = \cos\phi\cos\kappa$

$m_{12} = \sin\omega\sin\phi\cos\kappa + \cos\omega\sin\kappa$

$m_{13} = -\cos\omega\sin\phi\cos\kappa + \sin\omega\sin\kappa$

$m_{21} = -\cos\phi\sin\kappa$

$m_{22} = -\sin\omega\sin\phi\sin\kappa + \cos\omega\cos\kappa$

$m_{23} = \cos\omega\sin\phi\sin\kappa + \sin\omega\cos\kappa$

$m_{31} = \sin\phi$

$m_{32} = -\sin\omega\cos\phi$

$m_{33} = \cos\omega\cos\phi$

and x_a and y_a are the image coordinates of an image point a; f is the camera focal length;

X_A, Y_A and Z_A are the coordinates of object point A; and X_O, Y_O and Z_O are the coordinates of exposure stations (Wolf and Dewitt, 2000). The collinearity equations (Equations 2-5 and 2-6) can be written for each point, their form depending on which variables are treated as observables, knowns, or unknowns, and can be used for different purposes, such as space intersection, space resection, as well as for other tasks (Mikhail et al., 2001). It is noted that in order to implement photogrammetric models, the departures from collinearity (such as lens distortion and errors in interior orientation, which are discussed in the next section) have to be compensated (Fraser, 2006).

A bundle adjustment is a computational procedure that optimises all the unknown and observed data to solve the best orientation of the camera at time of exposure, and the 3D coordinates of the points observed. The standard collinearity equations are the basis of the bundle adjustment as applied to close range photogrammetry (Mikhail et al., 2001). When one camera is used to take an exposure, it is imagined that a bundle of rays or directions is recorded simultaneously in the image. In a set of images in close range photogrammetry, bundles of spatial directions are derived in individual images, and they are tied together by common object points (Kraus, 1993; Wolf and Dewitt, 2000). An example network of photogrammetric bundles is shown in Figure 2-17.

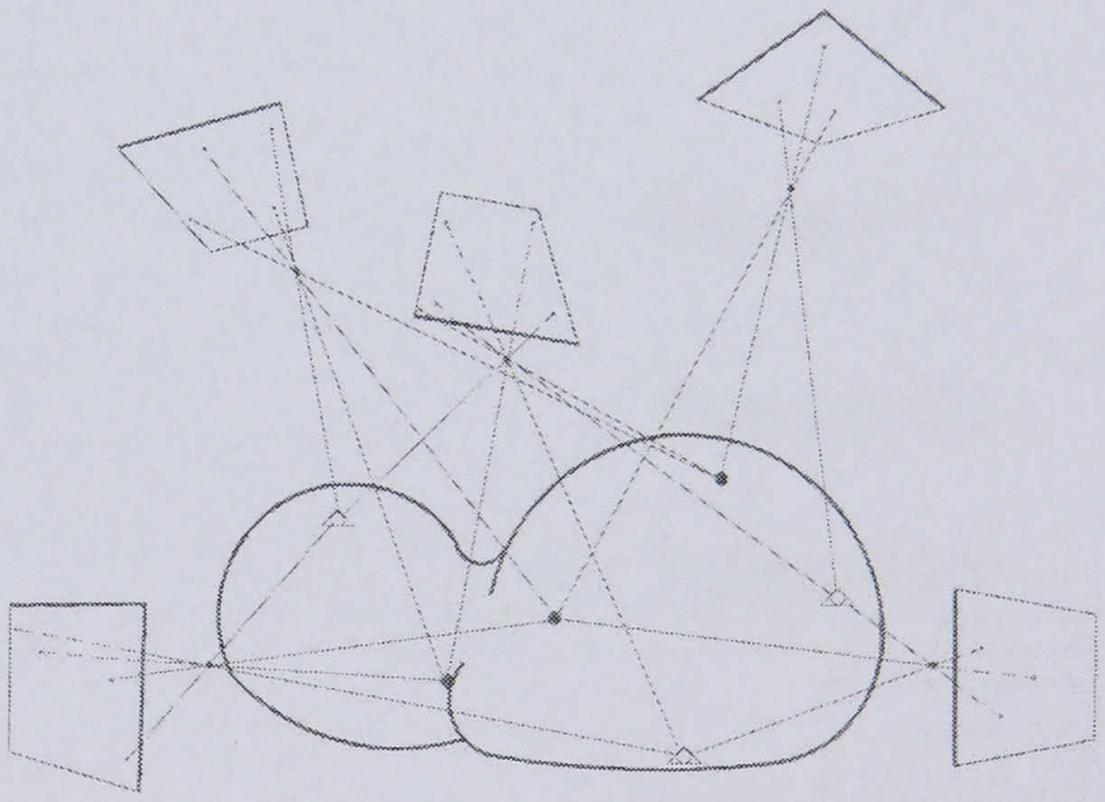


Figure 2-17: Network of photogrammetric bundles (Kraus, 1993).

A least squares adjustment of the photogrammetric bundles is performed as a bundle adjustment. To ensure the least squares solution is possible, an understanding of the number of observations required is needed. The unknown quantities to be obtained in a bundle adjustment are the six elements of exterior orientation of each exposure and the 3D coordinates of each object point. Assuming there are m images and n unknown object points, then the total number of unknowns is $(m\times6) + (n\times3)$. Normally the measurement associated with a bundle adjustment are image coordinates of object

points and 3D coordinates of control points, assuming p imaged points and q control points are measured, then a total of $(p\times2) + (q\times3)$ are derived. For solving the bundle adjustment, the number of observations $(p\times2) + (q\times3)$ should be greater than the number of unknowns $(m\times6) + (n\times3)$. Moreover, if the exterior orientations of each camera are also measured, $(m\times6)$ additional observations will be included in the adjustment.

2.4.2.3 Camera Calibration

In order to determine and evaluate the performance of a lens or an imaging data acquisition system employed in a photogrammetric application, a procedure of camera calibration is performed (Ziemann and El-Hakim, 1982). For a metric camera, this is normally carried out using a multicollimator or goniometer in a laboratory by camera manufacturers (refer to Wolf and Dewitt (2000) and Boland et al. (2004) for the detailed operations), while a non-metric camera generally requires a calibration each time it is used. Through the camera calibration, the elements of interior orientation of the camera, including focal length (f), principal point location (P_X, P_Y), and radial (dR_x, dR_y) and decentring lens distortion (dD_x, dD_y), are determined and used for refining the image measurement. Radial and decentring lens distortions are computed using the formulae below:

$$dR = k_1 \cdot r^3 + k_2 \cdot r^5 + k_3 \cdot r^7 \qquad \textbf{Equation 2-7}$$

$$dR_x = dR \cdot x / r \qquad \textbf{Equation 2-8}$$

$$dR_y = dR \cdot y / r \qquad \textbf{Equation 2-9}$$

$$dD_x = p_1(r^2 + 2x) + 2p_2 \cdot x \cdot y \qquad \textbf{Equation 2-10}$$

$$dD_y = 2p_1 \cdot x \cdot y + p_2(r^2 + 2y) \qquad \textbf{Equation 2-11}$$

where k_1, k_2 and k_3 are the coefficients of radial distortion, p_1 and p_2 are the coefficients of decentring distortion, r is the radial distance from the principal point, and x and y are coordinates of the image relative to the principal point.

For high accuracy applications, Mikhail et al. (2001) indicates it is common to perform

an initial laboratory calibration and then refine the camera parameters as part of a bundle adjustment. The later process is called a self-calibrating bundle adjustment (Granshaw, 1980). To this end, the collinearity equations (Equation 2-5 and 2-6) are augmented with additional terms to account for adjustment of the focal length, principal point offsets, and systematic radial and decentring lens distortion (Wolf and Dewitt, 2000). Once the adjustment is finished, the camera calibration parameters are solved along with the 3D coordinates of the object points and the exterior orientation of each camera. Compared with a calibration carried out in a fully controlled laboratory, self-calibration is performed under the operational environment as part of the bundle adjustment solution, thus avoiding the uncorrected systematic errors caused by the differences in environmental conditions between the laboratory calibration and the operational environment (Mikhail et al., 2001).

In order to guarantee the solution of a self-calibrating bundle adjustment, two issues have to be considered. The first point is the correlation between the interior and exterior orientation parameters added in the collinearity equations. If there is not enough geometric information to separate the effects of the parameters, they may be highly correlated to each other and the solution may not produce satisfactory results. For example, with narrow-angle lenses, a small change in principal point location produces image displacements nearly identical to those produced by a small tilt or shift of the camera (Mikhail et al., 2001). As the parameters involved and the level of correlation vary according to the imaging geometry, a photogrammetric system with strong network design (described in the previous section) is therefore used to minimise the affect of the correlation (Wolf and Dewitt, 2000). Secondly, Fryer (2001a) stated that the geometrical arrangement of the camera stations, the intersection angles of rays from object points to cameras, the number of targeted points seen from different camera locations, and the spread of targeted points across the image scene are all important factors influencing both the precision of the targets' coordinates on the object and the parameters of the camera calibration. As recommended by Robson and Shortis (2001), a minimum of 15-20 photographs and 20-50 targets arranged in a 3D site are ideal for a confident determination of the target coordinates and the camera calibration parameters for a self-calibrating bundle adjustment.

Camera calibration is also an interesting topic in the communities of computer/machine vision. Rather than adopting arranged points with known 3D coordinates, Tsai (1987) used a planar board containing aligned black square targets as an imaging target for calibration. The board was set at different distances from the camera and exposures

made. The corners of the black squares are used as control points and the parameters of exterior and interior orientations are then solved in the calibration. Following this idea, a number of calibration procedures were developed, such as Zhang (2000), Scaramuzza (2007), Stoyanov (2007) and Strobl et al. (2007). In most of these projects, a stand-alone GUI program was developed for performing the calibration (Figure 2-18). Although this type of calibration is convenient, simple and accurate enough for most computer vision applications (Mikhail et al., 2001), Heikkila (2000) points out that the simplifications may reduce the precision of the estimated parameters, and as a consequence, they are not suitable for applications in accurate 3D metrology.

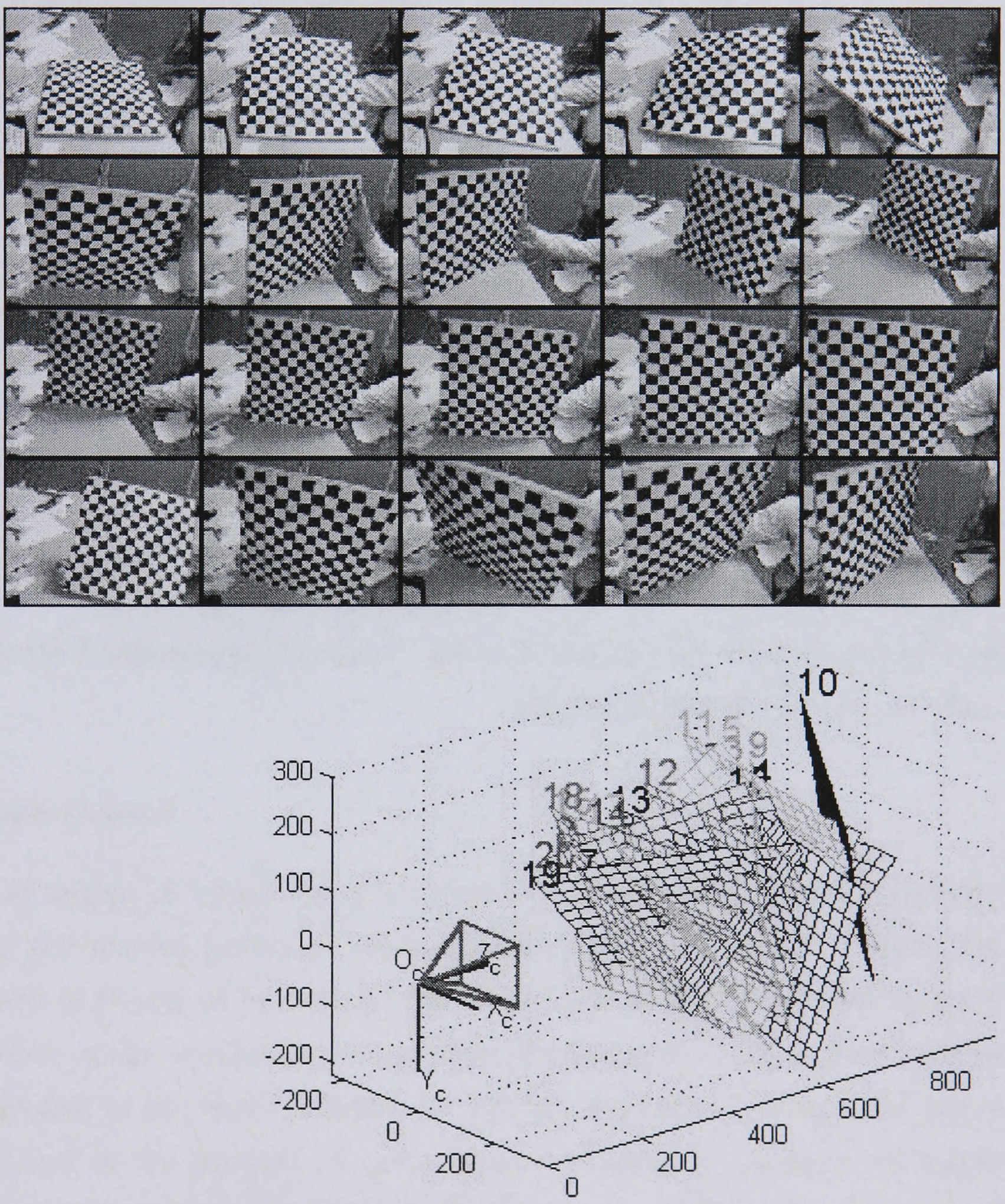


Figure 2-18: Images of a calibration planar checkerboard (top) and the solved 3D positions of the grids with respect to the camera (bottom) (Strobl et al., 2007).

In some machine vision applications where video cameras are employed, camera

calibration can be undertaken using the "moved reference bar" method (Maas, 1998a), which is based on moving a reference bar of known length through object space (Figure 2-19). This reference bar is imaged by all video cameras at a number of locations and orientations within the scene. Two targets attached at each end of the bar are then tracked and matched in the synchronous image sequences. The constant length of the reference bar is used as an additional geometric constraint in the self-calibrating bundle adjustment, and as a result the full calibration of each camera is determined. Due to its obvious simplicity, research conducted by Borghese et al. (2001), D'Apuzzo (2002) and Machacek et al. (2003) also adopted the moved reference bar for camera calibration. Based on the same concept, Svoboda et al. (2005) exploited a laser pointer as a "moved single-point" to calibrate a multi-camera system.

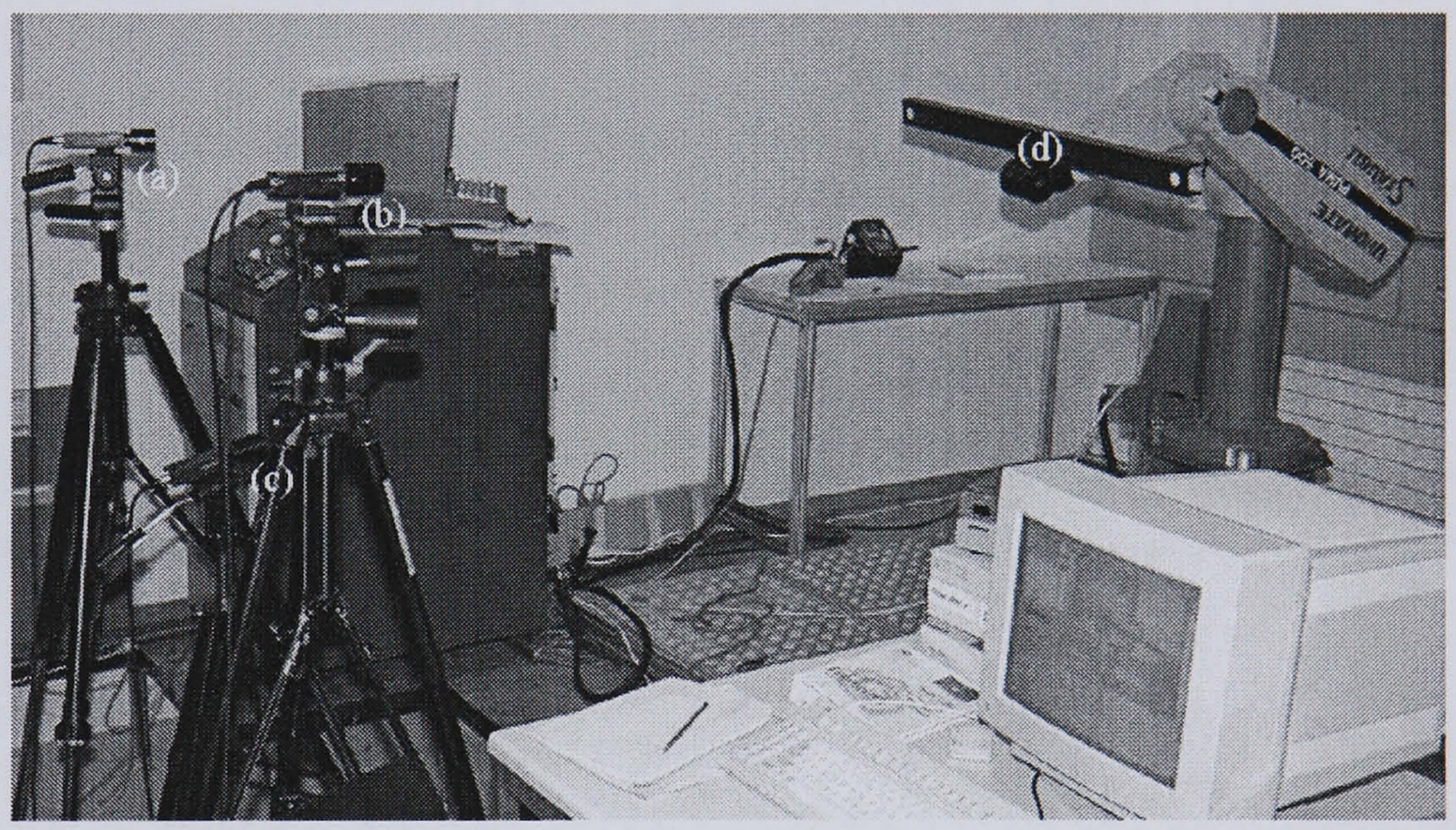


Figure 2-19: Calibrating the video cameras ((a), (b) and (c)) with a moved reference bar (d) (Maas, 1998a).

2.4.2.4 Image Measurement

A certain number of targets in object space are generally required in photogrammetric applications. Being the control points or representation of the objects of interest, the targets are positioned at points of interest on the object and imaged from two or more camera stations. When image acquisition is complete, the imagery is either processed in real-time or downloaded to the host computer for off-line processing. In general, there are two tasks required in the process of computing the subpixel locations of target images, namely target recognition and location (Robson et al., 1999). The detection of the target images is firstly performed to unambiguously identify targets within a scene and their coarse locations are determined. Once located, the centres of these targets are then precisely and accurately computed (Shortis et al., 1994a). The resulting image measurements are converted to object coordinates in a bundle adjustment.

Some applications of target recognition concentrate on separating the target images from a cluttered background using a combination of patterned targets and filtering of the image. The targets are identified using a sufficient contrast between the target and its background, or specific patterns which are unlikely to be accidentally replicated by the background features (Wong et al., 1988; van den Heuvel et al., 1992). Image segmentation is an alternative technique to highlight the targets. By examining the intensity histogram of the image, the optimum threshold value is determined and it is used to segment the entire image and isolate the target images. The digital image may retain grey value intensities above the threshold, or be binarised for faster processing (Shortis et al., 1994a). Target detection can then be carried out using scan-line searches on binary images (Clarke et al., 1993), or image correlation on grey-scaled images (Shortis et al., 1994b).

Once the targets are recognised, target measurement can be performed manually or automatically to determine the subpixel position of the target images. Using the automated approach, it is typically achieved by centroiding techniques or least squares template matching (Mills, 1996). By using the centroid method, a subset rectangular window is employed to enclose the target image and the target centre is estimated by the formulae given by Trinder (1989):

$$x = \frac{\sum_{i=1}^{n}\sum_{j=1}^{m} j \cdot g_{ij}}{\sum_{i=1}^{n}\sum_{j=1}^{m} g_{ij}} \quad and \quad y = \frac{\sum_{i=1}^{n}\sum_{j=1}^{m} i \cdot g_{ij}}{\sum_{i=1}^{n}\sum_{j=1}^{m} g_{ij}} \qquad \textbf{Equation 2-12}$$

where (n, m) is the size of the rectangular window, g_{ij} is the digital number (DN) value of each pixel, either 0 or 1 located in row i column j in the binary centroiding. While in the grey scale centroid, there is no threshold being applied to the DN values (Chen and Clarke, 1992; Shortis et al., 1994a).

In template matching, the goal is to find whether a pre-defined sub-image is contained within a test image. The sub-image is called a template and should be an ideal representation of the pattern or object which is being sought in the image (Vernon, 1991). For determining the position of the target fitted to the template, the matching is performed by moving the template to every possible position in the test image. The optimum match is determined by a maximum "similarity measure", which is a mathematical function examining the degree of correlation between corresponding DN

values of pixels being matched. When the least squares matching technique is introduced, the match location can be determined to a fraction of a pixel, at which the subpixel level precision is achievable (Wolf and Dewitt, 2000).

Comparing the two techniques for determining target location, it is concluded that the least squares matching method is able to indicate the "goodness of fit" between the target and an ideal template, whereas efficient computing time is required by using centroiding methods (Clarke et al., 1993). Although there are some differences between the two methods, no significant differences are found between the results of least squares matching and centroiding techniques (Maas and Kersten, 1994). Therefore, target location can be determined by either method based on the specifications of the application, and the resulting targeting precision are both able to achieve 0.03 – 0.05 pixels if good quality image targets are measured (Fraser, 2006).

The use of retro-reflective targets has become widespread due to the advantageous characteristics of the high return of light in the direction of illumination (Clarke, 1994). Both the centroiding and template matching techniques can be applied to derive the centres of the retro-reflective targets. Since all the subsequent processes in high accuracy 3D measurement rely on the resulting target measurement, the task of targeting undertaken at the initial stage is important (Shortis et al., 1994a). For an accurate and reliable operation, three primary issues with using retro-reflective targets are summarised and the following principles should be considered jointly at the stage of network design:

- Target size

The size of the target shown in the image is the primary factor influencing the targeting accuracy. If targets are too small in the images, a deterioration of the measuring accuracy will occur due to the small signal and discrete sampling. Conversely, if targets are too large, they may interfere with other targets or the background, or even produce systematic errors which will affect accuracy as well (Robson and Shortis, 2001). To optimise the target image measurement, Beyer (1992) and Clarke et al. (1993) suggest the optimum retro-reflective target should have a diameter of at least 6 pixels to attain utmost internal precision. A similar recommendation from Robson and Shortis (2001) point out the target image diameters should be approximately 5-10 pixels in the imagery.

□ Imaging angle

In order to understand the factors causing targeting offsets, the fabrication of a retro-reflective target is introduced. The cross-section of a retro-reflective target is shown in Figure 2-20, at which small glass spheres glued onto a base paper are responsible for reflecting light rays. To create a circular target, a circular mask is painted or glued onto the retro-reflective material. Since the glass spheres reflect light rays back in the same direction from which they came, the resulting edge of the glass spheres will change if the target is viewed from different angles. In Figure 2-20, for example, the target centre is shifted to the right if it is viewed from the left (Zumbrunn, 1995; Otepka, 2004).

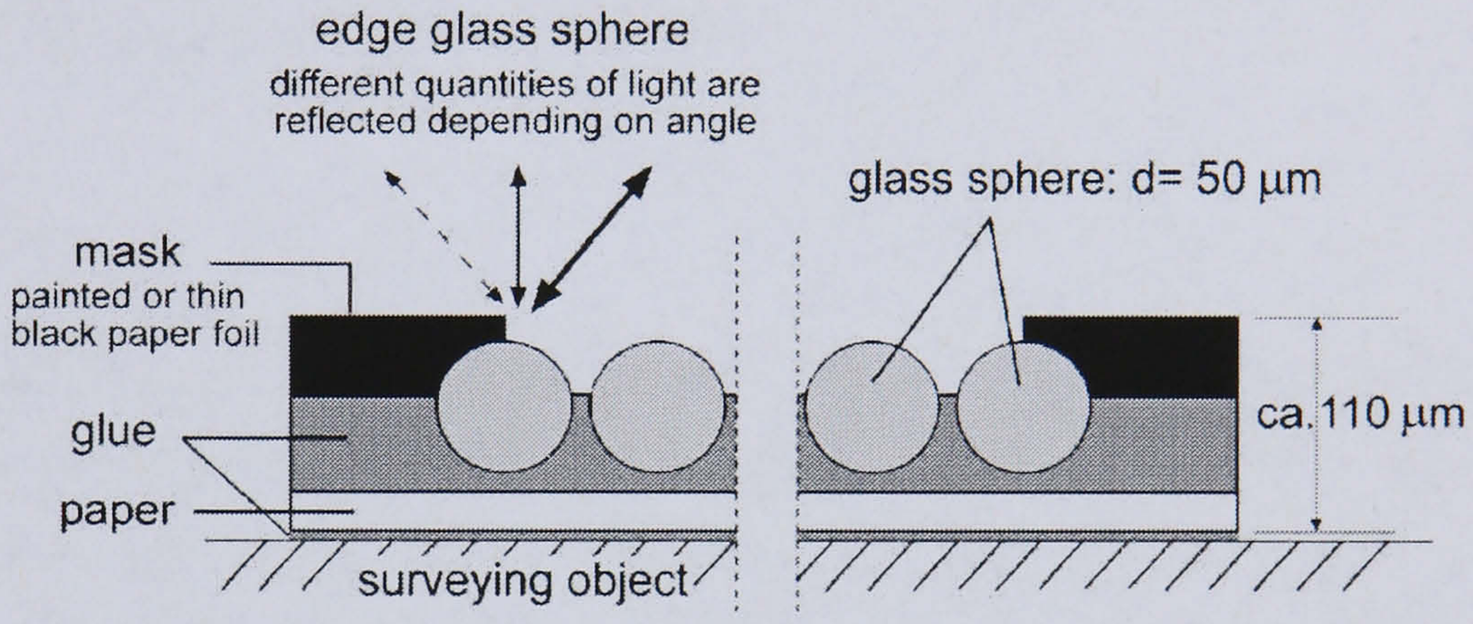


Figure 2-20: Cross section of retro-reflective target (Zumbrunn, 1995)

Zumbrunn (1995) indicates this shift is only caused by the changing degree of light reflection of edge spheres, although the thickness of the edge mask will further affect the shift. As a result, the centre of a target (constructed of 50 µm diameter glass spheres) shifted by +/- 30 µm when the viewing angle altered by +/- 40°. Moreover, from the experiment conducted by Clarke (1994), it is specified that the targets should present an angle of less than 45° to the camera to obtain sufficient light return for consistent high precision target location.

□ Illumination

The illumination of the working environment can considerably influence the achievable targeting quality (van den Heuvel, 1993). By repeating measuring targets illuminated at different intensities, Fraser and Shortis (1995) found the RMS error of image coordinates residuals of saturated targets to be 0.17 µm, while it was 0.19 µm with the non-saturated targets. Moreover, Clarke et al. (1994) stated that uneven illumination will cause poor target location. It would therefore indicate that a higher and even illumination produces superior targeting accuracy.

2.4.3 Instrumentation for Data Acquisition

As addressed in Section 2.4.2.1, a multi-station convergent imaging configuration is essential for photogrammetric applications where accurate results are required. In practice this can be accomplished by employing a single camera to take exposures at different stations or set one camera at each station. The general prerequisite in adopting the first method is that the shape of the object is invariant throughout the period when the imagery is recorded (Ryall and Fraser, 2002). However, in the latter approach if multiple cameras capable of shooting synchronous image sequences are utilised, this camera configuration is also suited to dynamic event monitoring since the object is recorded at each measurement epoch at a particular instant of time. Because the object to be observed in this research is a dynamic membrane roof, the potential cameras for recording image sequences simultaneously are introduced.

2.4.3.1 CCD Video Cameras

A charge coupled device (CCD) is the most commonly used device for recording digital images for photogrammetric applications. In a CCD video camera, a CCD sensor, which consists of a two dimensional array of closely spaced light sensitive elements, is arranged to record the light falling onto the two dimensional surface at a particular instant of time. Each element on the CCD sensor generally represents a pixel in a subsequently derived digital image array. The CCD works by converting light photons which fall onto the sensor surface into electrons. These are accumulated in capacitors and then put through Analogue / Digital (A/D) conversion to convert into digital form for output (Dowman, 2001). The size of the array and the pixel size are the most important characteristics of a camera for photogrammetric use, as accurate measurement is more achievable when larger and higher resolution CCD sensors are utilised (Uffenkamp, 1993; Mills, 1996). A full description of sensor technology for close range applications can be found in Shortis and Beyer (2001).

For analogue video cameras, additional equipment called a frame grabber is required for performing the A/D conversion and storage of a complete image frame (Figure 2-21). Standard single circuit frame grabber boards usually come with an A/D converter, one or more frame memories, arithmetic processors, control and clocking circuits as well as three D/A converters for red, green and blue (RGB) outputs to a colour computer monitor. In addition, some advanced frame grabbers are able to channel the image data directly into the host computer memory at video rate (Gruen, 1997).

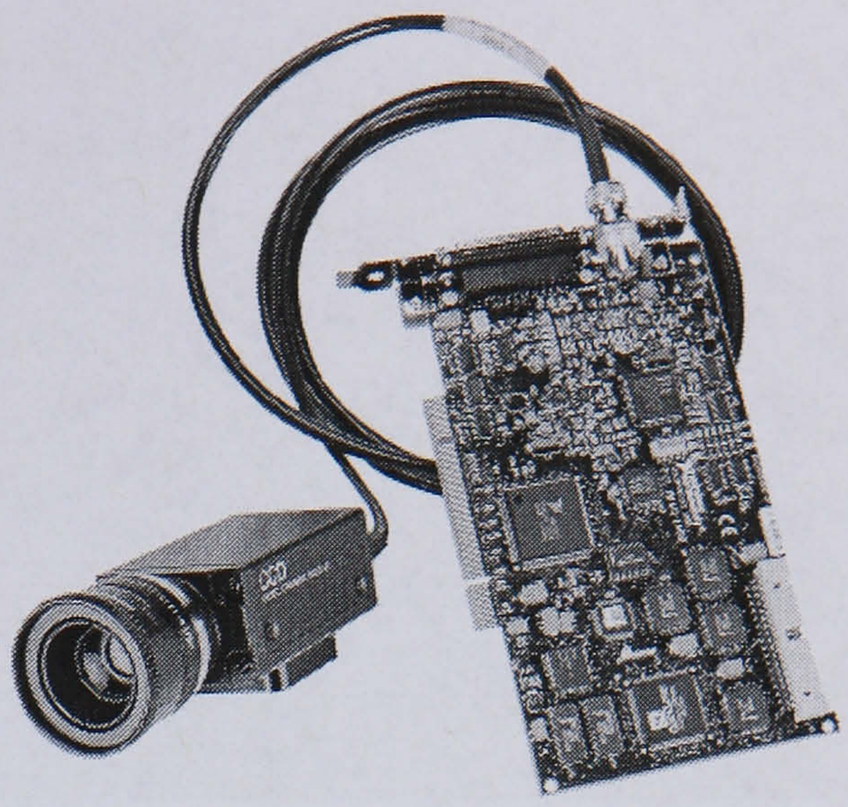


Figure 2-21: CCD analogue video camera and frame grabber (National Instruments, 2007).

Video signals are normally generated at the output of a camera by one of two scanning methods. If a frame is formed by the single scanning of an image, it is called progressive scanning. Alternatively, two images may be scanned at two different times, with the lines interleaved, such that two consecutive lines of a frame belong to alternate fields to form a frame (Figure 2-22). In this case, each scanned image is called a field and the scanning is then described as interlaced (Ghanbari, 1999). The concept behind interlaced scanning is to trade-off vertical-spatial resolution with that of temporal. For example, when recording a moving object, it will be in different positions between the first and second scans, resulting in the even and the odd fields being horizontally disarranged, thus causing a saw pattern effect (D'Apuzzo, 2003). The simplest solution to this problem is to use only the odd or even field, however, the resolution in the vertical direction is halved. Therefore if a moving object is recorded and the full resolution is required, the employment of progressive scan CCD cameras offers better measurement quality and is more appropriate.

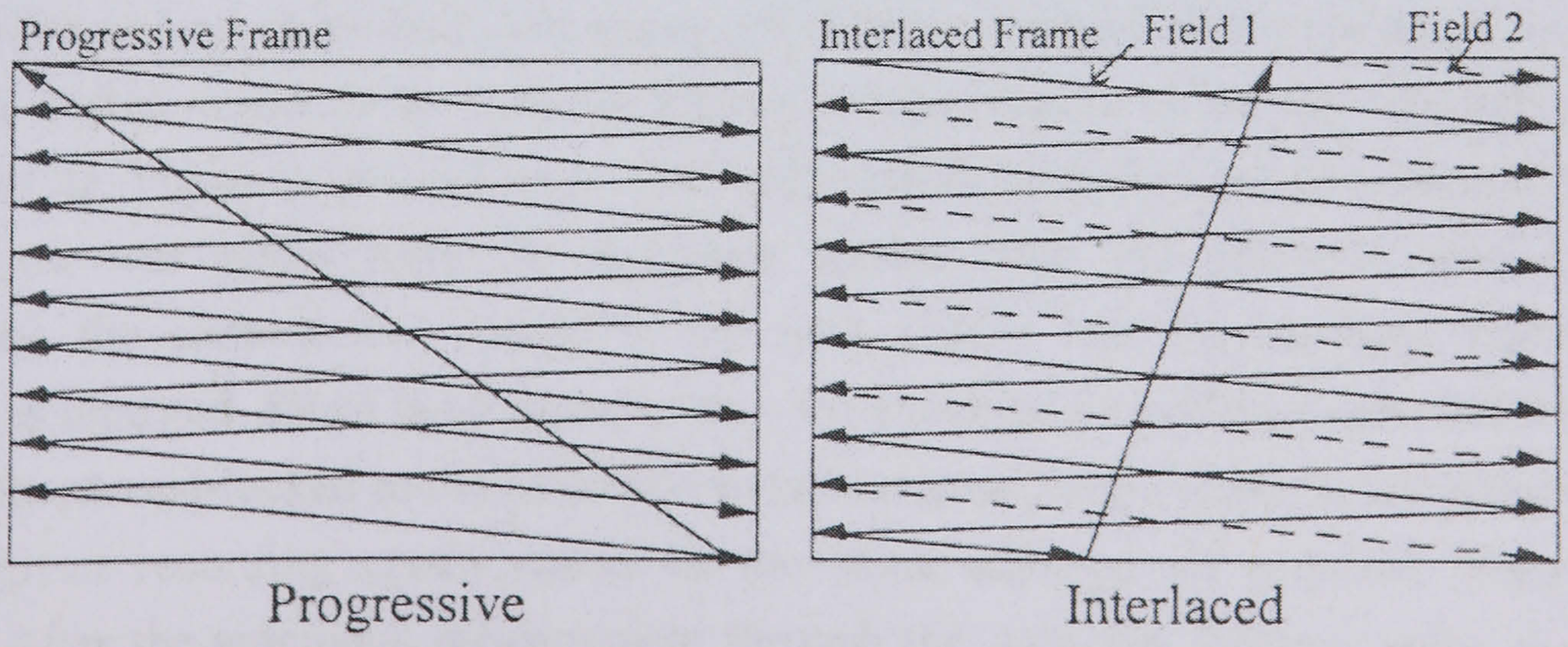


Figure 2-22: Progressive and interlaced frames (Ghanbari, 1999).

High resolution CCD video cameras have been developed and are widely used in scientific, machine vision, and close range photogrammetric applications. In the project of bridge deformation monitoring, Albert et al. (2002) used a CCD video camera to measure the bridge deformation under defined load and determine the amplitude and frequency of vibrations caused by traffic and wind (Figure 2-23). Due to the primarily one dimensional deformation was expected, data acquisition and processing were performed in monocular image sequences. As a result, the single image photogrammetric approach was proved reliable for determining the deformation. In addition, since the image sequences recorded the position of the controlled loading in each image, a better interpretation of the results was allowed.

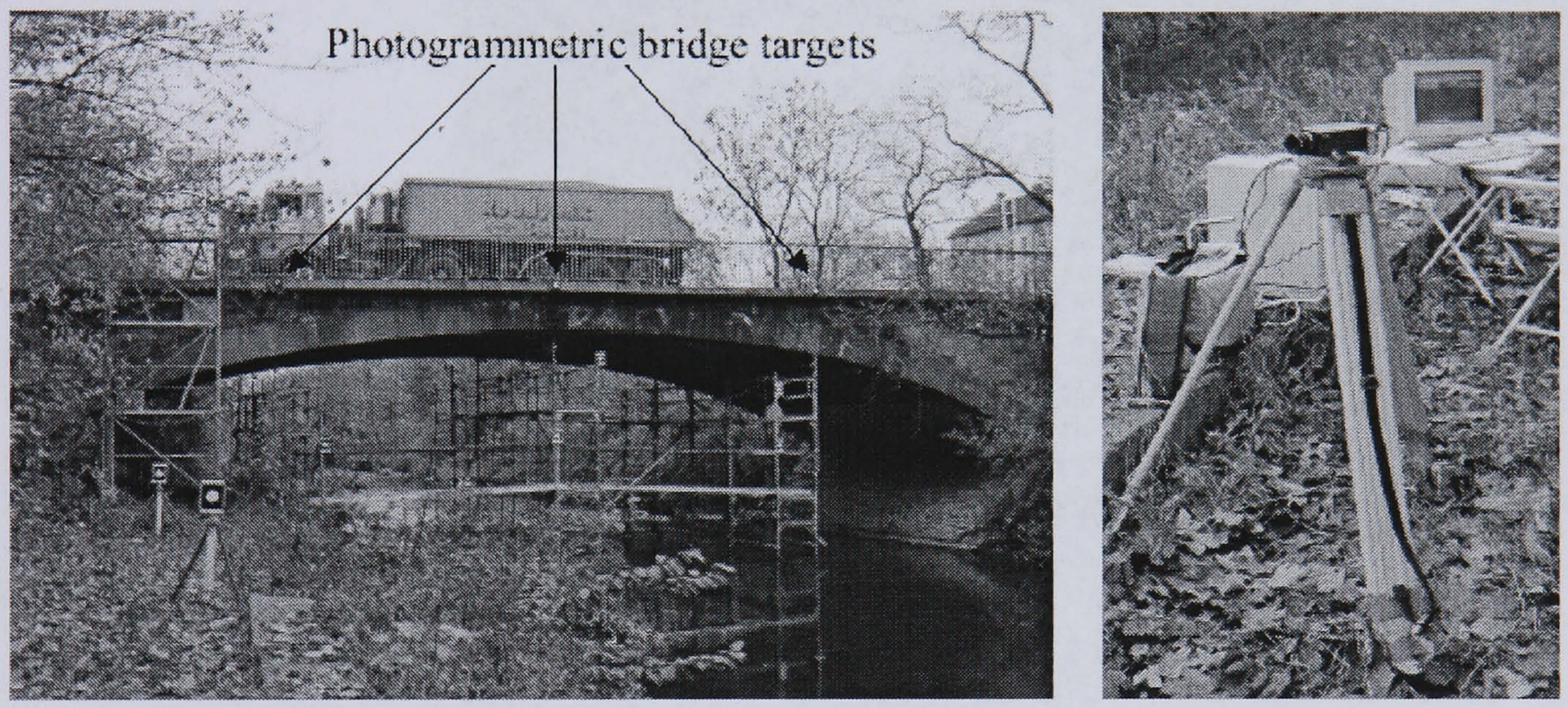


Figure 2-23: The observed bridge of the Franckestraße over the Flutgraben in Erfurt, Germany (left); the adopted CCD video camera (right) (Albert et al., 2002).

By applying a single CCD video camera (Sony XC-75CE), Ryall and Fraser (2002) conducted an off-line digital photogrammetric experiment to derive the 3D model of an oscillating structure. As the vibration was subject to a repeatable cycle of oscillation, which is induced via a controlled electromagnetic shaker, it could be assumed that the shape of the object would be the same at a given instant of time within the repeatable oscillation cycle. Figure 2-24 (top) shows the initial experimental setup and a sequence of 20 images was taken from the exposure station once the vibration started. Subsequently, the camera was moved to the next station and the identical shake sequence was repeated. Since the frame rate was fixed and the recording epochs for the imagery were phased-locked to the reference signal for generating vibration, the targets shot at a given recording epoch would be the same amongst all acquired image sequences. After the automatic measurement through the Australis software suite, the resultant mode of vibration of the wing structure was produced (Figure 2-24 (bottom)).

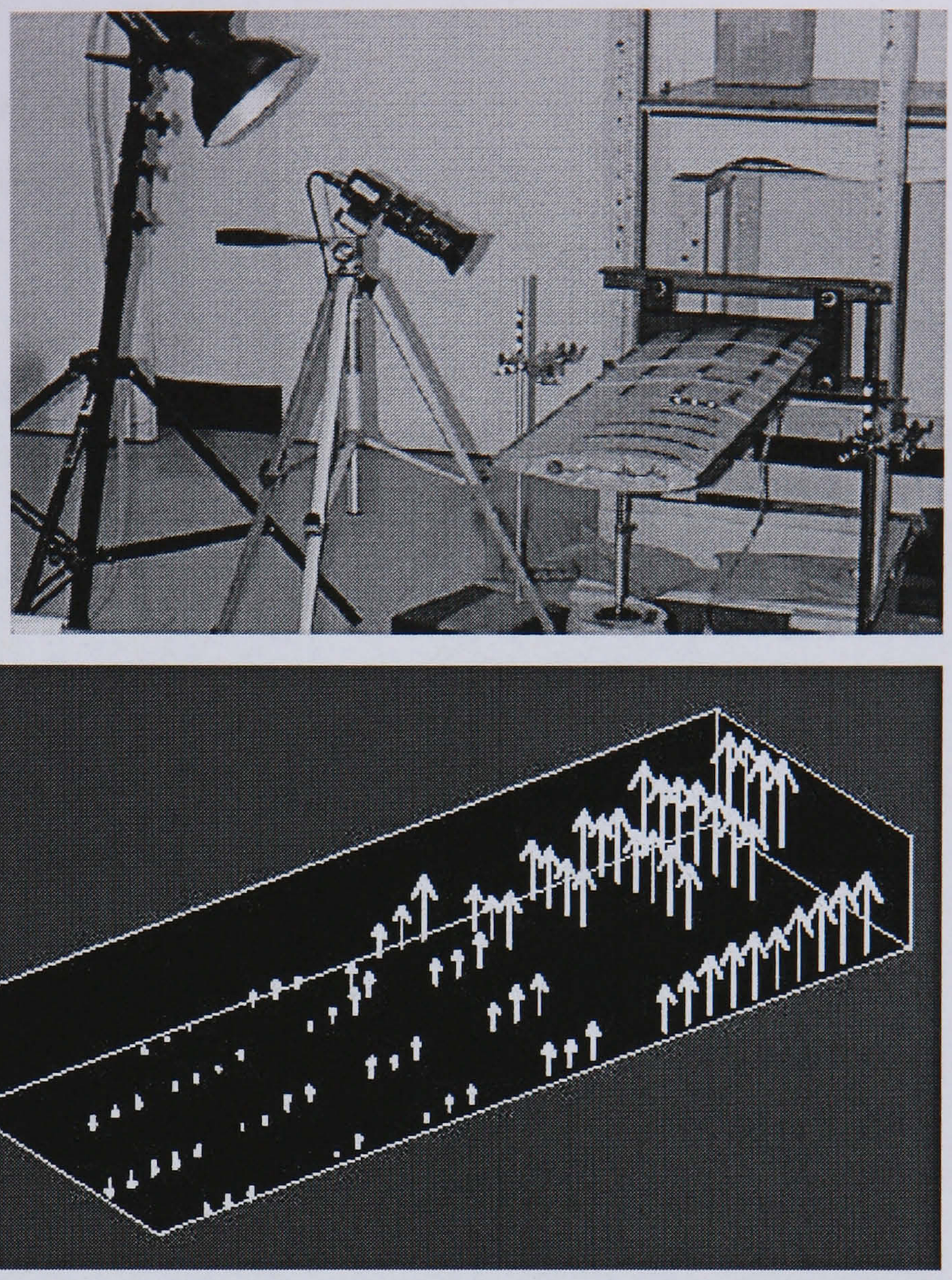


Figure 2-24: Experimental setup for the vibrating wing structure (top); the mode of vibration of the wing structure (bottom) (Ryall and Fraser, 2002).

For assessment of strength of beams and also for refinement of theoretical finite element models, Whiteman et al. (2002) used a stereo camera system to measure vertical deflections in concrete beams during a destructive testing. Two JAI CV-M50 CCD video cameras, each fitted with an 8 mm C-mount lens, were used to acquire video images. When the observations on three different types of concrete beams and the photogrammetric processing were complete, it was found that sub-millimetre object point precision was achieved. Moreover, compared to the traditional LVDTs measurement, the employment of CCD video cameras improved the problems of limited range, non-linearity of response and the ability to measure only in one dimension.

Other applications adopting CCD video cameras could also be found in robot vision systems (Zhu et al., 2002; Sumi et al., 2002), feature inspection and characterisation of industrial applications (Blahusch et al., 1999; Lee et al., 2000; Dai et al., 2005), and face measurement and human body tracking (D'Apuzzo, 2002).

2.4.3.2 Digital Video Camcorders

Before employing digital video (DV) camcorders in photogrammetric measurement, it is important to understand that DV camcorders are manufactured to meet different standard specifications, and this will result in different image formats and frame rates. With current standard colour cameras, the readout of the CCD sensor is transformed into a video signal conforming to one of the two internationally accepted standards. In Europe it is PAL (Phase Alternating Line) and in North America it is the NTSC (National Television Standards Committee) system (Poynton, 1996). In the former standard, the number of lines per frame is 625 and the number of frames per second is 25. In the latter these values are 525 and 30 respectively. The number of samples per active line (i.e. pixels) is 720 for both systems. Note that despite the differences in the number of lines and frame rates, the number of pixels generated per second under these two standards is the same, this is because in digital television only the active parts of the image are accounted for. The number of active lines per frame in PAL is 576 and the total number of pixels per second equals 10 368 000 (720×576×25). In NTSC the number of active lines is 480 and the total number of pixels per second is also 10 368 000 (720×480×30) (Ghanbari, 1999). Therefore, the frame rates and the formats of the images recorded by the DV camcorders manufactured under different standards will be different as well, and it is important to use camcorders of identical standard in photogrammetric operations.

DV camcorders store the recorded image sequence digitally on mini DV tapes, which can be transferred without loss of quality to a PC by FireWire connection and converted into common image formats. A frame grabber is therefore not required (D'Apuzzo, 2003). In addition, their portable size and internal LCD monitor allow handy adjustment of camera stations and on-site quality control for the acquired imagery. Due to these features, DV camcorders have been widely employed in diverse fields for measuring and monitoring. A videogrammetric system designed by Hobbs (2003) was adopted to track multiple targets. Two consumer grade DV camcorders for use have the same frame rate of 25 Hz and use the DV compression format (nominal frame size of 720 by 576 pixels). In the first experiment, measurement of the motion in the direction parallel to the mean wind velocity of a wheat plant was carried out. Several labels were placed on the plants and their motion was tracked while they moved in the wind. The motion measured for part of a wheat plant over a period of one minute is shown in Figure 2-25 (top). The system also used to determine the trajectories of a pair of bubbles used as airflow tracers in a vortex generated inside a wind tunnel. The resultant metric information and visualisation of the motion are illustrates in Figure 2-25 (bottom) and

proved helpful for analysing particular moving features.

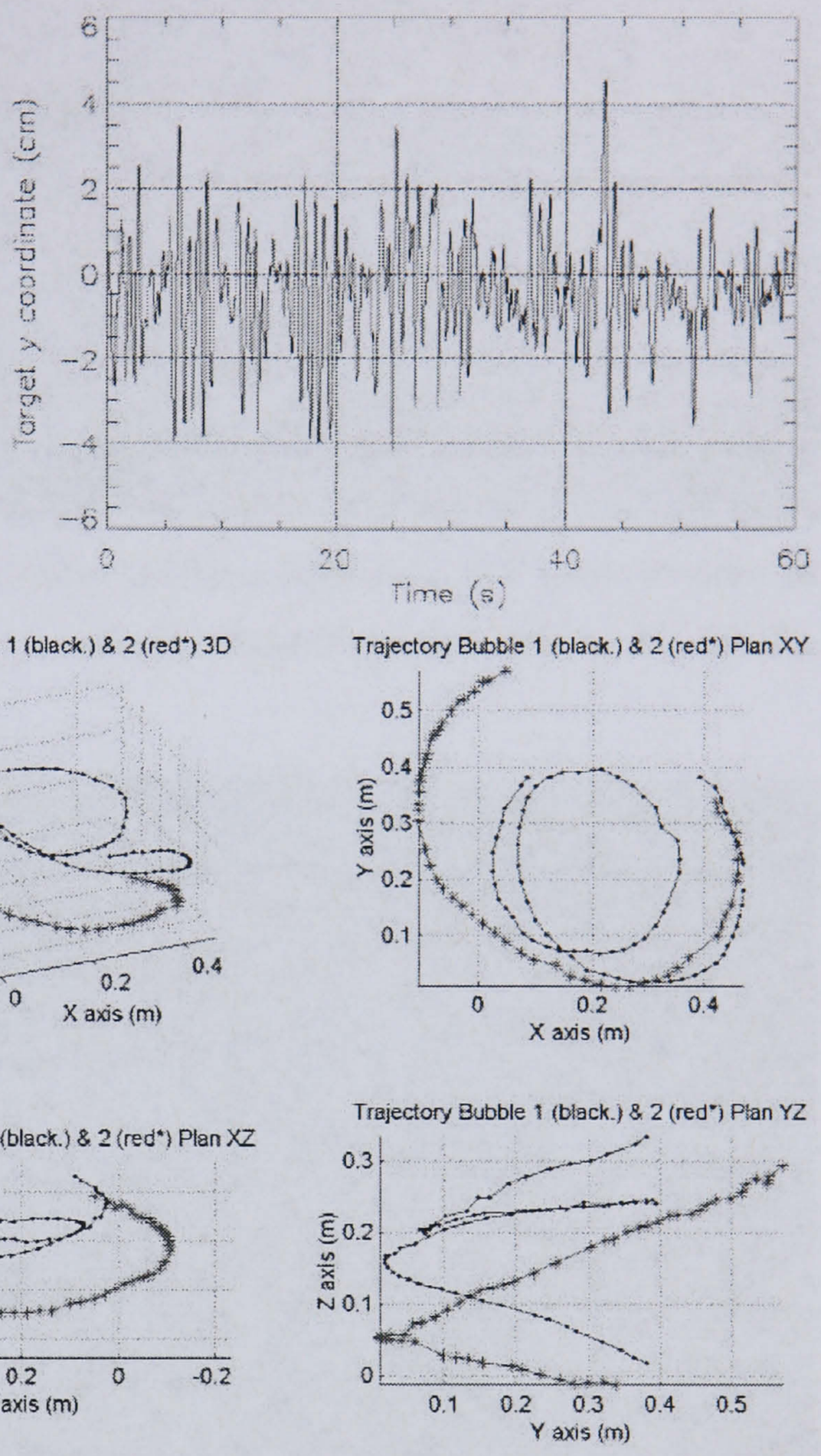


Figure 2-25: Example of motion measured for part of a wheat plant over a period of one minute (top); various projections of trajectories measured for two bubbles inside a low-speed vertical vortex (bottom) (Hobbs, 2003).

To accomplish a reliable and accurate catch monitoring for fishery management, Harvey et al. (2001) designed an underwater stereo-video system capable of measuring the fish body lengths. Figure 2-26 shows the developed underwater stereo-video system using two Sony TRV 900E DV camcorders in underwater housings. The system was applied in the monitoring campaign at Port Lincoln, Australia, to acquire video imagery of the Southern Bluefin Tuna. The measurement was made by locating the snout and tail of the tuna shown in the stereopair in the VMS software (Figure 2-27). When finished, an estimate of the length frequency distribution of the Southern Bluefin Tuna was obtained. Further projects utilising underwater stereo-video systems could be found in Shortis et al. (2007).

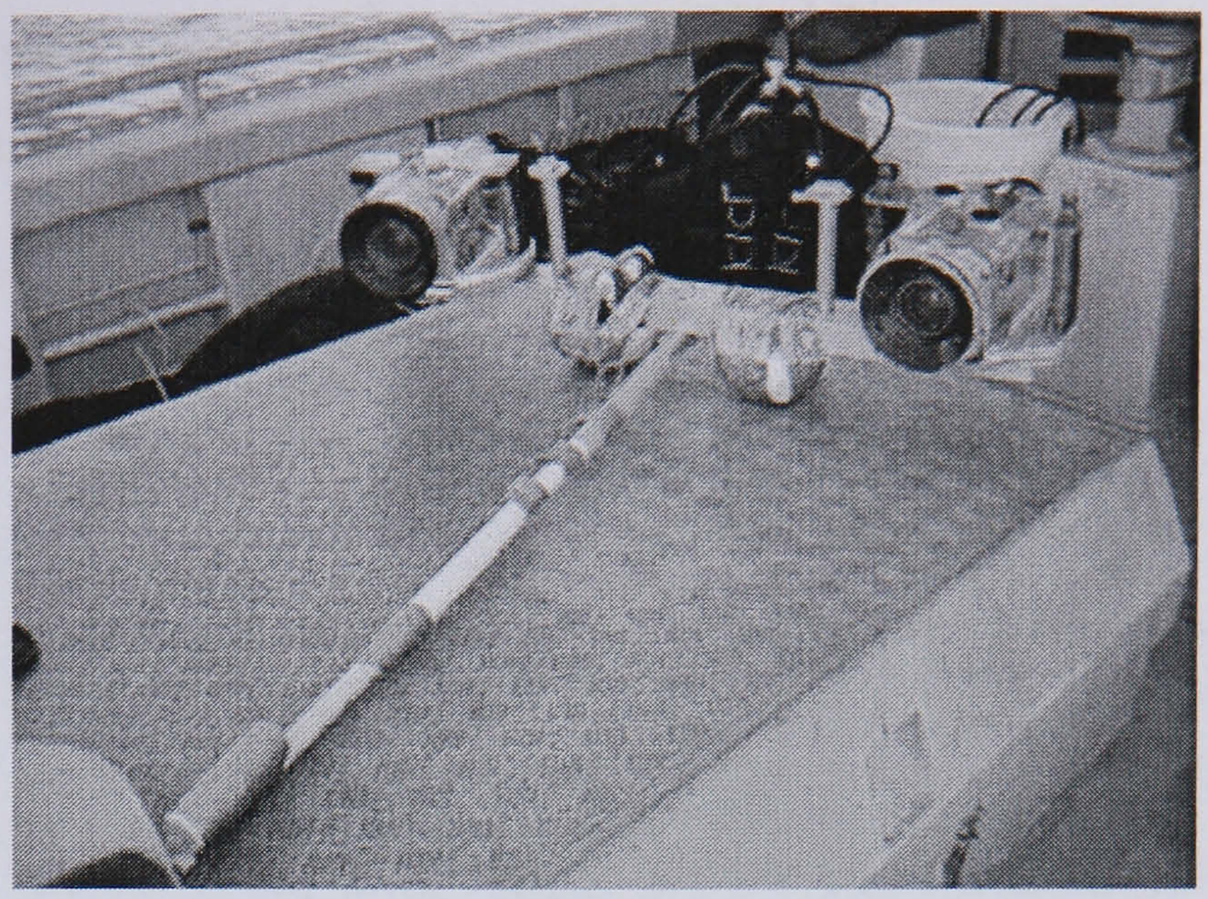


Figure 2-26: The underwater stereo-video system based on DV camcorders in acrylic housings (Shortis et al., 2007).

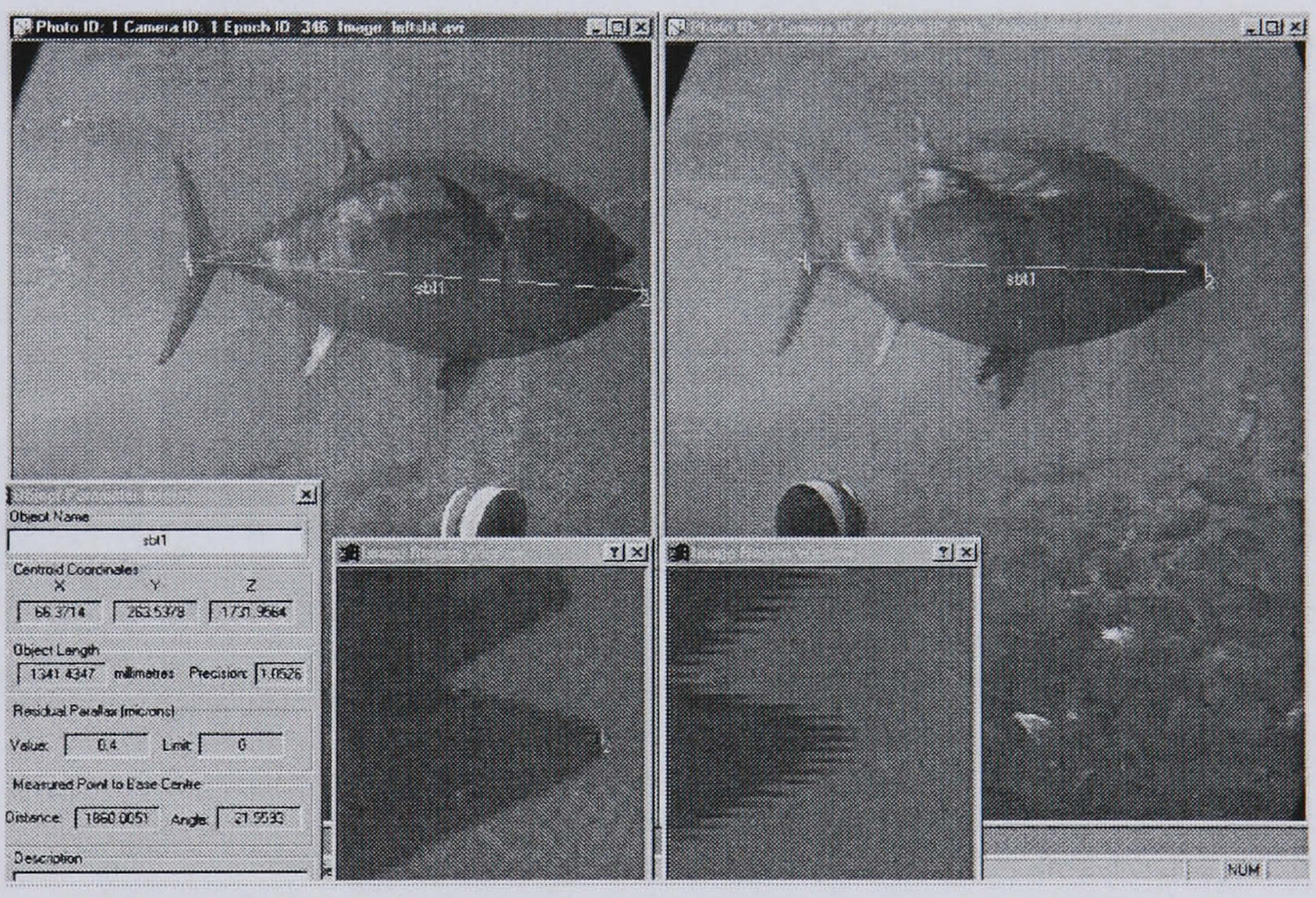


Figure 2-27: The software interface showing length measurements of a Southern Bluefin Tuna (Harvey et al., 2001).

In the field of biology, the technique of stereo videogrammetry was employed to study flight behaviour of aerial hawking bat Eptesicus bottae (Holderied et al., 2005). Two DV camcorders Sony DCR-PC100E were set up overlooking a gorge in Nachal Zin, Israel, where bats hunted for insects in open space. By using multiple images of a 3D calibration frame in combination with photogrammetric bundle adjustment techniques (Granshaw, 1980), the mathematical determination of the relative orientation and internal geometric imaging properties of each camera was simultaneously achieved. The resulting camera orientations were then used for triangulating the position of flying bats visible in both cameras' field of view by the method of intersection. Figure 2-28 shows

a representative reconstruction of a flight path of Eptesicus bottae, illustrating the positions of the bat relative to the cameras.

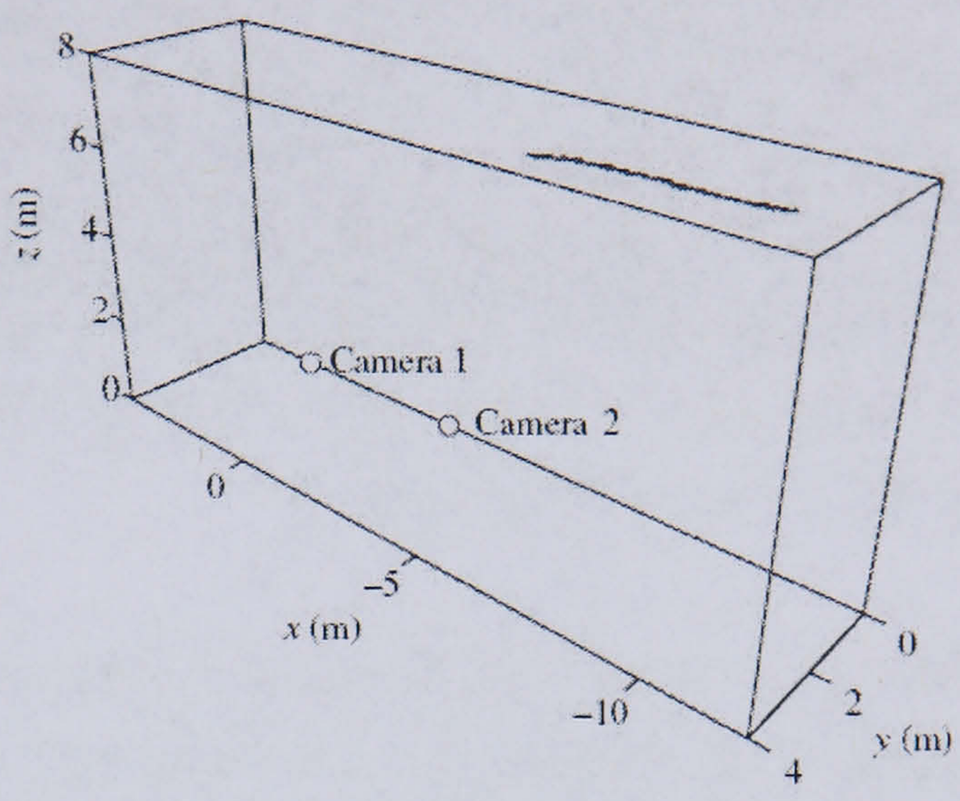


Figure 2-28: The reconstruction of a flight path (the red curve) of Eptesicus bottae (after Holderied et al., 2005).

Overall, it was concluded that consumer DV camcorders are very useful tools for research purposes, as they are readily available, low cost, well-suited to fieldwork and compatible with current personal computers (Hobbs, 2003). However, Hobbs also pointed out that moving targets could lead to image problems due to interlaced scanning of consumer video camcorders. Therefore higher frame rate or progressive scan video camera should be considered if fast-moving target was monitored.

2.4.3.3 Video Cameras with IEEE-1394 Interfaces

Inexpensive digital imaging sensors equipped with an IEEE-1394 port are also an option in applications involving the monitoring of dynamic objects. The computer communicates with the camera through the IEEE-1394 interface (also called FireWire or i-link), allowing control of some camera parameters (such as brightness, exposure, gain, shutter and white balance) and digital transmission of images. Therefore no frame grabber is required for image acquisition. The additional advantages of this type of connection are that only a single input port on the PC is required; and that multiple cameras can be connected to each other in series (D'Apuzzo, 2003). An imaging system consisting of five IEEE-1394 video cameras is shown in Figure 2-29, and was used for human face measurement; results of which can be found in D'Apuzzo and Kochi (2003).

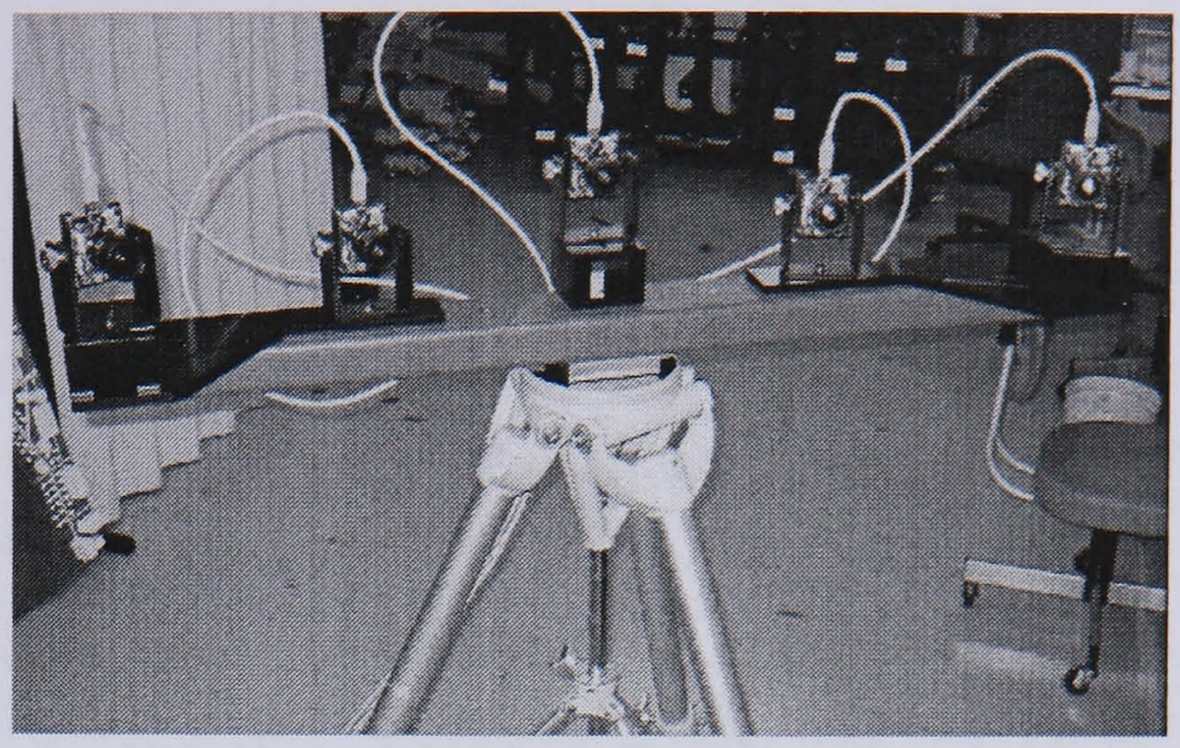


Figure 2-29: An imaging system consisting of five IEEE-1394 video cameras (D'Apuzzo and Kochi, 2003).

Although not originally designed for photogrammetric measurement purposes, another system applying multiple IEEE-1394 video cameras was developed at Stanford Computer Graphics Laboratory, in which a total of 100 cameras were employed (Levoy, 2002). Each camera used a complementary metal-oxide-semiconductor (CMOS) imaging sensor, Moving Picture Experts Group (MPEG) compression, and an IEEE-1394 chipset. Depending on the alignment of the camera array, the multi-camera system can function in various ways (Levoy, 2002). Figure 2-30 (A) shows the configuration of tightly packed cameras with telephoto lenses and splayed fields of view, this system being used for high-resolution imaging (Wilburn et al., 2005). Figure 2-30 (B) illustrates a tightly packed camera configuration with wide-angle lenses, and is proposed for high-speed video capture and hybrid aperture imaging (Wilburn et al., 2004). Cameras in a widely spaced configuration are shown in Figure 2-30 (C), the system functioning as a multiple centre-of-projection camera used to construct multi-perspective panoramas (Wilburn et al., 2002). In addition to these applications, the camera array is also potentially exploitable for scientific imaging, remote sensing, underwater photography, surveillance, and cinematic special effects.

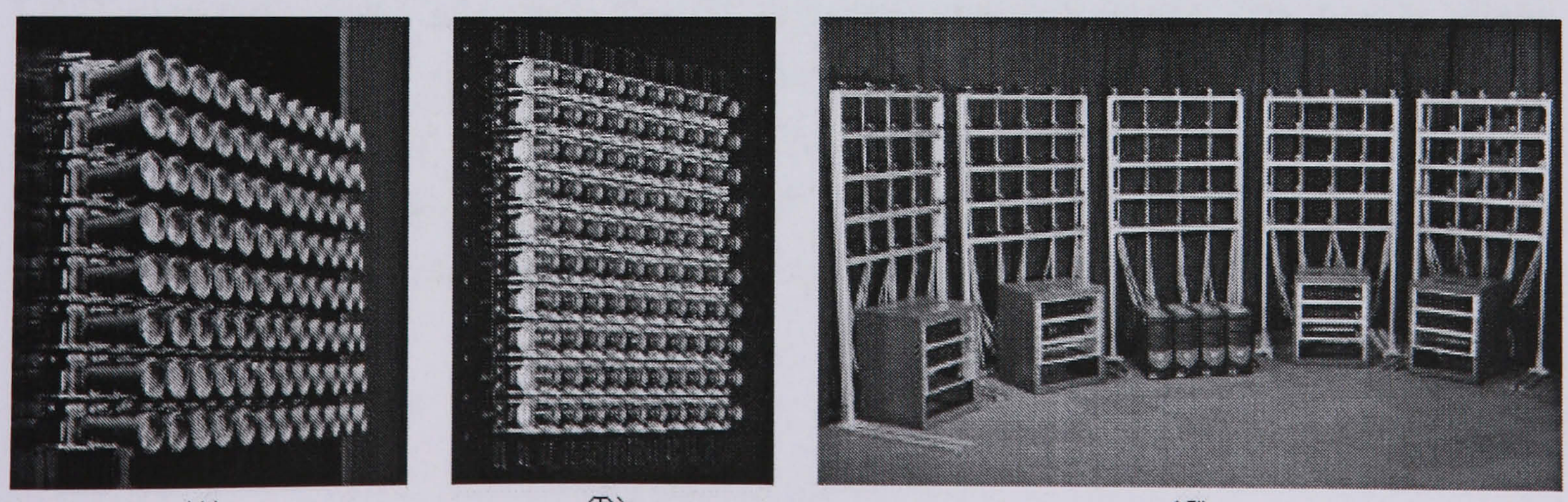
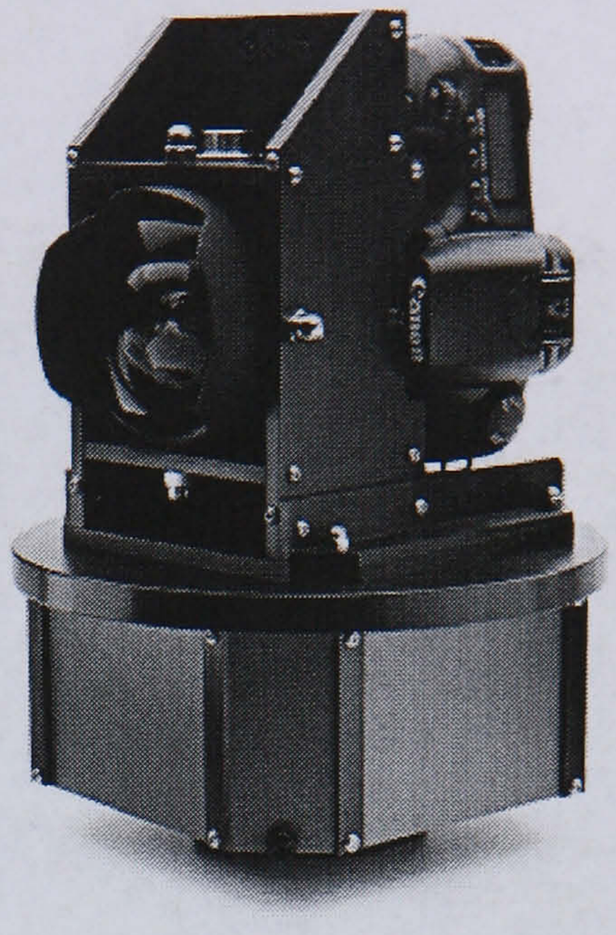


Figure 2-30: Different configurations of camera array (Wilburn et al., 2005).

2.4.3.4 Still Video Cameras

In most cases, still video cameras, e.g. the Kodak DCS series cameras (Shortis and Beyer, 2001), are used to observe static objects. However, if the movement is modest or predictable, the configuration of multiple still video cameras is able to offer a solution for accurate measurement. Such application was found in the deformation monitoring of concrete parts during a dehydration process (Maas and Niederost, 1997), a Kodak DCS 200 camera was used to acquire images in seven epochs over six months. When the processing was complete, the deformation relative to reference points was computed. With the high accuracy potential, Maas and Niederost depicted that digital photogrammetry was an unrivalled tool for this kind of relative measurement task due to low instrumental effort and the possibility of fully automatic data processing. In another application of monitoring the deformation of the reservoir wall Nalps in Switzerland, a total of 60 retro-reflective targets were attached evenly onto the wall surface and a Kodak DCS 460 camera equipped with an 18 mm lens was then used to shoot the images covering the whole surface (Maas, 1998b). Although the relatively low precision and accuracy were derived in this research, the deformation was still able to be estimated by comparing surface determined in different epochs. Moreover, photogrammetry using still video camera showed a viable alternative when a densification of geodetic measurements (e.g. total station measurement) was required.

Hazmap is a commercial digital photogrammetric system to undertake spatial data collection, analysis and address problems associated with as-built engineering (As-Built Solutions Ltd., 2007). The system was initially developed towards nuclear engineering application (European Commission, 1995). In order to operate remotely in the high radiological environment, panoramic imaging system was arranged in the nuclear plant to take images and the panoramic mosaic was generated afterwards. It was found qualitative assessment of plant condition, coordinates and distance measurement, and CAD modelling were all achievable through the acquired image data and resultant panoramic images (Chapman, 2000). In the latest version of the Hazmap system, a Canon EOS 5D digital camera, incorporating a high precision rotation system was adopted to capture eight images in a full 360° scan (Figure 2-31). The acquired images were used for undertaking deformation investigation, measurement and modelling.



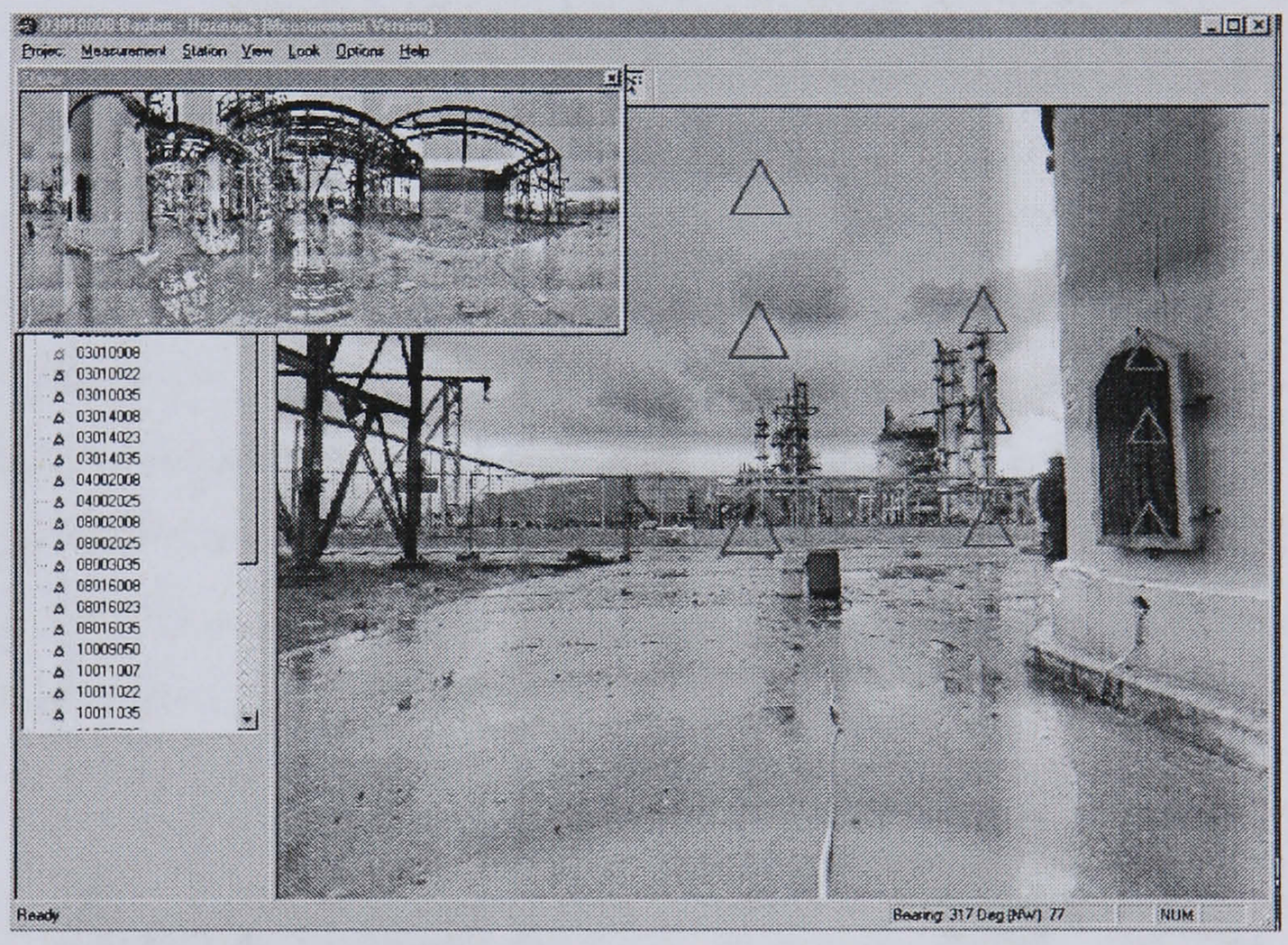


Figure 2-31: The panoramic camera system for the capture of 360° images (top); the panoramic browser interface (bottom) (As-Built Solutions Ltd., 2007).

Photogrammetry was also introduced into the field of sports science for measuring the structural deformation of a golf club as it was being swung (Smith et al., 1998). A measurement system based on the use of two Nikon F301 (35 mm) single length reflex cameras was developed. Due to the high speed of the golf club movement, obtaining an image sequence of the moving club was not achievable by successively winding on the film for individual frames. To accommodate this situation, Smith et al. (1998) captured image sequence by repeating exposures on the same frame. A typical exposure frame of a club during a swing is shown in Figure 2-32, at which butterfly type targets were arranged on posts as control points and critical points on the golf club were computed by both bundle adjustment and direct linear transformation (DLT) technique. The image

acquisition method provided a suitable solution for the applications tracking small number of moving points.

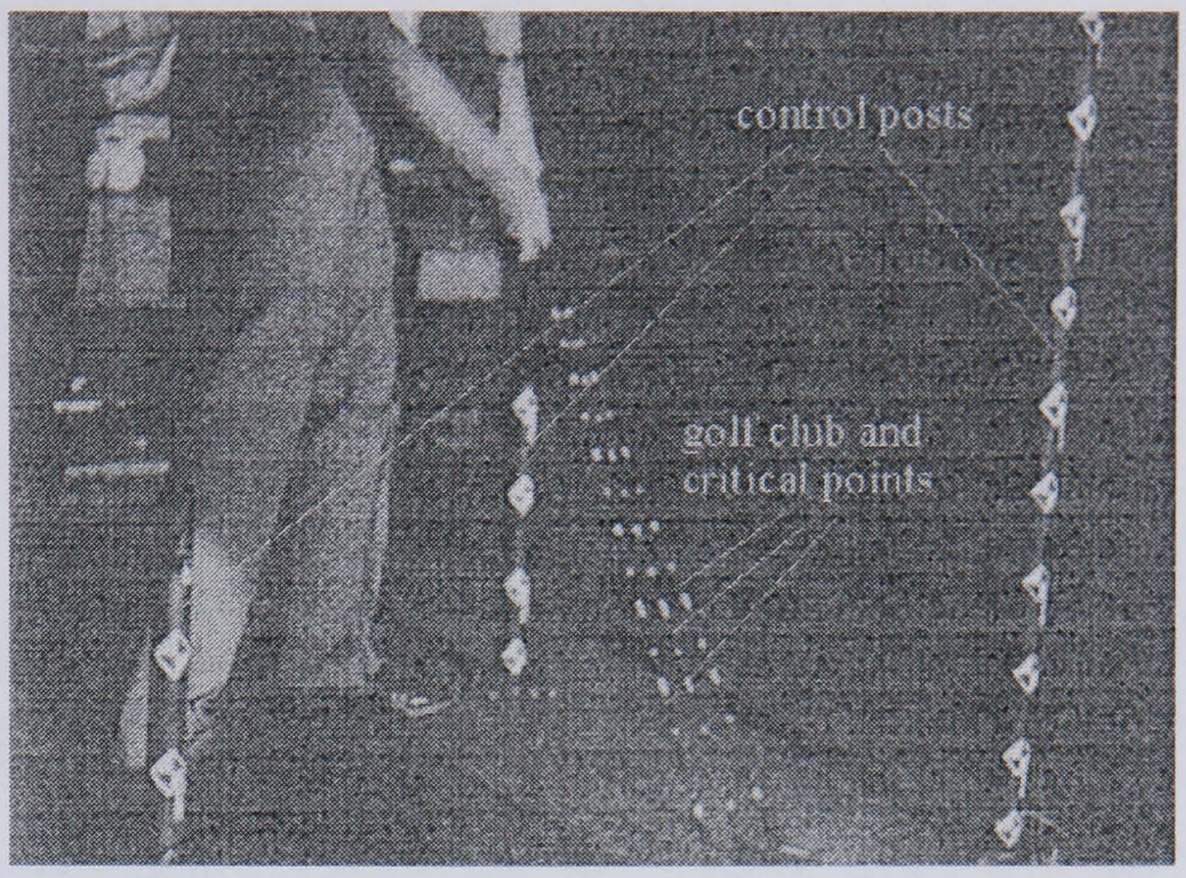


Figure 2-32: Typical frame recording moving golf club (after Smith et al., 1998).

The use of additional equipment to synchronise still video cameras (refer to Figure 2-33 for examples) or to acquire a set of simultaneous image sequences is achievable. This modification broadens the range of object monitoring applications using still cameras. However, due to the short delay between the acquisition of the sequential images (caused by saving the image in the camera), this configuration is more suitable in projects where low temporal resolution are required.

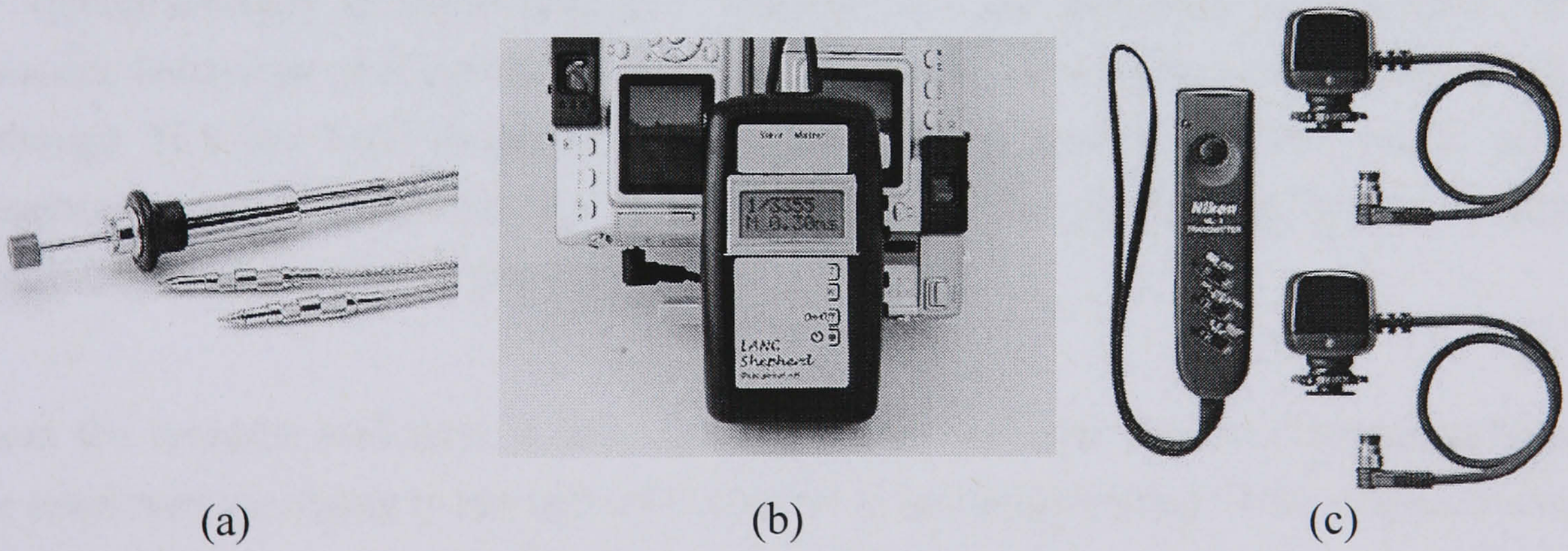


Figure 2-33: Kits for synchronising cameras: (a) synchronisation cable release; (b) wired controller; (c) wireless controller and receivers.

2.4.4 Suitability for Membrane Structure Measurement and Monitoring

The image-based methods of photogrammetry and videogrammetry have remained a popular technique in structural measurement and deformation monitoring for some time.

For observing the deformation of a series of super-hot steel beams (maximum temperature was about 1100°C), videogrammetry was considered as the most suitable method for the monitoring. To achieve this, Fraser and Riedel (2000) used three Jai CCD video cameras to record image sequences of the beams. The video imagery was then input to the Australis software and videogrammetric processing was performed. Once finished, the pattern of surface deformation exhibited by each steel beam as it underwent a change of temperature of close to 1100°C was determined. In the project conducted by Psaltis and Ioannidis (2006), a concrete beam was again monitored. By employing photogrammetry technique, its deformation occurred during a loading experiment was accomplished. Also, the results showed that the standards of an automatic, inexpensive, almost on-line calculation of displacements with accuracy better than 1 mm were fully met. In the research presented by Jauregui et al (2003), photogrammetry was suggested as an attractive method for the purpose of structural health monitoring due to the characteristic of non-contact measurement and capability of offering absolute displacement. A photogrammetric monitoring system was therefore developed to determine the vertical deflection of a bridge, and the damage occurred was further detected. The applications for structural measurement and monitoring can also be found in the projects conducted by Shortis (1986), Woodhouse et al. (1999), Li and King (2002), Fraser et al. (2003), Heath et al, (2004), and McClenathan et al. (2006). The broad applications are mainly due to the advantages of non-contact measurement, rapid data acquisition and capability to simultaneously sample all of the data points within the field of view of the camera (Blandino et al, 2003). Therefore, the technique of videogrammetry is considered as a suitable tool and proposed to determine the dynamic behaviour of a membrane roof structure in the monitoring scheme. Moreover, although TLS has been proposed as the technique for generating static model of a membrane roof, photogrammetry is also of potential for performing this task. The feasibility will be further explored.

From the research reviewed, it has been found that different camera instrumentations are employed according to the type of deformation being monitored. If the displacement is controllable (e.g. pressed concrete beams or bridges), the use of cameras introduced in Section 2.4.3 are all possible data capture solutions. When monitoring fast-moving or unpredictable movements (e.g. structural vibration or thermal deformation of steel beams), the employment of DV camcorders and CCD video cameras is necessary. Considering the moving characteristics of the membrane roof being observed in this research, DV camcorders and CCD video cameras are more appropriate equipments for image data acquisition. In addition, as addressed by D'Apuzzo (2003), different levels

of measurement quality can be achieved depending on the video imaging systems employed. Thereby research into the performance of these two types of cameras for dynamic surface modelling will be further investigated.

2.5 Additional Technologies

An overview of additional technologies for monitoring and measurement is briefly described in this section. This includes the other metrological techniques of laser tracking and laser vibrometry.

2.5.1 Laser Tracking

Laser tracking is a technique capable of performing surface measurement and inspection. Normally a laser tracking system comprises a laser based tracking unit, handheld locating device (e.g. retro-reflector targets), and a computer for tracker operation and data demonstration. To undertake laser tracking, a target is placed at the point to be measured. The laser tracker then communicates with the target to acquire its position information, to which the pitch, yaw and roll rotation angle of the target, and the spherical coordinates of the target relative to the tracking unit are obtained (Figure 2-34) (Lau, 2003). The target is kept moving to occupy all positions of interest, meanwhile the laser tracker will track the target according to the equipped high-speed positioning sensor and the targets' 3D coordinates relative to the tracking unit are estimated.

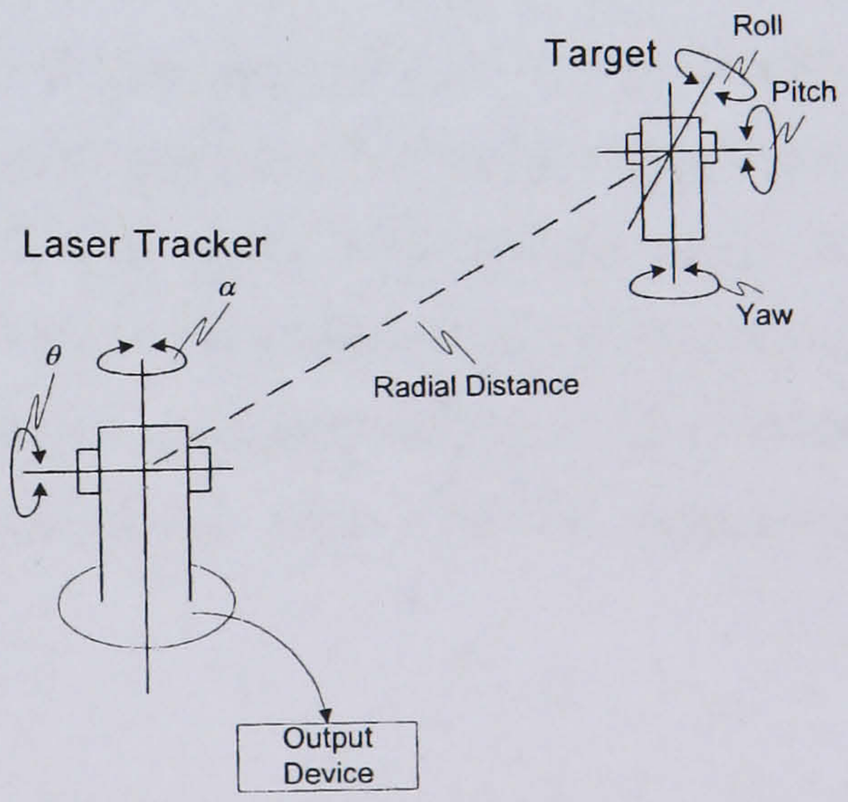


Figure 2-34: Schema of laser tracking technique (Lau, 2003).

As the continuous development of the commercial laser tracking systems (e.g. Leica LTD 840 Laser Tracker, FARO Laser Tracker X, and API Tracker3 Laser Tracking System), accurate and rapid measurement results derived from laser tracking have been

largely achieved. Due to these features, the Boeing Company adopted laser tracking as a digital tooling in the aircraft Major Structural Repair (MSR) scheme, determining whether a part is located properly within a defined tolerance band (Boyer, 2001). In addition, the technique of laser tracking has been broadly adopted in a range of industrial applications, such as aerospace, automotive, energy and power supply, generating plants, shipbuilding and railway supply industry (API Systems, 2007; FARO International USA, 2007; Leica, 2007). For example in a shipbuilding application, laser tracking could be used for alignment of propeller shafts, assembling of prefabricated components, inspection of tubings, fixture construction, and inspection of machine foundations (API Systems, 2007).

2.5.2 Laser Vibrometry

Laser vibrometry is considered as the "gold standard" for structural vibration testing (Blandino et al., 2003). Unlike traditional contact vibration transducers, laser vibrometers require no physical contact with the test object. The measurement principle of a laser vibrometer is based upon the Doppler Effect. When monochromatic laser light is scattered back from a vibrating target, it undergoes a frequency shift which is proportional to the velocity of the target (Brüel & Kjær, 2007). This is known as the Doppler Effect. As the target moves towards the light source, the back-scattered light undergoes an increase in frequency. When the target moves away, the back-scattered light undergoes a lowering of frequency. By detecting the Doppler shift in the frequency of coherent light scattered by a moving target, a time-resolved measurement of the target velocity is made (Halkon and Rothberg, 2003). Due to the feature of non-contact measurement, laser vibrometry is therefore feasible in the applications where remote or/and mass-loading-free vibration measurements were required. Nowadays two types of laser vibrometers are commercially available. Single point vibrometers must be moved manually from point to point on a surface. While by incorporating optical mirror systems with the laser source in the scanning vibrometers, complete vibration data from up to thousands of individual points on a user-defined area can be measured automatically and consecutively (Ching, 2005).

In recent years, the technique of laser vibrometry has been employed in structural vibration monitoring, in which examples can be found in ventilated walls, historical theatres, bridges and castle towers (Castellini et al., 2006). Esposito et al. (2004) applied a scanning laser Doppler vibrometer (SLDV) to diagnose the ventilated walls facades of the JWT building in Milan, Italy. Normally, structural excitation is caused by acoustic

waves radiation. Therefore, this experiment focused on examining the vibrations and structural state of the wall under acoustic radiation. The monitoring system, including the SLDV, loudspeaker systems, plus additional instrumentation such as a sound meter to monitor emitted sound level, is illustrated in Figure 2-35.

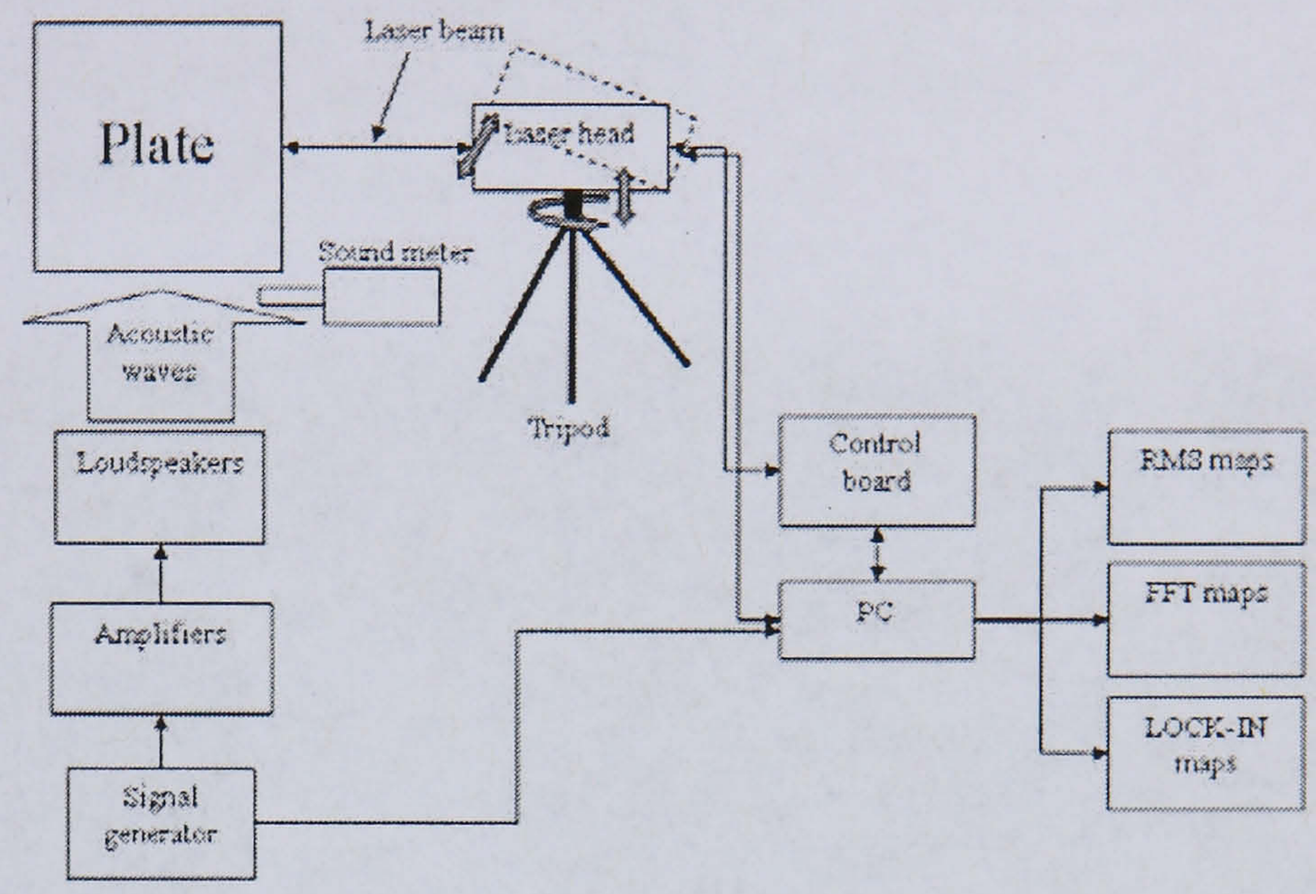


Figure 2-35: Monitoring system for measuring vibration of ventilated walls (Esposito et al., 2004).

The experimental setup is shown in Figure 2-36 (left), at which the laser head was positioned at about ten meters from the facade, while the loudspeakers were at about five meters. Consequently, a single frequency excitation from the loudspeakers was employed and the resulting vibrations map was rapidly acquired. From the map, it was found that the dangerous loosening plates were determined by inspecting the area where high vibration occurred (Figure 2-36, right).

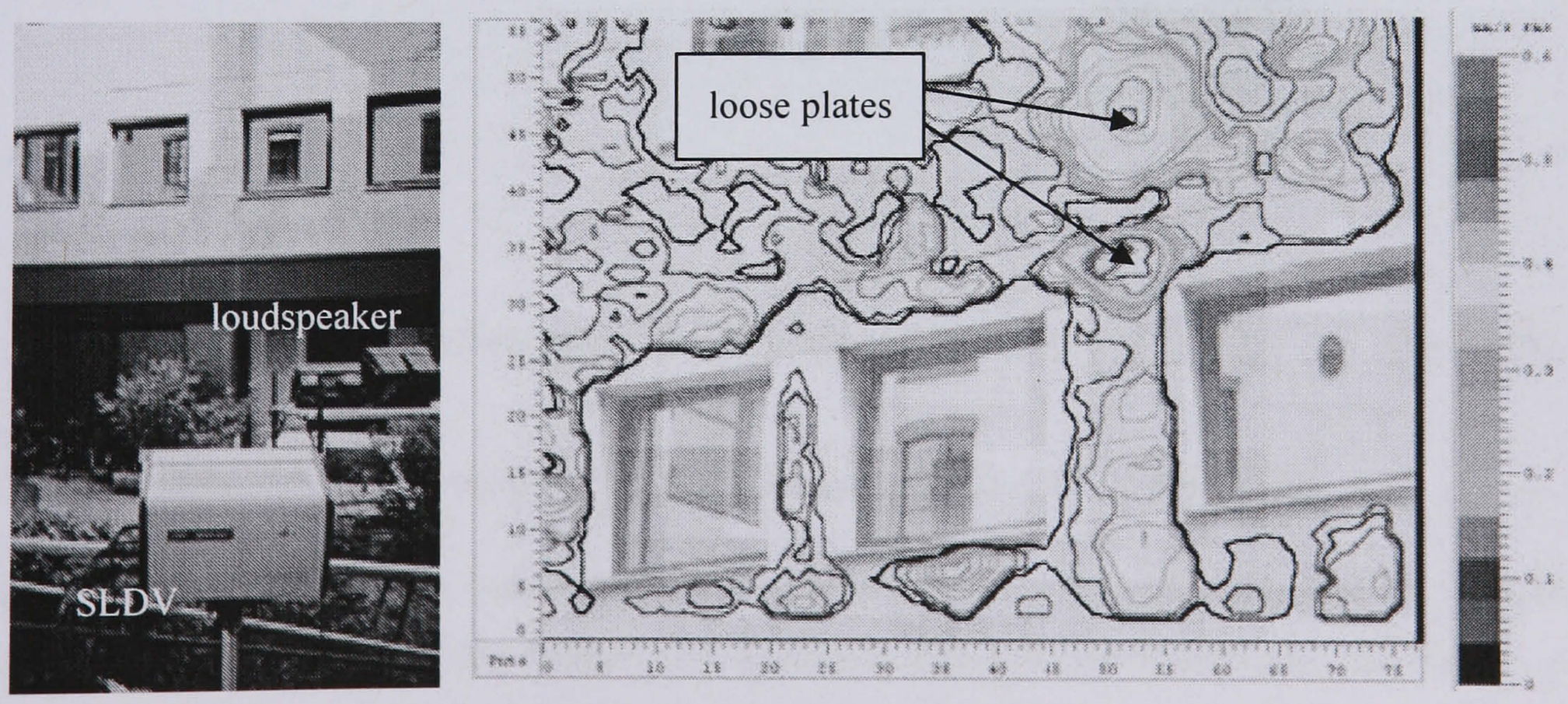


Figure 2-36: Experimental setup of the monitoring system (left); map of the resulting vibrations (right) (after Esposito et al., 2004).

In addition to the solid structures, an application of the laser vibrometry for studying gossamer structures was conducted by Blandino et al. (2003). A Polytec Model PSV-300-H scanning laser vibrometer was used to observe the vibration occurred across the solar sail model (Figure 2-37, left). The vibration was triggered by the signal from a force transducer mounted between the shaker stinger and the sail support rod (Figure 2-37, right). Once finished, the vibration map of the observed quadrant surface, at 3.34 Hz frequency, was generated and shown in Figure 2-38.

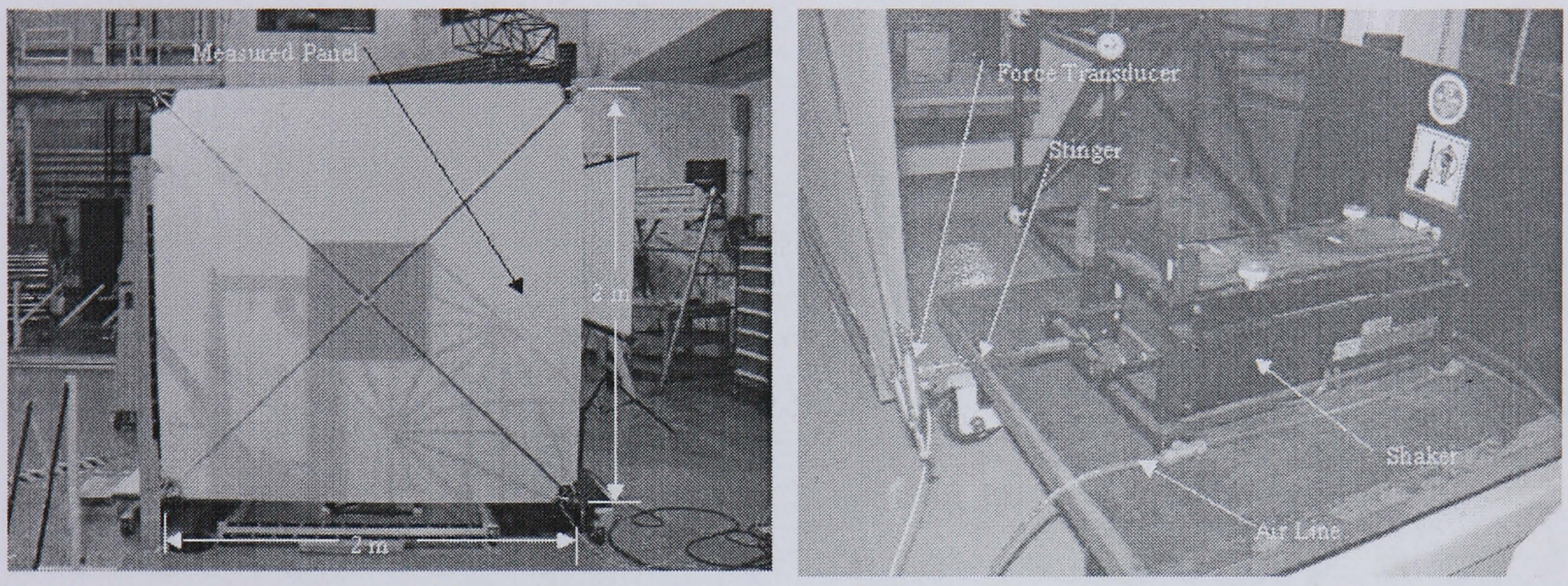


Figure 2-37: The observed solar sail model (left); shaker with attachment to sail model (right) (Blandino et al., 2003).

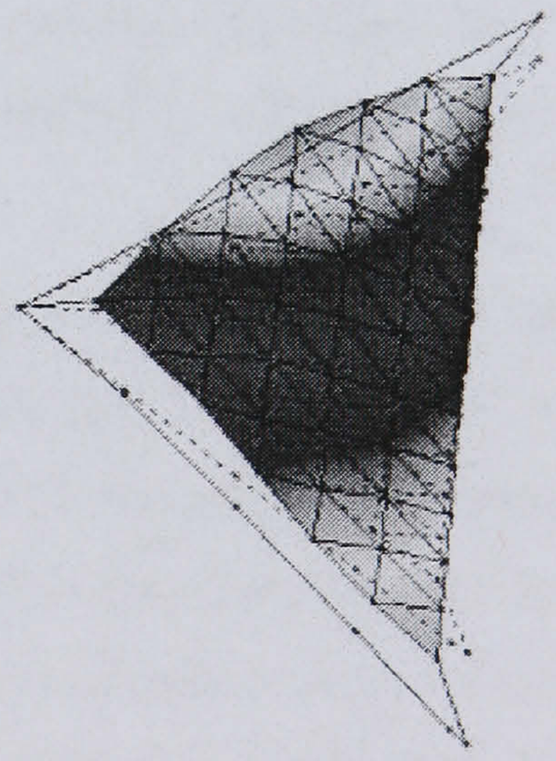


Figure 2-38: Vibration map of the observed surface (Blandino et al., 2003).

2.5.3 Suitability for Membrane Structure Measurement and Monitoring

Two metrological techniques based on laser technology were introduced. The technique of laser tracking possesses the feature of accurate surface measurement, however, a contact on the surface of interest is necessary. As the fabric roof of the membrane structure is inaccessible, this contact measurement manner limits the employment of laser tracking in the membrane structure measurement scheme.

Laser vibrometry is practicable for performing dynamic membrane surface modelling. However, in the membrane structure monitoring scheme it is desirable to measure displacement of more than one degree of freedom at each point and measure all points simultaneously. Moreover, laser vibrometry is a costly technology (Blandino et al., 2003). Considering the cost involved in acquiring a vibrometer, a less expensive and acceptable alternatives are more advantageous in the membrane structure monitoring scheme.

2.6 Chapter Summary

A review of the potential geomatics techniques for solving the issues involved in membrane structure monitoring has been presented in this chapter. In the first task of comparing the designed and finished membrane roofs, the main operation is to produce a surface model of the as-built structure. To this end, the feasibility of terrestrial surveying with total station instruments was inspected. Due to the relatively new feature of reflectorless measurement, total stations are currently employed in many structural measurement applications. However, the measurement time is long, making it inefficient for the application of generating the membrane roof model. Alternatively, terrestrial laser scanning demonstrates the capability of rapid, intensive and non-contact data acquisition, and therefore is considered as a more suitable technique for undertaking membrane roof measurement. Moreover, as the technique of convergent videogrammetry is also of potential for this task, the feasibility will be explored as well.

Subsequently, this research project focuses on the determination of the displacement of the membrane roof over a potentially extended period of time. Using a total station with targets or prisms attached on the object of interest, the function of automatic target tracking can be performed to define the movement of the observed object. Nevertheless the arrangement of the targets is not applicable on the membrane roof, so total stations are not employable. Moreover, these targets can not be observed simultaneously so the comparison between specific temporal epochs is not achievable. The latter point also limits the utilisation of TLS and laser vibrometry in determining the displacement of the membrane roof. To solve this problem, the technique of videogrammetry is proposed to simultaneously sample and measure all of the data points occurring within the field of view of the cameras. By repeating this process in sequential epochs, the displacement can be further estimated.

In summary, the principles, instruments, relevant applications or research, and advantages or disadvantages of the techniques have been presented in Chapter 2. It is subsequently concluded that a possible solution to membrane structure monitoring is a hybrid approach, combining the techniques of terrestrial laser scanning and videogrammetry. Modifications are absolutely necessary when they are applied to the observation of real-world membrane structures. The development and practical work that has been undertaken will be provided throughout the remainder of the thesis.

CHAPTER THREE

METHODOLOGIES FOR MEMBRANE STRUCTURE MONITORING

3.1 Introduction

A generic membrane structure monitoring system capable of inspecting the static and dynamic behaviour of the membrane roof surface is proposed. After reviewing the possible solutions of structure monitoring in the previous chapter, the geomatics technologies of terrestrial laser scanning and videogrammetry are introduced into the system. In addition, to accommodate the monitoring system in the working environment, some alternatives and modifications are necessary. In this chapter, the details of the proposed methodologies for monitoring the membrane structure are reported, and proof-of-concept tests are described to prove the feasibility of the adopted methods.

3.2 Static Surface Modelling

The first issue regarding the membrane structure to concern the engineer relates to the differences that exist between the designed model and the finished structure. To understand this problem two kinds of models are investigated and compared. The first model is the mathematical one, which is produced by structural engineers in the design stage of the membrane structure construction. The methods and principles of creating a mathematical model were introduced previously in Section 1.2.1. The second model is that of the finished structure. The technique of terrestrial laser scanning was used to generate the physical models of the membrane structures. Once the two surface models are acquired they are compared statistically, and the differences between two surfaces, if

existing, could be discovered.

3.2.1 Terrestrial Laser Scanning

3.2.1.1 Instrumentation

To acquire the as-built model of a membrane surface, the technique of terrestrial laser scanning was applied. In this monitoring scheme two laser scanning systems, a Leica HDS2500 and Leica HDS3000 (Figure 3-1), were employed to observe the membrane surface. Their specifications are given in Table 3-1 (Leica, 2003; Leica, 2004).

The primary difference between the two laser scanning systems is the field of view of each scan. The HDS2500 scanner was able to perform a 40° by 40° scan at a single station while the HDS3000, equipped with a drive motor and dual (front and top) windows, allowed a 360° by 270° scan per station. Due to this feature less scan stations were required when using HDS3000 laser scanner, and the network configuration of scan stations was different when using each laser scanning system to observe the same membrane structure.

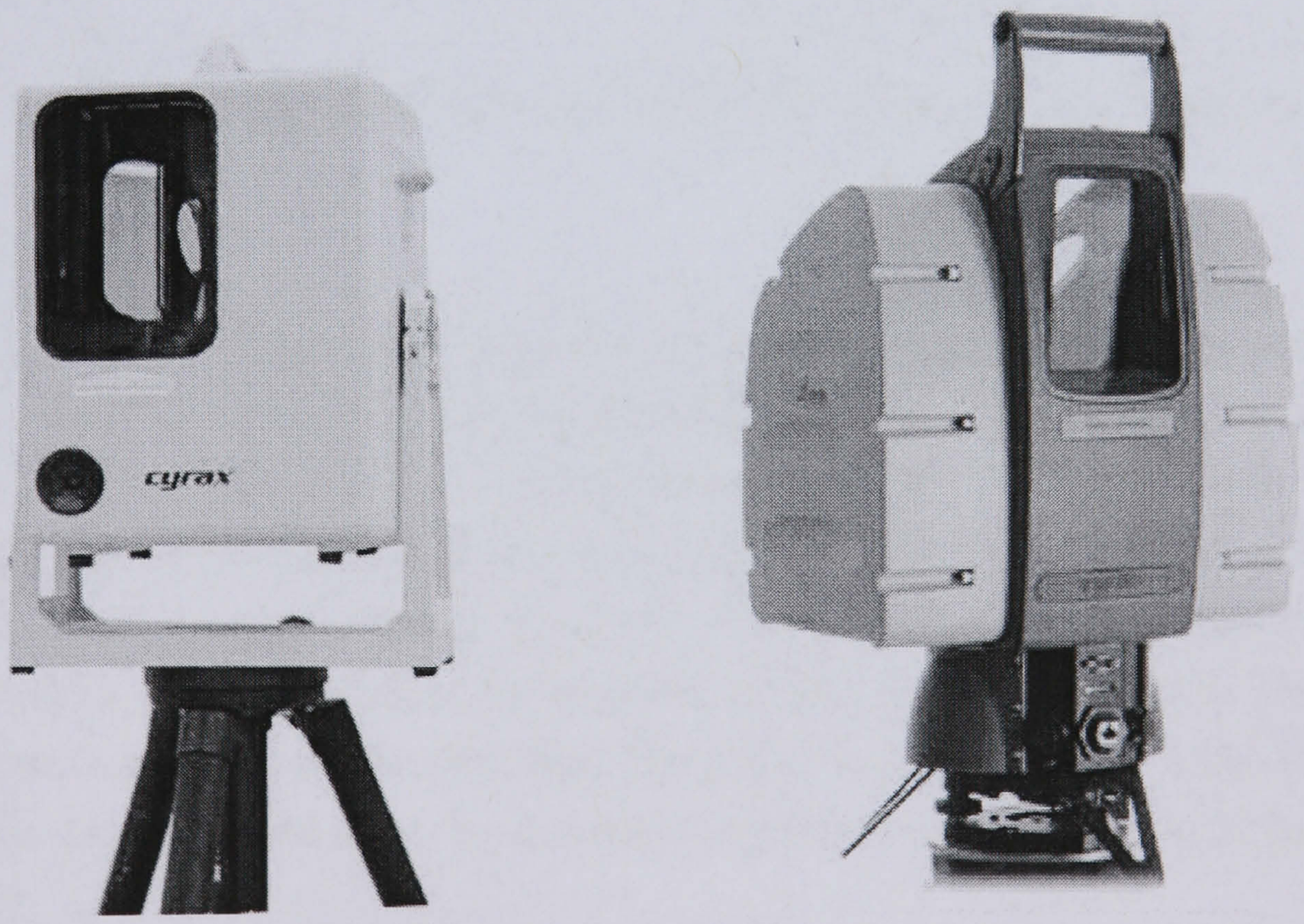


Figure 3-1: Terrestrial laser scanners employed (left: Leica HDS2500; right: Leica HDS3000).

	Leica laser scanner	
	HDS2500	*HDS3000*
Type	Pulsed (time-of-flight method)	
Optical viewer	Integrated video camera	
Optimal effective range	1.5 m – 50 m	1 m – 100 m
Spot size	≤ 6 mm from 0 m – 50 m	
Scan rate	Up to 1000 points/second	Up to 1800 points/second
Point position precision	+/- 6 mm	
Point distance precision	+/- 4 mm	
Point angle precision	+/- 60 micro-radians	
Scanning optics	Dual mirrors, random access	Single mirror, panoramic, dual window design
Scan motors	N/A	Direct drive
FOV (Horizontal)	40°	360°
FOV (Vertical)	40°	270°
Operating temperature	0°C to 40°C	
Lighting	Fully operational between bright sunlight and complete darkness	

Table 3-1: Specifications of HDS2500 and HDS3000 terrestrial laser scanners.

3.2.1.2 Software

Cyclone, the proprietary software for scanner control, data storage, visualisation and processing, is the main tool used to perform terrestrial laser scanning with the Leica HDS2500 and HDS3000 laser scanners. Whilst working on-site the parameters for operating the laser scanner, such as scan area determination and scan resolution, are introduced to the laser scanner through Cyclone. The collected scanned data is displayed in real-time during scanning. In addition, in the applications where the reflective targets were arranged in the scan area, the positions of the targets could be detected and their centres could then be estimated semi-automatically through the Cyclone software.

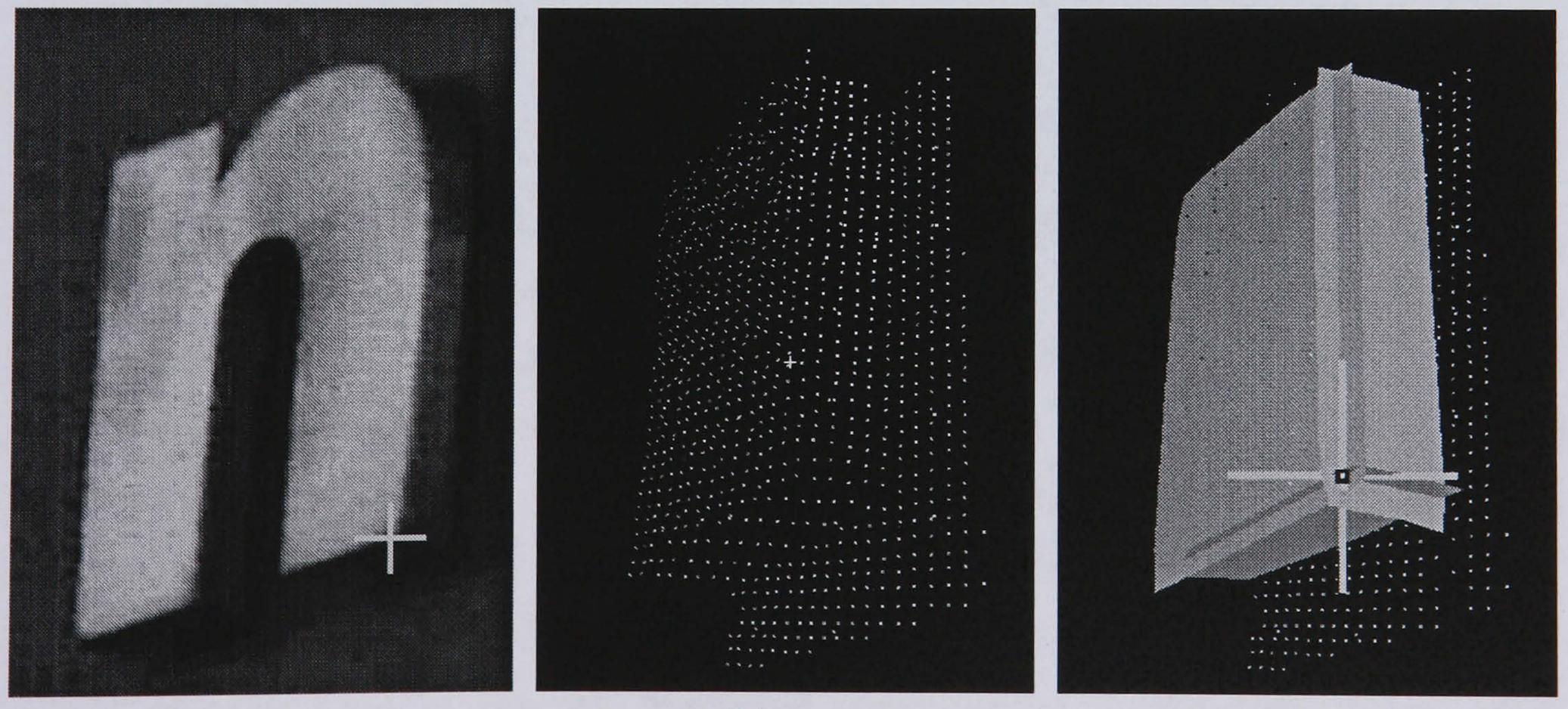
Once the scanning is finished, Cyclone is again used to manipulate the scanned data. At this stage, the functions most frequently used include registration, point cloud modelling and metric measurement. All the results can be exported as ASCII text or CAD drawing

files for further investigations.

3.2.1.3 Considerations

The general workflow of observing the membrane surface follows that introduced in Section 2.3.3.3, although one additional aspect has to be considered in this monitoring scheme. Under normal terrestrial laser scanning procedures, reflective targets are usually arranged in the overlapping scan areas between any two adjoining scan stations for the registration of the scanned models to the reference (site) coordinate system. In this case however, the object of interest (i.e. the membrane surface) is of unreachable height, making the attachment of reflective targets difficult and inefficient. Due to this constraint, natural features were used as control points for model registration instead of attached targets.

The intersection of three modelled planes was used for registration (Barber, 2003). Figure 3-2 illustrates the method to locate a control point from point cloud model. Figure 3-2 (a) is the photo showing the position of the selected control point (the blue cross). In order to obtain accurate positions of the control feature, the object was scanned with a dense point cloud (Figure 3-2 (b)). Subsequently the plane primitive was repeated to model three faces of the point cloud (Figure 3-2 (c)). The corner point could be extracted by selecting the intersection of the three modelled planes and it was taken as the control point for registration.



(a) (b) (c)

Figure 3-2: The strategy of extracting corner points from a dense point cloud.

3.2.2 Surface Model Comparison – Surface Matching

3.2.2.1 Overview

In order to investigate the disparity between the mathematical and laser scanned models, both should be aligned in the same coordinate system in advance. To accomplish this, a surface matching technique, which allowed a surface in the model coordinate system to be matched to a surface in the object space coordinate system (Besl and McKay, 1992), was applied. Based on the 3D conformal coordinate transformation this match enabled the conversion by means of three rotations (ω, ϕ, κ), three translations (Tx, Ty, Tz), and a scale factor (s) (Wolf and Dewitt, 2000).

Surface matching is of great use in situations where it may not be possible to identify sufficient control points from both datasets in order to perform this transformation by conventional means (Karras and Petsa, 1993; Mitchell and Chadwick, 1999; Schenk, 1999; Habib et al., 2000). This is the situation encountered in the membrane structure monitoring scheme, where the lack of accessibility makes traditional registration approaches difficult. By far the most common algorithms used in surface matching have been based on some form of least squares adjustment, minimising the differences in position between the surfaces. Once the matching is finished one of the by-products is the ability to detect changes, as the residuals from the least squares calculation are the surface separations. Examination of these may reveal actual differences that may have occurred between the surfaces produced by different techniques (Pilgrim, 1996). Therefore, surface matching was an ideal method to be applied in this case.

3.2.2.2 Software

To implement the surface matching algorithm the 3D Surf software was employed in the monitoring scheme. The software was originally developed for regular gridded data, where matches were performed only on subsets of the same datasets (Pilgrim, 1991; Mitchell, 1994). Consequently the fundamental algorithm of the software was modified for further applications such as the use of irregular datasets and large complex topographic DEMs, and results were successfully demonstrated in both simulated and real world datasets (Buckley, 2003; Mills et al., 2005). As the characteristics of the simulated surfaces used in the test matching were similar to the ones in the static monitoring scheme, it was inferred that 3D Surf was suitable for performing surface matching in this scheme.

Figure 3-3 illustrates the procedure adopted by the surface matching algorithm implemented in 3D Surf. In the beginning there are two surfaces S_1 and S_2 being matched, where S_1 is the reference surface and S_2 is the surface to be transformed. Instead of simply taking the nearest point on S_2 to a point on S_1 and using its height value, a better approximation can be made with the enclosing surface patch. A Delaunay triangulation of S_1 is therefore constructed to give a table of triangles describing the surface. This can be used to find the enclosing triangle in the triangulation for a point on S_2, enabling a better Z_1 value to be interpolated than if a single closest point was used. Clearly, any consistently large difference between the interpolated height values will imply that the surfaces are not in the correct position, and then the computation of least squares minimisation of vertical differences globally across the surfaces will be iterated. The transformation parameters are updated until the convergence criterion is achieved and the transformation of S_2 will take place at the end of the match (Buckley, 2003).

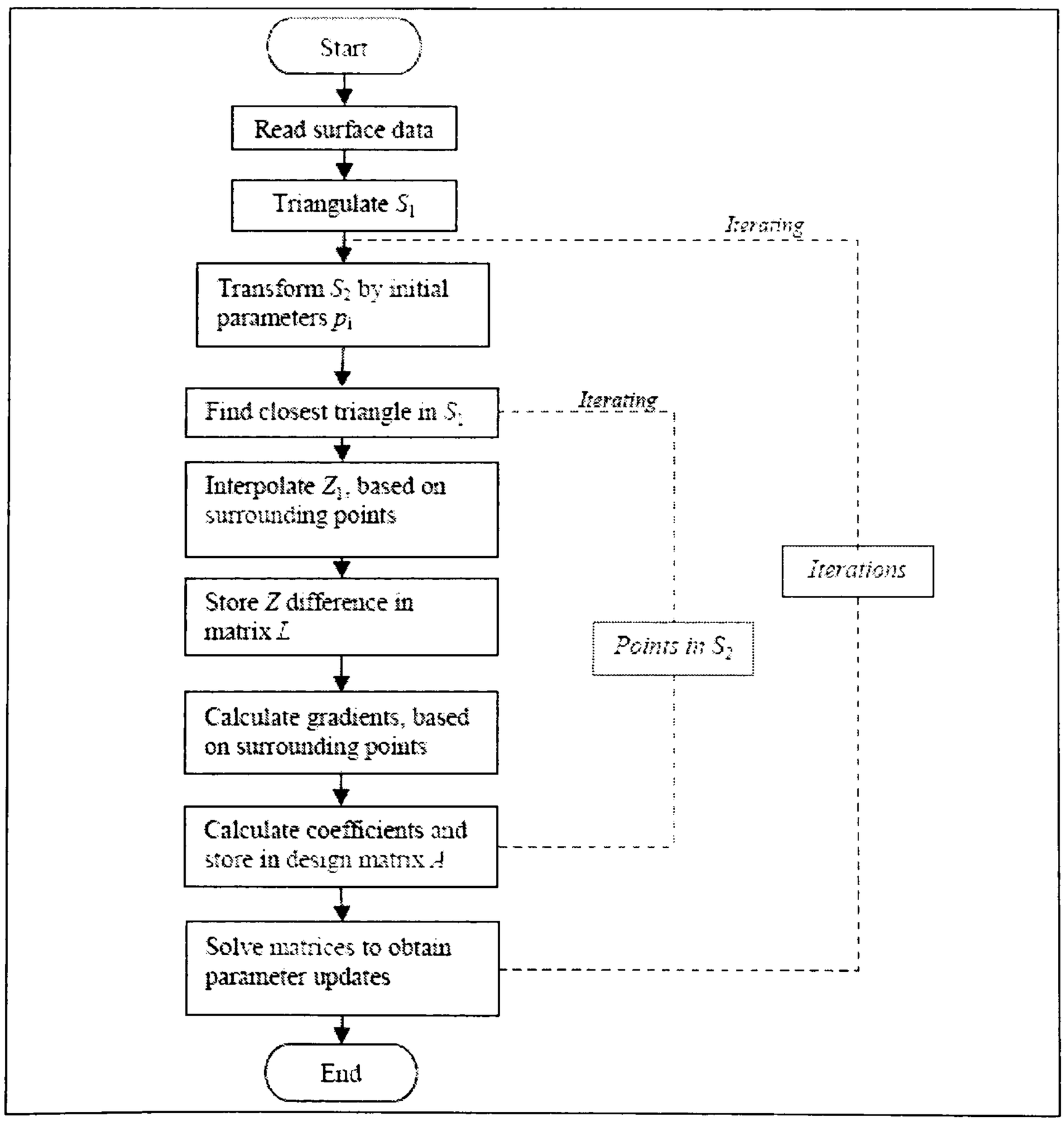


Figure 3-3: Surface matching procedure in the 3D Surf program (Buckley, 2003).

When implementing 3D Surf in this scheme, the laser scanned model was deemed as the true model of the membrane surface and was thus input as the reference surface (S_1), and the mathematical model (S_2) was matched to the scanned model. Once the matching was finished, the mathematical model was transformed and the residuals which represented the surface disparities were calculated. The information would be examined to find out the actual differences that may have occurred between two surfaces.

3.2.2.3 Considerations

As introduced above, surface matching was the means of avoiding having to adopt common control points for aligning the two surface models. Without physical constraints (i.e. control points), however, surface matching relied on a least squares matching principle and the best fit was found by minimising the vertical distances between surfaces. This may result in a statistically correct, but alternate, match being found. In order to avoid this situation, it has been suggested that care is needed in the use of surface matching (Mills et al., 2003a). Therefore the results derived from surface matching were compared to standard conformal transformation (introduced in the next section) in the static surface comparison scheme (Chapter Five).

3.2.3 Surface Model Comparison – 3D Conformal Transformation

In the previous section, a surface matching algorithm was proposed to solve the transformation problem where common points were unavailable. However if enough common points can be found between two models (at least three points were necessary), one of the models could be directly related to the other based on the three-dimensional conformal transformation, a standard seven-parameter adjustment common in photogrammetry and surveying (Dewitt, 1996).

As the designed model was composed of 3D points, lines and curves, the detailed points were clear enough to be identified in the designed CAD drawings of the membrane structure. Their corresponding points in the TLS model were, however, difficult to recognise. One of the reasons was that the data recorded in the TLS model was discrete points rather than continuous information, the success of selecting correct points would be affected by the scan resolution and the shape of the observed object. If the scan density was not high enough to represent the object, it would result in the failure of selecting specific points, e.g. the end point of the mast. In addition, as some components of the membrane structure were flexible, e.g. the corner point of the fabric membrane

roof, they were not suitable for selection as control points.

Considering these factors, the intersection points of the supporting steelworks, which were the fixed components of the structure, were employed as control points. They would be identified in the mathematical and TLS model for solving the transformation parameters. Once the transformation was complete, the two surface models were compared and the discrepancies between them were obtained.

3.3 Dynamic Surface Modelling

The second issue relating to the behaviour of the membrane structure this project aims to investigate is the displacement of the membrane surface under external loading, which may be caused by rain, snow or wind. Based on the methods reviewed in Chapter Two, videogrammetry was considered as the most suitable method to offer a potential solution. Furthermore, a software package, Membrane Structure Monitoring System (MS^2), was developed to process acquired video imagery and construct sequential surface models. By inspecting the dynamic model, the surface displacement could be determined.

3.3.1 Videogrammetric Instrumentation

3.3.1.1 DV Camcorders

Three consumer-grade DV camcorders, JVC GR-D30U, Sony DCR-PC101 and Sharp VL-Z1, capable of capturing image sequences were employed in the monitoring system (Figure 3-4; with specifications listed in Table 3-2). Their portable size and internal LCD monitor allowed handy adjustment of camera stations and on-site quality assurance of the acquired imagery. The recorded imagery was directly downloaded to the host computer via an IEEE-1394 interface. These DV camcorders are all manufactured to meet NTSC standard, which defines the sampling rate as 30 frames per second and the image resolution of a single frame grabbed from a video image sequence as 720 by 480 pixels (Buehler, 2003; PCTechGuide, 2003). To assure the geometric accuracy of using non-metric DV camcorders, the zoom lenses were fixed at their shortest focal lengths and were calibrated using the PhotoModeler Calibration Module before being used for image acquisition (a standard procedure independently verified in Hanke and Ebrahim (1997)). Example interior orientation parameters for the three DV camcorders, derived from camera calibration, are shown in Table 3-3.

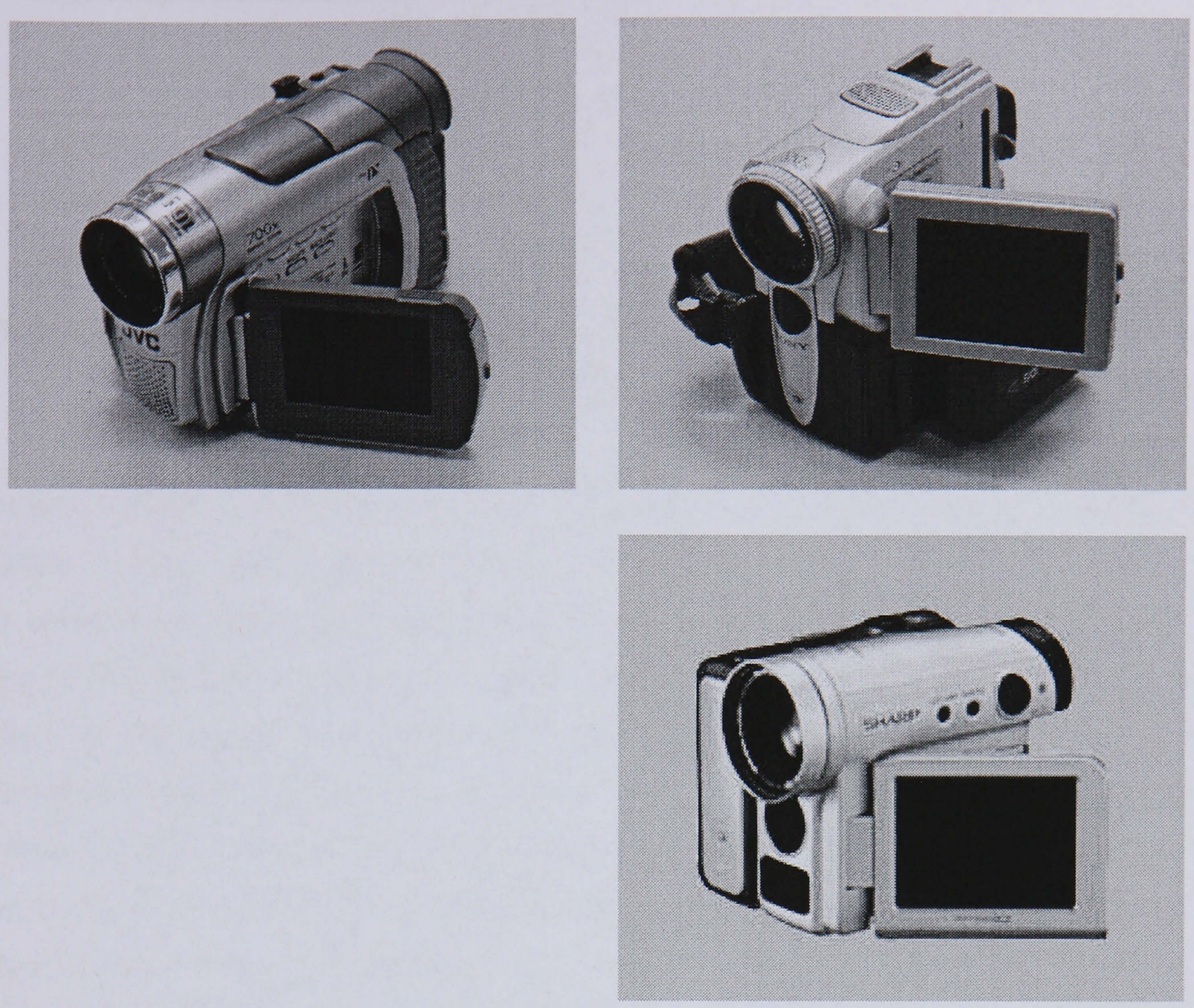


Figure 3-4: Employed DV camcorders (top left: JVC GR-D30U; top right: Sony DCR-PC101; bottom right: Sharp VL-Z1).

		JVC GR-D30U	*SONY DCR-PC101*	*SHARP VL-Z1*
Signal system			NTSC	
Frame rates (fps)			30	
Nominal focal length (mm)		2.7 ~ 43.2	3.8 ~ 38	3.7 ~ 37
CCD size (diagonal: mm)		2.7	6.4	3.8
Image formation			Interlaced scanning mode	
Effective pixels	*Still mode*	–	1,250,000	1,000,000
	Moving mode	680,000	690,000	690,000
Recording time (min)	*Standard play*		60	
	Long play		90	
Interface			IEEE-1394	
Power			Lithium battery/Alternating current (AC) power	
Weight (g)		525	510	480
Operating temperature (°C)			0 ~ 40	

Table 3-2: Specifications of the DV camcorders employed.

	f (mm)	P_X (mm)	P_Y (mm)	$k_1(10^{-3})$	$k_2(10^{-3})$	$p_1(10^{-3})$	$p_2(10^{-3})$
JVC	2.738	0.005	0.063	-5.315	-2.999	-0.671	-0.002
Sony	3.830	0.018	-0.018	1.533	2.578	-0.357	0.821
Sharp	3.850	0.040	-0.014	-1.436	3.773	-0.915	-0.282

Table 3-3: Example interior orientation parameters of the three DV camcorders (the coefficients are pre-defined in Section 2.4.2.3).

In experiments where more than one DV camcorder is adopted, the methods of synchronisation of these camcorders have to be considered. There are several examples of methods to achieve frame synchronisation reported in the literature. For example, Lee and Faig (1999) attached a stopwatch to the front of the test object. Synchronisation was achieved by matching the frames with the same clock indication, which was presented on each recorded frame. Harvey and Shortis (1996, 1998) used a single Light Emitting Diode (LED), which could be switched on and off manually or automatically switched on every five seconds, to synchronise the left and right camera images from which measurements were made. Harvey et al. (2001) further produced an improved unit by arranging a circular array of 25 LEDs. The synchronous images were then chosen by identifying the differentiation of colour and position of individual LEDs. In addition to the utilisation of visible signal, D'Apuzzo (2003) and Hobbs (2003) proved that the multiple cameras can be synchronised using a clapper or something generating a "clap" sound.

In summary, the method used to synchronise the DV camcorders was to trigger a simultaneous event which was video or audio sensible in all video images. As a data projector was essential equipment in the videogrammetric monitoring (the purpose will be introduced in Section 3.3.3) it was also utilised to project a "swift recurring dot" for synchronising the camcorders. When performing the monitoring at the test site, the camcorders and projector were firstly arranged in their appropriate positions, the projector was connected to a computer and a dot was projected onto a suitable position where it could be viewed by all cameras. The dot was then projected quickly and regularly and recorded by the DV camcorders.

Because the sampling rates of the three DV camcorders were the same, the frame intervals between recurring dots appeared in one video image would correspond to those in the other images. So after transferring the image sequences to the host computer,

the next stage was to mark the serial numbers of frames in which the dot was recorded in each camcorder. Comparison of these numbers from the three image sequences could determine the offset between the synchronous dots. Finally the synchronous image sequences could be defined.

3.3.1.2 CCD Video Cameras

Two machine vision type CCD video cameras, Oscar OF-810C (Figure 3-5), were the other type of instrumentation used for collecting the video imagery. In future discussions they will be referred to as Oscar cameras. Different to the DV camcorders, there are no control buttons on the Oscar camera body but only two jacks at the rear of the camera, which are IEEE-1394 and HiRose plugs. All the camera controls were accomplished through these two ports. The IEEE-1394 interface was used to supply power, control the camera and output recorded frames. In order to work with the Oscar camera a laptop/desktop computer equipped with IEEE-1394 interface was therefore necessary. After they were connected, the camera settings could be adjusted through an operations interface in the host computer, and the change would be reflected in the images and displayed in real time. Note that the DV camcorder also provides an IEEE-1394 port but this is only for transferring image files between the camcorder and computer.

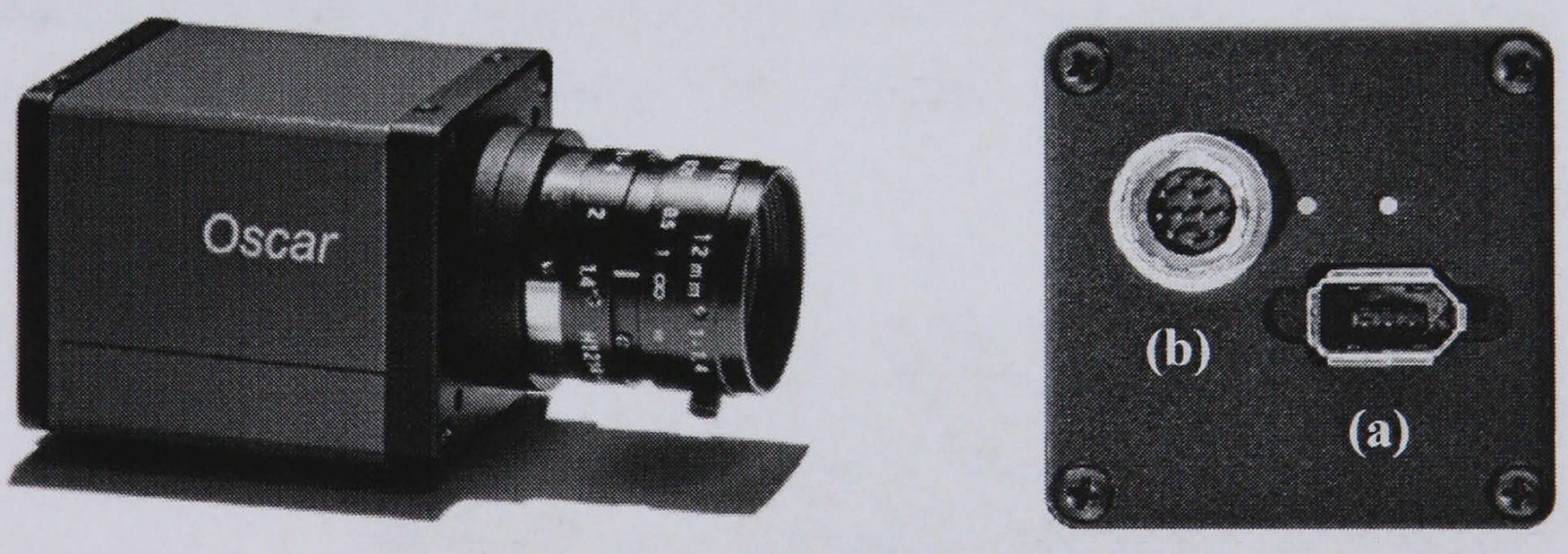


Figure 3-5: The CCD video camera employed, Oscar OF-810C and the rear of the camera ((a): IEEE- 1394 plug; (b): HiRose plug).

The HiRose plug was mainly used to receive an external electrical signal for triggering the camera's shutter. In the experiments of applying external triggering, a pulse generator (Figure 3-6) was connected to the camera and used to transmit square waveform signals to the camera. Since the signals were generated regularly according to the pre-set frequency (range is from 0.002 Hz to 2000 Hz), the image sequences could be obtained in that order.

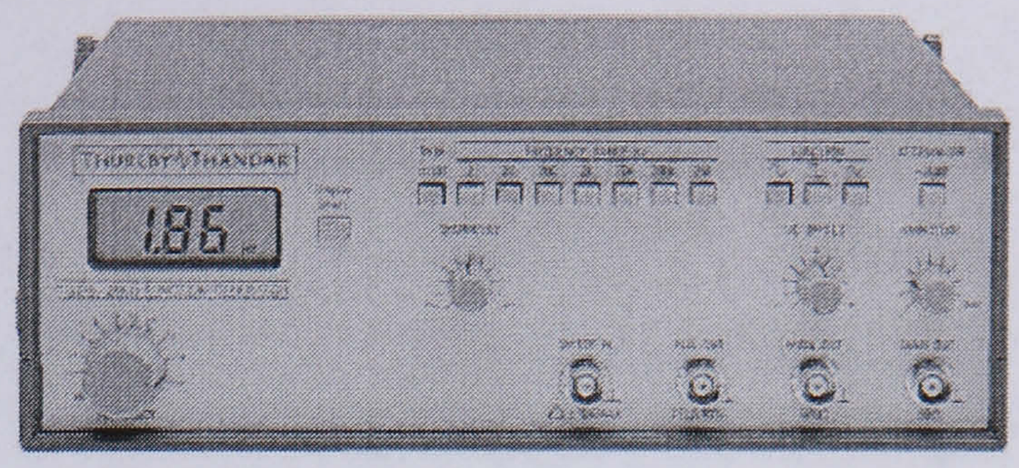


Figure 3-6: The pulse generator employed (Thurlby Thandar Instruments (TTi) TG 215), the frequency was adjustable and displayed in the window.

One of the features of the Oscar camera was the flexibility of image format. Attributes (Table 3-4) such as image size, image formation method, shutter mode and frame rate could be changed based on different requirements. To determine suitable camera settings in the dynamic monitoring scheme various image formats were tested. As a result the Sub-sampling Mode, at which the image was formed by the progressive scan method and the image size was 1088 pixels by 822 pixels, was adopted. In addition, in order to cover the area of interest at the test site a 12 mm lenses was fitted to the Oscar camera. With this setting, the Oscar cameras were calibrated in a close range 3D calibration field (Figure 3-7) immediately before being applied in the videogrammetric monitoring. A total of 69 stick-on targets were arranged and four images of different rotation angles were taken from each of five camera stations (Figure 3-8). The calibration was carried out in the manner described in Mills et al. (2003b), using a self-calibration bundle adjustment in the VMS software. Compared to PhotoModeler, more complete information from the adjustment (e.g. standard deviations of the interior orientation parameters) was offered by using VMS. Example parameters for the two cameras are shown in Table 3-5.

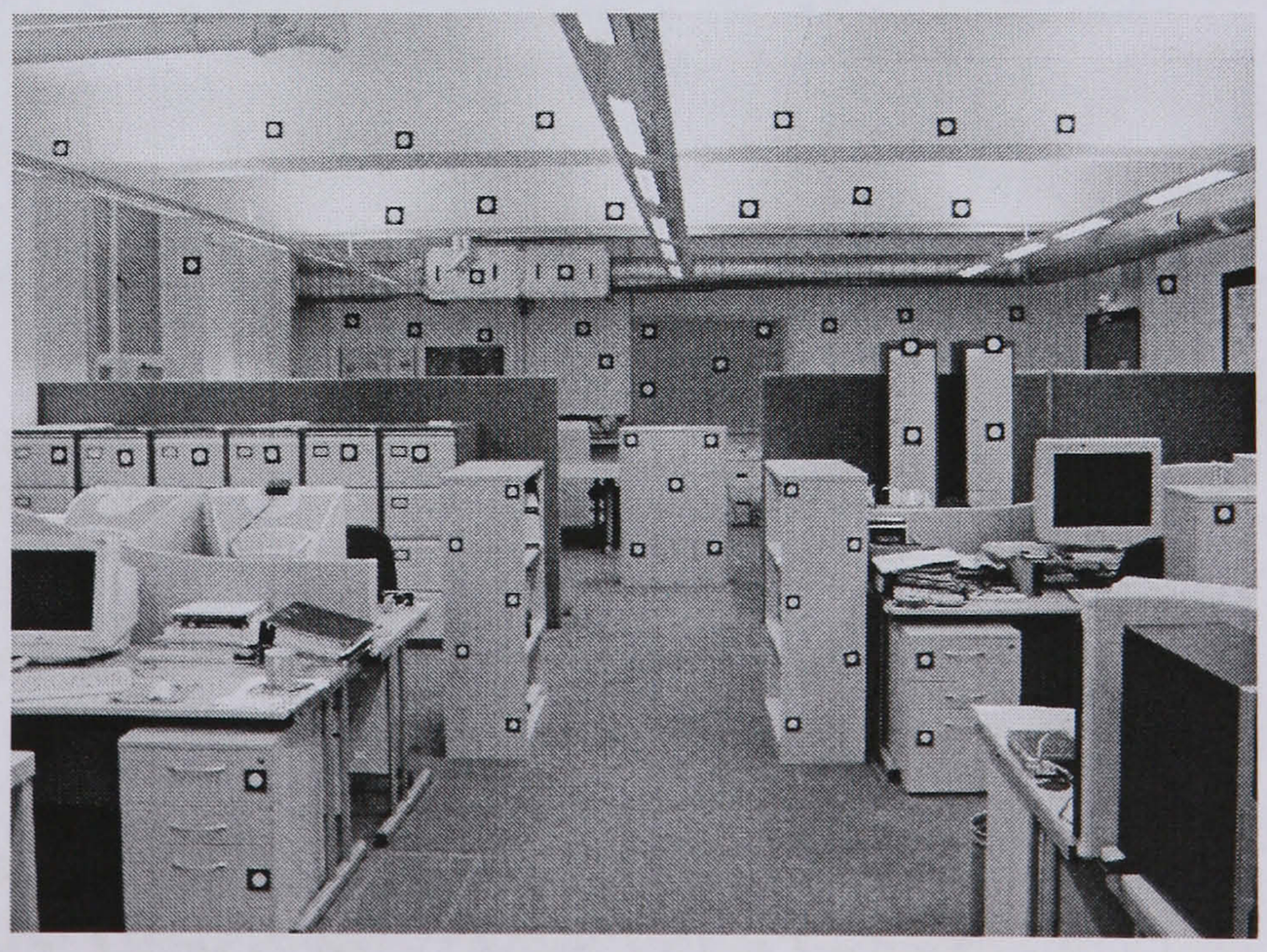


Figure 3-7: The close range calibration field.



Figure 3-8: The camera network in the close range calibration field.

CCD size (diagonal: mm)		11
Effective pixels		3288 x 2470
Pixel size (μm)		2.7 x 2.7
Image size (pixels)	*Format1*	1024 x 768
	Format7 Mode0	3272 x 2469
	Format7 Mode1	3272 x 2469
	Format7 Mode2	1088 x 822
Image formation	*Format1*	
	Format7 Mode0	Frame readout mode
	Format7 Mode1	
	Format7 Mode2	Sub-sampling mode
Shutter mode	*Format1*	–
	Format7 Mode0	Joint shutter
	Format7 Mode1	Split shutter
	Format7 Mode2	–
Frame rate (fps)	*Format1*	–
	Format7 Mode0	Up to 3.1
	Format7 Mode1	
	Format7 Mode2	Up to 8.9
Shutter speed (sec)		1/4095 ~ 1
Interface		IEEE-1394
Power requirements		DC 8 V ~ 36 V
Weight (g)		170 (without lens)
Operating temperature (°C)		5 ~ 45

Table 3-4: Specifications of the Oscar camera (Allied Vision Technologies, 2005).

		f (mm)	P_X (mm)	P_Y (mm)	$k_1(10^{-4})$	$k_2(10^{-5})$	$p_1(10^{-4})$	$p_2(10^{-5})$
Oscar 1	*Value*	12.847	-0.030	0.047	-6.464	1.714	0.057	-1.354
	Std. dev.	0.001	0.006	0.004	0.127	0.049	0.124	1.002
Oscar 2	*Value*	12.827	0.057	0.034	-6.138	1.496	-0.561	-0.593
	Std. dev.	0.001	0.005	0.004	0.117	0.043	0.116	0.960

Table 3-5: Example interior orientation parameters determined in camera calibration.

In the videogrammetric monitoring scheme, the two Oscar cameras were employed to shoot sequential stereo pairs of the area of interest on the membrane roof. As mentioned before a computer equipped with an IEEE-1394 port was essential, additionally a connection hub for IEEE-1394 devices called a repeater, was used to connect the two Oscar cameras with the host computer. A pulse generator, not only for external triggering but also synchronisation was adopted. The final hardware configuration of the monitoring system is illustrated in Figure 3-9.

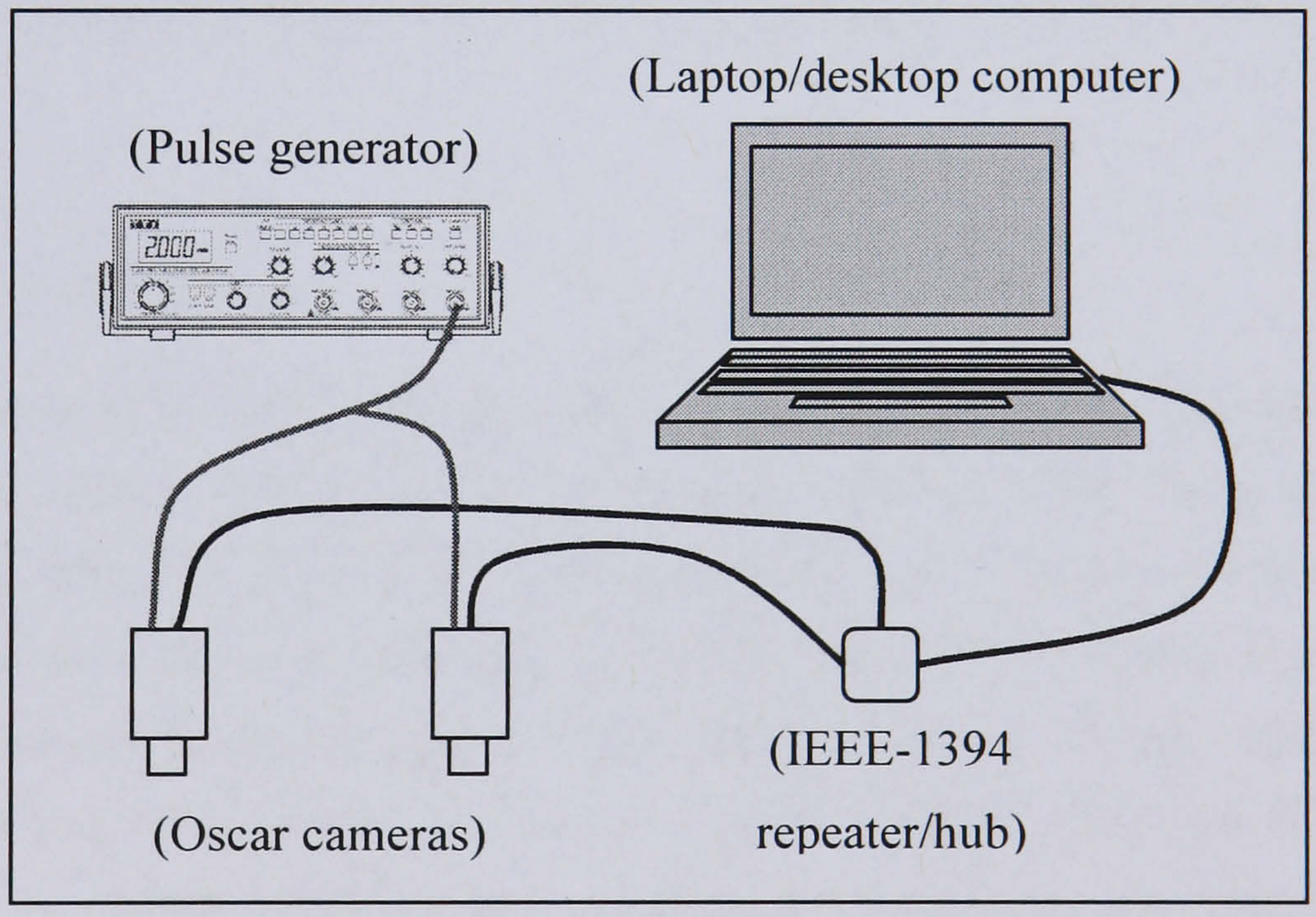


Figure 3-9: Hardware configuration of the videogrammetric monitoring system.

3.3.2 Non-contact Control Method

3.3.2.1 Introduction

A certain number of control points in object space are generally required for photogrammetric or videogrammetric applications. Object space coordinates of control points, which must be image-identifiable features, are normally determined via some type of field survey technique such as GPS or total station instrument (Wolf and Dewitt,

2000). However, in some situations it is difficult to identify reliable features or attach physical targets as control points. Therefore, conventional control methods cannot be applied. As a solution to this problem, it was proposed to adopt a technique based on the use of laser footprints.

Nowadays total station instruments, which incorporate a theodolite with electronic circles and an EDM unit, are used commonly in surveying. As reviewed in Chapter Two, the reflectorless measurement mode, in which a prism or special reflector is not necessary, has become a standard feature of total stations. To take a reflectorless measurement, the telescope cross hairs are simply aimed at the point to be measured and the observation is recorded. If a reflectorless observation is made by a system adopting a visible red laser, a red footprint will appear on the aimed point therefore it can be used to locate the measurement point exactly instead of using the telescope cross hairs. Meanwhile the horizontal and vertical angles, together with slope distance, are recorded and the 3D coordinates of the object point can be determined. As a visible laser footprint is generated at the moment the triggered laser beams touched the surface of the target and is of accurate 3D coordinates, the laser footprint has the potential to be used as a control point and can be utilised to efficiently perform the videogrammetric control task.

3.3.2.2 Methodology and Consideration

For reflectorless measurement taken with a phase shift system, the range that can be obtained is about 100 metres, with a similar accuracy to that obtained when using a prism or foil. Moreover, phase shift systems tend to have a smaller laser divergence than a pulse system and can locate objects more precisely (Uren and Price, 2006). Therefore a Leica TCRA1103 total station applying phase shift method (Leica, 2002) and featuring a distance measurement with visible laser beam (quoted angular precision of +/- 3" and range precision +/- (2mm+2ppm)) was employed to generate the laser footprint. Once the video cameras were positioned, the total station was manipulated to make a series of reflectorless measurements. The laser footprints, complete with 3D coordinates determined by the total station, were simultaneously recorded by the video cameras.

In the sequence of video frames, the laser footprints were shot regularly. For extracting the footprints, an image containing all laser footprints was firstly generated. Because the intensity of the laser footprints was higher than the monochromatic fabric membrane

roof in the image, the pixels with higher pixel values were considered as the laser footprints. Based on this principle an image arithmetic algorithm was performed frame by frame, to compare the intensity values pixel by pixel. During the comparison the pixels with higher intensity were extracted and stored in a temporary image. For example there were 15 laser footprints recorded in the image sequence of *N* epochs (Figure 3-10). A footprint was shot in the frame of epoch 1 but no footprint in epoch 2. After comparing the frame of epoch 1 against epoch 2, the footprint in epoch 1 was detected and stored in the temporary image. Subsequently the temporary image was compared with the frame of epoch 3, in which another footprint was recorded, and the second footprint was stored in the temporary image. By repeating the procedure to the frame of epoch *N*, an image containing 15 footprints was produced. The laser footprints were then extracted and introduced in the videogrammetric process as control points. For automated processing, the image arithmetic algorithm was executed by a routine programmed in MATLAB.

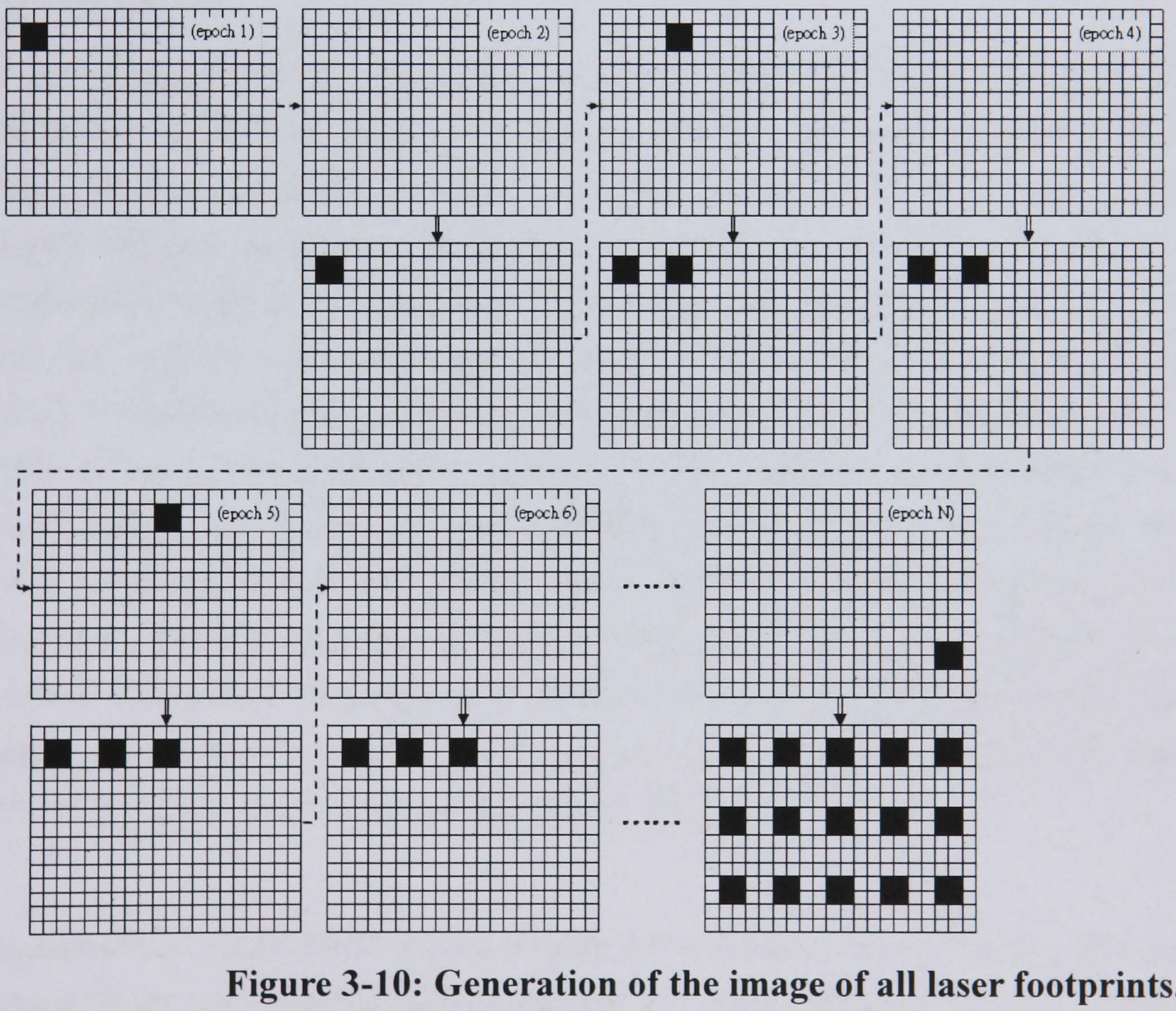


Figure 3-10: Generation of the image of all laser footprints.

Whilst undertaking a reflectorless observation, the measurement accuracy is highly affected by the angle of incidence of the measurement and the reflectivity of the target (Uren and Price, 2006). Kavanagh (2003) also suggests that targets with light-coloured,

flat surfaces perpendicular to the measuring beam provide the best range and accuracies. Considering the incidence angle of the measurement, the total station is arranged at an appropriate position when performing non-contact control, to assure the measurement quality. Regarding the target reflectivity, as the fabric roof observed is with characteristics of white and smooth surface, it should be an ideal reflector for performing reflectorless measurements. To prove this, a spectral reflectance test had been carried out to inspect the reflectivity of the observed fabric membrane (Section 3.4.2). As to the equipment for generating the laser footprints with 3D coordinates, a terrestrial laser scanner possessed similar characteristics as total station and was therefore considered of potential for supplying control laser footprints. The feasibility of employing a laser scanner in the non-contact control method was investigated in the proof-of-concept experiment and is reported in Section 3.4.5.

3.3.3 Projected-dot Videogrammetry

3.3.3.1 Background

A complete and accurate surface model will be determined from videogrammetry if there are sufficient artificial targets or natural features on the surface to measure. However, the membrane surface lacked identifiable texture and its height made attaching targets difficult. Moreover, the membrane roof surface is thin and flexible, so applying traditional targets to the surface may deform its original shape. To accommodate this problem, a non-contact targeting method utilising structured light was considered. Normally structured light is used either in an active or a passive manner (Maas, 1992b). In the former applications a light spot (or a line, grid) generating by a laser was recorded by a location-sensitive photoelectric detector, since the geometry of projection and recording device was known the position of the light spot could be solved (Fisher et al., 1999; Li and Zhang, 2004). The practice of passive structured light is used to texture a surface with a projected random pattern, the 3D surface model can be subsequently determined by correlating the pattern shown on the recording devices (Maas, 1992a; D'Apuzzo, 2002; Schmidt and Tyson, 2003).

In the videogrammetric applications where similar circumstances were met, the passive use of structured light was adopted (Greenwood et al., 2001; Black and Pappa, 2003; Pappa et al., 2003; Blandino et al., 2003). In these applications, a regular projected-dot pattern was designed and projected onto the surfaces of interest, replacing the physical targets. Due to the advantages of time-effective, non-invasion of the surface, relatively simple hardware and fast algorithms, and greater flexibility for allowing customisation

to any density or size (Ganci and Brown, 2000), this method was introduced in the videogrammetric monitoring scheme.

3.3.3.2 Methodology and Consideration

A regular dot pattern was designed and projected onto the area of interest using a data projector. For pursuing higher measurement precision discussed in Section 2.4.2.4, the dot image diameter was designed as 10 pixels. Moreover, as recommended by Brown (1985), a pattern of white dots against black background was projected onto the fabric membrane. During dynamic surface monitoring, the dot pattern was projected onto the surface of interest and the changes in position of the projected dots over time were recorded in the employed videogrammetric instrumentation. The centres of these dots were extracted following the centroiding algorithms described in Section 2.4.2.4 and then imported to the videogrammetric system for computing their 3D coordinates.

As the projected dots were not physically attached to the membrane roof surface, it is noteworthy that they would not arbitrarily move along all directions when the surface vibrated or changed shape. The path of each target, as measured by videogrammetry, instead always follows a straight line moving either towards or away from the projector, regardless of how the surface moves in reality (Maas, 1992b; Pappa et al., 2003). In this monitoring scheme, the dominant direction of displacement was expected to occur almost parallel to this direction, the method of using projected-dots therefore providing satisfactory targeting.

3.3.4 Workflow

To summarise the procedure of applying non-contact control and projected-dots videogrammetry in dynamic surface modelling, a general workflow at the stage of image acquisition is:

(i) Determine the area of interest and arrange data projector at the appropriate position to cover the area.

(ii) Arrange video cameras and total station at appropriate positions to achieve optimal geometry.

(iii) Perform non-contact control method.

(iv) Project dot pattern onto the membrane surface and start videogrammetric monitoring.

3.4 Laboratory Experiments

3.4.1 Overview

In order for the proposed methodology to be considered suitable for monitoring a real membrane structure, proof-of-concept tests were conducted to prove the feasibility, accuracy and reliability of the methodology. As the laser technology was applied in the membrane structure monitoring scheme, the characteristics of spectral reflectance of the observed fabric membrane was inspected in Test 1. In Test 2 the visibility of laser footprints in the video imagery collected by the DV camcorders and CCD video cameras was evaluated. Also, the proposed non-contact controlling was compared against conventional methods to inspect its feasibility and reliability. Once finished, the non-contact control method and projected-dots videogrammetry were applied to construct the surface model of a stairwell ceiling in Test 3. In addition, the performance of the off-the-shelf software, PhotoModeler Pro 5, was investigated.

In Test 4 a terrestrial laser scanner was used for implementing the non-contact control method. Along with the projected-dots videogrammetry, a sequential 3D model of a dynamic surface was determined. Also, for improving the automated processing the routines were programmed using the MATLAB language and used to perform the measurements and computations. By employing two CCD video cameras and a total station, a test dynamic surface was monitored in Test 5. The PhotoModeler Video (PMV) module was introduced to construct the sequential 3D model. The performance of the monitoring system and the limitations of the software were discussed in this test.

3.4.2 Test 1 – Spectral Reflectance Analysis

3.4.2.1 Methodology

As introduced in the previous sections, laser technology was broadly applied for both producing the laser scanned model of the finished as-built membrane roof and to serve as control footprints in the videogrammetric monitoring system. Because the accuracy of distance measurements depends on the intensity of the reflected laser beam (Lichti et al., 2000; Boehler et al., 2001; Schulz and Ingensand, 2004b), the characteristics of spectral reflectance of the observed fabric membrane was therefore inspected prior to practical experiments. To achieve this, an Analytical Spectral Devices (ASD) FieldSpec Pro FR spectroradiometer with a full spectral range (350 – 2500 nm), equipped with a contact reflectance probe was employed to analyse the spectral characteristics of the

woven polyester yarns with a PVC coating, which was the identical material used in the membrane structure to be subsequently observed.

Two measurements, the spectral response of a reference sample and the spectral response of the target material, were required in order to determine the reflectance of the fabric. The reflectance was then computed immediately by dividing the spectral response of the target object by that of the reference sample (Analytical Spectral Devices, Inc., 2001). A white panel served as the reference sample and a sample PVC-coated polyester fabric were placed separately on two flat boards in the laboratory (Figure 3-11). The inspection began by positioning the contact reflectance probe directly on the white reference panel to collect the reference measurement. Subsequently the probe was moved onto the PVC-coated polyester fabric to collect its spectra. The measurement of the sample PVC-coated fabric was repeated several times, also the reference measurement was performed regularly. The resultant spectral reflectance of the PVC-coated fabric was displayed in real-time and stored in the host computer. By using this method, the spectral response curve shown on the screen was the final product as the reflectance calibration was carried out during the operation and most errors were mathematically eliminated (Anderson, 2002).



Figure 3-11: Spectral reflectance test by using the contact reflectance probe.

3.4.2.2 Results

The average spectral response curve of the PVC-coated polyester fabric observed by contact reflectance probe is shown in Figure 3-12. A similar spectral reflectance curve

was found in Navin's report (2005) (Figure 3-13). By inspecting both curves it is revealed that strong reflectance of the PVC-coated polyester fabric is anticipated between the wavelengths of 400 nm to 1350 nm. The two items of equipment applied in the membrane structure monitor scheme, a Leica TCRA1103 total station and a Leica HDS2500/3000 laser scanning system, whose central laser wavelengths were 670 nm and 532 nm respectively, are plotted as dashed lines in Figure 3-12. The diagram shows that PVC has high reflectance across the wavelengths of both the total station and laser scanning system. The abundance of reflectance from the PVC fabric that could be expected at 532 nm and 670 nm therefore indicates that the laser scanning system and total station could perform well on the PVC surface.

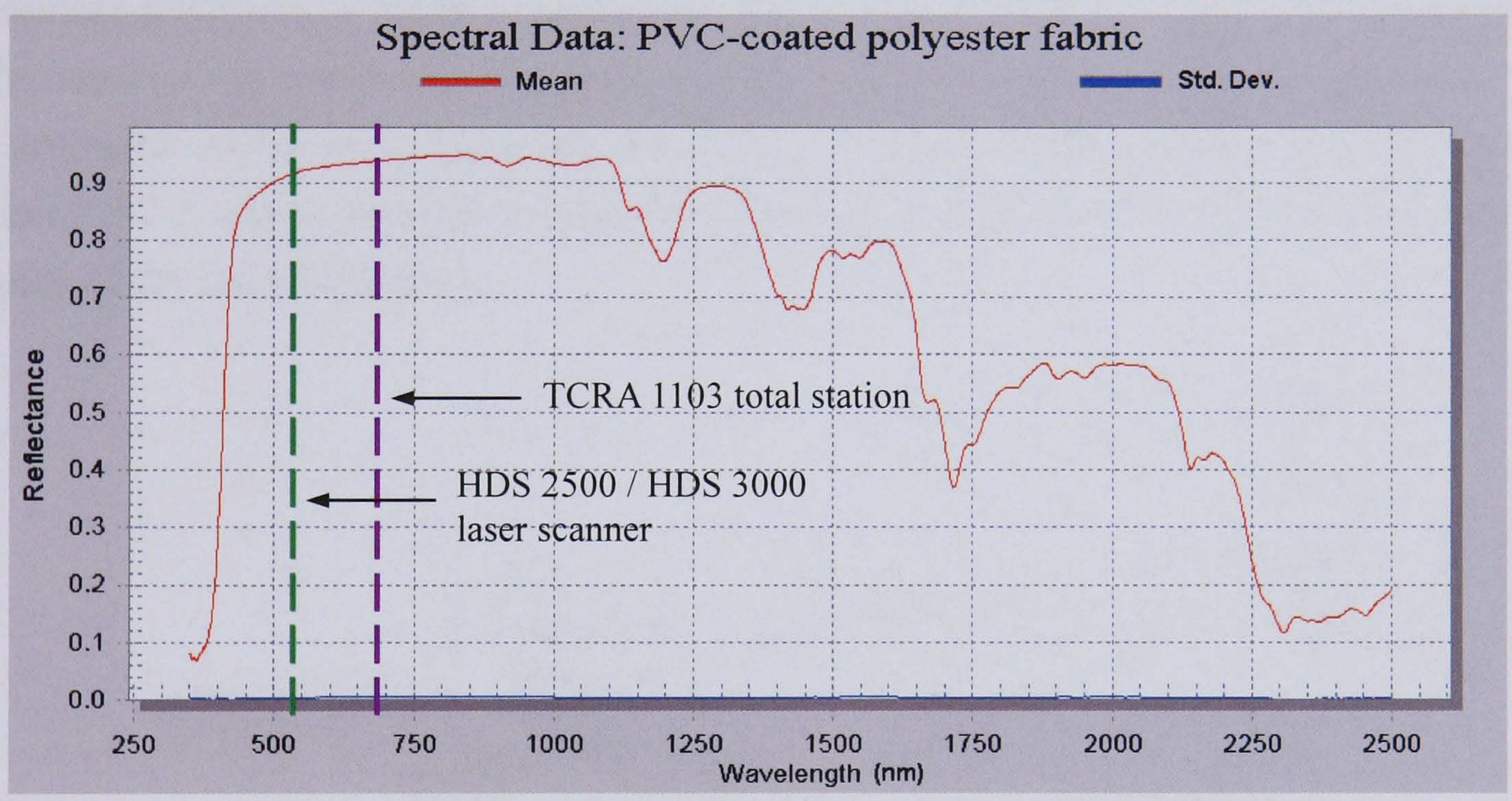


Figure 3-12: Spectral reflectance of the PVC-coated polyester fabric.

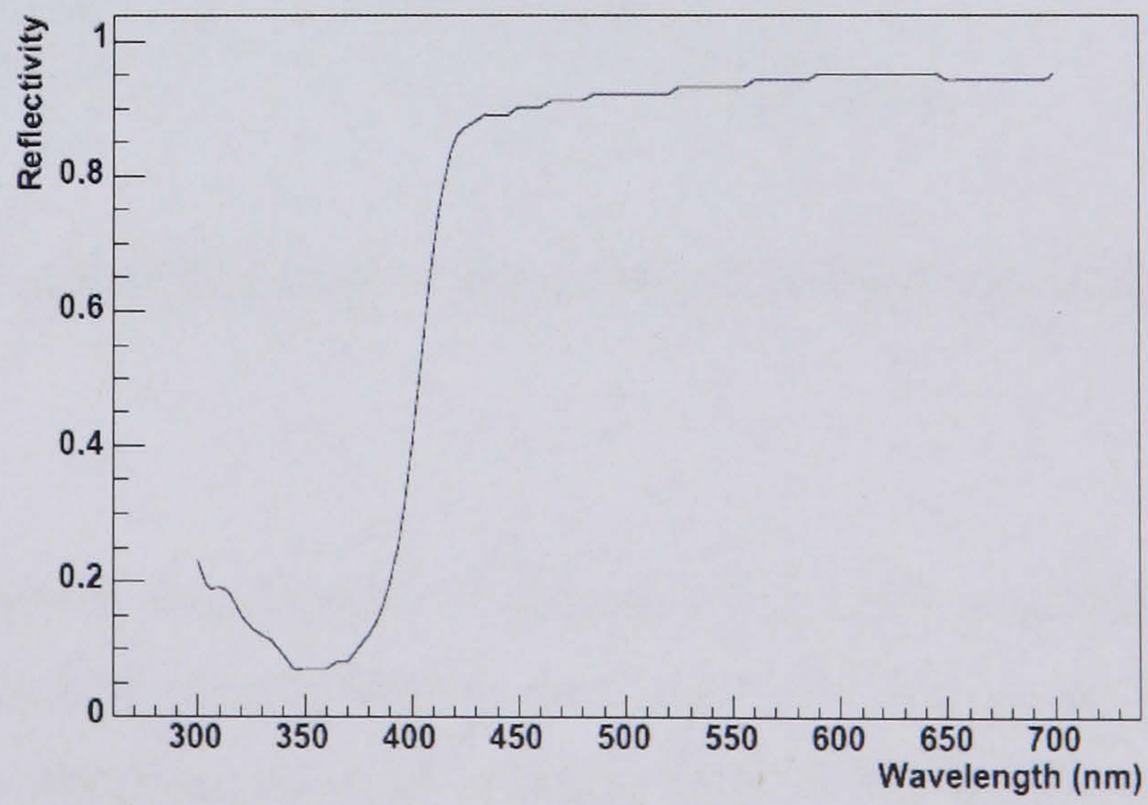


Figure 3-13: Spectral reflectance of PVC fabric obtained by Navin (2005).

3.4.3 Test 2 – Reliability Test of Using Laser Footprint as Control

3.4.3.1 Methodology

Conventional targets and the laser footprints from the total station were separately used as control points for determining the exterior orientations of the cameras. By investigating the root mean square (RMS) error of the check points, the feasibility and reliability of the non-contract control was determined in this test. Twenty targets with high colour contrast were attached across a wall surface, and the polar method was applied to measure their three dimensional coordinates using a Leica TCRA1103 total station. Three DV camcorders (Sony DCR-PC101, Sharp VL-Z1 and JVC GR-D30U), whose lenses were fixed at their shortest focal lengths, were then arranged in appropriate positions to capture the surface area (Figure 3-14). For realising the system performance at the test field a simulation of the configuration that would be used on-site was arranged in this test. Subsequently the non-contact control method described in Section 3.3.2.2 was performed and the DV camcorders were switched on to shoot video imagery of the laser footprints.

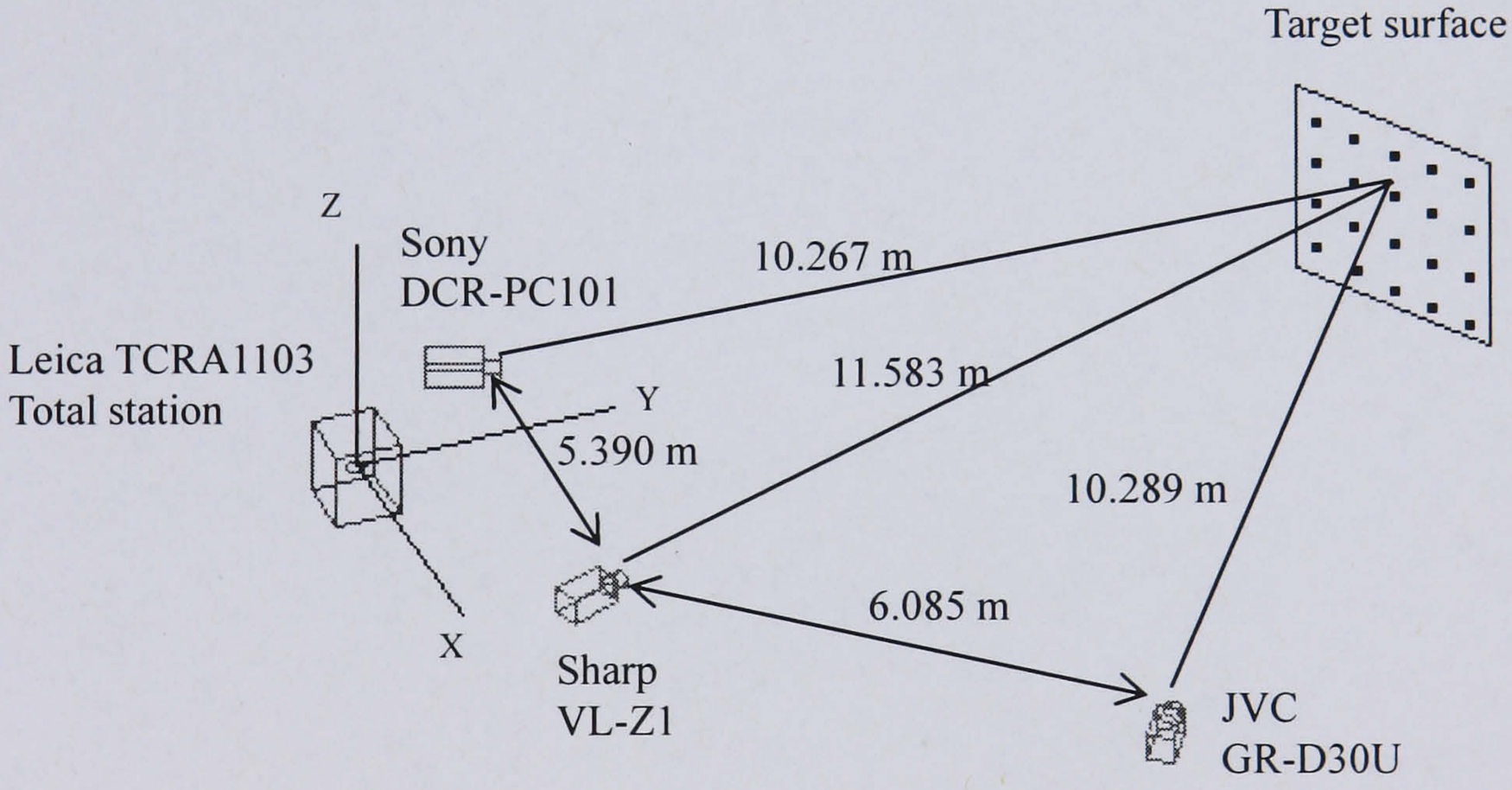


Figure 3-14: Setup of reliability test of non-contact control method.

3.4.3.2 Results

By applying the image arithmetic algorithm described in Section 3.3.2.2 the complete control images, which recorded both attached control targets and laser control footprints, were produced (Figure 3-15). From the zoom-in view of a single laser footprint it was found that the footprint was easily determined due to the obvious difference of the colour intensity between the laser footprint and the background. These three images were subsequently input into the PhotoModeler Pro5 software and the targets were

extracted automatically by a centroiding algorithm. A total of 20 attached targets and 76 laser footprints were derived from each image. In the first part of the test 10 attached targets, distributed evenly across the surface, were selected as control points. Meanwhile the 10 remaining attached targets were used as check points and their coordinates were estimated via a bundle adjustment. The second part of the test began by selecting 10 laser footprints as control points, and the same 10 attached targets used before were adopted as check points. Once computed the coordinates of the check points were compared with the total station measurement, and the RMS error of check points were solved and are summarised in Table 3-6.

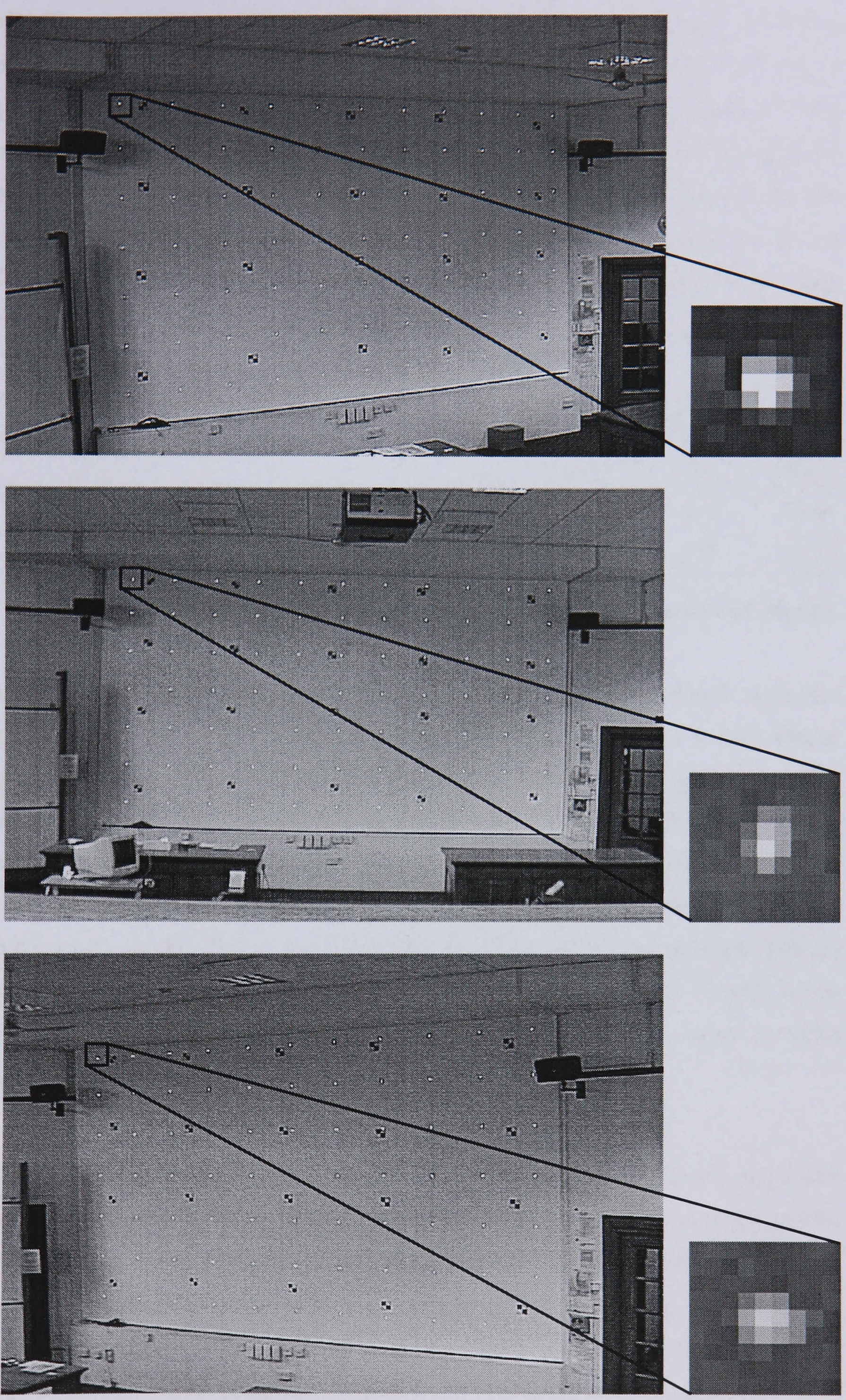


Figure 3-15: Images of complete control footprints and attached targets. Top to bottom are images taken from left (Sony DCR-PC101), middle (Sharp VL-Z1) and right (JVC GR-D30U) camera stations.

Based on the RMS error values listed in Table 3-6, the overall accuracy of using attached targets as control points is 12.0 mm, while it is slightly improved to 11.3 mm when adopting laser footprints as control. Although the size of the laser footprint was small (less than the ideal target image size suggested by Clarke et al. (1993)), and the pointing precision may be less than optimal as a result, the accuracy indicates that the use of laser footprints generated by the total station as control is comparable to the traditional methodology. Non-contact controlling can therefore be considered suitable for use in videogrammetric applications (Lin and Mills, 2005a).

		RMS error of check points (mm)			
		σ_X	σ_Y	σ_Z	σ_{All}
Control points	*Attached targets*	1.5	11.2	4.0	12.0
	Laser footprints	6.1	7.5	5.8	11.3

Table 3-6: Check point quality from the two control methods.

In order to understand the performance of the non-contact control method with the Oscar cameras, an experiment similar to the previous one was repeated. The two Oscar cameras equipped with the 12 mm lenses and the image size of 1088 pixels by 822 pixels were introduced to collect the image sequences. Before the start of the image acquisition, various frame rate and shutter speeds were tested to determine the most suitable values for shooting the laser footprints. As a result they were set to 3 fps and 1/4095 seconds respectively for clearly recording the laser footprints (as discussed later). Since the optimal settings for the Oscar cameras to apply non-contact control were determined, the synchronous signal was generated by the pulse generator to start shooting the image sequences.

The resulting images of 20 attached targets and 40 laser footprints are shown in Figure 3-16. 10 attached targets and 10 footprints were respectively selected as control points and the identical 10 attached targets were employed as check points. Automatic extraction by using a centroiding algorithm was performed to determine their centres and the bundle adjustment was then applied in PhotoModeler. Finally the RMS error values of the check points were obtained (Table 3-7), showing that the measurement accuracy of using traditional controlling and non-contact method was 5.3 mm and 6.3 mm respectively. While the accuracy of the proposed non-contact controlling is less than the conventional one in this experiment, it was nevertheless still considered an appropriate control method for the measurements whose requirements were at this level.

Also, no extra preparations were necessary for the execution of the non-contact control method, minimizing the effort of arranging a network of control points.

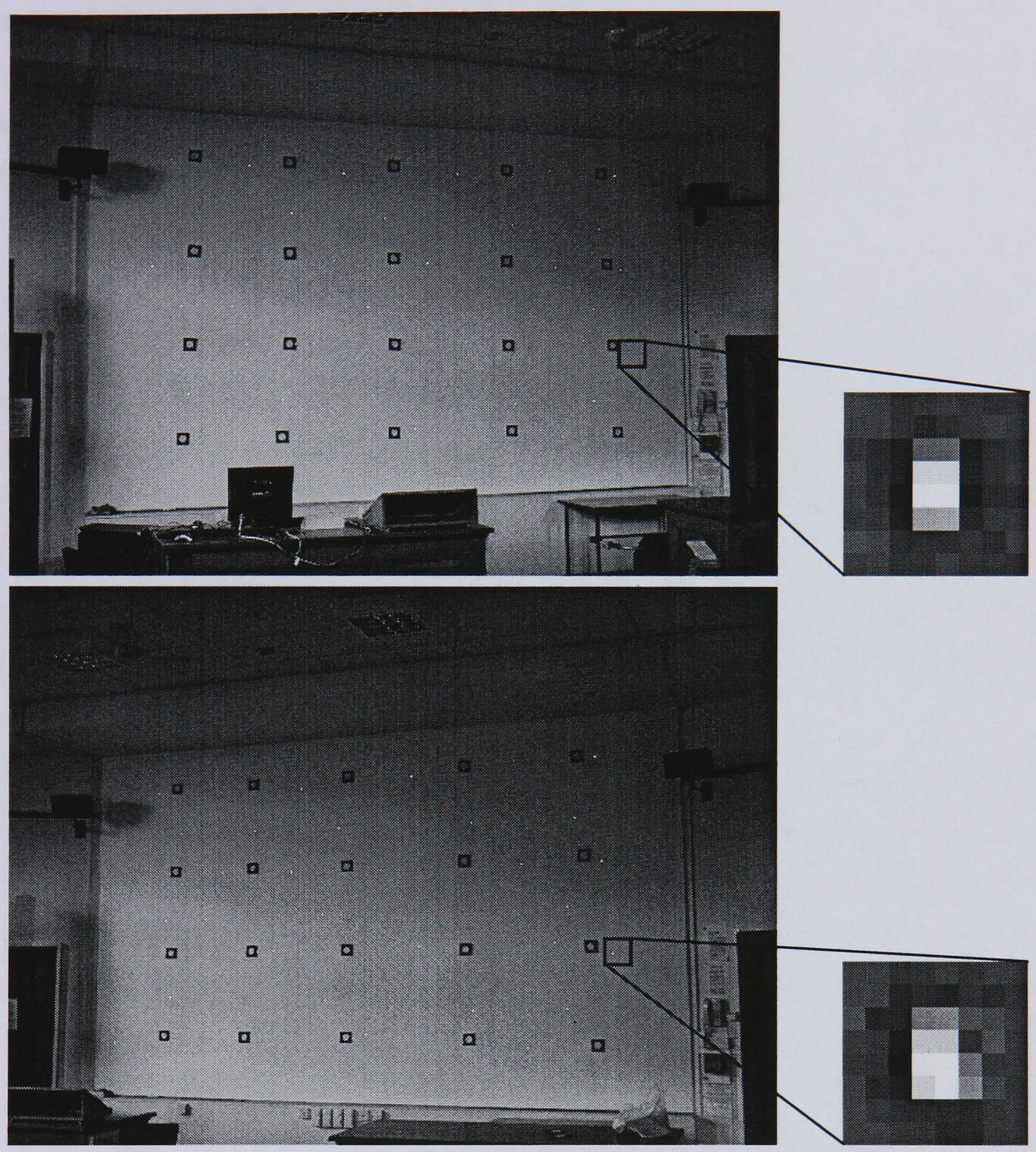


Figure 3-16: Images of complete control footprints, single zoom-in footprint and attached targets, taken by the two Oscar cameras.

		RMS error of check points (mm)			
		σ_X	σ_Y	σ_Z	σ_{All}
Control points	*Attached targets*	2.8	2.3	3.9	5.3
	Laser footprints	4.0	2.6	4.2	6.3

Table 3-7: Check point quality from the two control methods – Oscar cameras.

3.4.3.3 Discussion and Summary

The feasibility of adopting a non-contact control method in videogrammetric

applications was evaluated in this test. Although the proposed method proved reliable, there are still three points that have to be considered during implementation. In order to ensure that the laser footprints and the projected dots are clearly recorded in the acquired image sequences during the image acquisition stage, the brightness of the test site has to be first examined. If the working environment is too bright, failure to completely recognise all targets may occur. In this case image processing skills are required to highlight the laser footprints prior to the subsequent target extraction.

The second factor that determined the clarity of laser footprints on the images was the chosen frame rate. As the laser footprint appeared instantly on the observed object, a high frame rate of the camera was required to capture the laser footprints. However by doing this, the required storage space would be augmented and processing time would be increased. For the DV camcorder the imaging frequency was fixed to 30 fps, which was sufficiently high enough to capture complete laser footprints. While the frame rate of the Oscar camera was adjustable, after testing and considering the above factors the optimal rate was determined as 3 fps during the collection of the control laser footprints.

In the reliability test, it was noted that significant deteriorations of the accuracy in X and Z axes occurred when adopting laser footprints as control points (Table 3-6 and Table 3-7). This could be explained by the shape of the laser footprint. According to the test setup and the specifications given by the Leica TCRA1103 total station, the size of the laser dot is approximately 6 mm by 12 mm when the instrument was setup 10 metres from the observed object. Theoretically the laser dot should be imaged on the frame of each DV camcorder and Oscar camera with approximately 0.7 by 1.2 pixels and 0.9 by 1.8 pixels respectively, but diffusion occurred at the moment that the laser beam touched the surface meaning that one laser footprint generally occupied 3 by 3 pixels on the both images. The quality of measurements in the X and Z axes were therefore reduced in both tests. In addition, by comparing the RMS error computed from the tests using the three DV camcorders and the two Oscar cameras, higher accuracy was achieved when the latter cameras were adopted. The improved measurement accuracy was contributed by higher image resolution (Uffenkamp, 1993; Peipe, 1999) and good geometric stability (Maas and Hampel, 2006) of the CCD video cameras.

In summary, the proposed non-contact control method which implements the control arrangement and control survey simultaneously has been proved practicable. The methodology and workflow of the control method have been described under laboratory

conditions, demonstrating that this method is comparable with the conventional control method and could be applied in further videogrammetric applications.

3.4.4 Test 3 – Static Ceiling Surface Modelling

3.4.4.1 Methodology

This test was conducted in a stairwell simulating the real working environment, where the observed surface was high and not reachable, to evaluate the feasibility of introducing non-contact control method and projected-dots videogrammetry for constructing the surface model of the ceiling. In the test site one data projector (Philips ProScreen 4750), one total station (Leica TCRA1103) and two DV camcorders (Sony DCR-PC101 and Sharp VL-Z1) were arranged as outlined in Figure 3-17 to cover the part of the ceiling of interest.

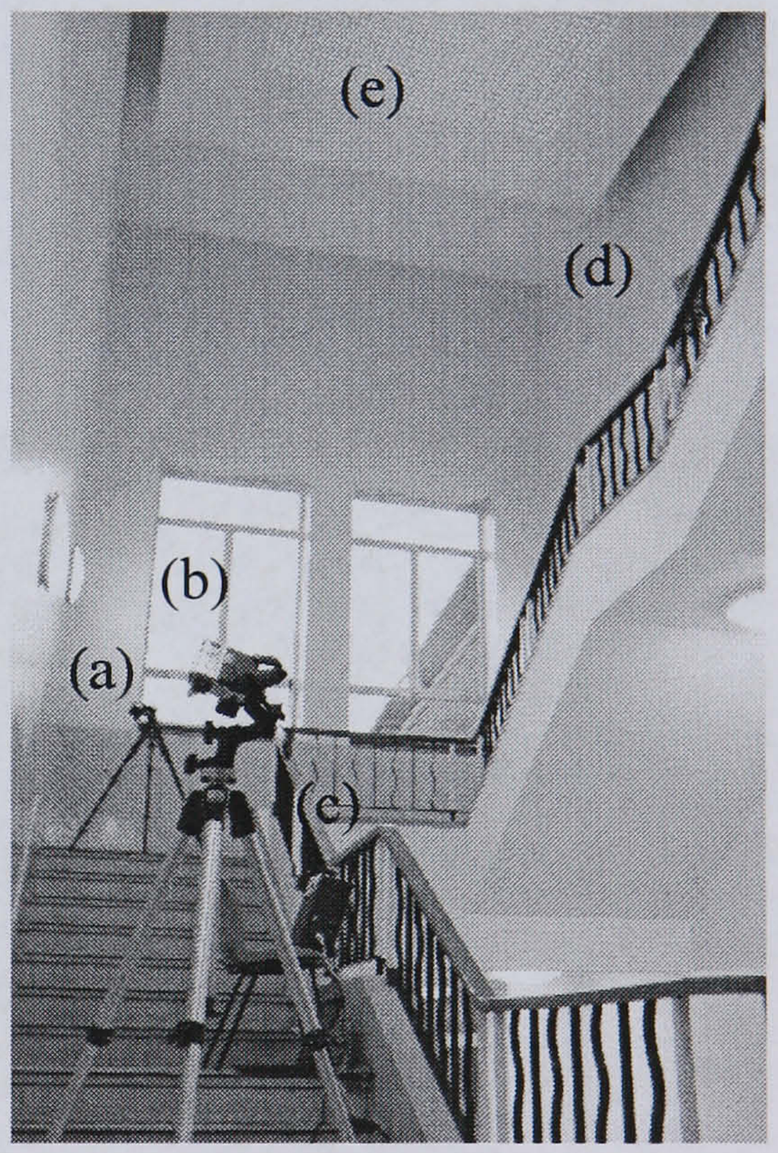


Figure 3-17: Setup of the Test 3: Sharp VL-Z1 camcorder (a); Sony DCR-PC101 camcorder (b); data projector (c); total station (d); projected pattern (e).

At the first stage the total station, which was treated as the control footprint generator, was used to scan the ceiling. Meanwhile the two DV camcorders were aimed at the area being scanned and were used to shoot image sequences. The laser footprints, complete with accurate 3D coordinates determined by the total station, were detected in the image sequences and introduced in the videogrammetric process as the control points. The second stage of the experiment was to project the pattern of dots (51 points by 38 points), which acted as the videogrammetric targets, onto the ceiling. The two DV

camcorders were continuously used to acquire stereopairs of the projected-dot pattern.

3.4.4.2 Results

When the image acquisition was finished, the video imagery was downloaded into the host computer. By using the image processing routine described in Section 3.3.2.2, the images of complete laser footprints were produced (Figure 3-18). Also, the stereopair of projected-dots is shown in Figure 3-19.

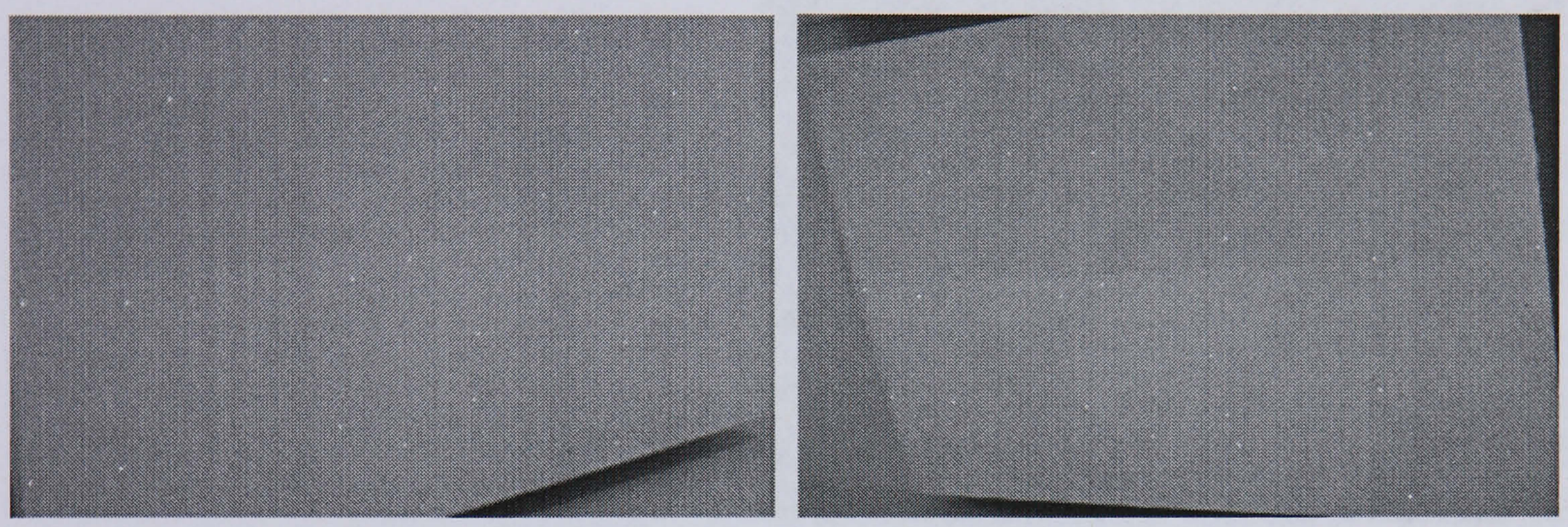


Figure 3-18: Images of the complete laser footprints.

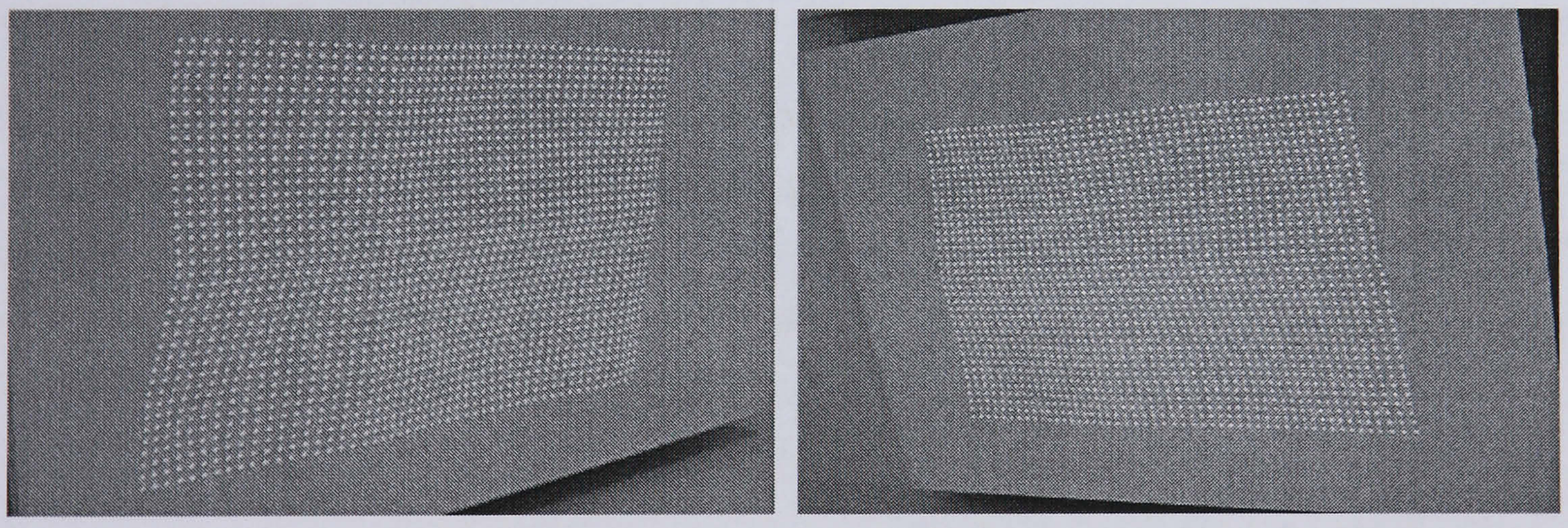


Figure 3-19: Stereopair of the projected-dots.

For videogrammetric processing, the images of complete laser footprints and the stereopair of projected-dots were input into the PhotoModeler software. By performing target extraction function in PhotoModeler, a total of 21 laser footprints were extracted automatically. However, a number of projected-dots failed to be identified and therefore manual interference was required. Consequently, a bundle adjustment was performed to compute the 3D coordinates of the projected-dots. Based on the solved positions of these points, the point model and meshed model of the observed ceiling are established and illustrated in Figure 3-20, from which the pattern of the ceiling could be recognised.

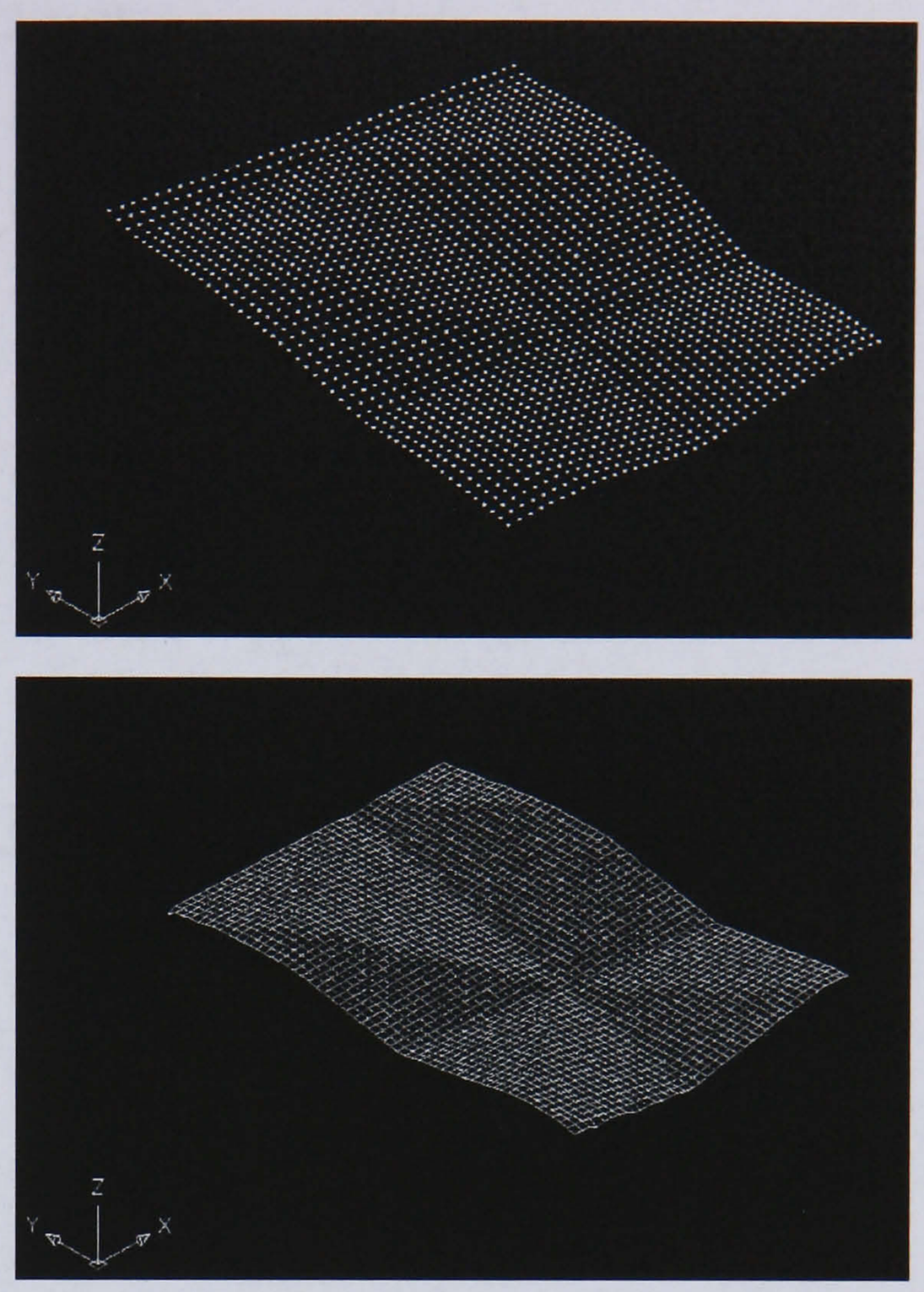


Figure 3-20: The point model (top) and meshed model (bottom) of the ceiling.

3.4.4.3 Discussion and Summary

During the operation of the test, it was realised the laser footprints generated at the stage of non-contact control shared identical characteristics with the "swift recurring dot" for synchronising the DV camcorders (Section 3.3.1.1). Therefore, in the case of using DV camcorders the synchronisation was achieved simultaneously with the implementation of non-contact control, making the image acquisition more efficient.

Subsequently the measurement precision was inspected. With the two-camera configuration, in which the average camera-to-object distance was 5.5 m and the baseline distance was 7.3 m, and an image coordinate measurement precision of 0.1 pixel, an anticipated precision of 1.0 mm was derived at the network pre-planning stage. After the computation was finished, however, the root mean square standard deviations of X, Y, Z axes of the 1 938 adjusted targets were solved as 1.3 mm, 1.3 mm and 2.0 mm respectively. The resultant precision in the position of targets indicated that the videogrammetric data was precise to 2.7 mm, which did not meet the predicted precision. Target extraction precision was the main factor causing the degradation of the measurement precision. To improve the performance, fully automatic target extraction was necessary.

The non-contact control method and projected-dots videogrammetry have been demonstrated practicable and could be applied in the videogrammetric monitoring scheme. However, at the data processing stage it was found some functions supplied in PhotoModeler software, such as automatic target extraction and target referencing, were constrained by the software conditions (e.g. insufficient image enhancement tools and the required number of cameras and images) and were not achievable. Therefore an in-house software package specifically developed for supporting non-contact control and projected-dots videogrammetry would be beneficial for monitoring the membrane structures.

3.4.5 Test 4 – Simulated Dynamic Membrane Modelling I

3.4.5.1 Methodology

By applying non-contact control and projected-dots videogrammetry, a sequential model of a flexible whiteboard simulating the dynamic fabric membrane was produced. Three DV camcorders employed in Test 3 were used in this test to capture the image sequence of the moving whiteboard, whose size was approximately 2.2 m by 1.5 m. Instead of using the total station, a terrestrial laser scanner (Leica HDS2500) was adopted for generating control footprints. The procedure of image acquisition followed the flow chart shown in Section 3.3.4. As summarised in the Test 3, the laser footprints were used as a tool for synchronising the three DV camcorders. After non-contact control a dot pattern was projected, at which 280 points appearing on the whiteboard were extracted and monitored. To test the feasibility of developing an in-house software, part of videogrammetric processing and computation were undertaken by routines programmed in MATLAB and City University Bundle Adjustment (CUBA) program.

Once the video imagery was downloaded to the host computer and the synchronisation was complete, the footprint extraction, coupled with specific image processing tasks, was performed in the following stage. For demonstrating the manner of extracting laser footprints the fourth scan line recorded in three sequential frames is shown in Figure 3-21. It was found the footprints presented in the image were not clear enough to be identified due to the interlaced scanning of the DV camcorder. According to the theory of interlaced scanning, a frame is formed by two fields (odd and even) which are scanned at two different times (Section 2.4.3.1). In dynamic image capture, by the time the second field is scanned, the object has already moved. As a result a ghosting effect or saw pattern occurred once the two fields are combined to create the whole interlaced frame (PULNiX, 2004). Because the odd (or even) field is captured per shutter event,

for fast moving objects the information would be more continuous between adjacent odd (or even) scan lines of the frame. Therefore the frames were restored separately to odd and even fields in the image processing stage, and then in the odd (or even) field the blank even (or odd) lines were generated by interpolating two adjacent odd (or even) scan lines. Figure 3-22 illustrates the resulting interpolated images of odd and even fields of the frames shown in Figure 3-21, proving the ghosting effect was reduced successfully (Lin and Mills, 2005b). Furthermore, Ryall and Fraser (2002) indicated that the use of video fields alone would have only a minor impact on the precision of measuring targets centroids within the imagery.

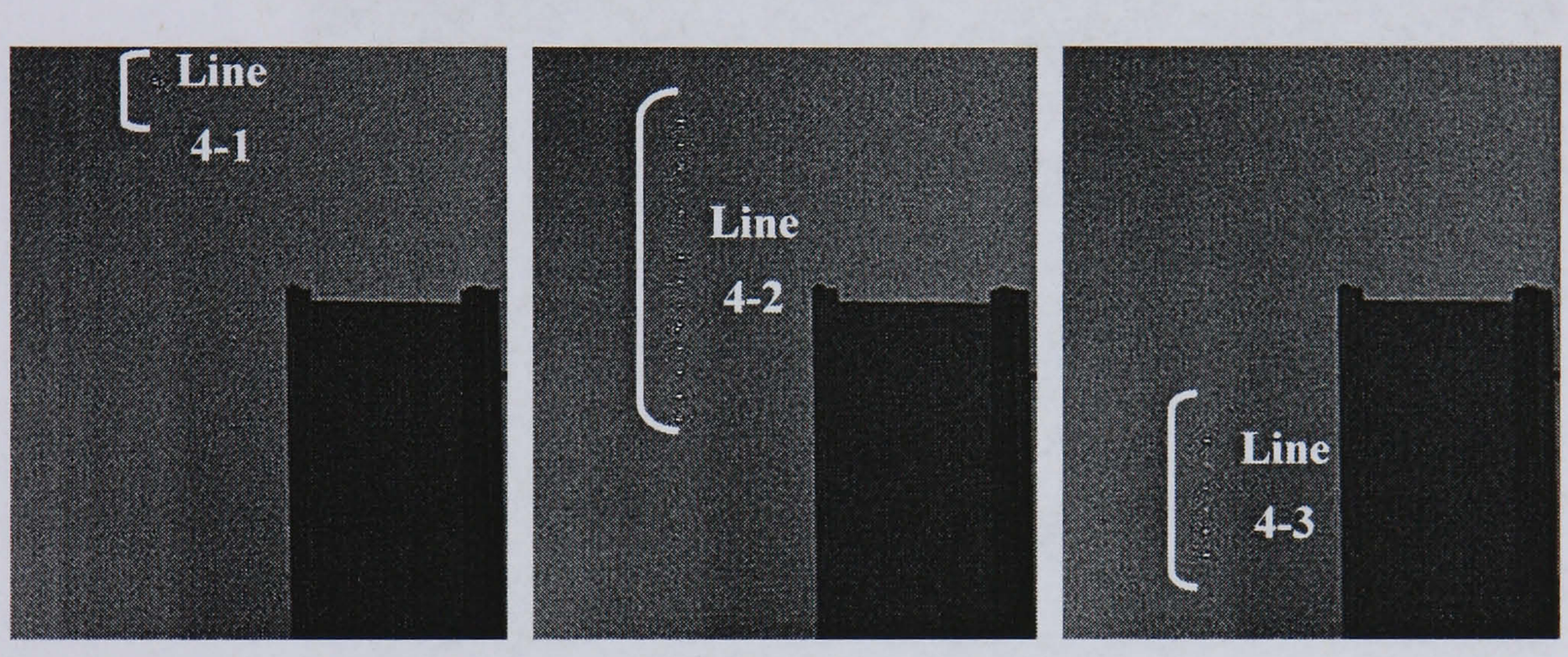


Figure 3-21: Close up views of sequential frames (frame 593 to 595) recorded laser footprints (Sony DCR-PC101), showing three consecutive sections of scan line 4.

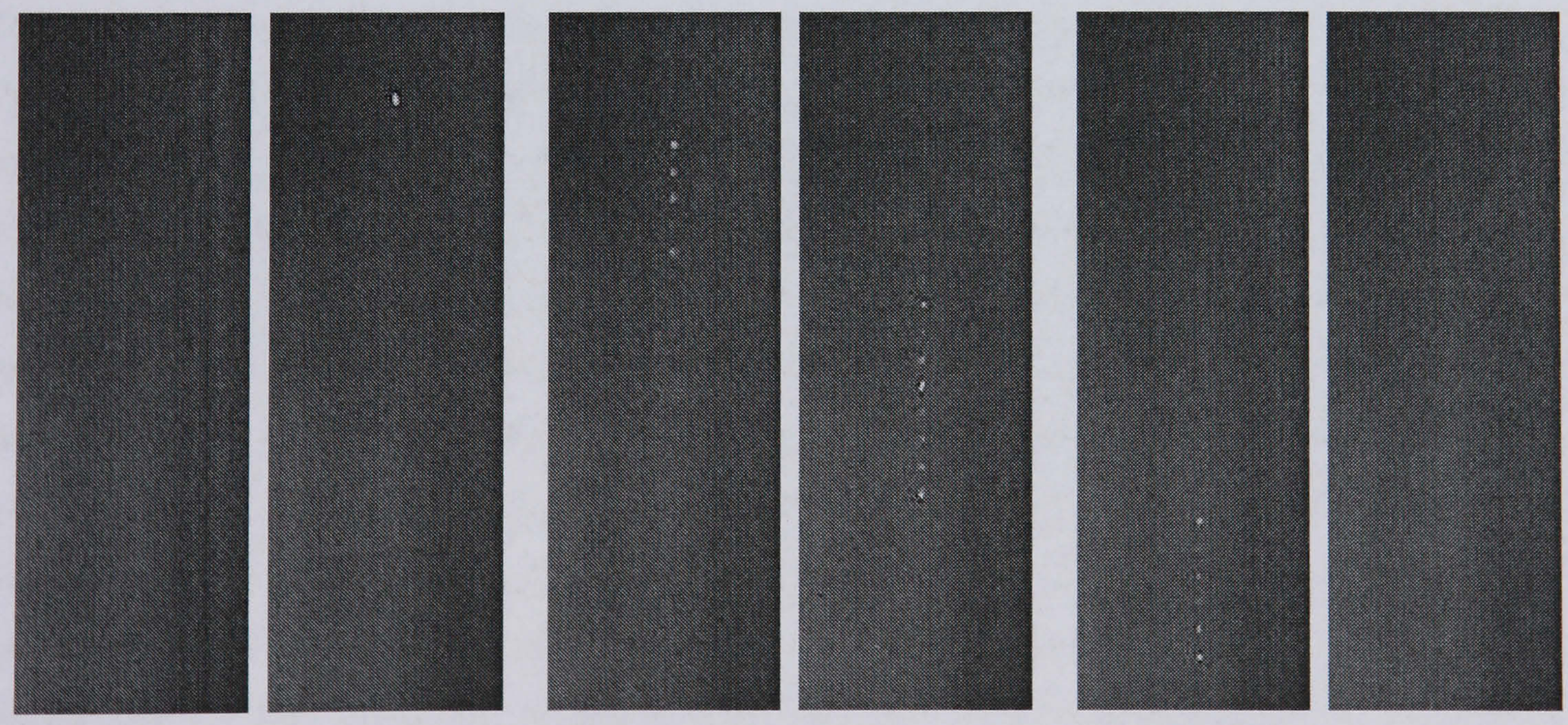


Figure 3-22: Close up views of interpolated laser footprints. From left to right: even and odd field of 593rd frame, even and odd field of 594th frame, even and odd field of 595th frame.

A scan was collected over the given surface in this test. Six lines were selected and their

interpolated images were produced separately following the steps described above. They were then integrated together to obtain a complete control image and 13 high contrast footprints were identified as control points (Figure 3-23). Moreover, their 3D coordinates, based on an arbitrary reference frame with its origin located at the scanner location, were abstracted from the scan data. The precision of the control footprints was commensurate with the precision of the laser scanner and was quoted to be +/- 6 mm.

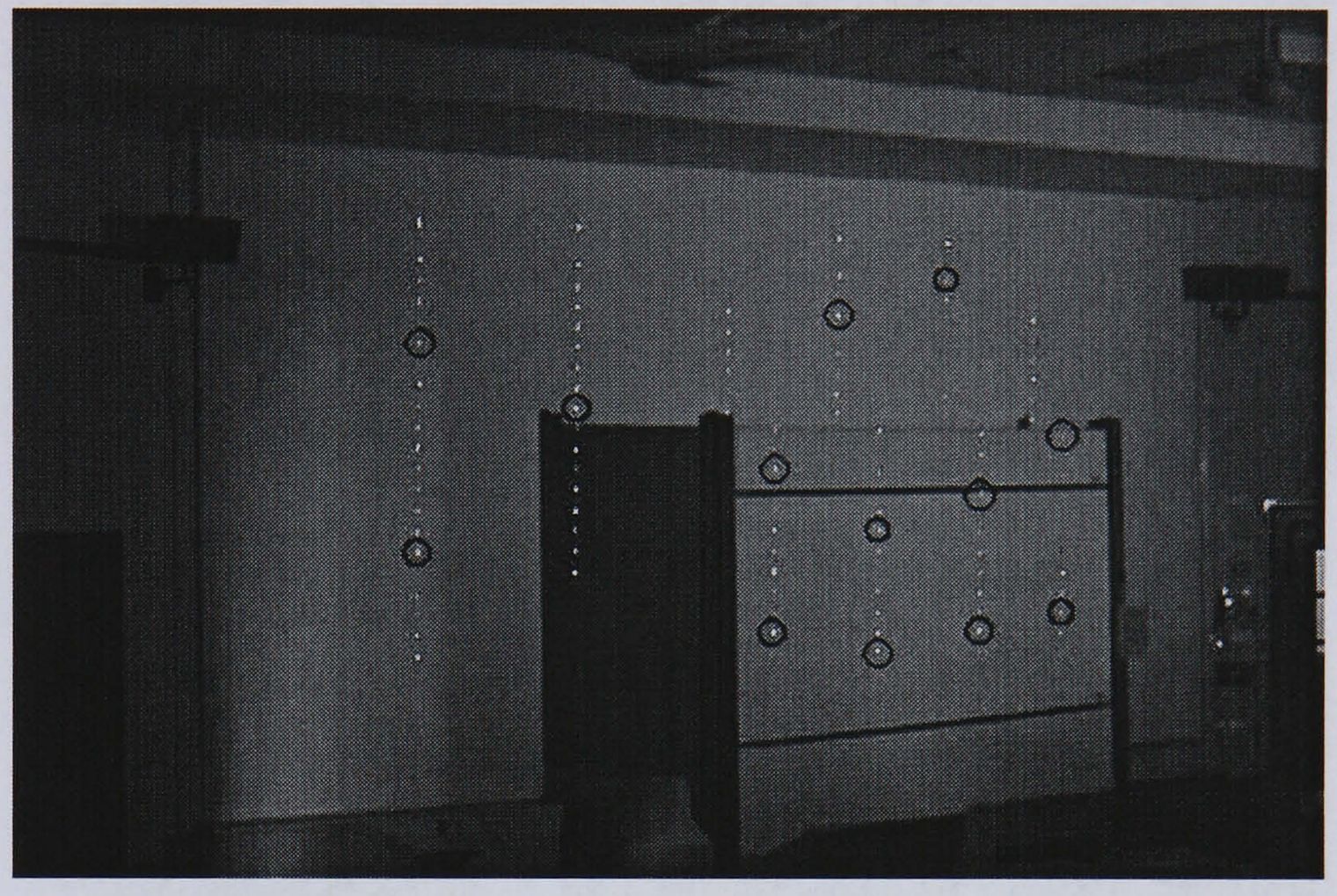


Figure 3-23: Complete control image (shot by Sony DCR-PC101) and the selected control footprints in Test 4 (outlined by black circles).

At the data capture stage, the designed dot pattern was projected onto the surface once the laser scanning was complete, and all of the DV camcorders continued to record the image sequences of the moving surface. When the monitoring ended, 10 epochs of synchronous frames (Figure 3-24), representative of the movement being applied, were grabbed from the left, middle and right DV camcorders for measurement. These images were firstly processed to enhance the projected dots. A total of 280 targets on the dynamic surface were determined, their subpixel image locations were then computed automatically by a centroid targeting algorithm. Consequently, a file containing the resultant positions, as well as the 3D coordinates of control footprints, approximate values of camera orientation and calibration parameters were generated and used as input for the CUBA program, where a least squares bundle adjustment program was executed to compute target coordinates. Once computed, the adjusted 3D coordinates of the 280 targets were exported for dynamic surface modelling. To achieve automated processing, routines programmed in MATLAB were used to handle the tasks included the generation of interpolated field images, extraction of the laser footprints and projected targets, and file exchange in CUBA.

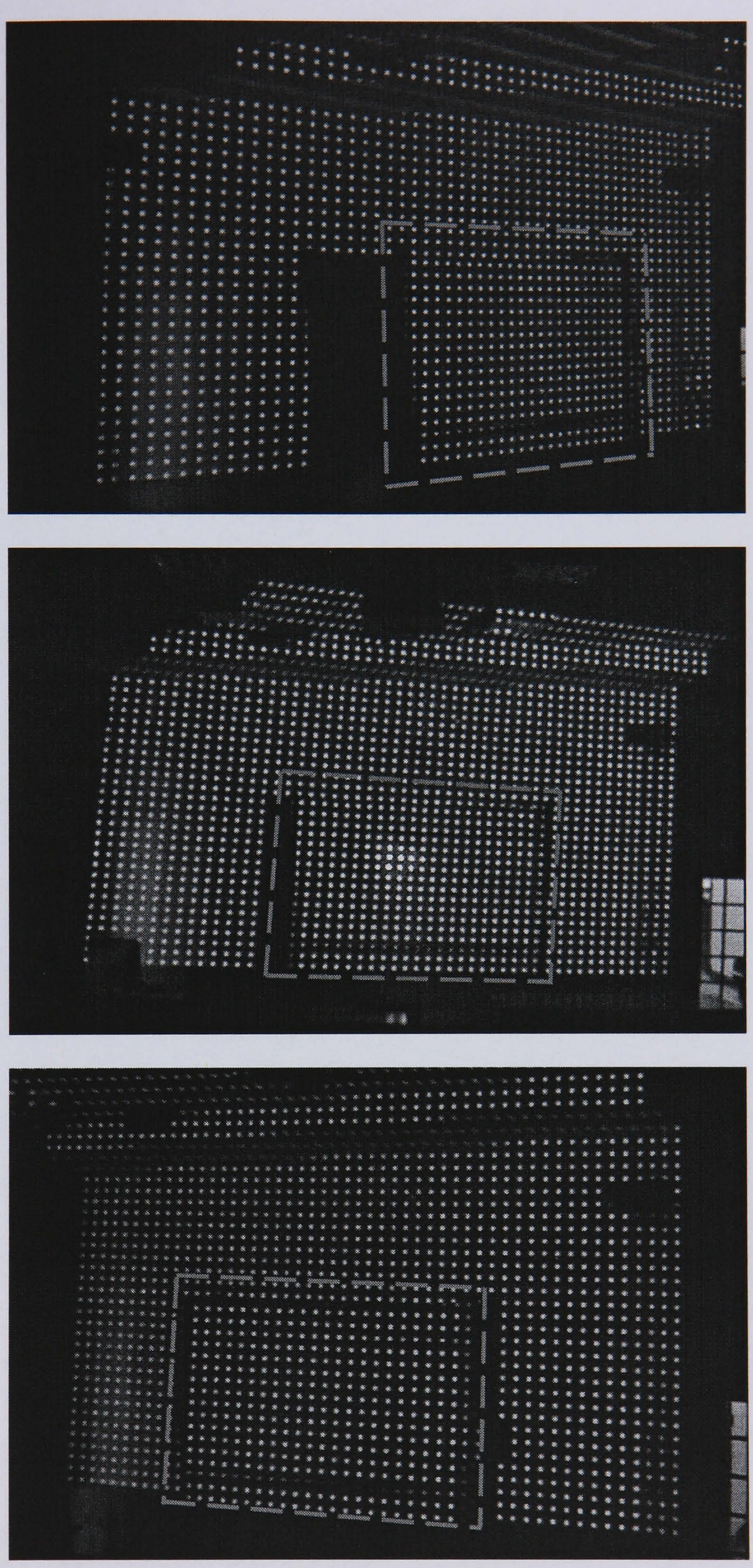


Figure 3-24: Example of synchronous frames set and the monitored dynamic surface was outlined by dotted lines. From top to bottom are images of projected-dots taken from left camera station (Sony DCR-PC101), middle camera station (Sharp VL-Z1) and right camera station (JVC GR-D30U).

3.4.5.2 Results

To generate the dynamic surface model, a smooth surface was fitted to the discrete target points solved by CUBA. This was achieved by interpolating the estimated target coordinates into a uniform mesh with a finer grid (0.05 m in this case). After this, the surface model of the whiteboard surface was constructed. The procedure was applied in a routine program repeatedly at various epochs. As a result the surface movement that occurred over 20 seconds, with a time interval between each surface of approximately two seconds, is demonstrated in Figure 3-25.

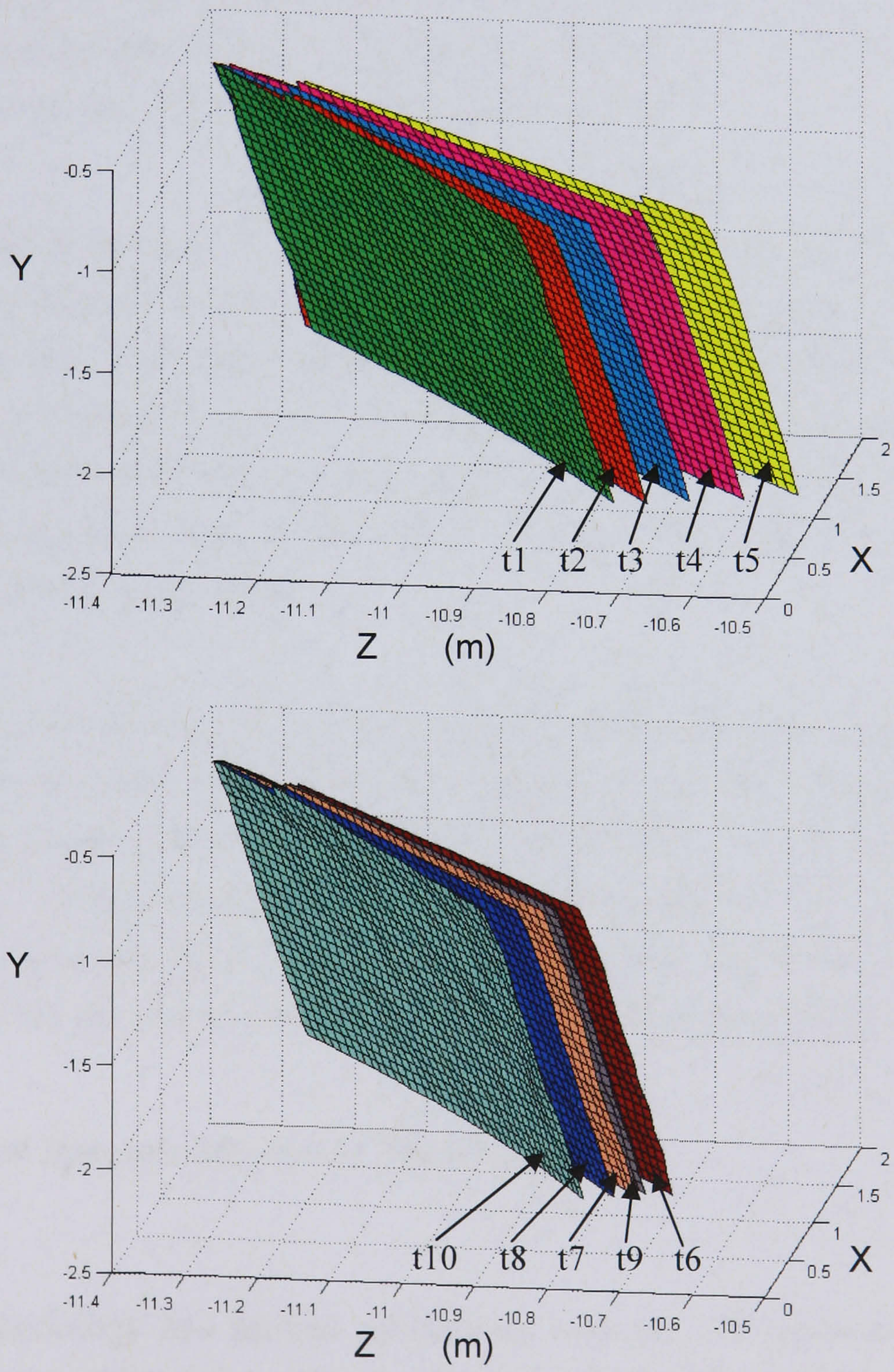


Figure 3-25: Dynamic surface movement (up: the movement occurring between t1 to t5; bottom: the movement occurring between t6 to t10).

3.4.5.3 Discussion and Summary

Although the targeting methods, both laser footprints control and projected videogrammetric targets, are feasible for application to the dynamic surface modelling, some issues need to be considered. Firstly, the visibility of laser footprints in images was significantly affected by the light condition. To ensure the laser footprints were clearly visible in the images a dark environment was preferred. This limitation would constrain the applications of integrating terrestrial laser scanner into videogrammetry. The second issue was the considerable manual manipulation involving in selecting appropriate control footprints, as the small size of the laser footprints the images have to be checked carefully to distinguish the footprints from the noises. Moreover, due to the enormous amount of scanned points more attention has to be paid when matching corresponding footprints amongst the three complete control images.

The other limitation is about the capability of the videogrammetric instrumentations. As the scan rate of the laser scanner is very fast (up to 1000 points per second), only a camera equipped with a high sampling frequency is capable of clearly capturing the laser footprints. In this test the DV camcorders, whose frame rate was 30 fps, were unable to record all laser footprints when a scan was performed. Although the manual operations made searching for corresponding control points achievable, the overall processing was time and labour consuming.

Owing to the issues outlined above, the use of a terrestrial laser scanner to provide videogrammetric control was only suitable under a well-controlled environment and with video cameras with a high frame rate. Therefore, it would not be introduced into the subsequent on-site videogrammetric monitoring. Nevertheless, the routines programmed for the test were beneficial for improving the automation of the processing and were introduced into the developed software for dynamic surface modelling.

3.4.6 Test 5 – Simulated Dynamic Membrane Modelling II

3.4.6.1 Methodology

Since the proposed methodology had proved satisfactory with the DV camcorders in Tests 3 and 4, the feasibility of the other videogrammetric instrumentation, the Oscar cameras, were evaluated in this test for dynamic membrane monitoring. In this dynamic surface modelling experiment, a projector screen was used to simulate the membrane roof surface to be observed at the real-world test site. The two Oscar cameras with the

settings determined in Test 2 were setup, and the proposed equipment and methodology were applied following the procedure shown in Section 3.3.4 to measure the surface movement, which was generated by manually shaking the screen. The camera configuration is illustrated in Figure 3-26, in which the camera-to-object and base distances were 10.667 m and 8.753 m respectively. With an image coordinate measurement precision of 0.1 pixel, a precision of 1.5 mm was anticipated for this experiment.

For measuring dynamic subjects, the PhotoModeler Video (PMV) module, off-the-shelf commercial software specifically designed for the videogrammetric applications applied projected-dots as targets, was used to perform the processing and computation.

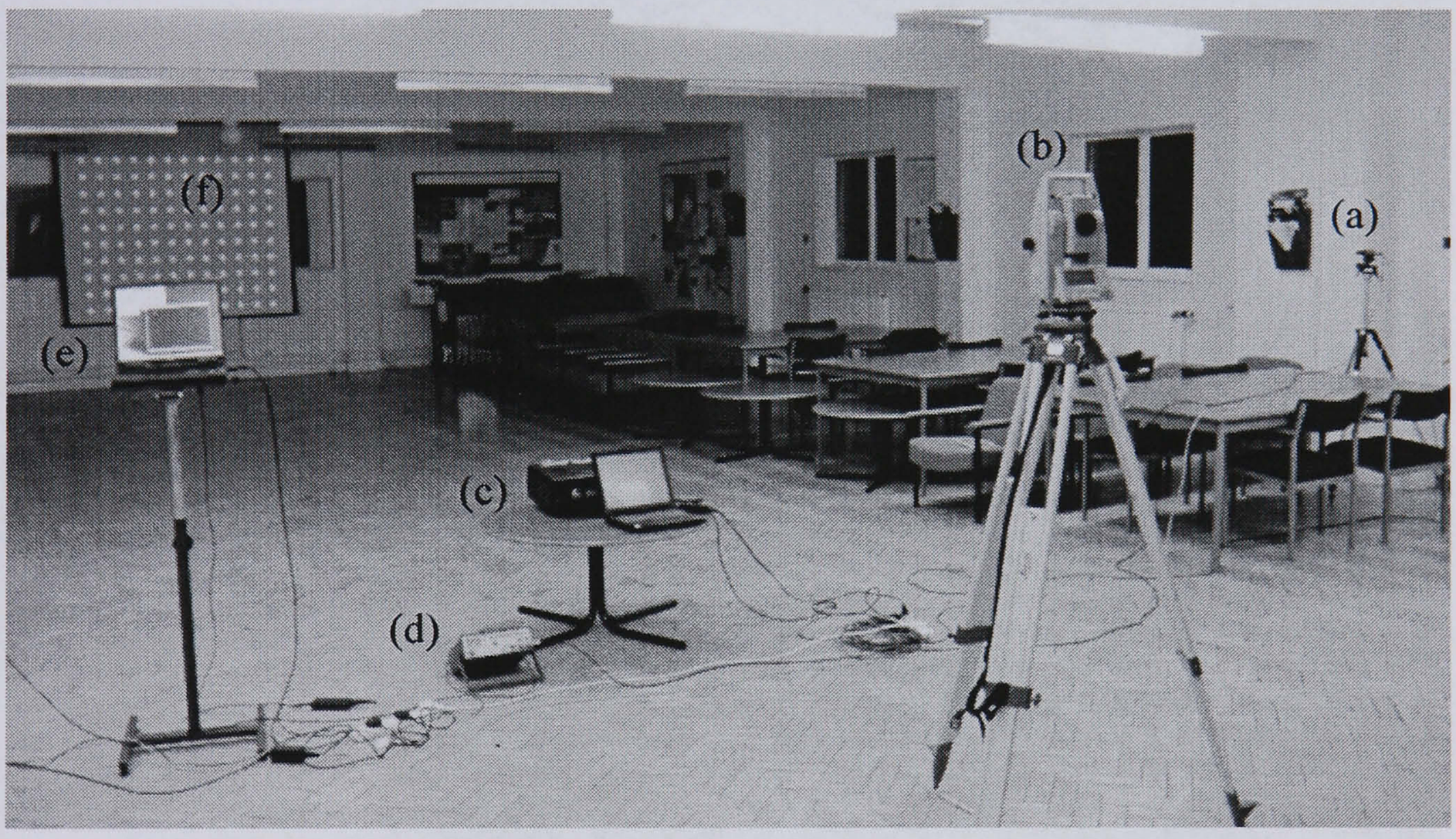


Figure 3-26: Configuration in Test 5: Oscar camera (right exposure station) (a); Leica TCRA1103 total station (b); data projector (c); pulse generator (d); host laptop computer (e); moving projector screen (f).

3.4.6.2 Results

By using the Oscar cameras the frames captured were stored in the host computer in near real-time. When the image acquisition was finished, a total of 119 frames were derived during the implementation of non-contact control, and 180 frames were collected at the stage of shooting the projected pattern. Subsequently, the routine developed in Section 3.3.2.2 was applied to produce the images of complete laser footprints. Along with the image sequences recording projected-dots, they were input to the PMV module for dynamic surface measurement.

Target Extraction, Target Referencing and coordinates determination were performed consecutively for the stereopair of the first epoch, at which 8 control laser footprints and 120 projected-dots were detected. The centres of the control footprints and the dots were extracted automatically by a centroiding algorithm (Figure 3-27). Their 3D coordinates were solved by a bundle adjustment, with a resultant precision of 1.0 mm. At next stage, the function Target Tracking was carried out to automatically extract the projected targets appeared in the remaining stereopairs and their 3D coordinates were computed immediately. The displacement of the projected-dots could therefore be presented in the end. For example, an obvious movement of the screen occurred between epoch 43 to epoch 50 were visualised in Figure 3-28.

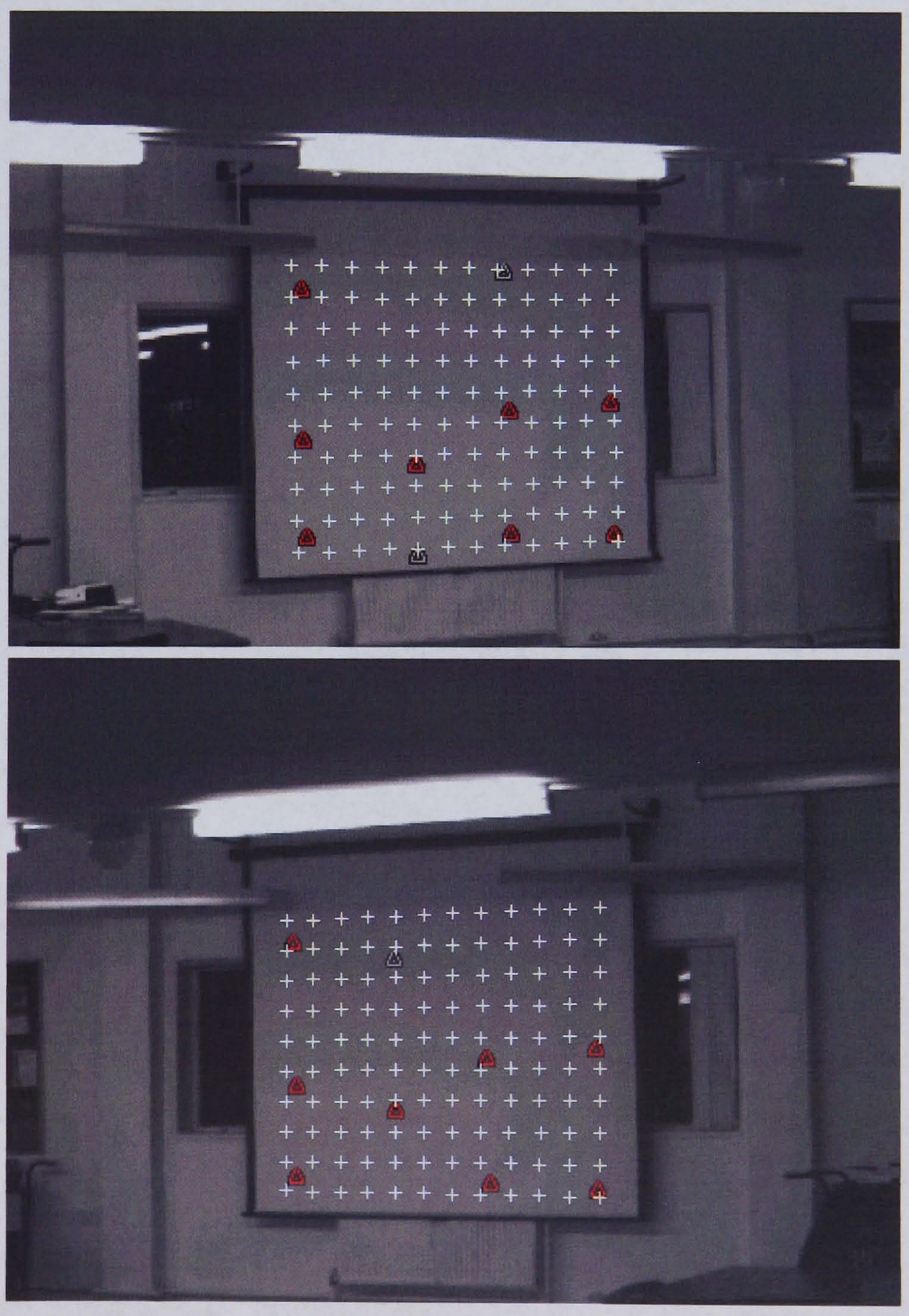
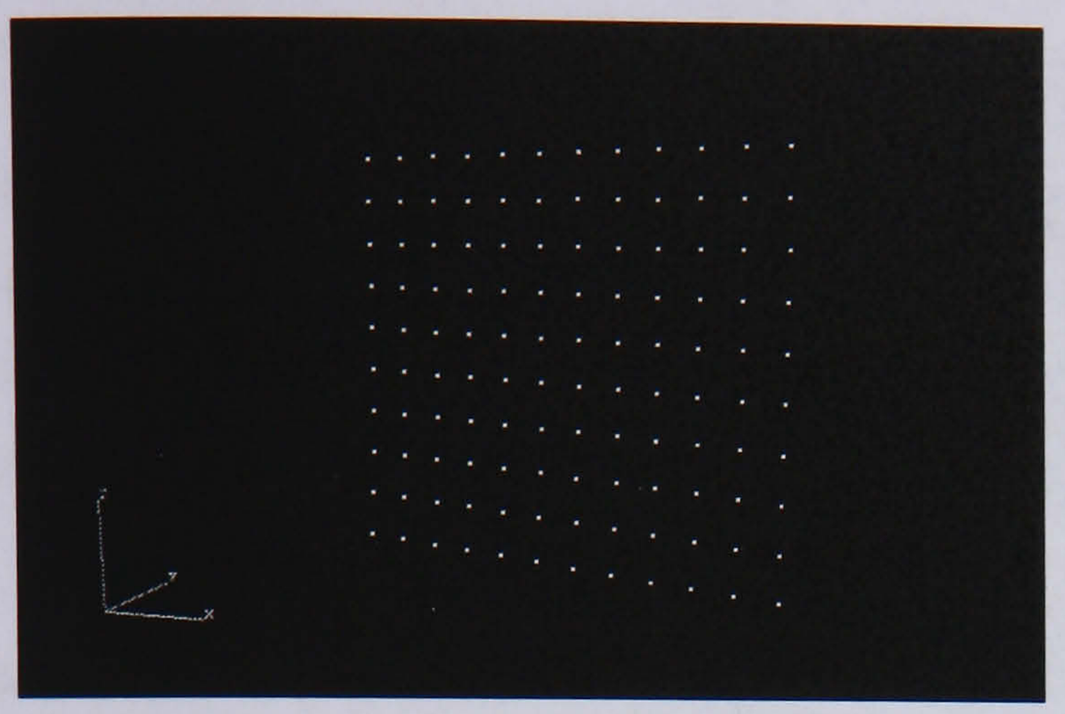
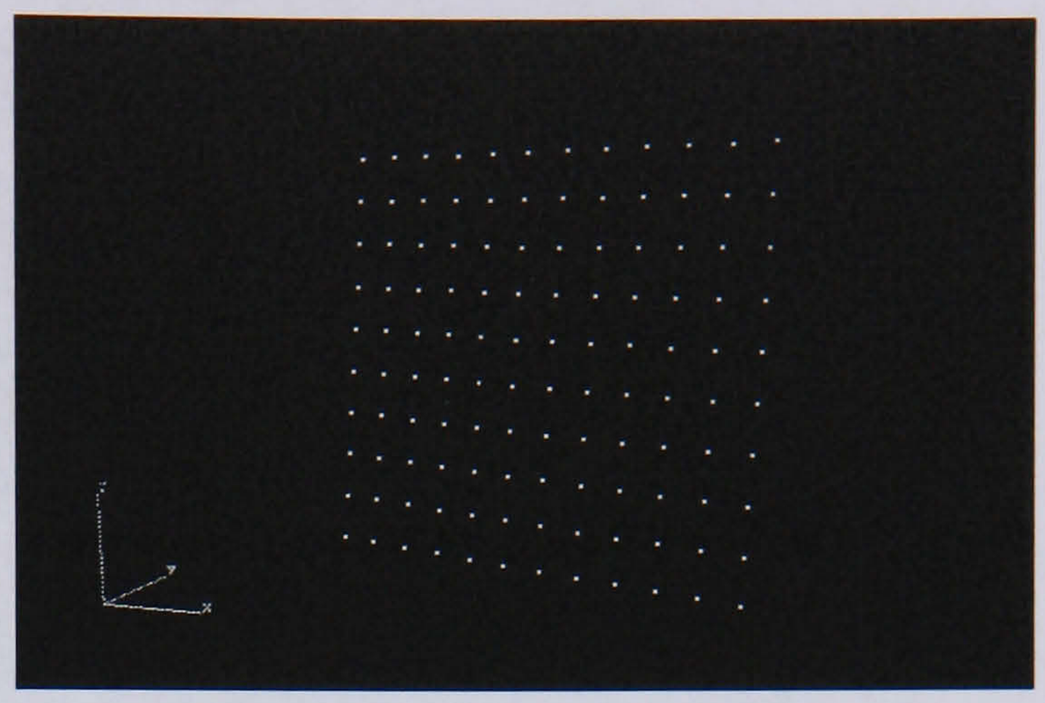


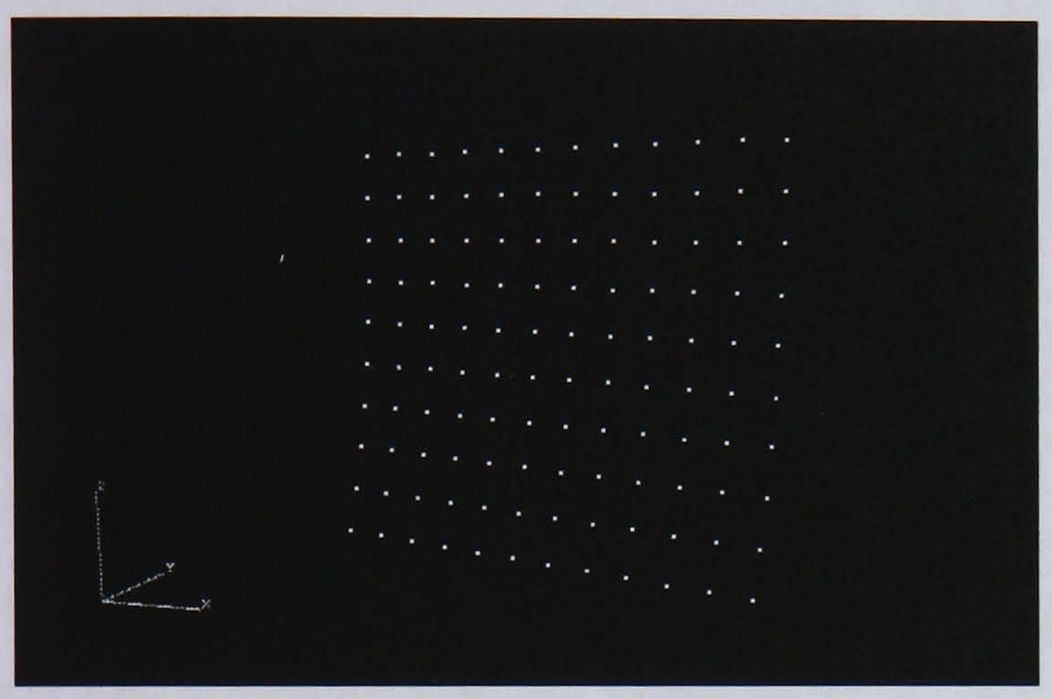
Figure 3-27: Extracted laser footprints (outlined by red triangles) and projected-dots (outlined by white crosses).



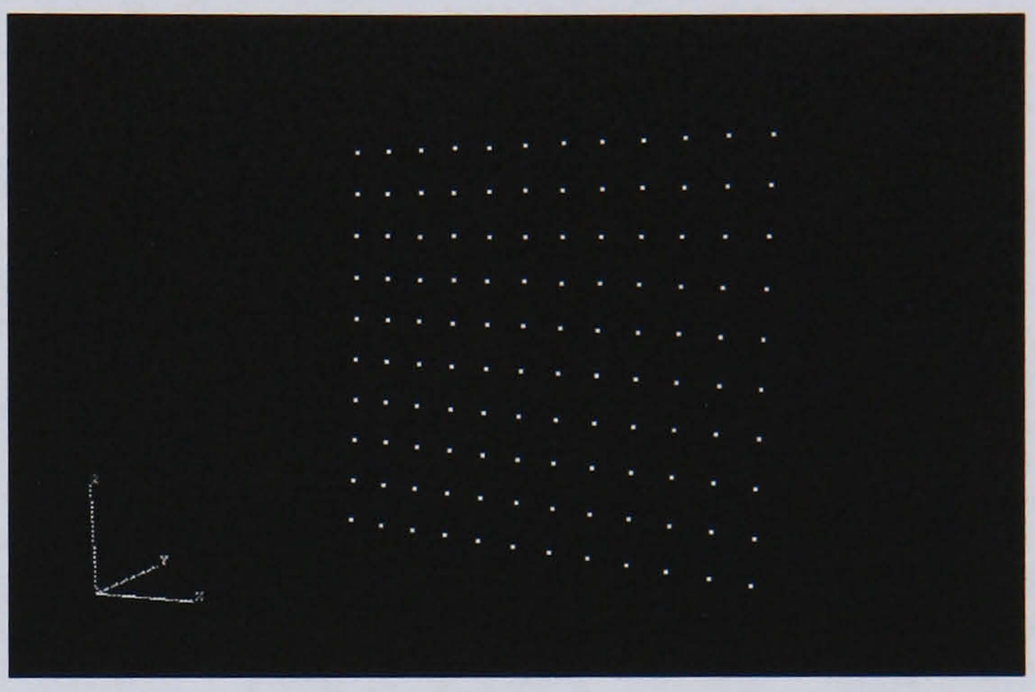
Epoch 43



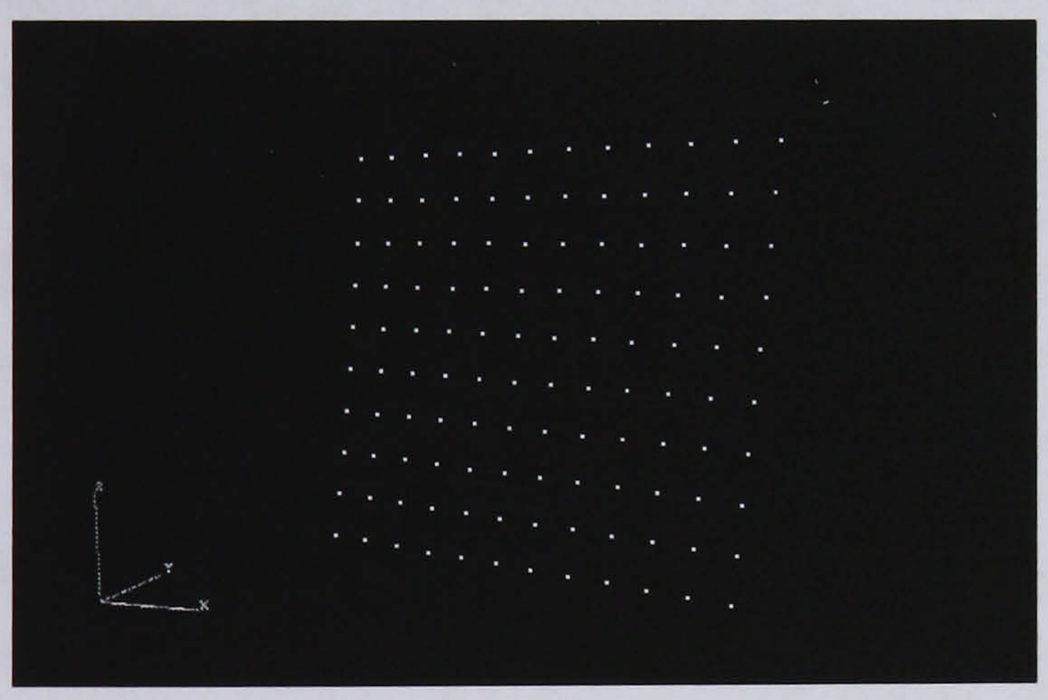
Epoch 47



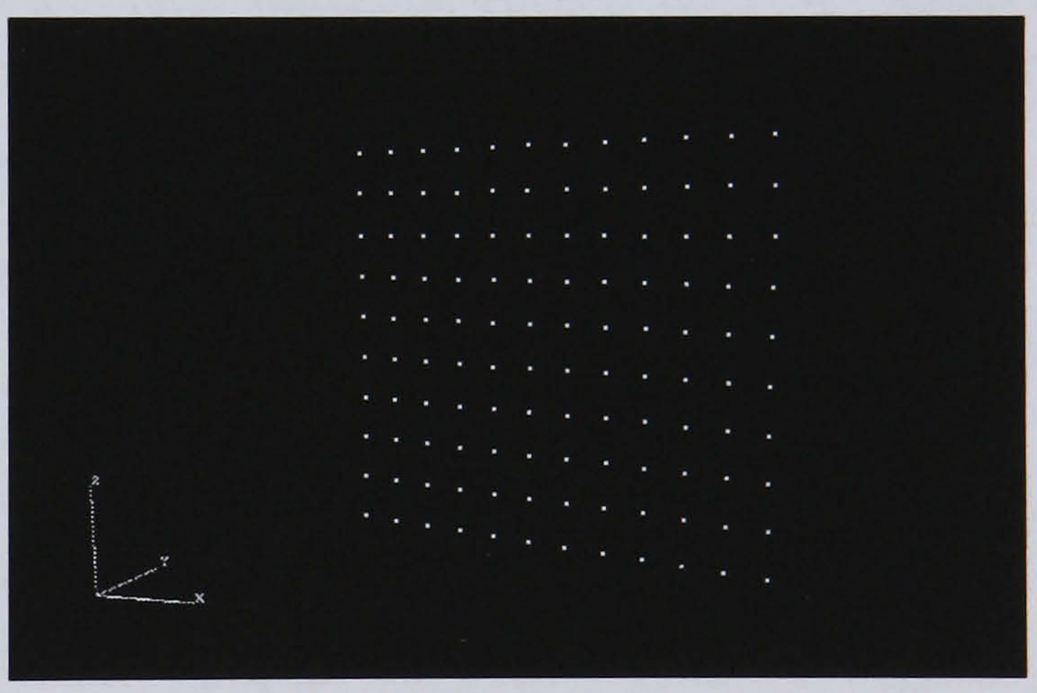
Epoch 44



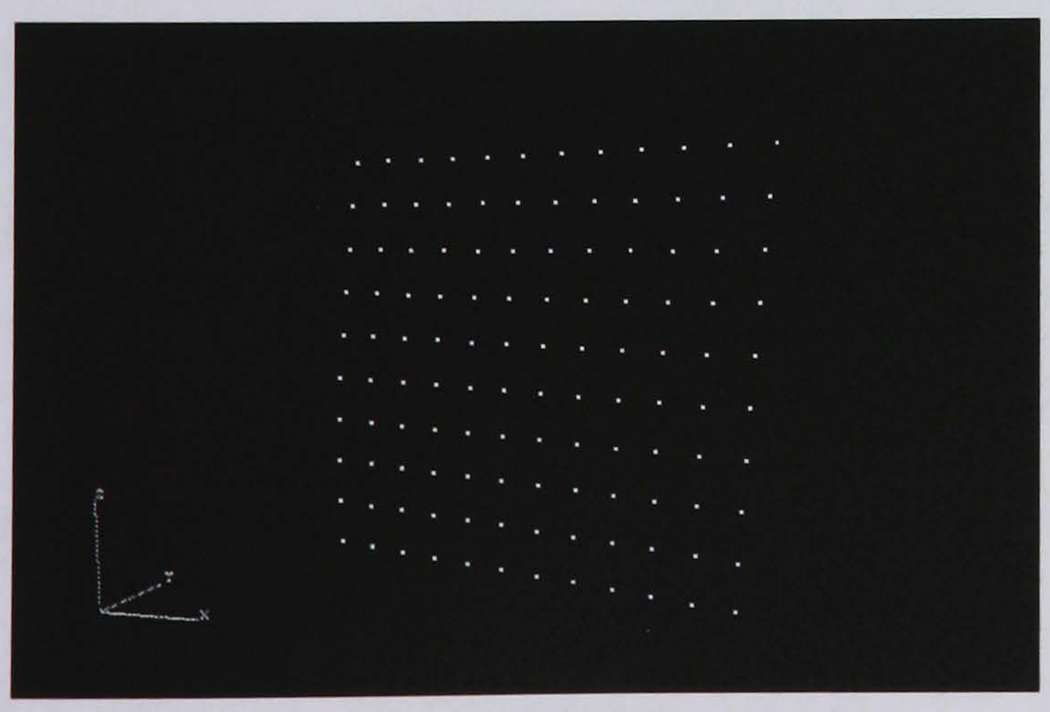
Epoch 48



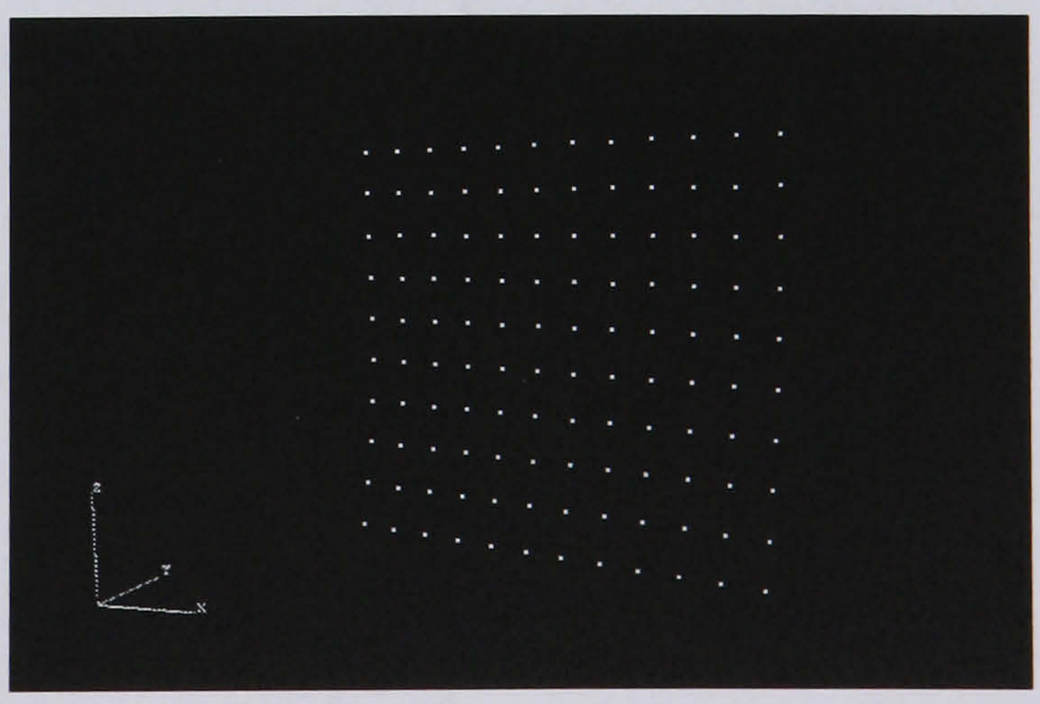
Epoch 45



Epoch 49



Epoch 46



Epoch 50

Figure 3-28: Example sequential point model of the dynamic surface in Test 5.

3.4.6.3 Discussion and Summary

The test showed the feasibility of applying CCD video cameras to the proposed methodology. Different from the DV camcorder, the shoot setting and frame rate of the Oscar camera were adjustable, making the image acquisition more flexible for fitting in various environments.

As for the performance of the applied software, the dynamic surface modelling was considered to be achieved automatically by implementing Target Extraction, Referencing and Tracking in the PMV. In the experiment, the Target Extraction performed well to mark the laser footprints and projected-dots with the sub-pixel accuracy. However, the Target Referencing, in which corresponding targets are matched, failed due to the insufficient number of cameras adopted (at least three cameras were needed). The second issue was in the task of Target Tracking, where some points were lost between epochs. As indicated by EOS System Inc. (2004), this might be caused by fast or unpredictable moving of the monitored targets. Furthermore, once a target has been lost it would not be re-acquired in later epochs. This limitation would affect the complete investigation of the sequential model over the monitoring. Thirdly, when Target Tracking was finished, the solved 3D coordinates of the points at each epoch could be derived. Nevertheless, there is no metric information about the displacement supplied, making the analysis of the surface movement unachievable through the PMV module.

The overall execution of monitoring dynamic surfaces by employing the Oscar cameras and the PMV module was investigated in the test. The cameras adopted were capable of capturing images of clear laser footprints and projected-dots occurred dynamically. The operation through a friendly interface also made processing in PMV straightforward. However, due to the weaknesses of the software discussed above, the development of a software package for more efficient videogrammetric processing and robust analysis of dynamic behaviour was proposed in this project.

3.5 Chapter Summary

3.5.1 Summary of Findings

A number of points raised from the laboratory tests are summarised below.

- Justification of laser applications

The equipment adopting laser technology, the terrestrial laser scanner and total station, were proposed to be applied in the membrane structure monitoring scheme. To ensure accurate measurement was achievable, the employment of the laser applications on the fabric membrane has been justified by the spectral reflectance test (Test 1).

- Instrumentation

Although both the DV camcorder and the CCD video camera (Oscar camera) demonstrated the capability of clearly capturing dynamic targets, some differences existed during the operations in the laboratory tests. A comparison between the DV camcorder and the Oscar camera is made in Table 3-8. Due to the advantages listed below, the two Oscar cameras were deployed in the further membrane structure modelling schemes.

	DV camcorder	*Oscar camera*
Advantages	• Relatively low cost. • Compact and easy setup.	• Flexible shooting setting. • Higher measurement accuracy. • Captured images were saved into the computer in near real-time. • Synchronisation was accomplished on-site.
Disadvantages	• Fixed shooting mode. • Relatively lower measurement accuracy. • Captured images were recorded in the internal tape, so time for image downloading and frame grabbing was required. • Extra operation for camera synchronisation was required.	• Additional components were needed, hence specific setup was required.

Table 3-8: A comparison of the DV camcorder and the Oscar camera.

For performing non-contact control, a total station and a terrestrial laser scanner were used to generate laser footprints in Test 3 and Test 4 respectively. As too much manual interference was required when using a terrestrial laser scanner, while automatic processing is accomplishable by using the total station, the total station was employed in the further operations of non-contact control. In addition, as determined in Test 2, the optimal frame rate of the Oscar camera was set as 3 fps during the collection of the control laser footprints

- Proposed methodology

  The reliability of the proposed non-contact control method was firstly proved comparable with the conventional control method in the Test 2. Subsequently, through the operations of the Test 3, Test 4 and Test 5, the non-contact control and projected-dots videogrammetry were demonstrated as feasible for the static/dynamic surface modelling applications.

- Applied software

  The PhotoModeler software and PMV module were adopted for videogrammetric processing in the laboratory tests. Nevertheless, owing to the weaknesses in the functions of Target Extraction, Referencing and Tracking, the development of an in-house software package specific for monitoring membrane structures was therefore proposed. Since the routines programmed in MATLAB and the exploit of CUBA had been proved feasible for videogrammetric processing and computation in Test 4, they were introduced as the fundamental of the software to this end.

3.5.2 Concluding Remarks

The applied equipment and methodology for membrane structure monitoring were introduced in Sections 3.2 and 3.3. Five proof-of-concept experiments were conducted (Section 3.4) to evaluate the performance, thereby proving the feasibility of the monitoring system. As a result the proposed method, coupled with a Leica TCRA1103 total station and the two Oscar cameras offering efficient and accurate measurement are employed in the further observations on finished as-built membrane structures. Moreover, an in-house software package for investigating the behaviour of membrane structures is developed. The specific modules in the developed software for video image processing, dynamic surface modelling, and displacement determination are outlined in Chapter Four.

CHAPTER FOUR

MEMBRANE STRUCTURE MONITORING SYSTEM (MS^2)

4.1 Introduction

The methodology for monitoring membrane structures was introduced in the previous chapter. For analysing data collected using the proposed methodology, an in-house software package called Membrane Structure Monitoring System (MS^2) has been developed, offering tools for static and dynamic surface modelling. The background, software structure and the applied algorithms of MS^2 are reported in this chapter. The performance of the MS^2 is evaluated by processing data derived from two simulated experiments.

4.2 Required Software

Due to the high performances in mathematics and computation, data acquisition, analysis, exploration, visualisation, and application development, MATLAB was selected as the programming environment for building the Membrane Structure Monitoring System (MS^2). In MS^2, a series of modules are programmed to perform video imagery processing, non-contact targeting, sequential 3D surface model construction, and surface comparison. The graphical user interface (GUI) was designed to ease MS^2 operation.

To determine the 3D positions of the targets, the City University Bundle Adjustment

(CUBA) program was introduced in MS^2. CUBA was developed at City University as a general purpose observation case least squares bundle adjustment program which handled geodetic and photogrammetric observations either singly or in combination (Short, 1994). In MS^2, CUBA is served as a videogrammetry engine to solve the camera orientations and target coordinates based on image observations. A text file containing initial estimates of calibration parameters, camera orientations, target locations, and the determined image coordinates of target centres is produced. CUBA is then triggered to run through the file and perform least squares computations. The resulting files are saved for further measurement in MS^2.

4.3 System Structure

4.3.1 Main Menu

Two panels, Static Surface Comparison and Dynamic Surface Modelling are included in the Main Menu of MS^2 (Figure 4-1). The former panel is developed for detecting the differences between the designed mathematical model and the as-built structure model, while the latter panel offers the solution for videogrammetric measurement. In addition, the instructions for manipulating the system are displayed in the Info Box, providing the working procedures and reminders for each step.

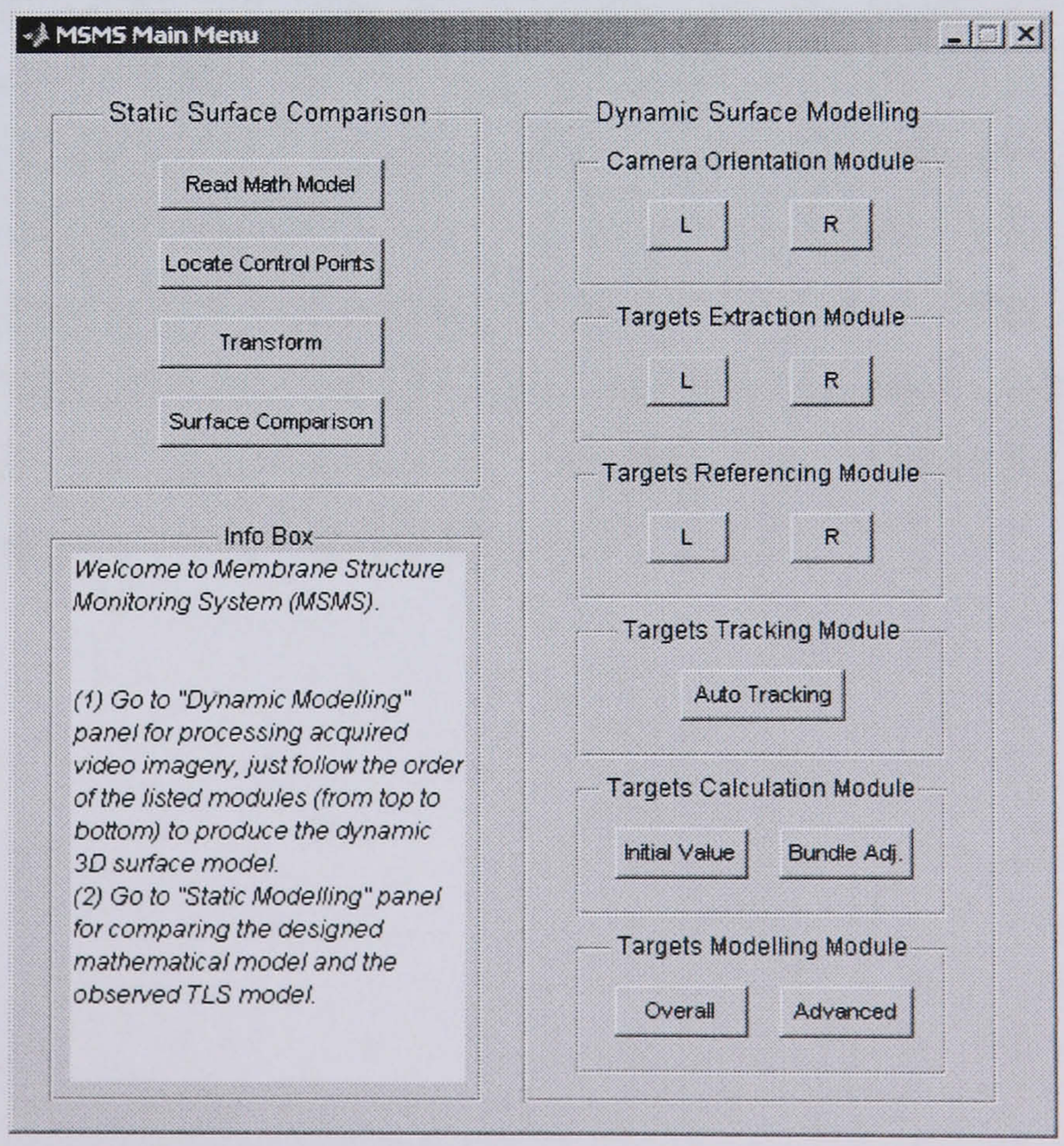


Figure 4-1: User interface of the Main Menu.

4.3.2 Static Surface Comparison

4.3.2.1 Read Math Model

To detect the differences between the designed and finished models of membrane structures, the models of two different sources are employed. The former one is the mathematical model, which is produced by structural engineers in the design stage of the membrane structure construction and is delivered as a CAD meshed drawing. The finished model is derived by using the technique of terrestrial laser scanning. When the processing is finished, a point cloud of the membrane structure is generated. For undertaking the area-based comparison (details are explained in Section 4.3.2.4), the mathematical model is firstly converted into a point model. The task is accomplished by triggering the "Read Math Model". A routine programmed specifically for extracting the nodes of the meshed model was subsequently called to produce the point model of the design structure (refer to A1.1.1 for code). The two models are imported into MS^2 for further processing and analysing.

4.3.2.2 Locate Control Points

This is the module for determining the corresponding control points between the two models for performing a 3D conformal transformation. As proposed in Section 3.2.3, the intersection points of the supporting steelworks of the membrane structures are selected as the control points. These points are directly identified in the designed mathematical model and filled in the column (B) of the interface (Figure 4-2). Nevertheless, in the laser scanned model the control points cannot be positioned directly, instead they are estimated by computing the intersections of modelled steelwork (refer to Section 3.2.3 and 5.3.2.2 for the introduction and implementation). To achieve this, the end points of centre lines of the modelled steelwork are input into the sections in the column (A). The intersection points are then solved by pressing the "Calculate Intersection" button. The code for implementation was shown in A1.1.2.

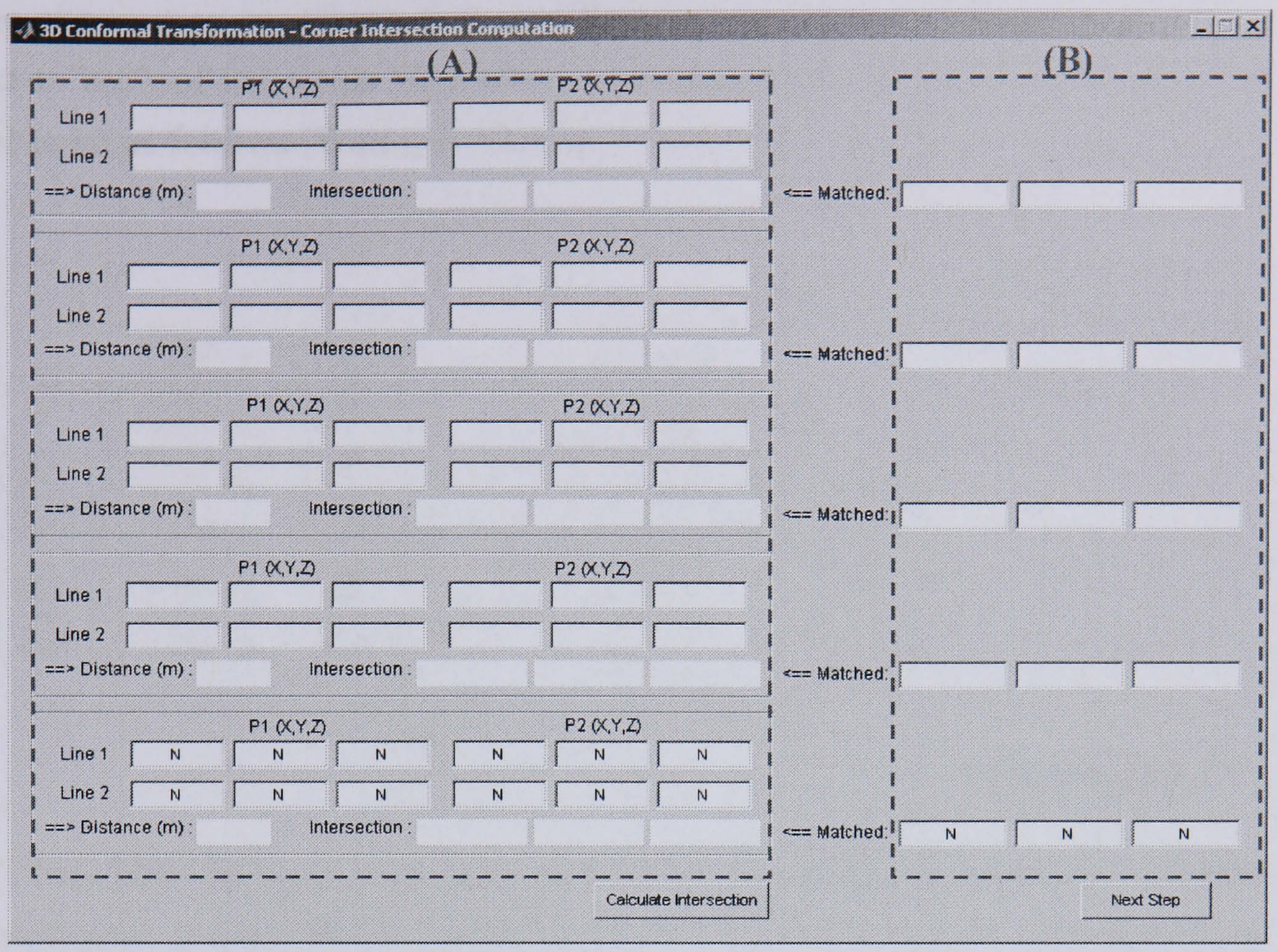


Figure 4-2: User interface of the Locate Control Points Module.

4.3.2.3 Transformation

Since the corresponding control points are determined in both the mathematical and laser scanned model, they are introduced in this module for performing 3D conformal transformation. For each control point, three observation equations (Equation 4-1) are formed to compute the transformation parameters, including three translations (T_X, T_Y, T_Z), three rotations (ω, ϕ, κ) and one scale parameter (s).

$$X = s(m_{11}x + m_{21}y + m_{31}z) + T_X$$

$$Y = s(m_{12}x + m_{22}y + m_{32}z) + T_Y \qquad \textbf{Equation 4-1}$$

$$Z = s(m_{13}x + m_{23}y + m_{33}z) + T_Z$$

In the above equations, (X, Y, Z) represent the points in the laser scanned model and (x, y, z) represent the points in the designed mathematical model. Parameters m_{11} to m_{33} are the elements of the rotation matrix which are used for relating the two axis systems (refer to Section 2.4.2.2 for details of the rotation parameters). Since there are seven unknowns in Equation 4-1, the minimum of three 3D control points are required to obtain the solution. If more control points are introduced, an improved solution is achievable through least squares techniques.

To solve the observation equations, they are linearised using a Taylor series expansion with respect to each of the seven parameters. The linearised equations are written for each control point as follows (Wolf and Ghilani, 1997):

$$\begin{bmatrix} \left(\frac{\partial X}{\partial s}\right)_0 & 0 & \left(\frac{\partial X}{\partial \phi}\right)_0 & \left(\frac{\partial X}{\partial \kappa}\right)_0 & 1 & 0 & 0 \\ \left(\frac{\partial Y}{\partial s}\right)_0 & \left(\frac{\partial Y}{\partial \omega}\right)_0 & \left(\frac{\partial Y}{\partial \phi}\right)_0 & \left(\frac{\partial Y}{\partial \kappa}\right)_0 & 0 & 1 & 0 \\ \left(\frac{\partial Z}{\partial s}\right)_0 & \left(\frac{\partial Z}{\partial \omega}\right)_0 & \left(\frac{\partial Z}{\partial \phi}\right)_0 & \left(\frac{\partial Z}{\partial \kappa}\right)_0 & 0 & 0 & 1 \end{bmatrix} \begin{bmatrix} ds \\ d\omega \\ d\phi \\ d\kappa \\ dT_X \\ dT_Y \\ dT_Z \end{bmatrix} = \begin{bmatrix} X - X_0 \\ Y - Y_0 \\ Z - Z_0 \end{bmatrix}$$

Equation 4-2

where $(\partial X/\partial s)_0, (\partial X/\partial \phi)_0$, etc., are the partial derivatives with respect to the indicated unknowns evaluated at the initial approximations; X_0, Y_0 and Z_0 are the right-hand side of Equation 4-1 evaluated at the initial approximations; and ds, $d\omega$, $d\phi$, $d\kappa$, dT_X, dT_Y, dT_Z are corrections to the initial approximations which will be computed during the solution (Wolf and Dewitt, 2000). Once the equation including all the control points is written, it is solved using least squares. During the adjustment the corrections are given at the end of each iteration, they are then added to the initial approximation of the unknowns and X_0, Y_0 and Z_0 are re-computed then Equation 4-2 re-run. The procedure is iterated until negligible small corrections are obtained, and the latest approximations for the unknowns are the values for the transformation parameters. Finally the points in the designed mathematical model are transformed to the coordinate system of the laser scanned model using Equation 4-1. To perform the computation described above, the routine programmed by Wolf and Dewitt (2000) is modified and integrated in MS^2.

4.3.2.4 Surface Comparison

Figure 4-3 shows the interface of the Surface Comparison Module, which is used for determining the discrepancies between the laser scanned model and the transformed mathematical model. As the point intensities in X-Y plane of these two models are different, they can not be compared directly. To achieve this, the solution offered in Section 2.3.4 is applied. Two new meshed surfaces with a uniform grid interval are fitted to the data in the non-uniformly spaced points. The meshed surfaces are interpolated at the identical points specified by (X, Y) to produce respective Z-values,

therefore the two output surfaces always pass through the same points (Figure 2-10). The comparison is then performed based on the Z-values of each node in the two output meshed surface. The resultant statistics are shown in the interface when the computation was finished. In addition to the metric information, the planimetric discrepancy map and the profiles of the surfaces are created for inspecting the positions of obvious differences, and further analysing and interpreting the discrepancies between the two surface models. The core codes for performing this module were shown in A1.1.3.

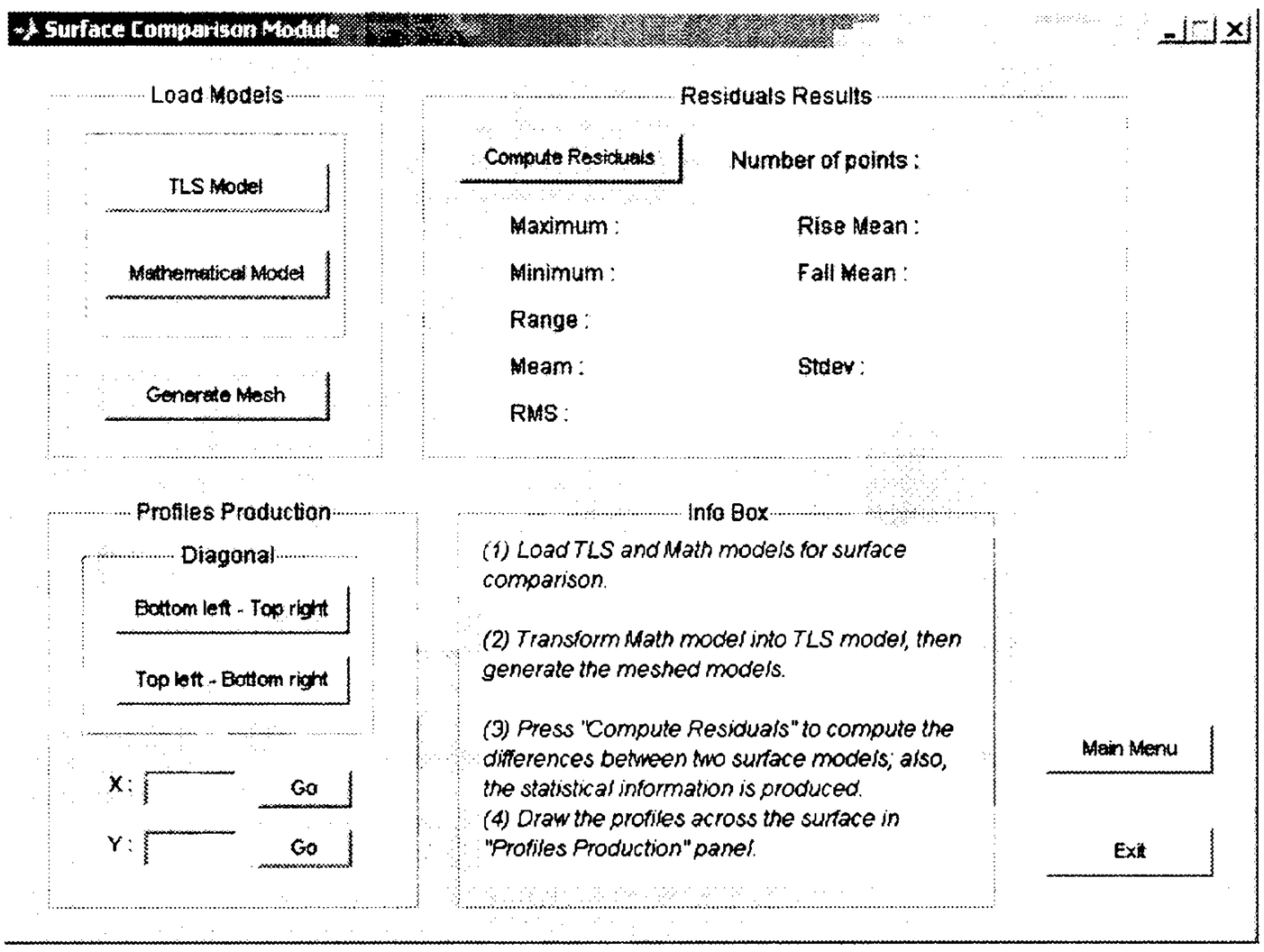


Figure 4-3: User interface of the Surface Comparison Module.

As the surface comparison is carried out on the two interpolated surface models, the results of the comparison will be influenced by different interpolation methods. In order to determine the most optimal solution, three interpolation methods, including triangle-based nearest neighbour, linear and cubic interpolation, were examined. All the methods are based on a Delaunay triangulation of the point data in the original laser scanned model and the transformed mathematical model, therefore the two sets of point data are triangularised prior to the interpolation. In the nearest neighbour interpolation, the Z-value of the vertex closest to the specified point is assigned as the output coordinate. During the triangle-based linear interpolation procedure, the first step is to find the triangle nearest to the specified point. Then barycentric coordinates for the point are computed and they are used to solve the Z-value of the output point (Watson, 1992; The Mathworks, Inc., 2004). Whereas when the cubic interpolation was performed, the finite element method is used to compute the optimal surface fit to the point data. More details and formulae about the employed triangular plate bending finite element are given in Yang (1986).

These three interpolation methods were implemented on an identical mathematical point model and the resulting surfaces are illustrated in Figure 4-4. In general, smooth surfaces are produced by using linear or cubic interpolation, while discontinuities are derived by adopting the nearest neighbour method. In addition, it was also found that some error spikes (outlined by circles in Figure 4-4) occasionally occur in the edge of the surface generated by cubic interpolation. As a result, the surface interpolated by the linear method presented the most appropriate and true surface, hence the triangle-based linear interpolation was introduced in MS^2.

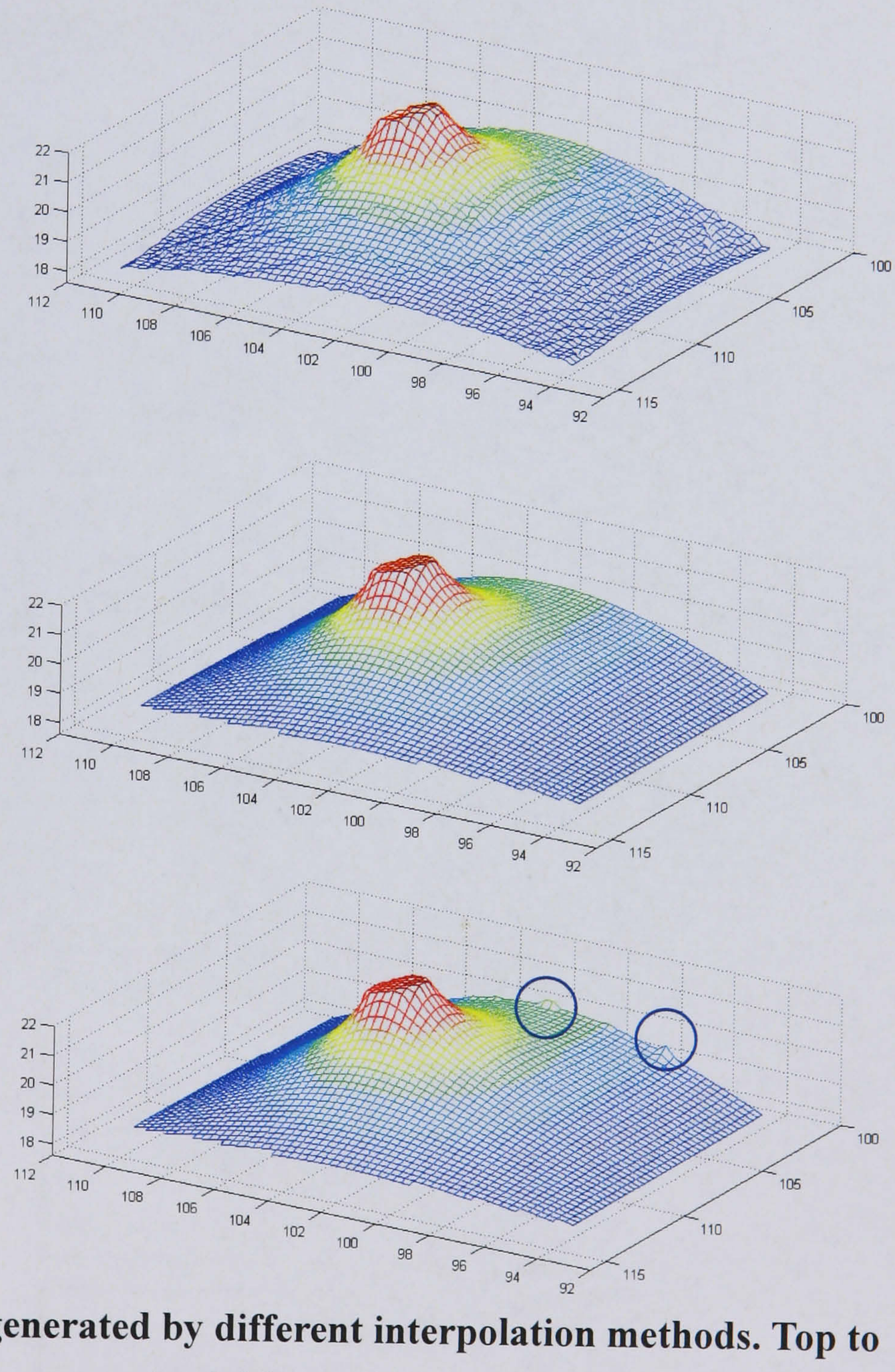


Figure 4-4: Meshed model generated by different interpolation methods. Top to bottom: nearest neighbour, linear and cubic interpolation.

4.3.3 Dynamic Surface Modelling

Once the video imagery is downloaded to the host computer, the Dynamic Surface Modelling panel in MS^2 is used to perform target extraction, target referencing, target

tracking, model construction and surface displacement query. In the main menu all the tasks are arranged in the order of a normal videogrammetry/photogrammetry workflow, allowing straightforward operation of the software.

4.3.3.1 Workflow

Figure 4-5 indicates the data processing procedures of videogrammetric monitoring in MS^2. Generally, the operations described in each block are realised through the modules arranged in the Dynamic Surface Modelling panel. In addition, as a considerable volume of data is expected, the results obtained from each module are assigned to save as a matrix structure for efficient retrieval and further computation and analysis.

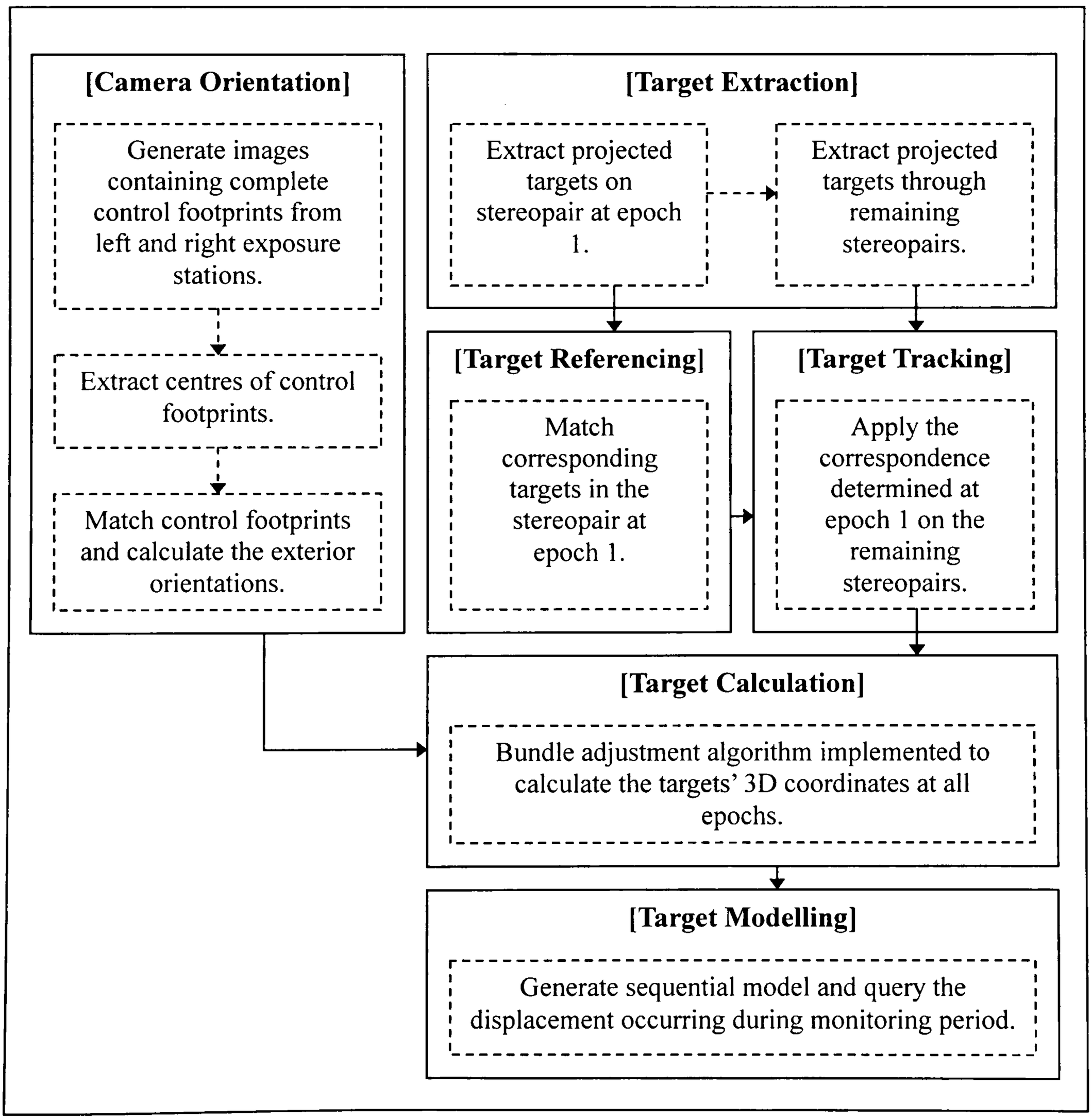


Figure 4-5: Computation sequence of the dynamic surface modelling in MS^2.

4.3.3.2 Camera Orientation Module

At the image acquisition stage, laser footprints were employed as control points for determining the orientations of cameras. As the laser footprints were captured in separate images, they were loaded and combined by the image arithmetic algorithm introduced in Section 3.3.2.2. Once the image containing complete control footprints was produced, image filtering and segmentation were performed to enhance the laser footprints. They are then extracted and labelled automatically. Consequently, a centroiding algorithm is used to estimate the centres of the laser footprints. For data visualisation and footprint matching, the extracted control footprints were coded and marked in the resultant images. All the tasks are implemented through the user interface (Figure 4-6) and the core code for this module was shown in A1.2.1.

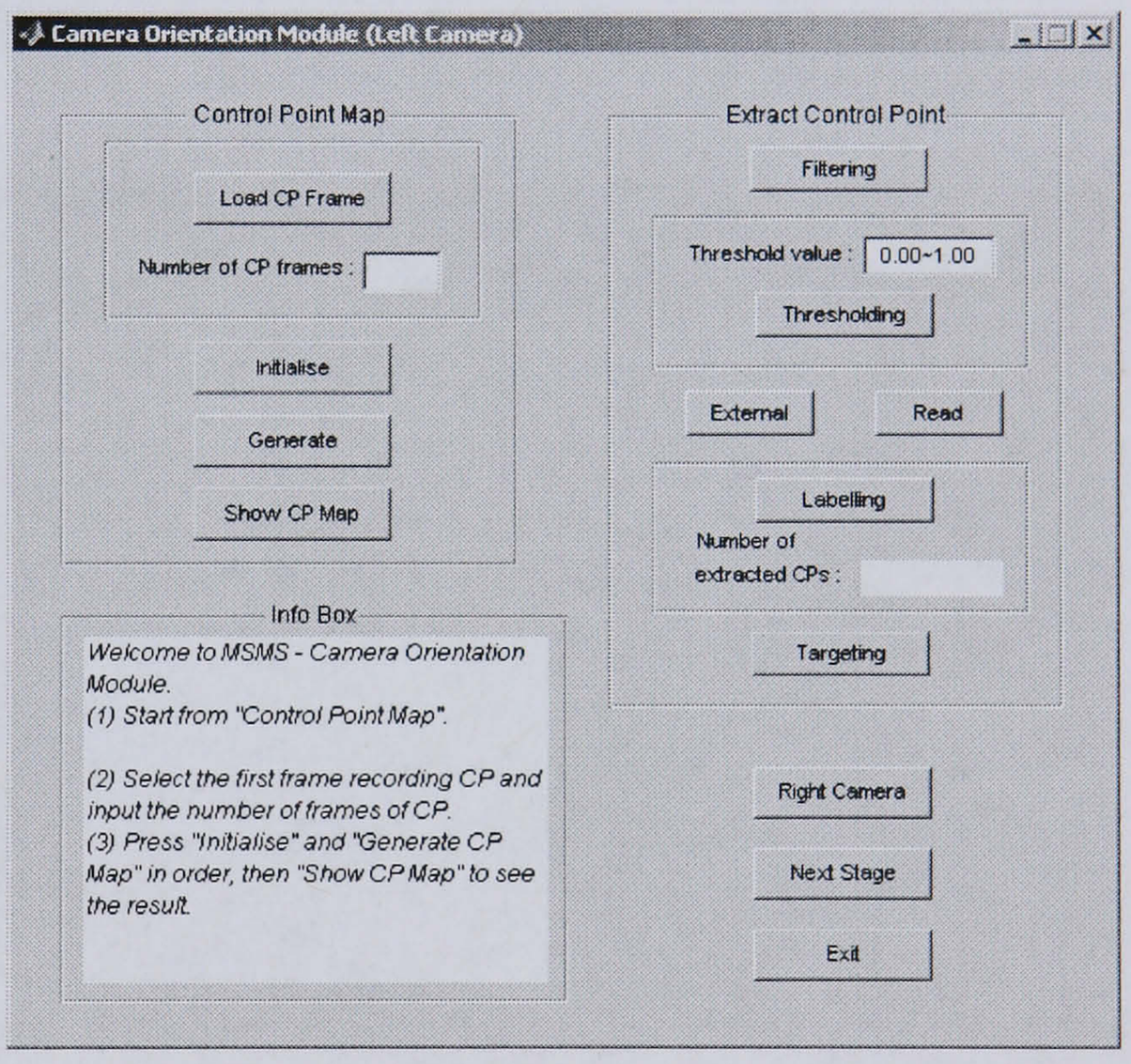


Figure 4-6: User interface of the control footprints extraction in Camera Orientation Module.

Considering the size of the laser footprints in the image, enhancement of the footprints may be required in this module. For highlighting the point feature, a spatial convolution filtering technique (a Laplacian mask) is introduced for enhancing the laser footprints (Jenson, 1996; Pratt, 2001). The Laplacian filter adopted is shown in Equation 4-3. In addition, during image segmentation, a normalised intensity value that lies between 0 and 1 was used as a threshold value to convert an intensity image to a binary image. The output binary image has values of 1 (white) for all pixels in the input image with luminance greater than the given threshold value, and 0 (black) for all other pixels.

$$Laplacian\ mask = \begin{bmatrix} -1 & -1 & -1 \\ -1 & 8 & -1 \\ -1 & -1 & -1 \end{bmatrix} \qquad \textbf{Equation 4-3}$$

The overall implementation is repeated on the images shot by the second camera to produce the image of extracted control points. The two resulting images are then brought to the next stage for matching corresponding control points. To speed up the matching, the 3D coordinates of the laser footprints observed by the total station are loaded to generate a 3D map of the footprints. Thereby the corresponding control footprints can be matched by searching the marked control footprints shown in the images of complete control points and the 3D map of the laser footprints. The results are input into the interface (Figure 4-7), and CUBA is subsequently prompted to compute the exterior orientations of the two cameras.

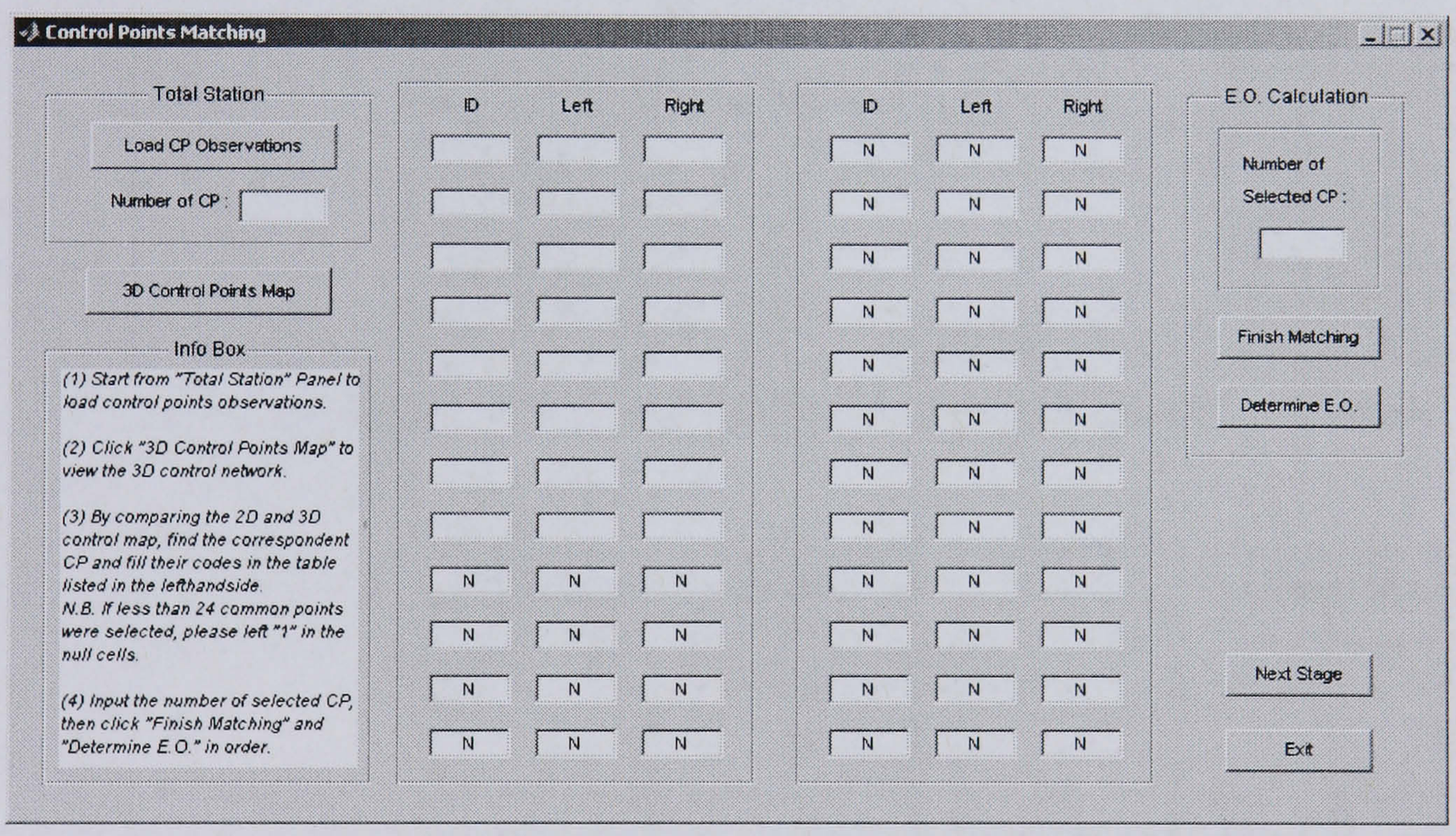


Figure 4-7: User interface of the control footprints matching in Camera Orientation Module.

4.3.3.3 Target Extraction Module

For extracting projected targets, image segmentation is firstly applied on the stereopair from the first epoch by applying an appropriate threshold value in the user interface (Figure 4-8). Meanwhile the function of de-noise is performed if necessary. Once all the projected-dots are highlighted, an algorithm is used to visit all pixels within the image for identifying the rough positions of the targets and also labelling the targets. Consequently, a centroiding algorithm is executed to measure the precise centres of the

targets pre-identified. If the number and positions of the extracted targets in the first stereopair are correct, the parameters and settings applied for the extraction are repeatedly implemented on the remaining stereopairs. The extracted targets of each epoch are saved in the structure shown in Figure 4-9. It is noteworthy that there is no specific order for the targets extracted in this module.

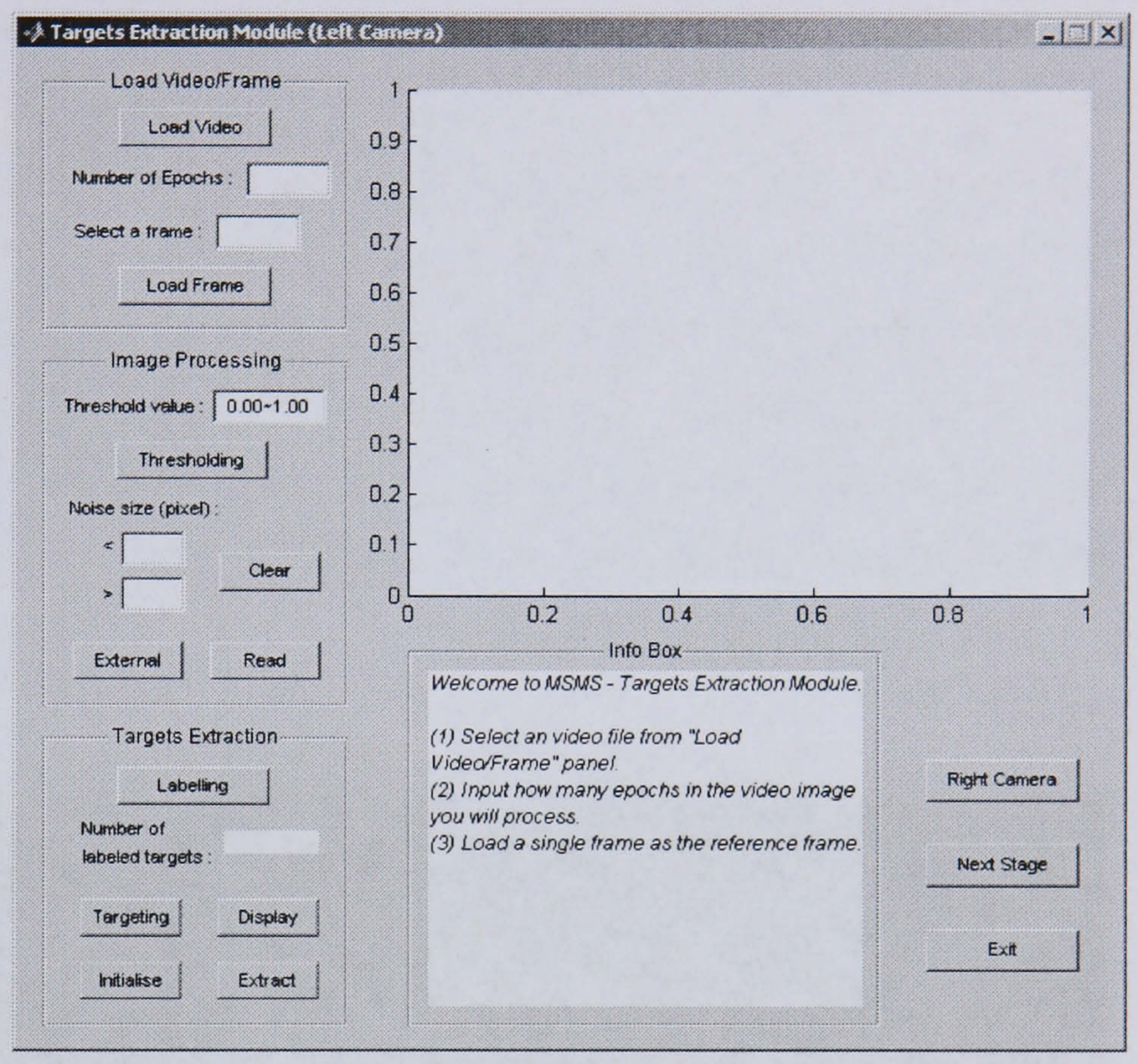


Figure 4-8: User interface of Target Extraction Module.

Epoch 1	
L	
X	Y

Epoch 2	
L	
X	Y

.....	
L	
X	Y

Epoch N	
L	
X	Y

Epoch 1	
R	
X	Y

Epoch 2	
R	
X	Y

.....	
R	
X	Y

Epoch N	
R	
X	Y

Figure 4-9: Saved data structure of the projected targets extracted from left and right cameras at each epoch.

4.3.3.4 Target Referencing Module

The goal of this module is to establish the correspondence of the extracted targets in the

stereopairs. Epipolar geometry is routinely applied for searching for corresponding points appearing in sets of photos. However, due to random and systematic errors in real imaging systems (e.g. inaccurate estimations of the camera orientation parameters, poor network geometry, and high point density), the corresponding points will not meet the epipolar constraint all of the time. Hence additional work is necessary for searching potentially corresponding points, then removing ambiguous points, and finally determining the correct corresponding point (Maas, 1992a; Chen et al., 1993; Ariyawansa and Clarke, 1999; Remondino, 2002; Megyesi and Chetverikov, 2003). In this project, the issues mentioned above also occurred if epipolar geometry was applied. A stereopair acquired from the fieldwork is shown in Figure 4-10. The match of corresponding point "1627" is performed using epipolar geometry. In the right image the epipolar line is generated and a total of 17 potentially corresponding points are found (marked by blue crosses). Supplementary operations are therefore required to eliminate the ambiguities. In order to make the matching more efficient, an alternative solution was proposed in this module.

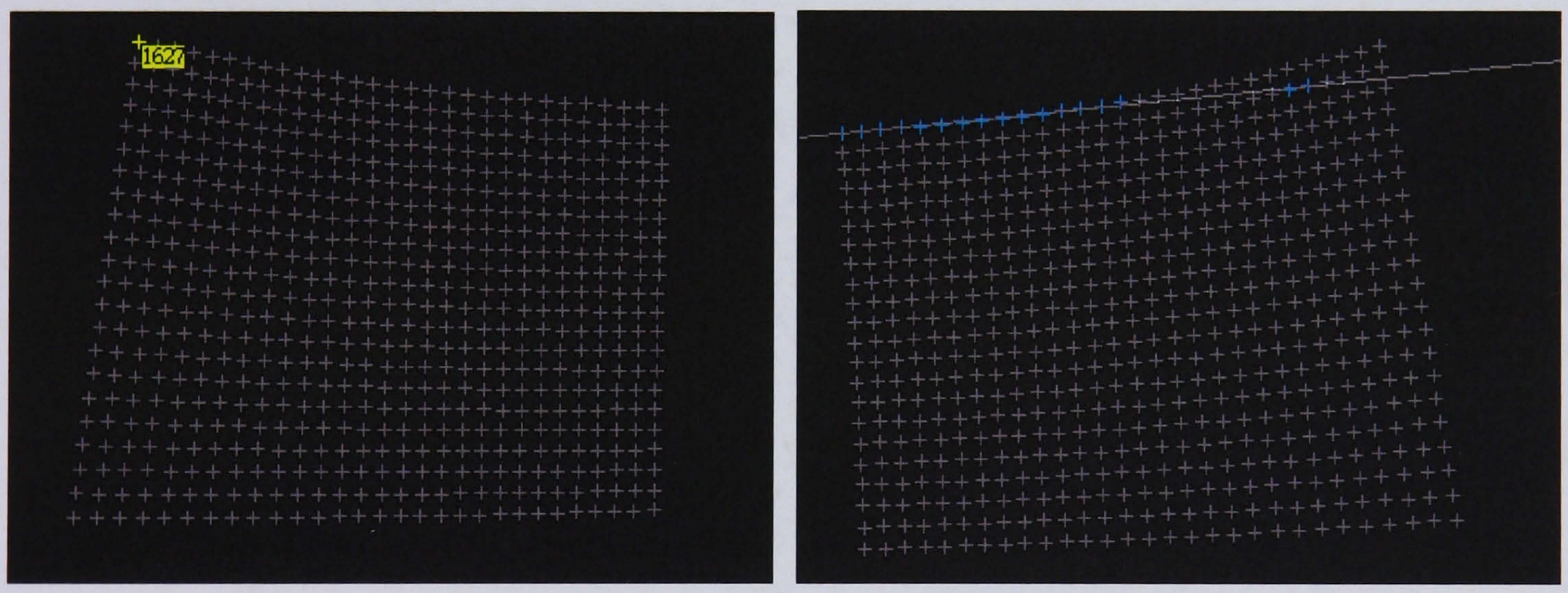


Figure 4-10: Ambiguities of applying epipolar geometry in the dynamic monitoring scheme.

In the previous module, a centroid algorithm was implemented to derive the centre of each target. The collection of extracted targets started from the top most left pixel of the image and was searched pixel by pixel, in the order of top to bottom row and left to right column, across the whole image. Based on this sequence, if the projected pattern was shown as a regular rectangle in the frames taken from different exposure stations, the most top left target of the projected pattern would be collected first and the remaining targets would be extracted and labelled with sequential point identifications (PtID) as shown at the top of Figure 4-11. After the collection of extracted targets is complete, the corresponding points could be matched by simply calling the points of

identical PtID. However, due to the diverse view angles of the cameras, the projected pattern rarely appears as a regular rectangle in the imagery, therefore the first target collected would not for certain be the most top left point of the projected pattern. Furthermore, the order of the collection of the remaining targets would be randomly stored (e.g. Figure 4-11, middle). Accordingly, the correspondence could not be achieved by requesting the targets of the same PtID.

The strategy of matching corresponding projected targets is to "re-label" the extracted targets from irregular into regular order, which is from the middle to the bottom diagram shown in Figure 4-11. Once finished, the corresponding points can be matched by collecting the points of identical updated PtID. The re-label task is undertaken by the following procedures:

(i) Work on the column basis from the left to identify the adjacent targets of each target. To achieve this, appropriate numbers of pixels, called "Max X/Y interval" in the user interface (Figure 4-12), are input. When the X and Y intervals between any two targets are both smaller than the given Max X/Y intervals, these two targets are determined as connection targets.

(ii) The number of connection(s) of each target should be one or two. The targets with one connection are either top or bottom targets of each column of the projected pattern. The targets with two connections are the interior targets between the top and bottom targets. They are saved separately into two groups.

(iii) Identify the top targets of each column in the group of targets with one connection. They are sorted in an order of left to right column.

(iv) Commence re-labelling from the most left column, where the top target determined in the previous step is re-labelled as PtID 1. Its connection target is derived from the group of targets with two connections (finished in step (ii)) and is re-labelled as PtID 2. The updated PtID and their image coordinates are saved in the matrix structure shown in Figure 4-13.

(v) Obtain the remaining connection target of PtID 2 in the group of targets with two connections and re-label it as PtID 3. The updated PtID and the image coordinates are saved. The re-labelling and storage is repeated until reaching the bottom-most target of the column.

(vi) The re-labelling and storage is continually applied to the remaining columns by repeating steps (iv) and (v).

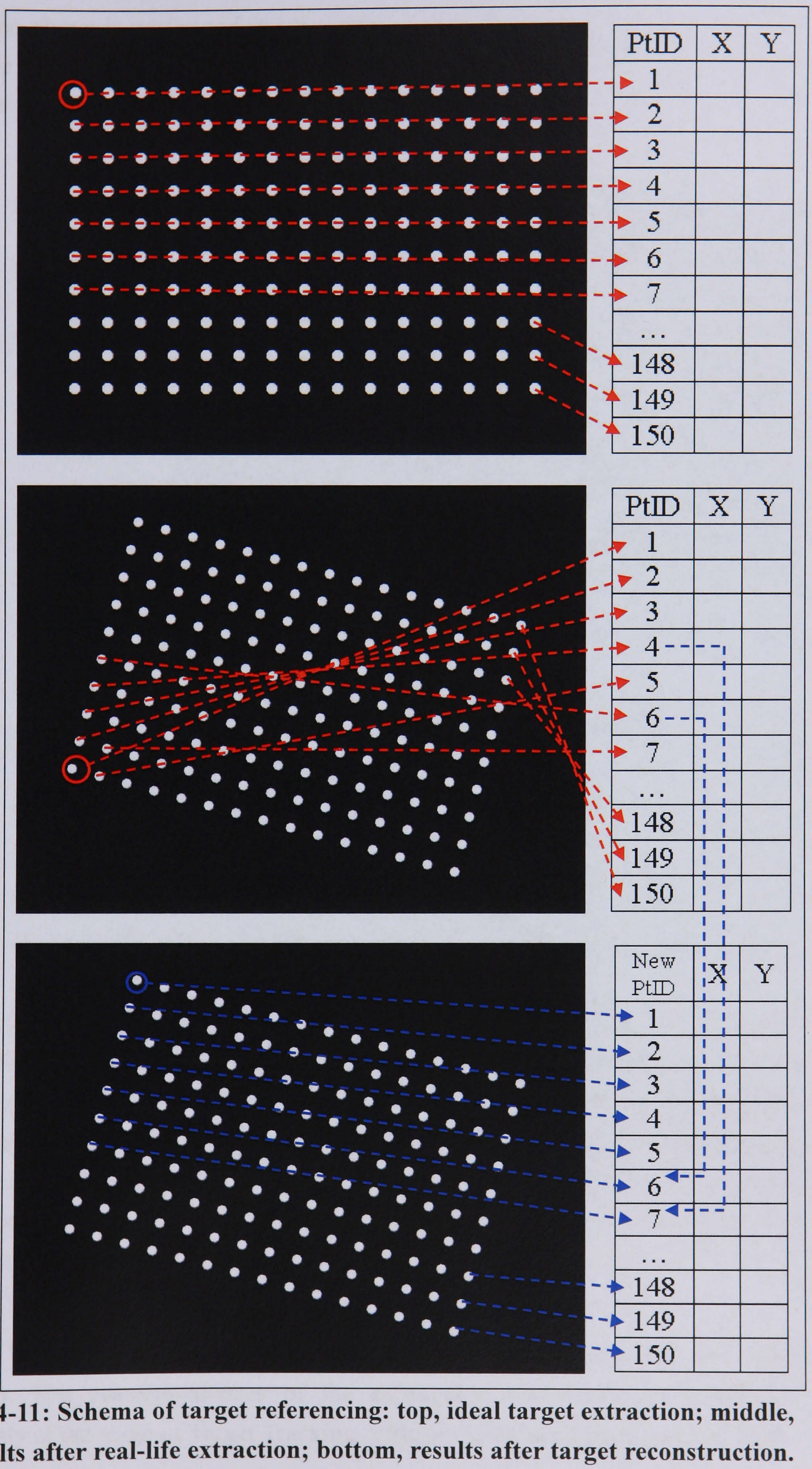


Figure 4-11: Schema of target referencing: top, ideal target extraction; middle, results after real-life extraction; bottom, results after target reconstruction.

The operation above is performed in the other image and the results are also saved in the structure shown in Figure 4-13. In the end, the corresponding points can be determined by collecting the points with the identical PtID.

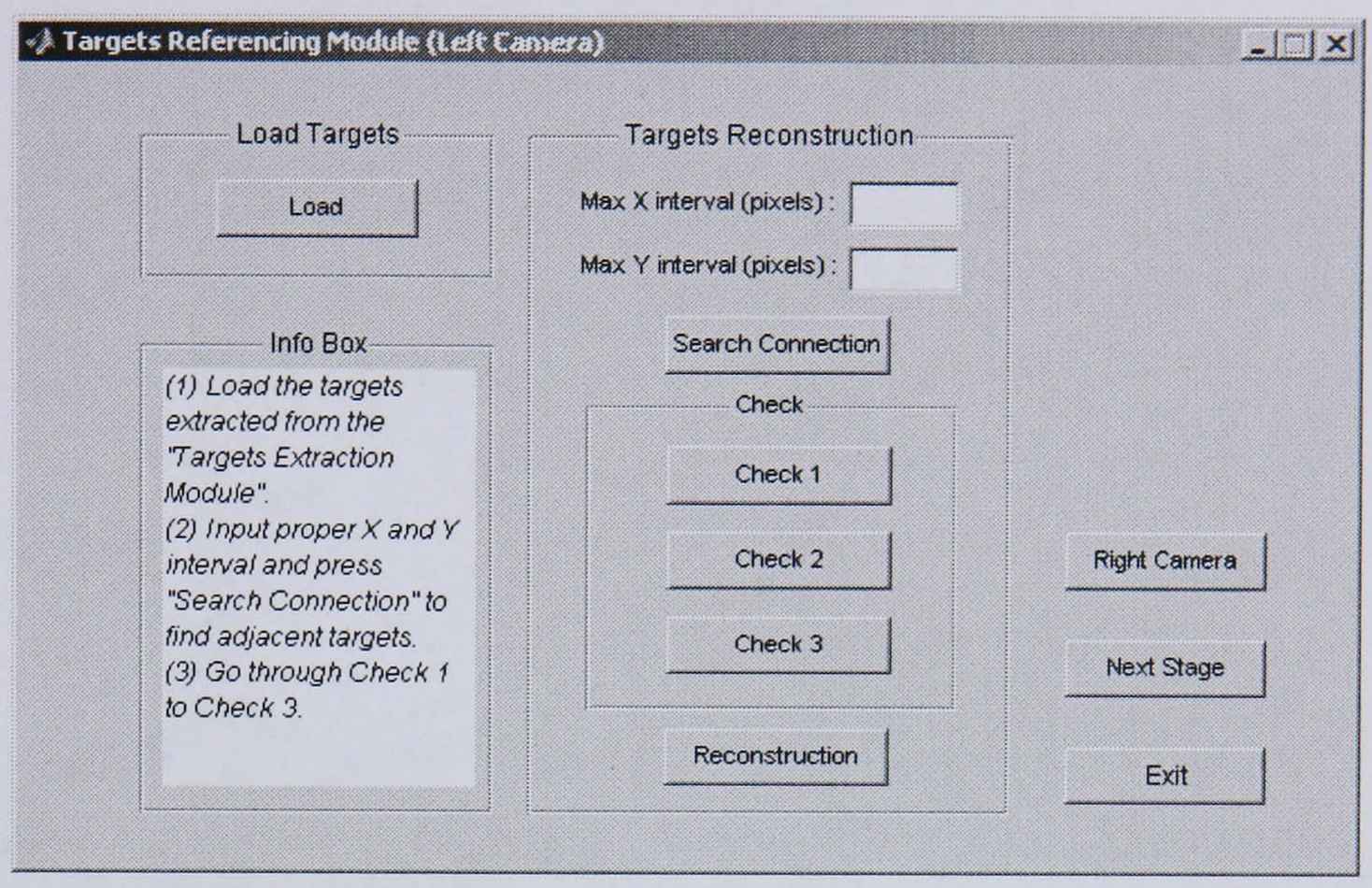


Figure 4-12: User interface of Target Referencing Module.

PtID	Epoch 1			
	L		R	
	X	Y	X	Y
1				
2				
...				
m				

Figure 4-13: Data structure of the corresponding targets at first epoch.

The key factor for a successful reconstruction is defining an appropriate "Max X/Y interval" in the user interface (Figure 4-12). To ensure the accomplishment, three steps of checking are carried out during the processing. The first two checks are performed to confirm if any points have less than one connection or more than three connections by applying the given X and Y interval values. The third check is to ensure the number of the top and bottom targets are correct. The overall workflow is illustrated in Figure 4-14 and the implemented code is demonstrated in A1.2.2.

In MS^2, the Target Referencing is only executed on the stereopair at the first epoch (Figure 4-5). The correspondences of the subsequent stereopairs are established simultaneously at the stage of Target Tracking, which is introduced in the next module.

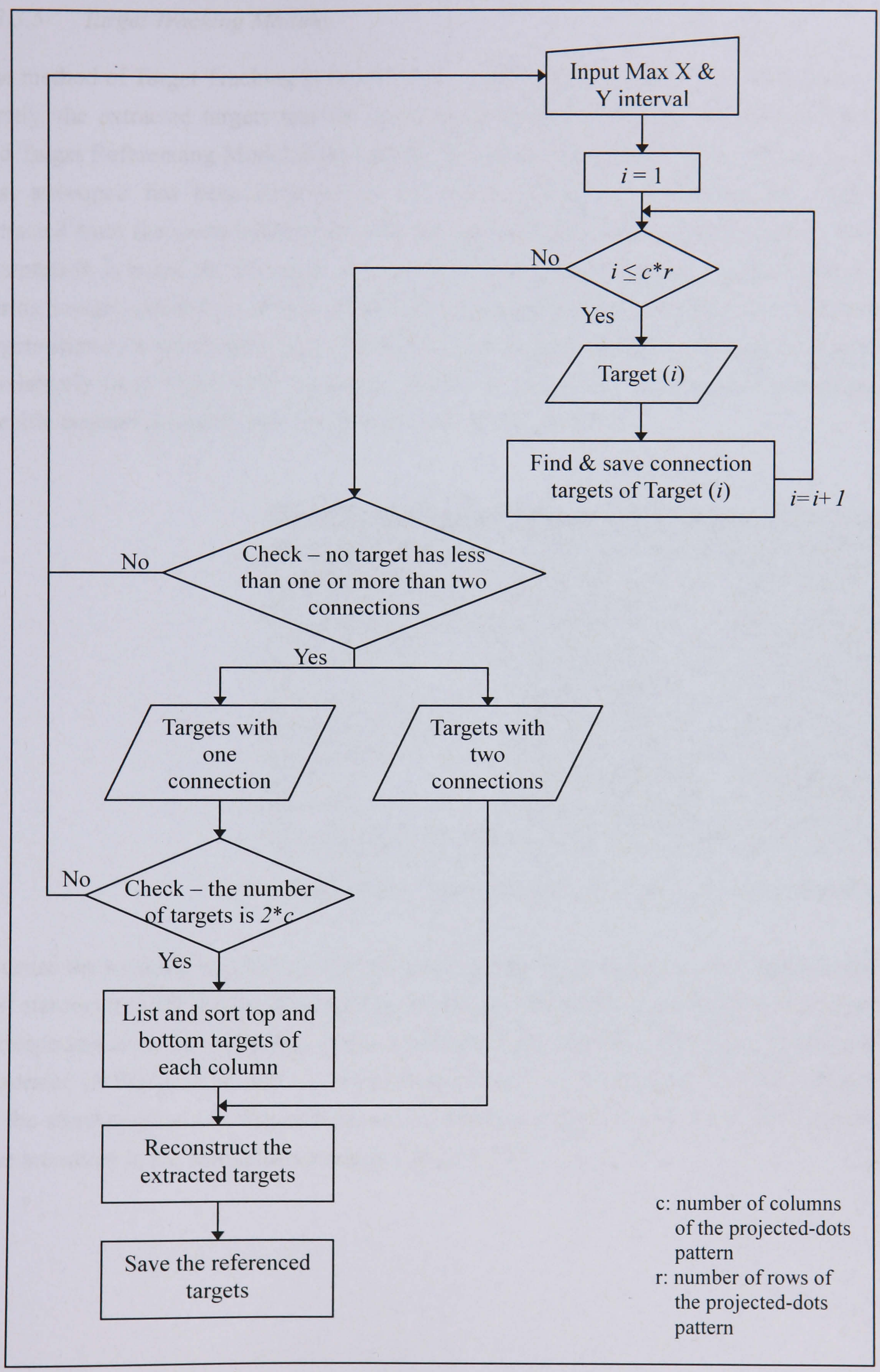


Figure 4-14: Workflow of the Target Referencing Module.

4.3.3.5 Target Tracking Module

The method of Target Tracking is based on the results derived from Target Referencing. Firstly, the extracted targets and the correspondences derived from Target Extraction and Target Referencing Modules are loaded. As the correspondence of the targets in the first stereopair has been determined, the tracking starts by comparing the targets extracted from the second stereopair with the targets derived at the first stereopair. This comparison is based on the range of movement that occurred on the observed surface during image acquisition. Where significant displacement had occurred, the identical targets shown in sequential images would be shifted significantly. In this circumstance, a relatively large "Max X/Y tolerance" should be given in the interface for tracking specific targets throughout the image sequences (Figure 4-15).

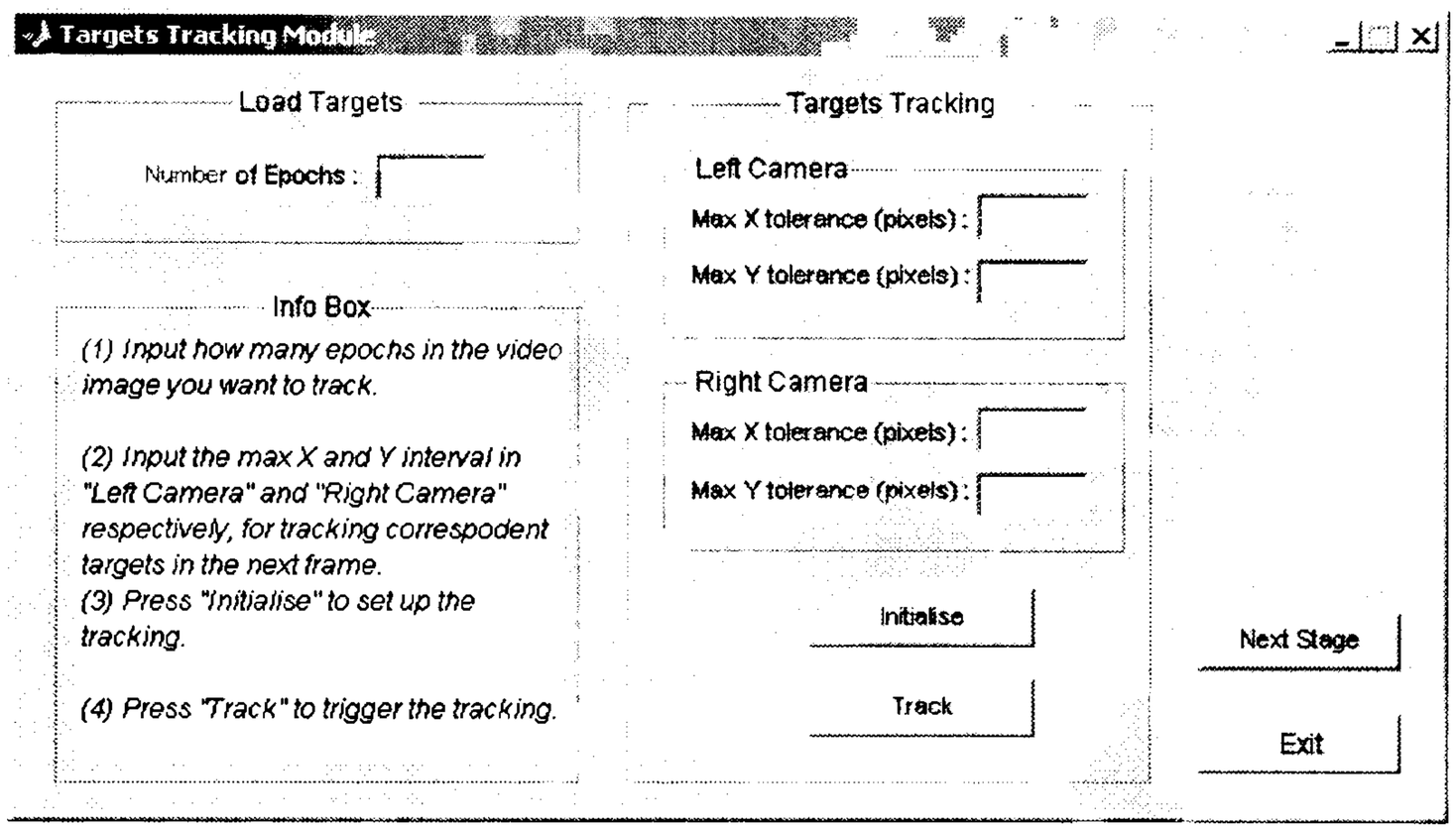


Figure 4-15: User interface of Target Tracking Module.

Because the tracking is performed in the order of the points being reconstructed in the first stereopair, once the tracking applied in the second stereopair is finished, the target correspondence is accomplished in the meantime. The workflow of Target Tracking is illustrated in Figure 4-16 and the implemented code is demonstrated in A1.2.3. Based on the structure saved in Target Referencing Module (Figure 4-13), the results derived here are saved in the format described in Figure 4-17.

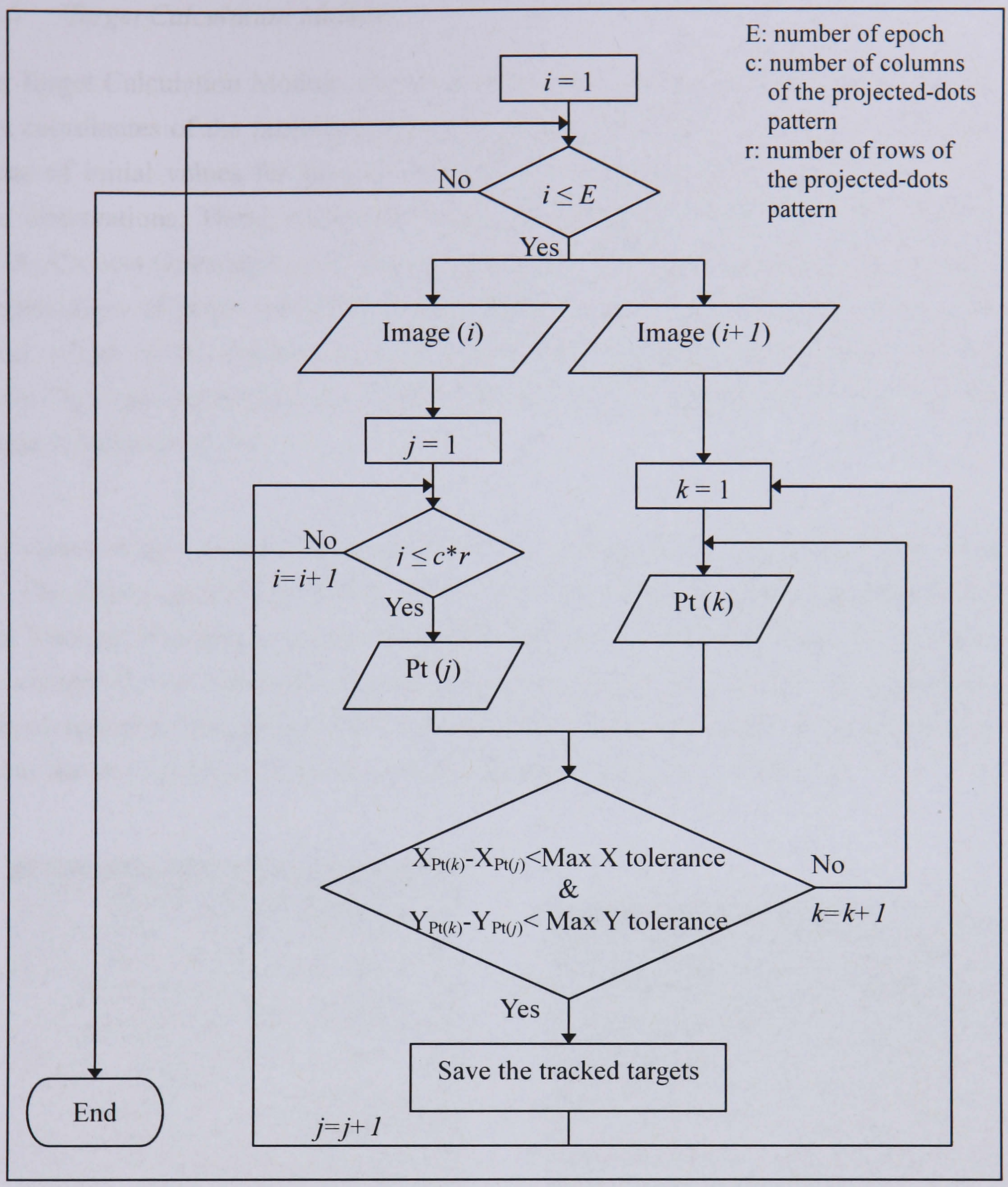


Figure 4-16: Workflow of Target Tracking Module.

PtID	Epoch1				.....				Epoch N			
	L		R		L		R		L		R	
	X	Y	X	Y	X	Y	X	Y	X	Y	X	Y
1												
2												
...												
m												

Figure 4-17: Data structure of the tracked target, based on the structure saved in Target Referencing Module.

4.3.3.6 Target Calculation Module

In the Target Calculation Module, the CUBA software is introduced to compute the 3D object coordinates of the projected targets at each epoch. The data file input to CUBA consists of initial values for interior and exterior orientations of the cameras and for image observations. These values are respectively retrieved from the results derived from the Camera Orientation and Target Tracking Modules. The input file also contains the estimations of target locations. To determine these values the space intersection method, which is the application of the collinearity equations, is introduced in this module. The formulae applied are listed in Section 2.4.2.2 (Equations 2-5 and 2-6) and the code is listed in A1.2.4.

Initial values of the target locations are computed in the interface shown in Figure 4-18 (left). The values are combined with the results derived from Camera Orientation and Target Tracking Modules to create a batch file for input into CUBA (Figure 4-18, right). Once computed, the adjusted 3D positions of the targets are saved. The procedures above are repeated through the whole sequence and the solved targets at each epoch are saved as the structure shown in Figure 4-19, for future retrieval and analysis.

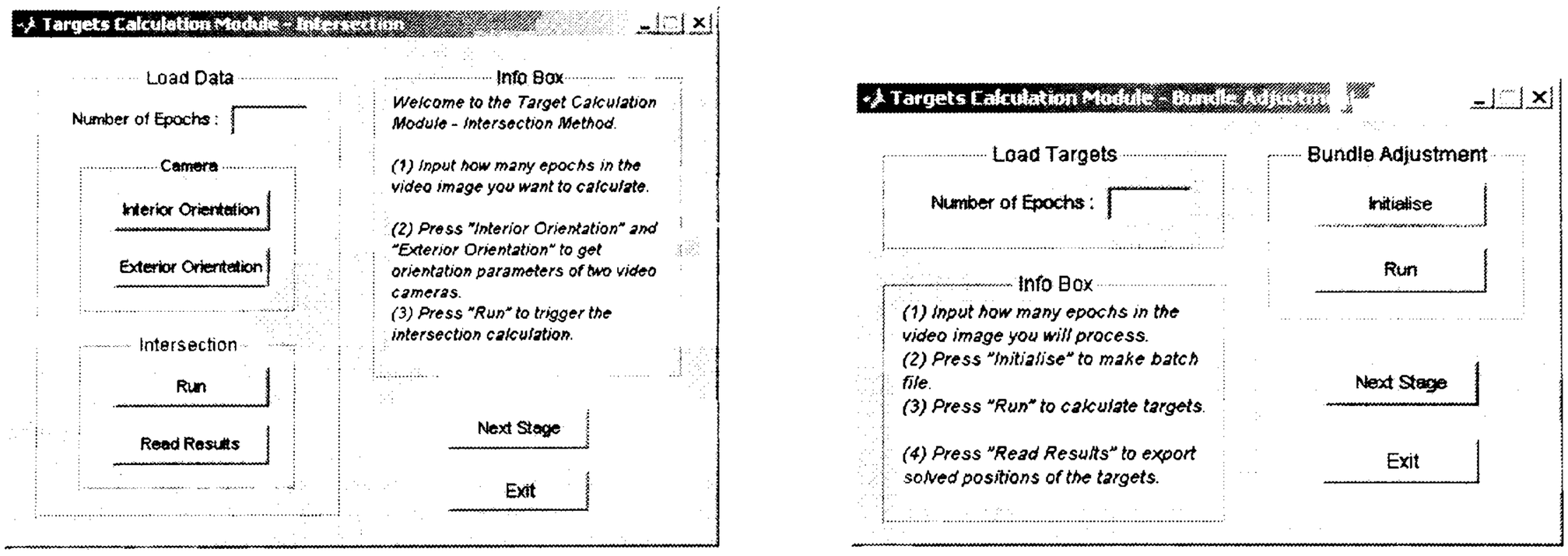


Figure 4-18: User interface of Target Calculation Module – Intersection (left) and Bundle Adjustment (right).

PtID	Epoch 1			.....			Epoch N		
	X	Y	Z	X	Y	Z	X	Y	Z
1									
2									
...									
m									

Figure 4-19: Saved data structure of the determined 3D positions of projected targets at each epoch.

4.3.3.7 Target Modelling Module

The Target Modelling Module is the last stage of the videogrammetric processing, at which the construction of the point or meshed model at a specified epoch is accomplished. They can be exported as a CAD file for detailed investigations through MS^2. Also, the sequential displacements of the surface are derived in this module. For computing the surface movement, meshed surfaces of uniform grid are generated by the method described in Section 4.3.2.4. Subsequently the comparison is performed based on the Z-values of each node in the selected meshed surfaces. MS^2 offers two interfaces for querying the displacement occurred through the complete sequence or only some specified epochs, referring to Overall Query (Figure 4-20) and Advanced Query (Figure 4-21) respectively.

To compute the displacement, the base surface is selected at the beginning. For deriving clearer results, the positive (moving upwards) and negative (moving downwards) displacements occurred at each epoch are separated during the comparisons in MS^2, the corresponding diagrams and statistics are displayed in the panels of Positive and Negative Z-displacement shown in Figure 4-20 and Figure 4-21. In summary, the queries are categorised into the following subjects:

(A) Displacements occurred through the whole sequence: Average positive and negative displacements, as well as the maximum displacements that occurred at each epoch, are computed. The statistical information is presented and the respective histograms are created.

(B) Movement of one specific target on the observed surface through the whole sequence.

(C) Displacements occurred at any specific epochs: The movements are calculated and they are plotted as 3D vectors based on the base surface points.

(D) Comparisons of the profiles across the surface: The difference value and the shape of the specific part of the membrane surface can be investigated through the extracted profiles.

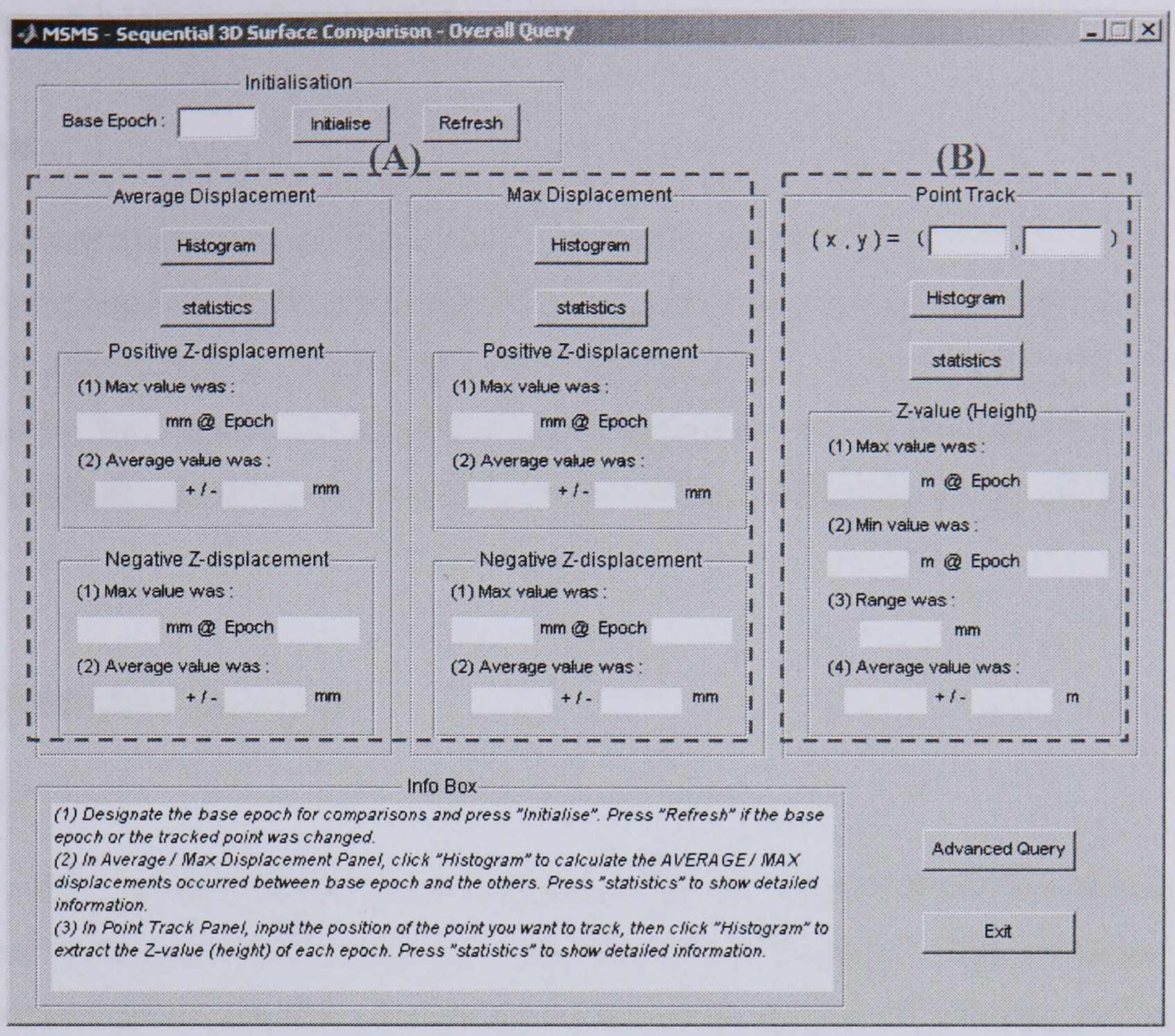


Figure 4-20: User interface of Target Modelling Module – Overall Query.

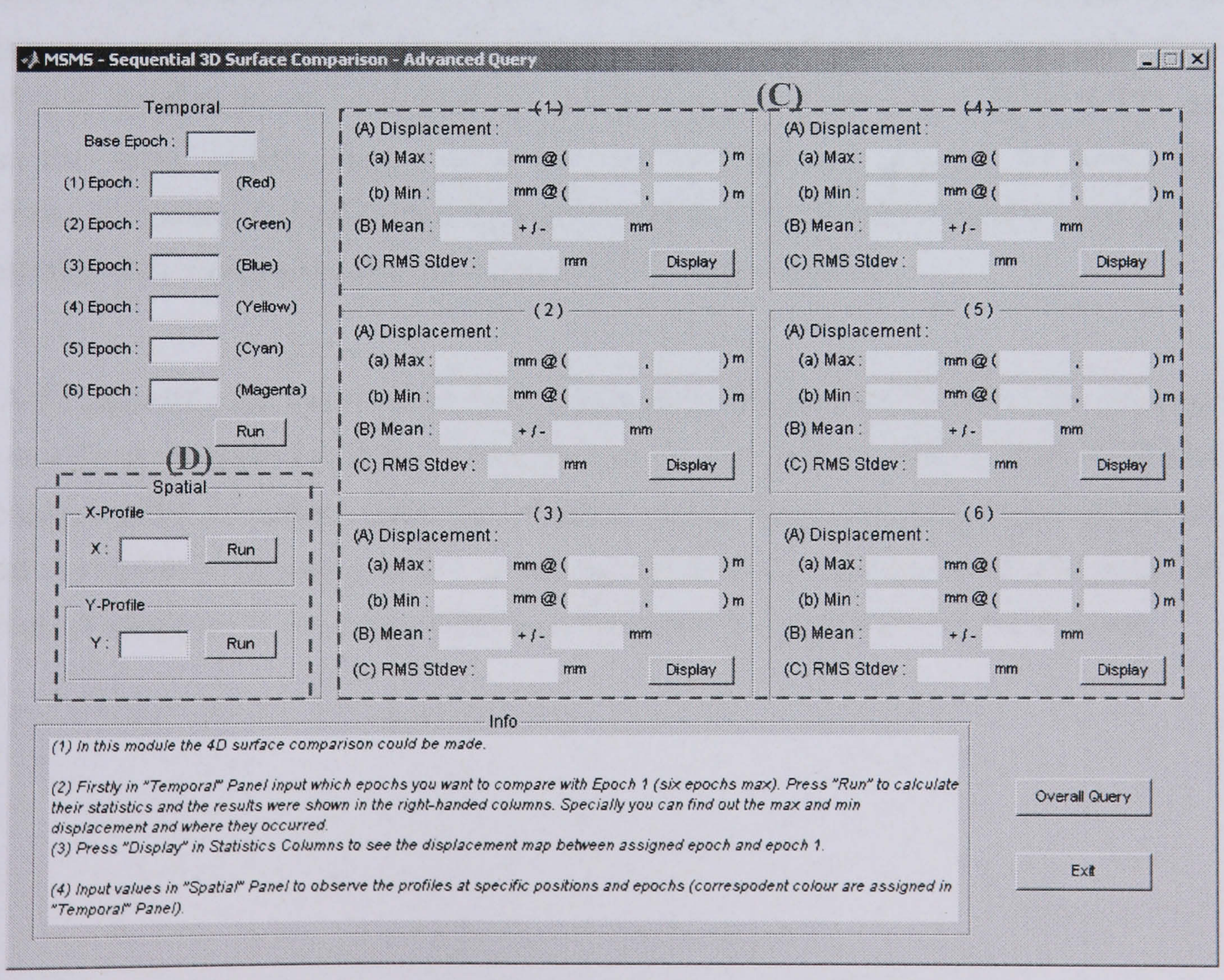


Figure 4-21: User interface of Target Modelling Module – Advanced Query.

4.4 Assessment of MS^2 Performance

4.4.1 Introduction

In order to assess the performance of MS^2, two tests were conducted under laboratory conditions. Imagery was acquired of both a static and dynamic surface and subsequently input into MS^2 for measurement. The tests were designed to simulate the type of network configuration that would be subsequently adopted in the field. The overall performance of the videogrammetric system and the resulting modelling are assessed in this section.

4.4.2 Static Monitoring Performance

4.4.2.1 Test Setup

In the first test, a static object (a laboratory internal wall) was selected and modelled using the developed videogrammetric system. The two Oscar cameras, with the same settings as the ones in Test 2 (Section 3.4.6), a Leica TCRA 1103 total station, and a data projector (Philips ProScreen 4750) were arranged in a configuration observing the wall surface that simulated the real test site. When the collection of control laser footprints was complete, a dot pattern of 450 targets was continuously projected onto the wall and simultaneously recorded using the two Oscar cameras (Figure 4-22). In addition, the video camera frame rates were set to three and one fps for collecting control laser footprints and projected-dots respectively. The images of control footprints and projected-dots were subsequently input to MS^2 for processing.

Figure 4-23 indicates the two-station convergent network geometry, where the average camera-to-object distance for the two cameras was 9.1 m (image scale 1:760). With this stereo configuration of camera network, coupled with an image coordinate measurement precision via centroid targeting of 0.1 pixel, triangulation precision (at 68.3% probable error level) of close to +/- 1.4 mm could be anticipated for points across the surface.

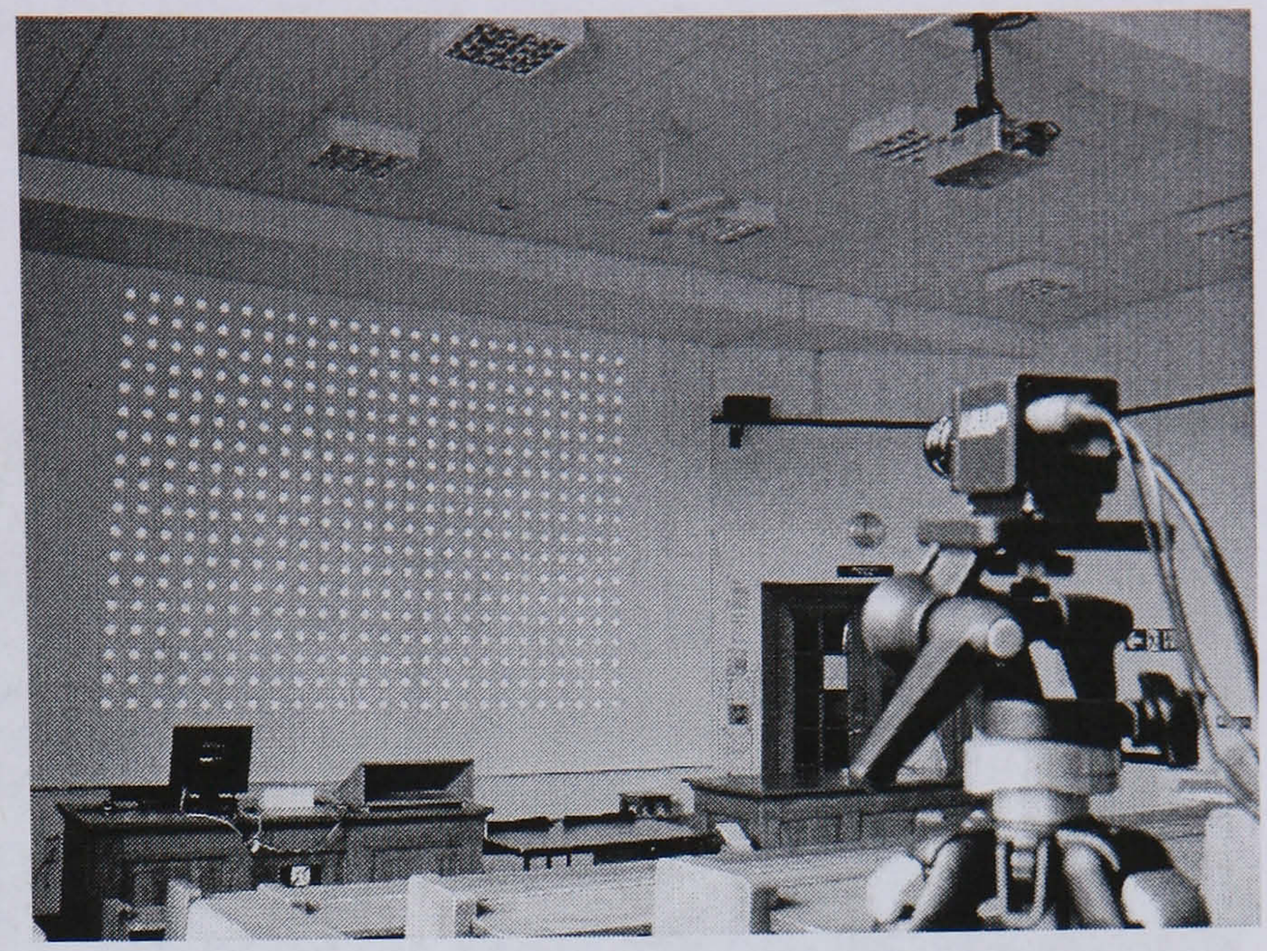


Figure 4-22: Dot pattern projected onto the static wall, observed by the left camera.

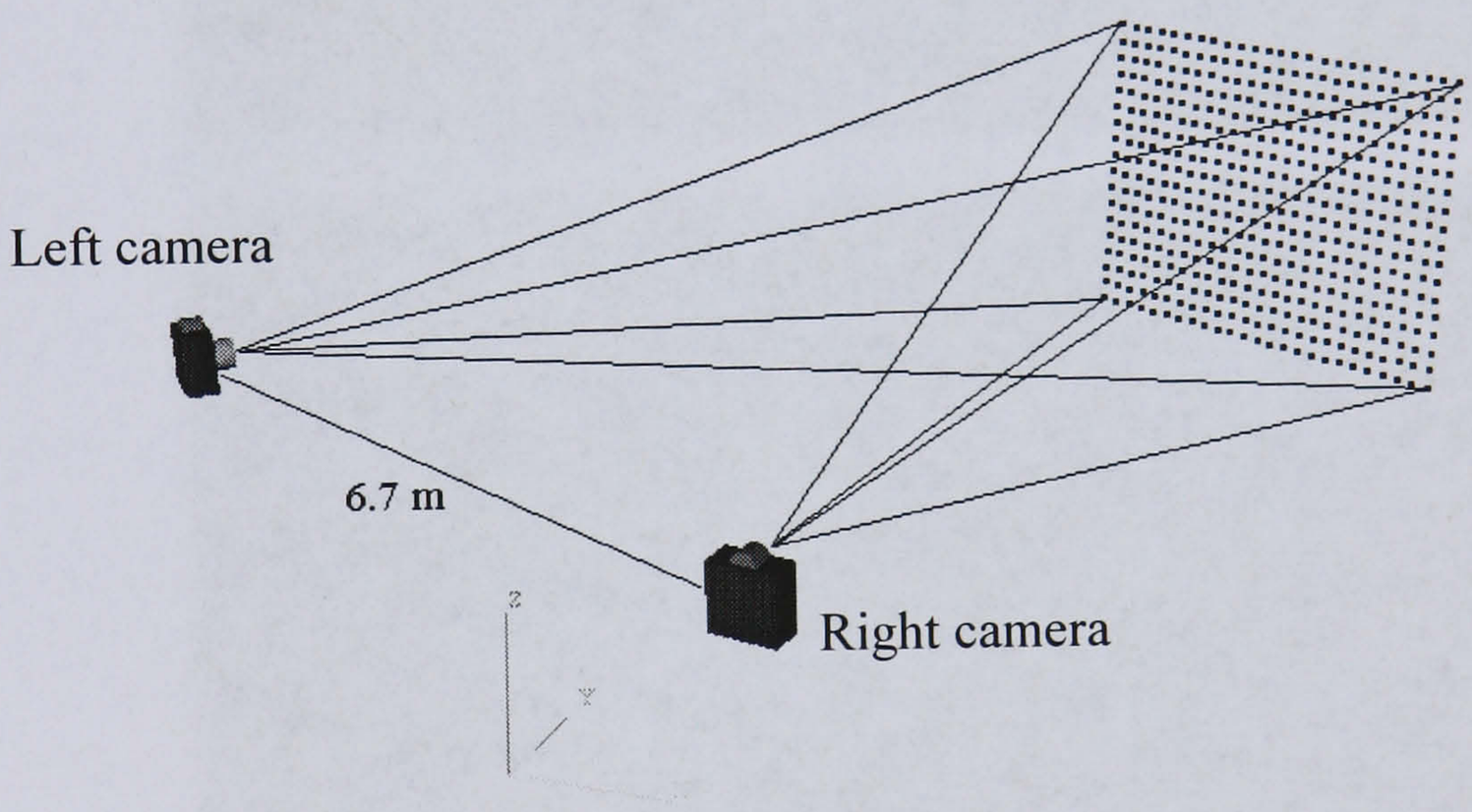


Figure 4-23: Videogrammetric network comprising two camera stations and the projected-dot pattern.

4.4.2.2 MS^2 Implementation

- Camera Orientation Module

During the data collection stage, 21 control footprints were generated across the area being imaged and they were recorded in 226 frames by each camera. The image sequences were then processed in the Camera Orientation Module in MS^2 (threshold values of 0.2 were used in the images shot in both the left and right camera stations). Once complete, all the laser footprints were successfully extracted from the left exposure station, while 19 footprints were acquired by the right camera (Figure 4-24). Subsequently, the 3D map of control footprints observed by the total station was

produced (Figure 4-25) and the corresponding footprints were matched manually. The results were input to the interface (Figure 4-26) for computing the exterior orientation parameters of the two cameras (Table 4-1).

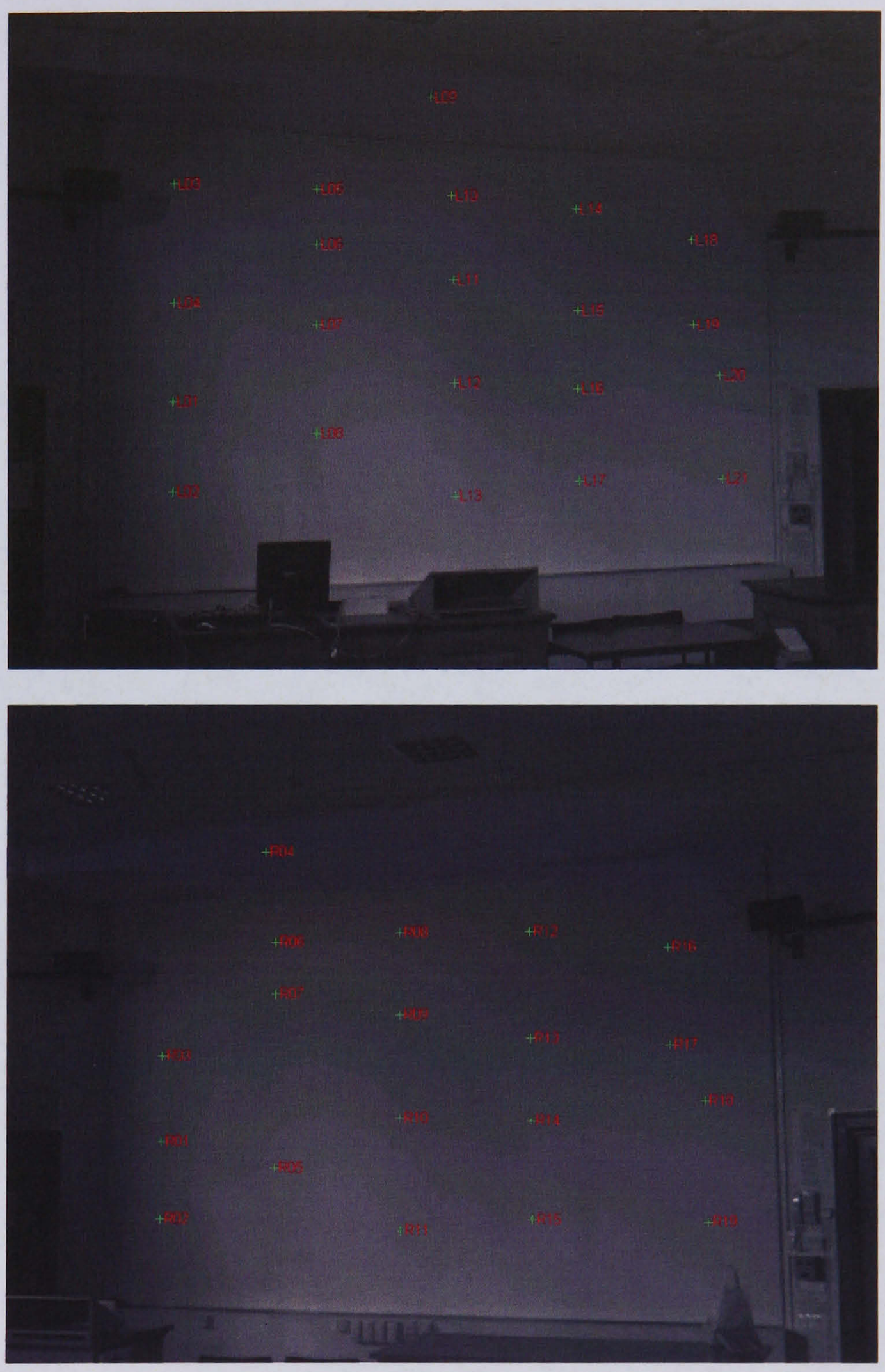


Figure 4-24: Image of extracted control footprints from left and right exposure stations.

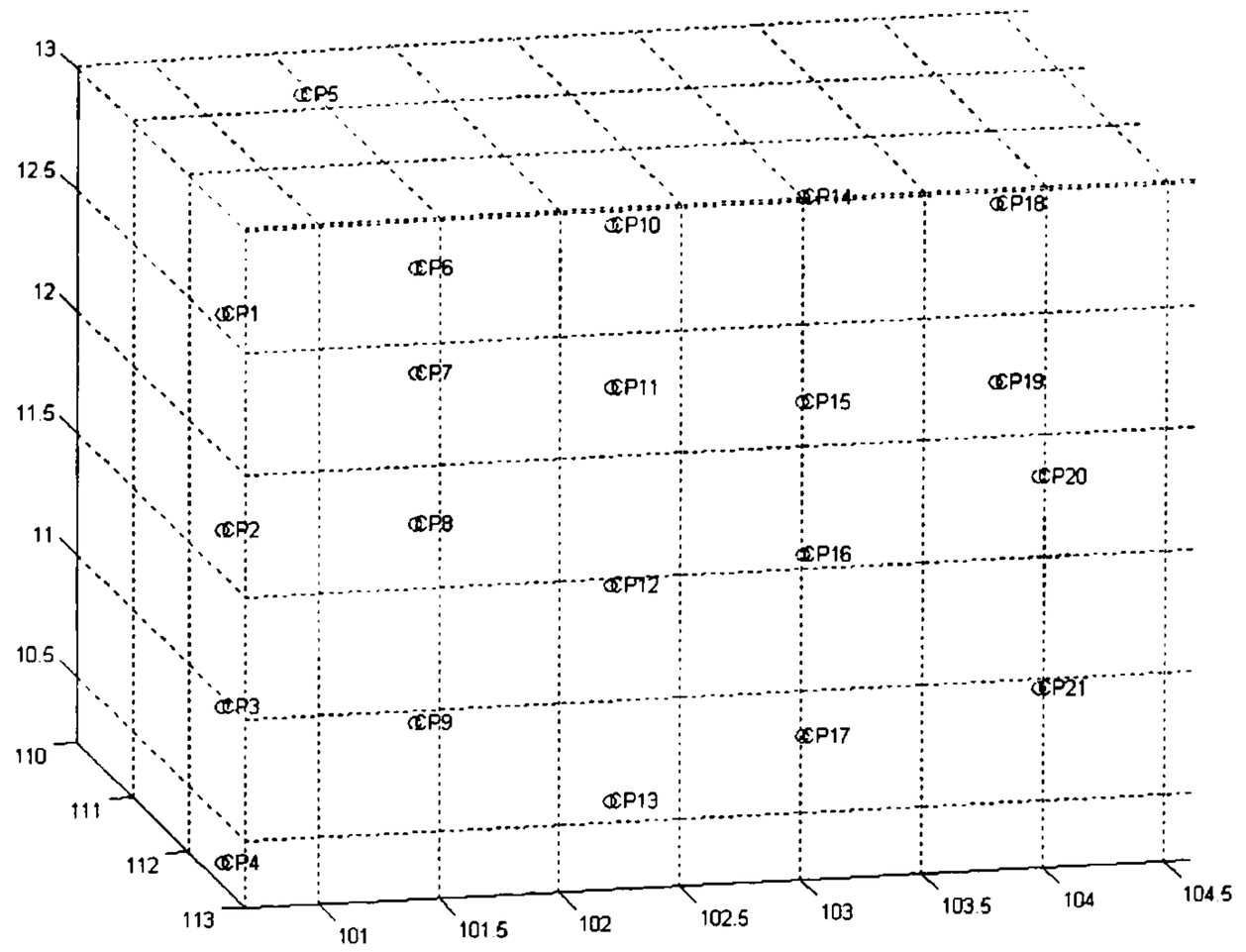


Figure 4-25: 3D map of the control footprints observed by the total station.

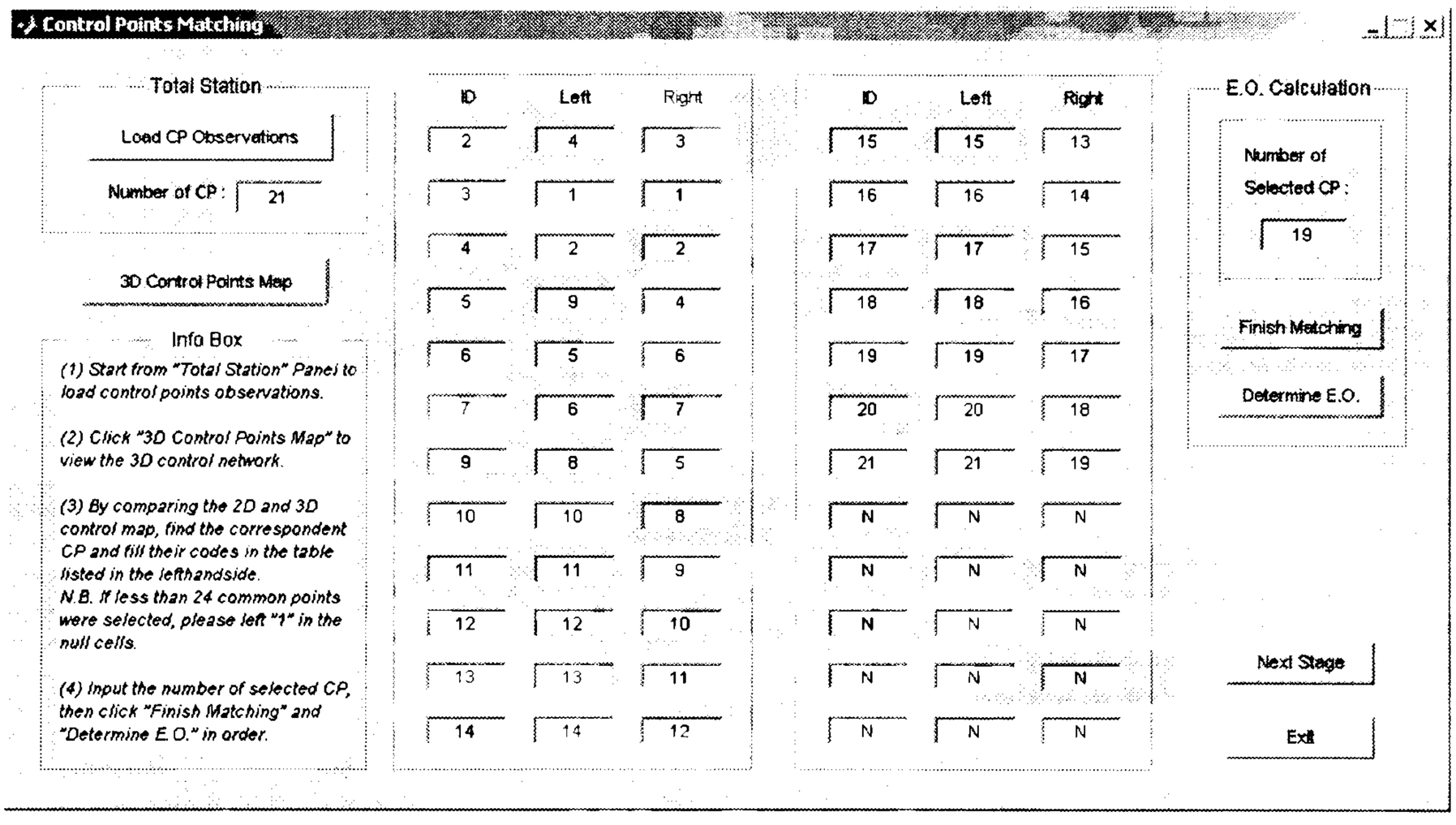


Figure 4-26: The resulting match of control footprints.

	Left Exposure Station	*Right Exposure Station*
X (m)	94.874	100.991
Y (m)	105.198	101.587
Z (m)	10.681	10.738
ω (degrees)	97.103	96.155
ϕ (degrees)	-49.918	-11.132
κ (degrees)	4.798	0.646

Table 4-1: Orientation results for the static surface monitoring test.

□ Target Extraction Module

A dot pattern of 450 points was adopted as the targets for constructing the surface model and imaging of the dot pattern lasted for 500 epochs. The first stereopair was processed in the Target Extraction Module in MS^2 and the centres of all 450 points were derived (Figure 4-27). The parameters applied were listed in Table 4-2 and they were consequently carried out in the remaining sequential stereopairs. The resultant coordinates of the points were saved for further implementation of Target Referencing, Tracking and Calculation. The parameters required in these modules are also listed in Table 4-2.

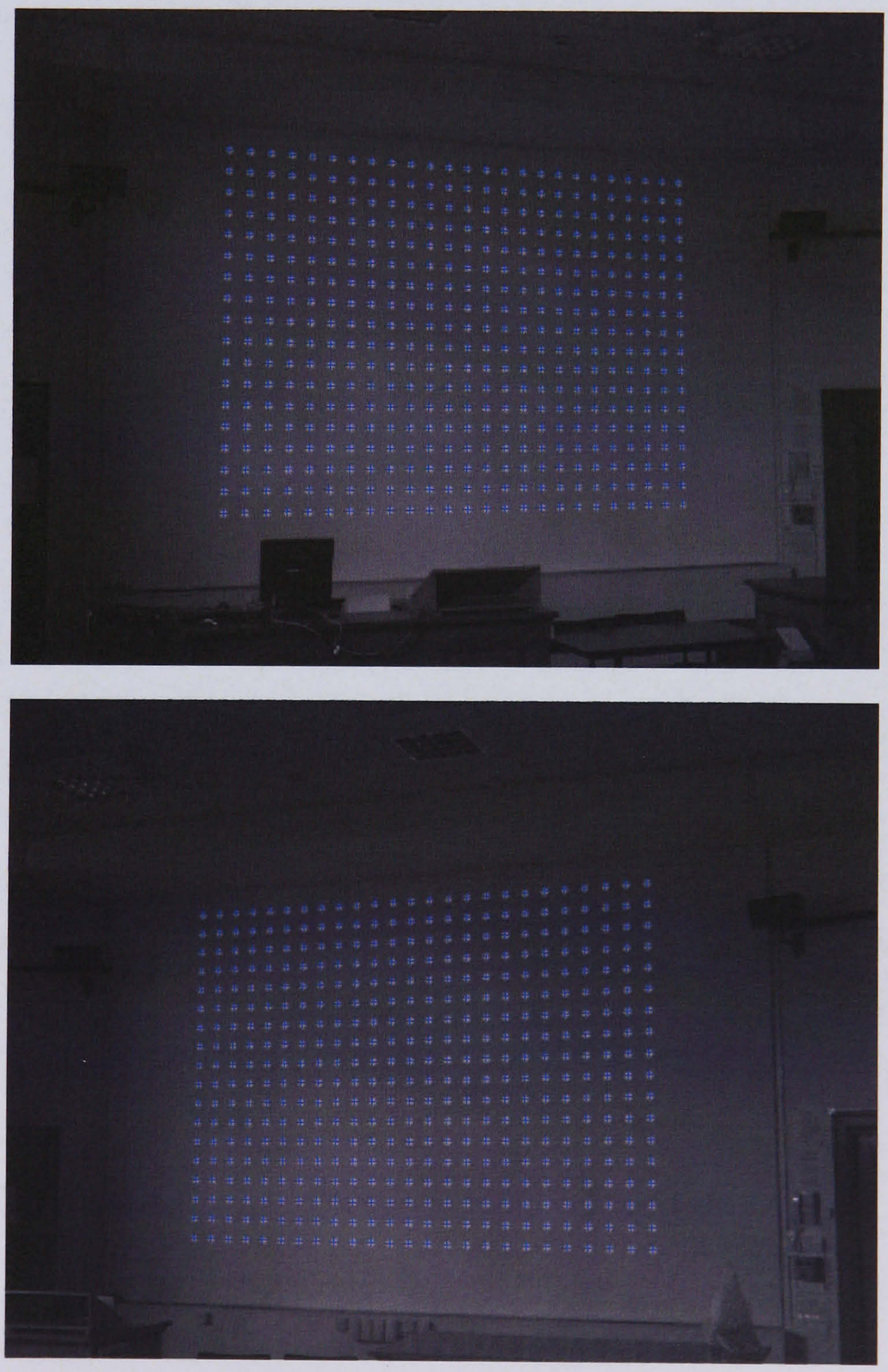


Figure 4-27: Image of extracted projected targets from left and right exposure stations.

Target Extraction	*Left*	*Number of epochs*	500
		Normalised threshold value	0.18
		Noise size (pixels)	<13 and >200
	Right	*Number of epochs*	500
		Normalised threshold value	0.17
		Noise size (pixels)	<4 and >400
Target Referencing	*Left*	*Max X interval (pixels)*	5
		Max Y interval (pixels)	30
	Right	*Max X interval (pixels)*	5
		Max Y interval (pixels)	30
Target Tracking	*Left*	*Max X tolerance (pixels)*	3
		Max Y tolerance (pixels)	3
	Right	*Max X tolerance (pixels)*	3
		Max Y tolerance (pixels)	3
Target Calculation	*Number of epochs*		500

Table 4-2: Input parameters for MS^2 implementation.

4.4.2.3 Results

When the calculation in MS^2 was complete, the 3D position of each projected-dot at each epoch was solved with a resultant standard deviation of +/- 1.0 mm. The measurement precision was therefore shown to be of the same order as the value predicted in network pre-planning. In order to determine the displacement that occurred through the whole sequence, the surface model from the first epoch was selected as the reference surface. The positive (points where forwards movement occurred) and negative (backwards movement) movements that occurred during the monitoring were computed separately. The resulting maximum and average displacements of each epoch that occurred over the 500 epochs are shown in Figure 4-28.

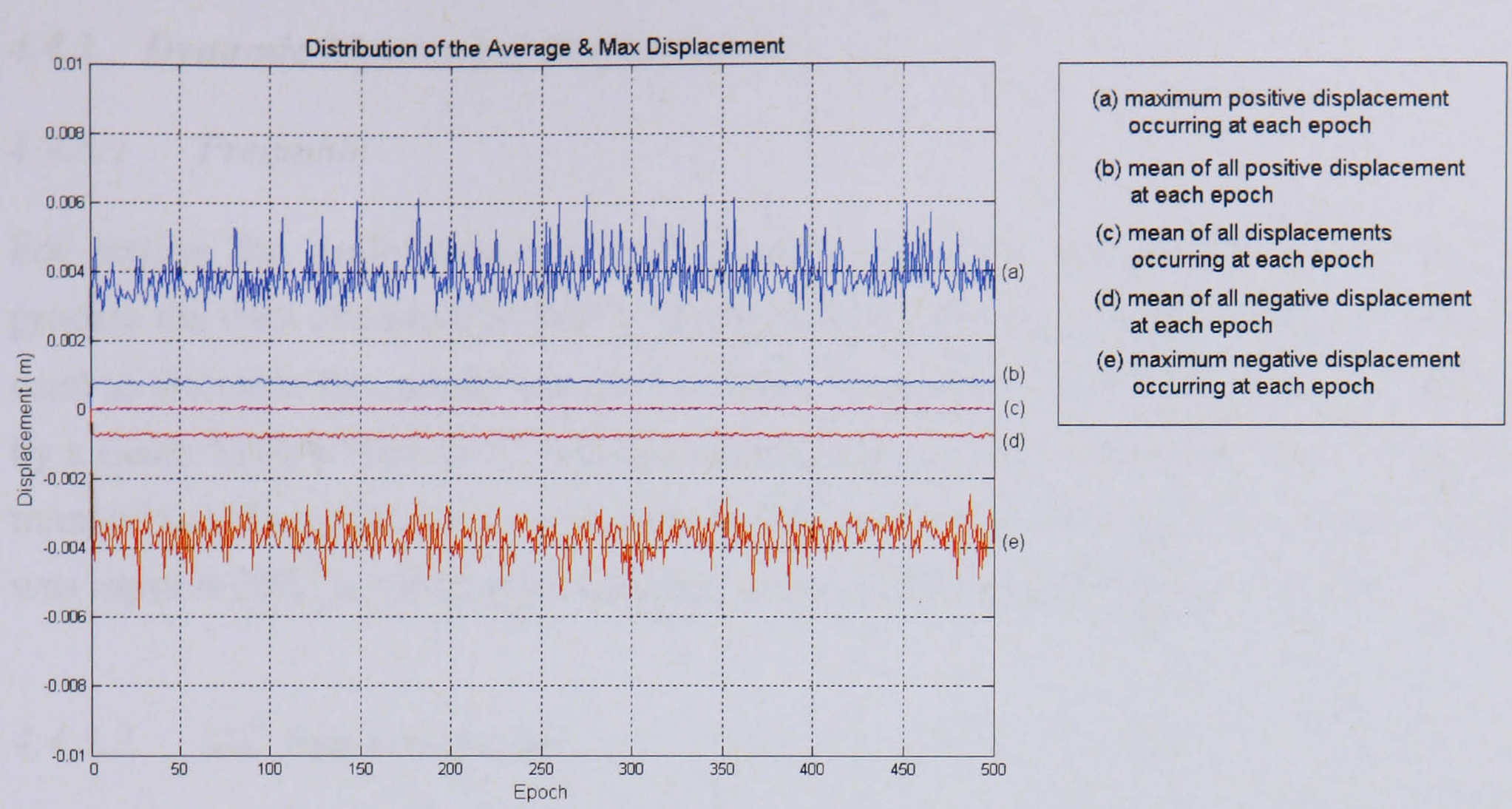


Figure 4-28: Resulting displacement for the static surface monitoring test.

Since the observed wall surface was static there should obviously be no movement determined by the measurement system. The resulting plots of mean and maximum displacements (Figure 4-28), however, revealed that non-zero differences were observed throughout the test. In Figure 4-28 the mean of curves (b) and (d) are 0.8 mm and -0.8 mm respectively. Comparison of these values against the measurement precision (+/- 1.0 mm), suggests the resolved displacements are measurement noise rather than real movement of the wall.

In addition to the non-zero mean movement, the resolved maximum displacements that occurred over 500 epochs varied from 6.2 mm to -5.8 mm (curve (a) and (e) in Figure 4-28). As the static surface modelling experiment was conducted in a well-controlled laboratory environment, the results were considered as the best performance the videogrammetric monitoring system could be expected to achieve. That is, when the system was subsequently applied in real-world dynamic monitoring tasks, the videogrammetric system was only able to detect displacements occurring above these threshold values. According to the design specification (Section 1.2.6), the "safe" acceptable movement tolerance of the membrane structures to be tested was +/- 250 mm, with any movement outside of this value expected to subsequently cause damage to the structure. The monitoring system was therefore deemed very capable of inspecting displacements within the tolerance value.

4.4.3 Dynamic Monitoring Performance

4.4.3.1 Preamble

For testing the performance of monitoring a dynamic surface, MS^2 was applied to process the data acquired in Test 5 (Section 3.4.6), during which a projector screen was used to simulate the membrane roof surface; the control laser footprints were generated by a Leica TCRA 1103 total station; and the surface movement, which was generated by manually shaking the screen, was shot by the two Oscar cameras. The acquired imagery was input to MS^2 for further processing, with a potential precision of 1.5 mm.

4.4.3.2 MS^2 Implementation

The parameters required during the implementation of MS^2 are listed in Table 4-3. Once the processing was finished, the camera orientation (Table 4-4) was determined using eight common control points (Figure 4-29) and the 3D coordinates of 120 projected-dots at each epoch were solved with a final precision of 1.3 mm. The value was again of the same magnitude as the predicted measurement precision in network design stage. Figure 4-30 and Figure 4-31 illustrate an example session of the stereo image sequence and the determined meshed model, showing the movement of the observed surface.

Camera Orientation	*Left/Right*	*Number of frames*	119
		Normalised threshold value	0.1
Target Extraction	*Left/Right*	*Number of epochs*	180
		Normalised threshold value	0.12
		Noise size (pixels)	<4 and >400
Target Referencing	*Left*	*Max X interval (pixels)*	10
		Max Y interval (pixels)	30
	Right	*Max X interval (pixels)*	8
		Max Y interval (pixels)	30
Target Tracking	*Left/Right*	*Max X tolerance (pixels)*	10
		Max Y tolerance (pixels)	10
Target Calculation	*Number of epochs*		180

Table 4-3: Input parameters for MS^2 implementation.

	Left Exposure Station	*Right Exposure Station*
X (m)	96.648	105.562
Y (m)	104.294	101.453
Z (m)	10.515	10.545
ω (degrees)	99.610	96.962
ϕ (degrees)	-41.105	5.624
κ (degrees)	2.970	0.125

Table 4-4: Orientation results for the dynamic surface monitoring test.

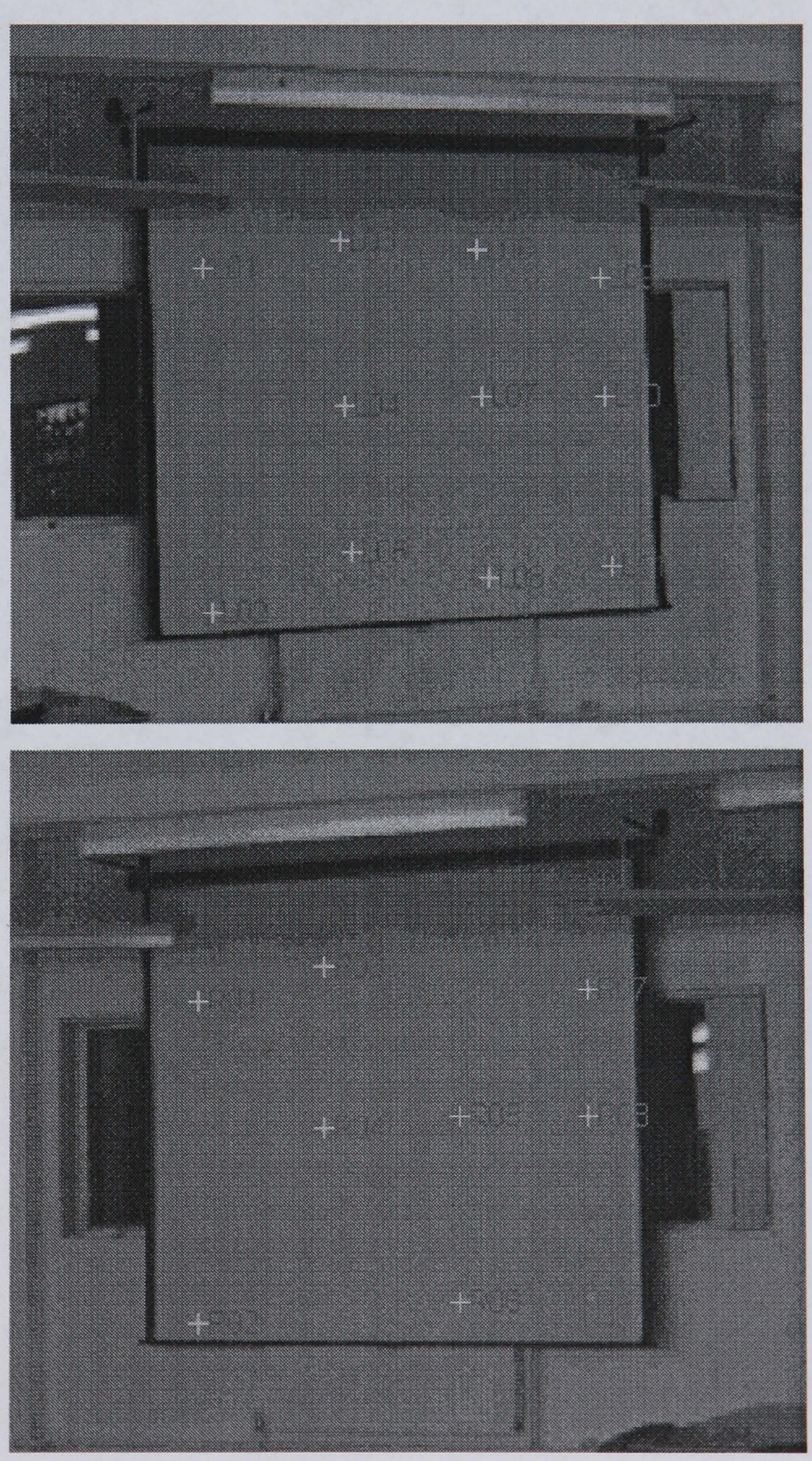
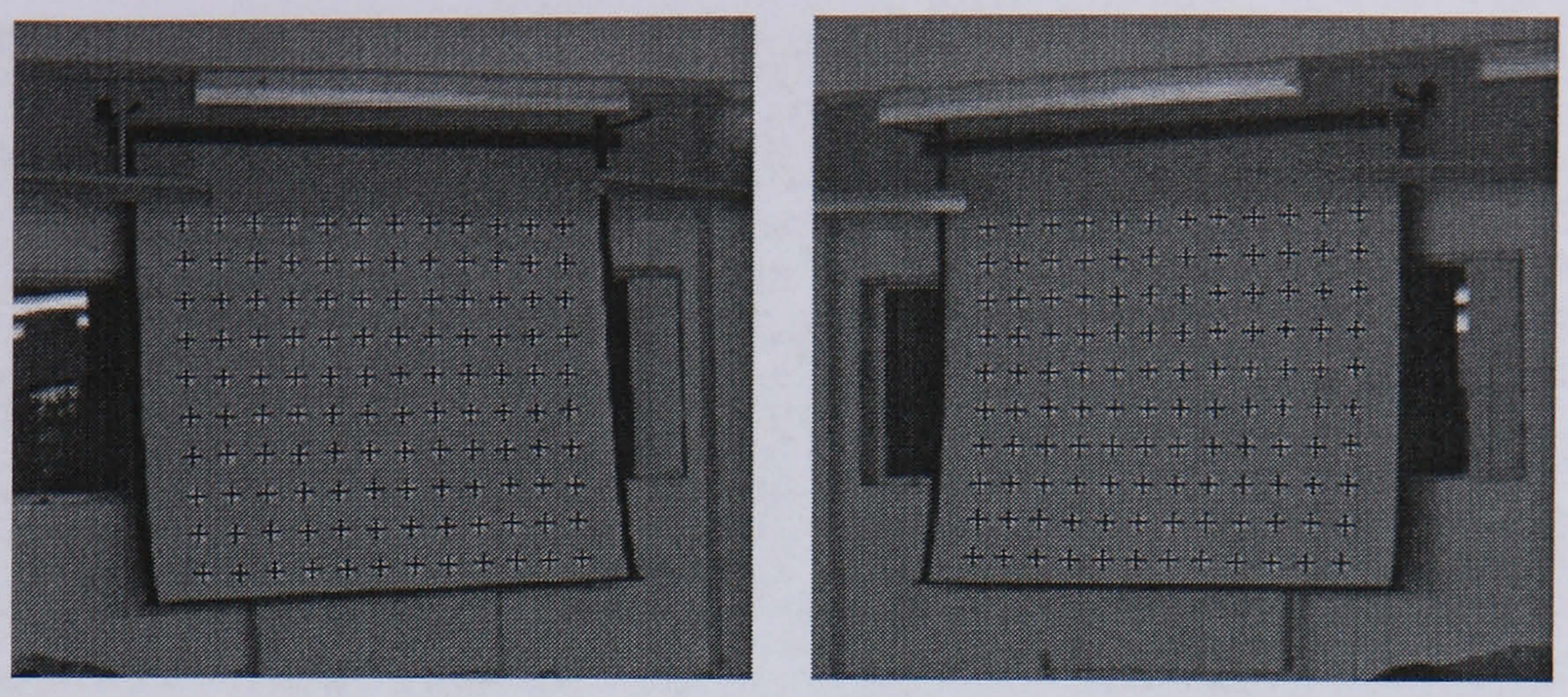
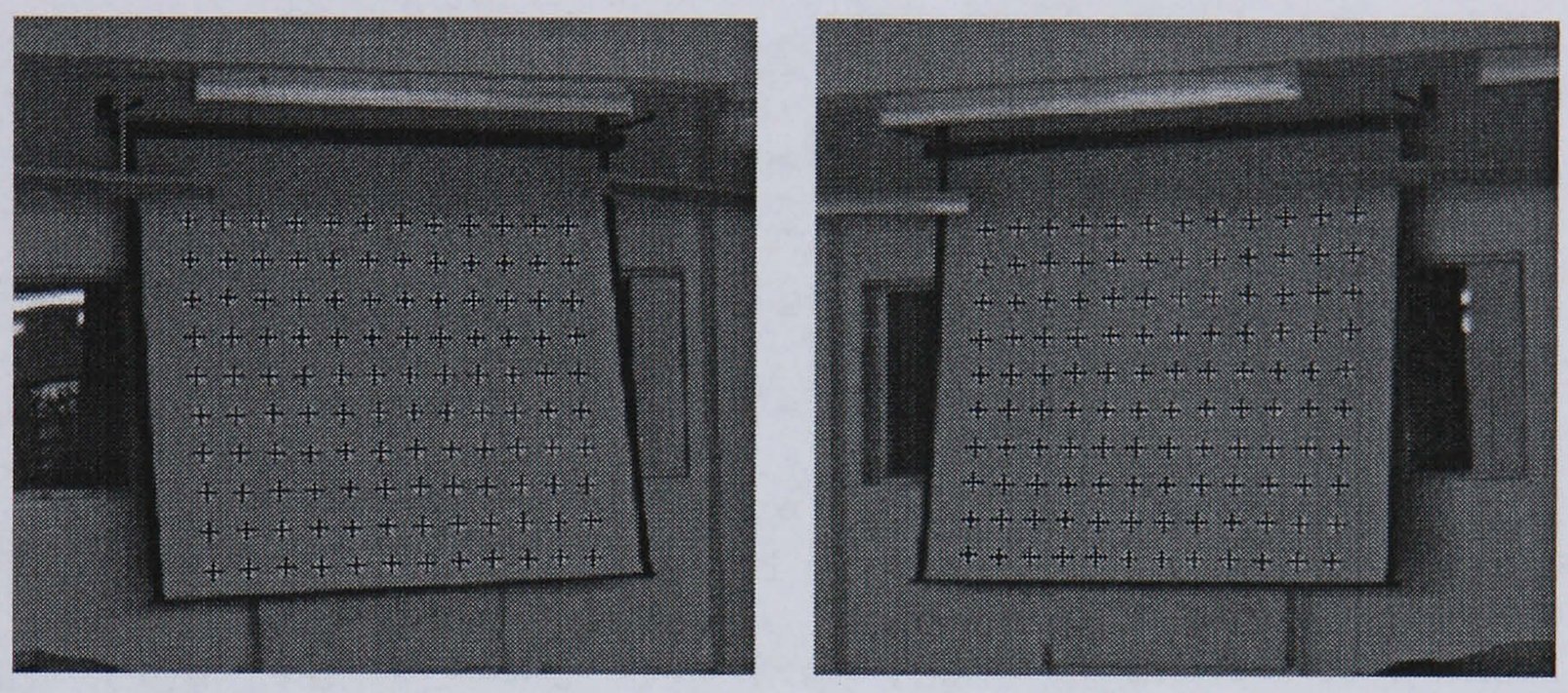


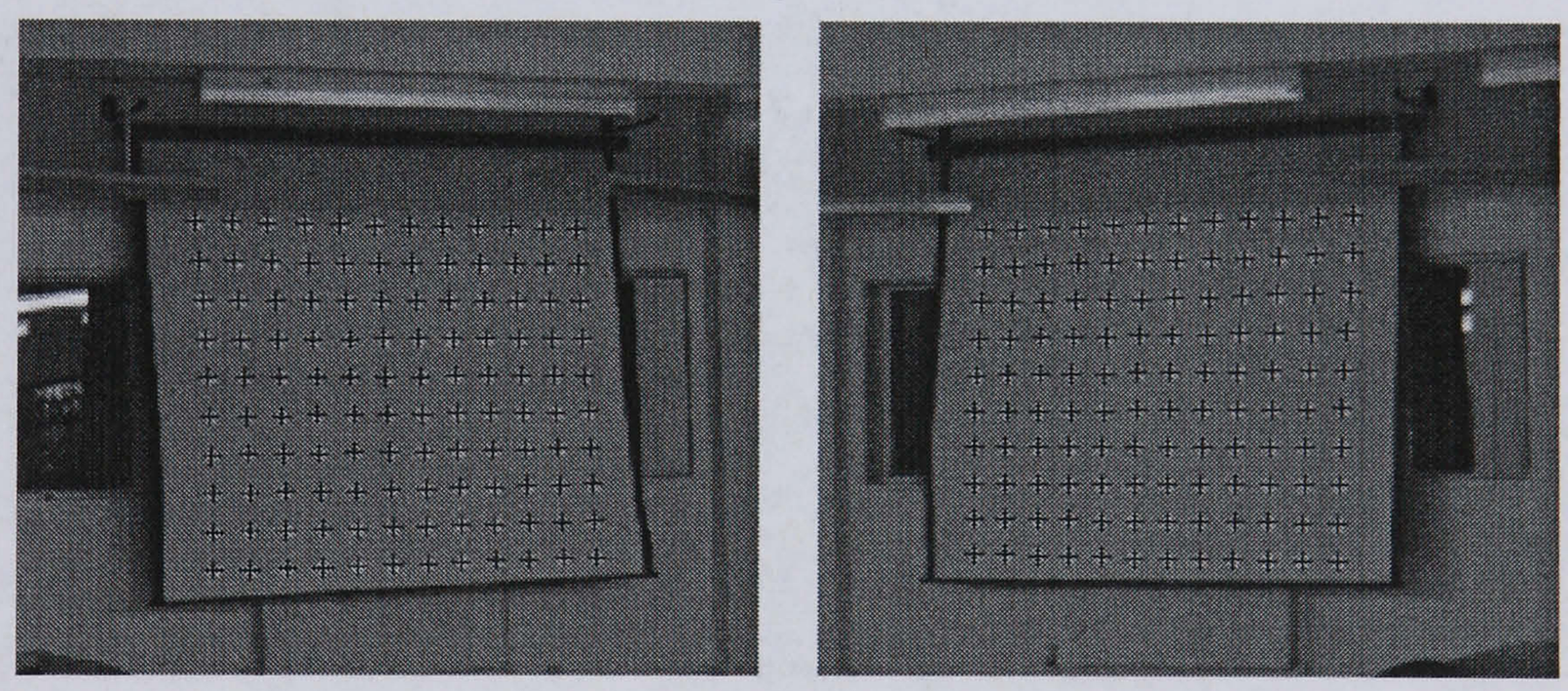
Figure 4-29: Images of extracted control footprints from left and right exposure stations, produced by MS^2.



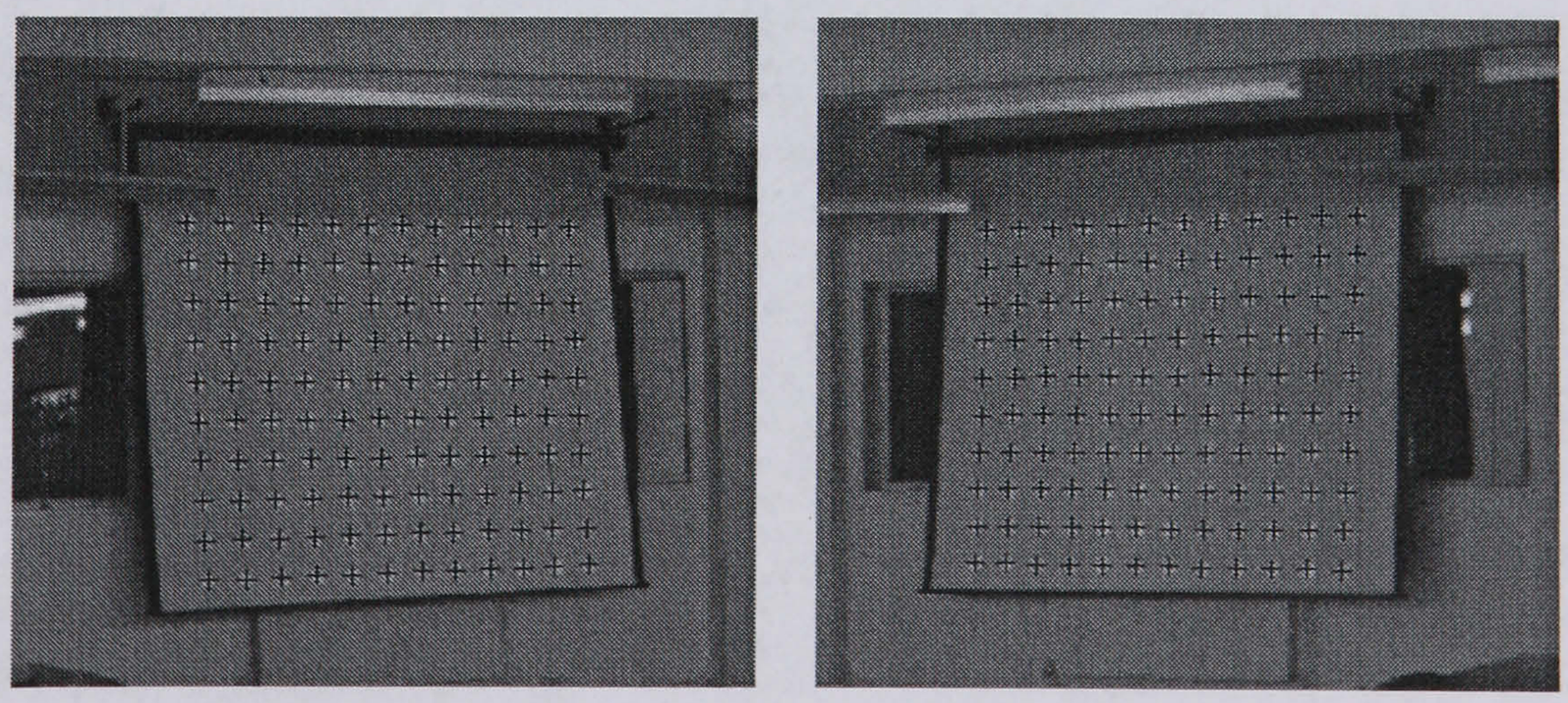
Epoch 44



Epoch 45

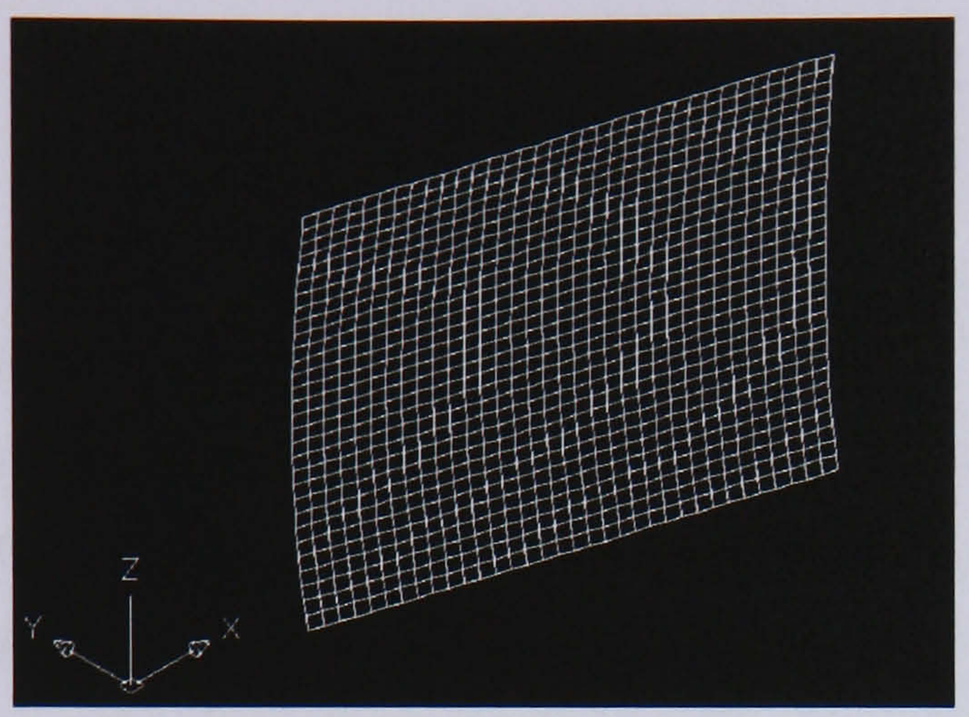


Epoch 46

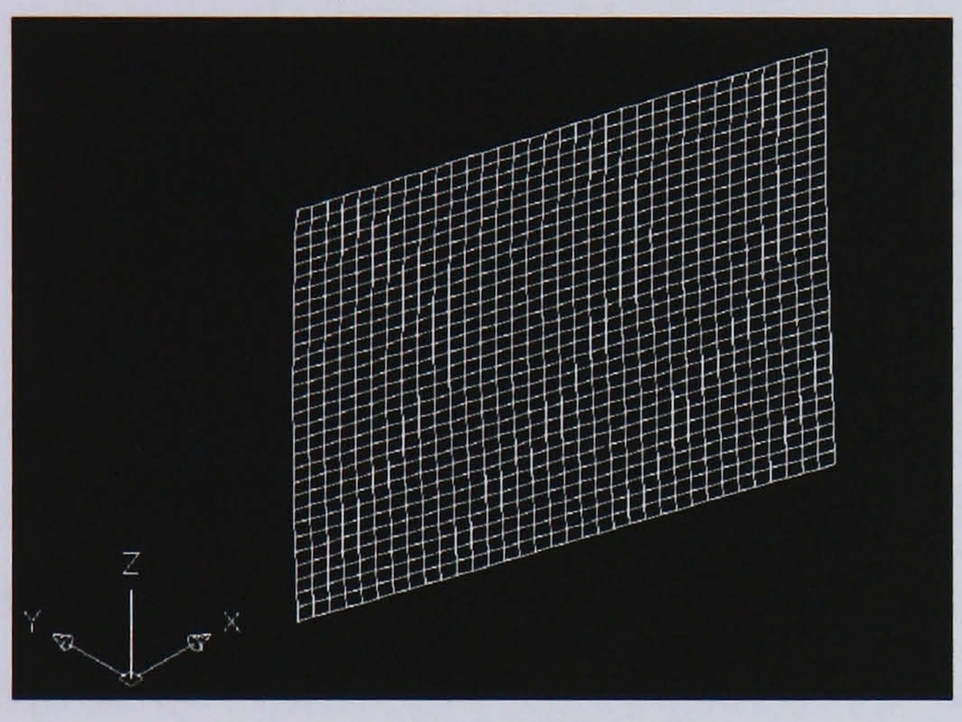


Epoch 47

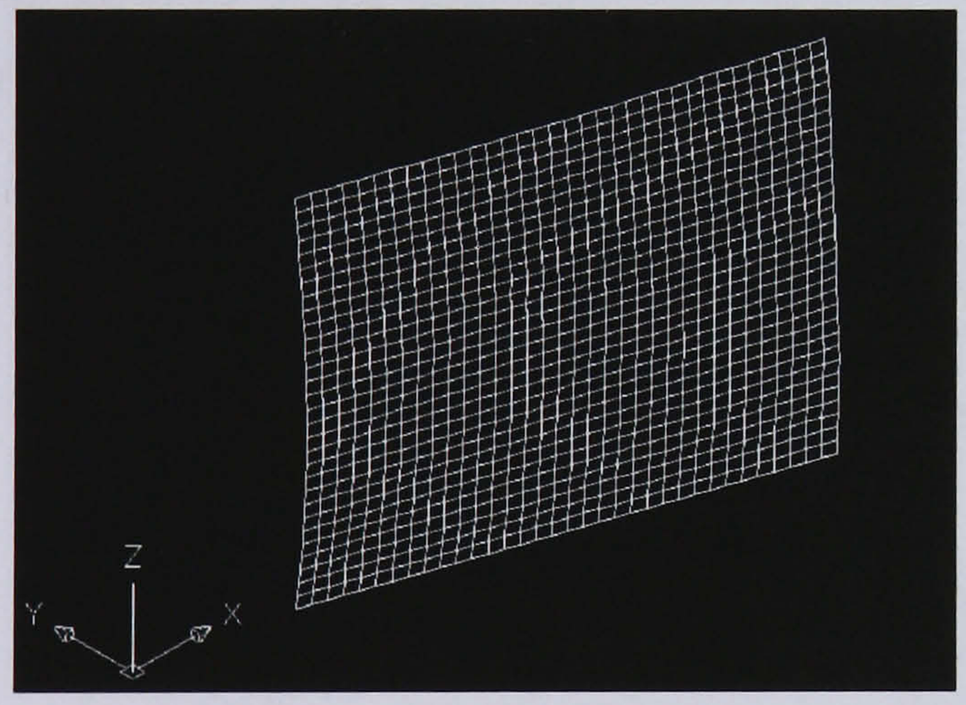
Figure 4-30: Example sequential stereopairs of extracted projected targets.



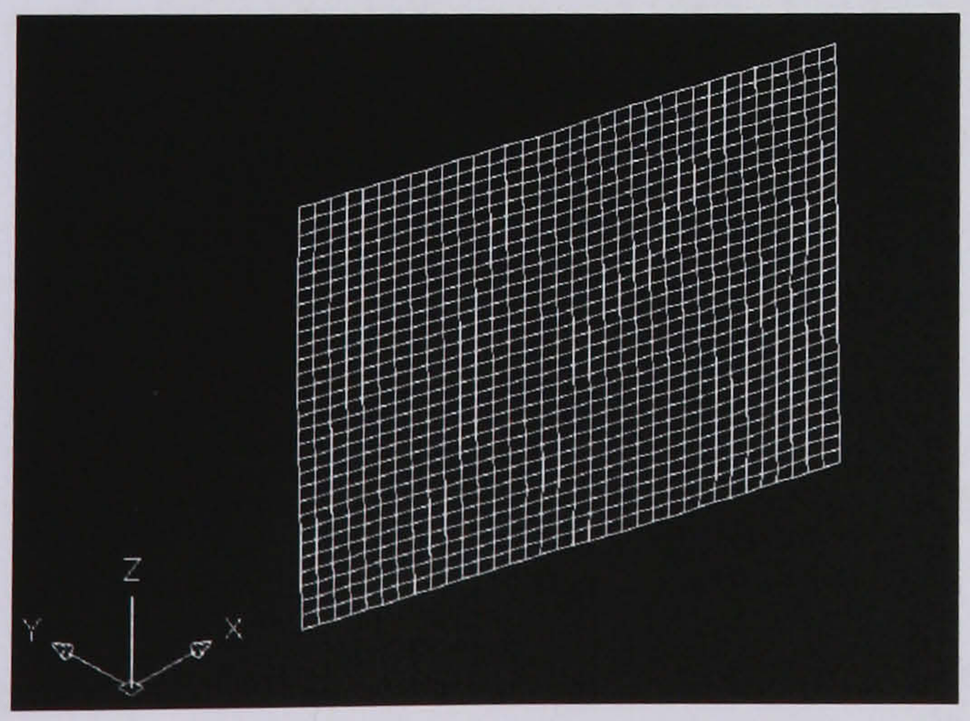
Epoch 43



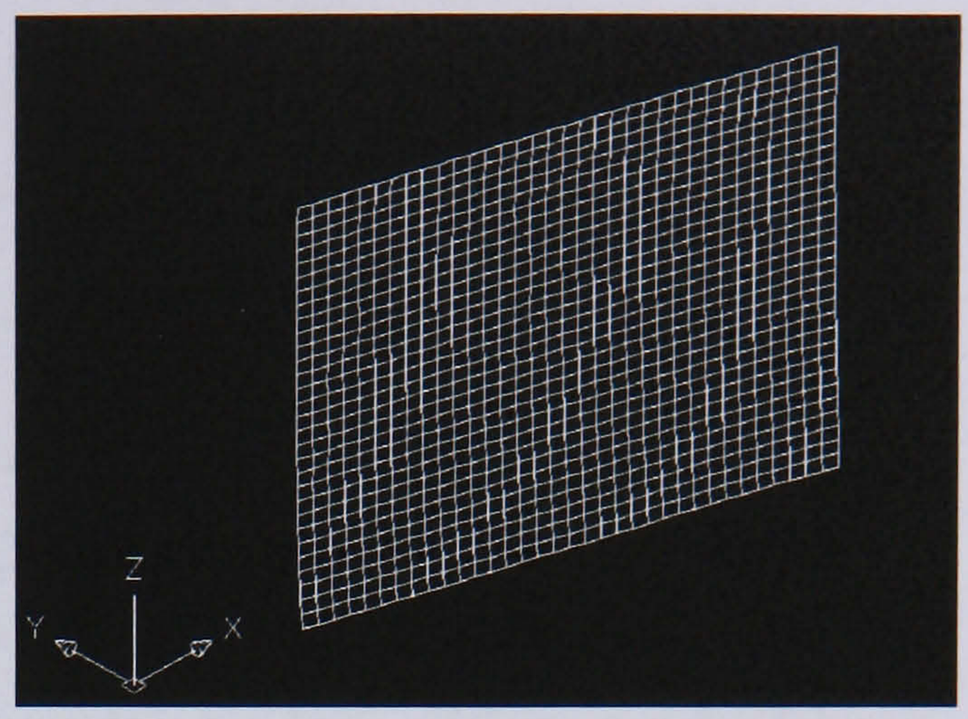
Epoch 44



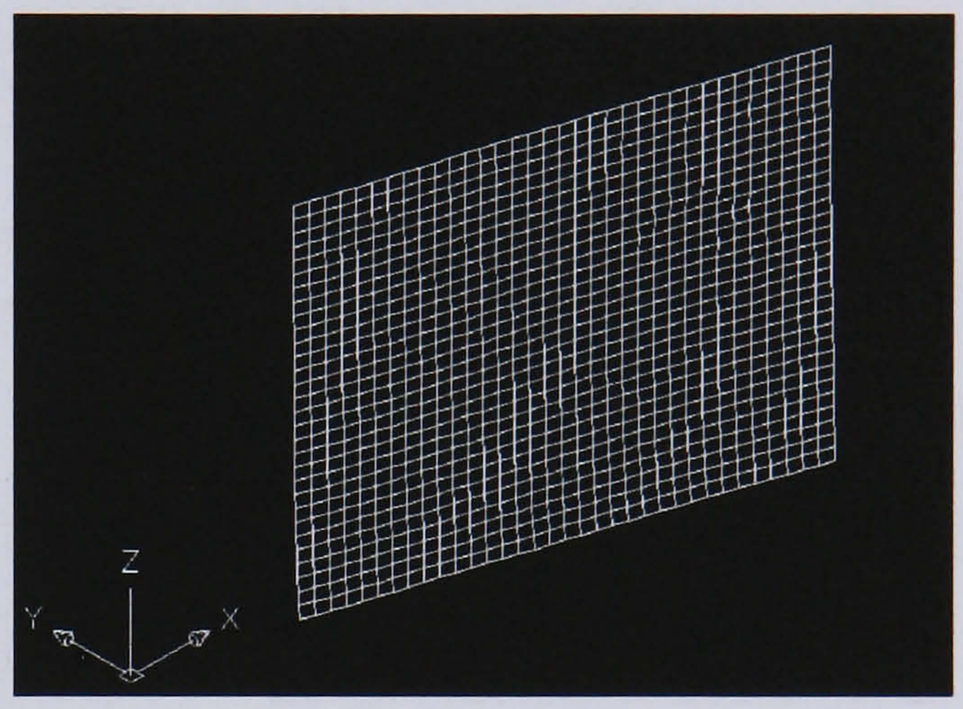
Epoch 45



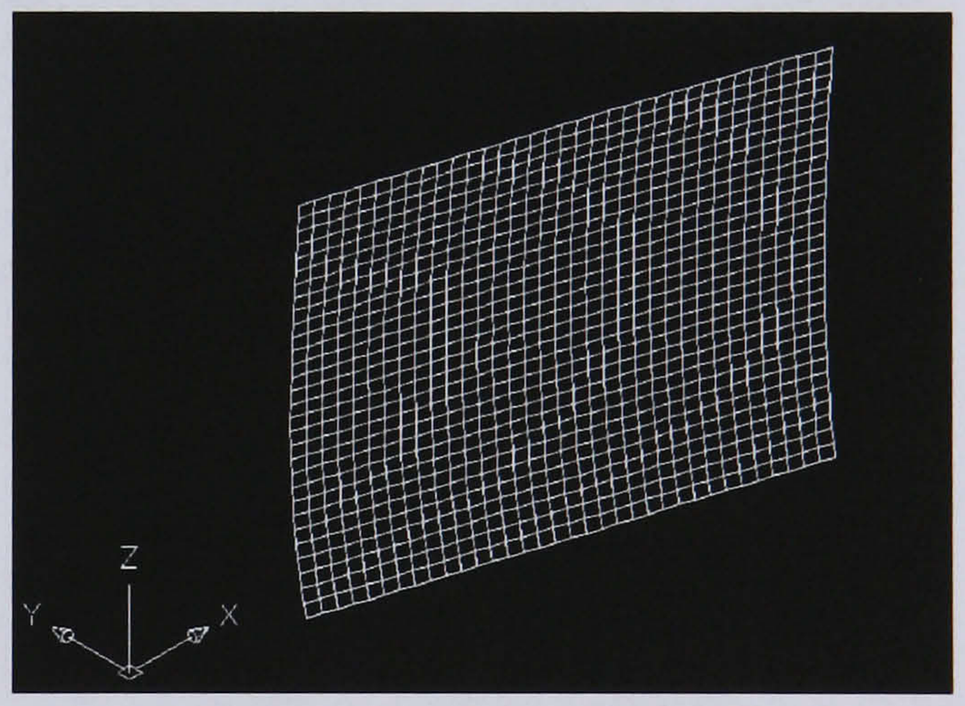
Epoch 46



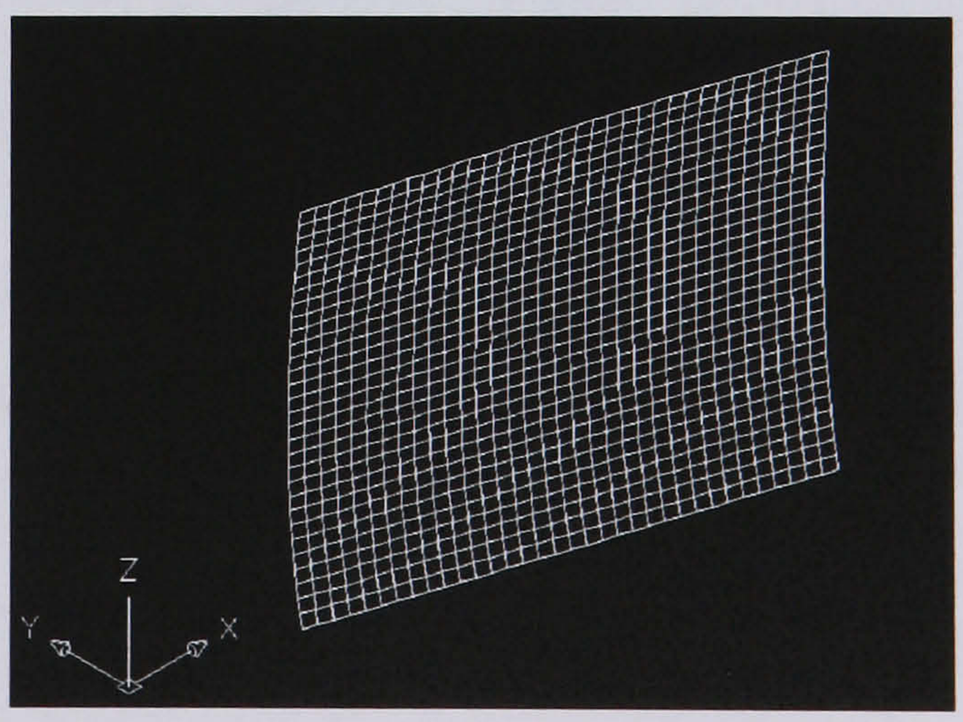
Epoch 47



Epoch 48



Epoch 49



Epoch 50

Figure 4-31: The example sequential meshed model of the dynamic surface (from epoch 43 to epoch 50).

4.4.3.3 Displacement Analysis

In order to determine displacement, the surface model at the first epoch was selected as the base surface, and the positive and negative movements that occurred during the monitoring period were computed relative to this. The average and maximum displacements at each of the 180 epochs is illustrated in Figure 4-32. In the initial period of monitoring the average positive and negative displacements varied from 0.9 to 1.1 mm (curve (b) and (d)), and the maximum movements were 5.6 mm and -6.3 mm (curve (a) and (e)) in positive and negative directions respectively. This period related to the time where no movement was applied to the screen and can be seen to be generally commensurate with the findings derived from the static surface modelling test (Section 4.4.2).

In comparison with the motionless period, it is clear from Figure 4-32 that the movement started from around the 40th epoch and continued to the 150th epoch. Figure 4-32 shows that the maximum positive movement of 40.4 mm, occurring at the 44th epoch, whilst the maximum negative displacement of -38.6 mm occurred at the 46th epoch. According to the curve of displacement, it is shown that the surface remained stationary again after the 160th epoch until the end of monitoring.

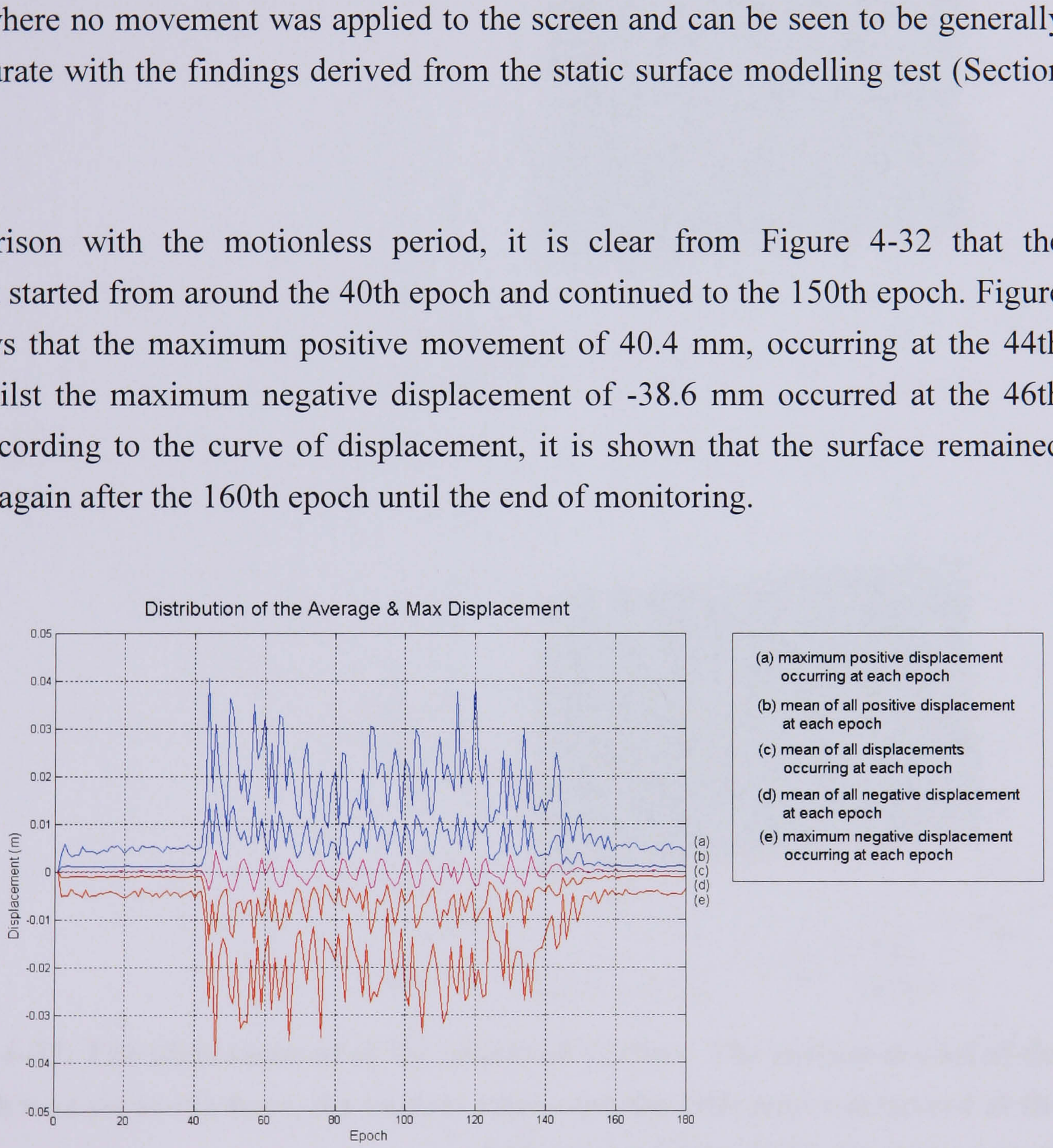


Figure 4-32: Average and maximum movement occurred at each epoch.

From the statistics shown in the Overall Query Module and the diagrams produced, some surfaces of interest were selected and input to the Advanced Query interface for further inspection. In this experiment the surfaces at the 20th, 44th, 46th, 70th, 120th and 160th epochs were selected. Once the computation was finished, the statistics such

as the maximum values of positive and negative displacements, and the positions they occurred, were derived. The movements are plotted as 3D vectors at the base surface points (Figure 4-33). The magnitude and direction of the movement across the surface is realised by inspecting the displacement maps.

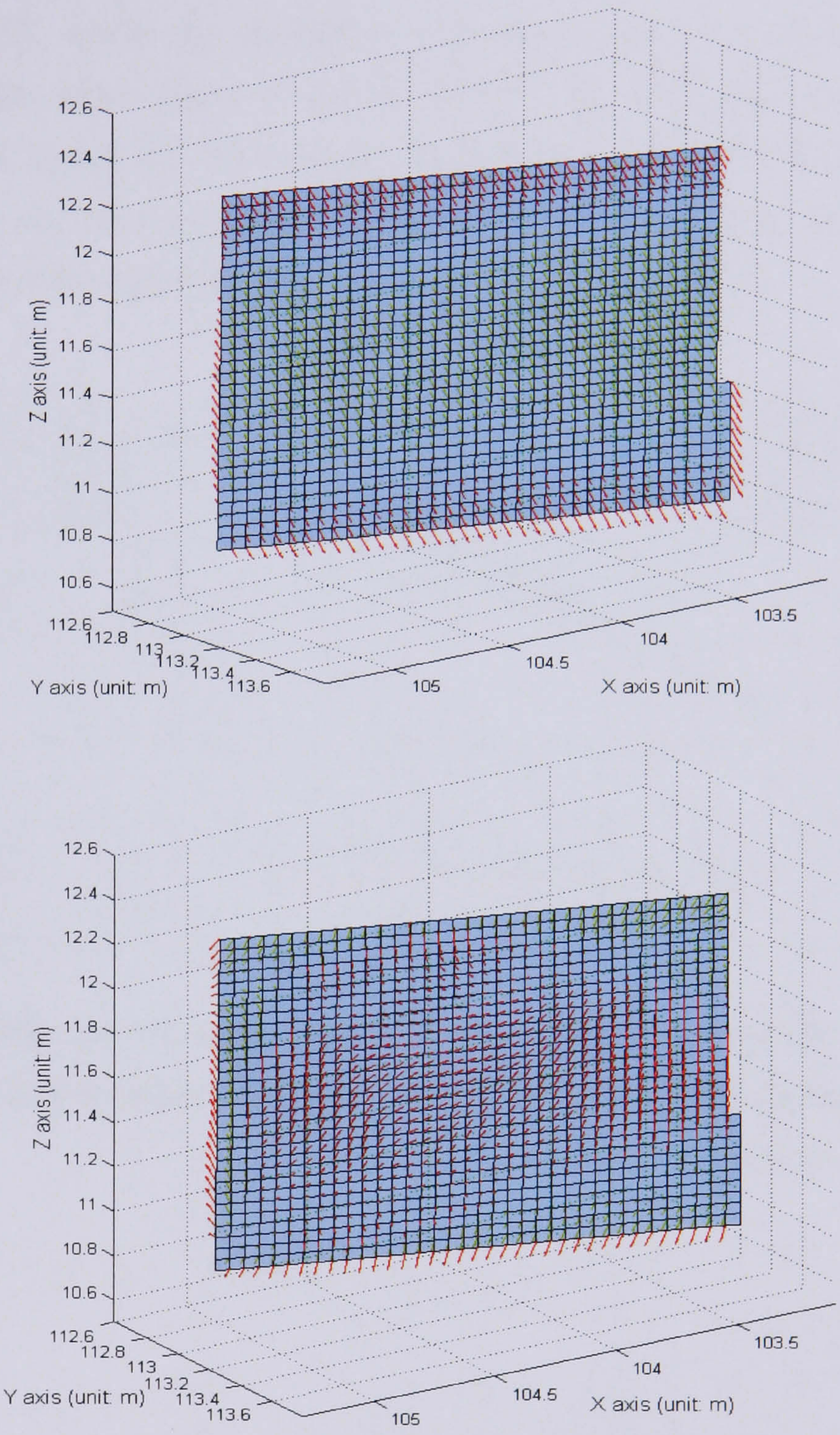


Figure 4-33: The displacement of the observed surface. The surface model of the 1st epoch was set as the base, the vectors represent the differences occurred at the 44th (top) and the 120th (bottom) epoch.

Another feature in the Advanced Query Module was the creation of the profiles across the screen surface. Two profiles passing through the point (105.1 m, 10.9 m) in the sequential meshed model are depicted in Figure 4-34, in which the differences between the base and six input surface models are presented. Along the profiles, the obvious discrepancies that occurred at particular areas in the specific epochs were discovered.

Moreover, the movement of any specific point on the observed surface could be tracked. Take two points located around the top right and bottom left corners of the surface as examples, their moving trajectories along range direction (Y-axis) are illustrated in Figure 4-35, in which the epochs that the projector screen reach the maximum and minimum Y–values are inspected. For point (105.1 m, 12.3 m), the maximum Y–value was 113.277 m, occurred at epoch 57, while the minimum one was 113.231 m which was happened at epoch 46. On the other hand in point (103.95 m, 10.8 m), the maximum Y–value was 113.469 m at epoch 46, whereas the minimum one was 113.423 m at epoch 120. The ranges of the movement at these two points were both 46 mm. All the queries and results were performed through the interfaces shown in Figure 4-36.

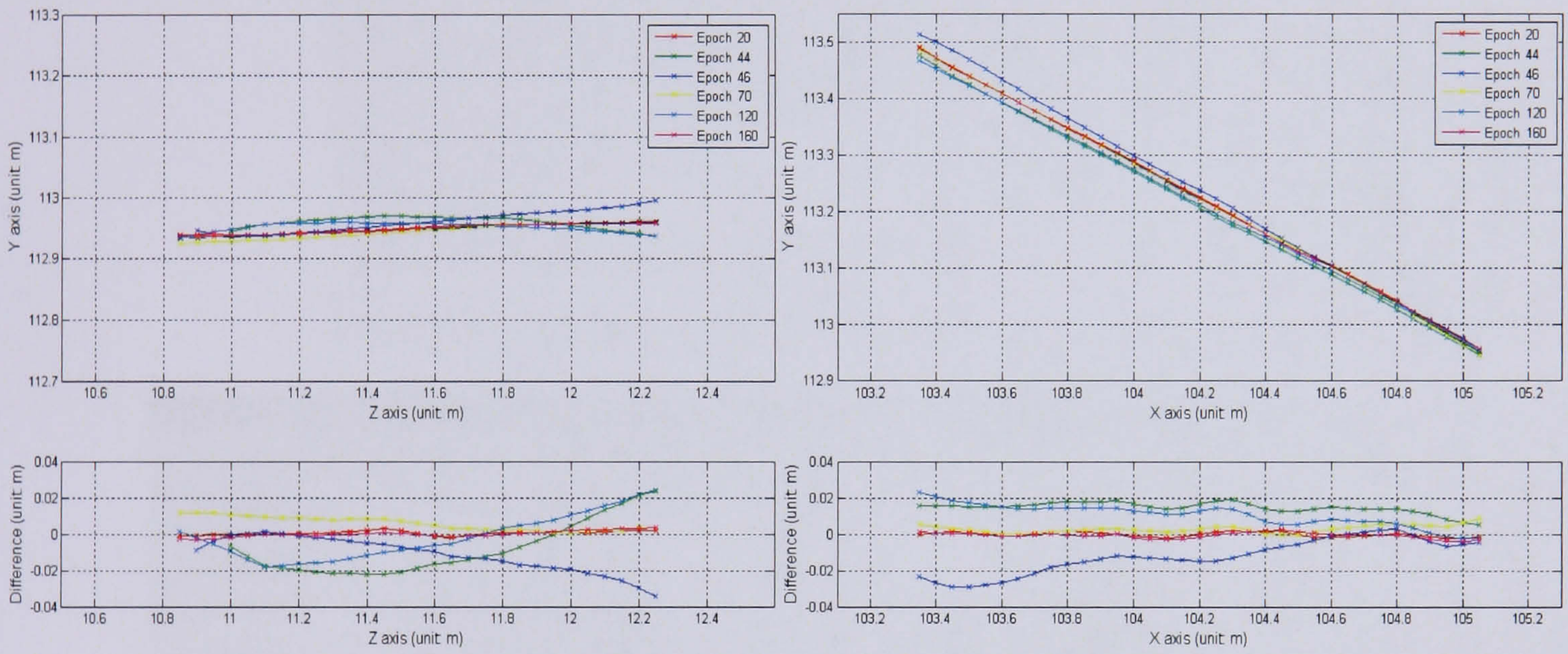


Figure 4-34: Differences in profiles between the base and the selected six surface models. Left: the profile along Z-axis where X=105.1 m; right: the profile along X-axis where Z=10.9 m.

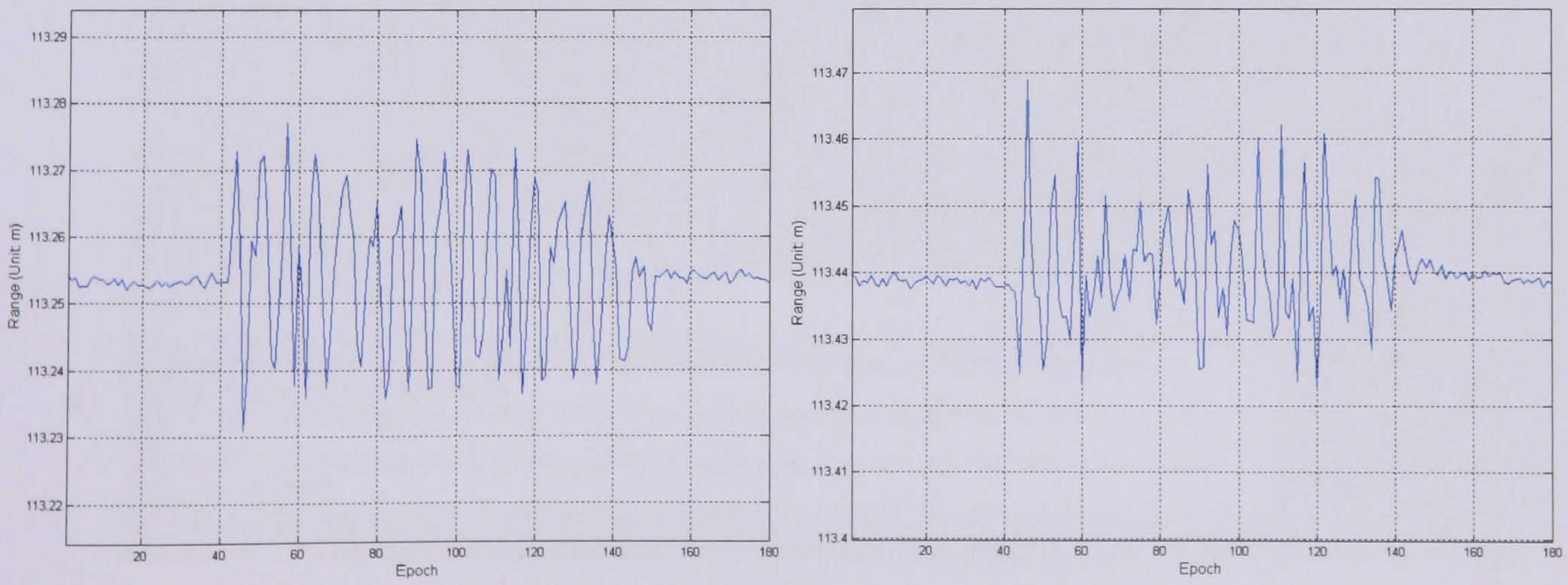


Figure 4-35: The moving trajectory along the range direction of the specific points (105.1 m, 12.3 m) (left) and (103.95 m, 10.8 m) (right) occurred during the monitoring.

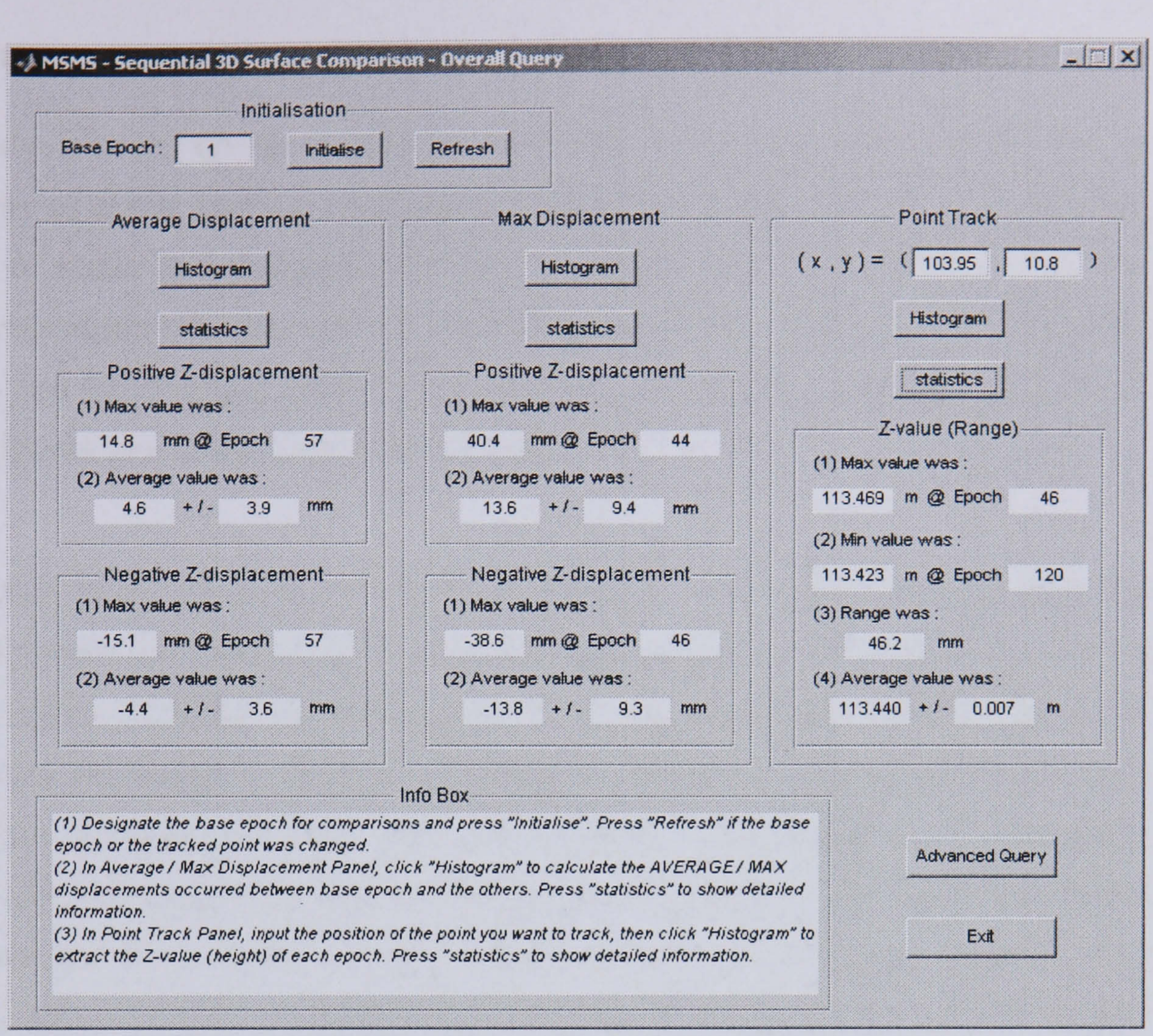


Figure 4-36: The resulting interfaces of the overall and advanced queries of the surface movement.

4.4.4 Discussion

This chapter mainly focuses on the performance of the dynamic surface modelling in MS^2, while the part of static surface comparison will be examined in the next chapter. Through the tests of static and dynamic surface modelling, MS^2 was proved a success for complete videogrammetric processing, including the video processing, sequential surface modelling and the displacement determinations. However, there were also some issues during the operations that are now discussed.

The first issue relates to the processing efficiency of MS^2. The frame rate is adjustable when the Oscar cameras are employed. For monitoring fast moving objects, the given high frame rate makes detailed movement investigation possible. Nevertheless, the increase of triggering frequency will result in a higher number of shot images, not only augmenting the data storage space but also extending the processing time, especially devoted to the modules of Target Extraction and Target Calculation. Therefore the frame rate has to be decided by making a compromise between monitoring requests and system processing efficiency. As a result the image sequence frame rate was set as one fps when shooting the projected-dots in this project.

Secondly, in some experiments it was noted that some control laser footprints were missed in the final control footprint imagery. This was affected by the threshold value used for image segmentation in the target extraction stage. This was primarily due to some laser footprints of low colour contrast being ignored after image segmentation. Additionally, as two different threshold values were applied on the images taken in left and right exposure stations, the missing footprints may be varied between the stereopairs. An increased image sequence frame rate may solve the problem, however the storage space for recorded imagery would need to be augmented. As the number of missing control footprints insufficiently affected the performance of camera orientation (as long as more than 10 laser footprints were available, as explained later in Chapter Six), a frame rate of three fps during capturing the laser control footprints produced acceptable results.

When performing target tracking in the off-the-shelf software PMV (refer to the experiment conducted in Section 3.4.6), the loss of targets between epochs is a problem, which is mainly caused by fast or unpredictable moving of the monitored surface. In order to test the system capability for target tracking, the simulated projector screen was moved rapidly and irregularly in the dynamic surface monitoring experiment (Section

4.4.3). Once the processing was complete no targets were missed over the tracking, furthermore, the results showed the system was capable of capturing an instantaneous movement of around 40 mm within a second, which is sufficient for determining the displacement of the real membrane roof structures. In some cases if some points were missed between epochs, as the entire projected-dots at each epoch are estimated at the target extraction stage, they can still be re-acquired in later epochs by using the last locations of the missed targets, solving the problem of lost targets that occurred in the PMV software.

The final discussion comes to the measurement accuracy itself. Both the experiments reported in Section 3.4.3 and 4.4.2 indicated that the system measurement is accurate to about 6 mm, which is satisfactory for investigating displacement that exceeds the design tolerance value on the membrane structure at the test site. For the request of advanced accuracy, increasing the number of cameras employed would be beneficial. However accompanying issues such as image storage space and processing efficiency, but primarily cost, would also need to be considered. The final solution would be a compromise between required accuracy, processing time and budget limitations.

4.5 Chapter Summary

The MS^2 software has been developed in order to inspect the surface geometry of membrane roof structures. The task of static surface comparison is firstly performed, in which the transformation parameters between the designed mathematical model and the physical laser scanned model are determined. Once the transformation is finished, the differences between the two models of the fabric membrane are statistically computed. Subsequently, for understanding the dynamic behaviour of membrane roof surfaces, the sequential surface model is derived by undertaking videogrammetric processing through MS^2. Some considerations mentioned in Chapter Three, such as the failure of target referencing, tracking and shortage of metric information about the displacement, are also addressed and resolved. Having proved to work well under laboratory conditions, the developed monitoring system and the proprietary software were subsequently deployed to a real-world site (Dalton Park, a retail outlet centre in the north east of England), to verify the feasibility. Details are provided in Chapter 5.

CHAPTER FIVE

DALTON PARK MONITORING SCHEME – SITE ASSESSMENT

5.1 Introduction

To prove the devised methodology as a standard practice, a process of testing, evaluation and application to real world problems was necessary. In the previous two chapters, the proposed methodology and the developed software were demonstrated feasible under laboratory conditions. This chapter presents the results from the application of the developed methodology to a real world test site. Workflows of static surface comparison and dynamic surface modelling are proposed. The differences between the designed model and the as-built structure, and the displacements of the fabric membrane are addressed in the two schemes. The issues involved in the process are discussed and the overall performance is evaluated.

5.2 The Observed Membrane Structure

Dalton Park is a retail outlet centre in the north east of England. It features a variety of fabric membrane canopies. At the outlet centre, two lines of single shop units are arranged on either side of a central street. The street is partially covered by various fabric canopies based on single and multiple conic forms (Figure 5-1).

The canopies of Tent Type 1 are 60 m long by 14 m wide and consist of four linked conics supported by four straight flying masts, which are supported in turn by cables

back to the main high-level steelwork (Figure 5-2). The edges of the fabric membranes are supported by boundary cables along the long side, with the short sides being clamped directly to inclined steel arches (Bridgens et al., 2004). In this chapter, a membrane structure of Tent Type 1 (outlined in Figure 5-1) was selected to evaluate the developed methodology.

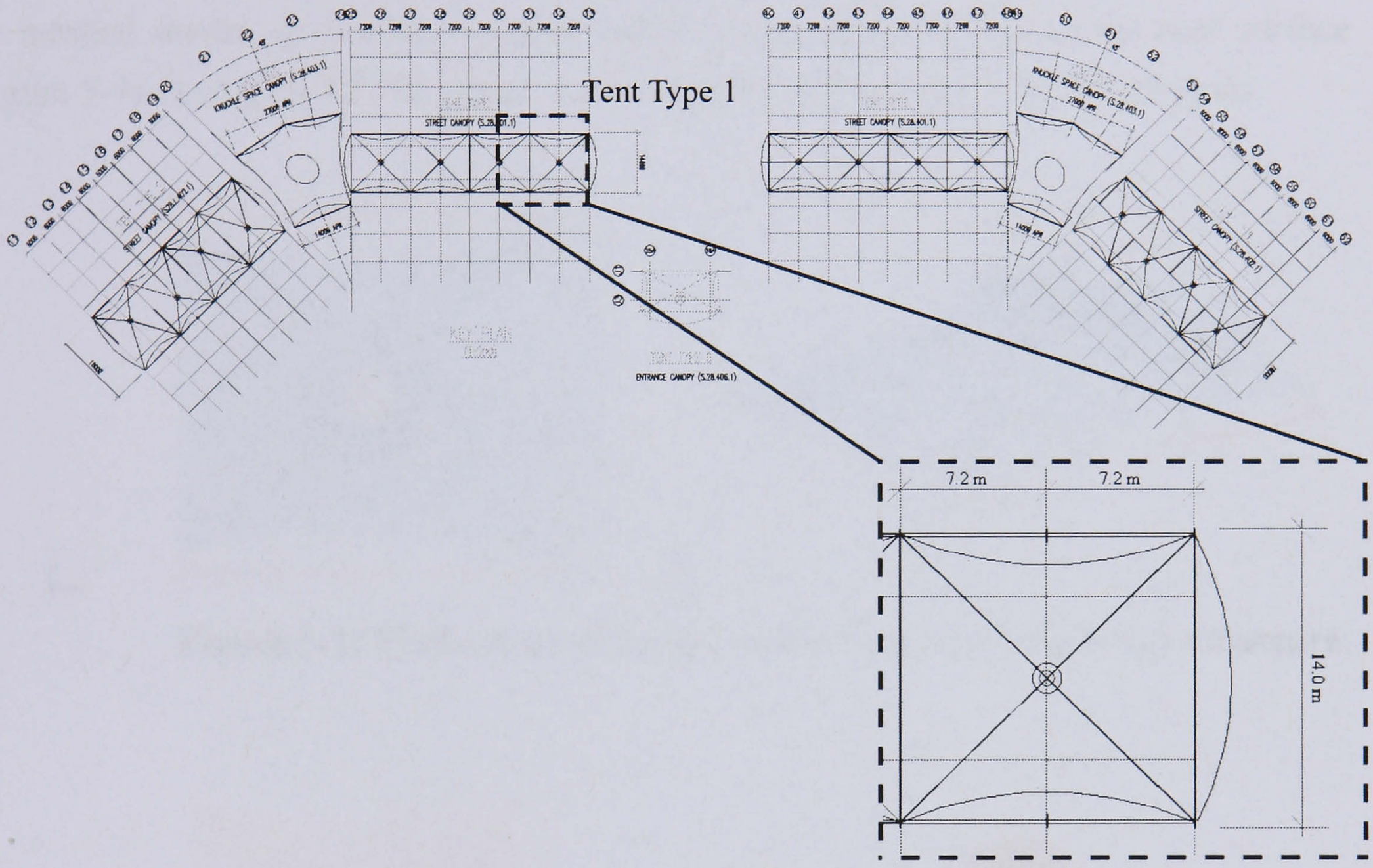


Figure 5-1: Design plan of Dalton Park, the observed membrane structure of Tent Type 1 is outlined by dashed line.

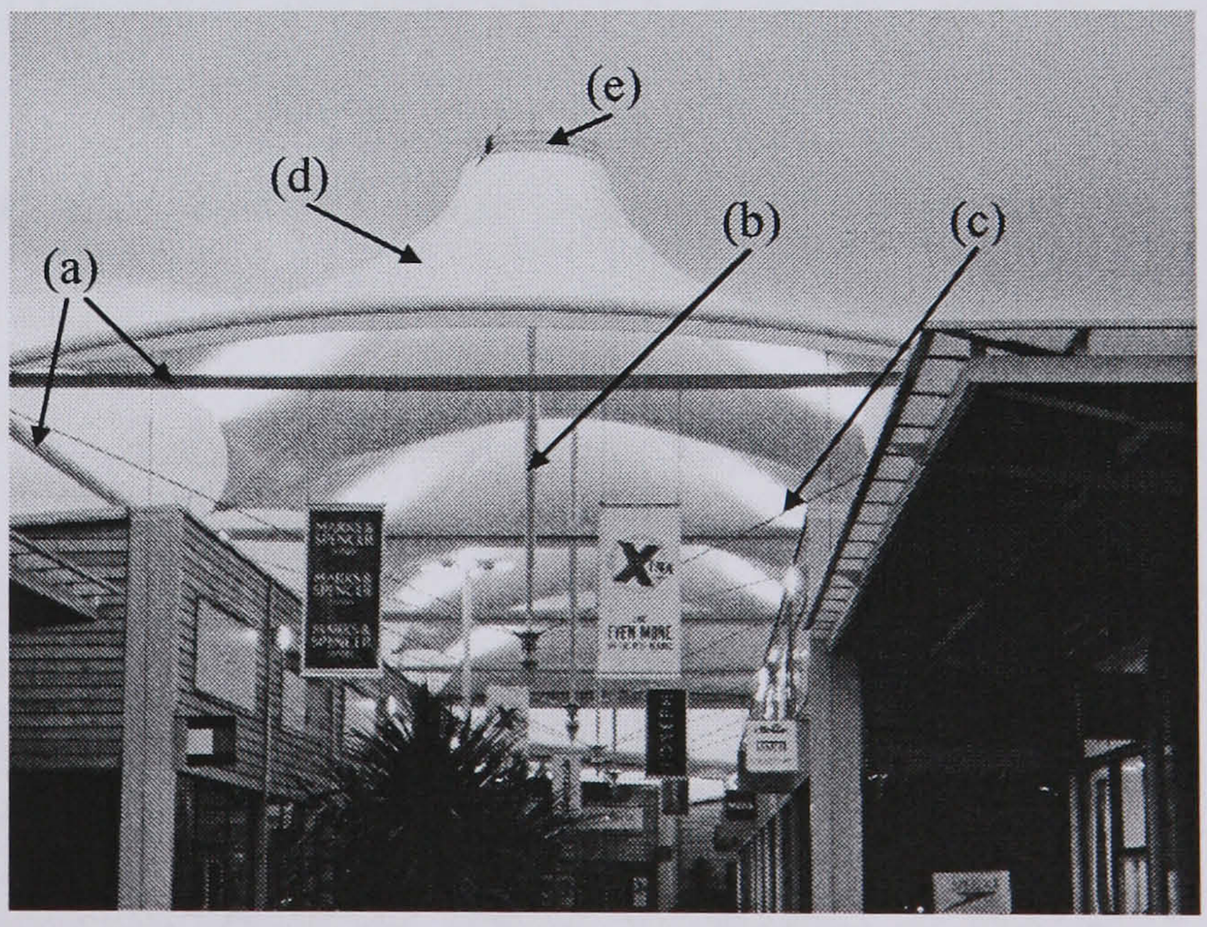


Figure 5-2: Components of the observed membrane structure: beams (a); flying mast (b); cables (c); fabric membranes (d) and top ring (e).

5.3 Static Surface Modelling

5.3.1 Mathematical Model

Figure 5-3 shows the mathematical model as designed by the consulting structural engineers. For performing surface comparison, the designed meshed model was initially converted to a point model. The directory path of the mathematical model was specified in the interface, and the "Read Math Model" module was used to extract the nodes of the meshed model, generating a point model of the observed membrane roof surface (Figure 5-4). A total of 12 768 points were extracted and saved for further analysis.

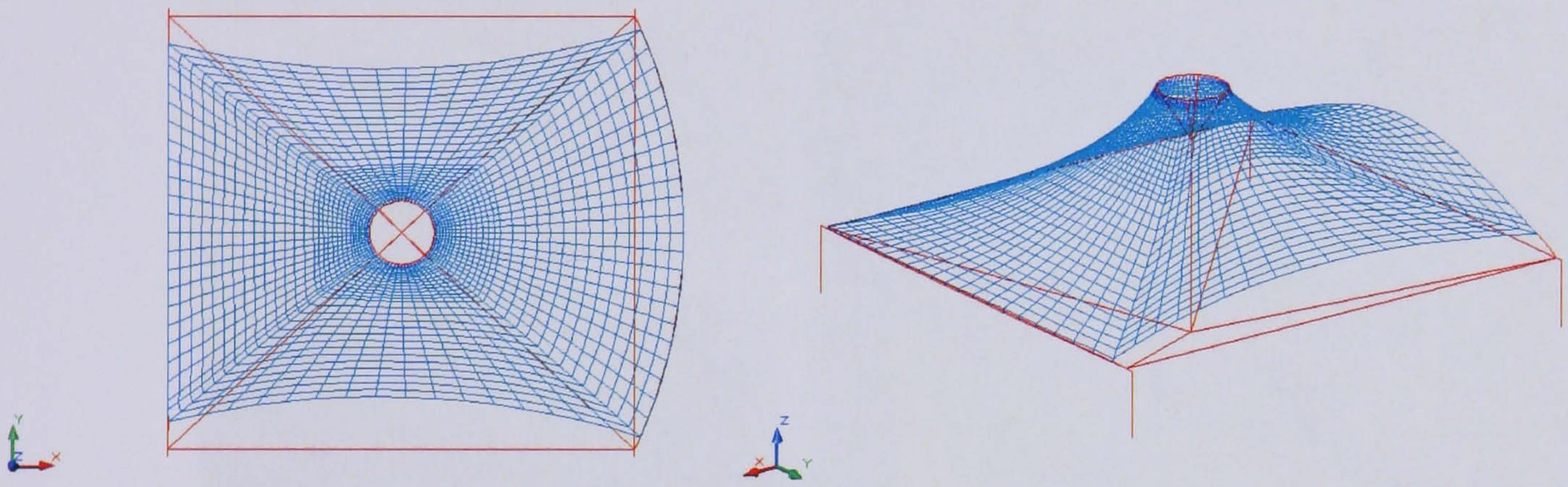


Figure 5-3: Mathematical model of the observed membrane structure.

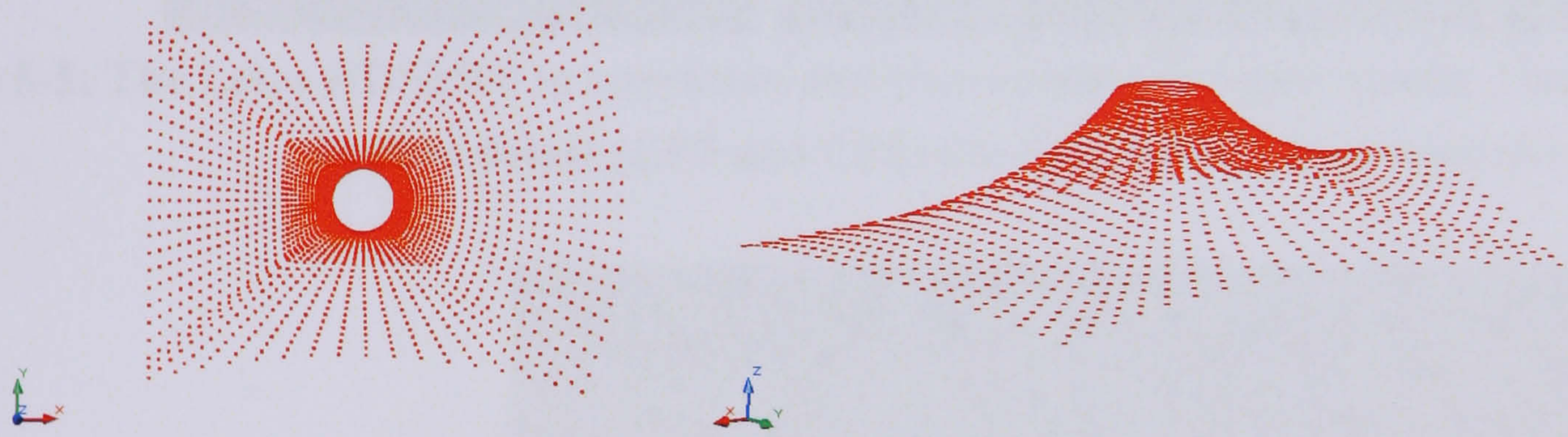


Figure 5-4: Point model of the observed membrane structure.

5.3.2 TLS Model

5.3.2.1 On-site Methodology

Terrestrial laser scanning was used to acquire a three dimensional model of the finished membrane structure. Following the terrestrial laser scanning procedures outlined in Chapter Two, Leica HDS2500 and Leica HDS3000 laser scanning systems were employed to acquire models of the membrane structure. Firstly the model control was collected. Due to the inefficiency of arranging attached targets in the working environment, existing features on the shop façades were selected as control points and

scanned at high resolution. For the registration of scanned models, 14 control points were collected in total, with a scan resolution of 4 mm. Their 3D model coordinates were determined in the manner described in Section 3.2.1.3, while object coordinates were measured using a Leica TCRA1103 total station by the polar method (Section 2.2.2). The scanning setup is illustrated in Figure 5-5 and the resulting control network is shown in Figure 5-6. The coordinates of the control points were estimated in a rigorous least squares estimation in the STAR*NET software package providing control points with an average standard deviation of 0.8 mm, 1.7 mm and 0.8 mm (one sigma) in the X, Y and Z axes respectively.

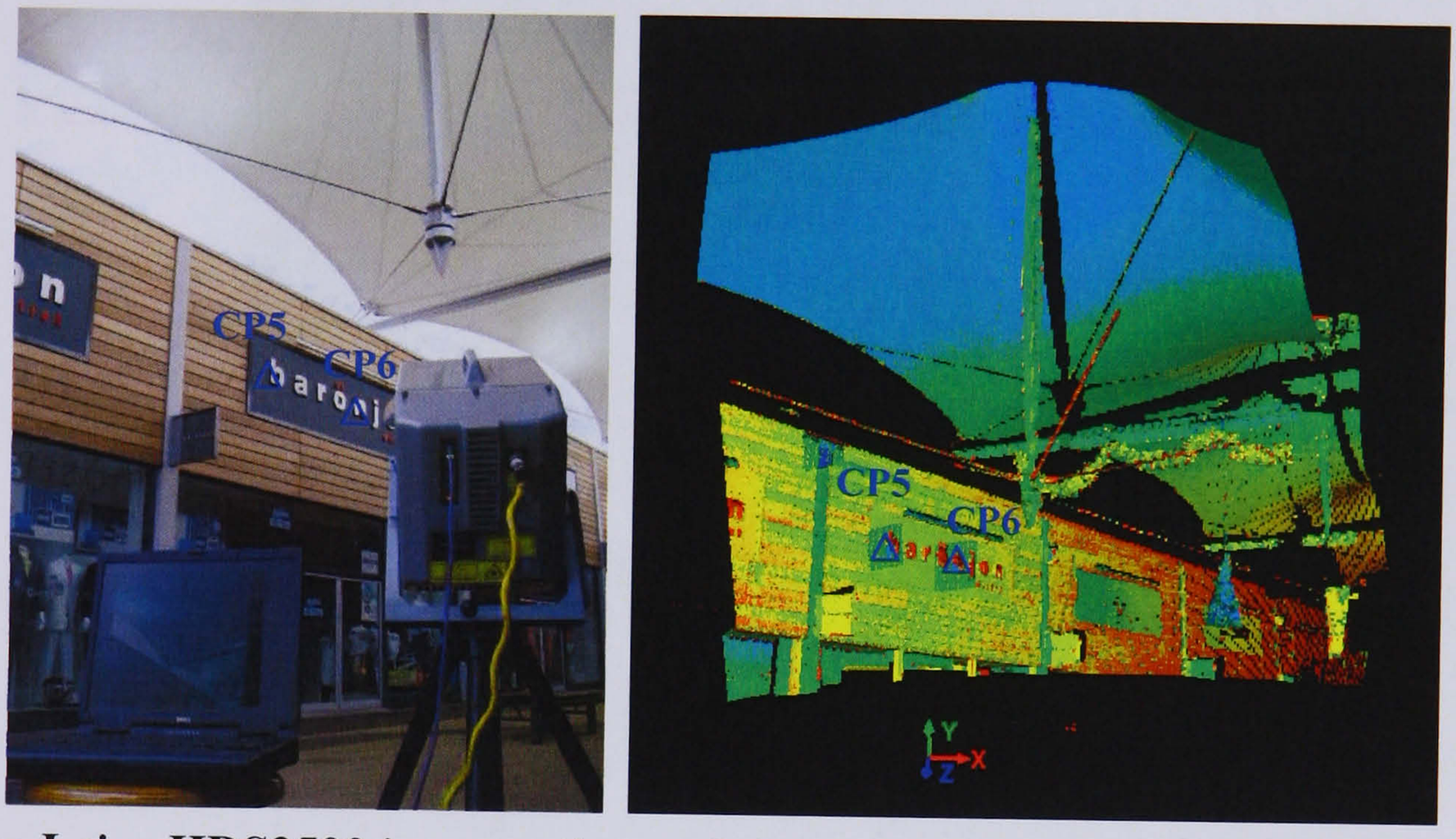


Figure 5-5: The Leica HDS2500 in operation and the resulting scanned model. Two control points (CP5 and CP6) are indicated by blue triangles.

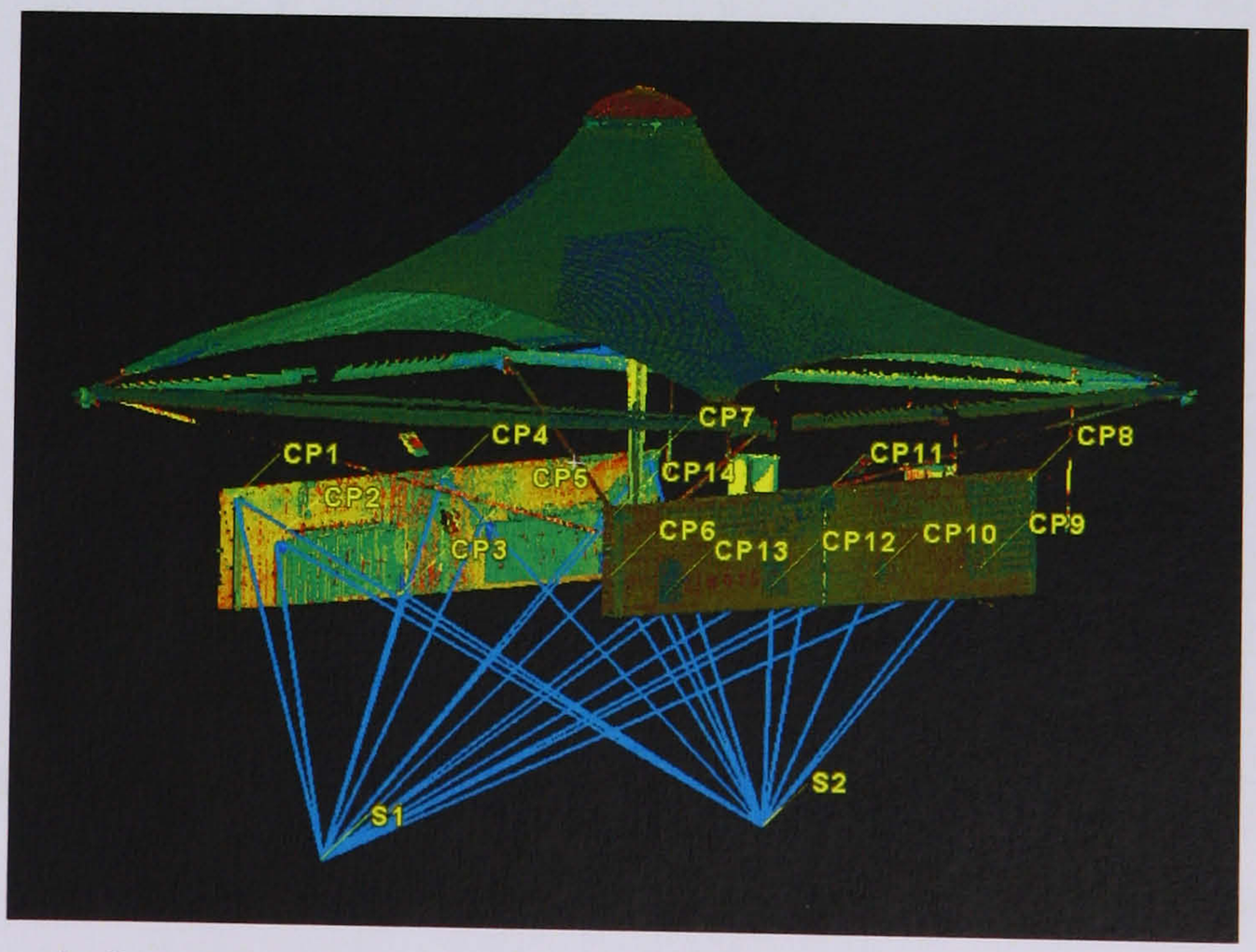


Figure 5-6: Control network for the registration of the laser scanned models.

When using the Leica HDS2500, with its 40˚ by 40˚ field of view in the horizontal and vertical directions, it was necessary to scan the membrane roof from four scanner positions in order to completely cover the fabric roof. The scan resolution was set to 0.04 m for the membrane roof scanning. In addition to the roof surface, a scan of the supporting steelwork was also undertaken. To achieve an appropriate perspective, a raised platform was used to elevate the instrument viewpoint sufficiently to capture the structural components (Figure 5-7). The overall scanner network is shown in Figure 5-8.



Figure 5-7: Scanning from the raised platform.

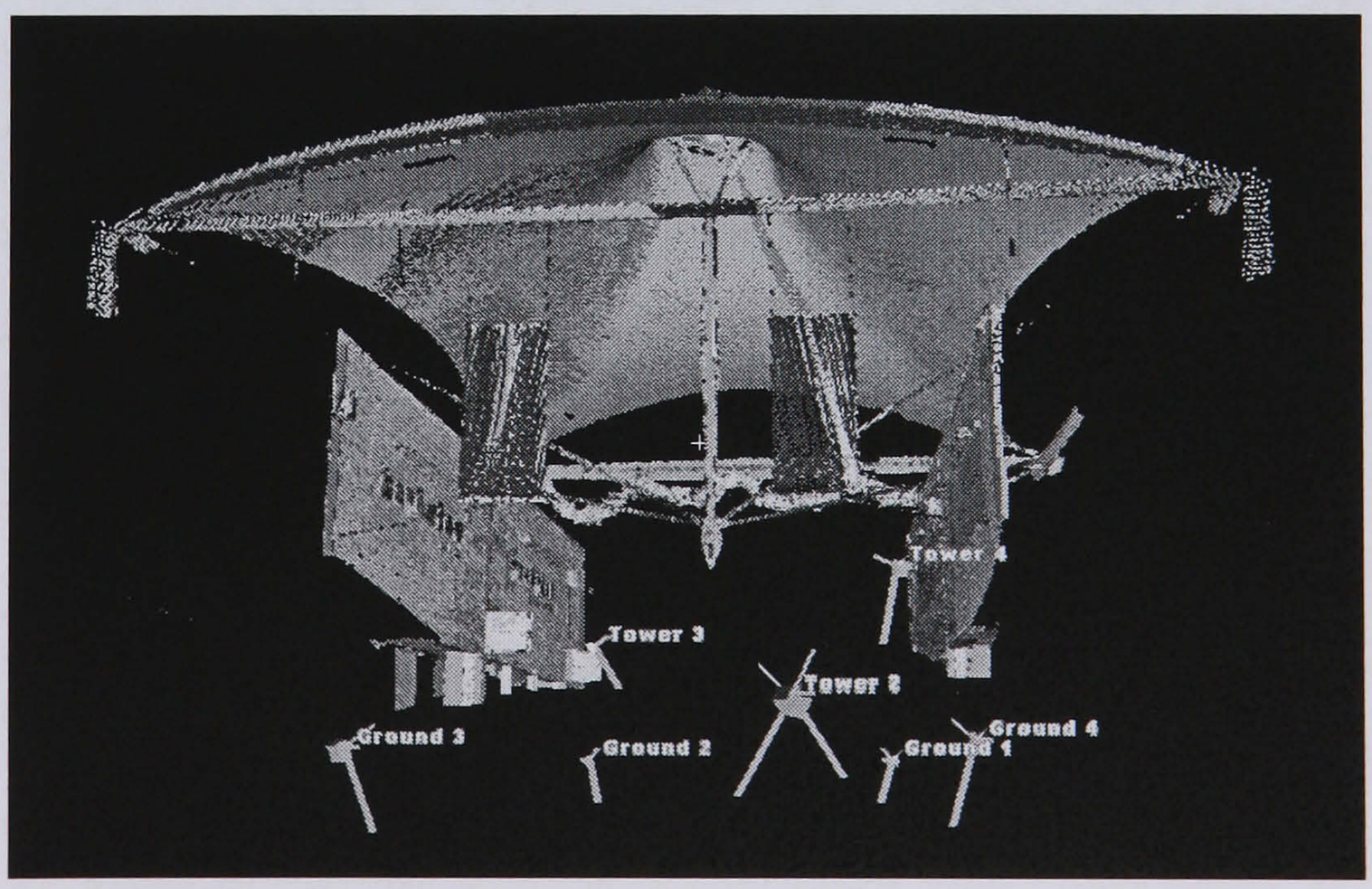


Figure 5-8: Scanner network using a Leica HDS2500 for the membrane structure observation; including four ground scanning stations (Ground 1 – 4) and four platform-mounted scan stations (Tower 1 – 4).

A Leica HDS3000 laser scanning system was also applied in the fieldwork. This more versatile system incorporates a 360˚ by 270˚ field of view in the horizontal and vertical scanning directions respectively. In this case scanning from three stations on the raised platform was sufficient to cover the entire membrane roof surface and supporting steelwork (Figure 5-9).

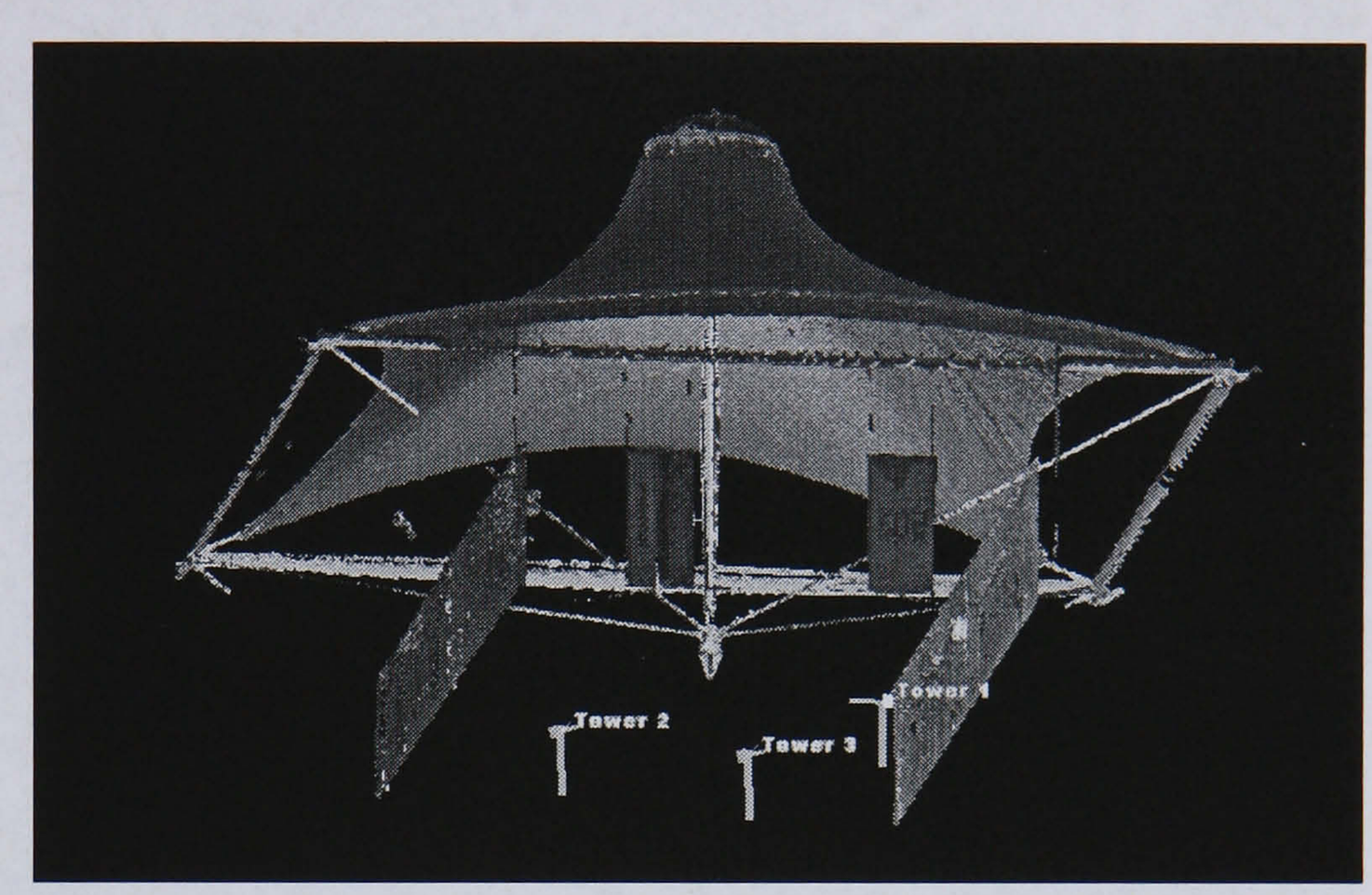


Figure 5-9: Scanner network of using Leica HDS3000 (Tower 1-3) in the membrane structure observation.

5.3.2.2 Data Processing

A total of eight and three scanned models were collected with the Leica HDS2500 and HDS3000 laser scanner respectively. The 14 control points were determined in each scan, and then the models were aligned based on their positions by performing registration. The resultant registered model of the membrane structure is shown in Figure 5-10. As the more comprehensive model was derived using the HDS3000, the resultant model from HDS3000 was used in the subsequent tasks. For surface comparison, the corresponding part of the membrane surface to that in the mathematical model was extracted from the laser scanned model (Figure 5-11).

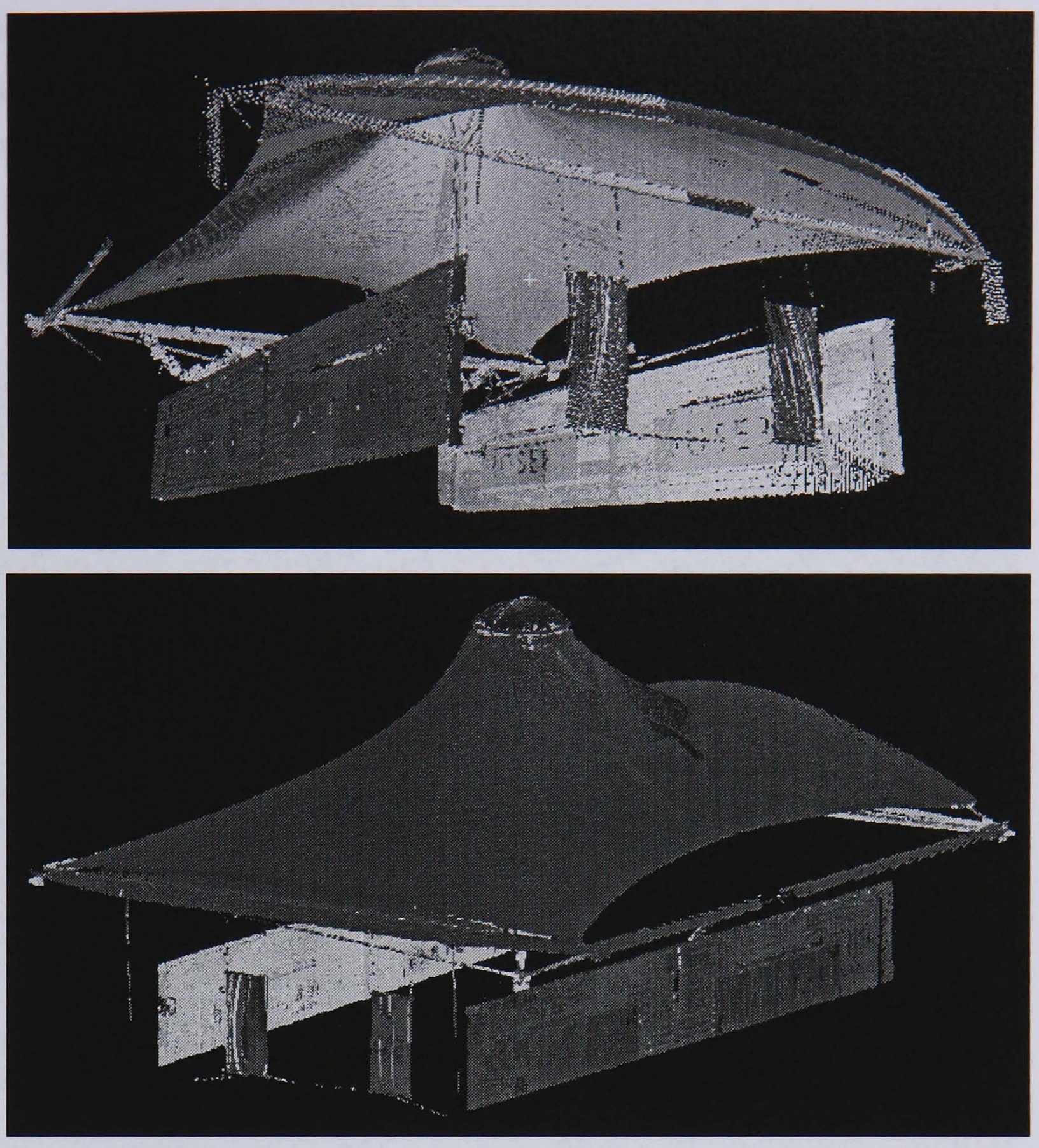


Figure 5-10: Amalgamated laser scanned model of the membrane structure generated by Leica HDS2500 (top) and HDS3000 (bottom) laser scanners.



Figure 5-11: Fabric membrane roof extracted from the HDS3000 laser scanned model for surface comparison.

In order to compare the designed mathematical model with the laser scanned model, the modelling of supporting steelwork was necessary (details will be explained later in Section 5.3.3.2). Cylinder primitives were used to represent the point cloud of beam components. The determined model of the supporting steelwork and the centre lines of the cylinders are shown in Figure 5-12.

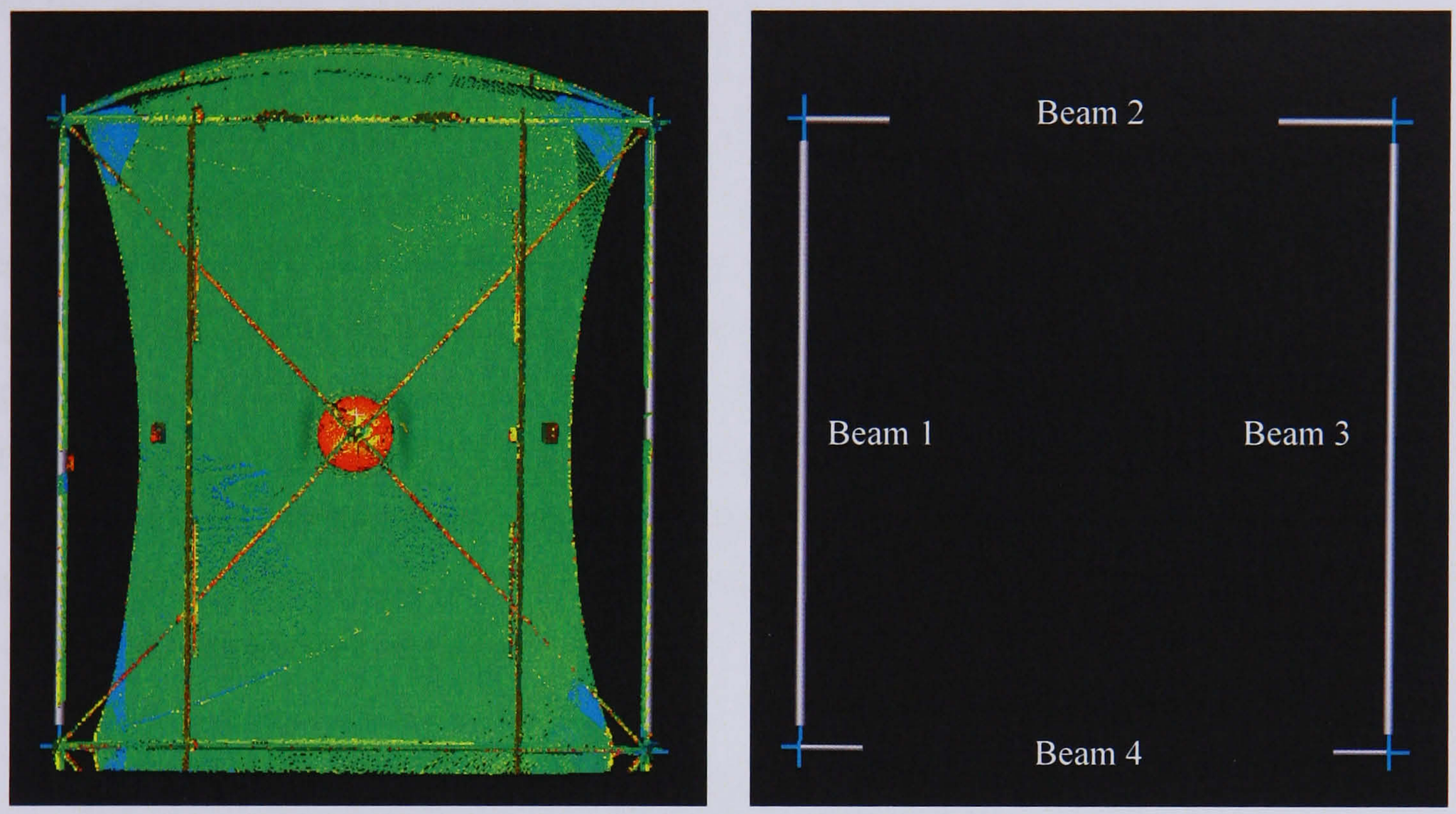


Figure 5-12: The scanned supporting steelworks and the resulting cylinder models (grey pipes) and centre lines (blue lines).

5.3.2.3 Validation of Laser Scanned Model

The accuracy of the laser scanned model was further validated before being introduced into the static surface comparison scheme. The aligned error generated at the stage of model registration was the first indicator. After the processing of laser scanned data was complete, the registration error of the amalgamated laser scanned model was solved as 6.0 mm, proving the TLS model was accurate enough for examining the membrane structure whose construction tolerance was 10.0 mm (refer to Section 1.2.6 for the description of the tolerance).

In addition, independent observations from a Leica TCRA1103 total station were introduced for evaluating the accuracy of the TLS model. To achieve this, normally, some common identifiable points in both the TLS model and physical structure are selected. Then their coordinates, derived from the TLS model and measured by total station, are compared to determine the accuracy. However, as the laser scanned model

was presented as a discrete point cloud, it was difficult to identify exact points in the TLS model corresponding to those on the physical structure. Therefore a line feature, the centre line of the modelled beam, was adopted for determining the accuracy of the TLS model using a total station. The area for comparison is illustrated in Figure 5-13, in which the centre line of Beam 4 was derived in the previous section, and the total station was applied on-site to observe along the beam as outlined by the dashed line. After the observations were finished, these points were imported into the TLS model, and the normal distances between them to the centre line of Beam 4 were computed. In theory the distances should be equal to the radius of the beam, however in practice, the disparities between the normal distances and the radius were deemed as the error of the TLS model (Figure 5-14). In the fieldwork, a total of 15 points were observed by total station, and the mean difference was calculated as 10.9 mm. Considering the ambiguity of pointing along the vague line by total station, the relatively degraded accuracy derived was expected. Nevertheless, the fact that the TLS error was at the same level of the construction tolerance of the membrane structure at Dalton Park, again demonstrated that the resultant TLS model was satisfactory for measuring and analysing the observed membrane structure.

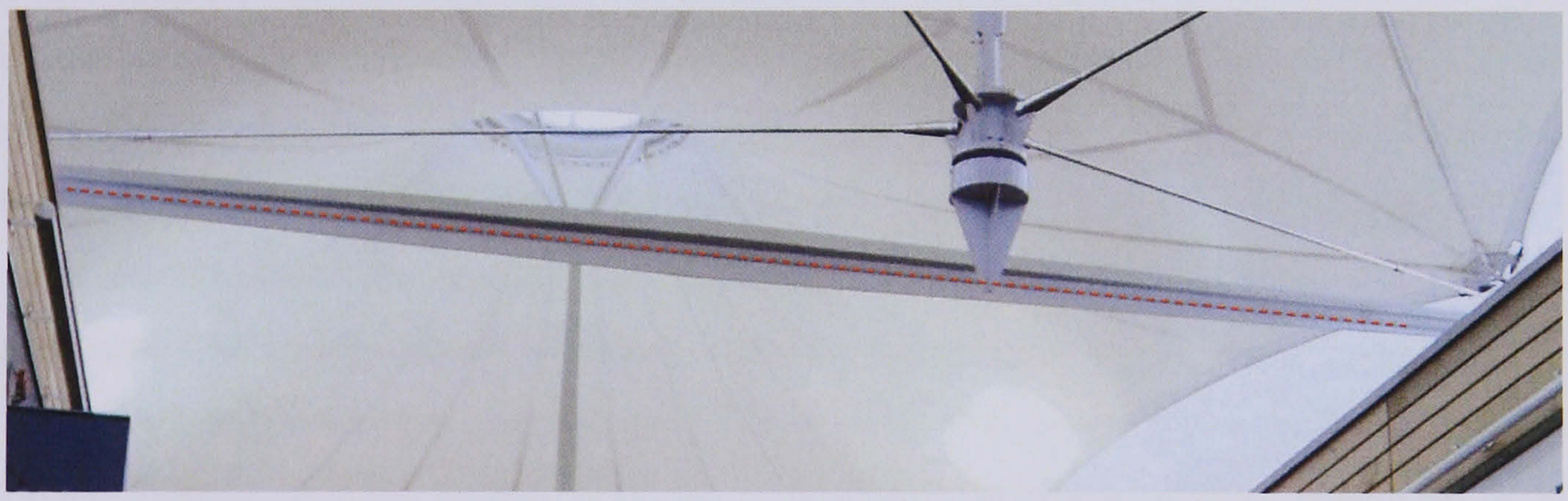


Figure 5-13: The beam (Beam 4) used in the estimation of the accuracy of the laser scanned model.

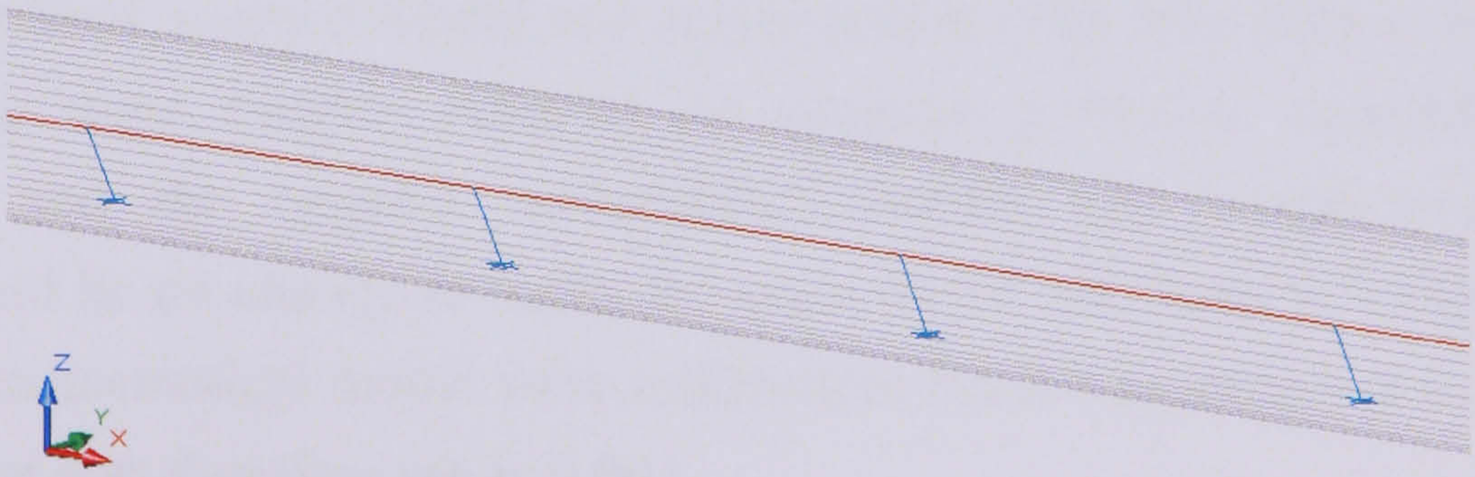


Figure 5-14: The example section of Beam 4 showing discrepancies between the check points (blue points) and the centre line of the beam (red line).

The final part of the justification was the evaluation of the beam modelling. The accuracy was derived by comparing the diameters of the modelled beams with the values noted in the mathematical model. From the results (Table 5-1), it is revealed that the average difference varies from 1 to 3 mm, showing the correctness of the cylinder modelling. The centre lines of the modelled beams were also verified.

	Physical Beam (m)	*Modelled Beam (m)*	*Difference (m)*
Beam 1	0.245	0.247	0.002
Beam 2	0.193	0.196	0.003
Beam 3	0.245	0.246	0.001
Beam 4	0.139	0.142	0.003

Table 5-1: Diameter differences between the physical and the modelled beams.

5.3.3 Static Surface Comparison

5.3.3.1 Surface Matching

For static surface comparison the technique of surface matching was applied. Identical parts of the membrane surface were extracted from both the mathematical and laser scanned model (Figure 5-4 and Figure 5-11). They were then input into the 3D Surf surface matching software. The laser scanned model was deemed as the true model of the membrane surface and thus was used as the reference surface, and the mathematical model was transformed to match the scanned model. After an initial approximate transformation, the computation of least squares minimisation of vertical differences between the two surfaces was carried out. The solution was iterated until convergence, and the final transformation parameters, as well as the residuals which represented the surface separations, were calculated.

To make the matching more efficient in 3D Surf, a coarse transformation of the mathematical model to the laser scanned model was implemented. The four corners of the two fabric membrane were roughly selected as common points to compute parameters (Table 5-2), and the original mathematical model was transformed accordingly. As there should be no change in scale, the scale factor was fixed to unity. However, the units in the mathematical model were millimetres but it was metres in the TLS model. The scale factor was therefore set as 0.001.

Translation (m)			*Rotation (°)*		
T_X	T_Y	T_Z	ω	ϕ	κ
107.855	61.518	-82.932	-0.171	-0.014	91.688

Table 5-2: Parameters for transformation before running 3D Surf.

Once convergence was reached, a total of 13 122 points, evenly distributed across the surface, were used to calculate the residuals. The transformation parameters and statistics of residuals are listed in Table 5-3. The residual values have been derived by subtracting the Z-values of the points on the transformed mathematical model from those values on laser scanned model. The maximum positive difference was 0.328 m, while the lowest negative residual was 0.342 m.

Transformation Parameters	*Translations (m)*	T_X	1.097
		T_Y	-1.740
		T_Z	-1.033
	Rotations (°)	ω	-0.661
		ϕ	0.095
		κ	0.323
Surface Disparity (m)	*Maximum*		0.328
	Minimum		-0.342
	Range		0.670
	Mean		0.000
	Std. deviation		0.148
	RMS		0.148

Table 5-3: Solved transformation parameters and surface comparison results.

For further analysis of the resolved vertical difference between the two surfaces, the points used for calculating the surface transformation in 3D surf were plotted in their correct planimetric positions. Moreover, these points were classified into six levels according to the discrepancy values and colour-coded. As shown in Figure 5-15, the points with a negative value indicated the positions in which the transformed mathematical model was higher than the laser scanned model; the points with a positive value represented the positions where the transformed mathematical model was lower than the laser scanned model. From the rendered colour it was evident that the discrepancies occurred symmetrically over the observed surface. Positions (a) to (f) marked in Figure 5-15 are areas with apparent differences. Monitored sections (a), (c)

and (d) were lower than the transformed mathematical model, while (b), (e) and (f) were above.

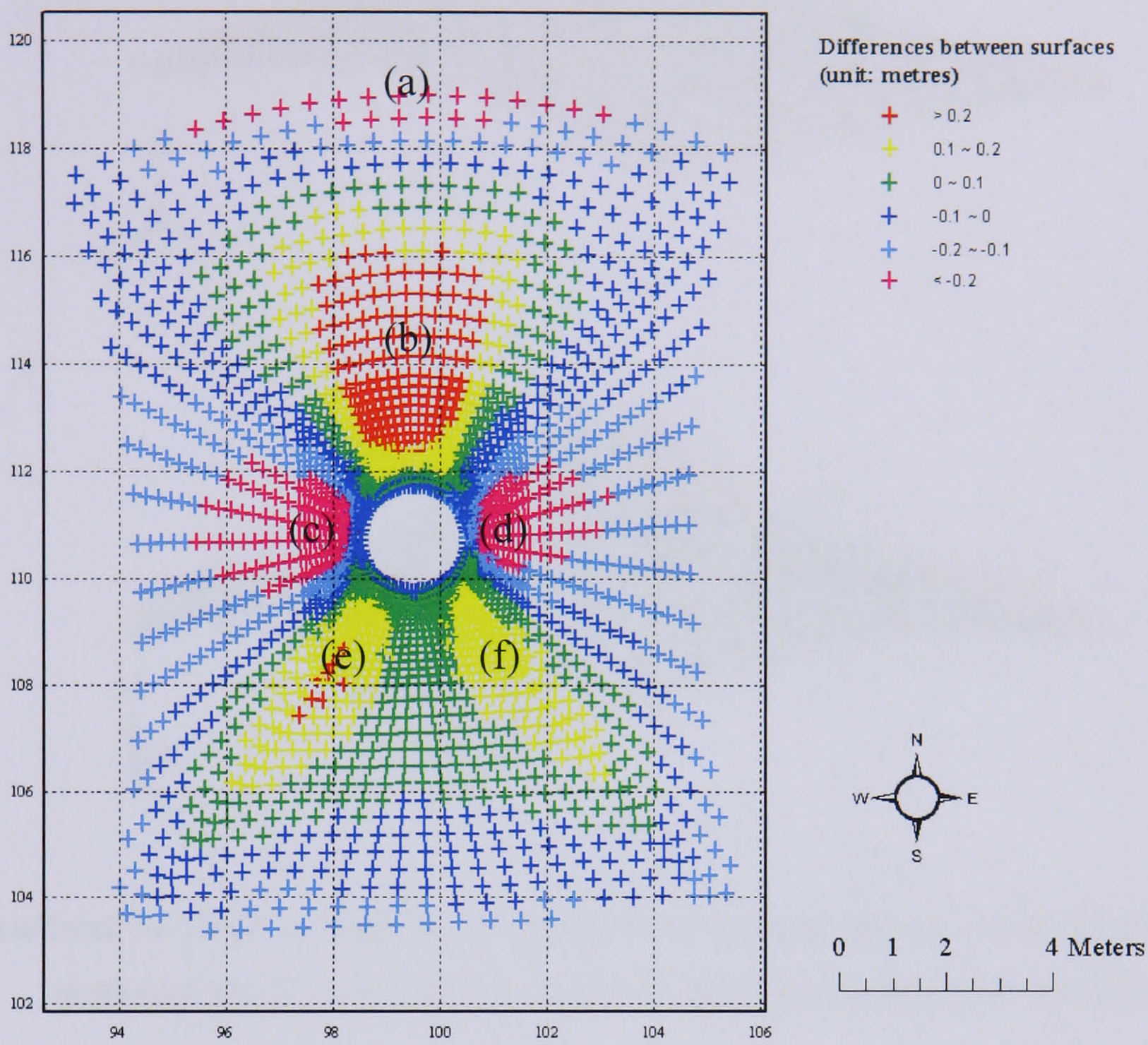


Figure 5-15: Discrepancy map derived from surface matching.

Perspective visualisation was used to quantitatively assess the disparities between the two surfaces. ArcMap and GLView software were employed to create and display the perspective scenes of the matched results. The mathematical surface model was transformed using the final parameters and then both surfaces were input into ArcMap for meshed model generation and editing. The TLS meshed surface and the matched mathematical model could then be displayed in ArcMap and GLView. Examples of the perspective scene shown in GLView are illustrated in Figure 5-16, and the areas of obvious difference specified in Figure 5-15 are pointed out in the 3D surface model.

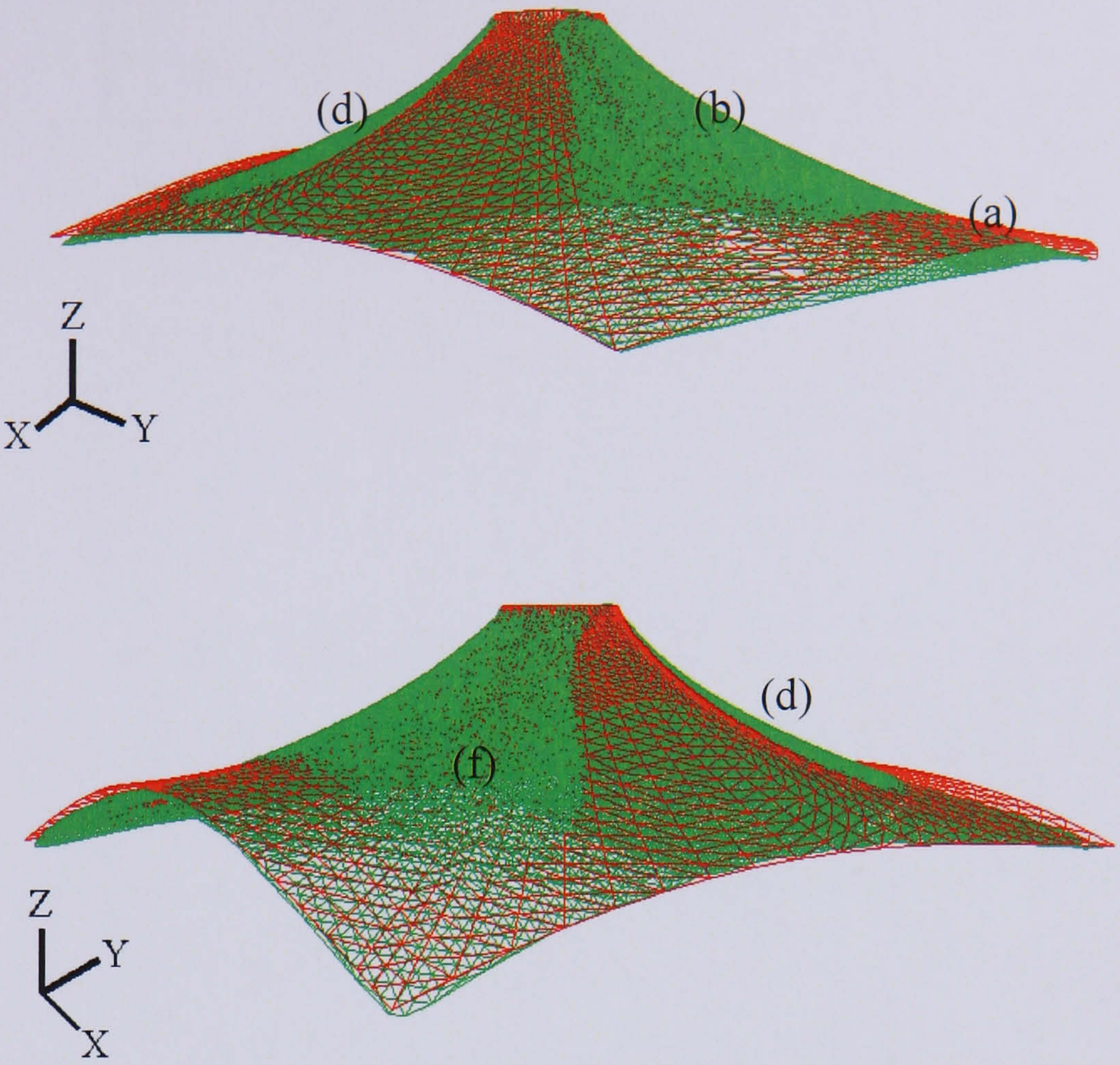


Figure 5-16: Resultant meshed models after surface matching (green mesh: laser scanned model; red mesh: transformed mathematical model).

Furthermore, the disparity value and the shape of the specific part of the membrane surface have been investigated by inspecting extracted profiles. The profiles along the Y-axis where X=99 m and along the X-axis where Y= 111 m are depicted in Figure 5-17. The green profile line was derived from the laser scanned model, and the red line represented the profile of the transformed mathematical model. The blue curve shown in the figure below illustrates the difference values between the two profiles. Along the profiles drawn, the discrepancies occurred in areas (a) and (b), areas (c) and (d) were inspected.

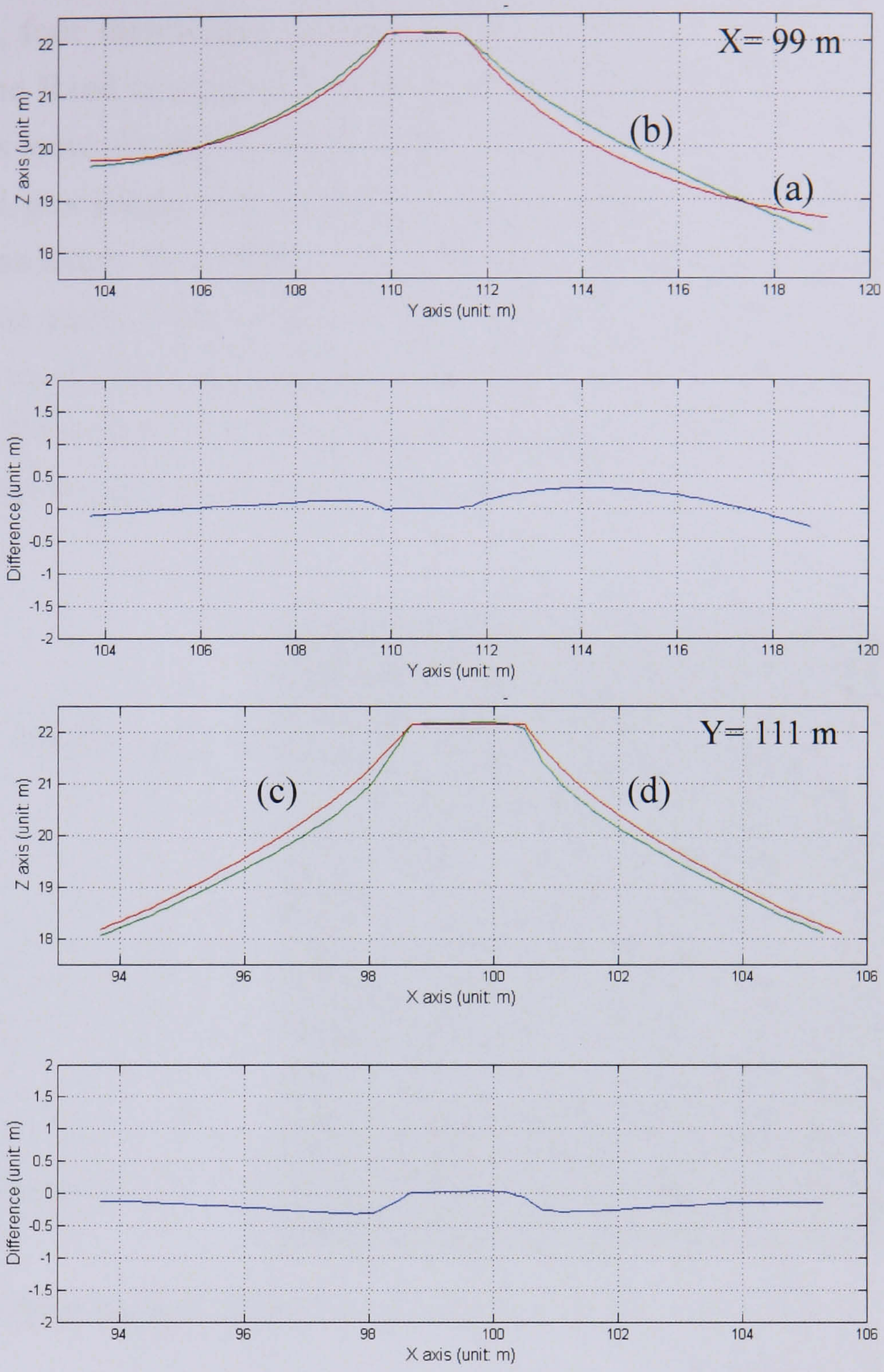


Figure 5-17: Differences in profiles between the two surface models (top: profiles along the Y-axis; bottom: profiles along the X-axis).

Based on the metric information and the model visualisation presented above, it is shown that significant differences exist between the finished "as-built" membrane roof structure and the designed mathematical model, especially in the areas (a), (b), (c) and (d) highlighted in Figure 5-15. Another method, 3D conformal transformation, to define the differences between the two surface models was subsequently performed to validate these findings.

5.3.3.2 3D Conformal Transformation

As described in Section 3.2.3, the intersection points of the supporting steelwork were utilised as control points for performing a 3D conformal transformation. In the Tent

Type 1 membrane structure, four intersection corner points (points 1 – 4 indicated in Figure 5-18), which were the fixed components of the structure, were used as control points. Their 3D coordinates were directly extracted in the mathematical model, while in the TLS model additional processing was necessary. First of all the point clouds of the steelwork have to be modelled by cylinder primitives and the points were then determined by intersecting the centre lines of the modelled cylinders. The task has been accomplished at the laser scanned data processing stage (Section 5.3.2.2). Figure 5-19 depicts the procedure of determining the corresponding common point (Point 2) between the two models and the resulting coordinates are listed in Table 5-4.

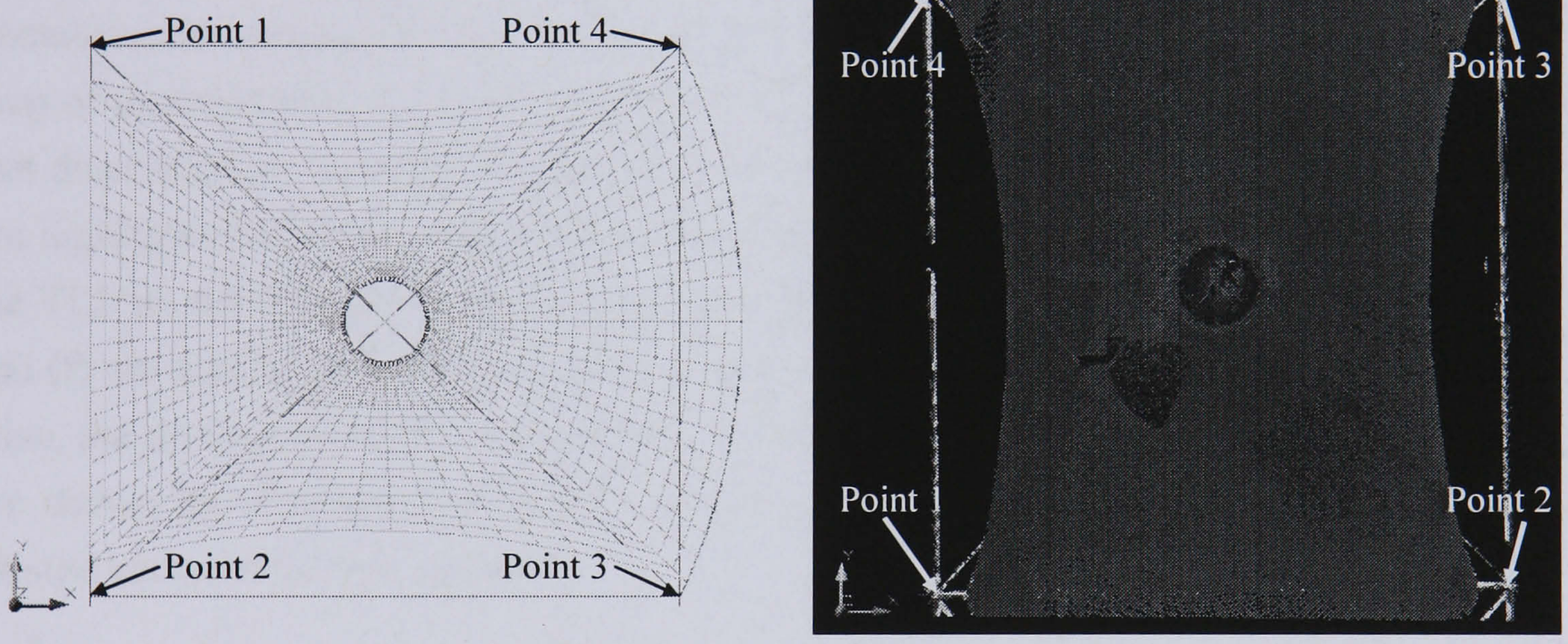


Figure 5-18: Four common control points in the mathematical model and laser scanned model.

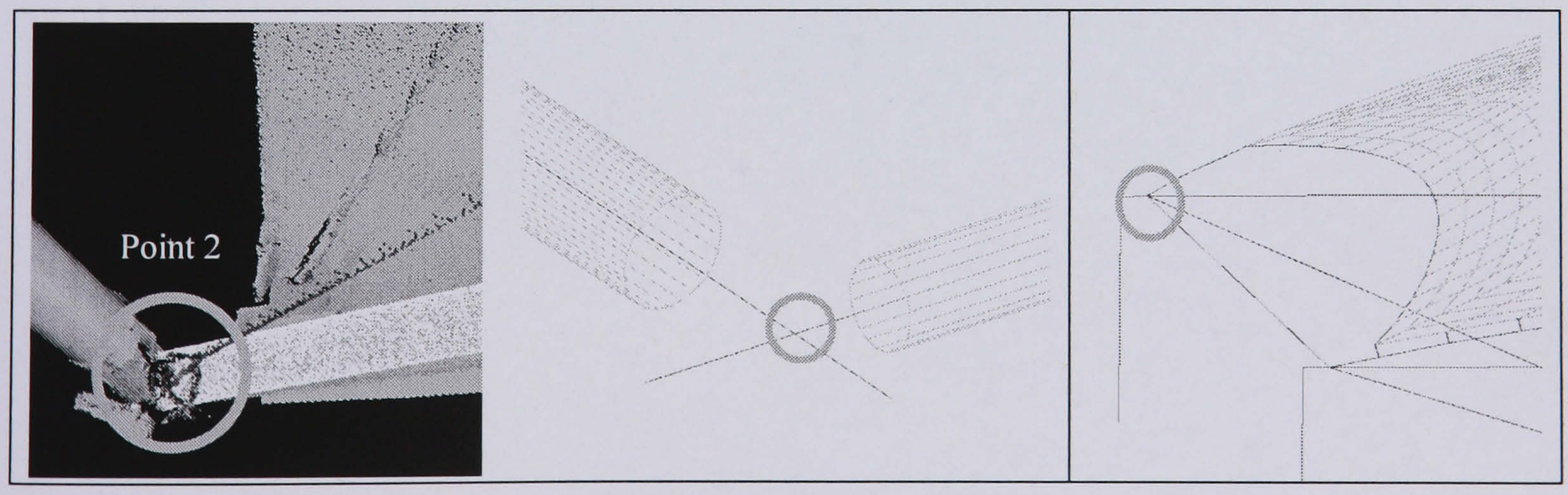


Figure 5-19: Control point (outlined by the circle) in laser scanned model (left), modelled beams (centre), and mathematical model (right).

	Mathematical Model (mm)			*TLS Model (m)*		
	X_M	Y_M	Z_M	X_T	Y_T	Z_T
Point 1	43200.000	13770.100	103150.000	93.056	103.262	17.642
Point 2	43200.000	229.900	103150.000	106.550	103.770	17.640
Point 3	57600.000	229.900	103150.000	106.033	118.118	17.558
Point 4	57600.000	13770.100	103150.000	92.520	117.658	17.538

Table 5-4: 3D coordinates of corresponding control points in mathematical and TLS model.

Following the determination of the four common points, a 3D conformal transformation was performed. The laser scanned model and the transformed mathematical model were then statistically compared via the Surface Comparison Module in MS^2. The resolved transformation parameters and surface comparison results are listed in Table 5-5 and the map of discrepancies is shown in Figure 5-20. From the rendered colours it is obvious that discrepancies occurred symmetrically over the observed surface. Positions (a) to (f) are highlighted to show areas with apparent differences. Areas (a), (c) and (d) are parts the TLS model that are lower than the transformed mathematical model, while (b), (e) and (f) are higher, with the maximum discrepancy of -0.288 m and 0.445 m respectively. Also, the profiles along the Y-axis where X=99 m and along the X-axis where Y= 111 m are drawn for detailed investigation (Figure 5-21), showing that obvious differences existed between the two surfaces.

Transformation Parameters	*Translations (m)*	T_X	108.438
		T_Y	60.008
		T_Z	-85.052
	Rotations (°)	ω	-0.370
		ϕ	-0.051
		κ	92.077
	Scale		0.001
Surface Disparity (m)	*Number of Points*		2043
	Maximum		0.445
	Minimum		-0.288
	Range		0.733
	Mean		0.086
	Std. deviation		0.134
	RMS		0.159

Table 5-5: Solved transformation parameters and surface comparison results.

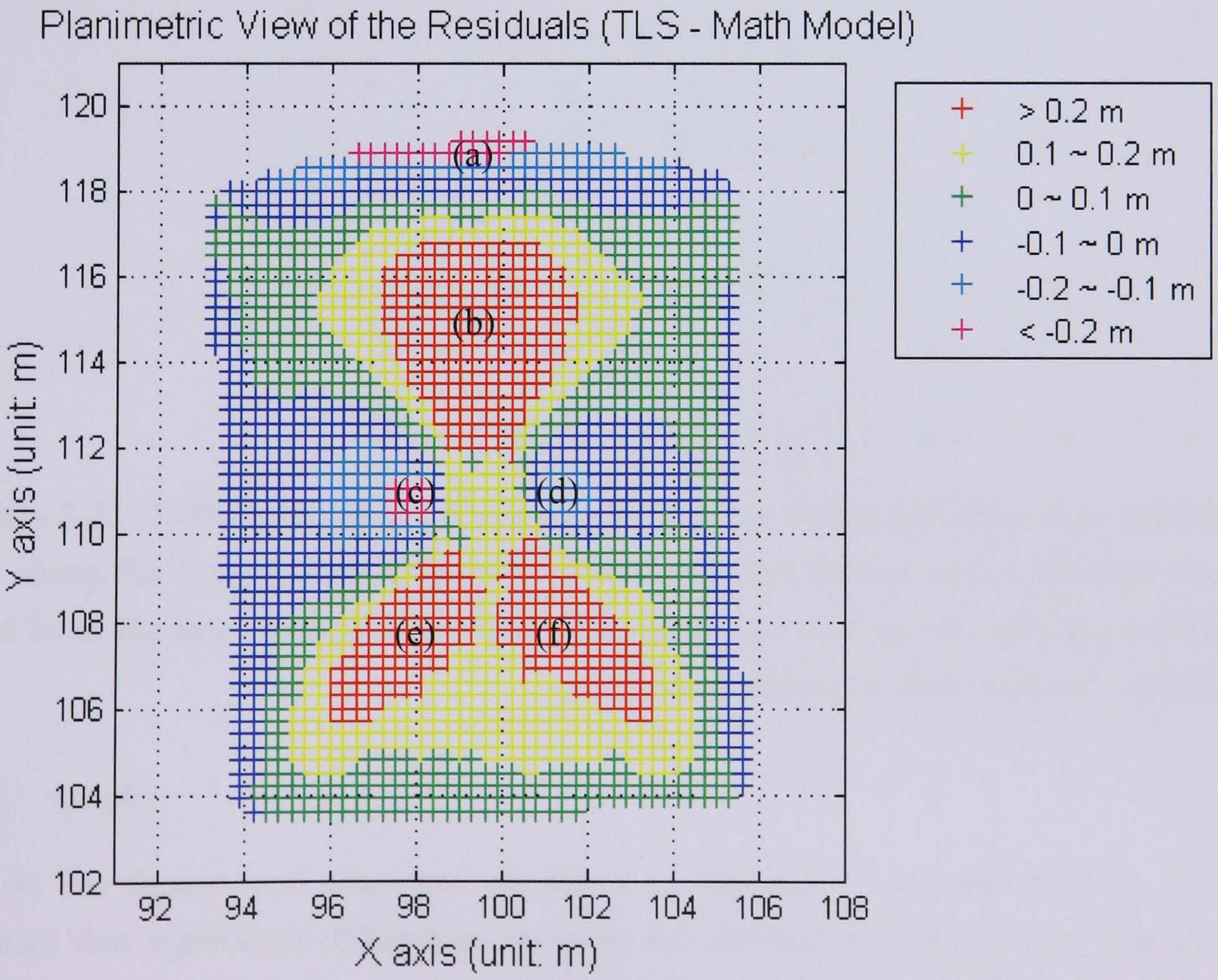


Figure 5-20: Discrepancy map derived from 3D conformal transformation.

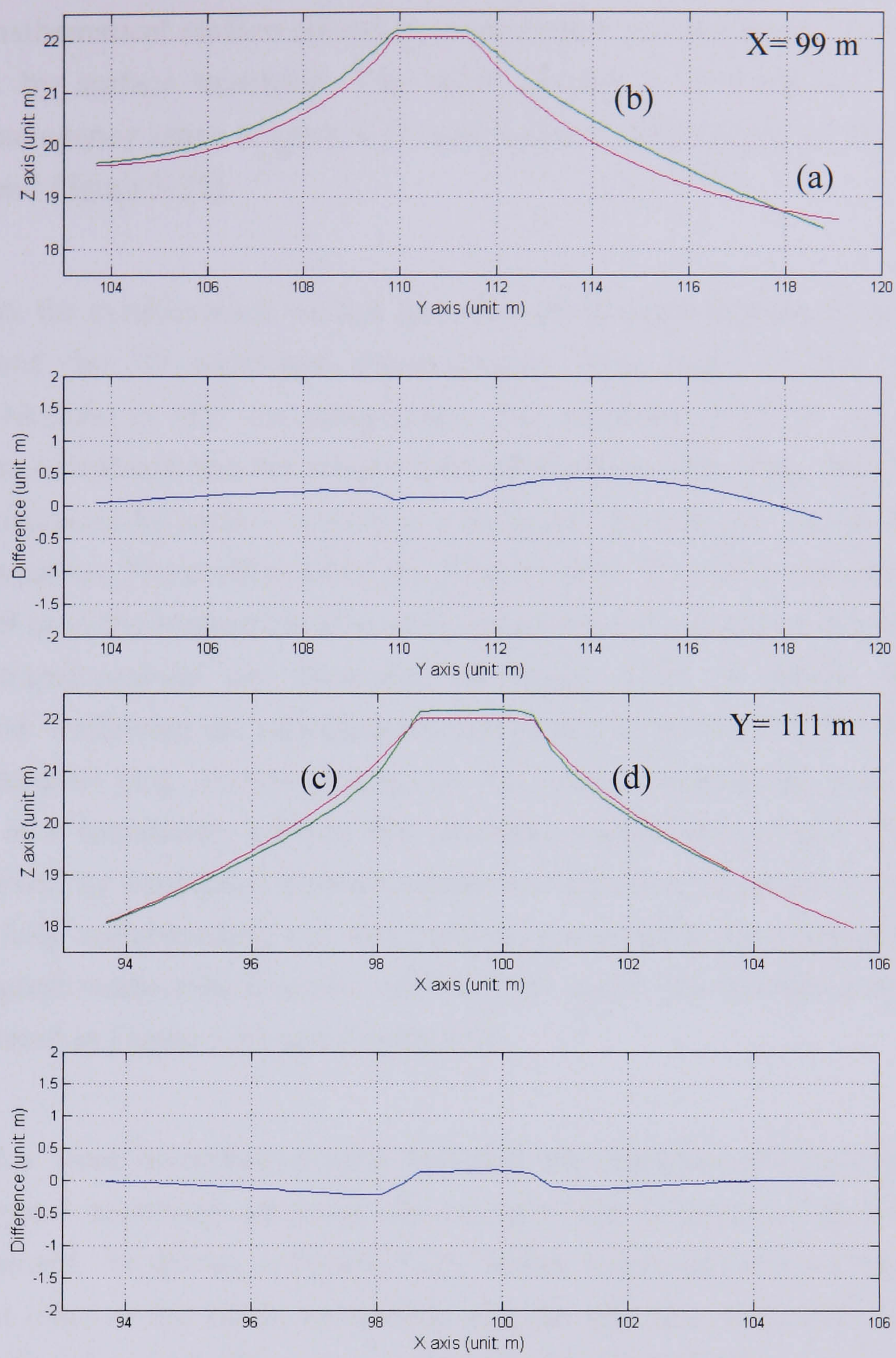


Figure 5-21: Differences in profiles between the two surface models. Top: profile along the Y-axis; bottom: profile along the X-axis (the green profile line was derived from the laser scanned model, and the magenta line represented the profile of the transformed mathematical model).

5.3.3.3 Results

Based on the figures and diagrams presented in Section 5.3.3.1 and 5.3.3.2, it is determined that significant differences between the finished membrane roof structure and the designed mathematical model existed. However, from the computed maximum, minimum and mean values of residuals, it is also noted that the magnitude of the residuals vary according to the technique of surface matching or 3D conformal

transformation. The mathematical surface solved by conformal transformation is lower than that determined by surface matching. The same finding is also inferred by comparing the two discrepancy maps (Figure 5-15 and Figure 5-20) and the extracted profiles (Figure 5-17 and Figure 5-21).

For further exploration, the mathematical models transformed through both the surface matching algorithm and the 3D conformal transformation were imported into the Surface Comparison Module in MS^2 for comparison. The residuals of 2 119 points across the surface were calculated and the results were all positive, indicating that the mathematical model produced by surface matching was higher than the one solved by 3D conformal transformation. The profiles along the X-axis where Y= 111 m and along the Y-axis where X=99 m of the mathematical models transformed by surface matching and 3D conformal transformation are illustrated in Figure 5-22, in which this discrepancy is observed. Following the consideration mentioned in Section 3.2.2.3, the lack of physical constraints (e.g. control points) in the implementation of surface matching may result in a statistically correct, but alternate, match being found. The surface model determined by conformal transformation was therefore regarded as the correct solution. For fully understanding the discrepancies occurred at the membrane roof between the designed mathematical model and the TLS model, the profiles across the surface were generated in Figure 5-23 and Figure 5-24.

Since the discrepancies were identified existed between the designed and finished version of the Tent Type 1 membrane structure, the extent of the variances at specific areas was further inspected. As shown in Figure 5-25, further examinations have been performed at the front edge of the fabric membrane and the top ring steelwork. The finished structure was found to be 0.426 m lower than the designed model at the arch steelwork, while it was 0.082 m higher at the top ring. The results indicate that the main failure of Type 1 membrane structure occurred during the structure's construction, in which the middle flying mast was propped higher than designed, while the front arch steelwork was set lower than the designed height. The incorrect construction, rather than the inaccurate design, caused the deformation of the fabric membrane and explained the discrepancies determined in Section 5.3.3.1 and 5.3.3.2.

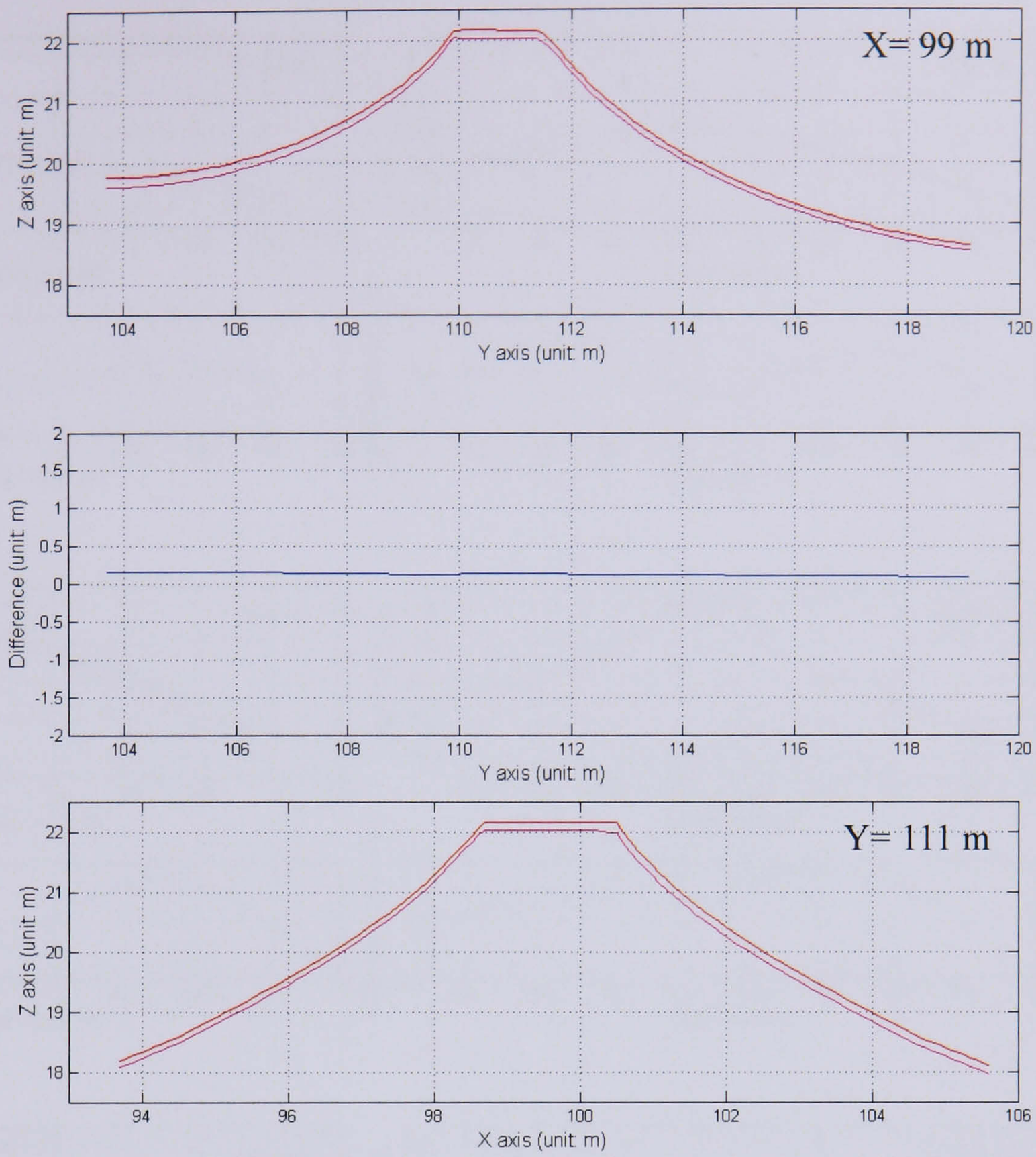


Figure 5-22: Differences in profile between the surface matched and 3D conformal transformed models (red: transformed mathematical model from surface matching; magenta: transformed math model from conformal transformation).

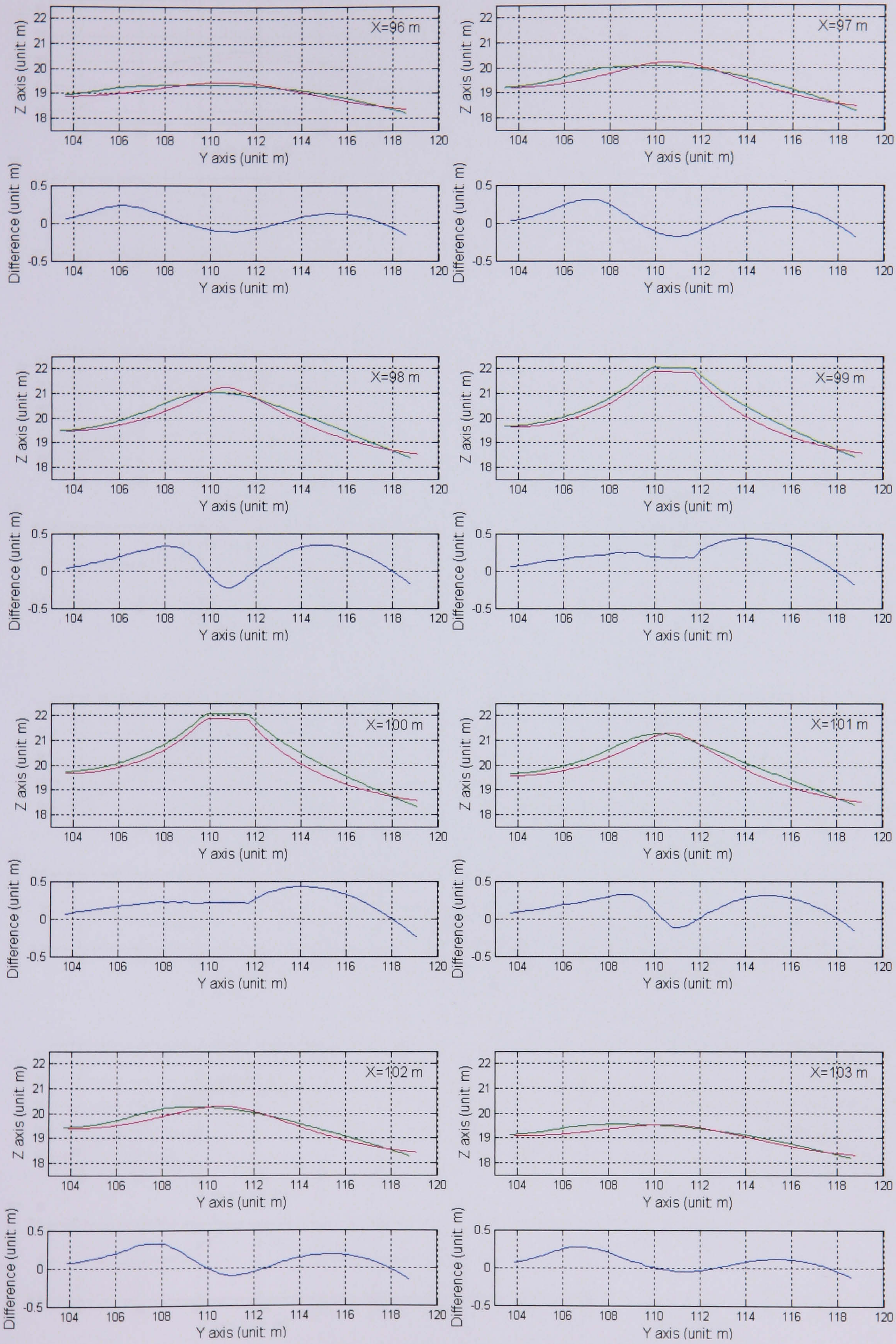


Figure 5-23: Differences in profile along the Y-axis between the transformed mathematical model (magenta curve) and the laser scanned model (green curve).

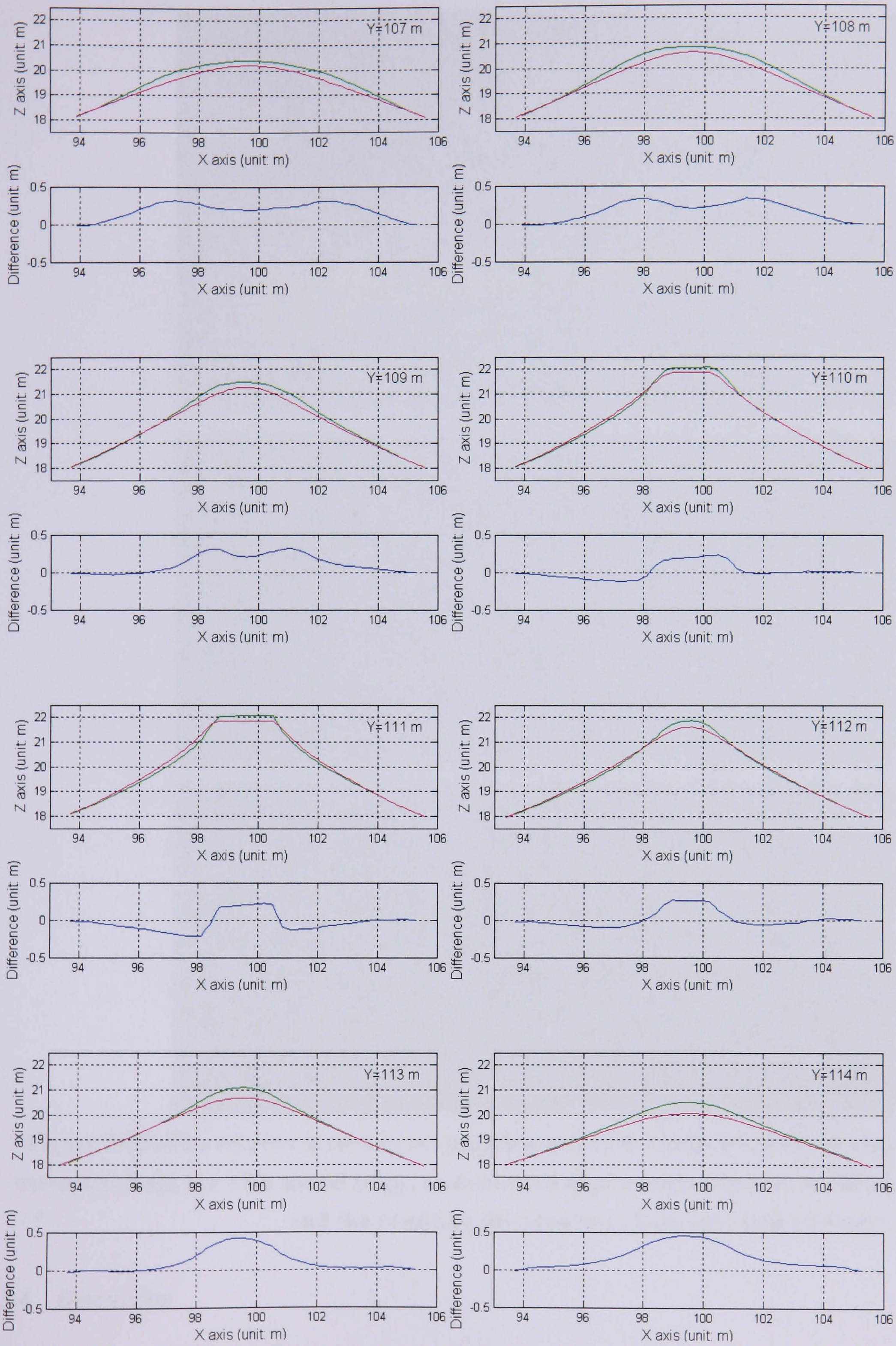


Figure 5-24: Differences in profile along the X-axis between the transformed mathematical model (magenta curve) and the laser scanned model (green curve).

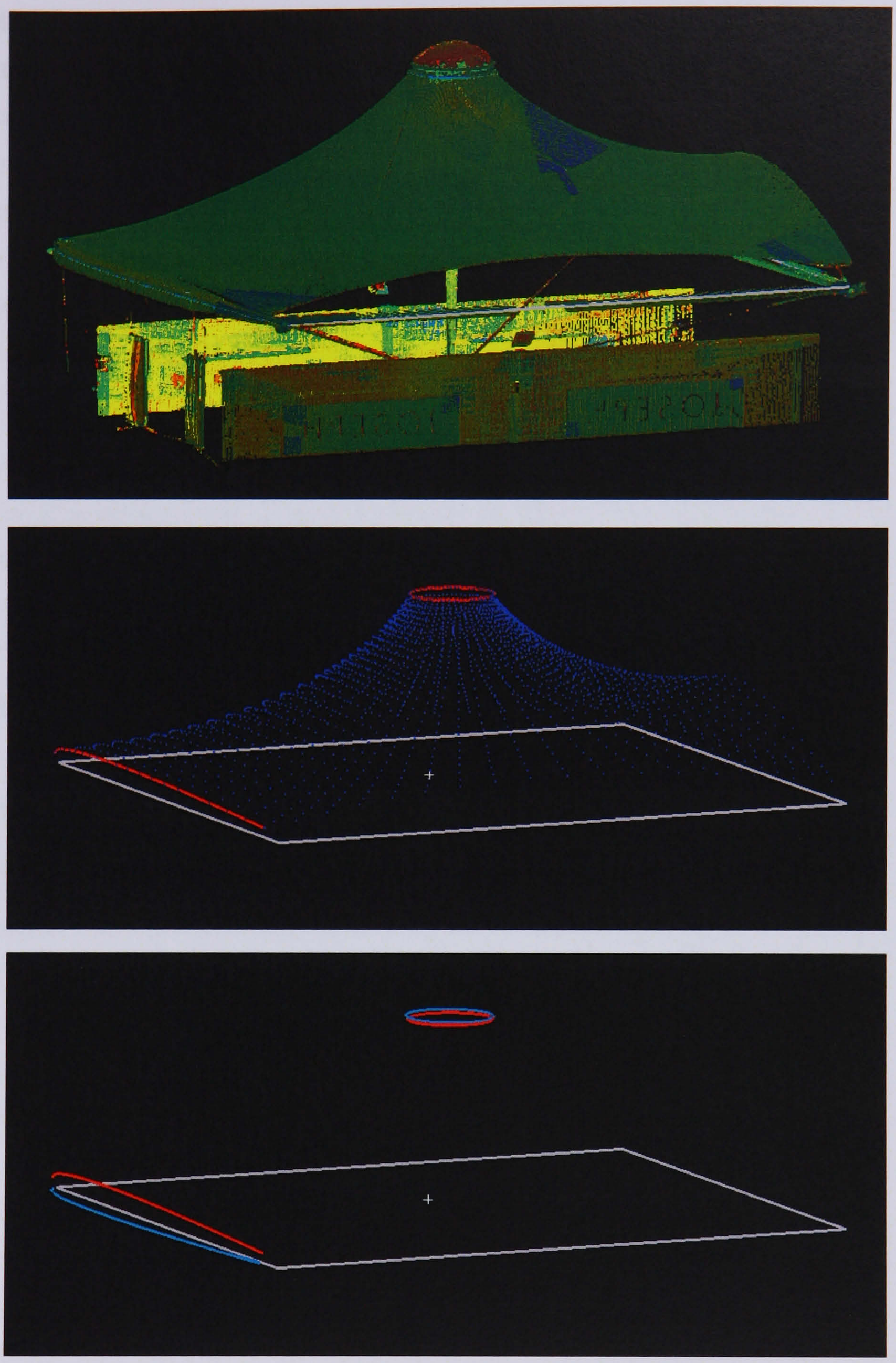


Figure 5-25: The reference steelwork (gray frame), arch steelwork and top ring extracted from the TLS model (top), transformed mathematical model (middle), and the resulting discrepancies between them (bottom).

5.3.4 Discussion

5.3.4.1 Terrestrial Laser Scanning

Terrestrial laser scanning was introduced to produce the as-built model of the membrane

structure in the static surface comparison scheme. The employment of Leica HDS2500 and HDS3000 laser scanning systems demonstrated the capability of producing 3D models of the membrane structures. However, due to different specifications of the laser scanners, the scanner network was different and consequently the working efficiencies varied. As mentioned in Section 5.3.2.1 less scanning stations were needed to cover the entire membrane roof surface and the detailed supporting steelworks when a Leica HDS3000 laser scanner was used. Thereby the procedures for data collection and post-processing were more effective, improving the overall efficiency.

Whilst scanning control features at the test site, it was occasionally found that points with weak reflectance were scanned. This was mainly affected by the distance, the angle of the incident beam and the properties of the surface (Schulz and Ingensand, 2004b). As the strength of the reflectance is associated with the accuracy of distance measurement, it is important to select objects with strong reflectance in the task of control points scanning.

5.3.4.2 Static Surface Comparison

The surface matching algorithm used in this scheme applied the principle of minimising the vertical differences between two surfaces. As a result it was realised that the match was in agreement with this principle as the mean value of computed residuals was 0.000 m. In order to minimise differences, however, the more extreme (but genuine) differences between the two surfaces have been treated as gross errors and removed during the matching process (Pilgrim, 1996), causing the real differences to be counterweighted improperly once the matching was converged. This was observed at areas (a) and (b) shown on the profiles in Figure 5-17 and Figure 5-21. In the latter the actual height of the finished structure at area (a) was around 0.2 m lower than that of designed model, and the finished structure was 0.5 m higher at area (b). Nevertheless using the surface matching algorithm, for minimising the vertical differences, the value at area (a) was raised to 0.3 m but at area (b) it was reduced to 0.3 m (Figure 5-17), demonstrating the real differences have been wrongly compensated during matching.

It was also realised that the symmetrical occurrence of the discrepancies over the observed surface was similar across the two approaches even though the solved differences varied. Therefore, the surface matching algorithm remained a useful approach for initially understanding the discrepancy that existed between two surface models under the circumstances that common points were unavailable.

5.3.5 Summary: Static Surface Modelling

Following the proposed methodology, the discrepancy of the fabric membrane roof between the designed mathematical model and the as-built structure model is determined by surface comparison. The differences that occurred across the surface can be investigated through the MS^2 software. For the membrane structure of Tent Type 1 observed in this chapter, the derived discrepancies mainly result from the incorrect erection of supporting steelwork. From the perspective of structural engineers, in order to avoid failures, more regular and rigid examinations should be carried out during construction. Moreover, since the error values of the steelwork locations are known, they can be re-introduced into the design stage to produce a new mathematical model of the fabric membrane. By comparing the new designed membrane roof with the acquired laser scanned model, the appropriateness of the design work can be reviewed. In summary, the proposed methodology is of significant value for understanding the characteristics of the fabric membranes and further improving the design of membrane structures.

5.4 Dynamic Surface Modelling

5.4.1 On-site Methodology

For monitoring dynamic behaviour of the observed surface, two Oscar cameras, a Leica TCRA 1103 total station and a data projector were set up at the test site. A workflow, based on the one addressed in Section 3.3.4, was followed to undertake the non-contact control method and videogrammetric monitoring (Figure 5-26). The frame rate of the image sequences was varied at these two stages. Moreover, for good quality assurance and closing the loop, the non-contact control method is proposed as an option to perform again at the end of the procedure.

The two calibrated Oscar cameras (refer to Section 3.3.1.2 for detailed calibration), fitted with the 12 mm lenses and an adopted image size of 1088 pixels by 822 pixels, were used for videogrammetric data acquisition. In order to avoid the appearance of the cables and flying mast in the images and also consider the network geometry, the positions of cameras should be arranged carefully for covering the area of projection. The average camera-to-object distance was 9.4 m and the scale of the images was 1:800. Figure 5-27 demonstrates the two-camera configuration and the area where the dots pattern was projected onto. When the total station and the data projector were ready, the cameras were triggered by the signals sent by the pulse generator to collect image

sequences of the control laser footprints and the projected-dots. Afterwards the acquired imagery was input to MS^2 for measurement.

Due to the limited projection distance, it was found that the projection area was not able to cover the whole membrane roof (Figure 5-27). This indicated that the developed videogrammetric method was applicable for monitoring the movements of the specific area of the membrane roof surface, however, it was not an ideal solution for generating complete static surface model of the membrane roof.

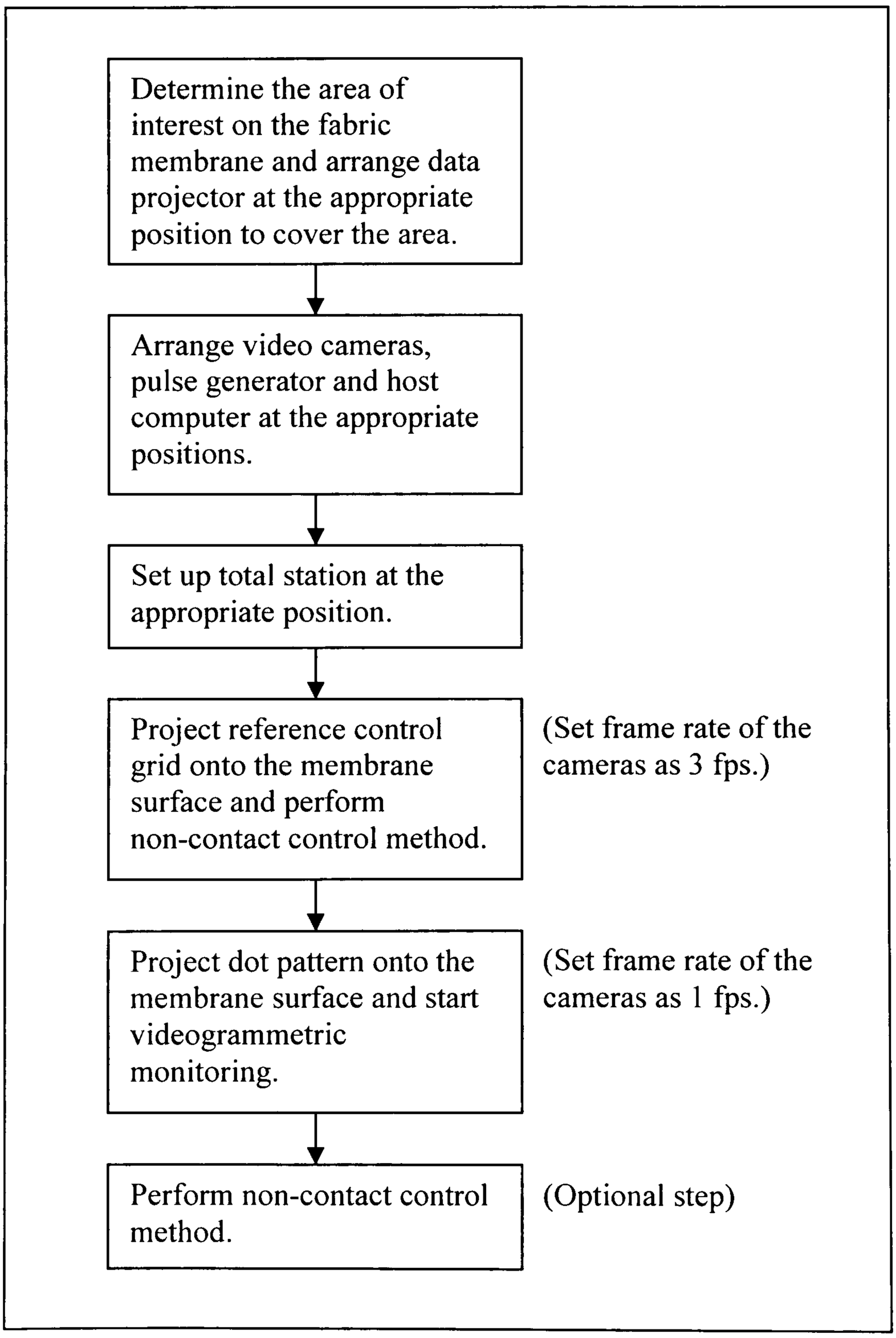


Figure 5-26: Workflow of on-site image acquisition.

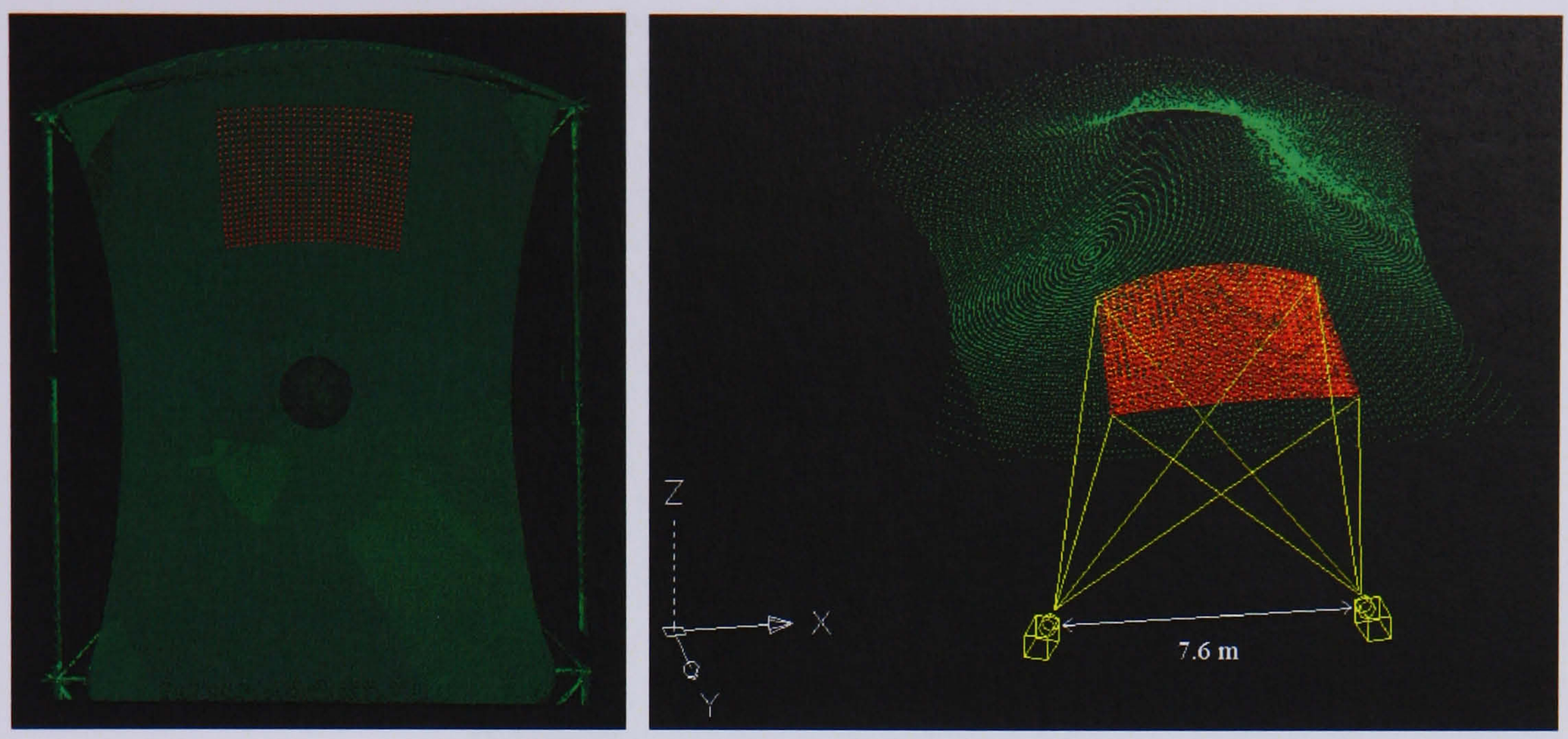


Figure 5-27: Laser scanned model (green points) and videogrammetric monitoring area (red points) on the observed membrane roof structure.

5.4.2 Data Processing – MS²

The measurement process was subsequently performed in the modules enclosed in MS², including Camera Orientation, Target Extraction, Target Referencing, Target Tracking and Target Modelling Modules. The computational sequence is illustrated in Figure 4–5.

5.4.2.1 Camera Orientation

During the implementation of non-contact control, a reference control grid was firstly projected onto the membrane surface for instructing the operator the proper positions for producing the control footprints. Then a total of 46 laser footprints were generated, which were recorded in 821 frames by each camera. Subsequently the images of complete laser footprints were produced (Figure 5-28), and the centres of footprints were extracted through the Camera Orientation Module (Figure 5-29) by applying the parameters listed in Table 5-6. From the left camera 40 laser footprints were extracted whilst 34 footprints were acquired in the right. Amongst them 18 correspondent footprints were matched and used for computing the exterior orientations of the two cameras (Table 5-7).

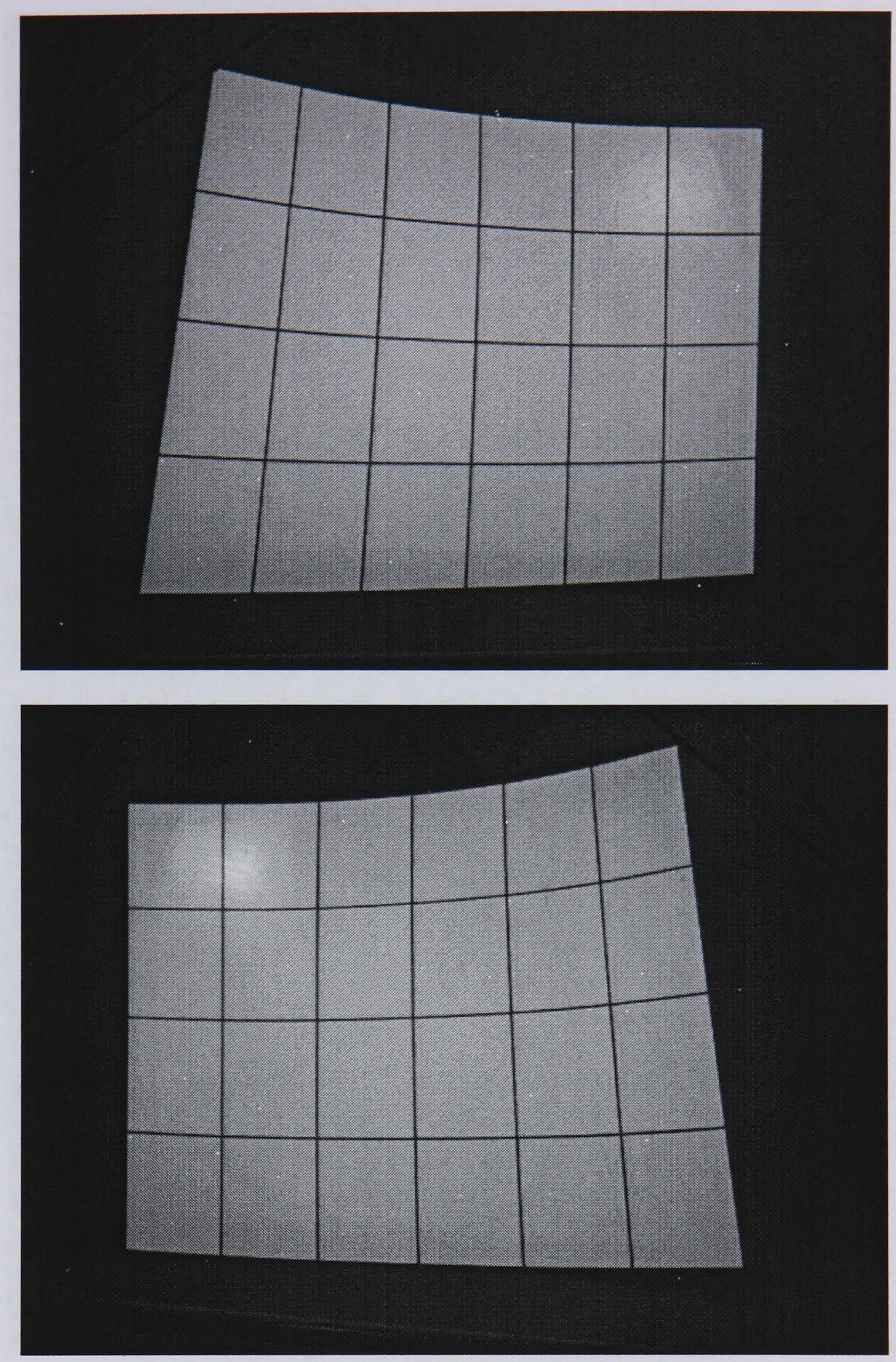


Figure 5-28: Stereopair of the complete control footprints (images being enhanced).

Camera Orientation	*Left*	*Number of frames*	821
		Normalised threshold value	0.3
	Right	*Number of frames*	821
		Normalised threshold value	0.2

Table 5-6: Input parameters for Camera Orientation Module.

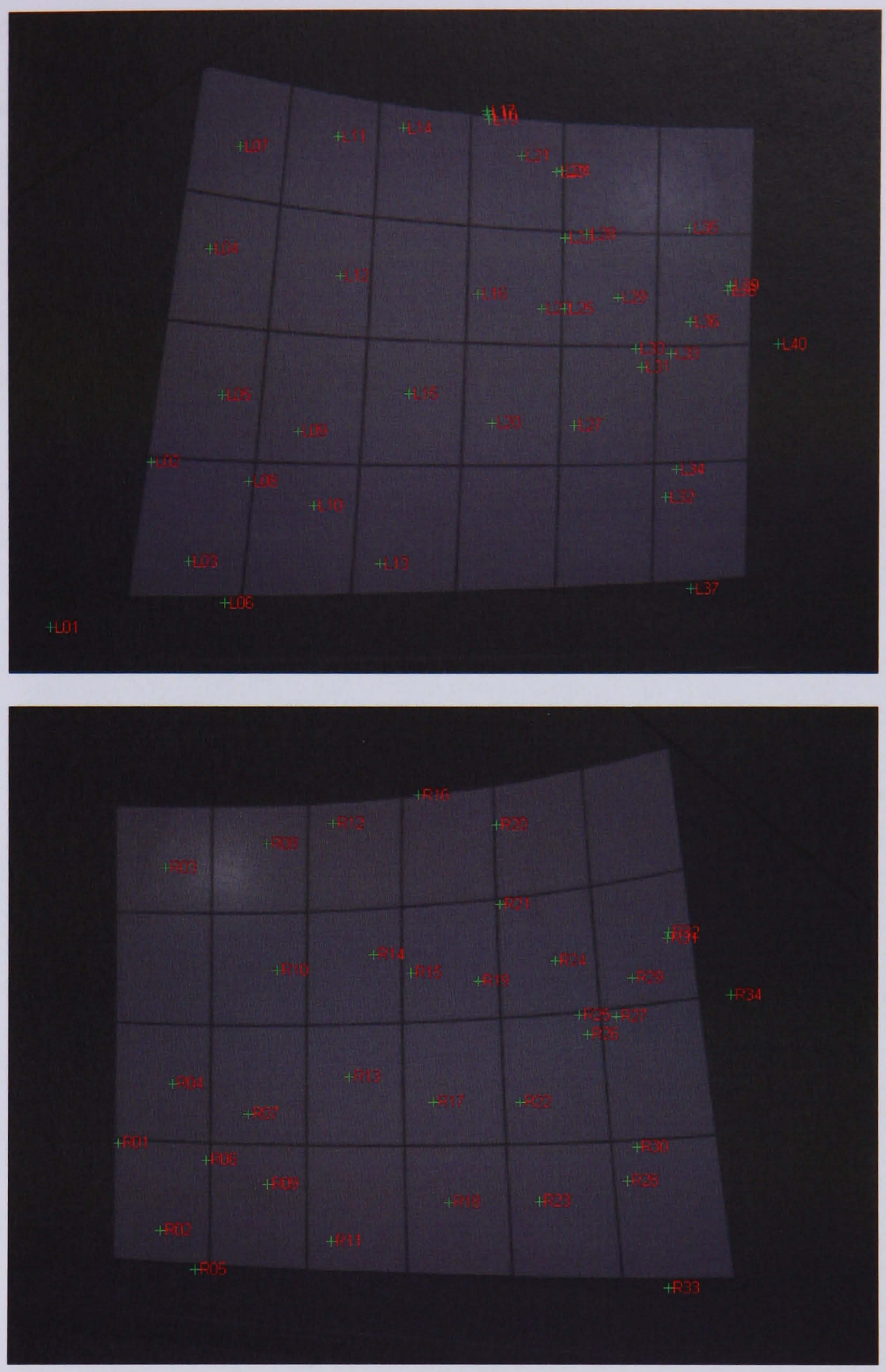


Figure 5-29: Stereopair of extracted control footprints.

	Left Exposure Station	*Right Exposure Station*
X (m)	95.655 ± 0.008	103.233 ± 0.008
Y (m)	112.661 ± 0.012	113.084 ± 0.012
Z (m)	10.682 ± 0.007	10.666 ± 0.007
ω (degrees)	157.999 ± 0.077	159.997 ± 0.077
ϕ (degrees)	-20.355 ± 0.048	20.546 ± 0.048
κ (degrees)	2.395 ± 0.031	-1.964 ± 0.031

Table 5-7: Orientation results for the static surface monitoring test.

5.4.2.2 Target Extraction

After the scanning of the control laser footprints, a dot pattern of 638 points was adopted as the targets for constructing the surface model and was projected onto the membrane surface. The stereopairs of 500 epochs were acquired during monitoring. The stereopair of the first epoch (Figure 5-30) was processed in the Target Extraction Module, by introducing the parameters listed in Table 5-8, to define the centres of points. The extracted targets are saved and indicated in Figure 5-31.

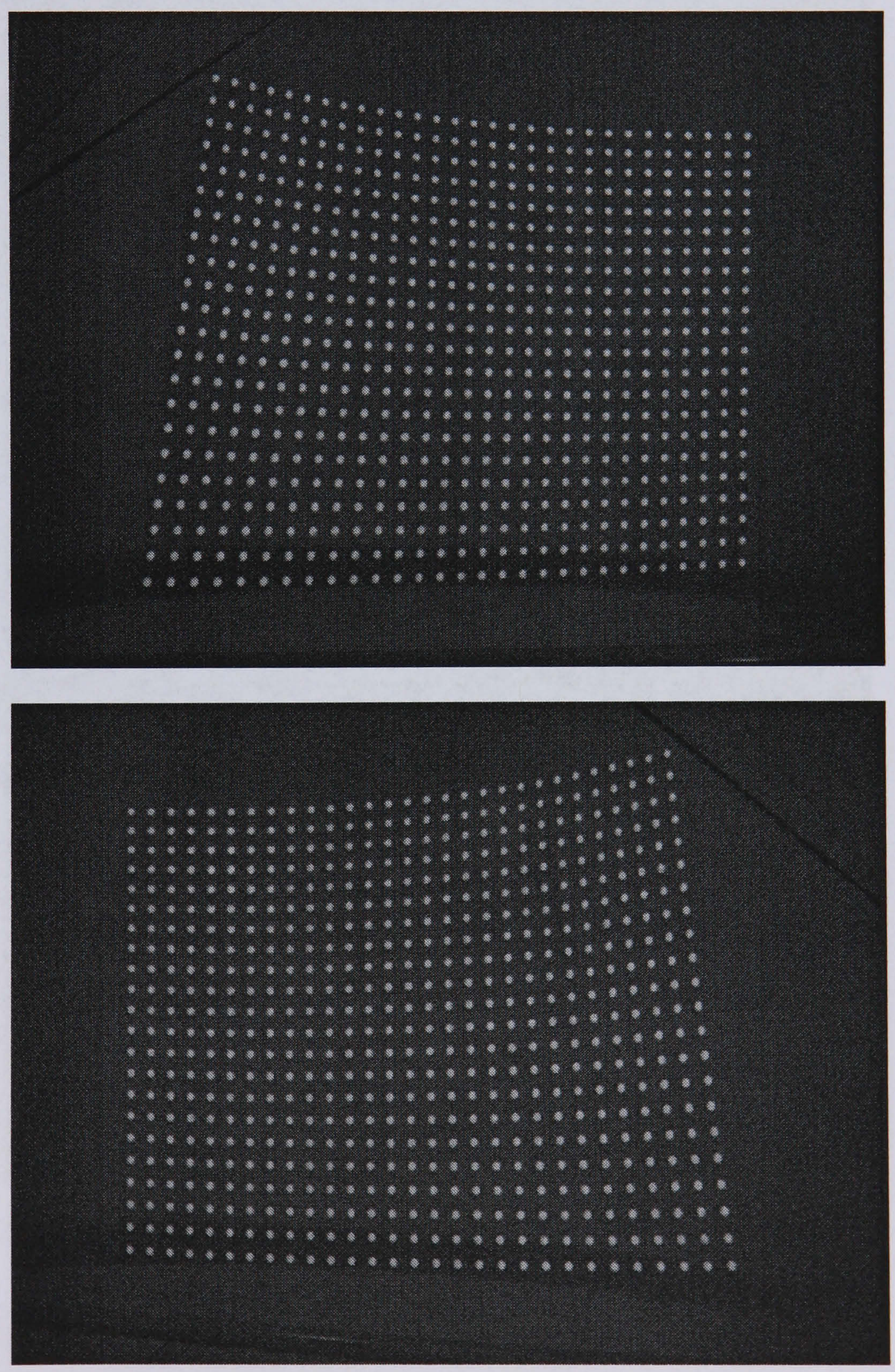


Figure 5-30: Stereopair of original projected targets at epoch 1.

Target Extraction	*Left/Right*	*Number of epochs*	500
		Normalised threshold value	0.05
		Noise size (pixels)	<4 and >200

Table 5-8: Input parameters for Target Extraction Module.

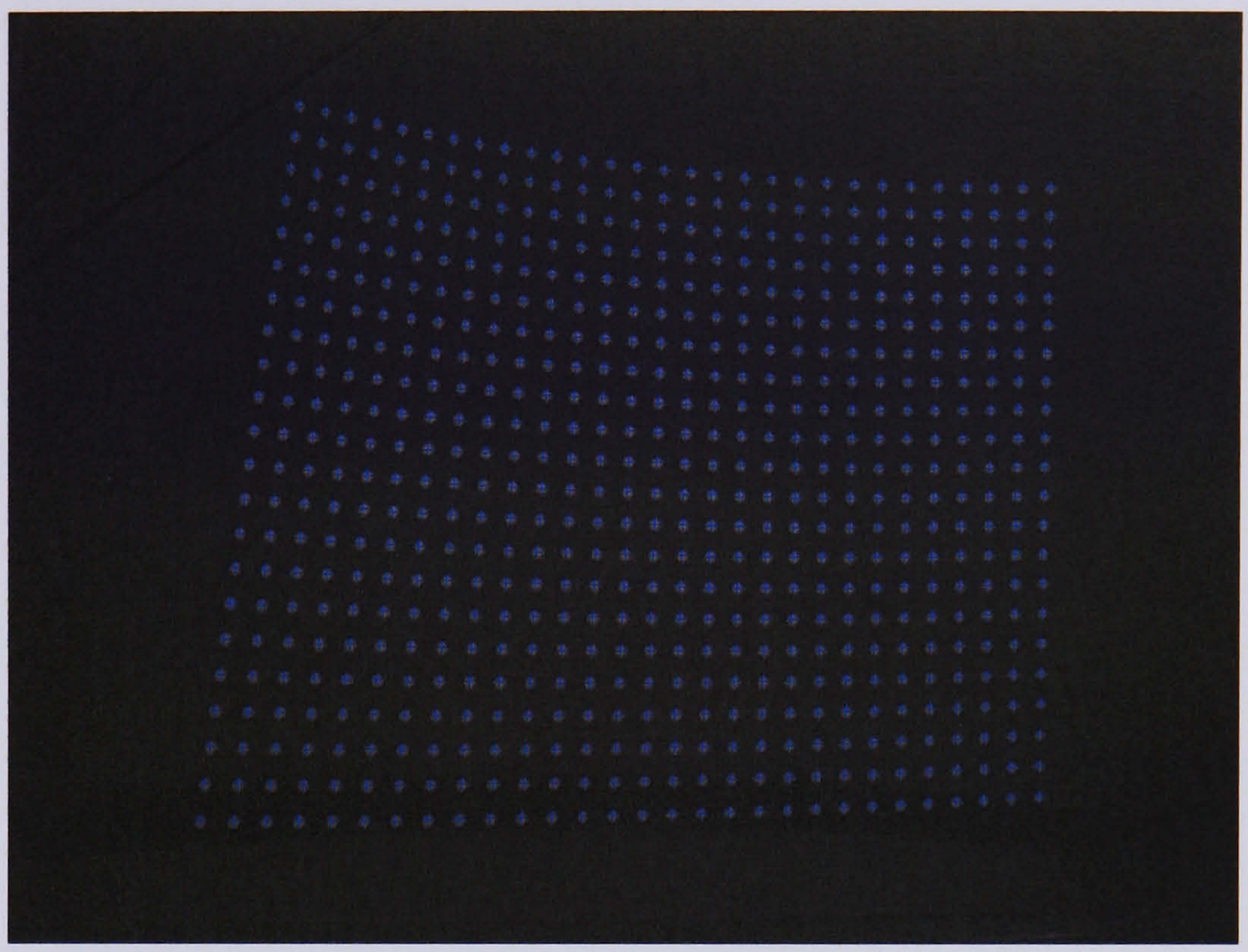


Figure 5-31: Stereopair of extracted projected targets at epoch 1.

At the next stage, the corresponding targets at the stereopair of the first epoch were matched and consequently the targets in the remaining stereopairs were tracked in the Target Referencing and Target Tracking Modules respectively. The required parameters are listed in Table 5-9.

Target Referencing	*Left/Right*	*Max X interval (pixels)*	5
		Max Y interval (pixels)	36
Target Tracking	*Left/Right*	*Max X tolerance (pixels)*	5
		Max Y tolerance (pixels)	5

Table 5-9: Input parameters for Target Referencing and Tracking Modules.

5.4.2.3 Targets Calculation

For high accuracy measurement, as Mikhail et al. (2001) suggested, self-calibrating bundle adjustment was performed at this stage. Once the adjustment was finished, the coordinates of projected targets shown at each epoch were solved and the resulting precisions derived from the calculation of bundle adjustment were 0.5 mm, 0.6 mm and 1.1 mm in X, Y and Z axes respectively. The overall precision (1.3 mm) was at the same level as the predicted precision of 1.5 mm.

Base Distance (m)	*Depth Distance (m)*	*Image Scale*	*Predicted Precision (mm)*				*Adjustment Precision (mm)*			
			σ_X	σ_Y	σ_Z	$\sigma_{Position}$	σ_X	σ_Y	σ_Z	$\sigma_{Position}$
7.6	9.4	1:800	0.6	0.9	1.0	1.5	0.5	0.6	1.1	1.3

Table 5-10: Results of the point measurement for the Type 1 membrane structure monitoring.

5.4.3 Results

5.4.3.1 Target Modelling

Since the coordinates of the projected-dots were solved, the point and meshed model of the observed surface could be produced in the Target Modelling Module (Figure 5-32).

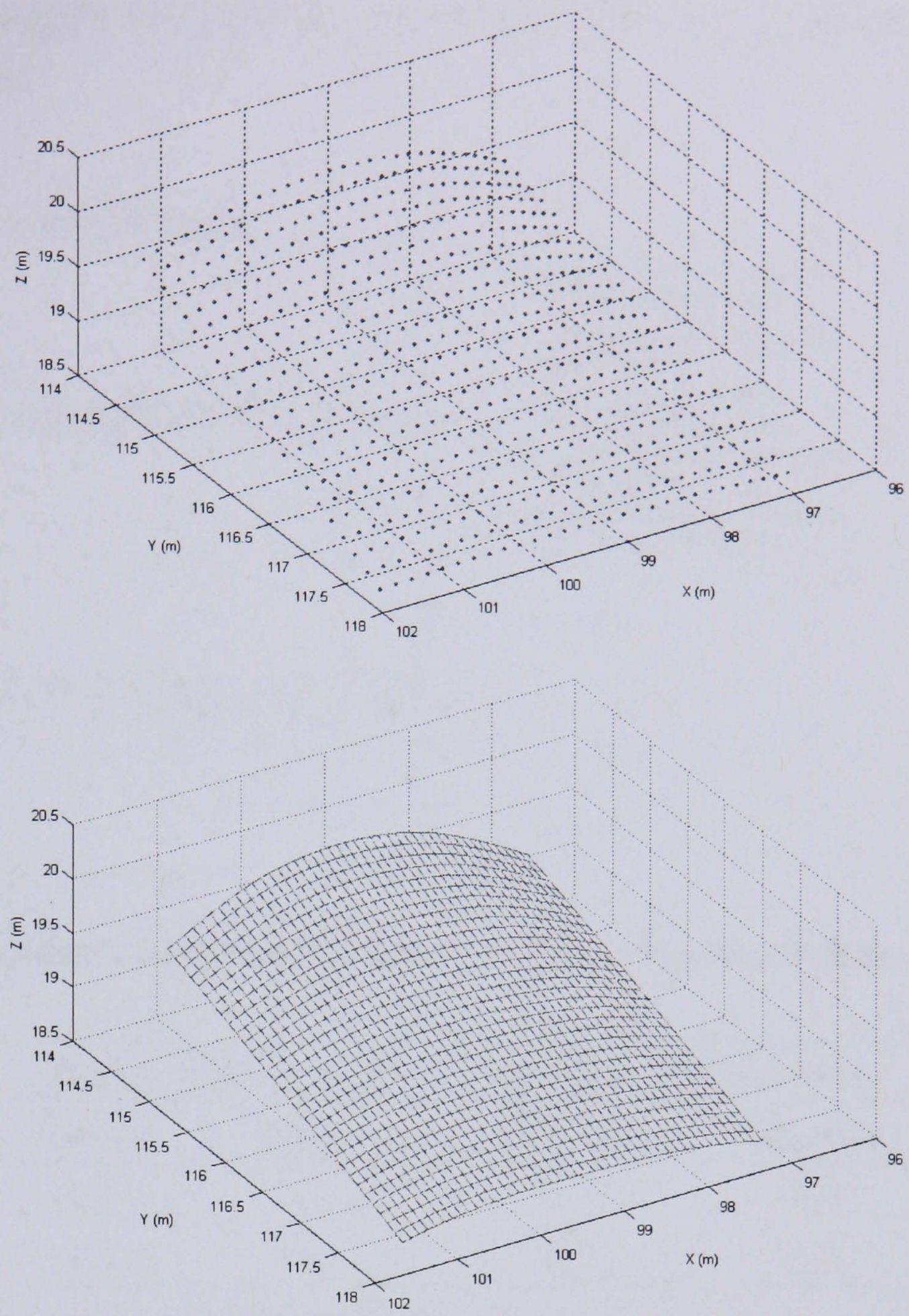


Figure 5-32: Point (top) and meshed (bottom) model of the observed surface.

5.4.3.2 Sequential Surface Analysis

In order to determine the displacement occurring through the whole monitoring sequence, the surface model at the first epoch was selected as the reference surface. The positive (points moving upwards) and negative (points moving downwards) movements were then computed relative to this. The resulting maximum and average displacements of each epoch occurred over the 500 epochs are shown in Figure 5-33 and Table 5-11. Although some evidence of movement could be observed, analysis showed the figures to be similar to those derived from the static surface modelling test (Section 4.4.2), with the maximum positive and negative displacements of 6.3 and -6.2 mm being of the same order of magnitude of the minimum movement that could be inspected using the system. This indicated that there was no unexpected movement being observed by the videogrammetric monitoring system. As the weather conditions were good on the day the experiment was conducted this result, in which the observed displacements in the

sequential surface model were largely insignificant, was as expected for a membrane structure in serviceable condition.

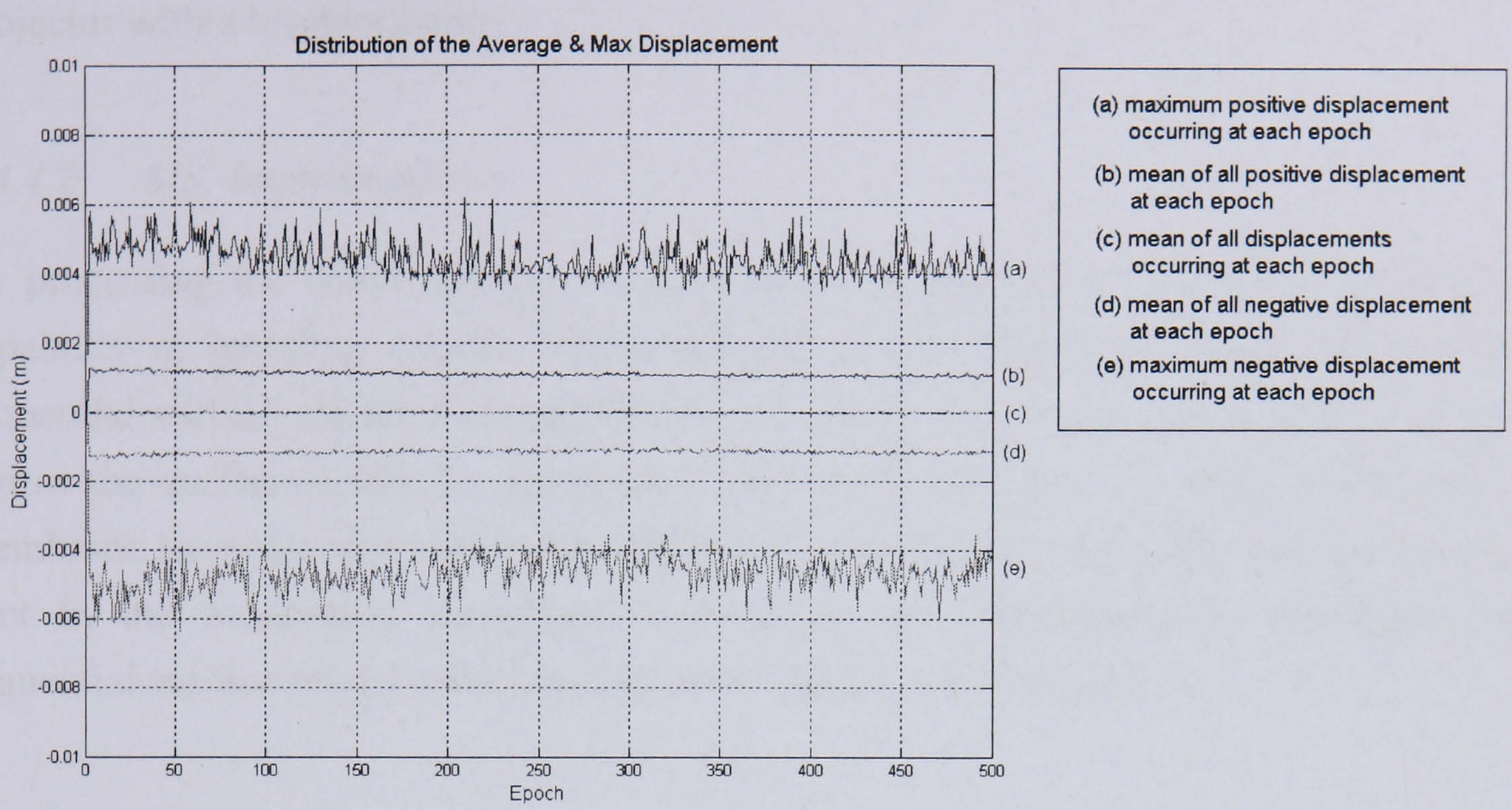


Figure 5-33: Resulting displacement for the observations on the fabric membrane.

	Average Displacement		*Maximum Displacement*	
	Positive	*Negative*	*Positive*	*Negative*
Mean (mm)	1.2	-1.1	4.7	-4.4
Max (mm)	1.4	-1.3	6.3	-6.2

Table 5-11: Solved displacement for the membrane structure monitoring.

5.4.4 Discussion

5.4.4.1 Non-contact Targeting Methods

During the videogrammetric monitoring described, non-contact targeting methods were adopted to produce the laser footprints for control and also the projected-dots for surface modelling. The former task was originally proposed to be automatically executed through the inbuilt face scanning program in the total station, however this function failed when performing at the test site. Manual operation was therefore introduced in producing the laser footprints. In order to have redundant control laser footprints and also ensure the footprints distributed evenly across the observed area, the reference control grid was projected onto the area observed at the implementation of non-contact control.

The other consideration relates to the execution of projected-dot videogrammetry. The shooting of projected-dots took place at night due to the use of a relatively low powered data projector, although this limitation could potentially be overcome by using a projector with a brighter lamp.

5.4.4.2 MS² Implementation

By processing the video imagery obtained from the fieldwork, MS^2 demonstrated the capability of handling overall videogrammetric computations. Through the resulting sequential surface model, the magnitudes and positions of displacements that occurred across the surface could be determined over time. As the roof of the Tent Type 1 membrane structure was seen to be stable during the monitoring, only 500 epochs were shot in the monitoring campaign. Accordingly, the displacements throughout the sequential surface model solved by MS^2 were largely insignificant.

5.4.4.3 Videogrammetric Measurement Performance

To achieve advanced measurement performance in photogrammetric applications of static object modelling, one camera is usually used to capture images of the object in redundant different positions and angles. However, in most dynamic surface monitoring tasks, as the images need to be taken simultaneously, the cameras have to be arranged in fixed positions during the monitoring period. Therefore the number of cameras adopted becomes a factor mainly affecting the measurement precision. In the videogrammetric monitoring system described, two CCD video cameras were used. Based on the camera network employed and image measurement precision, the precision derived from the Type 1 membrane structure monitoring schemes was 1.3 mm in object space. Such results are adequate for the membrane roof structure monitoring task, but could be improved by deploying more cameras in a stronger network configuration. For example the precision could be expected to improve to 0.6 mm if one more camera was adopted (Fraser, 2001). However accompanying issues such as image storage space and processing efficiency, but primarily cost, would also need to be considered. The final solution would be a compromise between required precision, processing time and budget limitations.

5.4.5 Summary: Dynamic Surface Modelling

In accordance with the feasibility demonstrated under laboratory conditions, the Oscar cameras also proved practicable in recording laser footprints and projected-dots at the

real test site. The videogrammetric tasks including Camera Orientation, Target Extraction, Referencing, Tracking and Calculation were performed successfully in the developed software package MS^2. When the processing was finished, the sequential surface model was determined and it was revealed that no unexpected movements had occurred over the monitoring period.

5.5 Chapter Summary

5.5.1 Summary of Findings

The proposed methodology adopts terrestrial laser scanning and videogrammetry to observe the real membrane structure at a test site. To accommodate the constraints in the working environment, some modifications were implemented during data collection. The physical model of the membrane structure and dynamic model of the fabric membrane were obtained. By inspecting the results derived from MS^2, the findings of the observed Tent Type 1 membrane structure were listed below.

- Two approaches were adopted in the static surface comparison scheme and different results were derived. As the employment of the physical control points, the 3D conformal transformation is treated as the more robust method for determining the true disparities between the designed mathematical model and the as-built membrane structure.

- Disparities between the designed mathematical model and the as-built Type 1 membrane structure existed, in which the differences varied between 0.288 m to 0.445 m. The deformation of the membrane roof resulted from the wrong arrangement of the supporting steelworks at the construction stage.

- The non-contacting control methods, videogrammetric monitoring system and the MS^2 software package worked successfully for determining the dynamic behaviour of the fabric membrane, although no unanticipated displacements occurred in the observed area of the membrane roof of Tent Type 1.

- The laser scanned model was generated under the same coordinate system as the videogrammetric surface. The combination of both models could provide a useful tool for understanding the areas that displacements occurred across the membrane

surface (Figure 5-27).

5.5.2 Concluding Remarks

Based on the results derived from static surface comparison, structural engineers are now able to better understand differences that exist between the designed mathematical model and the finished structure model. The surface comparison also allowed the cause of the disparities to be further investigated. Subsequently, the dynamic behaviour of the fabric membrane could be investigated through the sequential surface model. The surface movements of the area of interest are highlighted to identify the displacements which are over tolerance values.

Since the conclusive on-site methodology has been determined in this chapter, further surveying would be conducted to observe different types of membrane structures, testing the transferability of the monitoring system.

CHAPTER SIX

DALTON PARK MONITORING SCHEME – TRANSFERABILITY ASSESSMENT

6.1 Introduction

Considering the constraints in the working environment, the on-site methodology was established and outlined in the previous chapter. By applying the proposed methodology, a membrane structure of Tent Type 1 was observed. The disparities between the as-built structure and its designed mathematical model were determined, in addition to the displacements of the observed fabric membrane. In order to prove the transferability of the monitoring system, a static surface comparison and dynamic surface modelling have been performed in two different types of membrane structures.

6.2 Type 2 Membrane Structure

6.2.1 Background

The first roof observed in this chapter was a Tent Type 2 membrane structure (Figure 6-1). The line of canopies of Tent Type 2 is 50 m long by 18 m wide and consists of four linked conics. The construction components were similar to the Type 1 with the exception of the flying mast design. In the Type 1 membrane structure the flying mast was propped up vertically, while it was inclined in the Type 2 structure (Figure 6-2). The location of the structure is indicated in Figure 6-1 and its individual dimensions were 12 m by 18 m in plan, with the highest point being approximately 12 m above ground level.

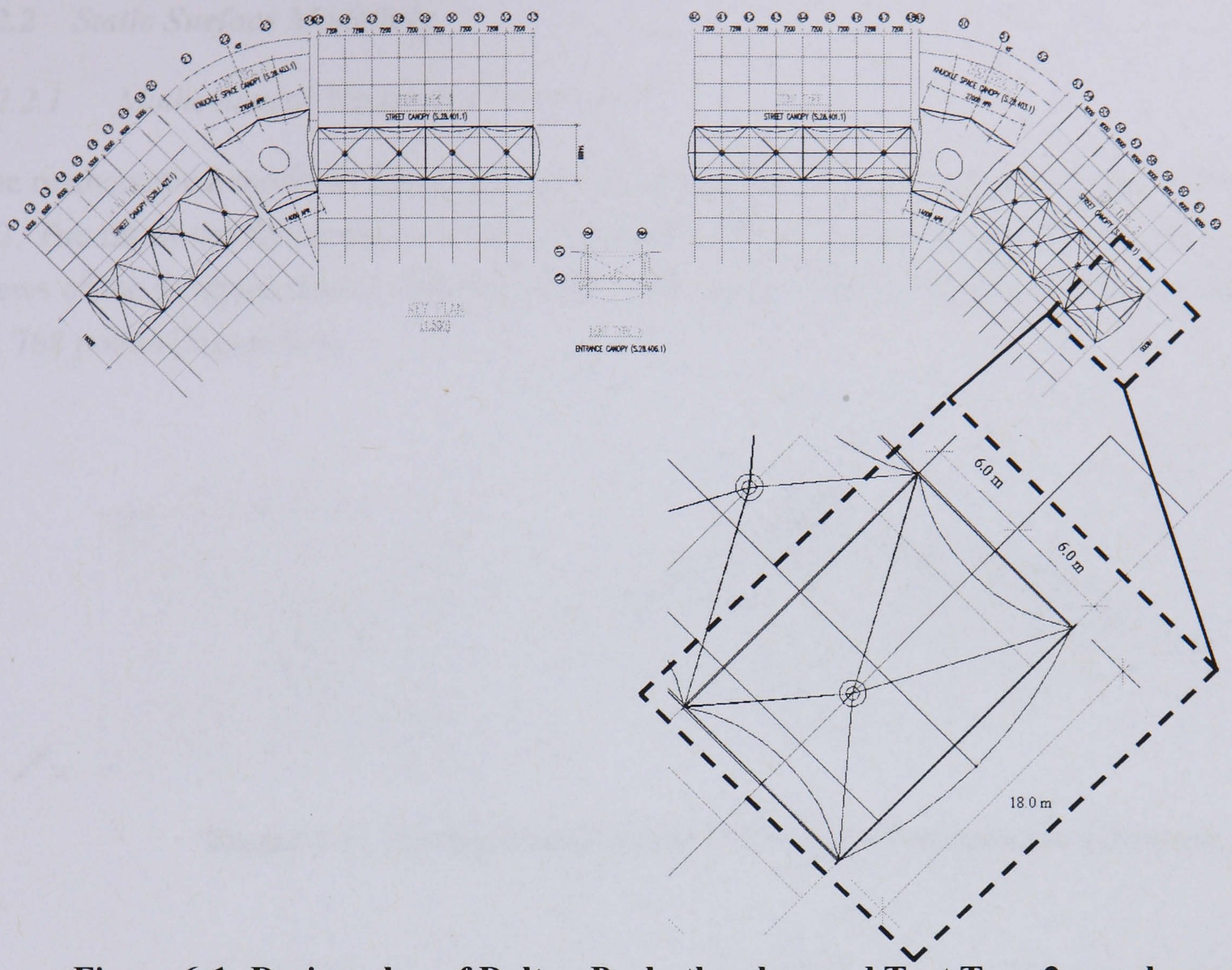


Figure 6-1: Design plan of Dalton Park, the observed Tent Type 2 membrane structure is outlined by the dashed line.



Figure 6-2: The Type 2 membrane structure.

6.2.2 Static Surface Modelling

6.2.2.1 Mathematical Model and TLS model

The mathematical model of the observed Type 2 membrane structure is shown in Figure 6-3. The tilt of the flying mast and the shape of the fabric membrane are evident in the views of the designed model. A point model of the fabric membrane was extracted with 12 768 points (Figure 6-4).

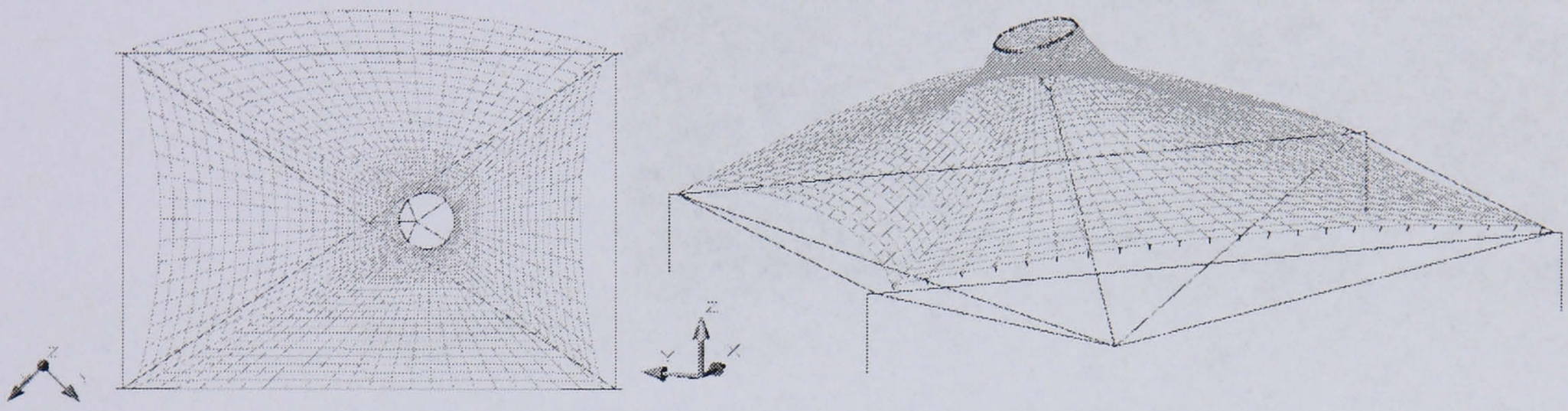


Figure 6-3: Mathematical model of the Type 2 membrane structure.

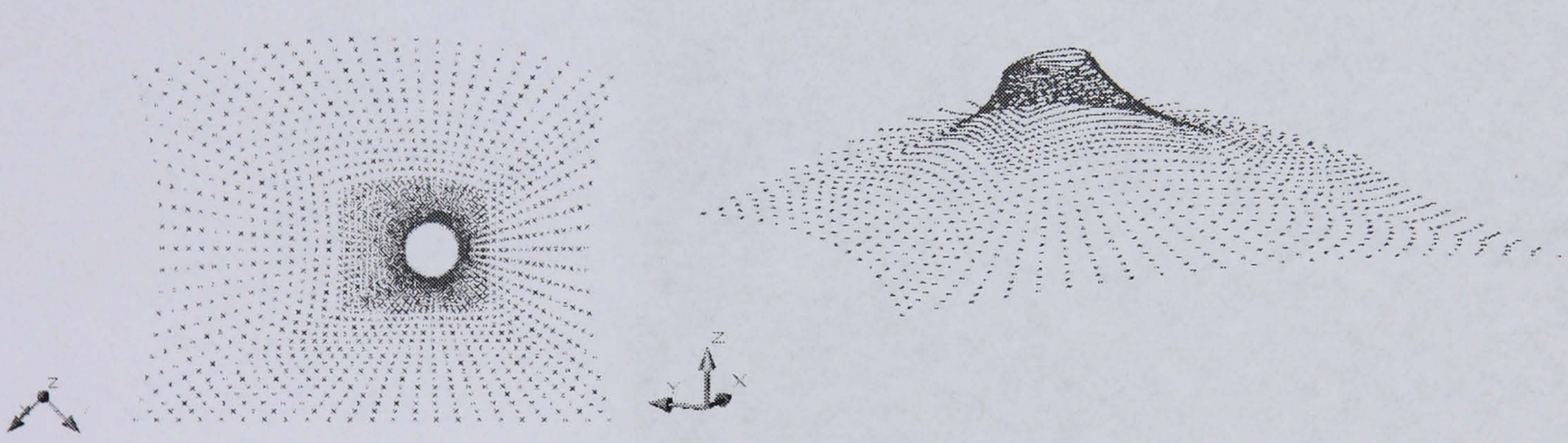


Figure 6-4: Point model of the Type 2 membrane structure.

During the data collection, Leica HDS2500 laser scanning system was adopted to acquire a physical model of the Type 2 membrane structure. Following the methodology proposed in Section 5.3.2.1, eight control points (Figure 6-5) were observed by a Leica TCRA1103 total station for model registration. Their coordinates were solved in a least squares estimation in the STAR*NET software, with an average standard deviation of 1.9 mm, 2.2 mm and 0.9 mm in the X, Y and Z axes respectively (one sigma). The scanning was performed from six positions, including four stations on the ground and two on a raised platform, to cover the complete canopy. The scanner network and resultant registered model of the membrane structure are shown in Figure 6-6. For performing surface comparison, the same part of the membrane roof as the one in mathematical model was extracted from laser scanned model (Figure 6-7). Additionally,

the point cloud of the supporting steelwork (Figure 6-8) was modelled to determine the control points used for a 3D conformal transformation.

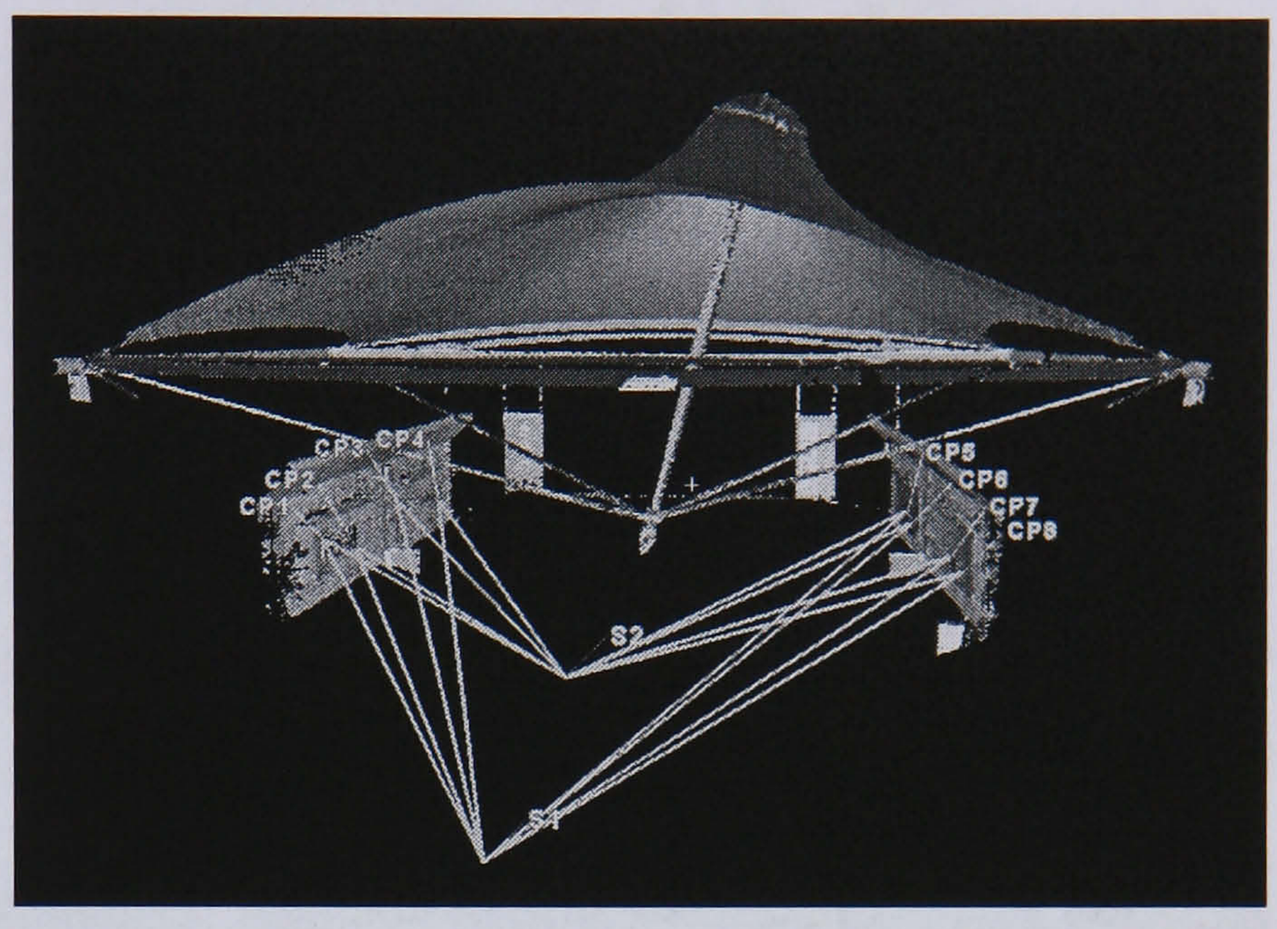


Figure 6-5: Control points (CP1 – CP8) for model registration.

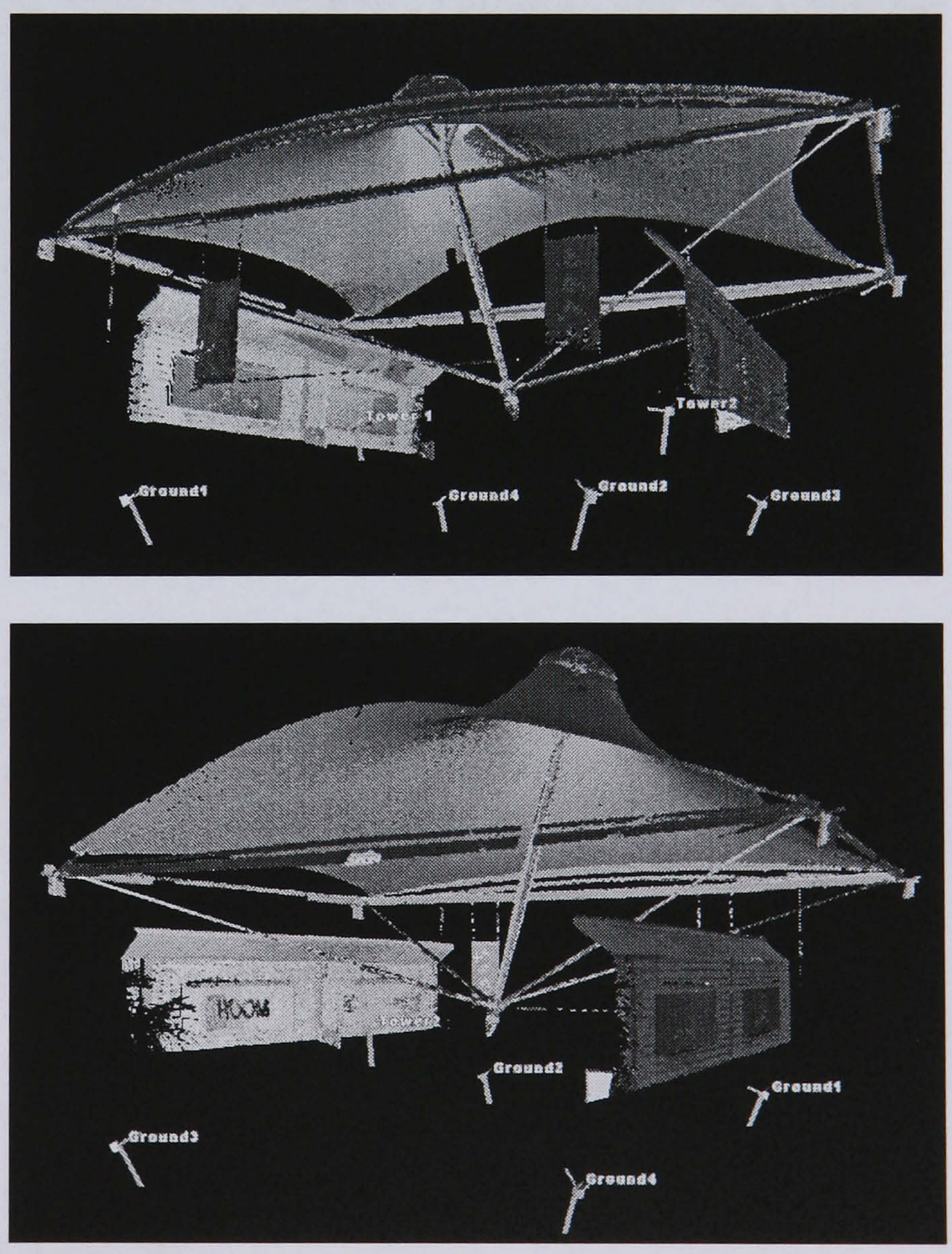


Figure 6-6: Scanner network and the resultant scanned model of the Type 2 membrane structure, the network includes four ground scanning stations (Ground 1 – 4) and two scan station on the platform (Tower 1 – 2).

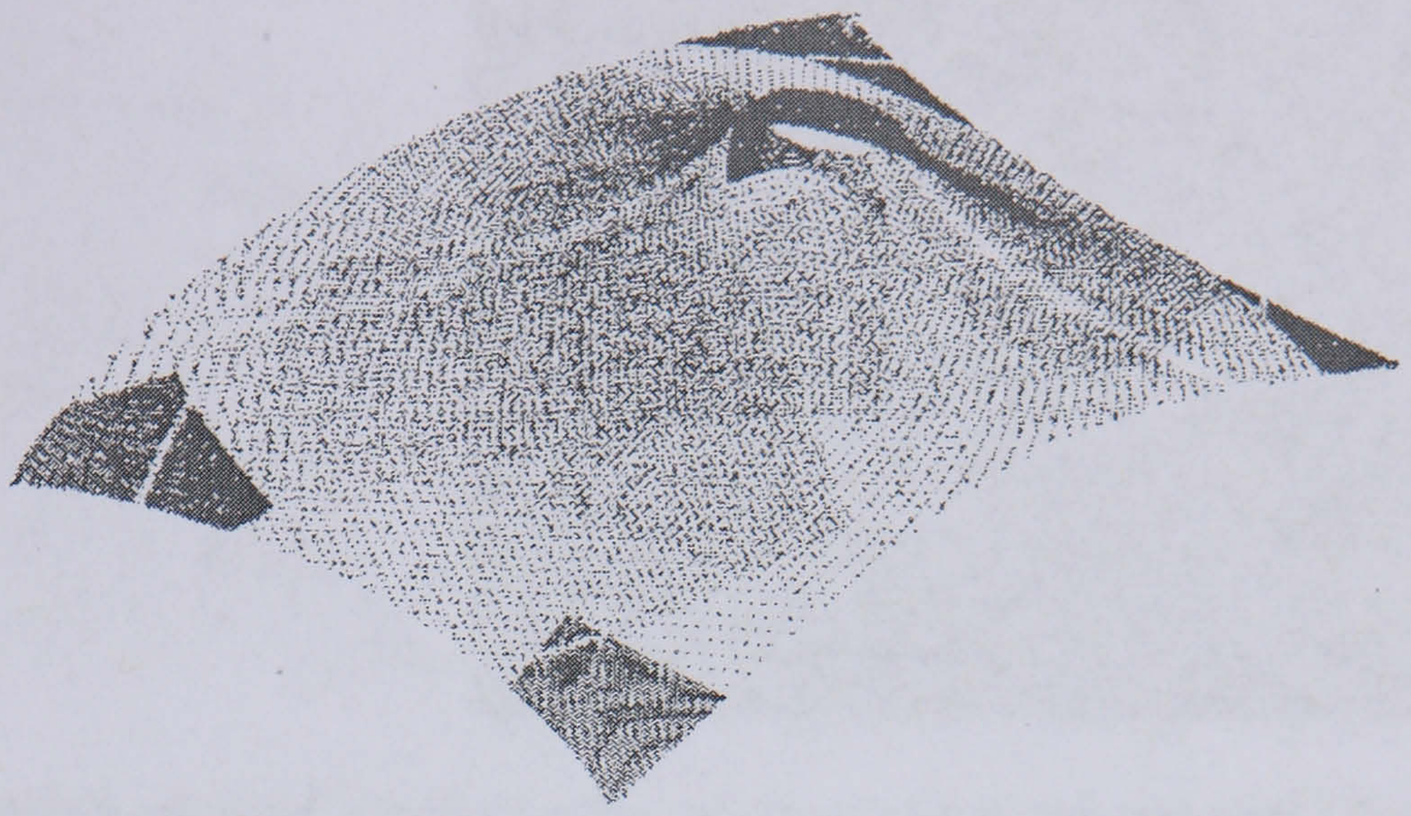


Figure 6-7: Fabric membrane roof extracted from laser scanned model for surface comparison.

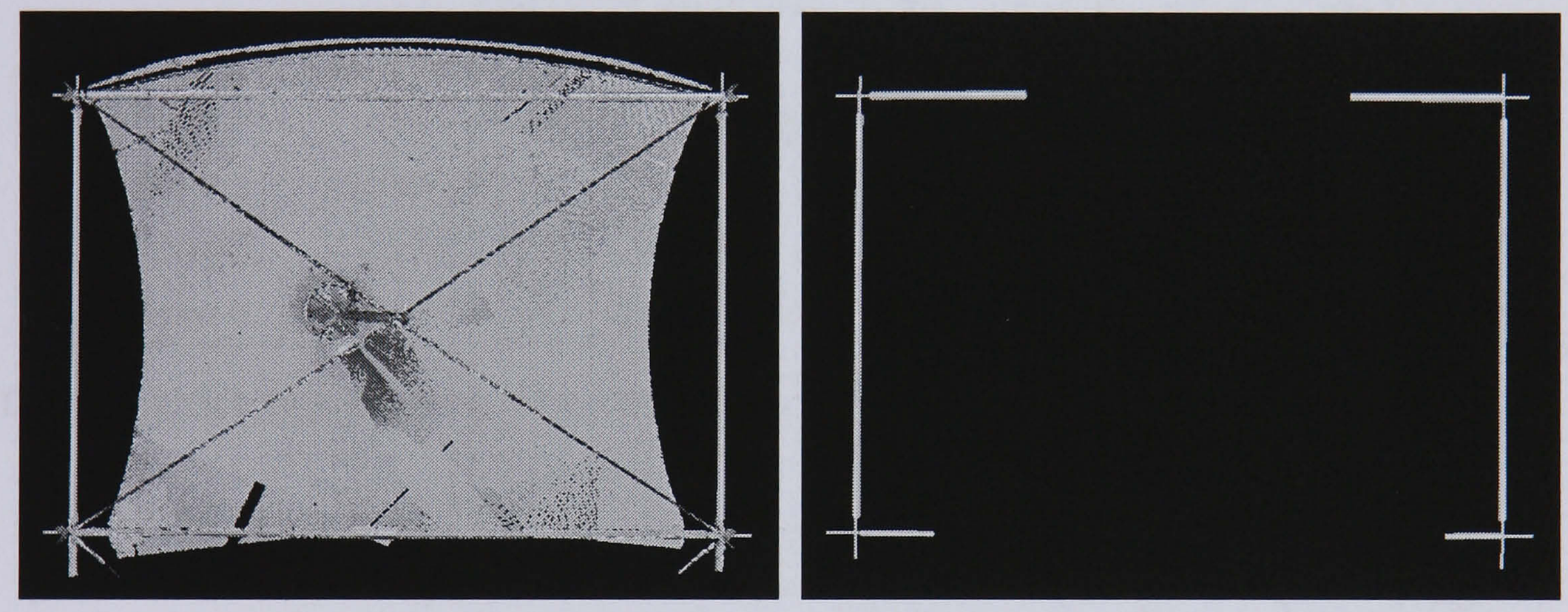


Figure 6-8: The modelled supporting steelwork and derived centre lines.

6.2.2.2 Surface Comparison

The mathematical model was compared against the laser scanned model to determine the disparities between the design model and finished building of the Type 2 membrane structure. As the two models were produced under different coordinate systems, four common control points were extracted (Figure 6-9 and Table 6-1) to perform a 3D conformal transformation, relating the mathematical model to the laser scanned model. The differences between the two surface models were then computed. The solved transformation parameters and comparison results are listed in Table 6-2. From the derived statistics, the discrepancies that existed between the two models were derived, the range of the differences reaching 0.435 m.

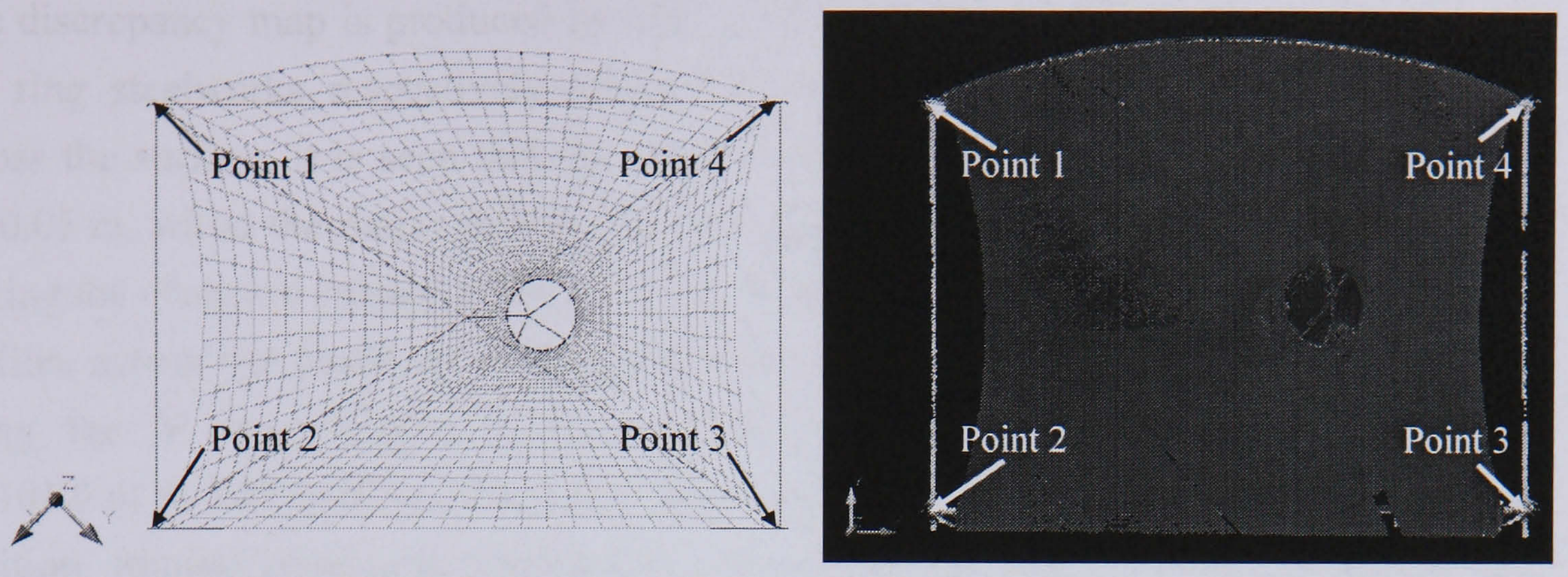


Figure 6-9: Four corresponding control points in the mathematical model and laser scanned model.

	Mathematical Model (mm)			*TLS Model (m)*		
	X_M	Y_M	Z_M	X_T	Y_T	Z_T
Point 1	1616196.17	255502.34	103150.00	93.612	103.440	17.684
Point 2	1624681.45	263987.62	103150.00	93.419	101.428	17.682
Point 3	1612278.80	276390.27	103150.00	110.971	101.160	17.672
Point 4	1603793.52	267904.99	103150.00	111.121	113.175	17.675

Table 6-1: 3D coordinates of corresponding control points in the mathematical and TLS model.

Transformation Parameters	*Translations (m)*	T_X	1075.418
		T_Y	1422.573
		T_Z	-85.738
	Rotations (°)	ω	0.012
		ϕ	0.031
		κ	-135.854
	Scale		0.001
Surface Disparity (m)	*Number of Points*		2361
	Maximum		0.345
	Minimum		-0.090
	Range		0.435
	Mean		0.075
	Std. deviation		0.104
	RMS		0.128

Table 6-2: Solved transformation parameters and surface comparison results.

The discrepancy map is produced by MS^2, in which area (a) and (b) were the arch and top ring steelworks respectively (Figure 6-10). By inspecting the rendered colours across the surface, it is seen that the major part of the area is within a discrepancy of +/- 0.05 m, while the major differences mainly occurred in area (c), which is the area linking the observed canopy to the next one. To further understand the discrepancies, the profiles across the positions of apparent disparities were extracted. From the profiles along the Y axis (Figure 6-11), obvious differences largely appeared between Y=101.0 m to 107.0 m, in which the laser scanned model is higher than its designed position. Similar results are detected in the profiles along the X axis, especially the profiles passed Y=105.0 m and 106.0m (Figure 6-12), demonstrating that the membrane roof of the finished structure is higher than the designed model.

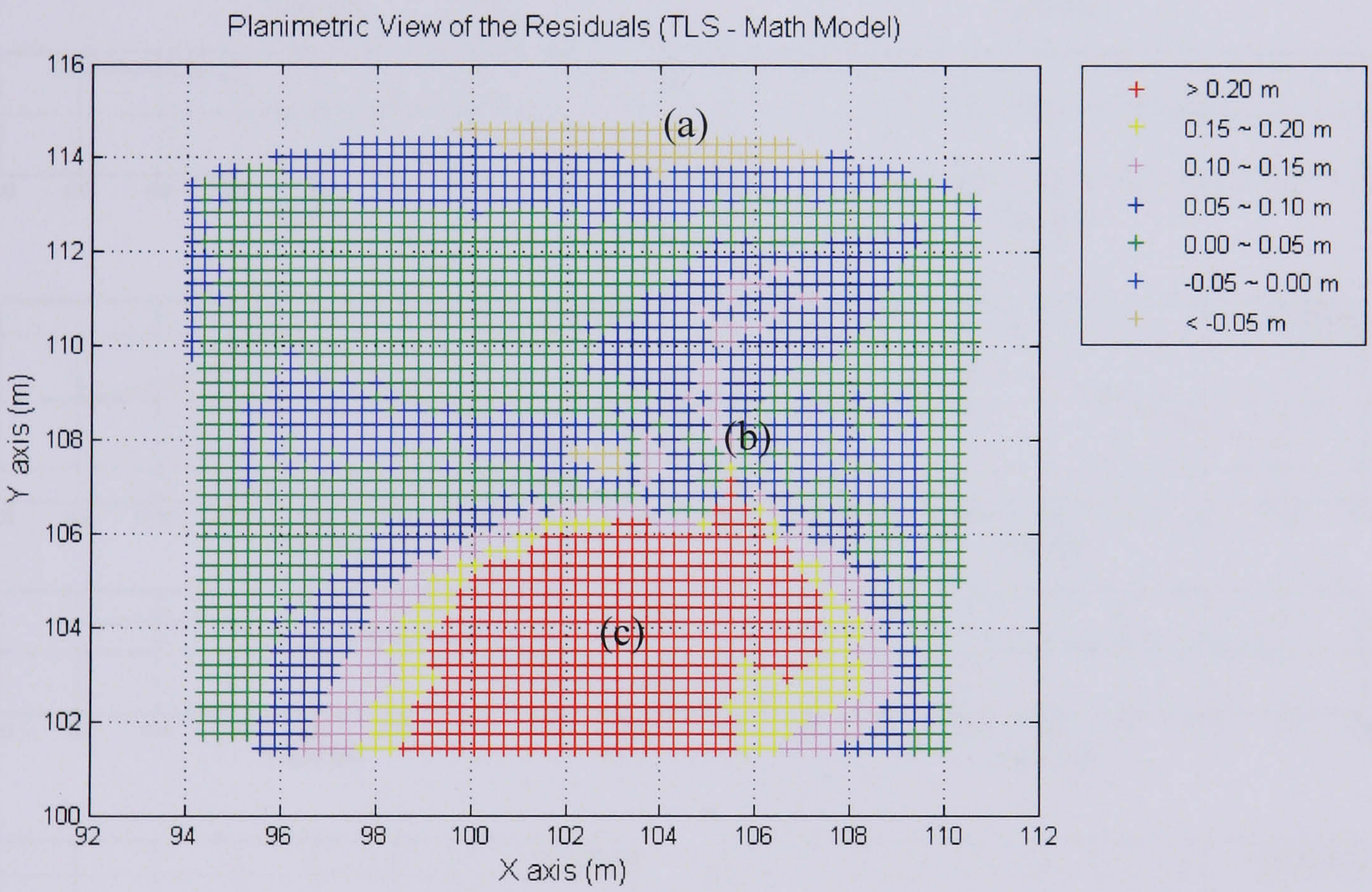


Figure 6-10: Discrepancy map derived from 3D conformal transformation.

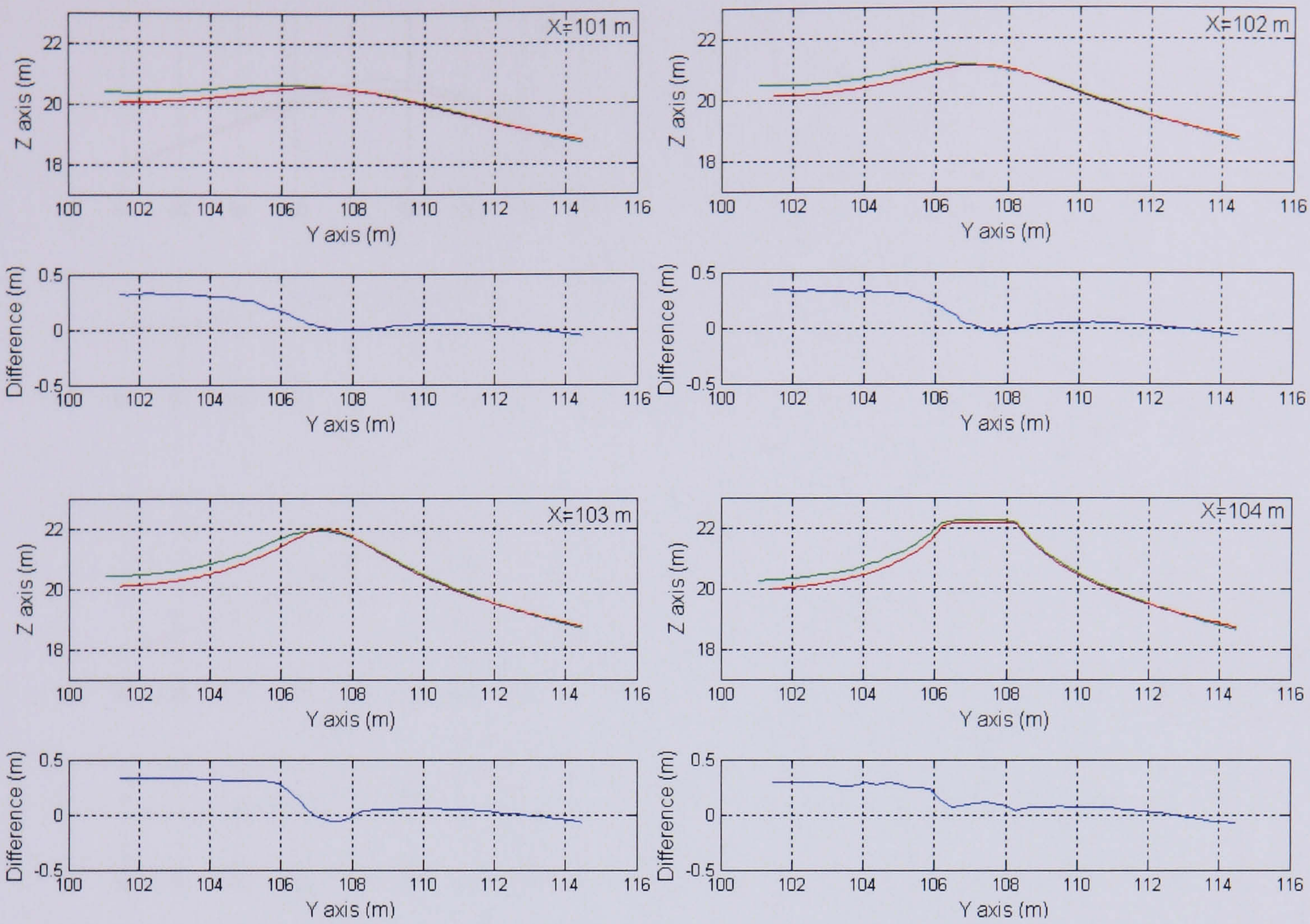


Figure 6-11: Differences in profiles along the Y axis between the two surface models (the green profile line is derived from the laser scanned model, and the red line represents the profile of the transformed mathematical model).

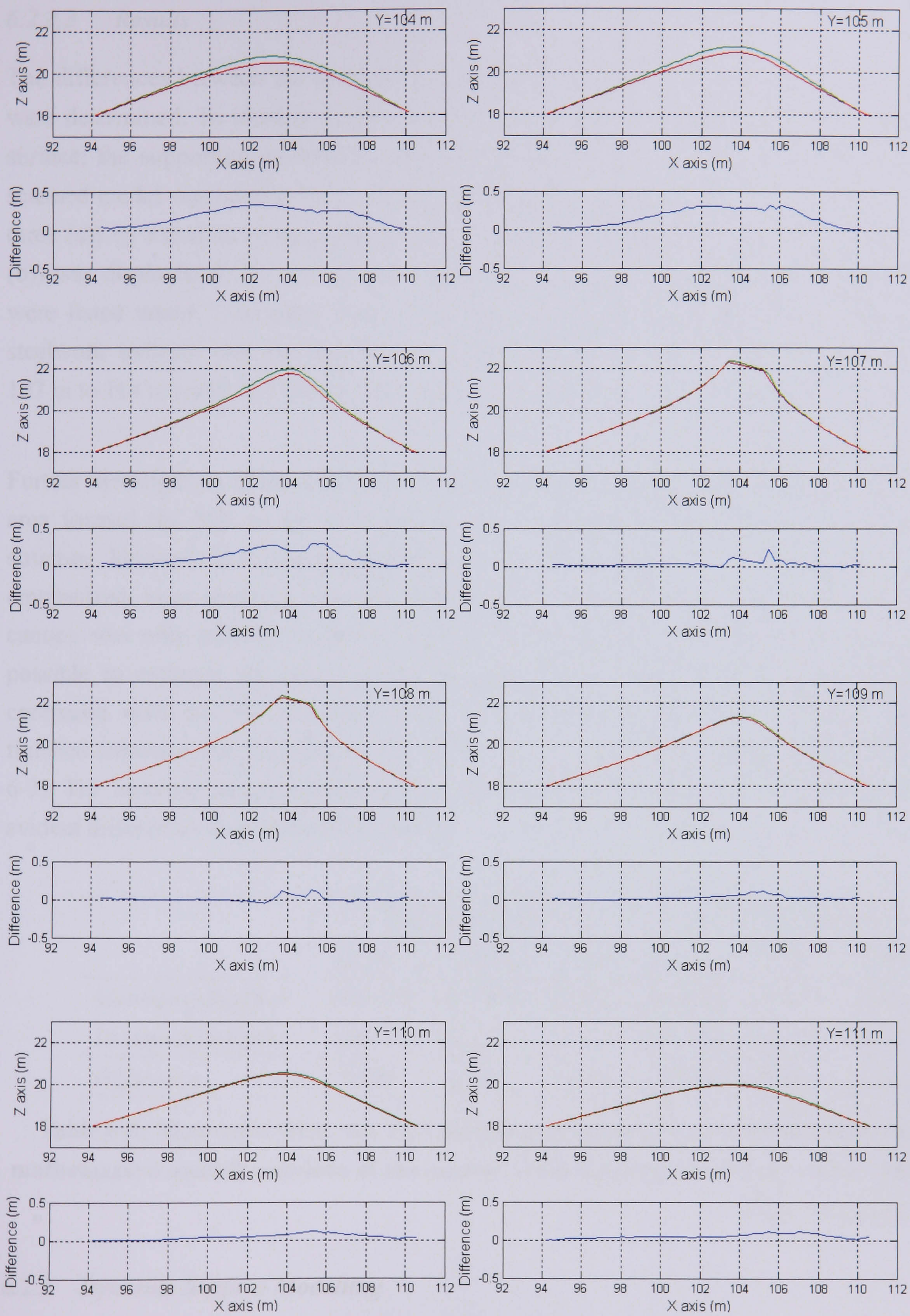


Figure 6-12: Differences in profiles along the X axis between the two surface models (the green profile line is derived from the laser scanned model, and the red line represents the profile of the transformed mathematical model).

6.2.2.3 Results

The differences between the designed model and the finished structure of Tent Type 2 were determined. To identify the factors causing the roof deformation on the observed surface, the supporting steelwork were firstly inspected. As a consequence, the laser scanned model was seen to be lower than the designed model along the arch steelwork (area (a)) by a maximum disparity of 0.051 m, whereas the centre of the top ring (area (b)) was displaced 0.101 m from the designed position (3D coordinates of the centres were listed under "The edge canopy" in Table 6-3). The construction errors of the steelwork indicate that the disparities occurred on the membrane roof between Y= 107 m to 114 m (refer to Figure 6-10), within a range of -0.1 m to +0.1 m.

Further investigation of the disparities occurring at area (c) has been conducted. As this area formed the link to the next canopy, the inspection was extended to the next structure. However in the monitoring campaign, as the edge canopy of Tent Type 2 was emphasized, laser scanning was mainly performed on this structure, while the linking canopy was only partially scanned. From the coarse point cloud derived, it was still possible to estimate the centre of the top ring of the linking canopy. It was then compared with the one extracted from the transformed mathematical model. The finished structure was calculated to be 0.259 m away from the designed model (Table 6-3). The incorrect raising arrangement of the flying mast and the top ring explain the evident differences that occurred at area (c).

	The edge canopy			*The linking canopy*		
	X (m)	*Y (m)*	*Z (m)*	*X (m)*	*Y (m)*	*Z (m)*
Measured position	104.459	107.279	22.224	99.980	95.334	22.431
Designed position	104.372	107.272	22.174	100.018	95.332	22.175
Difference	0.087	0.007	0.050	-0.038	0.002	0.256

Table 6-3: Measured (from the TLS model) and designed (from the transformed mathematical model) positions of the centres of the top ring steelworks at two Tent Type 2 canopies.

6.2.3 Dynamic Surface Modelling

6.2.3.1 Image Acquisition

By using the two Oscar cameras and following the methodology introduced in Section 5.4.1, video imagery of the control laser footprints and projected-dots were collected at

the test site (Figure 6-13). The camera configuration and the area observed were demonstrated in Figure 6-14.



Figure 6-13: Hardware configuration for Type 2 membrane structure monitoring.

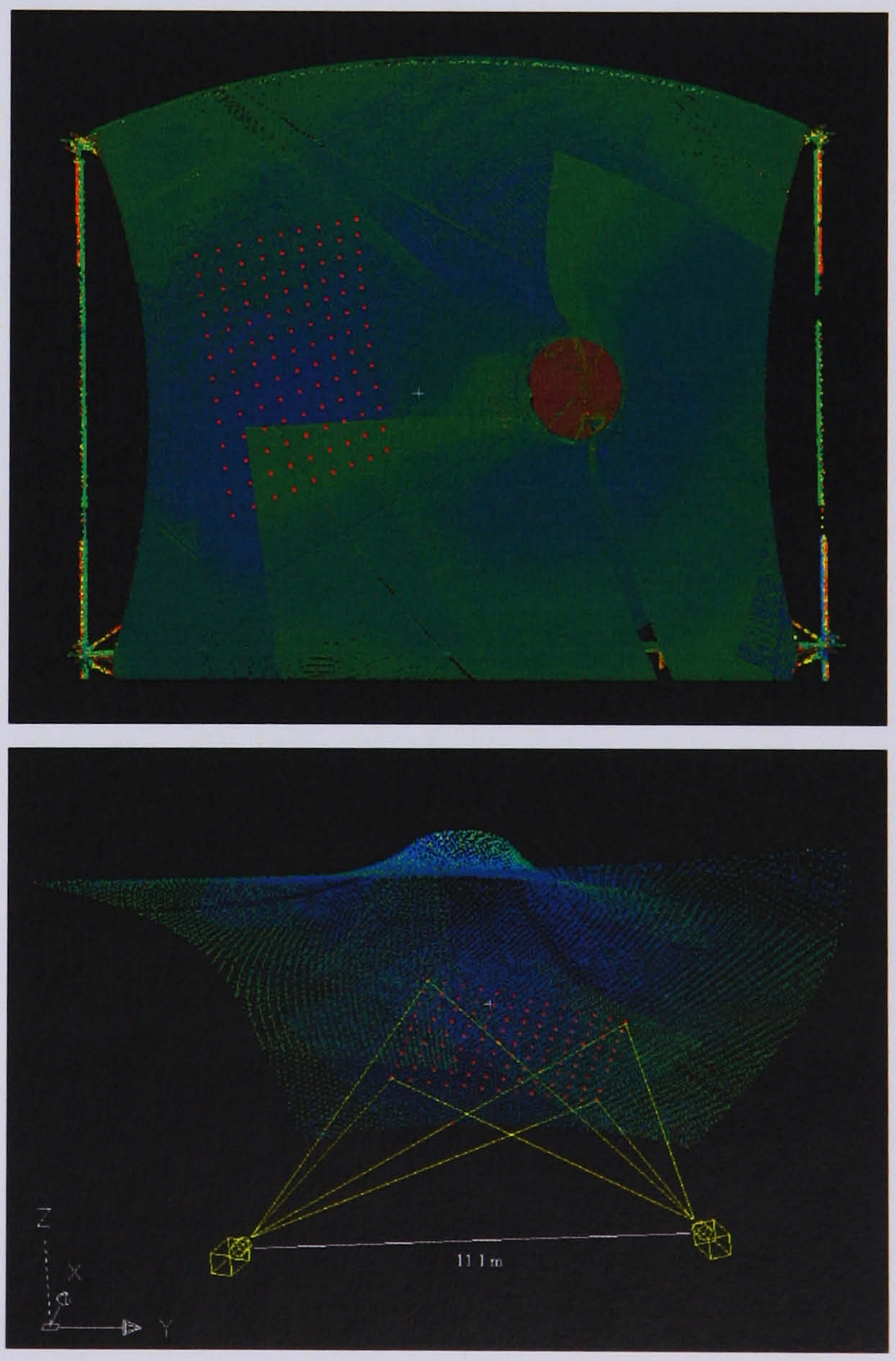


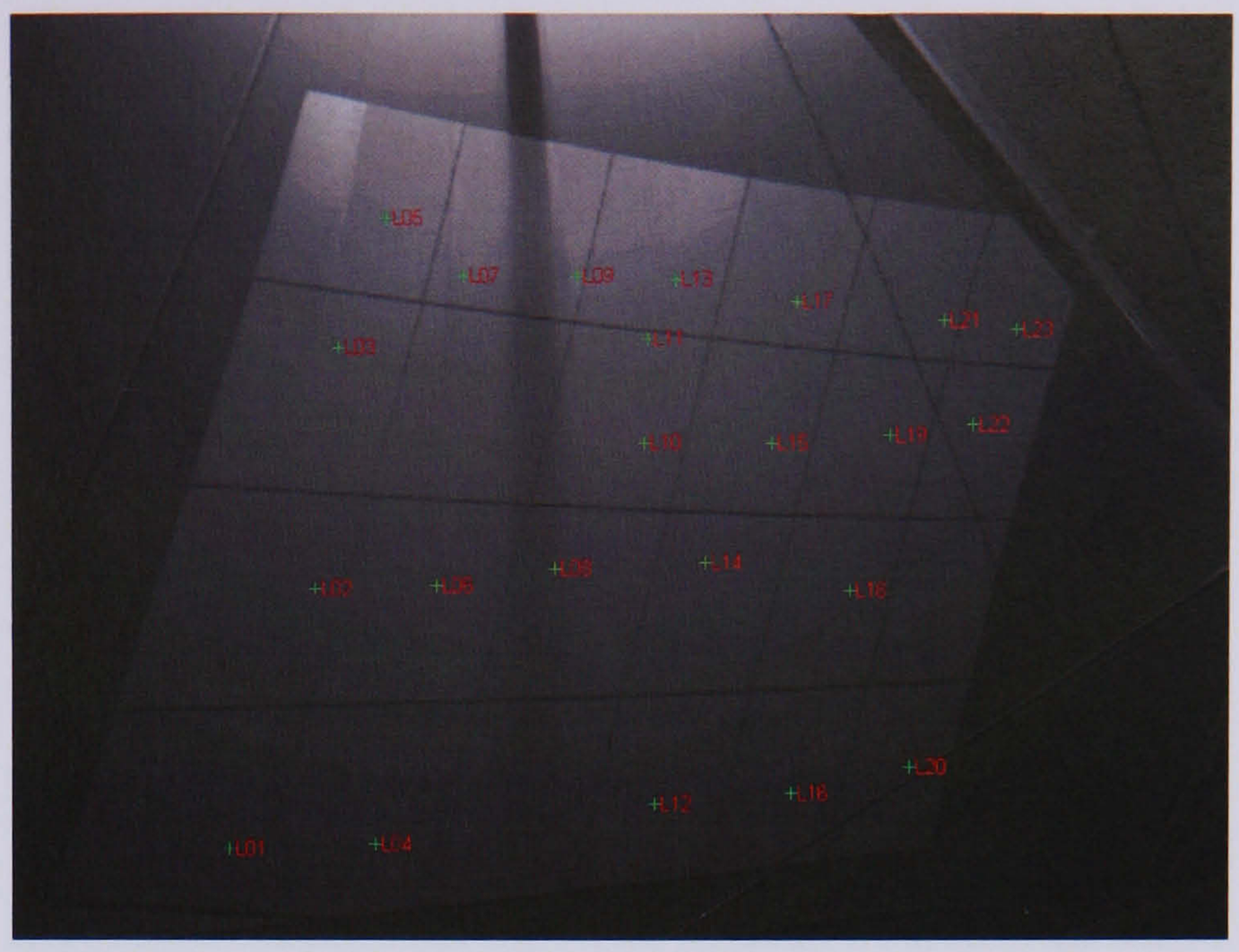
Figure 6-14: Laser scanned model and videogrammetric monitoring area (red points) of the Type 2 membrane structure.

6.2.3.2 Implementation of MS²

The acquired imagery was input into MS² for processing and measurement. All the parameters required during the implementation are listed in Table 6-4. In the Camera Orientation module, the laser footprints were extracted (Figure 6-15) and 20 control footprints were selected to solve the camera orientations (Table 6-5). Consequently, Target Extraction was performed to extract the centres of the projected dots (Figure 6-16). As the density of the points was reduced in this campaign, the input maximum interval values for Target Referencing were increased. Also, apparent movement was observed in the campaign, hence the relatively large maximum tolerance values were given for Target Tracking. Once the computation was finished, the 3D coordinates of each point at each epoch were solved and the measurement precision was shown in the same level as the predicted value (Table 6-6).

Camera Orientation	*Left*	*Number of frames*	378
		Normalised threshold value	0.15
	Right	*Number of frames*	378
		Normalised threshold value	0.14
Target Extraction	*Left*	*Number of epochs*	3600
		Normalised threshold value	0.8
		Noise size (pixels)	<10 and >400
	Right	*Number of epochs*	3600
		Normalised threshold value	0.8
		Noise size (pixels)	<10 and >300
Target Referencing	*Left*	*Max X interval (pixels)*	25
		Max Y interval (pixels)	75
	Right	*Max X interval (pixels)*	10
		Max Y interval (pixels)	60
Target Tracking	*Left*	*Max X tolerance (pixels)*	9
		Max Y tolerance (pixels)	9
	Right	*Max X tolerance (pixels)*	9
		Max Y tolerance (pixels)	9
Target Calculation	*Number of epochs*		3600

Table 6-4: Input parameters for MS² implementation.



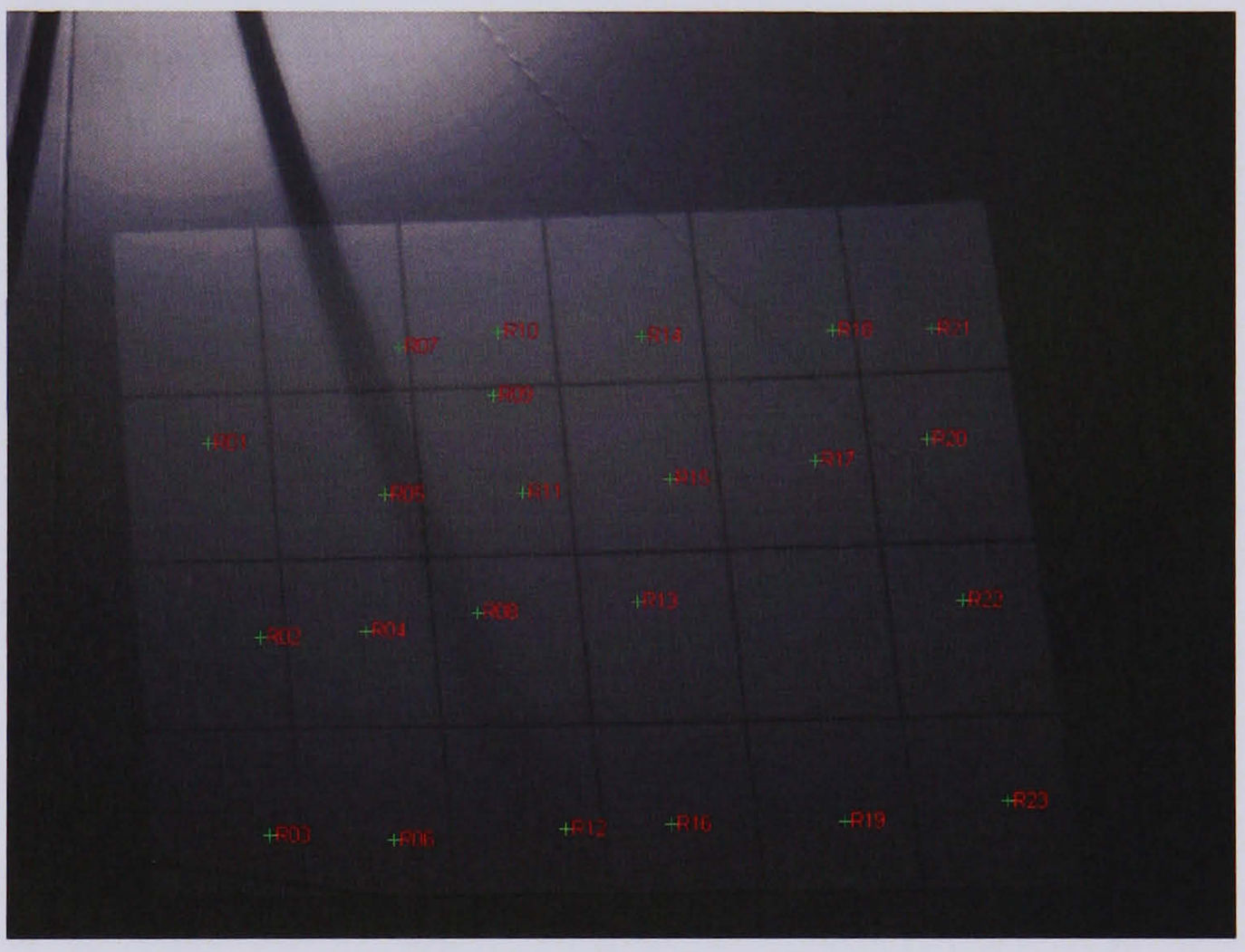


Figure 6-15: Stereopair of extracted control footprints.

	Left Exposure Station	*Right Exposure Station*
X (m)	97.160 ± 0.014	104.931 ± 0.012
Y (m)	99.504 ± 0.010	91.685 ± 0.010
Z (m)	11.095 ± 0.013	11.045 ± 0.013
ω (degrees)	172.630 ± 0.062	136.492 ± 0.072
ϕ (degrees)	-46.819 ± 0.068	-9.693 ± 0.067
κ (degrees)	38.131 ± 0.059	15.601 ± 0.065

Table 6-5: Orientation results for the Type 2 membrane structure monitoring.

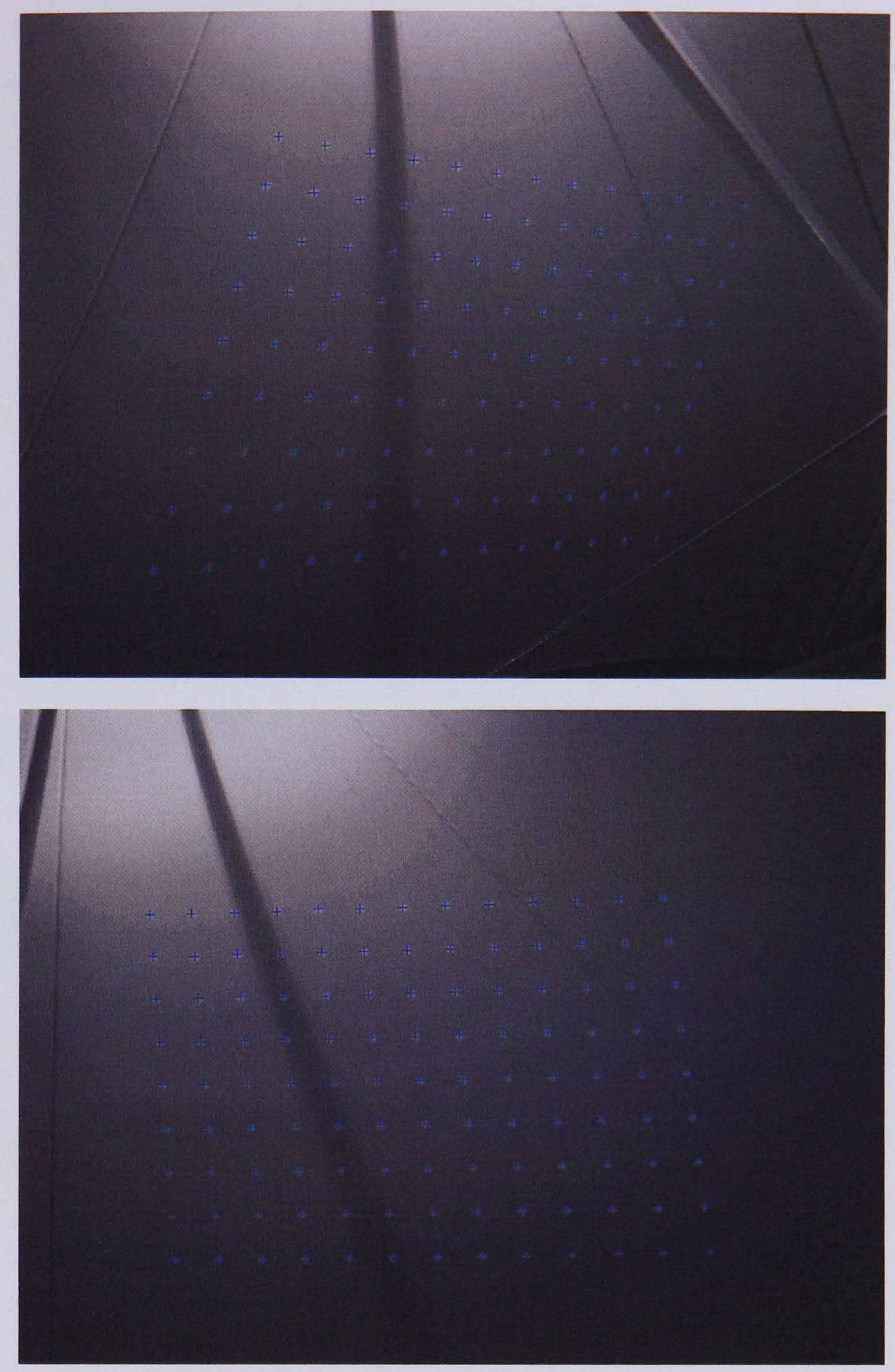


Figure 6-16: Stereopair of extracted projected-dots at epoch 1.

Base Distance (m)	*Depth Distance (m)*	*Image Scale*	*Predicted Precision (mm)*				*Adjustment Precision (mm)*			
			σ_X	σ_Y	σ_Z	$\sigma_{Position}$	σ_X	σ_Y	σ_Z	$\sigma_{Position}$
11.1	11.2	1:950	0.7	0.9	1.0	1.5	1.0	0.7	1.0	1.6

Table 6-6: Results of the point measurement for the Type 2 membrane structure monitoring.

6.2.3.3 Displacement Analysis

The surface created at the first epoch was used as the base model and the subsequent displacements occurring over 3599 epochs were then determined. During the

computation, the positive movements (points moving upwards) and negative movements (points moving downwards) across the observed area in each epoch were collected separately. For realising the characteristics of the movement, the mean and maximum values of positive and negative movements of each epoch were estimated and depicted. In Figure 6-17, it is shown that numerous significant movements were observed over the period of monitoring. From the derived statistics the maximum positive displacement was 22.9 mm, occurring at epoch 1645, while the maximum negative movement was -19.4 mm at epoch 1777. In addition to the epochs of these evident displacements, the epochs with maximum mean of positive and negative displacements were selected for further analysis of the observed membrane surface's dynamic behaviour.

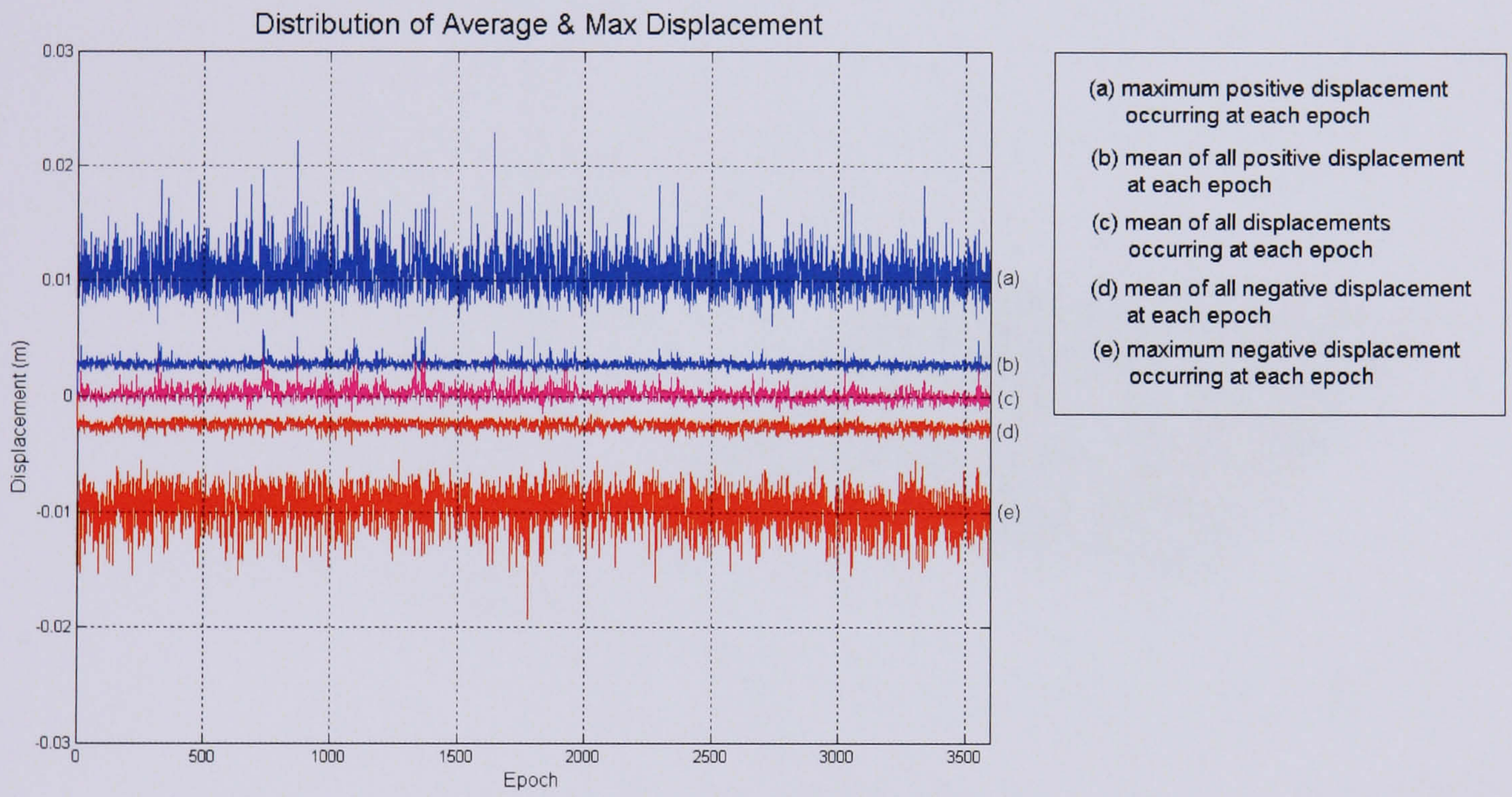
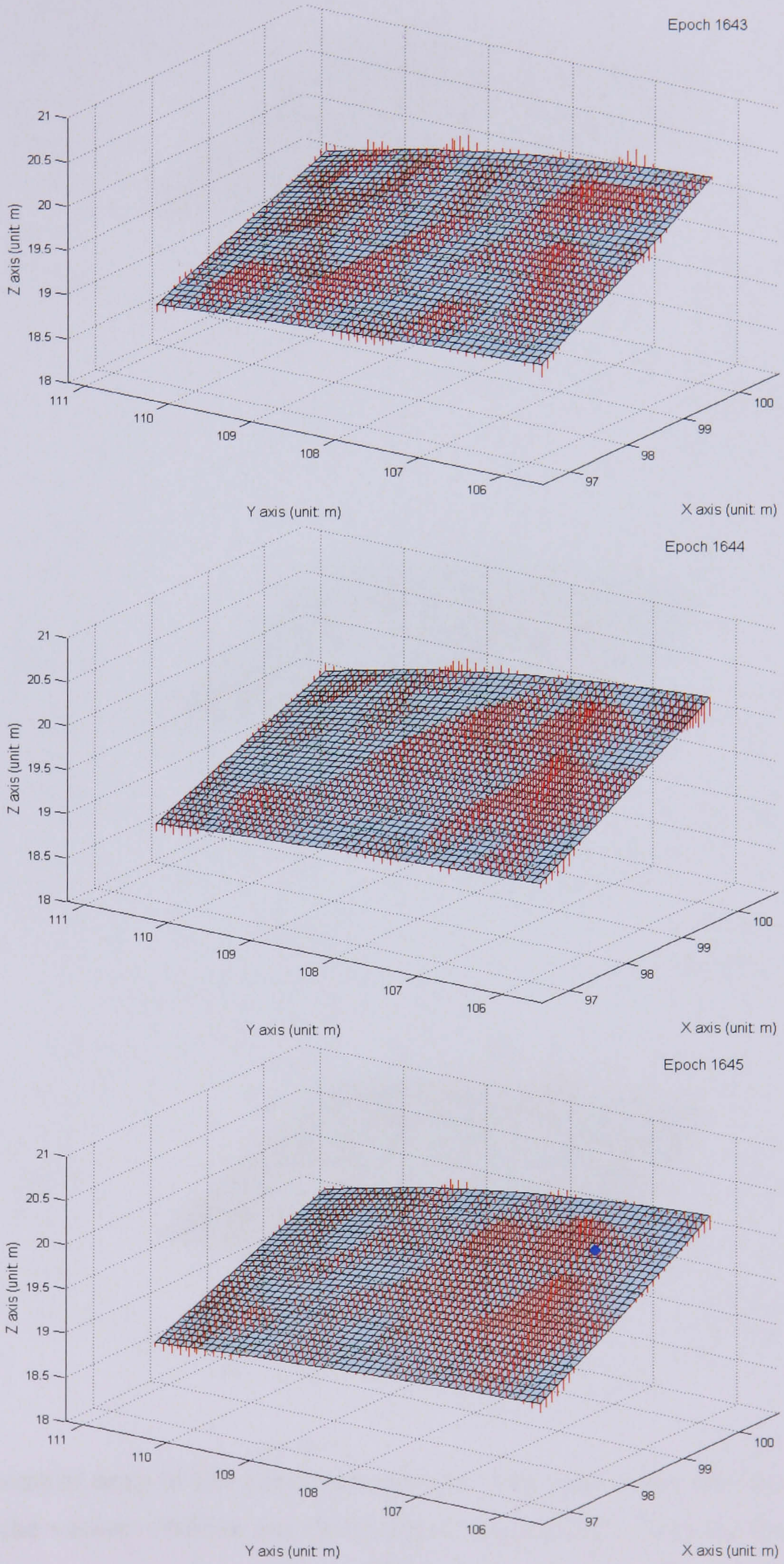


Figure 6-17: Resulting displacement for the observations on the Type 2 membrane structure.

Firstly, a session when maximum positive displacement had occurred was inspected (epoch 1643 to 1648). For a detailed investigation a displacement map, at which vectors were plotted to represent the differences of Z-ordinates between the base surface and any model of a specific epoch, was produced through an Advanced Query interface in MS^2. By viewing the maps, the positions and magnitudes of the displacements could be clearly identified. The displacement maps of epoch 1643 to 1648 are shown in Figure 6-18. The maximum value of maximum positive displacement over 3599 epochs was 22.9 mm, and it occurred at position (99.4 m, 107.1 m) at epoch 1645 (outlined by a blue point in the displacement map of epoch 1645 in Figure 6-18). By viewing the distribution of the vectors in the sequential surface model, it is revealed apparent

movements generally appeared in the area between Y=106.0 m to 108.0 m.



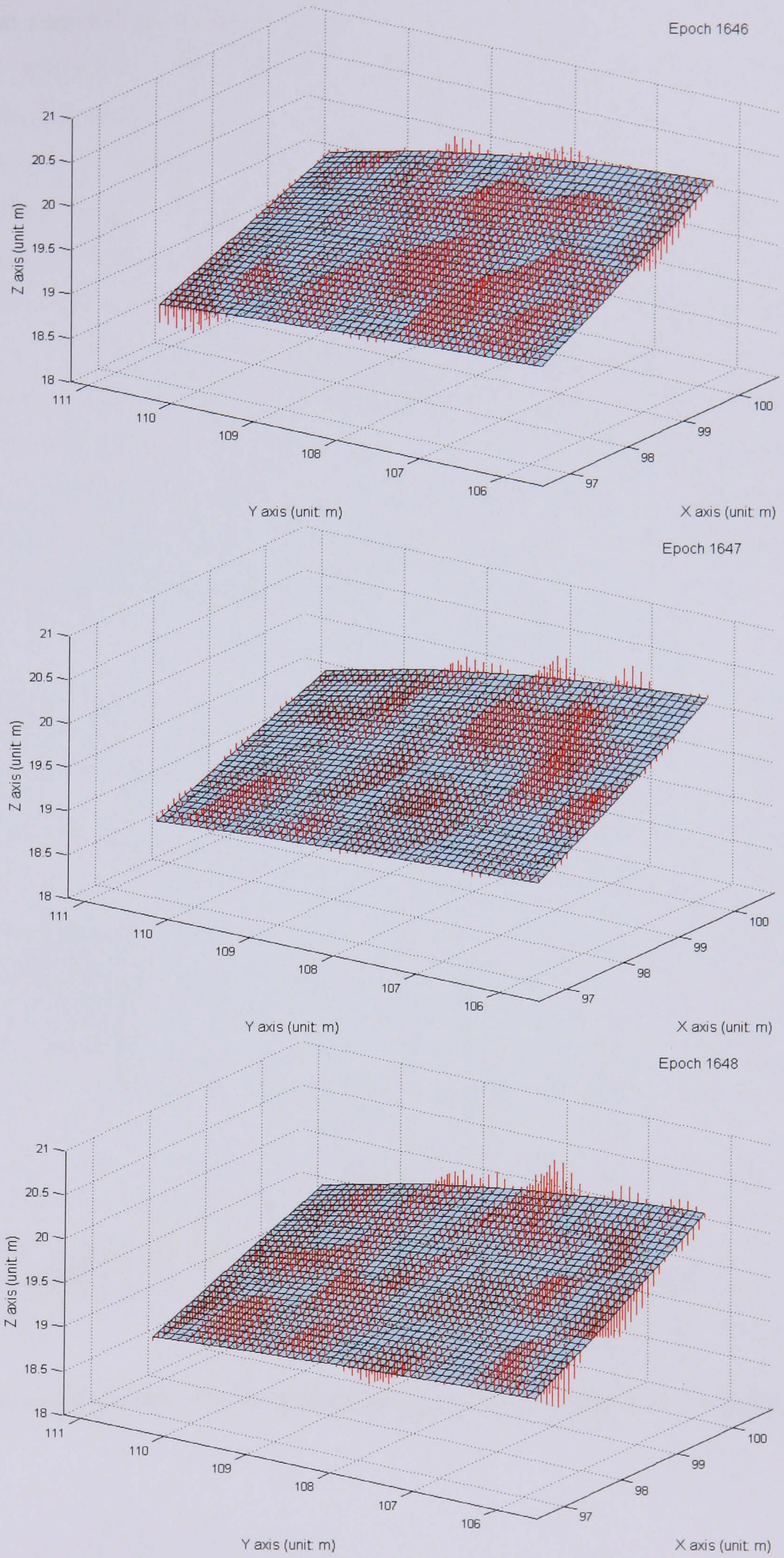


Figure 6-18: The displacement map of the observed surface. The base is the surface model of the 1st epoch, the vectors (which are three times magnified) represent the differences to the specific epoch.

In order to understand the sequential movement, further inspection was carried out by comparing the profiles extracted from different epochs. The task was again accomplished through the Advanced Query interface in MS^2. The displacement and shape of the specific part of the membrane roof surface were investigated along the profiles. Since the maximum value of maximum positive displacement occurred at position (99.4 m, 107.1 m), the profiles passing though this point were inspected first. In the upper diagram in Figure 6-19, the sequential profiles (epoch 1643 to 1648) along the Y axis where X=99.4 m are displayed in different colours. The curves shown in the lower plot illustrate the displacement along the profiles between the specific surface and base model. From Figure 6-19, obvious movements occurred in the section between Y=106.0 m to 108.0 m. Whereas the profiles along the X axis (Y=107.1 m) are illustrated in Figure 6-20, in which apparent movements appeared in the sections between X=97.5 m to 98.5 m and X=99.0 m to 100.0 m.

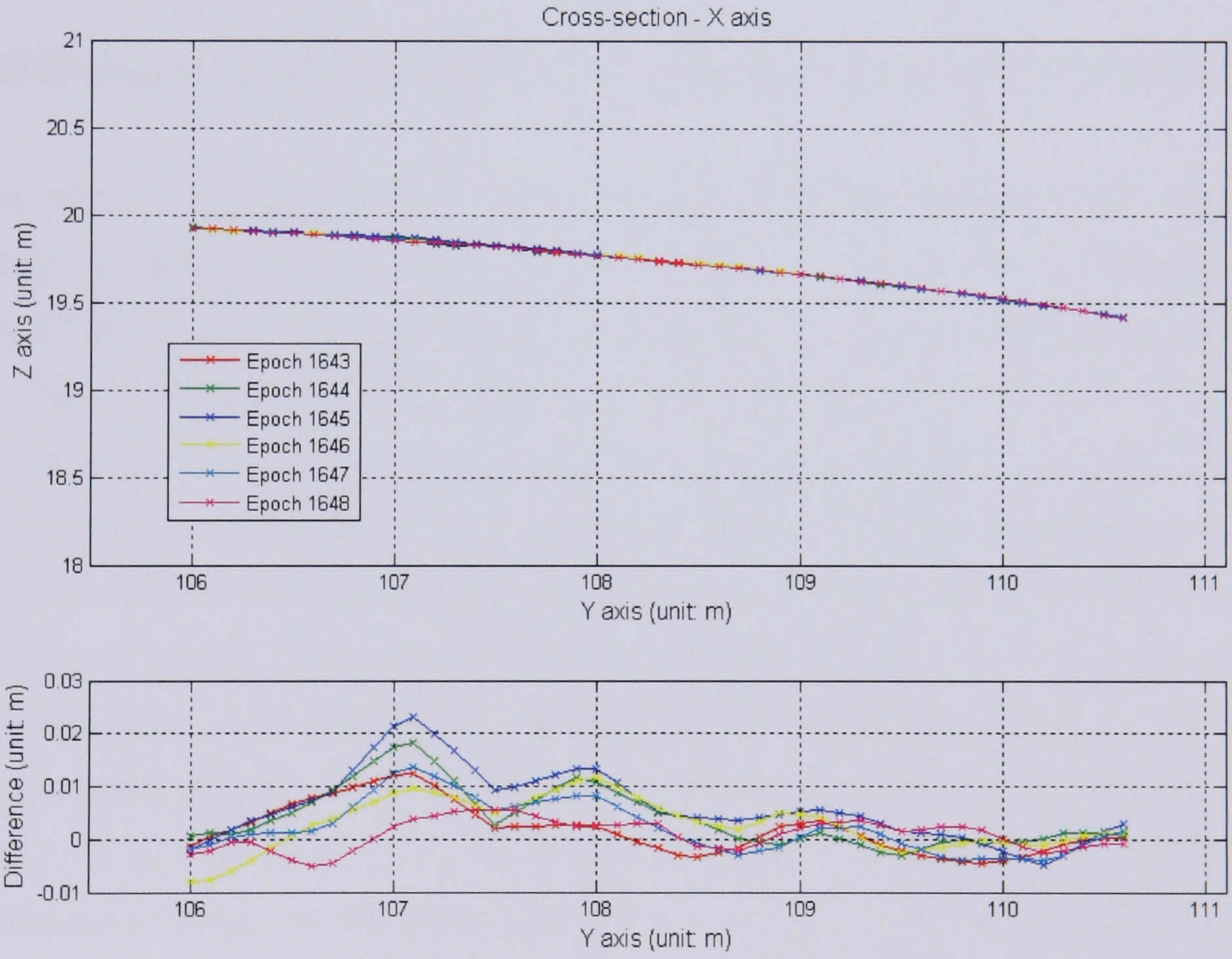


Figure 6-19: Differences in profile (X=99.4 m) amongst the six temporal epochs.

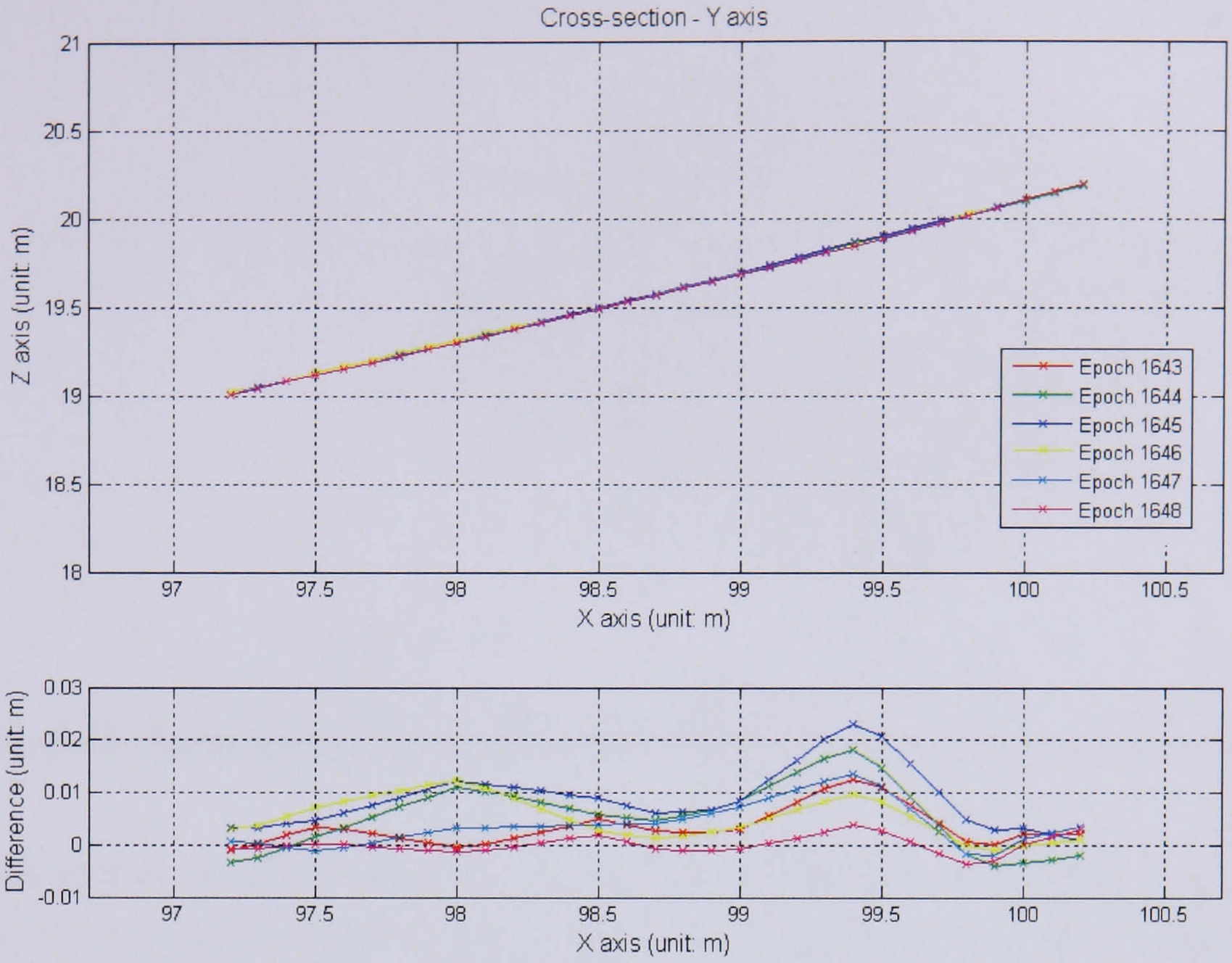


Figure 6-20: Differences in profile (Y=107.1 m) amongst the six temporal epochs.

In addition to the profiles passing through the point of maximum positive movement, ten profiles evenly distributed across the surface (Figure 6-21) were extracted to discover the overall dynamic characteristics of the membrane surface between epoch 1643 and 1648. The profiles along the Y and X axis are depicted in Figure 6-22 and Figure 6-23 respectively. Also, the range of displacements that occurred at each profile is estimated and listed in Table 6-7 and Table 6-8. By inspecting the ranges of displacement in Table 6-7, the mean value of overall range of displacement is 14.6 mm, thereby the profiles or epochs whose mean range of displacement over this value are deemed as possessing large movements. Accordingly, it is found that large movement mainly occurred along the profile where X=98.1 m and 99.5 m (mean values of range of displacements are 15.2 mm and 17.9 mm respectively), especially at epochs 1644, 1645 and 1647 (mean values of range of displacements are 15.1 mm, 18.7 mm and 14.7 mm). Along these two profiles shown in Figure 6-22, the obvious displacements mostly occurred between Y=106.0 m to 108.0 m.

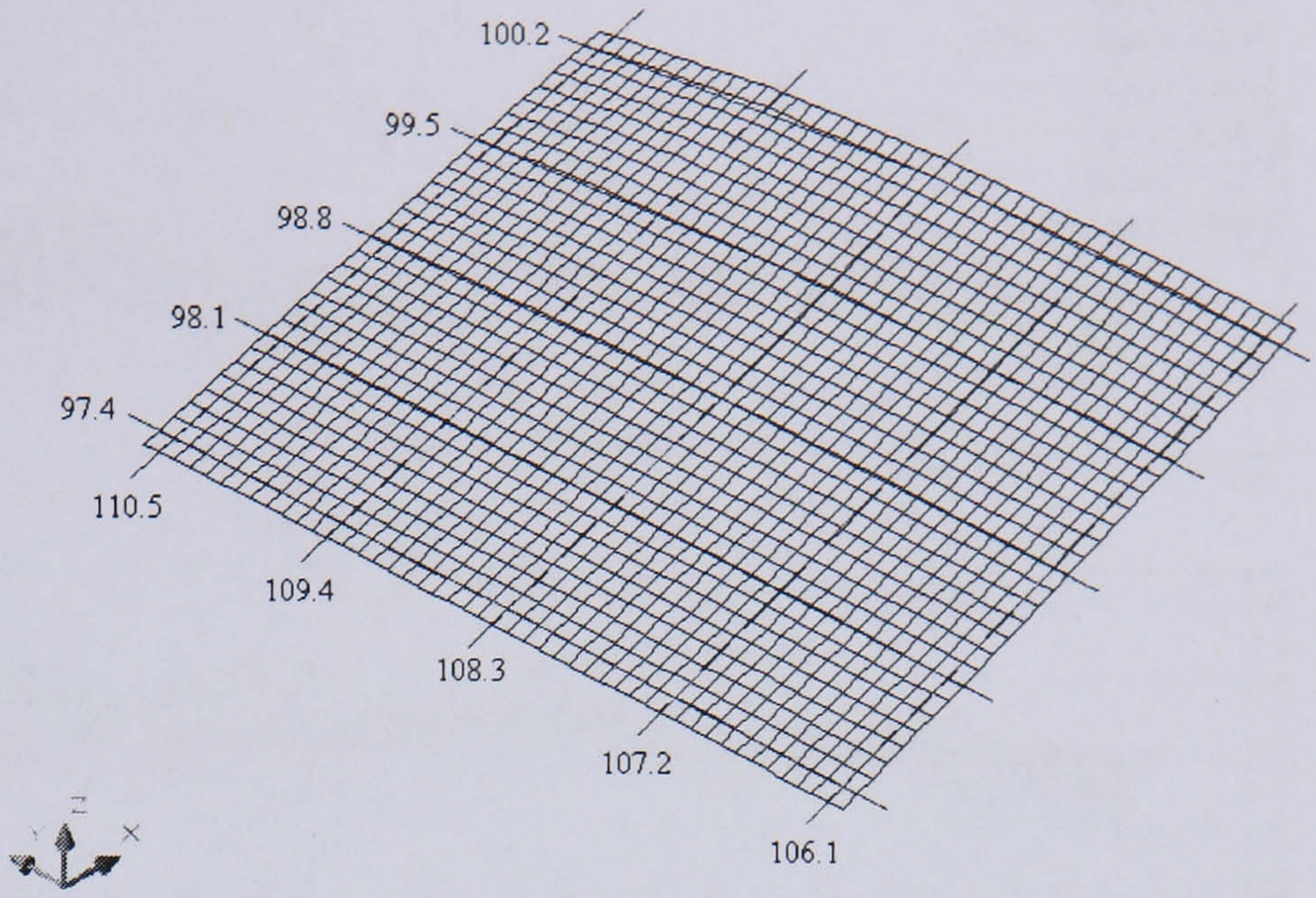


Figure 6-21: Indication of profiles investigated over the observed surface.

With regard to the profiles along the X axis, obvious movements were determined along Y=106.1 m and 107.2 m due to large mean values of range of displacements solved in Table 6-8 (15.1 mm and 16.4 mm). Along these two profiles, evident movements appeared at epochs 1644, 1645, 1646 and 1647. By viewing Figure 6-23, the relatively large movements occurred in the section where X=98.0 m to 99.0 m along Y=106.1 m, and between X=97.5 m to 98.5 m and X=99.0 m to 100.0 m along Y=107.2 m. On the other hand, small movements were also detected in the sequential surface model, which existed along the profile where Y=110.5 m. The mean value of range of displacements was found to be 7.7 mm.

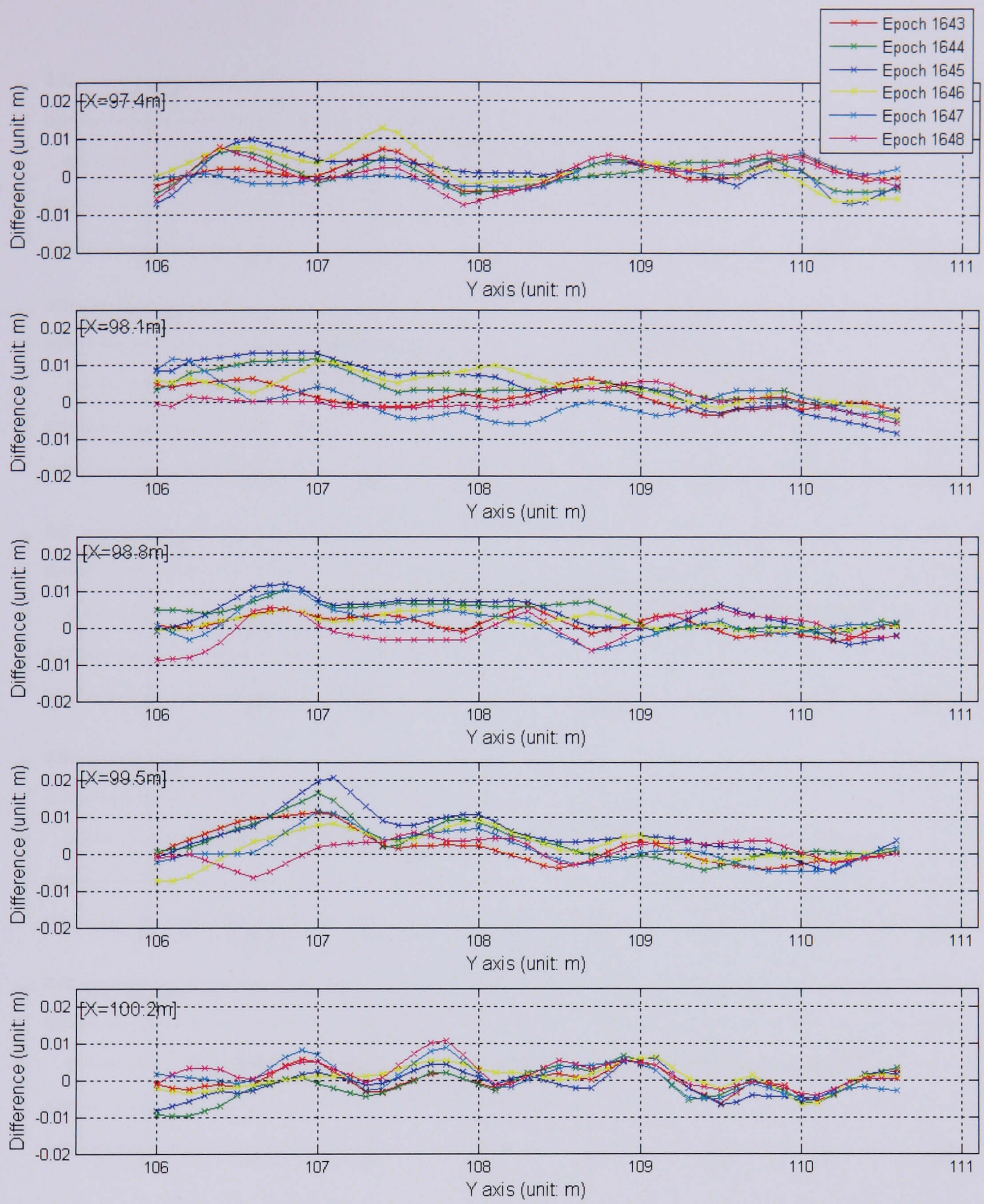


Figure 6-22: Movements that occurred along the Y axis across the surface.

	Range of Displacements (mm)						
X (m)	*Epoch 1643*	*Epoch 1644*	*Epoch 1645*	*Epoch 1646*	*Epoch 1647*	*Epoch 1648*	*Mean*
97.4	11.0	10.6	16.5	19.0	9.4	15.2	13.6
98.1	9.7	16.5	21.6	14.5	17.4	11.3	15.2
98.8	9.7	11.3	16.5	6.1	16.5	14.2	12.4
99.5	15.5	21.0	25.5	16.5	16.5	12.3	17.9
100.2	11.9	16.1	13.2	12.9	13.9	14.5	13.8
Mean	11.6	15.1	18.7	13.8	14.7	13.5	*14.6*

Table 6-7: Range of displacement that occurred along the Y axis.

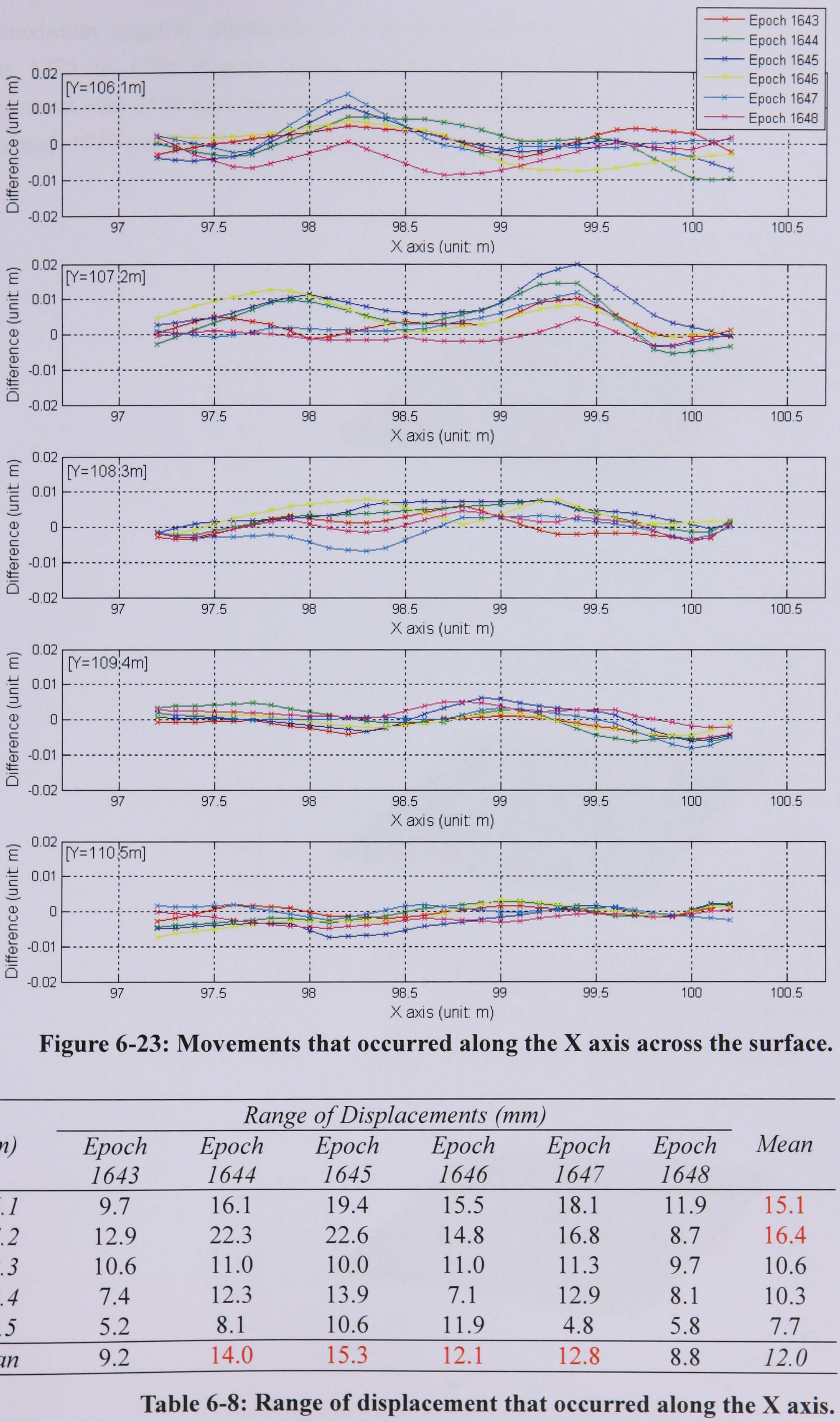
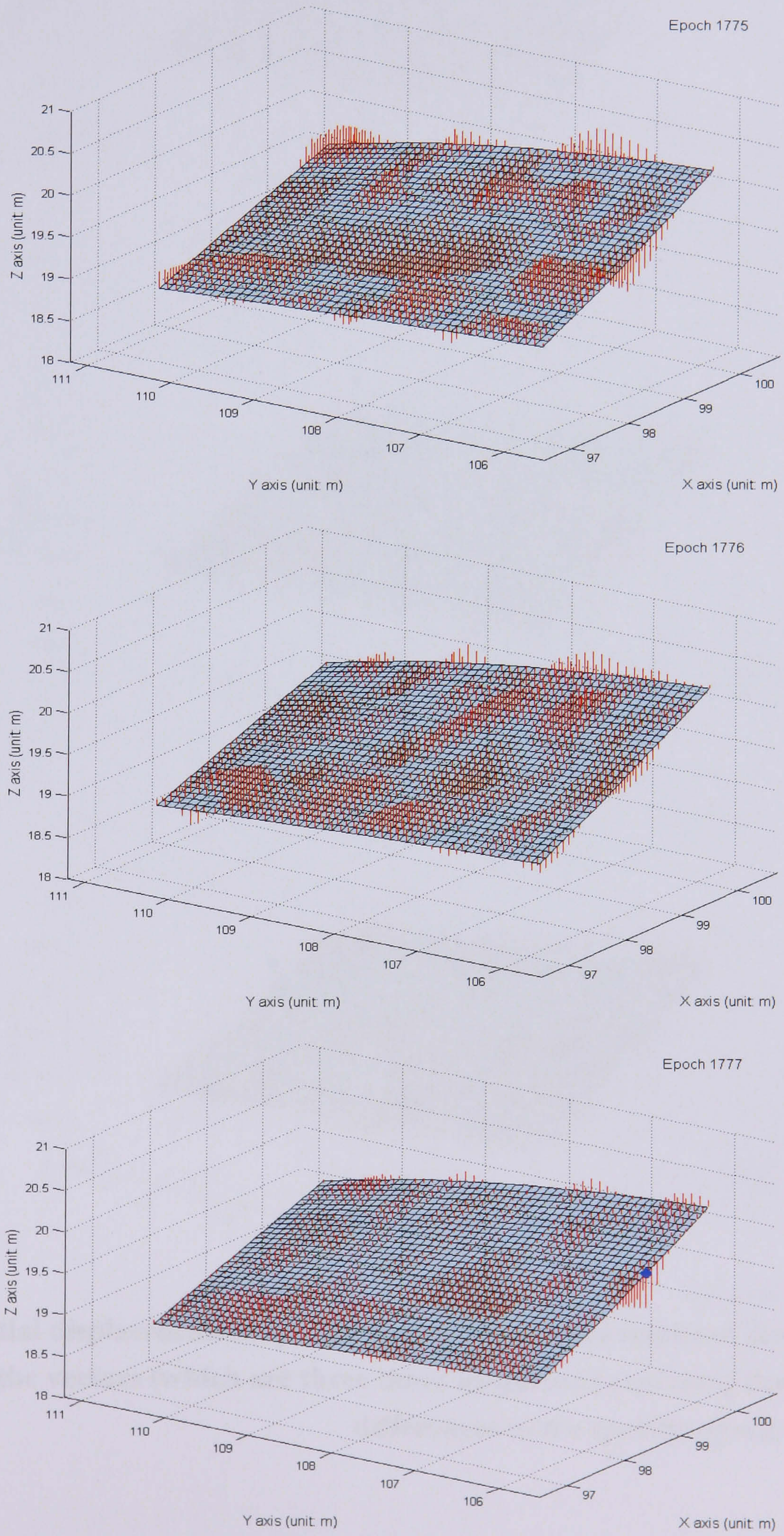


Figure 6-23: Movements that occurred along the X axis across the surface.

	Range of Displacements (mm)						
Y (m)	*Epoch 1643*	*Epoch 1644*	*Epoch 1645*	*Epoch 1646*	*Epoch 1647*	*Epoch 1648*	*Mean*
106.1	9.7	16.1	19.4	15.5	18.1	11.9	15.1
107.2	12.9	22.3	22.6	14.8	16.8	8.7	16.4
108.3	10.6	11.0	10.0	11.0	11.3	9.7	10.6
109.4	7.4	12.3	13.9	7.1	12.9	8.1	10.3
110.5	5.2	8.1	10.6	11.9	4.8	5.8	7.7
Mean	9.2	14.0	15.3	12.1	12.8	8.8	*12.0*

Table 6-8: Range of displacement that occurred along the X axis.

The maximum negative displacement was investigated with displacement maps of epochs 1775 to 1780 (Figure 6-24). The maximum value of maximum negative displacement over 3599 epochs was 19.4 mm, and it occurred at position (99.1 m, 106.0 m) at epoch 1777 (outlined by a blue point in Figure 6-24).



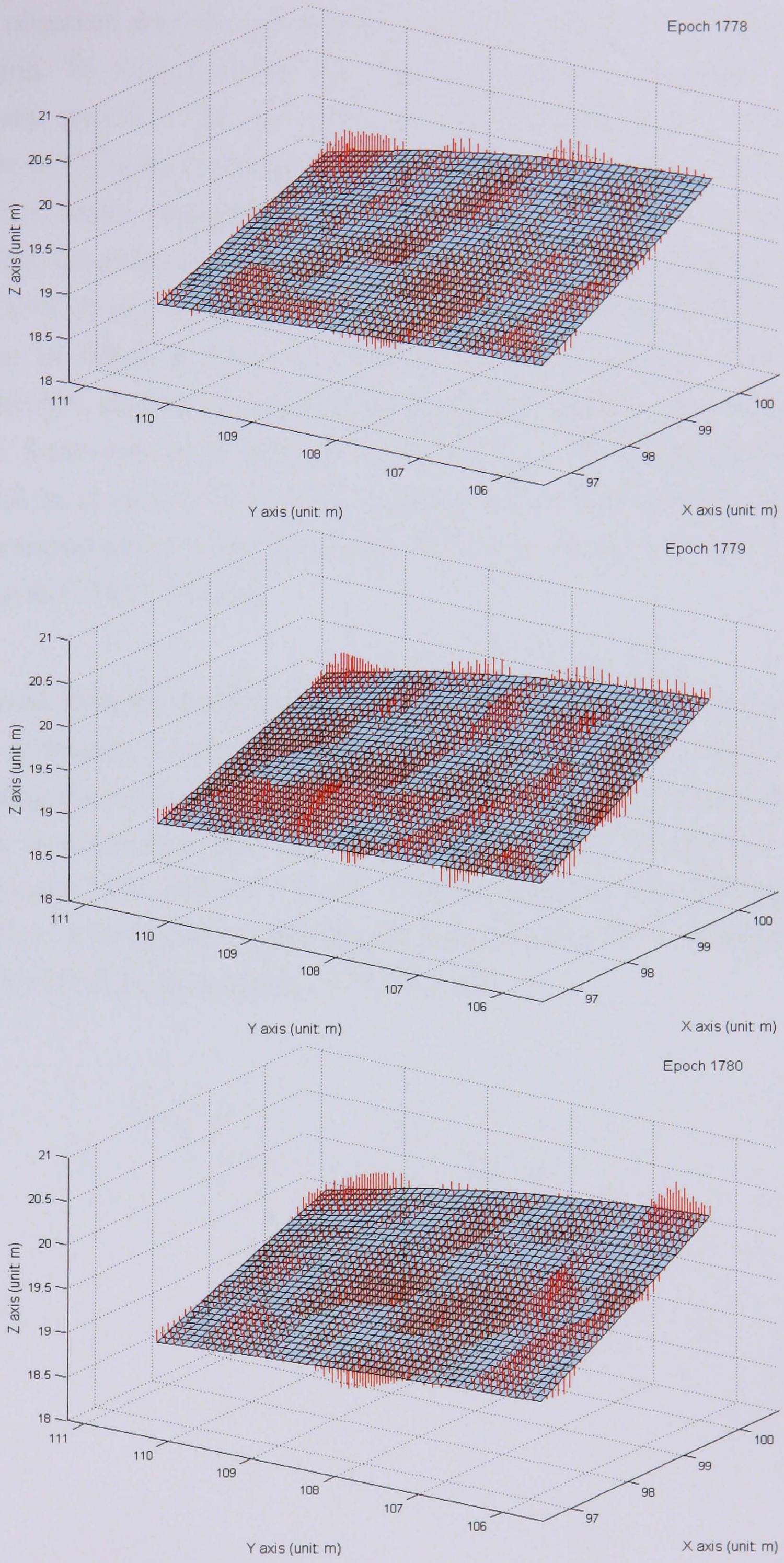


Figure 6-24: The sequential displacement map. The base is the surface model of the 1st epoch and the vectors (which are three times magnified) represent the differences to the specific epoch.

From Figure 6-24, it is observed that the movements occurred irregularly across the surface during this session. To further realise the dynamic manner of the observed membrane surface between epochs 1775 and 1780, ten profiles along X an Y axes across the surface (Figure 6-21) were extracted and the range of the displacement that occurred along the profiles were computed. In Figure 6-25, displacements occurred randomly along the profiles, for example they appeared between Y=107.5 m to 109.0 m along the profile where X=97.4 m; between Y=108.0 m to 109.5 m where X=98.8 m and between Y=106.0 m to 108.0 m where X=100.2 m. By inspecting the metric information listed in Table 6-9, equivalent range of displacements along Y axis across the surface was derived. Relatively large movements mainly occurred along profiles where X= 97.4 m and 98.8 m, at epochs 1775, 1776, 1778 and 1780. To be specific, the significant movements occurred along the profile where X=98.8 m at epoch 1780 (17.7 mm) and X=99.5 m at epoch 1776 (17.4 mm).

Similar results were derived from the profiles along the X axis (Figure 6-26). Obvious displacements occurred arbitrarily along the profiles, such as the section between X=98.0 m and 99.5 m along the profile Y=106.1 m. The solved range of displacements also reflects the situation, in which dramatic movements occurred along the profile Y= 106.1 m, especially at epochs 1775 and 1777 (range of displacements were 18.0 mm and 20.9 mm respectively). Alternatively, insignificant displacements were observed along the profiles where Y=110.5 m, from epochs 1776 to 1780.

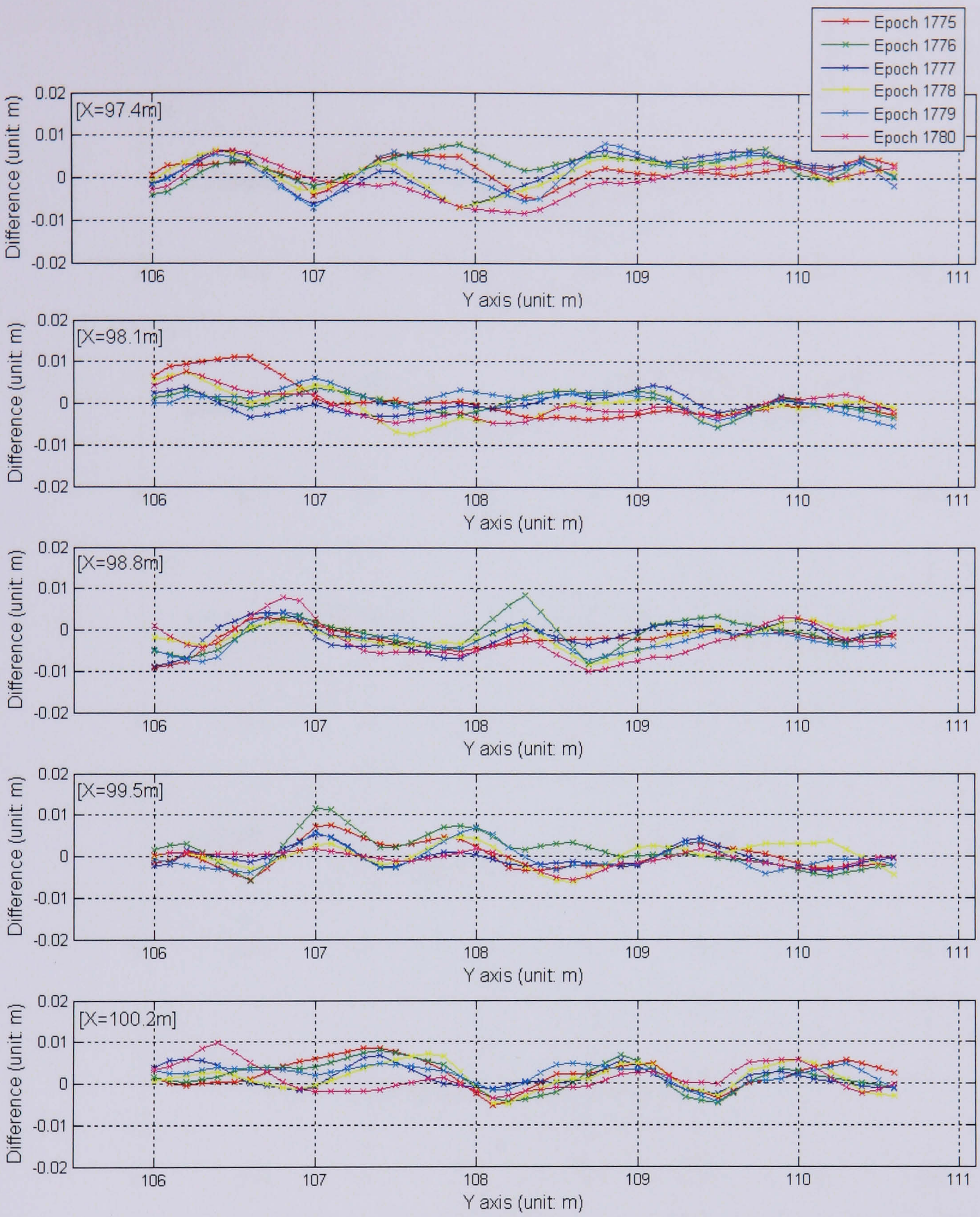


Figure 6-25: Movements that occurred along the Y axis across the surface.

Range of Displacements (mm)

X (m)	*Epoch 1775*	*Epoch 1776*	*Epoch 1777*	*Epoch 1778*	*Epoch 1779*	*Epoch 1780*	*Mean*
97.4	10.0	11.7	13.7	13.5	15.1	14.6	13.1
98.1	14.9	9.1	7.7	14.9	11.4	12.3	11.7
98.8	12.0	16.6	12.8	11.4	12.0	17.7	13.8
99.5	13.1	17.4	8.9	10.9	11.2	7.4	11.5
100.2	13.7	12.6	9.1	12.0	9.1	13.5	11.7
Mean	12.7	13.5	10.4	12.5	11.8	13.1	*12.3*

Table 6-9: Range of displacements that occurred along the Y axis.

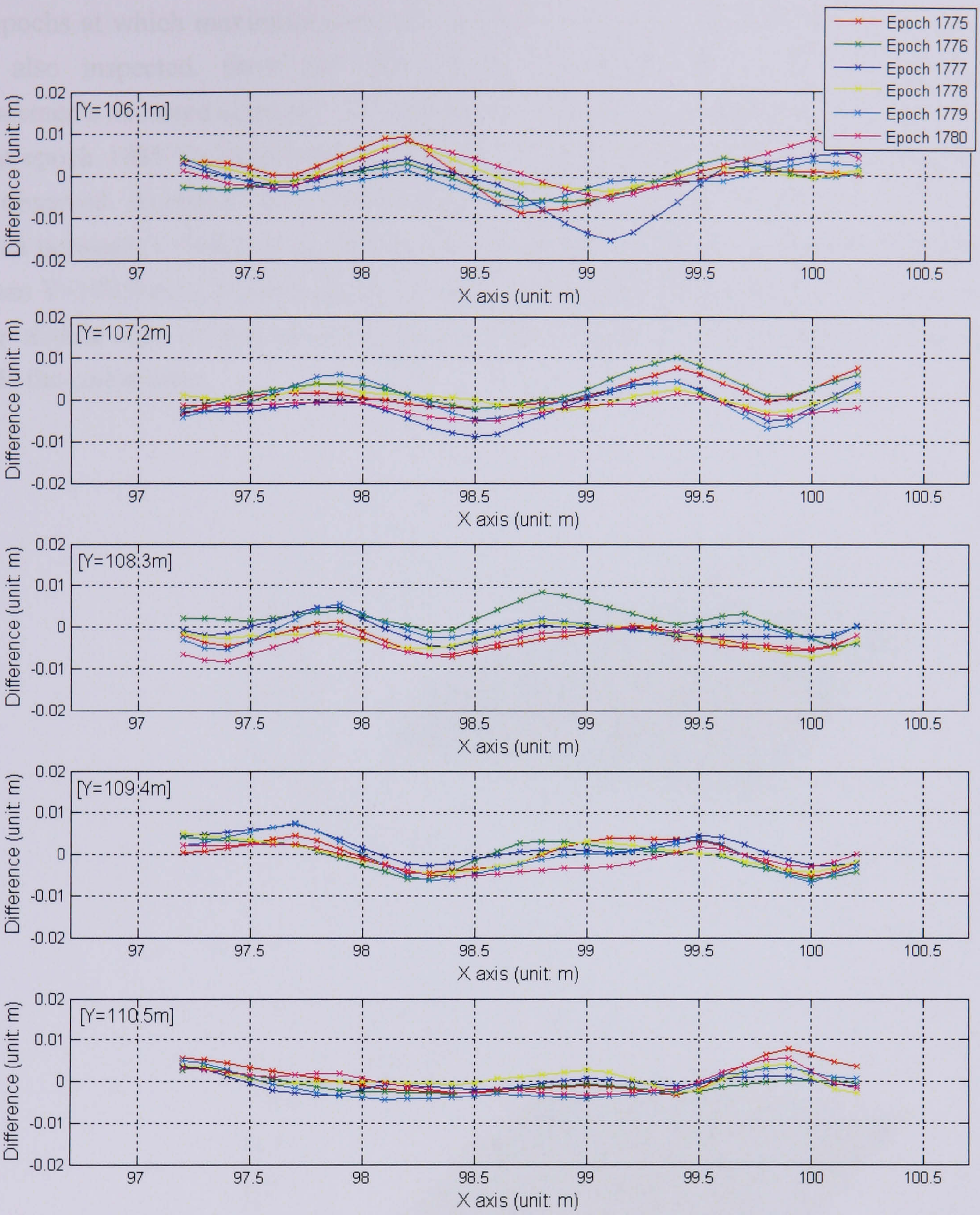


Figure 6-26: Movements that occurred along the X axis across the surface.

Range of Displacements (mm)

Y (m)	*Epoch 1775*	*Epoch 1776*	*Epoch 1777*	*Epoch 1778*	*Epoch 1779*	*Epoch 1780*	*Mean*
106.1	18.0	10.3	20.9	11.7	11.7	14.3	14.5
107.2	10.9	12.3	13.1	6.6	12.9	6.6	10.4
108.3	8.3	13.1	9.4	8.6	10.9	8.0	9.7
109.4	9.7	10.0	10.0	9.7	14.3	7.1	10.1
110.5	11.1	6.0	6.9	6.9	9.4	8.9	8.2
Mean	11.6	10.3	12.1	8.7	11.8	9.0	*10.6*

Table 6-10: Range of displacements that occurred along the X axis.

The epochs at which maximum mean of positive and negative displacements occurred were also inspected. Over the 3599 epochs, the maximum mean of positive displacements occurred at epoch 1371, while maximum mean of negative displacements was at epoch 1085. In Figure 6-27, the areas of positive and negative displacements were observed. At epoch 1371, the positive displacements were mainly distributed in the area between Y=106.0 m to 109.0 m, conversely the negative movements occurred between Y=109.0 m to 110.0 m. At epoch 1085, the negative displacements were spread in the middle area of the observed surface, while positive displacements occurred outside the centre area.

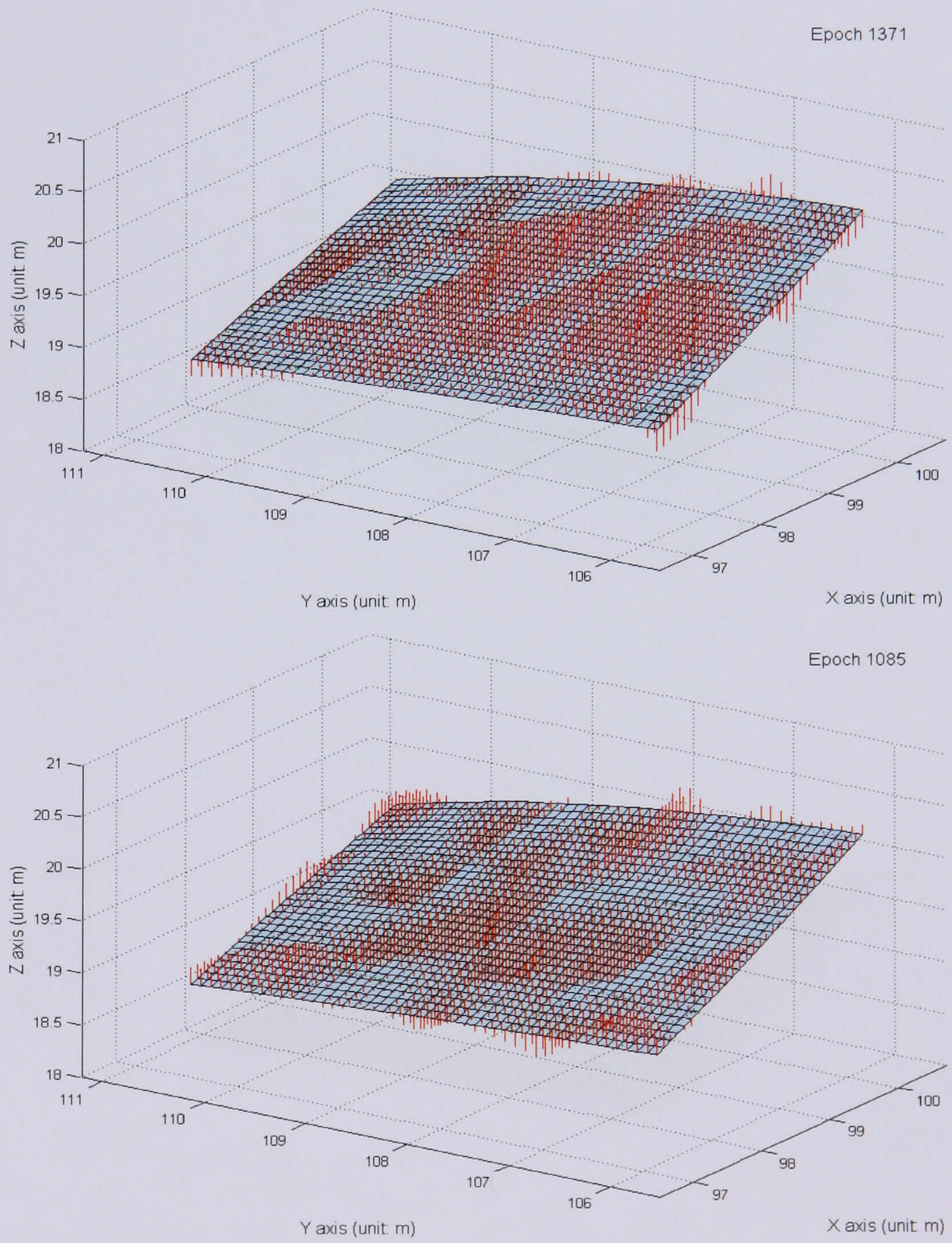


Figure 6-27: The displacement maps of epoch of maximum mean of positive (top, epoch 1371) and negative (bottom, epoch 1085) displacements.

In order to determine the dynamic behaviour of the fabric membrane, the instantaneous movement needed to be accounted for. The value is computed by comparing the two

sequential surface models. As the frame rate was one fps, the instantaneous movement within a second across the observed surface was derived. As a result, the maximum instantaneous movement was solved as 19.5 mm, which occurred between epochs 983 and 984. In order to view the magnitude and distribution of the instantaneous movements, the surface of epoch 983 was used as the base and the displacements occurred at epoch 984 were drawn as the vectors on the base surface (Figure 6-28, left). The maximum instantaneous movement happened at position (98.5 m, 108.0 m) (outlined by a red dot in the map). The minimum instantaneous movement of -20.2 mm occurred at point (98.1 m, 106.9 m) between epochs 3503 and 3504. The displacement map is shown in the right diagram of Figure 6-28.

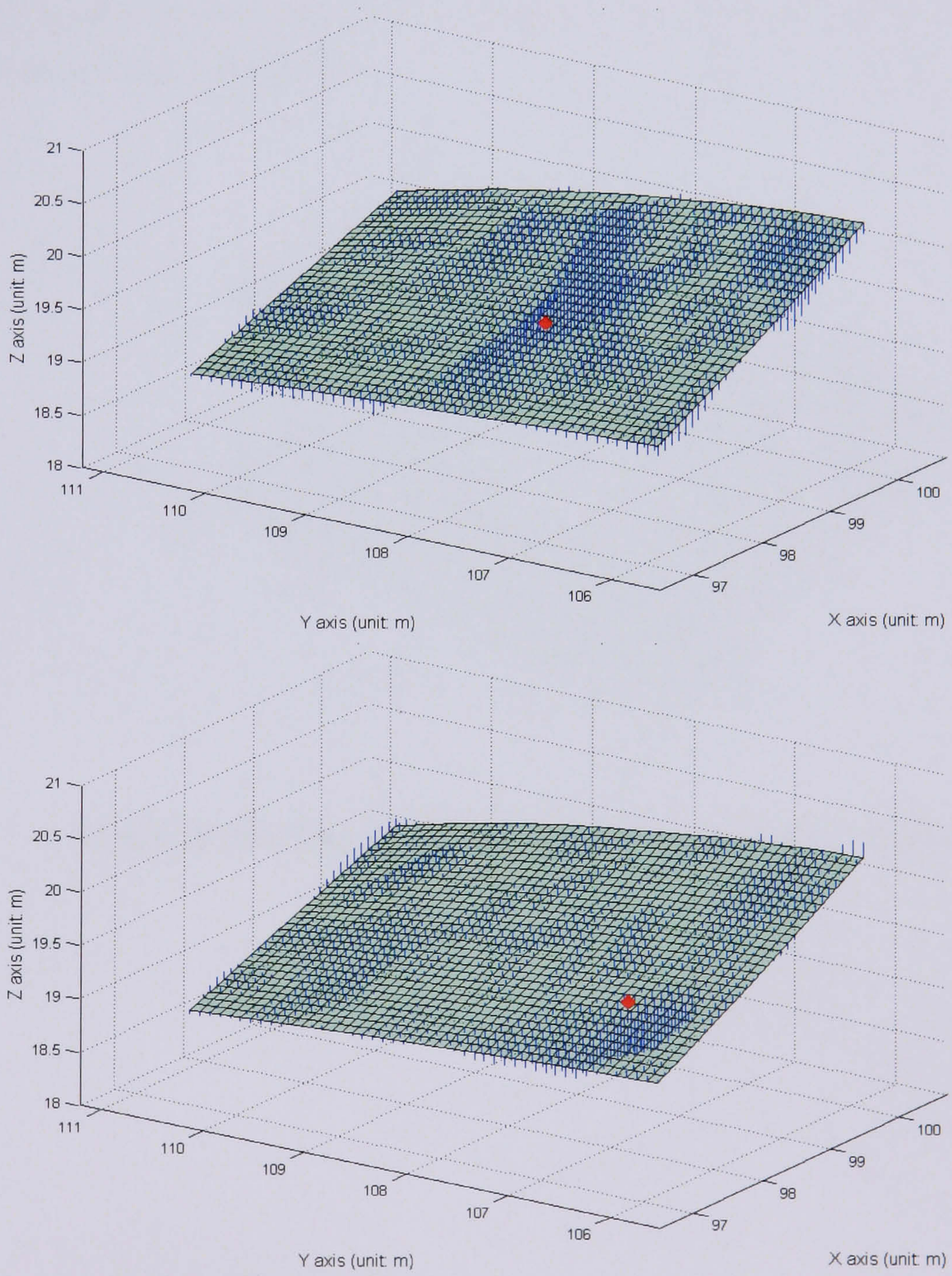


Figure 6-28: The displacement maps of epochs of maximum (top) and minimum (bottom) instantaneous movements. The base is the surface model of the epoch 983 and 3503 respectively, and the blue vectors (which are three times magnified) represent the displacements at epochs 984 and 3504.

By applying the Point Tracking function offered in the Advanced Query interface, the trajectory of Z-values over 3600 epochs were derived. To realise the movement of the surface, 25 points evenly distributed across the surface were tracked (Figure 6-29). The resultant trajectories of these 25 points were determined, and the statistics of solved Z-value of each point are listed in Table 6-11. Points whose range and standard deviation were in excess of the mean value of range (0.016 m) and standard deviation (2.3 mm) were treated as the positions with relatively obvious movements. For displaying the areas of large displacements on the fabric membrane roof, the videogrammetric monitored area (represented by the 25 points tracked) was superimposed on the laser scanned model, and the points where obvious displacements occurred were marked in red points in Figure 6-30. By inspecting the information offered in Table 6-11 and Figure 6-30, the part of the membrane roof where obvious and unapparent displacements occurred is identified.

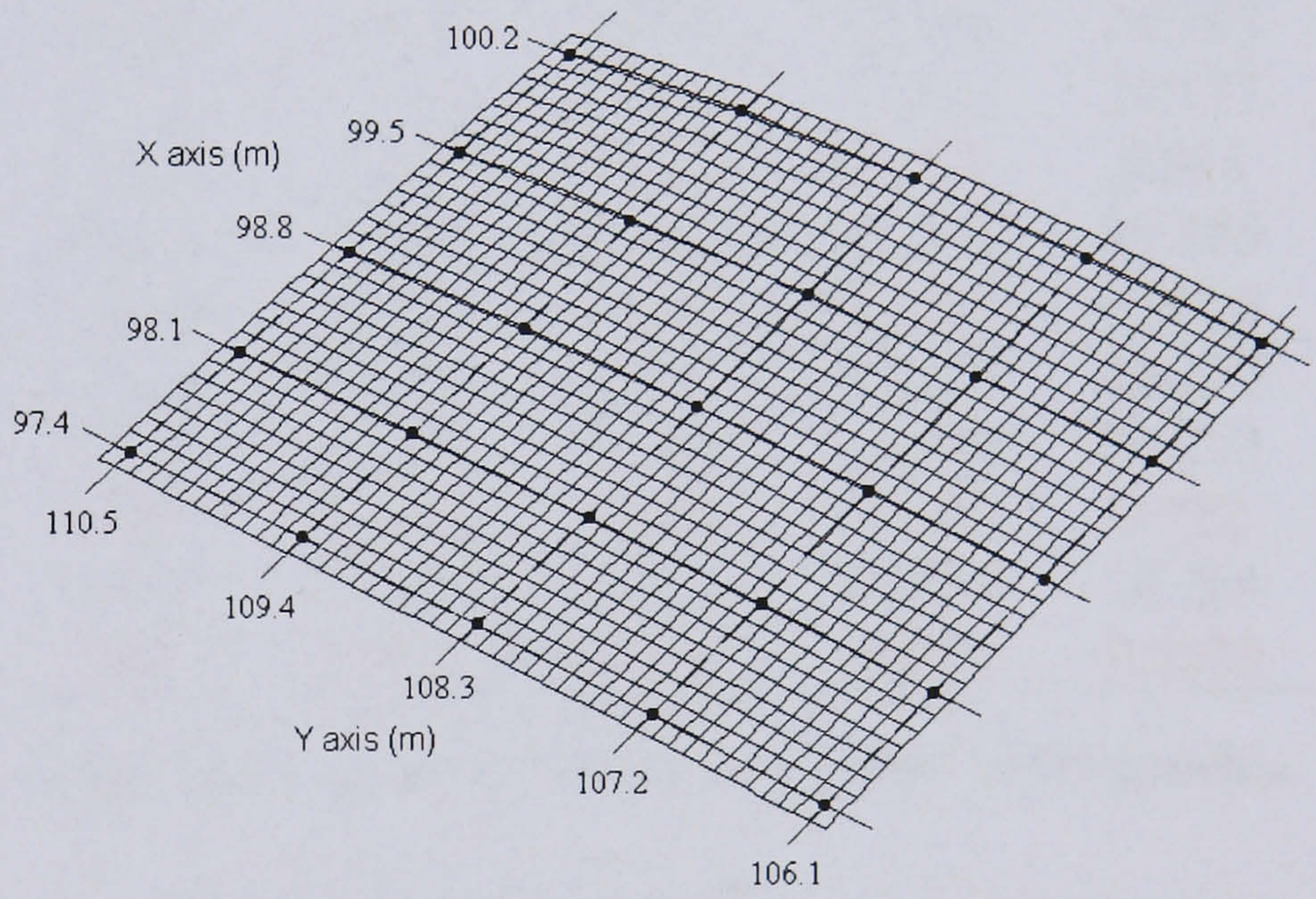


Figure 6-29: The 25 points observed across the surface.

			X (m)				
			97.4	*98.1*	*98.8*	*99.5*	*100.2*
Y (m)	*110.5*	*Max*	18.871	19.069	19.266	19.466	19.656
		Min	18.857	19.056	19.252	19.452	19.643
		Range	0.014	0.013	0.014	0.014	0.013
		Mean	18.865	19.063	19.260	19.459	19.649
		Std. dev	0.0019	0.0019	0.0019	0.0021	0.0019
	109.4	*Max*	18.952	19.174	19.408	19.648	19.896
		Min	18.937	19.160	19.395	19.630	19.884
		Range	0.015	0.014	0.013	0.018	0.012
		Mean	18.944	19.166	19.400	19.640	19.890
		Std. dev	0.0017	0.0019	0.0017	0.0024	0.0018
	108.3	*Max*	19.021	19.266	19.520	19.784	20.067
		Min	19.003	19.246	19.496	19.766	20.051
		Range	0.018	0.020	0.024	0.018	0.016
		Mean	19.011	19.255	19.507	19.774	20.059
		Std. dev	0.0026	0.0023	0.0030	0.0022	0.0022
	107.2	*Max*	19.080	19.341	19.610	19.894	20.193
		Min	19.064	19.322	19.590	19.873	20.177
		Range	0.016	0.019	0.020	0.021	0.016
		Mean	19.072	19.330	19.599	19.881	20.185
		Std. dev	0.0020	0.0022	0.0023	0.0025	0.0026
	106.1	*Max*	19.134	19.403	19.677	19.970	20.275
		Min	19.116	19.379	19.660	19.948	20.253
		Range	0.018	0.024	0.017	0.022	0.022
		Mean	19.125	19.390	19.667	19.959	20.264
		Std. dev	0.0025	0.0029	0.0023	0.0031	0.0028

Table 6-11: Statistics of the Z-values of the 25 points occurring over 3600 epochs.

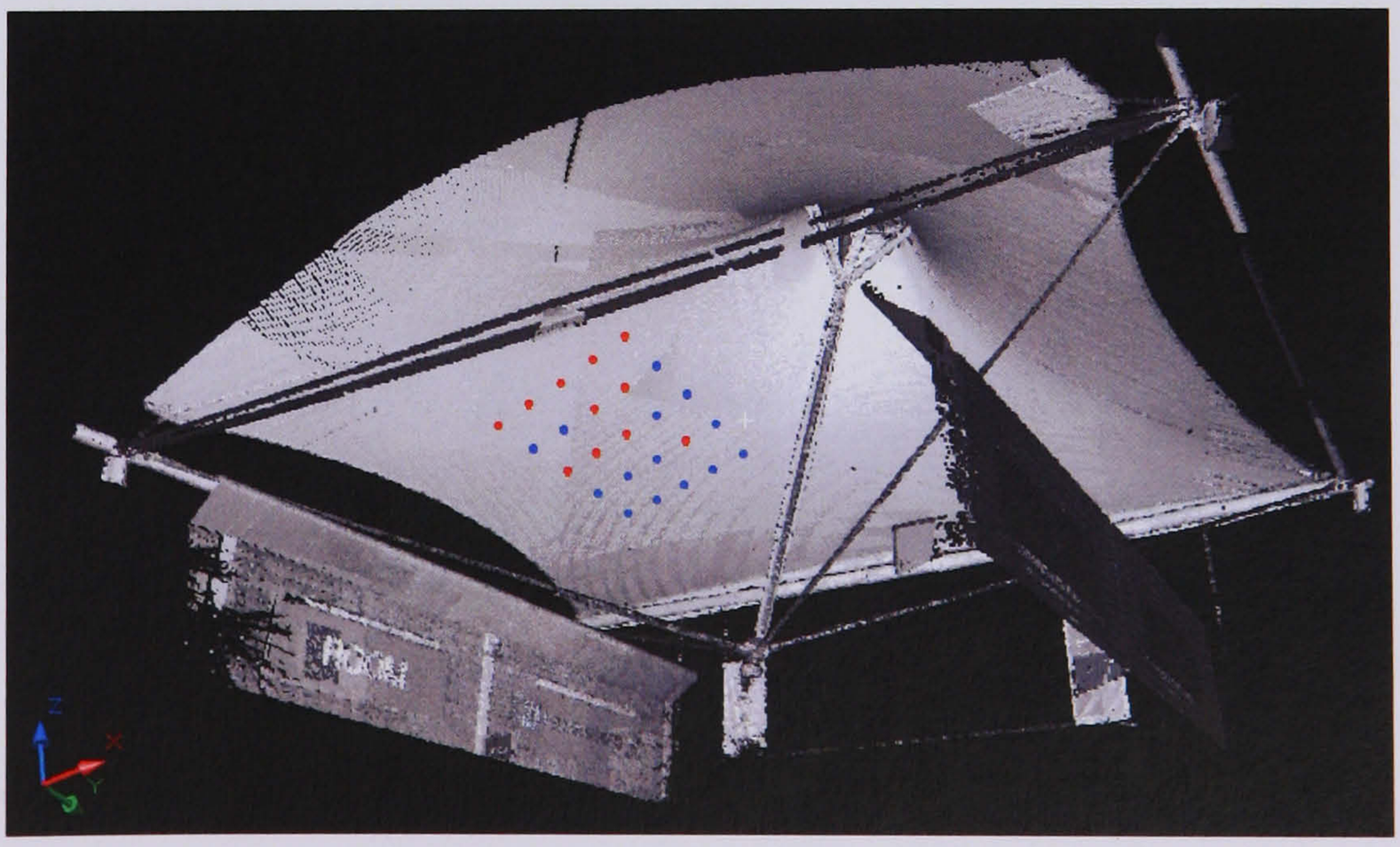


Figure 6-30: The videogrammetric monitored area on the membrane roof; points measured with obvious displacements are marked by red points.

6.2.3.4 Discussion: Dynamic Surface Modelling of Type 2 Membrane Structure

- Consistency of on-site non-contact controlling

  In addition to the standard monitoring task, the consistency of the non-contact control implementation was inspected on-site. The operation of generating and recording laser footprints was conducted three times at the beginning and repeated twice at the end of the Type 2 monitoring campaign. The data derived from each set was input to MS^2 for footprint extraction and matching. As a result, a total of 20, 22, 23, 21 and 23 common points were obtained respectively from the five scanning tasks. Consequently, 6 footprints located evenly across the observed area were specified as check points in each task and diverse numbers of remaining footprints were systematically selected as control points, to estimate the RMS error values of the remaining check points. A plot of accuracy against the number of employed control points is depicted in Figure 6-31. In general, higher accuracy is achieved by adopting more control points in the computation, however, RMS errors are shown to become more stable when at least 10 control points are employed. When 10 control points were used the RMS errors ranged from 6.7 to 7.5 mm. The accuracies of the same order demonstrate the consistency of the on-site non-contact control approach, although on-site results were slightly degraded compared with those obtained in the indoor experiments.



Figure 6-31: RMS error values vs. diverse number of adopted control points.

- Displacements of the observed surface

  The weather on the day for observing membrane structure of Tent Type 2 was windy. Whilst videogrammetric monitoring was carried out, the displacement of the

membrane roof was very clear to see at the test site. The dynamic surface model solved by MS^2 reflected the scene accordingly. The displacement of the membrane roof reached over 20 mm, caused by external wind loading. By inspecting the displacement maps (Figure 6-18, Figure 6-24, Figure 6-27, Figure 6-28) and extracted profiles (Figure 6-22, Figure 6-23, Figure 6-25, Figure 6-26) generated through the Advanced Query interface in MS^2, the non-linear waved movements that occurred due to the wind loading were observed. Furthermore, as Scheuermann and Boxer (1996) stated, once an arrangement of supports of membrane structures has been established, any change of compression member results in an immediate change of structural behaviour. To inspect this point, the displacements derived from the 25 tracking points (where obvious movements occurred were marked by red points) were superimposed onto the discrepancy map generated from the static surface comparison scheme (Section 6.2.2.2). In Figure 6-32, it was generally found that small displacements occurred in the area built close to the designed model, while the points with evident displacements were distributed closer to the area where large discrepancies were determined. The dynamic behaviour of the roof was therefore suspected as having a connection with the roof deformation, at which the relatively obvious displacements were possibly caused by the incorrect arrangement of the membrane roof.

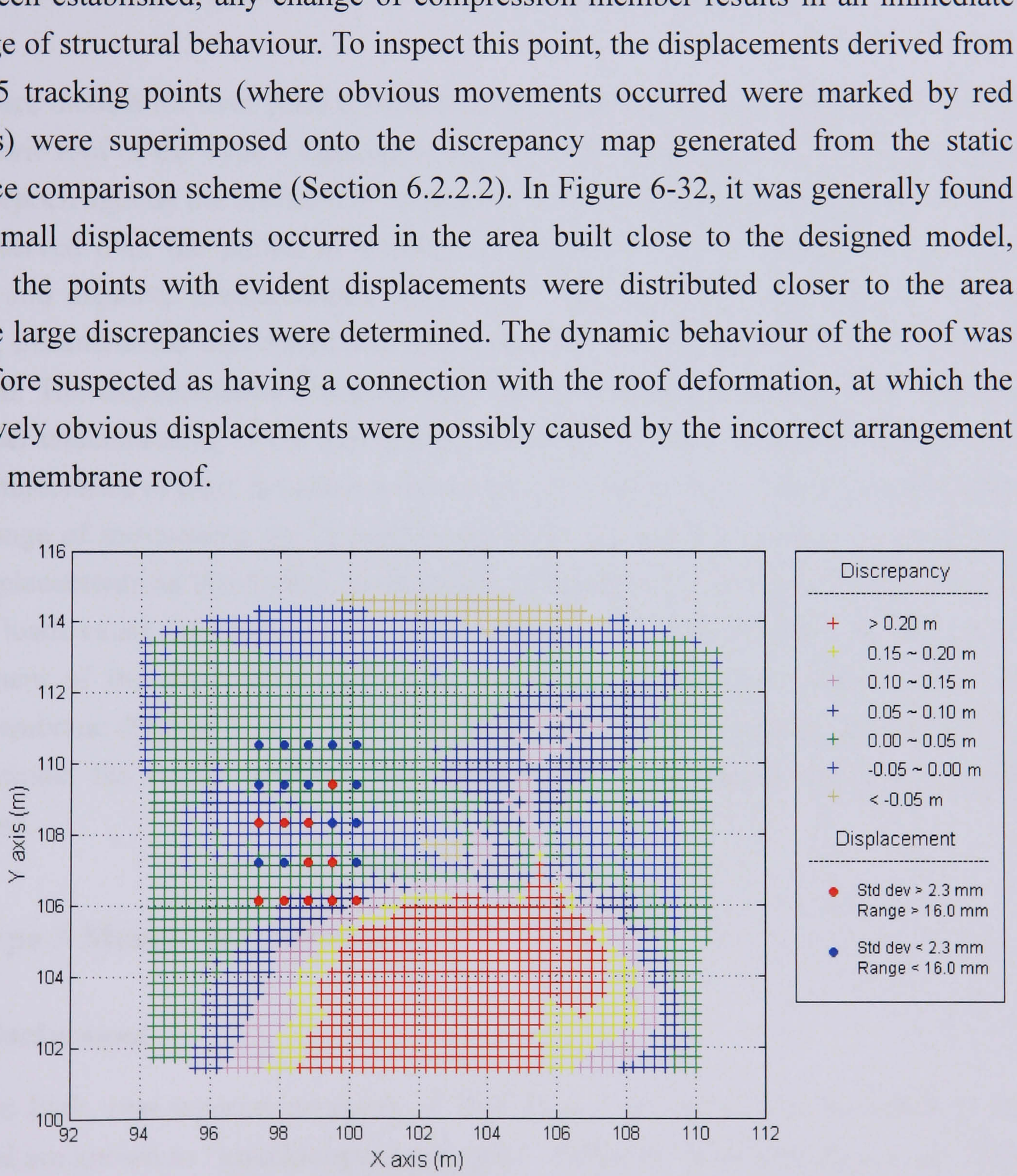


Figure 6-32: The superimposed map of displacements and discrepancy map.

6.2.4 Summary: Monitoring of Type 2 Membrane Structure

Through the implementation of static surface comparison, the disparities between the

designed mathematical model and the finished structure could be determined. Similar to the results derived from the monitoring of the Type 1 membrane structure, the disparities of the observed Type 2 membrane roof were identified. The solved discrepancies varied from -0.09 m to +0.345 m and their magnitude and distribution across the fabric roof was illustrated in Figure 6-10. The common factor causing the differences determined in the Type 1 and Type 2 membrane roofs was the incorrect erection of the arch steelworks and flying masts in the observed structures. Furthermore, in the Type 2 membrane structure monitoring scheme, it was also proved that the roof deformation would be affected by the steelworks of the connected canopy.

The surface models for over 3600 epochs were analysed to determine the displacements of the fabric roof of the Type 2 membrane structure. By comparing the surface model of the first epoch against the surfaces of remaining epochs, numerous obvious movements were observed over the period of monitoring (Figure 6-17), in which the maximum positive and negative displacements were +22.9 mm and -19.4 mm respectively. In addition, instantaneous movement was also computed and it varied from +19.5 mm to -20.2 mm. The displacements observed were mostly caused by external wind loading. For further understanding of the movements across the surface, 25 points were selected and the trajectories of their Z-values were tracked over time. As a result, the mean value of the range of movements on 25 points was 0.016 m, and the positions of relatively large displacements on the canopy were shown in Figure 6-30. Furthermore, not only do external loads cause the displacement of a membrane structure surface, the changes of arrangement of the supporting steelworks also affect the dynamic behaviour of the fabric membrane (Figure 6-32). Hence, when inspecting the movements in a sequential surface model the results derived from static surface comparison should be jointly considered.

6.3 Type 3 Membrane Structure

6.3.1 Background

At Dalton Park, two separate canopies of Tent Type 3 are located at the bends in the street, and are known as "knuckle space canopies". Different from Tent Type 1 and Type 2, these form single low conics, with large elliptical rings suspended from cable-stayed masts (Bridgens et al., 2004). A relatively flat roof is the other characteristic of the Tent Type 3 membrane structure. In this section, one of the Tent Type 3 structures was observed, its position and dimensions are illustrated in Figure 6-33 and Figure 6-34.

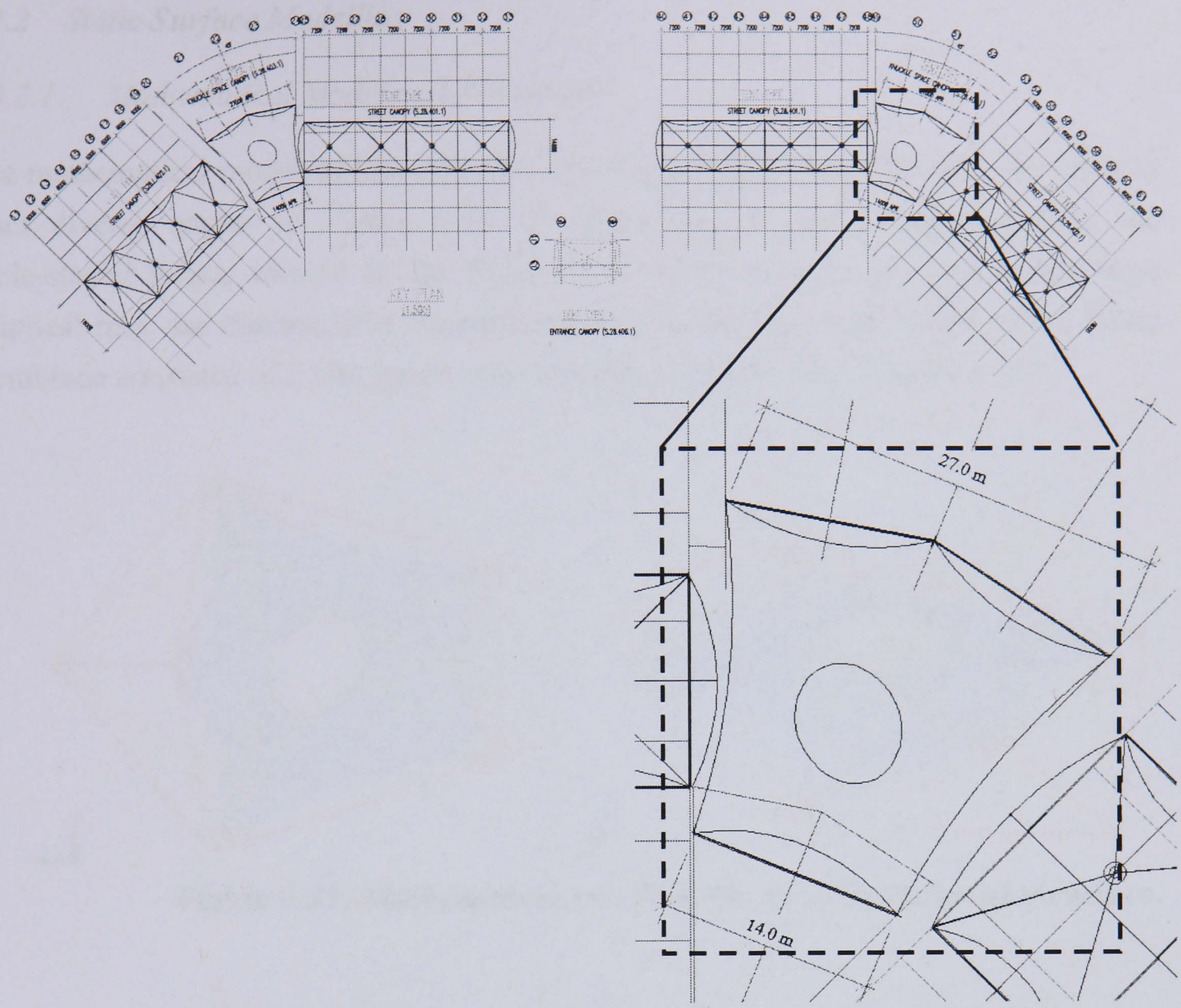


Figure 6-33: Design plan of Dalton Park, the observed membrane structure of Tent Type 3 is outlined by the dashed line.

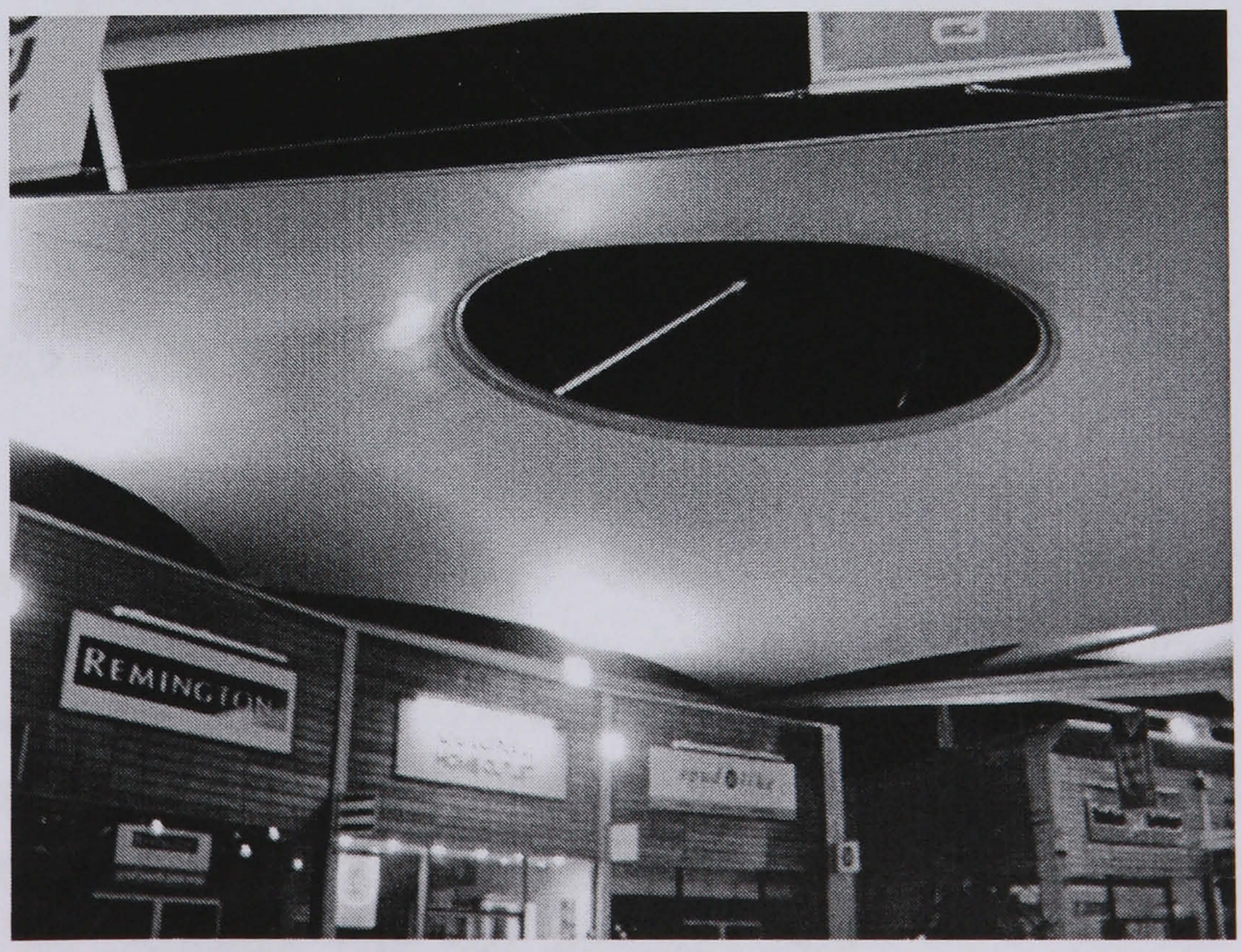


Figure 6-34: The Tent Type 3membrane structure.

6.3.2 Static Surface Modelling

6.3.2.1 Mathematical Model and TLS model

The mathematical model of the observed Tent Type 3 membrane structure was viewed from diverse angles in Figure 6-35. As introduced in the previous section, the cable-stayed masts, instead of the flying mast, which were used to carry the large elliptical ring, are illustrated in the mathematical model. The point model of the fabric membrane consisted of 2 040 points was then extracted with MS^2 (Figure 6-36).

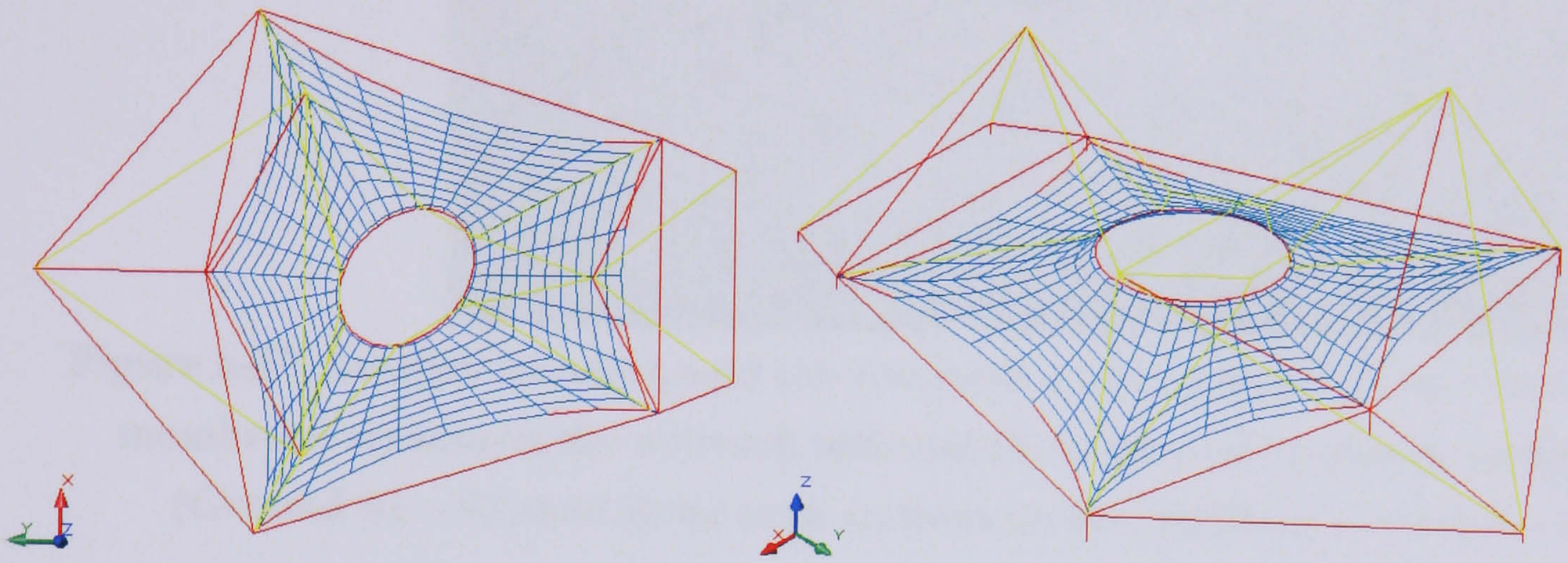


Figure 6-35: Mathematical model of the Type 3 membrane structure.

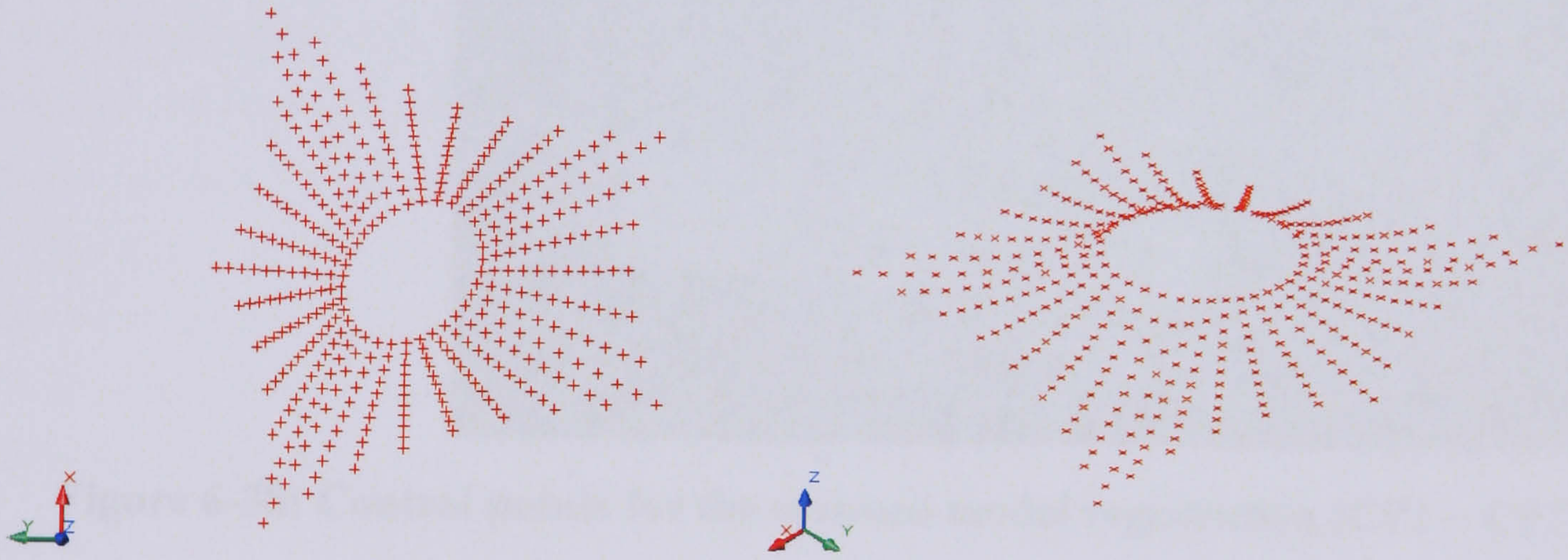


Figure 6-36: Point model of the Type 3 membrane structure.

The laser scanned model of the Tent Type 3 membrane structure was derived using a Leica HDS2500 laser scanner. A scanner network comprising nine scans performed at five stations was arranged to scan the membrane structure (Figure 6-37). Twelve control points for model registration were observed by a Leica TCRA 1103 total station, with an average standard deviation of 2.7 mm, 2.5 mm and 1.7 mm in the X, Y and Z axes (Figure 6-38). After the registration was finished, the amalgamated scanned model was produced. Subsequently, the membrane roof was extracted (Figure 6-39) and the supporting steelwork was modelled (Figure 6-40) for the task of surface comparison.

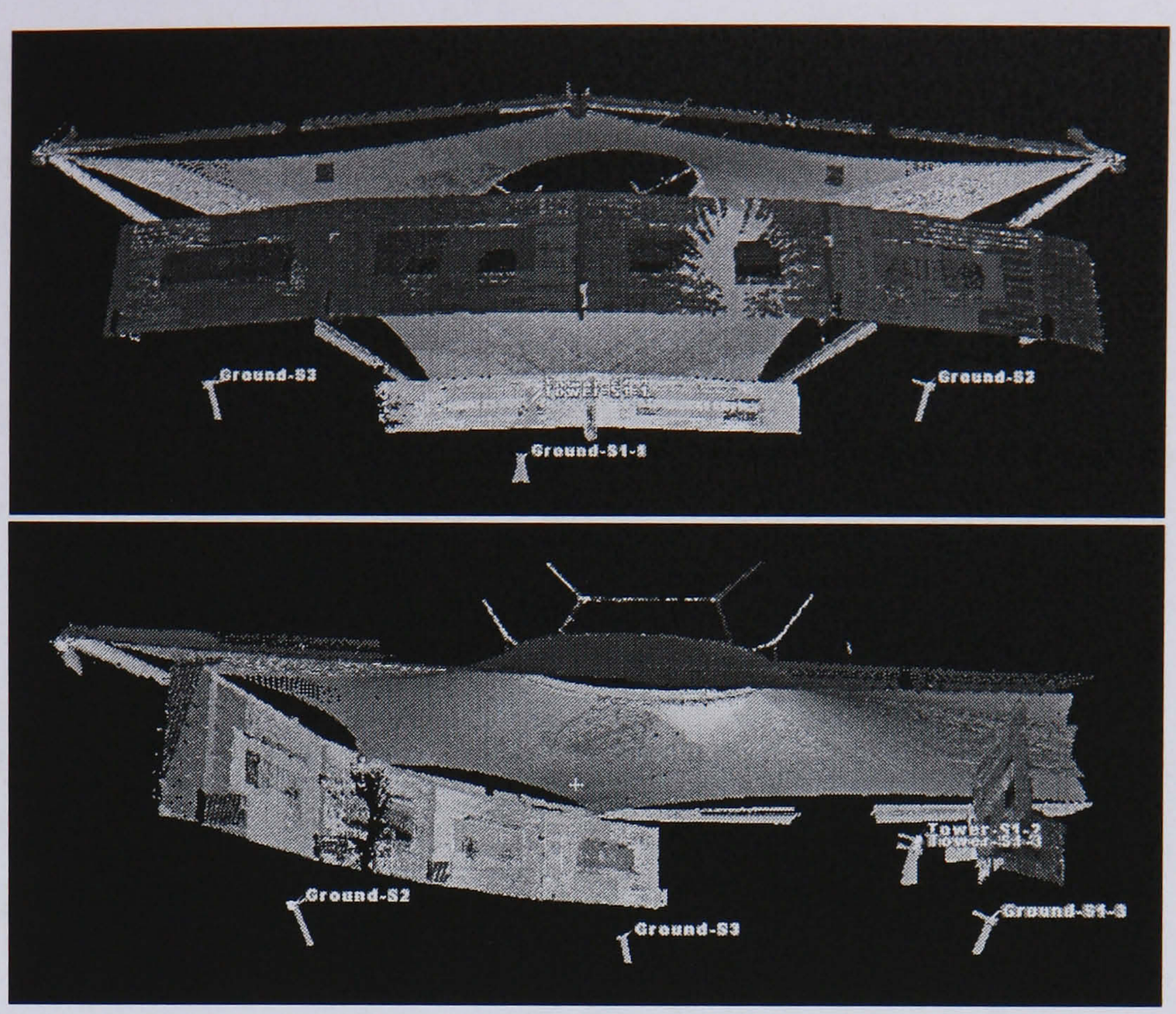


Figure 6-37: Scanner network and the resultant scanned model of the Type 3 membrane structure, the network includes three ground scanning stations (Ground S1 – S3) and three scan stations on the platform (Tower 1 – 2).

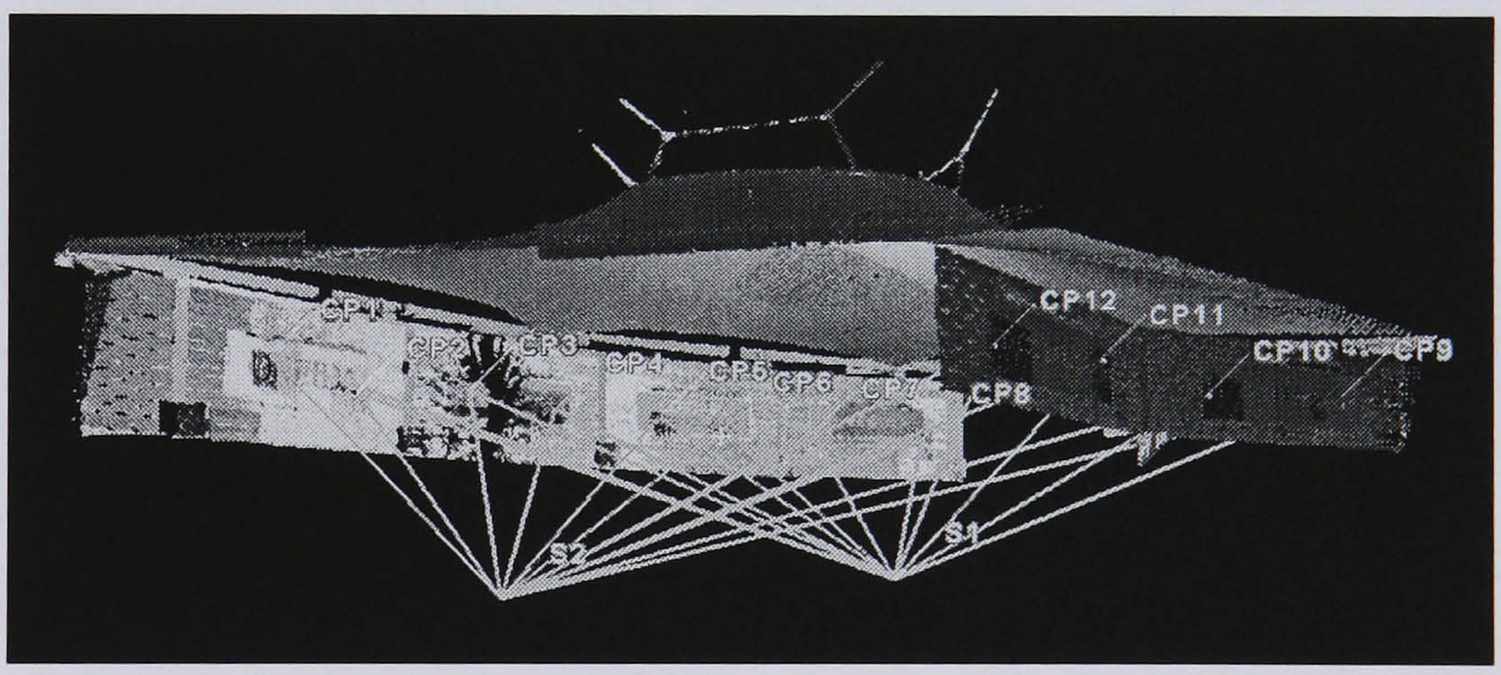


Figure 6-38: Control points for the scanned model registration (CP1 – CP12).

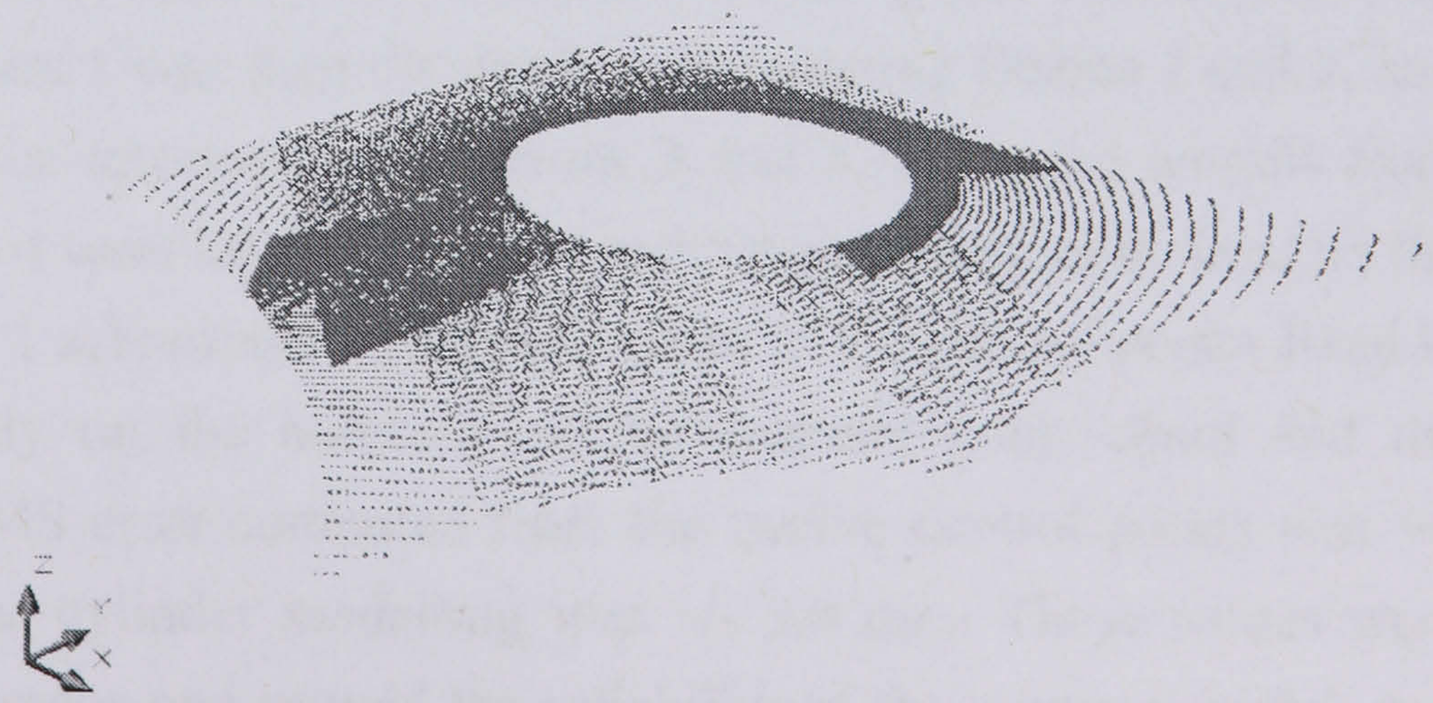


Figure 6-39: Fabric membrane roof extracted from laser scanned model.

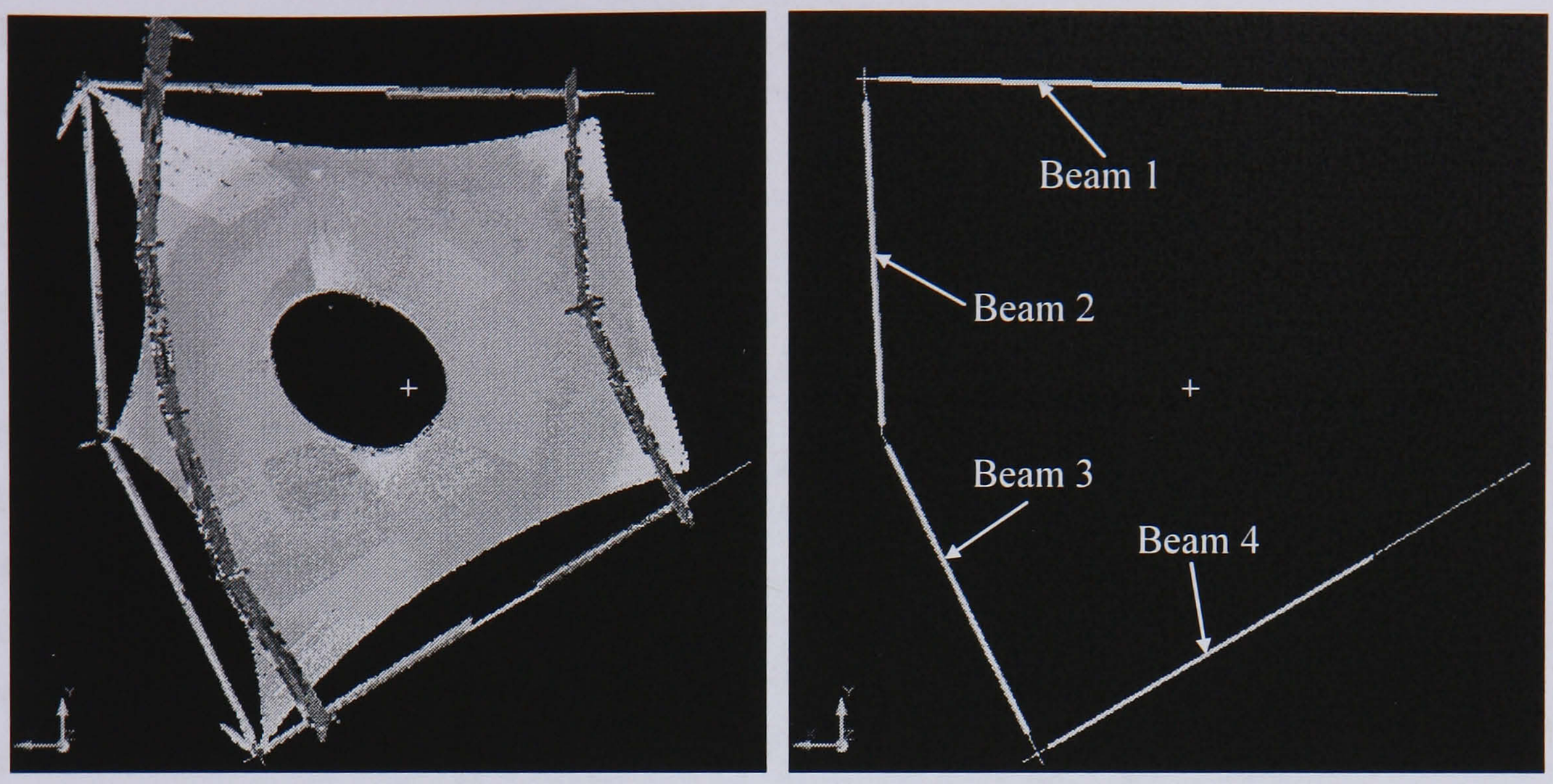


Figure 6-40: The modelled supporting steelwork and derived centre lines.

6.3.2.2 Surface Comparison

In order to compare the design model and finished structure of Tent Type 3, the control points for transforming the mathematical model were firstly determined. Both in the Type 1 and Type 2 structure monitoring schemes, four control points positioned approximately in the four corners were derived by computing the intersection points of the supporting steelwork. In applying this method to the observation of the Type 3 membrane structure, ideally five control points should be obtained. However, two of them on one side (Points 4 and 5 in Figure 6-41) were obscured by the declined canopy and could not be viewed even on the raised platform. Therefore only three control points were intersected (Points 1, 2 and 3 in Figure 6-41). Although the use of three control points would still be able to perform a 3D conformal transformation, the improper alignment of these three points (almost aligned on a straight line) might result in a solution with wrong rotation parameters. To avoid this, the determination of Points 4 and 5 was necessary. Four beams were modelled in the point cloud modelling procedure (Figure 6-40), Point 1 was then obtained by intersecting Beams 1 and 2, and Point 3 was derived from the intersection of Beams 3 and 4. Since the lengths from Points 1 to 5 and Points 3 to 4 were known, Points 4 and 5 were therefore defined on the centre lines of Beams 4 and 1 accordingly. The correctness of the control points fixed in this method depends largely on the accuracy of the scanned point cloud and the modelled cylinders. The RMS error computed from the twelve control points was +/- 5.9 mm and the error of the cylinder modelling was +/- 3.0 mm. These values were within the construction tolerance and proved the reliability of the scanned model, and further validated the control points determined.

The five control points were derived from both models (Table 6-12) and a 3D conformal transformation was carried out to relate the mathematical model into the same coordinate system as the laser scanned model. Consequently, the two surfaces were compared statistically. The solved transformation parameters and the surface comparison results are listed in Table 6-13. The discrepancies between the two surfaces were estimated and the range of the differences reached 0.954 m. From the discrepancy map produced by MS^2 (Figure 6-42), it is apparent that disparities occurred in area (a), the top ring steelwork. In addition, the area affected by the top ring is identified by the systematic distribution of the discrepancies. A number of profiles across the area where obvious discrepancies occurred are illustrated in Figure 6-43 and Figure 6-44. By viewing the profiles, the positioning differences of the top ring steelwork were identified. The small disparities in the five corners demonstrate the satisfactory performance of the transformation.

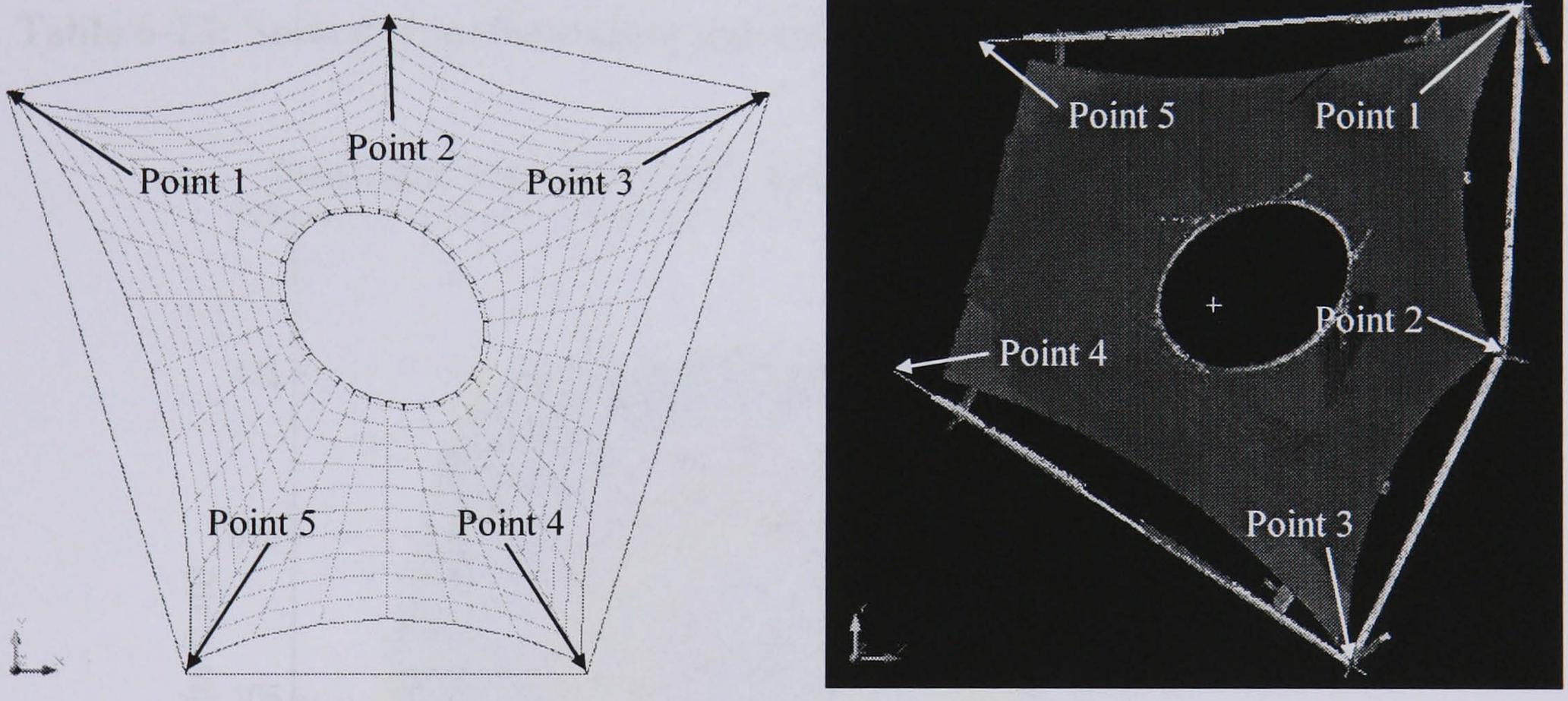


Figure 6-41: Five corresponding control points in the mathematical model and laser scanned model.

	Mathematical Model (mm)			*TLS Model (m)*		
	X_M	Y_M	Z_M	X_T	Y_T	Z_T
Point 1	-13581.161	38487.488	102500.008	110.677	117.041	17.064
Point 2	0.544	41189.801	102499.930	109.969	103.183	16.999
Point 3	13582.535	38488.180	102500.000	103.879	90.724	17.092
Point 4	7133.000	17482.402	100574.984	85.147	102.292	14.914
Point 5	-7132.928	17482.027	100574.977	88.681	116.021	14.912

Table 6-12: 3D coordinates of corresponding control points in mathematical and TLS model.

Transformation Parameters	*Translations (m)*	T_X	70.852
		T_Y	113.223
		T_Z	-85.976
	Rotations (°)	ω	-0.175
		ϕ	-0.494
		κ	-104.503
	Scale		0.001
Surface Disparity (m)	*Number of Points*		4157
	Maximum		0.147
	Minimum		-0.807
	Range		0.954
	Mean		-0.133
	Std. deviation		0.165
	RMS		0.212

Table 6-13: Solved transformation parameters and surface comparison results.

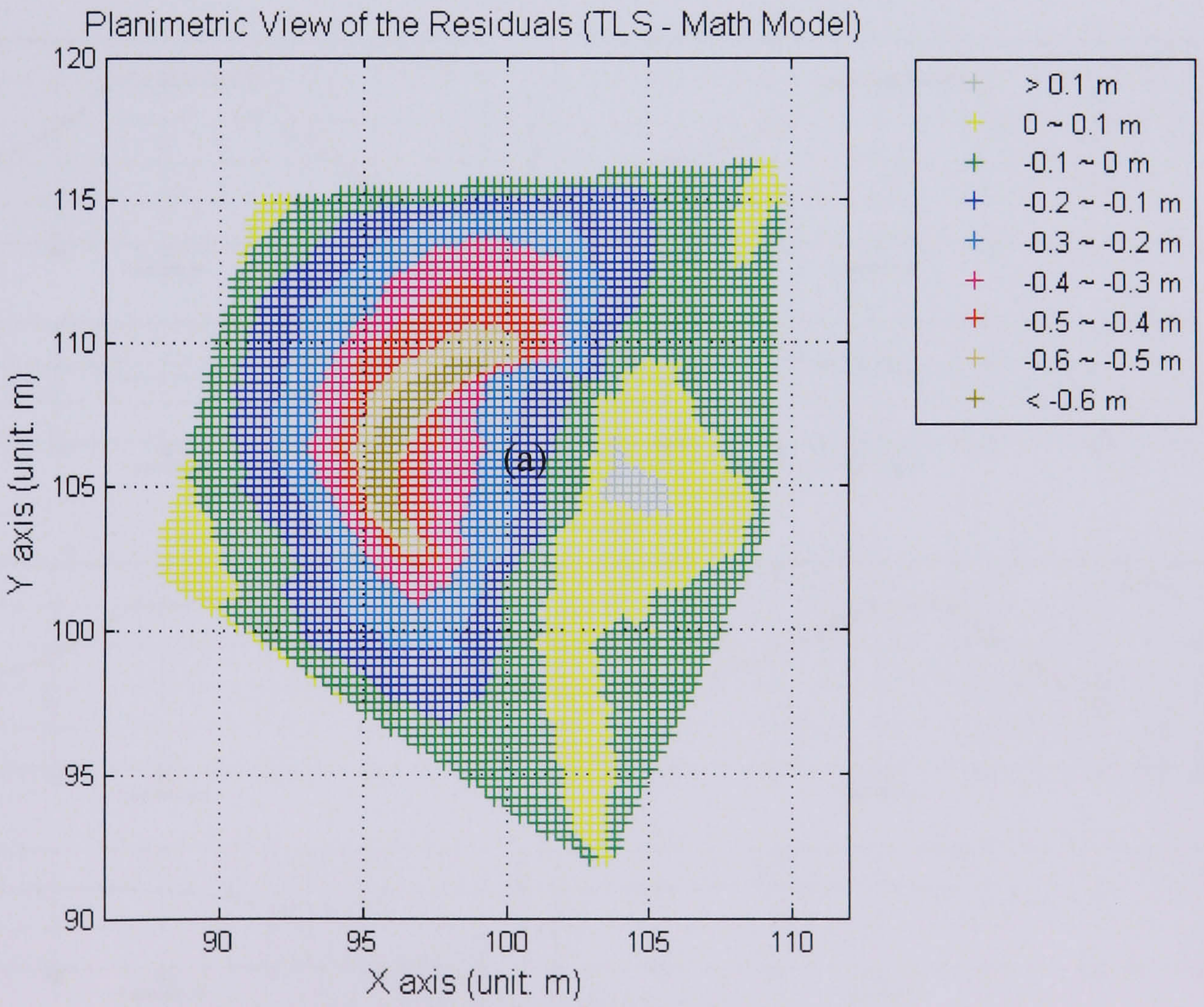


Figure 6-42: Discrepancy map derived from 3D conformal transformation.

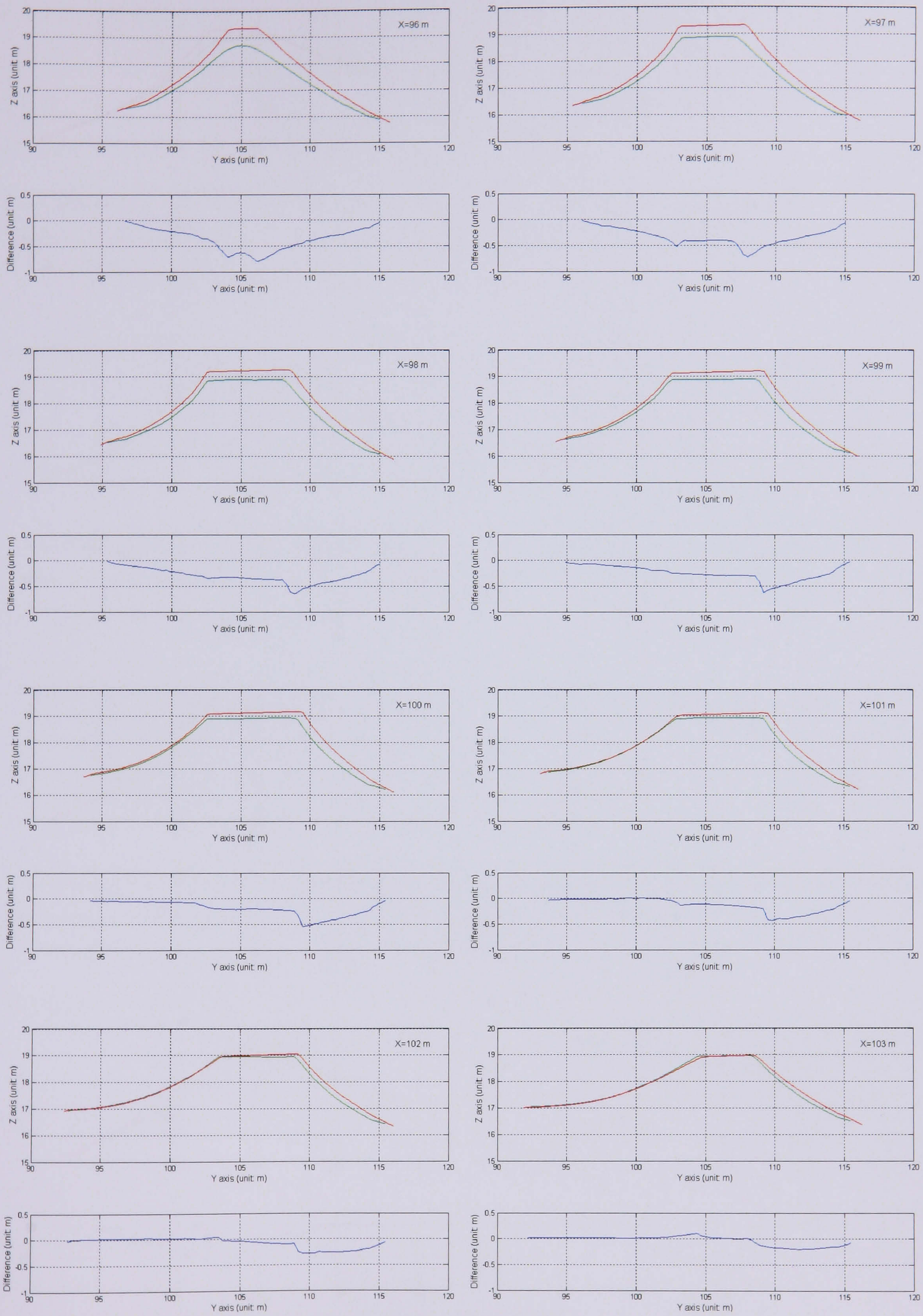


Figure 6-43: Differences in profiles along Y axis between the two surface models (the green profile line is derived from the laser scanned model, and the red line represents the profile of the transformed mathematical model).

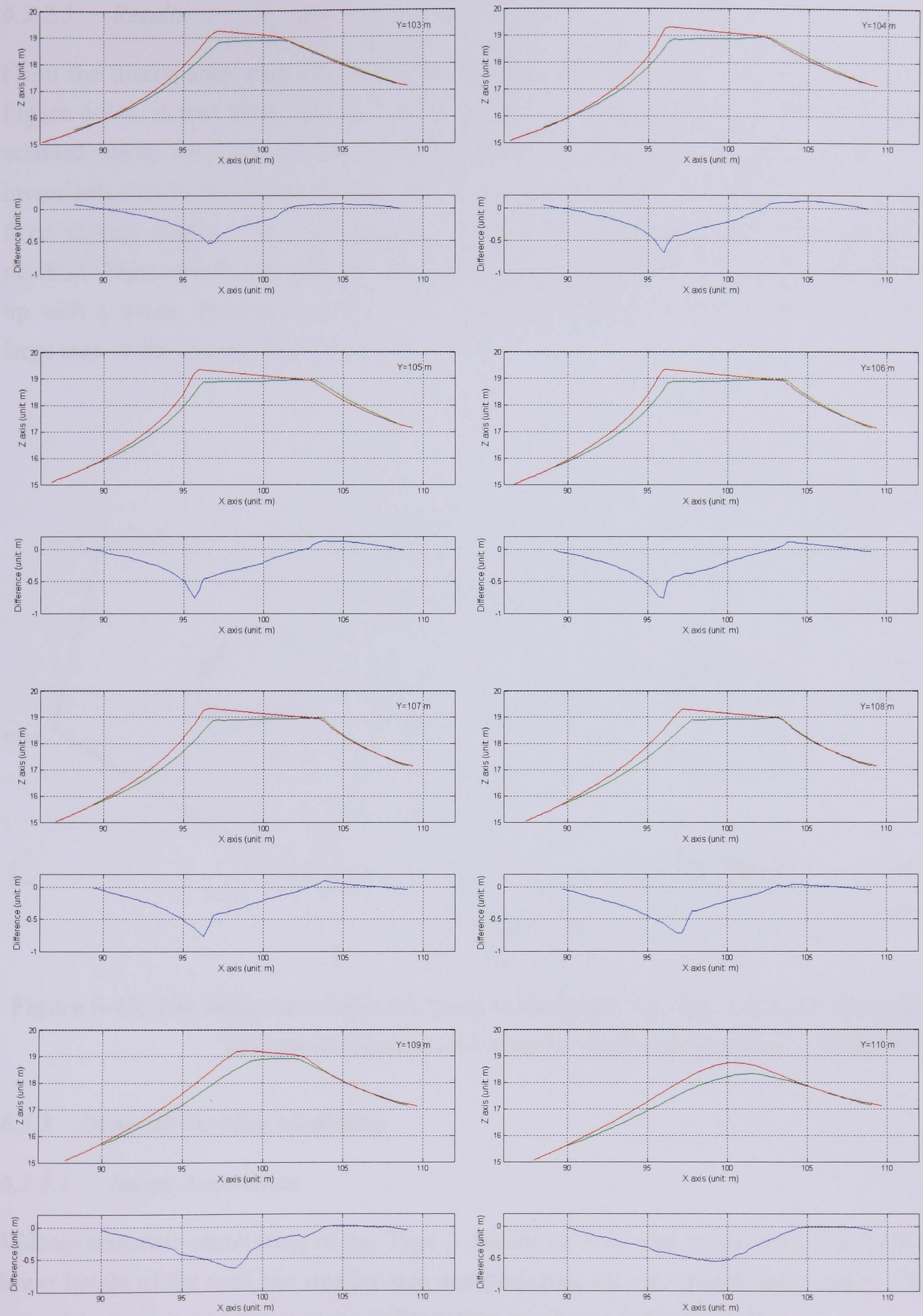


Figure 6-44: Differences in profiles along X axis between the two surface models (the green profile line is derived from the laser scanned model, and the red line represents the profile of the transformed mathematical model).

6.3.2.3 Results

From the discrepancy map (Figure 6-42) and the extracted profiles (Figure 6-43 and Figure 6-44), it was clear that the disparities between the mathematical and the laser scanned model were caused by the wrong arrangement of the top ring steelwork. To investigate this further, the top elliptical rings derived from both models were viewed from diverse angles. The top ring was found to be shifted from the designed plan position (Figure 6-45, left) and the ring suspended by the cable-stayed masts was pulled up with a wrong declined angle (Figure 6-45, right). Due to the construction error a large area of the canopy was deformed.

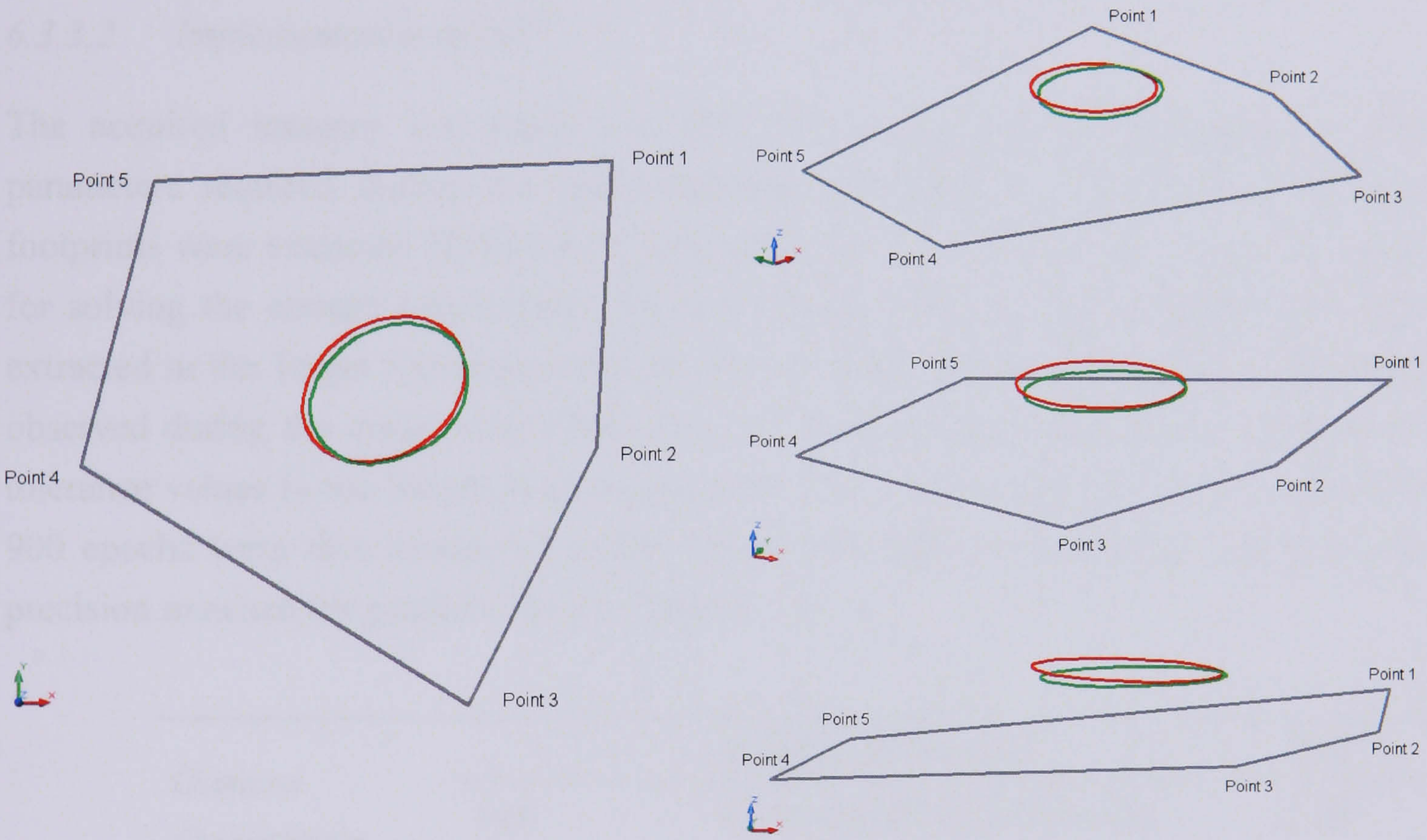


Figure 6-45: The reference steelwork (gray frame) and top ring extracted from the TLS model (green) and transformed mathematical model (red).

6.3.3 Dynamic Surface Modelling

6.3.3.1 Image Acquisition

Videogrammetric monitoring of the Type 3 membrane roof was undertaken. Due to the lower height of the roof, the smaller area was projected onto the membrane surface. The area of projection and the camera configuration are shown in Figure 6-46.

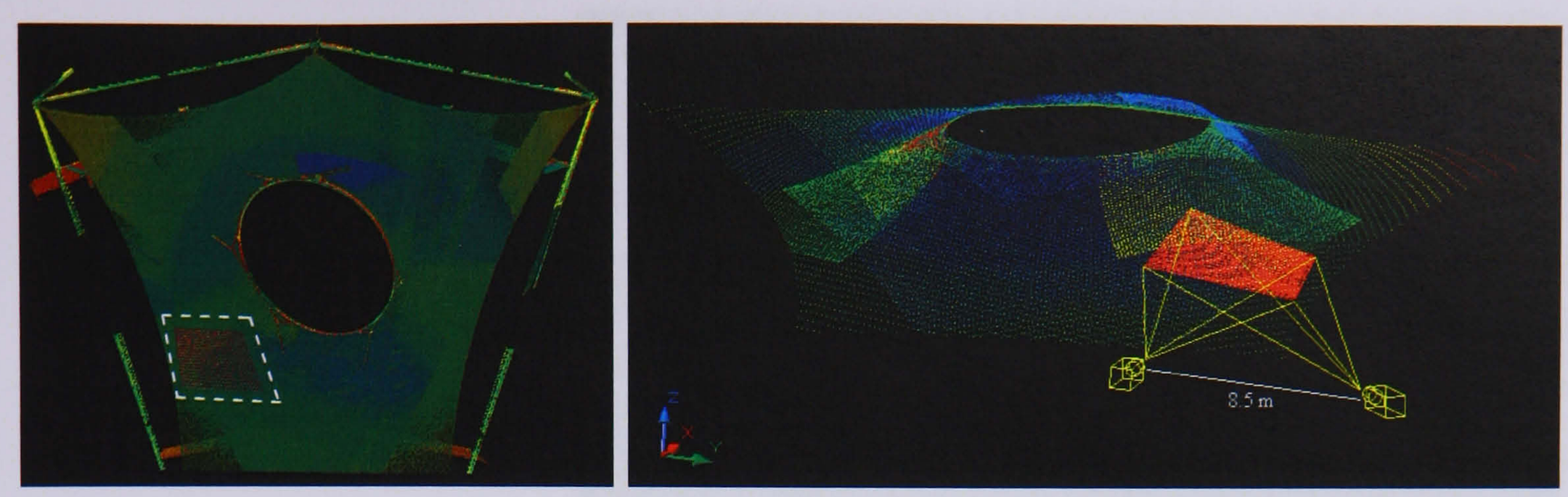


Figure 6-46: Laser scanned model and videogrammetric monitoring area (red points) of Type 3 membrane structure.

6.3.3.2 Implementation of MS²

The acquired imagery was input into MS² for processing and measurement. The parameters required during the implementation are listed in Table 6-14. The laser footprints were extracted (Figure 6-47) and 20 of them were selected as control points for solving the camera orientations (Table 6-15). In addition, the projected dots were extracted in the Target Extraction module (Figure 6-48). As no obvious movement was observed during the monitoring at the test site, small values were given for maximum tolerance values in the Target Tracking module. The 3D coordinates of each point over 900 epochs were then computed in the Target Calculation module, the measurement precision matched the predicted value (Table 6-16).

Camera Orientation		*Number of frames*	768
	Left	*Normalised threshold value*	0.30
	Right	*Normalised threshold value*	0.18
Target Extraction		*Number of epochs*	900
	Left	*Normalised threshold value*	0.084
	Right	*Normalised threshold value*	0.064
Target Referencing	*Left*	*Max X interval (pixels)*	10
		Max Y interval (pixels)	35
	Right	*Max X interval (pixels)*	5
		Max Y interval (pixels)	38
Target Tracking	*Left / Right*	*Max X tolerance (pixels)*	5
		Max Y tolerance (pixels)	5

Table 6-14: Input parameters for MS² implementation.

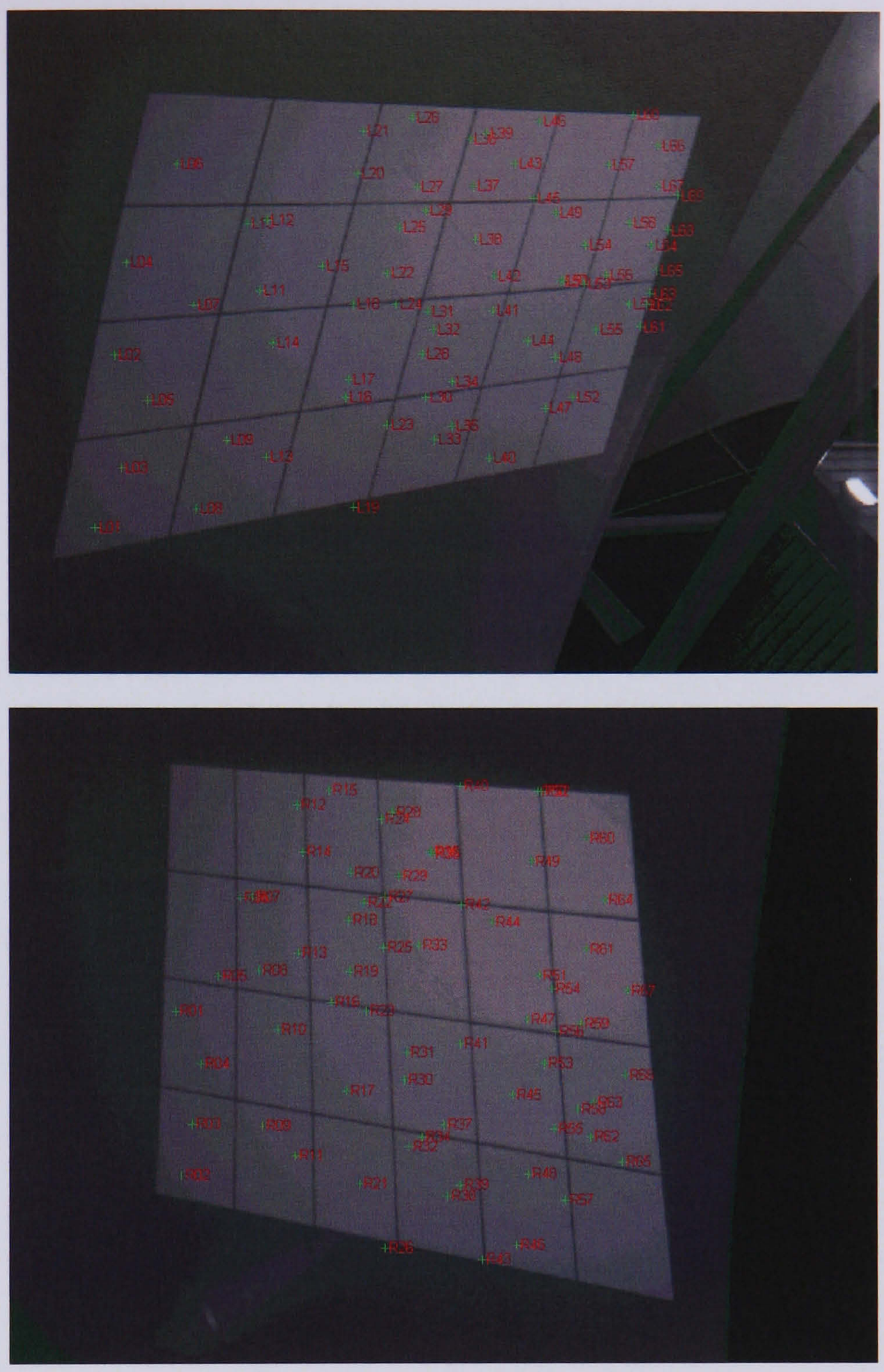


Figure 6-47: Stereo pair of extracted control footprints.

	Left Exposure Station	*Right Exposure Station*
X (m)	101.289 ± 0.019	101.279 ± 0.014
Y (m)	106.385 ± 0.014	114.880 ± 0.013
Z (m)	11.112 ± 0.021	11.151 ± 0.012
ω (degrees)	132.833 ± 0.155	-156.191 ± 0.120
ϕ (degrees)	31.880 ± 0.128	38.142 ± 0.123
κ (degrees)	-63.391 ± 0.114	-93.456 ± 0.129

Table 6-15: Orientation results for the Type 3 membrane structure monitoring.

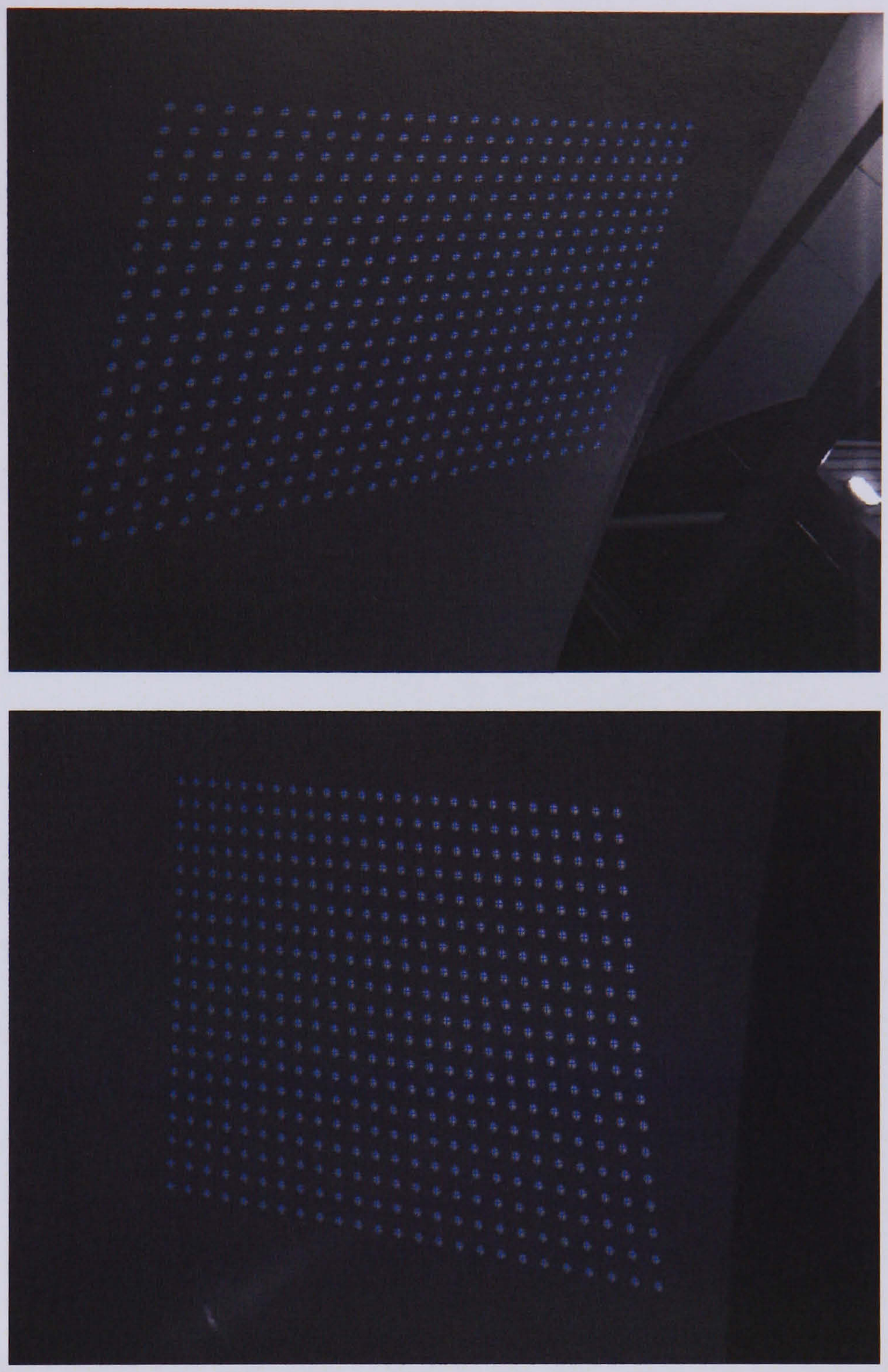


Figure 6-48: Stereo pair of extracted projected-dots of epoch 1.

Base Distance (m)	*Depth Distance (m)*	*Image Scale*	*Predicted Precision (mm)*				*Adjustment Precision (mm)*			
			σ_X	σ_Y	σ_Z	$\sigma_{Position}$	σ_X	σ_Y	σ_Z	$\sigma_{Position}$
8.5	7.5	1:625	0.5	0.6	0.6	1.0	0.6	0.5	0.6	1.0

Table 6-16: Results of the point measurement for the Type 3 membrane structure monitoring.

6.3.3.3 Results

At the displacement analysis stage, the surface from the first epoch was chosen as the base model and it was statistically compared with the surfaces from the remaining

epochs. The resultant diagram of the maximum and average displacements through 899 epochs is drawn in Figure 6-49, and the maximum positive and negative movements were found to be as +4.3 mm and -5.0 mm respectively (Table 6-17). As the resulting movements were under the minimum displacement that could be measured using the videogrammetric system, it indicated there was no unexpected movement being observed. Similar to the situation in observing the membrane structure of Tent Type 1, the weather conditions were good on the day the experiment was conducted, therefore this result, in which the observed displacements in the sequential surface models were largely insignificant, was as expected.

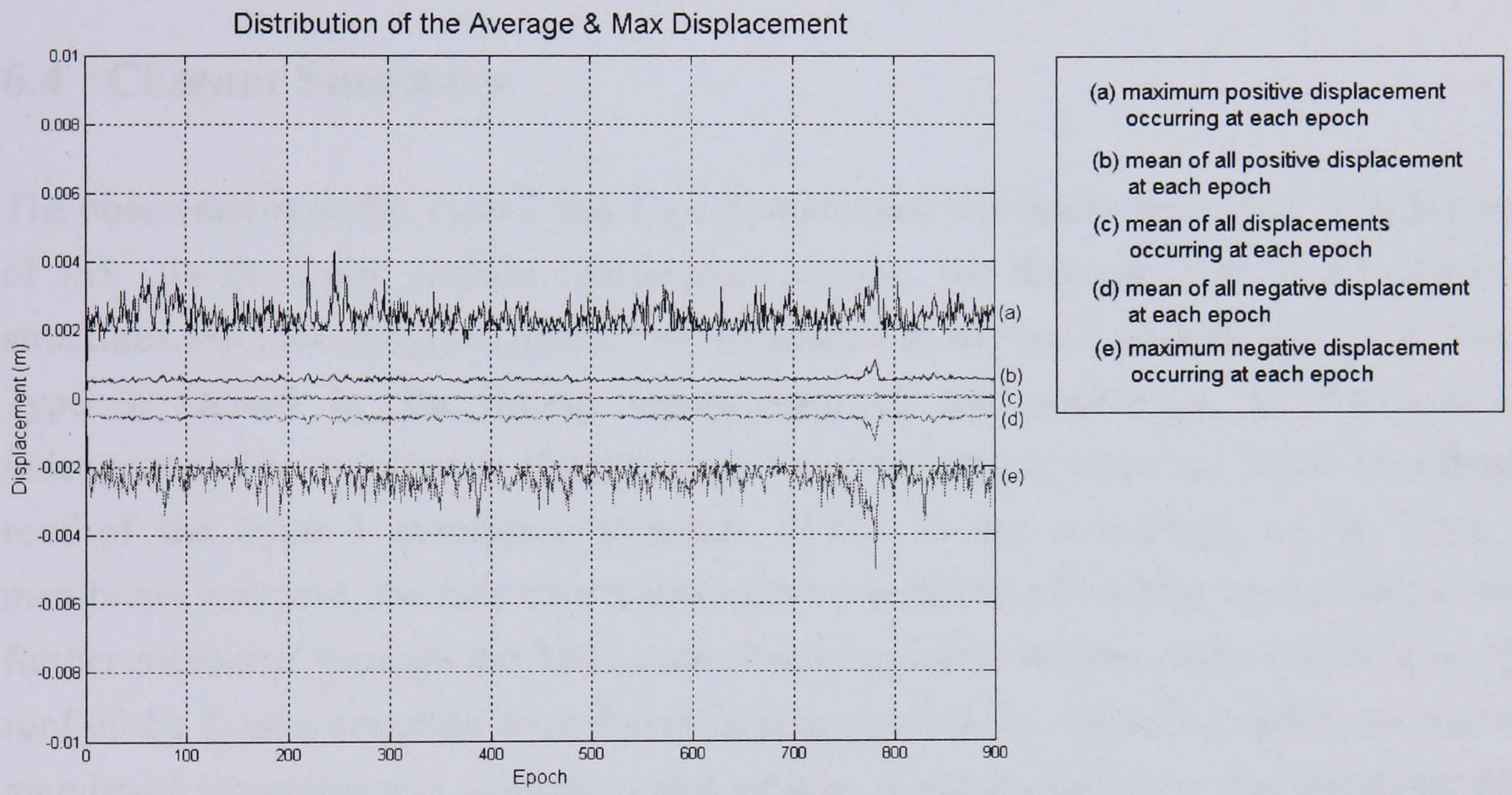


Figure 6-49: Resulting displacement for the observations on the Type 3 membrane structure.

	Average Displacement		*Maximum Displacement*	
	Positive	*Negative*	*Positive*	*Negative*
Mean (mm)	0.6	-0.6	2.4	-2.3
Max (mm)	1.1	-1.3	4.3	-5.0

Table 6-17: Solved displacement for the Type 3 membrane structure monitoring.

6.3.4 Summary: Monitoring of Type 3 Membrane Structure

According to the results derived from the Type 1 and Type 2 monitoring scheme, the discrepancies of the membrane roofs between the mathematical and TLS model were mainly affected by the incorrect arrangement of the steelwork. After the investigation, it

was realised this was also the case in the Type 3 membrane structure. Without the erection of the flying masts, the membrane roof of the Type 3 membrane structure was suspended from the cable-stayed masts. The results derived from the surface comparison scheme revealed the discrepancies between the designed model and the finished as-built structure existed and varied from -0.807 m to 0.147 m (Table 6-13; Figure 6-42). Furthermore, the incorrect suspension angle and position of the top ring caused the large deformation of the membrane roof of the observed structure (Figure 6-43; Figure 6-44; Figure 6-45). During the dynamic surface modelling scheme, as no external loading was applied, there was no unexpected displacement being observed by the videogrammetric monitoring system.

6.4 Chapter Summary

The observations of the Type 2 and Type 3 membrane structures were made with the use of MS^2. In the static surface comparison scheme, the discrepancies of the finished structures from the designed models were detected in the roofs of both Tent Type 2 and Type 3, caused by the wrong arrangement of the steelworks. In the task of videogrammetric monitoring, there was no movement being observed in the membrane roof of the Type 3 membrane structure. While in the monitoring of the Type 2 membrane structure, the movements caused by external wind loading were recorded and further measured through the MS^2, a number of evident displacements occurred in the roof of the Type 2 structure were determined as a result. By observing different types of membrane structures and working under various weather conditions, the transferability of MS^2 was proved in this chapter.

CHAPTER SEVEN

CONCLUDING REMARKS

7.1 Conclusions

This thesis has demonstrated the development of a monitoring system for determining the disparities between the designed and finished structure, and for modelling the dynamic behaviour of the membrane roof surface. The feasibility of the system has been proven through the investigation of three different types of finished membrane structures. Based on the implementation, results and discussions that followed the research, the important conclusions regarding the applied geomatics techniques, the monitoring system, on-site observation by the monitoring system, transferability of the monitoring system, and investigations into the various membrane structures are presented.

7.1.1 Applied Geomatics Techniques

In order to investigate solutions to the issues involved in the membrane structure measurement and monitoring, geomatics techniques including terrestrial surveying adopting total station instruments, terrestrial laser scanning, photogrammetry and videogrammetry have been reviewed and discussed in Chapter Two. In addition, the metrological techniques of laser tracking and laser vibrometry were introduced. By inspecting the principles and relevant applications of these potential techniques, their limitations and applicability to the monitoring system have been assessed. As a result, terrestrial laser scanning was determined as a suitable technique for undertaking membrane roof measurement due to the capability of rapid, intensive and non-contact

data acquisition. Also, the technique of videogrammetry was proposed to estimate the displacement of the membrane roof over a potentially extended period of time.

7.1.2 Hardware and Software Aspects of the Monitoring System

The use of terrestrial laser scanning and videogrammetry have been recognised as suitable techniques for membrane structure measurement and monitoring, the methodology comprising these two techniques was subsequently proposed in Chapter Three. Firstly, the available hardware components including the Leica HDS2500 and HDS3000 laser scanning systems, DV camcorders and CCD video cameras employed in the monitoring system were introduced. Further, in order to accommodate the constraints involved in videogrammetric monitoring such structures, e.g. the uniform surface texture and unreachable height, non-contact control and projected-dots videogrammetry methods were proposed to provide control and targets for measurement in this research. Through a series of proof-of-concept experiments, the proposed methodology was proved feasible, accurate and reliable for monitoring a real membrane structure.

In order to provide a comprehensive software for processing data acquired from the membrane structure observation, the MS^2 software has been developed for inspecting differences that exist between the designed model and the finished structure as well as for determining the displacements that occurred on the membrane surface under loading. The software was programmed using the MATLAB language and the algorithms adopted were introduced in Chapter Four. By importing the mathematical model and registered terrestrial laser scanned model of a membrane roof into the Static Surface Comparison panel, the disparities between the designed and finished version of the structures could be obtained. The magnitude and the distribution of the solved differences could be inspected from the resulting discrepancy map and the profiles extracted across the membrane roof surfaces.

To investigate the displacement occurring in the membrane surface under loading, the imagery data acquired from videogrammetric monitoring was input into the Dynamic Surface Modelling panel. In the panel, the image sequence was processed through the modules of Camera Orientation, Target Extraction, Target Referencing, Target Tracking, Target Computation and Target Modelling. These modules were also programmed in the MATLAB environment and the primary tool applied for bundle adjustment computation was the CUBA program. For advanced automation of the implementation, these tasks

were operated via the programmed GUIs. With the straightforward interface and the prompt operation guide, the dynamic model of the observed membrane roof would be generated easily. The sequential and instantaneous displacements were able to be determined from the resulting sequential surface model. The performance of MS^2 was evaluated by two tests simulating the type of network configuration that would be adopted in the field (Section 4.4). After the processing, the best accuracy that the videogrammetric monitoring system could be expected to achieve was in a level of +/- 6 mm, indicating the system was satisfactory for investigating displacement that exceeds the design tolerance value on the observed membrane structures. Moreover, the analysis of dynamic displacement has been accomplished in MS^2 by tracking points, profiles and surfaces extracted from the sequential surface model. Although the issues of processing efficiency and image feature extraction needed to be addressed as indicated in Section 4.4.4, the MS^2 software was still demonstrated as a success for complete videogrammetric processing and measurement.

7.1.3 On-site Observation using the Monitoring System

The developed monitoring system was first applied to observing a Tent Type 1 membrane structure at Dalton Park outlet centre. The Leica HDS2500 and HDS3000 laser scanning systems were employed to generate the as-built model of the membrane structures. Although the time required for performing scanning varied due to different specifications of the instruments (see Section 5.3.2), both scanners demonstrated the capability of producing 3D models of the membrane structures. The utilisation of the TLS technique enabled the membrane roof to be represented by a point model with high resolution. Moreover, the accuracy of the resulting scanned model (6.0 mm) indicated that the laser scanned model was accurate enough for examining the membrane structure whose permitted deviation of the position of steelwork was 10.0 mm. However, when considering the operation of TLS at the test site, inconveniences occurred occasionally, due to the heavy scanner head and battery. This is currently one of the main drawbacks of TLS. In addition, the terrestrial laser scanning system is still costly. This may limit the widespread deployment of the TLS technique in membrane structure monitoring.

To determine the discrepancies between the designed mathematical model and the laser scanned model, the surface matching and standard 3D conformal transformation methods were respectively applied in the circumstances where common control points were unavailable and available. From the resultant discrepancy maps (Figures 5–15 and

5–20), it was found that obvious difference between the two surface models did exist. Furthermore, the symmetrical occurrence of the discrepancies across the observed surface was similar through the implementation of the two approaches, even though the solved differences varied. As physical constraints (i.e. common control points) were employed, a 3D conformal transformation was deemed as a more robust method and used to investigate the discrepancy that existed between the two surface models.

The proposed methodology including non-contact control and projected-dots videogrammetry was applied to monitor the dynamic behaviour of the membrane roof structures. Sequential image data of the membrane roof was collected using a pair of CCD video cameras. According to the monitoring campaign addressed in Chapter Five, the proposed methodology proved feasible at the test site. As no additional arrangement of physical targets was needed, the efficiency of the videogrammetric monitoring was significantly improved. In addition, as image sequences were acquired, sequential movements of the membrane roof could be derived once the videogrammetric processing was complete through MS^2. The displacement was analysed in Section 5.4.3.

Regarding on-site operation of the videogrammetric monitoring, two issues are noted below. Firstly, the videogrammetric monitoring was mainly executed in an automatic way, with the exception of the non-contact control. In this task, the generation of control laser footprints was performed by the internal program of the Leica TCRA 1103 total station instrument. However, , this function experienced a high failure rate, as did the similar function in another total station that was trialled (a Leica TCR 307). To inspect possible factors causing the failure, an identical fabric sample was tested in the laboratory and the automatic measurement of the total station responded well with the material. As the malfunction still remained unexplained, the total station was operated manually to generate laser footprints during the implementation of non-contact control. Secondly, the steelwork constructed beneath the fabric membrane obstructs a direct observation in this application. In order to get a clear view of the projected area on the roof from each camera, the exposure stations therefore had to be arranged appropriately to avoid the steelwork. Due to the constraints that existed in the working environment, camera network design as a result had to be modified at the setup stage of videogrammetric monitoring.

7.1.4 Transferability of the Monitoring System

The monitoring system has been proved feasible in the previous observation campaign.

It was further employed to survey different types of membrane structures to sustain its transferability. Firstly the monitoring system was applied on a Tent Type 2 membrane structure at Dalton Park. The measurement and monitoring were adequately performed on site and the schemes of static surface comparison and dynamic surface modelling were processed successfully. This was also the case in the observation of the Tent Type 3 membrane structure. As a result the feasibility of the monitoring system was proved.

From the investigation of the on-site data, it was revealed that the videogrammetric monitoring system was capable of measuring membrane structures with an accuracy ranging from 6.7 to 7.5 mm (Section 6.2.3.4). Compared with the predicted displacements of the membrane roof (+/- 250 mm under extreme external loading), the achievable accuracy of the monitoring system was satisfactory for inspecting displacements within the tolerance value.

Taking into account the large displacements occurring in membrane structures, Balz and Dencher (2004) emphasized it is important that the results of a load combination are obtained by adding loads and then analysing, rather than analysing each load separately and then summing the results. As the videogrammetric monitoring system was employed at a real-world test site, the displacements recorded were exactly the ones that comprised various load combinations (such as self weight + prestress + wind). The use of the monitoring system therefore complied with the principle outlined by Balz and Dencher and presented an important benefit of allowing the further analysis of the displacements to be undertaken based on the combined loading. As no snow condition was met during the time frame of the observation campaign, no analysis of snow loading was available in this thesis. However, since the transferability of the monitoring system has been proved, it could be used in the assumption to observe the membrane structure under various conditions in further research.

7.1.5 Investigations into Membrane Structure Behaviour

By using the developed monitoring system, three different types of as-built membrane structures have been investigated. Also, the acquired data has been processed through the MS^2 software, enabling the potential issues involved in the membrane structures that were addressed in Section 1.2.5 to be resolved.

With regard to the first issue, the differences between the designed model and the finished membrane structure were investigated. As a result disparities between the

designed and finished membrane structure were found in all three observed structures. The primary factor causing the disparities occurred at the construction stage, at which the steelwork was installed in the wrong positions. For example, a maximum discrepancy of 0.445 m was determined in Tent Type 1 membrane structure, and this resulted from the incorrect erection of the flying masts and edge arch steelwork (Section 5.3.3.2). The issue highlighted the situation stated by Scheuermann and Boxer (1996), that a change of steelwork position or angle would result in variation of membrane form. More detailed descriptions of the discrepancies that occurred in Tent Types 2 and 3 were addressed in Sections 6.2.2 and 6.3.2 respectively.

In this research the deformation of the membrane roofs can be assumed to be the result of incorrect erection of steelwork. However, in the situation where disparities are determined but the steelwork is constructed correctly, the discrepancies can be treated as errors resulting from improper design. In this case the magnitude and distribution of the derived discrepancies can be brought back to the initial design stage for review and inspection of the design problems.

As for the second issue, involving the displacement of the membrane roof, the inspections were undertaken amongst the three membrane structures. The results suggested no obvious movements were detected in Tent Types 1 and 3. However in the Tent Type 2 membrane structure, evident displacements were determined over the monitoring, in which the range of the movement reached over 20 mm. Non-linear wave movements across the surface, primarily caused by wind loading, were observed. The travelling waves excited on the membrane surface by wind were similar to the phenomenon observed by Balz and Dencher (2004). Moreover, the dynamic behaviour of the Tent Type 2 membrane roof was suspected as having a connection with the roof deformation, at which the relatively obvious displacements were possibly caused by the incorrect arrangement of the membrane roof. Further inspection and analysis of the displacements was reported in Section 6.2.3.3.

7.1.6 Summary

The original objectives of the research project, as outlined in Section 1.3, have largely been met. The background of membrane structures was introduced in Chapter One and the issues associated with it were addressed. To determine suitable approaches for resolving the issues, potential techniques were reviewed in Chapter Two. As a result the non-contact geomatics techniques including terrestrial laser scanning and

videogrammetry were identified as appropriate tools for membrane structure measurement and modelling. Based on these two techniques, the applied monitoring methodology and software for data processing were proposed and developed in Chapters Three and Four respectively. Since they have been proved feasible through the conduction of a series of simulated experiments, the overall monitoring system was applied at the test site to observe an as-built membrane structure. The system has allowed success demonstration in Chapter Five, despite some modifications were required. The improved monitoring system was subsequently employed to observe other two types of membrane structures, as a result the transferability of the monitoring system was presented in Chapter Six.

As the laser scanned and the videogrammetric models were constructed under the same coordinate system, the two models could be combined. This enabled visualisation of the exact area of the membrane roof onto which the targets were projected. In summary, observations on three different types of as-built membrane structures have been successfully achieved, proving the system as a viable metrology system for structural engineers to monitor real-world membrane structures. Moreover, the system fulfilled the needs of further understanding for interaction of membrane surface geometry, applied loads and structural response, which were emphasized by Lewis (2003). The information acquired by the system is proving to be of great value to collaborating engineers who are involved in refining the designs of such membrane structures.

7.2 Suggestions for Future Work

Some suggestions for the continued development of the monitoring system are made:

- The Oscar cameras used in the videogrammetric monitoring used the IEEE-1394a interface for controlling the cameras and transferring acquired image data into the processing computer. There are some other camera buses with various specifications for performing this work. Currently IEEE-1394, Gigabit Ethernet (GigE) Vision and Camera Link are three possible camera buses for machine vision systems. The specifications regarding maximum bandwidth, frame grabber required, maximum cable length, power over cable, and camera availability are listed in Table 7-1. A camera with an appropriate bus is selected for specified requirements. For example, in the case that image acquisition with a high frame rate is important, cameras equipped with a Camera Link interface would make the best option.

	Maximum bandwidth (MB/Sec)	*Frame grabber required*	*Maximum cable length (m)*	*Power over cable*	*Camera availability*
IEEE-1394a	50	No	5	Yes*	High
IEEE-1394b	100	No	100	Yes*	Median
GigE Vision	125	No	100	No	Low
Camera Link	Base: 255 Medium: 510 Full: 680	Yes	10	No	High

* External power source is still required for high-power devices.

Table 7-1: Comparison of camera buses (summarised from National Instruments (2007)).

- In this research the camera synchronisation was accomplished by an external triggering method, where a signal was generated by a pulse generator and was transmitted to the cameras to trigger the shutters synchronously. This task can also be achieved by internal triggering, where the triggering command is synchronously broadcast to all connected cameras by software. By adopting this method, the use of a pulse generator can be withdrawn. Moreover, this function could be integrated into the developed MS^2 software, upgrading the MS^2 software to a more comprehensive videogrammetric monitoring solution.

In addition to improvements to the monitoring system, a number of suggestions are made for further valuable utilisation of the system regarding membrane structures:

- Within various load types, Essrich (2005) pointed out that wind loads are the most significant types of load in the case of membrane buildings, however the current methods of structural calculation for correcting the membrane shape were either too expensive (wind tunnel tests) or not rigorous enough (experiences from wind specialists). Therefore the videogrammetric monitoring system offers an ideal solution for determining the movement under wind loading, which could be applied to a simulated model of a membrane structure under controlled laboratory conditions.

- High speed cameras allow image rates of 1000 frames per second and even beyond, extending the applicability of photogrammetric techniques to highly dynamic scenes

and further improving the interpretability when sudden failure events occurred. Therefore it is worth introducing this type of camera to the scheme of dynamic surface modelling. As this type of high speed camera is still very costly, 3D information can be obtained by using only one camera, along with additional equipment, such as mirror systems, stereoscopic beam splitters or an integrated camera-projector system (Maas and Hampel, 2006).

- As addressed in Section 1.2.4, the installation of the membrane roof is usually accomplished only by experience and on-site observation. The method is not robust enough and easily results in incorrect installation. To improve the situation, the technique of TLS, which is capable of obtaining 3D coordinates in near real-time, could be used at the stage of membrane structure erection. During the installation, the erecting of the supporting steelwork would be monitored by TLS until their positions were confirmed to be arranged in the correct locations.

- For understanding the dynamic behaviour of the membrane roof in response to various weather conditions, the system could be prepared at the test field to record the displacements occurring on the surface. It could also be used as a tool for structural health monitoring, revealing the optimum time for re-tensioning the membrane roof.

- Once the processing through the Static Surface Comparison scheme was complete, not only were the disparities between the designed model and the as-built structure determined, but also the error values of the steelwork locations. The incorrect positions of the steelwork could be re-introduced into the design stage to produce a new mathematical model of the fabric membrane roof. By comparing the new designed membrane roof with the acquired laser scanned model, the appropriateness of the design work could be reviewed.

APPENDIX ONE

MATLAB CODES FOR MS^2

IMPLEMENTATION

A1.1 Static Surface Comparison

A1.1.1 Read Math Model

The code listed below is for extracting the nodes of the meshed mathematical model (specific for dxf file format).

```
[filenameE, pathnameE]=uigetfile_name({'*.dxf';'*.*'},'Select the meshed math model')

dxf = read_dxf([pathnameE filenameE]);
ccc=size(dxf);
C2 = dxf(:,:,1);
for i=2:ccc(3);
        C2 = cat(2,C2,dxf(:,:,i));
end

fid=fopen('DPFW-Math-PtModel.dat','w');
for a=1:(ccc(3)*3);
        fprintf(fid,'%.4f\t%.4f\t%.4f\n',C2(1,a),C2(2,a),C2(3,a));
end
fclose(fid)
```

A1.1.2 Locate Control Points

The code for computing intersection point between the two lines (Line 1 and Line 2):

```
a1 = str2num(get(handles.edit1, 'String'));                    % input Point 1 of Line 1
b1 = str2num(get(handles.edit2, 'String'));
c1 = str2num(get(handles.edit3, 'String'));
a11 = str2num(get(handles.edit4, 'String'));                   % input Point 2 of Line 1
b11 = str2num(get(handles.edit5, 'String'));
c11 = str2num(get(handles.edit6, 'String'));
d1 = a11-a1; e1 = b11-b1; f1 = c11-c1;

a2 = str2num(get(handles.edit7, 'String'));                    % input Point 1 of Line 2
b2 = str2num(get(handles.edit8, 'String'));
c2 = str2num(get(handles.edit9, 'String'));
a21 = str2num(get(handles.edit10, 'String'));                  % input Point 2 of Line 2
b21 = str2num(get(handles.edit11, 'String'));
c21 = str2num(get(handles.edit12, 'String'));
d2 = a21-a2; e2 = b21-b2; f2 = c21-c2;

i=e1*f2-f1*e2;j=f1*d2-d1*f2;k=d1*e2-e1*d2;
ShDist1=(((a2-a1)*i+(b2-b1)*j+(c2-c1)*k)/((i^2+j^2+k^2)^0.5))   % shortest distance
                                                               between two 3D lines
ShDist = num2str(ShDist1,'%.3f');
set(handles.text4, 'String', ShDist);

A=[i*e2-j*d2,i*(-e1)-j*(-d1);k*e2-j*f2,k*(-e1)-j*(-f1);k*d2-i*f2,k*(-d1)-i*(-f1)];
L=[j*(a2-a1)-i*(b2-b1);j*(c2-c1)-k*(b2-b1);i*(c2-c1)-k*(a2-a1)];
X=A\L;
p1=[a1+d1*X(2),b1+e1*X(2),c1+f1*X(2)]
p2=[a2+d2*X(1),b2+e2*X(1),c2+f2*X(1)]
pc=[(p1(1)+p2(1))/2,(p1(2)+p2(2))/2,(p1(3)+p2(3))/2]           % centre point of the
                                                               intersection line

set(handles.text1, 'String', pc(1));
set(handles.text2, 'String', pc(2));
set(handles.text3, 'String', pc(3));                           % display intersection point of Line 1
                                                               and Line 2 on the interface
```

A1.1.3 Surface Comparison

The following code was programmed for generating meshed model with uniform grid from TLS and mathematical models.

```
[Xtls,Ytls,Ztls] = textread([pathnameB filenameB],'%f %f %f');        % read TLS model
x=93.8:0.3:110.6;                    % set grid interval to 0.3 m
y=101.1:0.3:114.9;
[XItls,YItls] = meshgrid(x,y);
ZItls = griddata(Xtls,Ytls,Ztls,XItls,YItls);

[Xmw,Ymw,Zmw] = textread([pathnameC filenameC],'%f %f %f');    % read math model
x=93.8:0.3:110.6;                    % set grid interval to 0.3 m
y=101.1:0.3:114.9;
[XImw,YImw] = meshgrid(x,y);
ZImw = griddata(Xmw,Ymw,Zmw,XImw,YImw);

ans1=ZItls-ZImw;                     % calculate the difference in Z-direction
```

The code listed below was programmed for computing statistics of the differences in Z-direction between the two surface models. In addition, the code for drawing the planimetric discrepancy map and the profiles was shown.

```
% separate the positive and negative differences
    s=1;                             % find out negative differences
    for a=1:n1-1;                    % n1 is the number of points whose residuals being calculated
        if ans1(a)<0;
            res_minus(s,1)=XImw(a);
            res_minus(s,2)=YImw(a);
            res_minus(s,3)=ans1(a);
            s=s+1;
        end;
end;

s=1;                                 % find out positive differences
for a=1:n1-1;
    if ans1(a)>0;
        res_plus(s,1)=XImw(a);
        res_plus(s,2)=YImw(a);
```

```
            res_plus(s,3)=ans1(a);
            s=s+1;
        end;
    end;
```

% this is the example code for computing and displaying mean value of negative differences

```
Mean_res_Minus1=mean(res_minus(:,3));
Mean_res_Minus = num2str(Mean_res_Minus1,'%.3f');
set(handles.FallMean_Res, 'String', Mean_res_Minus);
```

% draw a planimetric discrepancy map (refer to Fig. 5-20 for example resultant map)
% this is the example code for plotting the points whose differences were over 0.2 m

```
s=1;
for a=1:n1-1;
    if ans1(a)>0.2;
        res_l1(s,1)=XImw(a);
        res_l1(s,2)=YImw(a);
        res_l1(s,3)=ans1(a);
        s=s+1;
    end;
end;

figure,plot(res_l1(:,1),res_l1(:,2),'r+','MarkerSize',6);
set(gca,'DataAspectRatio',[1 1 1],'PlotBoxAspectRatio',[1 1 1]);
axis equal;
hold all;
```

% draw a profile (refer to Fig. 5-21 for example resultant profiles)

```
XProf = str2num(get(handles.X_Profile, 'String'));

Q1 = interp2(XItls,YItls,ZItls,XProf,101.1:0.1:114.9);   % profile from TLS model
Q2 = interp2(XItls,YItls,ZImw,XProf,101.1:0.1:114.9);    % profile from math model
Q3 = interp2(XItls,YItls,ans1,XProf,101.1:0.1:114.9);    % profile of the difference
                                                         between the two models

figure,
subplot(2,1,1); subplot('Position',[0.13 0.42 0.775 0.5]);
plot(101.1:0.1:114.9,Q1,'g');
```

```
hold all;
plot(101.1:0.1:114.9,Q2,'r');
grid on;
xlabel('Y axis (m)','fontsize',12),ylabel('Z axis (m)','fontsize',12);
axis equal; axis ([100 116 17 23]);
hold off;
subplot(2,1,2); subplot('Position',[0.13 0.25 0.775 0.2]);
plot(101.1:0.1:114.9,Q3,'b');
```

A1.2 Dynamic Surface Modelling

A1.2.1 Camera Orientation Module

The code listed below includes the task of image filtering, thresholding, labelling and targeting in the Camera Orientation Module. The code was commonly adopted in the Target Extraction Module. Also, the code for triggering and implementing CUBA program is shown.

```
% image filtering by Laplacian mask
    aL=imread('TS_CP_L_Original.BMP');
    h=[-1 -1 -1;-1 8 -1;-1 -1 -1];
    jL=imfilter(aL,h);

% image thresholding
    nc=str2num(get(handles.thres_value_input, 'String'));        % read threshold value
    bwL=im2bw(jL,nc);
    imwrite(bwL,'TS_CP_L_Original2.bmp');
    figure, imshow(bwL);

% image labelling
    lL=bwlabeln(bwL,8);
    [yL,numL]=bwlabel(lL,8);
    set(handles.num_extra_target, 'String', numL);                % display the number of
                                                                  labelled targets (numL)
% image targeting (centroiding algorithm)
    for s=1:numL;
        [rL,cL] = find(yL==s);
        iL=double(diag(aL(rL,cL))):
```

```
        dL=[rL cL iL cL.*iL rL.*iL];
        eL(:,1)=sum(dL(:,1));
        eL(:,2)=sum(dL(:,2));
        eL(:,3)=sum(dL(:,3));
        eL(:,4)=sum(dL(:,4));
        eL(:,5)=sum(dL(:,5));
        ltest1cp(s,:)=[(eL(1,4)/eL(1,3)) (eL(1,5)/eL(1,3))];          % extracted targets
end
```

```
% trigger CUBA for computing exterior orientation of the cameras
    [status,result]=dos('cuba -AF DPFW-EO.txt');
```

A1.2.2 Target Referencing Module

The codes behind the command buttons on interface of Target Referencing Module are introduced below, including "Search Connection", "Check 1", "Check 2", "Check 3", and "Reconstruction".

```
% Search Connection – identify the adjacent targets of each target
    for i=1:num;
        m=1;
        for j=1:num;
            AL=[abs(ltest1m(i)-ltest1m(j)) abs(ltest1m(i+num)-ltest1m(j+num))];
            if (AL(1)<L_x_interval) & (AL(2)<L_y_interval);    % L_x_interval and
                                                               L_y_interval are suitable
                                                               "Max X/Y interval"

                BL(i,m)=j;
                m=m+1;
            end;
        end;
end;
```

```
% Check 1 – if any target has more than two connections
    size_BL=size(BL);
    s_size_BL=size_BL(1,2);
    if s_size_BL>3;
        clear BL;
        msgbox('Fail - Back to check the interval');
```

```
    else;
        msgbox('Pass - Go to "Check 2"');
    end;

% Check 2 – if any target has less than one connection
    n=0;
    for i=1:num;
        if BL(i,2)==0;
            n=n+1;
            CL(1,n)=i;
        end;
end;

if n>0;
    msgbox('Fail - Back to check the interval');
else;
    msgbox('Pass - Go to "Check 3"');
end;

% Check 3 – find top and bottom targets of each line
    [i1,j1]=find(BL==0);
    for n=1:50;                          % find top targets of each lines (25 lines)
        ltemp1(n,1)=ltest1m((i1(n,1)),2);
        [i2,j2]=find(ltemp1<411);        % 411=822/2 (image size: 1088*822)
    end;

    size_L_startdots=size(i2);
    s_size_L_startdots=size_L_startdots(1,1);
    if s_size_L_startdots==25;
        msgbox('Pass - Go to "Reconstruct Targets"');
    else;
        msgbox('Fail - Back to check the interval');
    end;

    for o=1:25;
        k(o,1)=i1(i2(o,1),1);
    end;
```

```
% Reconstruction – reconstruct the order of the targets
    for m=1:25;
    k1=k(m,1);
        for n=1:19;
            LineL(n,m)=k1;
            [i3,j3]=find(BL==k1);
            [i4,j4]=find(i3>k1 | i3<k1);
            m1=size(i4);
        if m1(1,1)==1;              % the top/bottom targets
            k1=i3(i4,1);
        else m1(1,1)==2;            % the targets with two adjacent targets
            k2=i3(i4,1);
            [i5,j5]=find(LineL==k2(1,1));
            if isempty(i5)==1;
                k1=k2(1,1);
            end;
            [i6,j6]=find(LineL==k2(2,1));
            if isempty(i6)==1;
                k1=k2(2,1);
                    end;
                end;
            end;
        end;

    save LineL;                     % LineL is the saved data shown in Figure 4-13
```

A1.2.3 Target Tracking Module

After the "Max X/Y tolerance" values are given, the following code is implemented to perform Target Tracking.

```
[xl2,yl2]=textread('DPFW_L2.txt','%f %f');
[xr2,yr2]=textread('DPFW_R2.txt','%f %f');
for i=1:num;
    for j=1:size(xl2);
        ALL=[abs(xl2(j)-ImageCoordComb(i,1)) abs(yl2(j)-ImageCoordComb(i,2))];
        if (ALL(1)<15) & (ALL(2)<15);       % "15" is the "Max X/Y tolerance" value
            ImageCoordComb(i,5)=xl2(j);
```

```
                ImageCoordComb(i,6)=yl2(j);
        end;
end;
if ImageCoordComb(i,5)==0;
        ImageCoordComb(i,5)=ImageCoordComb(i,1);
end;
if ImageCoordComb(i,6)==0;
        ImageCoordComb(i,6)=ImageCoordComb(i,2);
        end;
end;

for i=1:num;
        for j=1:size(xr2);
                ALL=[abs(xr2(j)-ImageCoordComb(i,3)) abs(yr2(j)-ImageCoordComb(i,4))];
                if (ALL(1)<15) & (ALL(2)<15);
                        ImageCoordComb(i,7)=xr2(j);
                        ImageCoordComb(i,8)=yr2(j);
                end;
        end;
        if ImageCoordComb(i,7)==0;
                ImageCoordComb(i,7)=ImageCoordComb(i,3);
        end;
        if ImageCoordComb(i,8)==0;
                ImageCoordComb(i,8)=ImageCoordComb(i,4);    % ImageCoordComb is the
                                                            saved data shown in Figure
                                                            4-17
        end;
    end;
```

A1.2.4 Target Calculation Module

The space intersection method is adopted for computing initial values of the target locations. The code for this task is shown below:

```
% get I.O. information
    [d1,f,d2,ppx,ppy,k1,k2,k3,p1,p2,p3,d3,d4,d5,d6,d7,d8]=textread('C_lens_a02372.cub','%s
     %f %f %f %f %f %f %f %f %f %f %f %f %f %f %f %s','commentstyle','shell');
```

```
fL=f(1);                    % left camera
ppx1L=ppx(1);
ppxL=544*0.0081+ppx1L;
ppy1L=ppy(1);
ppyL=411*0.0081-ppy1L;
k1L=k1(1); k2L=k2(1);
p1L=p1(1); p2L=p2(1);
fR=f(3);                    % right camera
ppx1R=ppx(3);
ppxR=544*0.0081+ppx1R;
ppy1R=ppy(3);
ppyR=411*0.0081-ppy1R;
k1R=k1(3); k2R=k2(3);
p1R=p1(3); p2R=p2(3);

% get E.O. information & rotation matrix
[campos,x,y,z,o,p,k,camname,dx,dy,dz,do,dp,dk]=textread('C_eo_a02372.cub','%s %f %f
 %f %f %f %f %s %f %f %f %f %f %f','commentstyle','shell');

XLL=x(1); YLL=y(1); ZLL=z(1);                    % left camera
OL=o(1)*pi/180; PL=p(1)*pi/180; KL=k(1)*pi/180;
ML=[cos(PL)*cos(KL) sin(OL)*sin(PL)*cos(KL)+cos(OL)*sin(KL)
 -cos(OL)*sin(PL)*cos(KL)+sin(OL)*sin(KL);-cos(PL)*sin(KL)
 -sin(OL)*sin(PL)*sin(KL)+cos(OL)*cos(KL)
 cos(OL)*sin(PL)*sin(KL)+sin(OL)*cos(KL);sin(PL) -sin(OL)*cos(PL)
 cos(OL)*cos(PL)]

XLR=x(3); YLR=y(3); ZLR=z(3);                    % right camera
OR=o(3)*pi/180; PR=p(3)*pi/180; KR=k(3)*pi/180;
MR=[cos(PR)*cos(KR) sin(OR)*sin(PR)*cos(KR)+cos(OR)*sin(KR)
 -cos(OR)*sin(PR)*cos(KR)+sin(OR)*sin(KR);-cos(PR)*sin(KR)
 -sin(OR)*sin(PR)*sin(KR)+cos(OR)*cos(KR)
 cos(OR)*sin(PR)*sin(KR)+sin(OR)*cos(KR);sin(PR) -sin(OR)*cos(PR)
 cos(OR)*cos(PR)]

% intersection calculation (Equations 2-5 and 2-6)
 for i=1:num;                % "num" is the number of extracted targets
```

```
A=[fL*ML(1,1)-(ppx1L-(ImageCoordComb(i,(1+(j-1)*4))*0.0081-4.4064))*ML(3,1)
 fL*ML(1,2)-(ppx1L-(ImageCoordComb(i,(1+(j-1)*4))*0.0081-4.4064))*ML(3,2)
 fL*ML(1,3)-(ppx1L-(ImageCoordComb(i,(1+(j-1)*4))*0.0081-4.4064))*ML(3,3);f
 L*ML(2,1)-(ppy1L-(3.3291-ImageCoordComb(i,(2+(j-1)*4))*0.0081))*ML(3,1)
 fL*ML(2,2)-(ppy1L-(3.3291-ImageCoordComb(i,(2+(j-1)*4))*0.0081))*ML(3,2)
 fL*ML(2,3)-(ppy1L-(3.3291-ImageCoordComb(i,(2+(j-1)*4))*0.0081))*ML(3,3);f
 R*MR(1,1)-(ppx1R-(ImageCoordComb(i,(3+(j-1)*4))*0.0081-4.4064))*MR(3,1)
 fR*MR(1,2)-(ppx1R-(ImageCoordComb(i,(3+(j-1)*4))*0.0081-4.4064))*MR(3,2)
 fR*MR(1,3)-(ppx1R-(ImageCoordComb(i,(3+(j-1)*4))*0.0081-4.4064))*MR(3,3);f
 R*MR(2,1)-(ppy1R-(3.3291-ImageCoordComb(i,(4+(j-1)*4))*0.0081))*MR(3,1)
 fR*MR(2,2)-(ppy1R-(3.3291-ImageCoordComb(i,(4+(j-1)*4))*0.0081))*MR(3,2)
 fR*MR(2,3)-(ppy1R-(3.3291-ImageCoordComb(i,(4+(j-1)*4))*0.0081))*MR(3,3)];

L=[XLL*(fL*ML(1,1)-(ppx1L-(ImageCoordComb(i,(1+(j-1)*4))*0.0081-4.4064))*
 ML(3,1))+YLL*(fL*ML(1,2)-(ppx1L-(ImageCoordComb(i,(1+(j-1)*4))*0.0081-4.
 4064))*ML(3,2))+ZLL*(fL*ML(1,3)-(ppx1L-(ImageCoordComb(i,(1+(j-1)*4))*0.
 0081-4.4064))*ML(3,3));XLL*(fL*ML(2,1)-(ppy1L-(3.3291-ImageCoordComb(i,(
 2+(j-1)*4))*0.0081))*ML(3,1))+YLL*(fL*ML(2,2)-(ppy1L-(3.3291-ImageCoordC
 omb(i,(2+(j-1)*4))*0.0081))*ML(3,2))+ZLL*(fL*ML(2,3)-(ppy1L-(3.3291-Image
 CoordComb(i,(2+(j-1)*4))*0.0081))*ML(3,3));XLR*(fR*MR(1,1)-(ppx1R-(Image
 CoordComb(i,(3+(j-1)*4))*0.0081-4.4064))*MR(3,1))+YLR*(fR*MR(1,2)-(ppx1R
 -(ImageCoordComb(i,(3+(j-1)*4))*0.0081-4.4064))*MR(3,2))+ZLR*(fR*MR(1,3)-
 (ppx1R-(ImageCoordComb(i,(3+(j-1)*4))*0.0081-4.4064))*MR(3,3));XLR*(fR*M
 R(2,1)-(ppy1R-(3.3291-ImageCoordComb(i,(4+(j-1)*4))*0.0081))*MR(3,1))+YLR
 *(fR*MR(2,2)-(ppy1R-(3.3291-ImageCoordComb(i,(4+(j-1)*4))*0.0081))*MR(3,2
 ))+ZLR*(fR*MR(2,3)-(ppy1R-(3.3291-ImageCoordComb(i,(4+(j-1)*4))*0.0081))*
 MR(3,3))];

XX=A\L;
Obj3DCoor(i,(1+(j-1)*3))=XX(1);
        Obj3DCoor(i,(2+(j-1)*3))=XX(2);
        Obj3DCoor(i,(3+(j-1)*3))=XX(3);
end;
save Obj3DCoor;
msgbox('Done !');
```

LIST OF REFERENCES

AGOURIS, P., DOUCETTE, P. and STEFANIDIS, A., 2004. Automation and digital photogrammetric workstations. *Manual of Photogrammetry*, fifth edition (Eds. J. C. McGlone, E. M. Mikhail and J. Bethel). American Society for Photogrammetry and Remote Sensing, Maryland, USA. 1151 pages: 949-981.

ALBA, M., FREGONESE, L., PRANDI, F., SCAIONI, M. and VALGOI, P., 2006. Structural monitoring of a large dam by terrestrial laser scanning. *International Archives of Photogrammetry, Remote Sensing and Spatial Information Sciences*, 36(A5): 6 pages.

ALBERT, J., MAAS, H.-G., SCHADE, A. and SCHWARZ, W., 2002. Pilot studies on photogrammetric bridge deformation measurement. *Proceedings, 2nd Symposium on Geodesy for Geotechnical and Structural Engineering*. Berlin, Germany: 133-140.

ALLIED VISION TECHNOLOGIES, 2005. *AVT Oscar Technical Manual*. Allied Vision Technologies GmbH, Germany. 155 pages.

ANALYTICAL SPECTRAL DEVICES, INC., 2001. Field Spectrometry: Techniques and Instrumentation. http://www.asdi.com/Field%20Spectroscopy-screen.pdf [accessed 12th September 2005].

ANDERSON, K., 2002. Field guide for the ASD FieldSpec Pro – White Reference Mode. 8 pages.

API SYSTEMS, 2007. Area of application: Shipbuiding. http://www.apisensor.com/shipbuilding.html [accessed 3rd April 2007].

ARIYAWANSA, D. D. A. P. and CLARKE, T. A., 1999. High speed multiple view image point correspondences using rectification. *Videometrics VI*, San Jose, USA, SPIE Vol. 3641: 92-103.

AS-BUILT SOLUTIONS LTD., 2007. Hazmap Browser / Modeller Version 3.x. http://www.absl.co.uk/HazmapBrowser3x.htm [accessed 3rd March 2007].

ASSOCIATED PRESS, 2005. FIFA confederation photo gallery. http://fifaworldcup.yahoo.com/06/de/c/photos/index.html?i=111&d=0 [accessed 5th April 2006].

BALLARD, D. H. and BROWN, C. M., 1982. *Computer Vision*. Prentice-Hall, Inc., New Jersey, USA. 523 pages.

BALZ, M. and DENCHER, M., 2004. Design loading conditions. *European Design Guide for Tensile Surface Structures* (Eds. B. Foster and M. Mollaert). TensiNet, Brussels, Belgium. 354 pages: 191-204.

BALZANI, M., PELLEGRINELLI, A., PERFETTI, N., RUSSO, P., UCCELLI, F. and TRALLI, S., 2002. CYRAXTM 2500 Laser scanner and GPS operational flexibility: from detailed close range surveying to urban scale surveying. *Proceedings, International Workshop on Scanning for Cultural Heritage Recording*. Corfu, Greece: 27-32.

BANNISTER, A., RAYMOND, S. and BAKER, R., 1998. *Surveying*, seventh edition. Addison Wesley Longman Limited, Essex, UK. 502 pages.

BARBER, D. M., 2003. *Terrestrial Laser Scanning for the Metric Survey of Cultural Heritage Structures*. PhD Thesis, University of Newcastle upon Tyne, Newcastle upon Tyne, UK (unpublished): 222 pages.

BARBER, D., MILLS, J. and BRYAN, P., 2003. Towards a standard specification for terrestrial laser scanning of cultural heritage. *CIPA International Archives for Documentation of Cultural Heritage*, 19: 619–624.

BARNES, M., FORSTER, B. and DENCHER, M., 2004a. Structural design basis and safety criteria. *European Design Guide for Tensile Surface Structures* (Eds. B. Foster and M. Mollaert). TensiNet, Brussels, Belgium. 354 pages: 177-190.

BARNES, M., GRUNDIG, L. and MONCRIEFF, E., 2004b. Form-finding, load analysis and patterning. *European Design Guide for Tensile Surface Structures* (Eds. B. Foster and M. Mollaert). TensiNet, Brussels, Belgium. 354 pages: 205-218.

BERGEVIN, R., SOUCY, M., GAGNON, H. and LAURENDEAU, D., 1996. Towards a general multi-view registration technique. *IEEE Pattern Analysis and Machine Intelligence*, 18(5): 540-547.

BESL, P. J. and MCKAY, N. D., 1992. A method for registration of 3-D shapes. *IEEE transactions on Pattern Analysis and Machine Intelligence*, 14(2): 239-256.

BEYER, H. A., 1992. Advances in characterisation and calibration of digital imaging systems. *International Archives of Photogrammetry and Remote Sensing*, 31(B4): 545-553.

BHALLA, S., YANG, Y. W., ZHAO, J. and SOH, C. K., 2005. Structural health monitoring of underground facilities – Technological issues and challenges. *Tunnelling and Underground Space Technology*, 20(2005): 487-500.

BLACK, J. T. and PAPPA, R. S., 2003. Videogrammetry using projected circular targets: proof-of-concept test. http://techreports.larc.nasa.gov/ltrs/PDF/2003/tm/NASA-2003-tm212148.pdf [accessed 21st November 2003].

BLAHUSCH, G., ECKSTEIN, W., STEGER, C. and LANSER, S., 1999. Algorithms and evaluation of a high precision tool measurement system. http://www9.in.tum.de/papers/1999/QACV-99-Blahusch-etal.pdf [accessed 3rd January 2004].

BLANDINO, J. R., PAPPA, R. S. and BLACK, J. T., 2003. Modal identification of membrane structures with videogrammetry and laser vibrometry. *AIAA Paper 2003-1745*: 11 pages.

BOEHLER, W., HEINZ, G., SCHERER, Y.and SIEBOLD, M., 2001. Topographic information in cultural and natural heritage visualization and animation. *International Archives of Photogrammetry, Remote Sensing and Spatial Information Sciences*, 34(5W1): 56-61.

BOEHLER, W. and MARBS, A., 2002. 3D scanning instruments. *Proceedings, International Workshop on Scanning for Cultural Heritage Recording*. Corfu, Greece: 9-12.

BOLAND, J., AGER, T., EDWARDS, E., FREY, E., TOTH, C., WALKER, S., WHITTAKER, E. F., ZAVATTERO, P. and ZUEGGE, H., 2004. Cameras and sensing systems. *Manual of Photogrammetry*, fifth edition (Eds. J. C. McGlone, E. M. Mikhail and J. Bethel). American Society for Photogrammetry and Remote Sensing, Maryland, USA. 1151 pages: 581-676.

BONORA, V., COLOMBO, L. and MARANA, B., 2005. Laser technology for cross-section survey in ancient buildings: A study for S. M. Maggiore in Bergamo. *Proceedings, CIPA 2005 XX International Symposium*. Torino, Italy: 6 pages.

BORGHESE, N. A., CERVERI, P. and RIGIROLI, P., 2001. A fast method for calibrating video-based motion analysers using only a rigid bar. *Journal Medical and Biological Engineering and Computing*, 39(1): 76-81.

BORNAZ. L., LINGUA, A., RINAUDO, F. and TORINO, P., 2003. Multiple scan registration in lidar close-range applications. *International Archives of Photogrammetry, Remote Sensing and Spatial Information Sciences*, 34(5/W12): 72-77.

BOYER, L. P., 2001. Digital tooling for major structural repair. http://ieeexplore.ieee.org/iel5/7542/20537/00949468.pdf [accessed 2nd April 2007].

BRADATSCH, J., PATZOLD, P., DE FREITAS, C. S., SCHEUERMANN, R., MONJO, J. and MOLLAERT, M., 2004. Form. *European Design Guide for Tensile Surface Structures* (Eds. B. Foster and M. Mollaert). TensiNet, Brussels, Belgium. 354 pages: 43-96.

BRIDGENS, B. N., GOSLING, P. D. and BIRCHALL, M. J. S., 2004. Tensile fabric structures: concepts, practice & developments. *The Structural Engineer*, 82(14): 21-27.

BRIESE, C., 2006. Structure line modelling based on terrestrial laser scanner data. *International Archives of Photogrammetry, Remote Sensing and Spatial Information Sciences*, 36(5): 6 pages.

BROWN, D., 1985. Tools of the trade. *Close-range Photogrammetry and Surveying – State of the Art*. American Society for Photogrammetry and Remote Sensing, Falls Church, USA. 941 pages: 83-252.

BRÜEL & KJÆR, 2007. Laser Vibrometry. http://www.bksv.com/1067.asp [accessed 2nd April 2007].

BRYAN, P. G., BARBER, D. M and MILLS, J. P., 2004. Towards a standard specification for terrestrial laser scanning in cultural heritage – one year on. *International Archives of the Photogrammetry, Remote Sensing and Spatial Information Sciences*, 35 (B7): 966–971.

BUCKLEY, S. J., 2003. *A Geomatics Data Fusion Technique for Change Monitoring*. PhD Thesis, University of Newcastle upon Tyne, Newcastle upon Tyne, (unpublished): 259 pages.

BUEHLER, T., 2003. Video guide – NTSC basics. http://people.csail.mit.edu/tbuehler/video/ntsc.html [accessed 3rd March 2005].

BULUT, F. and TUDES, S., 1996. Determination of discontinuity traces on inaccessible rock slopes using electronic tacheometer: an example from the Ikizdere (Rize) Region, Turkey. *Engineering Geology*, 44(1): 229–233.

CAMPBELL, D., 1991. The unique role of computing in the design and construction of tensile membrane structures. *Proceedings, American Society of Civil Engineers (ASCE) Second Civil Engineering Automation Conference*. New York, USA. http://www.geigerengineers.com/techpaper.cfm?RecordID=5 [accessed 20th February 2007].

CASTELLINI, P., MARTARELLI, M. and TOMASINI, E. P., 2006. Laser Doppler vibrometry: development of advanced solutions answering to technology's needs. *Mechanical Systems and Signal Processing*, 20 (2006): 1265-1285.

CHAPMAN, D. P., 2000. Megapixels, millimetres and microsieverts: Packaging digital photogrammetry for emerging industrial markets. *The Photogrammetric Record*, 16(95): 763-779.

CHEN, J. and CLARKE, T. A., 1992. The automatic recognition, location and labelling of targets in digital photogrammetric engineering measurement. *International Archives of Photogrammetry and Remote Sensing*, 29(B5): 686-693.

CHEN, J., CLARKE, T. A. and ROBSON, S., 1993. An alternative to the epipolar line method for automatic target matching in multiple images for 3D measurement. *Optical 3-D Measurement Techniques II* (Eds. A. Gruen and H. Kahmen). Wichmann, Karlsruhe. 624 pages: 197-204.

CHING, J., 2005. Velocity and vibrations measurement in a computer hard disk. http://dynamicslab.mpe.nus.edu.sg/dynamics/project0405/thesis0405/Non-intrusive%20velocity%20measurement%20of%20corotating%20disk%20flows.pdf [accessed 2nd April 2007].

CLARKE, T. A., 1994. An analysis of the properties of targets used in digital close range photogrammetric measurement. *Videometrics III*, Boston, USA, SPIE Vol. 2350: 251-262.

CLARKE, T. A., COOPER, M. A. R. and FRYER, J. C., 1993. An estimator for the random error in subpixel target location and its use in the bundle adjustment. *Proceedings, Optical 3-D Measurement Techniques II* (Eds. A. Gruen and H. Kahmen). Wichmann, Karlsruhe: 161-168.

CLARKE, T. A., ELLIS, T. J. and ROBSON, S., 1994. High accuracy 3-D measurement using multiple camera views. *IEE Colloquium on "3D Imaging and Analysis of Depth/Range Images"*, No.1994/054: 1/1-1/4.

COOPER, M. A. R. and ROBSON, S., 2001. Theory of close range photogrammetry. *Close Range Photogrammetry and Machine Vision* (Ed. K. B. Atkinson). Whittles Publishing, Caithness, UK. 371 pages: 9-51.

CURLESS, B. and LEVOY, M., 1995. Better optical triangulation through spacetime analysis. *Proceedings, the 5th International Conference on Computer Vision.* Cambridge, USA: 987-994.

DAI, J., GUAN, Y.-X., WANG, S.-L., WU, Z.-Y. and FANG, Z.-L., 2005. Feature characterization of microfabricated microfluidic chips by PDMS replication and CCD imaging. *Analytical and Bioanalytical Chemistry*, 381(4): 839-843.

DAKOV, D. and TANEV, V., 2005. Experimental investigation of a conical shaped textile membrane under snow loading. TensiNews, 8: 12-13.

D'APUZZO, N., 2002. Surface measurement and tracking of human body parts from multi-image video sequences. *ISPRS Journal of Photogrammetry and Remote Sensing*, 56(5-6): 360-375.

D'APUZZO, N., 2003. *Surface Measurement and Tracking of Human Body Parts from Multi Station Video Sequences*. PhD thesis, Swiss Federal Institute of Technology Zurich, Zurich, Switzerland: 147 pages.

D'APUZZO, N. and KOCHI, N., 2003. Three-dimensional human face feature extraction from multi images. *Proceedings, Optical 3-D Measurement Techniques VI* (Eds. A. Gruen and H. Kahmen). Zurich, Switzerland. Volume I: 140-147.

D'AYALA, D. and SMARS, P., 2003. Architectural and structural modelling for the conservation of cathedral. *Journal of Architectural Conservation*, 9(3): 51-72.

DEWITT, B. A., 1996. Initial approximations of the three-dimensional conformal coordinate transformation. *Photogrammetric Engineering & Remote Sensing*, 62(1): 79-83.

DOWMAN, I. J., 2001. Fundamentals of digital photogrammetry. *Close Range Photogrammetry and Machine Vision* (Ed. K. B. Atkinson). Whittles Publishing, Caithness, UK. 371 pages: 52-77.

EMS, 1999. Tunnelling monitoring system. http://www.emonitoring-system.com/cgi-bin/Info.cgi?page=menu_TMS&pagetitle=TUNNELING+MONITORING+SYSTEM&LsIm= [accessed 2nd January 2007].

EOS SYSTEM INC., 2004. *PhotoModeler Pro 5 User Manual*, Vancouver B. C., Canada. 500 pages.

ESPOSITO, E., COPPARONI, S. and NATICCHIA, B., 2004. Recent progress in diagnostics of civil structures by laser vibrometry. *Proceedings, the 16th World Conference on Nondestructive Testing*. Montreal, Canada: 9 pages. (on CD-ROM.)

ESSRICH, R., 2005. From draft design to installation. *Lecture Notes, Textile Roofs 2005 Workshop*, Berlin, Germany. 14 pages.

EUROPEAN COMMISSION, 1995. TELEMAN robotics and remote systems in hazardous or disordered nuclear environments. *Proceedings, TELEMAN Telerobotics Research Conference*. Nordwijkerhout, Netherlands: 401-412.

FARO INTERNATIONAL USA, 2007. Applications. http://www.faro.com/content.aspx?ct=us&content=app [accessed 3rd April 2007].

FENG, Q., FARDIN, N., JING, L. and STEPHANSSON, O., 2003. A new method for in situ non-contact roughness measurement of large rock fracture surfaces. *Rock Mechanics and Rock Engineering*, 36(1): 3-25.

FENG, Q., SJOGREN, P., STEPHANSSON, O. and JING, L., 2001. Measuring fracture orientation at exposed rock faces by using a non-reflector total station. *Engineering Geology*, 59(1): 133–146.

FISHER, R. B., ASHBROOK, A. P., ROBERTSON, C. and WERGHI, N., 1999. A low-cost range finder using a visually located, structured light source. *Proceedings, the 2nd International Conference on 3-D Digital Imaging and Modelling*. Ottawa, Canada: 24-33.

FORSTER, B., 1994. Cable and membrane roofs – a historical survey. *Structural Engineering Review*, 6(3-4): 145-174.

FRASER, C. S., 2001. Network design. *Close Range Photogrammetry and Machine Vision* (Ed. K. B. Atkinson). Whittles Publishing, Caithness, UK. 371 pages: 256-281.

FRASER, C. S., 2006. Photogrammetry - basics of interior orientation & network design. *Lecture Notes*: 26 pages.

FRASER, C., BRIZZI, D. and HIRA, A., 2003. Vision-based, multi-epoch deformation monitoring of the atrium of Federation Square. *Proceedings, the 11th FIG Symposium on Deformation Measurements*. Santorini, Greece: 6 pages.

FRASER, C. S. and RIEDEL, B., 2000. Monitoring the thermal deformation of steel beams via vision metrology. *ISPRS Journal of Photogrammetry and Remote Sensing*, 55(2000): 268-276.

FRASER, C. S. and SHORTIS, M. R., 1995. Metric exploitation of still video imagery. *The Photogrammetric Record*, 15(85): 107-122.

FROHLICH, C. and METTENLEITER, M., 2004. Terrestrial laser scanning – new perspectives in 3D surveying. *International Archives of Photogrammetry, Remote Sensing and Spatial Information Sciences*, 36(8/W2): 7-13.

FRYER, J. G., 2001a. Camera calibration. *Close Range Photogrammetry and Machine Vision* (Ed. K. B. Atkinson). Whittles Publishing, Caithness, UK. 371 pages: 156-179.

FRYER, J. G., 2001b. Introduction. *Close Range Photogrammetry and Machine Vision* (Ed. K. B. Atkinson). Whittles Publishing, Caithness, UK. 371 pages: 1-7.

GANCI, G. and BROWN, J., 2000. Developments in non-contact measurement using videogrammetry. http://www.geodetic.com/Downloadfiles/Developments%20in%20Non%20Contact%20Videogrammetry.pdf [accessed 24th November 2003].

GHANBARI, M., 1999. *Video Coding*. The Institution of Electrical Engineers, London, UK. 260 pages.

GIPPERICH, K., CANOBBIO, R., LOMBARDI, S. and MALINOWSKY, M., 2004. Fabrication, installation and maintenance. *European Design Guide for Tensile Surface Structures* (Eds. B. Foster and M. Mollaert). TensiNet, Brussels, Belgium. 354 pages: 243-258.

GODIN, G., LAURENDEAU, D. and BERGEVIN, R., 2001. A method for the registration of attributed range images. *Proceedings, International Conference on 3D Imaging and Modelling*. Quebec, Canada: 179-186.

GORDON, S. J. and LICHTI, D. D., 2004. Terrestrial laser scanners with a narrow field of view: the effect on 3-D resection solutions. *Survey Review*, 37(292):448-468.

GORDON, S. J., LICHTI, D. D., CHANDLER, I., STEWART, M. P. and FRANKE, J., 2003. Precision measurement of structural deformation using terrestrial laser scanners. *Proceedings, Optical 3-D Measurement Techniques VI* (Eds. A. Gruen and H. Kahmen). Zurich, Switzerland: 322-329.

GORDON, S. J., LICHTI, D. D., FRANKE, J. and STEWART, M. P., 2004. Measurement of structural deformation using terrestrial laser scanners. *Proceedings, the 1st FIG International Symposium on Engineering Surveys for Construction Works and Structural Engineering*. Nottingham, UK: 16 pages.

VAN GOSLIGA, R., LINDENBERGH, R. and PFEIFER, N., 2006. Deformation analysis of a bored tunnel by means of terrestrial laser scanning. *International Archives of Photogrammetry, Remote Sensing and Spatial Information Sciences*, 36(5): 167-172.

GOSLING, P. D., 2001. Non-linear material models for coated woven fabrics. http://www.staff.ncl.ac.uk/p.d.gosling/pdg/arup.pdf [accessed 24th January 2007].

GRANSHAW, S. I., 1980. Bundle adjustment methods in engineering photogrammetry. *The Photogrammetric Record*, 10(56): 181-207.

GREENWOOD, J. A., DARVE, C., BERNSTEIN, R., BLACK, E. and KUBIK, D., 2001. Failure-mode metrology using projected target videogrammetry. http://tspc01.fnal.gov/darve/public/publi/photogrammetry.pdf [accessed 4th January 2004].

GRUEN, A., 1997. Fundamentals of videogrammetry - a review. *Human Movement Science*, 16(1997): 155-187.

GRUEN, A., 2001. Development of digital methodology and systems. *Close Range Photogrammetry and Machine Vision* (Ed. K. B. Atkinson). Whittles Publishing, Caithness, UK. 371 pages: 78–104.

GRUEN, A. and AKCA, D., 2004. Least squares 3D surface matching. *International Archives of Photogrammetry, Remote Sensing and Spatial Information Sciences*, 34(5/W16): 8 pages.

GUARNIERI, A., PIROTTI, F., PONTIN, M. and VETTORE, A., 2005. Combined 3D surveying techniques for structural analysis applications. *International Archives of Photogrammetry, Remote Sensing and Spatial Information Sciences*, 36(5/W17): 6 pages.

GULYAEV, S. A. and BUCKERIDGE, J. S., 2004. Terrestrial methods for monitoring cliff erosion in an urban environment. *Journal of Coastal Research*, 20(3): 871–878.

HAASE, J., SCHEUERMANN, R., BLUM, R., LLORENS, J., FORSTER, B., HOUTMAN, R. and WERKMAN, H., 2006. Design development. http://www.tensinet.com/documents/Designing_Tensile_Structures/DesignDevelopment.pdf [accessed 10th February 2006].

HABIB, A., KELLEY, D. and ASMAMAW, A., 2000. New approach to solving matching problems in photogrammetry. *International Archives of Photogrammetry and Remote Sensing*, 33(B2): 257-264.

HALKON, B. AND ROTHBERG, S., 2003. Continuous scanning laser vibrometry for measurements on rotating structures. *Materials Science Forum*, Vols. 440-441: 245-252.

HANKE, K. and EBRAHIM, M. A.-B., 1997. A low cost 3D-measurement tool for architectural and archaeological applications. *International Archives of Photogrammetry and Remote Sensing*, 32(5C1B): 8 pages.

HAPPOLD, E., PUGH, J. W. E., LIDDELL, W. I., EALEY, T. A. and WEBSTER, R. H., 1987. The design and construction of the Diplomatic Club, Riyadh. *The Structural Engineer*, 65A(1): 15-26.

HARALICK, R. M. and SHAPIRO, L. G., 1992. *Computer and Robot Vision,* volume I. Addison-Wesley, Massachusetts, USA. 672 pages.

HARVEY, E. S., SEAGER, J. and CAPPO, M., 2001. The validation of the accuracy and precision of in situ length measurements of Southern Blue Fin Tuna by stereo-video. http://www.afma.gov.au/services/research/reports/r00_1181.pdf [accessed 10th March 2004].

HARVEY, E. S. and SHORTIS, M., 1996. A system for stereo-video measurement of subtidal organisms. *Journal of Marine Technology Society*, 29(4): 10-22.

HARVEY, E. S. and SHORTIS, M., 1998. Calibration stability of and underwater stereo-video system: Implications for measurement accuracy and precision. *Journal of Marine Technology Society*, 32(2): 3-17.

HEATH, D. J., CORVETTI, J., GAD, E. F. and WILSON, J. L., 2004. Development of a photogrammetry system to monitor building movement. *Proceedings, 2004 Annual Technical Conference of the Australian Earthquake Engineering Society* (Eds. K. McCue, M. C. Griffith and B. Butler). Mt. Gambier, South Australia: 19 pages.

HEIKKILA, J., 2000. Geometric camera calibration using circular control points. *IEEE Transactions on Pattern Analysis and Machine Intelligence*, 22(10): 1066-1077.

HERNANDEZ, E. S., GALATI, N., MYERS, J. J. and NANNI, A., 2006. Long term monitoring of bridges using a robotic tacheometry system. *Proceedings, the 6th International Symposium on NDT in Civil Engineering (NDT-CE)* (Eds. I. Al-Qadi and G. Washer). St. Louis, USA: 113-120.

VAN DEN HEUVEL, F. A., 1993. Automated 3-D measurement with the DCS200 digital camera. *Proceedings, Optical 3-D Measurement Techniques II* (Eds. A. Gruen and H. Kahmen). Wichmann, Karlsruhe: 63-71.

VAN DEN HEUVEL, F. A., KROON, R. J. G. A. and LE POOLE, R. S., 1992. Digital close-range photogrammetry using artificial targets. *International Archives of Photogrammetry and Remote Sensing*, 29(5): 222-229.

HOBBS, S., 2003. Target position and trajectory measurements by videogrammetry. *College of Aeronautics Report 0208*. School of Engineering, Cranfield University, Cranfield, UK. 67 pages.

HOFFMAN, E., 2005. Specifying laser scanning services. *Chemical Engineering Progress Magazine*, 101(5): 34-38.

HOLDERIED, M. W., KORINE, C., FENTON, M. B., PARSONS, S., ROBSON, S. and JONES, G., 2005. Echolocation call intensity in the aerial hawking bat Eptesicus bottae (Vespertilionidae) studied using stereo videogrammetry. *Journal of Experimental Biology*, 208: 1321-1327.

HOPPE, H., 1993. Mesh optimization. *Proceedings, SIGGRAPH 1993*. New York, USA: 19-26.

HOPPE, H., 1994. *Surface reconstruction from unorganized points*. PhD thesis, University of Washington, Washington D. C., USA. (unpublished): 134 pages.

HUNTER, G., PINKERTON, H., AIREY, R. and CALVARI, S., 2003. The application of a long-range laser scanner for monitoring volcanic activity on Mount Etna. *Journal of Volcanology and Geothermal Research*, 123(1/2): 203-210.

HUNTINGTON, C. G., 2004. *The Tensioned Fabric Roof*. American Society of Civil Engineers. 203 pages.

IOANNIDES, C., VALANIS, A., GEORGOPOULOS, A. and TSILIGIRIS, E., 2006. 3D model generation for deformation analysis using laser scanning data of a cooling tower. *Proceedings, 3rd IAG Symposium on Geodesy for Geotechnical and Structural Engineering and 12th FIG Symposium on Deformation Measurements*. Baden, Austria: 10 pages.

JAMES, H., 2005. Dynamic target surveying. http://www.gobridges.com/article.asp?id=44 [accessed 4th January 2007].

JAUREGUI, D., WHITE, K., WOODWARD, C. and LEITCH, K., 2003. Noncontact photogrammetric measurements of vertical bridge deflection. *Journal of Bridge Engineering*, 8 (4): pp 212-222.

JENSON, J. R., 1996. *Introductory digital image processing: A remote sensing perspective*. Prentice-Hall, Inc., New Jersey, USA. 318 pages.

JOHNSON, A. E., and HEBERT, M., 1999. Using spin images for efficient object recognition in cluttered 3D scenes. *IEEE Pattern Analysis and Machine Intelligence*, 21(5): 433-449.

KARARA, H. M., 1989. An introduction to non-topographic photogrammetry. *Non-topographic Photogrammetry*, second edition (Ed. H. M. Karara). American Society of Photogrammetry and Remote Sensing, Falls Church, USA. 445 pages: 1-4.

KARRAS, G. E. and PETSA, E., 1993. DEM matching and detection of deformation in close-range photogrammetry without control. *Photogrammetric Engineering & Remote Sensing*, 59(9): 1419-1424.

KAVANAGH, B. F., 2003. *Geomatics*. Pearson Education Inc., New Jersey, USA. 589 pages.

KAVANAGH, B. F. and BIRD, S. J. G., 1992. *Surveying Principles and Applications*, third edition. Prentice-Hall, Inc., New Jersey, USA. 667 pages.

KIL, Y. J., MEDEROS, B. and AMENTA, N., 2006. Laser scanner super-resolution. *Proceedings, Eurographics Symposium on Point-based Graphics*. Boston, USA: 8 pages.

KLIMOSKI, S., 2006. Using 3D terrestrial laser scanning to model the interior of an abandoned theater for renovation purposes. http://www.gis.smumn.edu/GradProjects/KlimoskiS.pdf [accessed 3rd January 2007].

KRAUS, K., 1993. *Photogrammetry*, volume one, fourth edition. Dummler, Bonn, Germany. 397 pages.

KREMEN, T., KASPAR, M. and POSPISIL, J., 2006. Operating quality control of ground machine by means of the terrestrial laser scanning system. *International Archives of Photogrammetry, Remote Sensing and Spatial Information Sciences*, 36(A5): 5 pages.

KRETSCHMER, U., ABMAYR, T., THIES, M. and FROHLICH, C., 2004. Traffic construction analysis by use of terrestrial laser scanning. *International Archives of Photogrammetry, Remote Sensing and Spatial Information Sciences*, 36(8/W2): 232-236.

KUHLMANN, H. and GLASER, A., 2002. Investigation of new measurement techniques for bridge monitoring. *Proceedings, the 2nd Symposium on Geodesy for Geotechnical and Structural Engineering*. Berlin, Germany: 10 pages.

LAHOZ, J. G., AGUILERA, D. G., FINAT, J., MARTINEZ, J., FERNANDEZ, J. and SAN JOSE, J., 2006. Terrestrial laser scanning metric control: assessment of metric accuracy for cultural heritage modelling. *International Archives of Photogrammetry, Remote Sensing and Spatial Information Sciences*, 36(A5): 6 pages.

LAU, K. C., 2003. Six dimensional laser tracking system and method. http://www.freepatentsonline.com/20030043362.html [accessed 25th April 2007].

LEE, C. K. and FAIG, W., 1999. Dynamic monitoring with video systems. *Photogrammetric Engineering & Remote Sensing*, 65(5): 589-595.

LEE, M. R., DE SILVA, C. W., CROFT, E. A. and WU, Q.M. J., 2000. Machine vision system for curved surface inspection. *Machine Vision and Applications*, 12(3): 177-188.

LEICA, 2002. *Leica TPS1100 Professional Series – Technical data*. Leica Geosystems, Switzerland. 2 pages.

LEICA, 2003. *Leica HDS 2500 Product Specifications*. Leica Geosystems, Switzerland. 2 pages.

LEICA, 2004. *Leica HDS 3000 Product Specifications*. Leica Geosystems, Switzerland. 1 page.

LEICA, 2007. Leica LTD709: Automotive applications CMM laser tracker. http://www.leica-geosystems.com/corporate/en/ndef/lgs_35315.htm [accessed 3rd April 2007].

LEMMON, T. and BIDDISCOMBE, P., 2006. Laser scanners improve survey workflow. *Professional Surveyor Magazine*, 26(3): 14-18.

LERMA, J. L. and BIOSCA, J. M., 2005. Segmentation and filtering of laser scanner data for cultural heritage. *Proceedings, CIPA 2005 XX International Symposium*. Torino, Italy: 6 pages.

LEVOY, M., 2002. The Stanford multi-camera array. http://graphics.stanford.edu/projects/array/ [accessed 15th January 2006].

LEVOY, M., GINSBERG, J., SHADE, J., FULK, D., PULLI, K., CURLESS, B., RUSINKIEWICZ, S., KOLLER, D., PEREIRA, L., GINZTON, M., ANDERSON, S. and DAVIS, J., 2000. The digital Michelangelo project: 3D scanning of large statues. *Proceedings, SIGGRAPH 2000*. New Orleans, USA: 131-144.

LEWIS, W. J., 2003. *Tension Structures: Form and Behaviour*. Thomas Telford, London, UK. 201 pages.

LI, C. and KING, B., 2002. Close range photogrammetry for the structural monitoring. *Journal of Geospatial Engineering*, 4(2): 135-143.

LI, Y. F. and ZHANG, B., 2004. A method for 3D measurement and reconstruction for active vision. *Measurement Science and Technology*, 15: 2224-2232.

LICHTI, D. D., 2005. Spectral filtering and classification of terrestrial laser scanner point clouds. *The Photogrammetric Record*, 20(111): 218-240.

LICHTI, D. D., STEWART, M. P., TSAKIRI, M. and SNOW, A. J., 2000. Benchmark tests on a three-dimensional laser scanning system. http://www.cage.curtin.edu.au/~geogrp/WordDocs/scancal.pdf [accessed 17th November 2003].

LIDDELL, W. I., 1994. Minnesota Metrodrome. A study on the behaviour of air supported roofs under environmental loads. *Structural Engineer Review*, 6(3-4): 215-235.

LIM, M.; PETLEY, D. N.; ROSSER, N. J.; ALLISON, R. J.; LONG, A. J., and PYBUS, D., 2005. Combined digital photogrammetry and time-of-flight laser scanning for monitoring cliff evolution. *The Photogrammetric Record*, 20(110): 109-129.

LIN, S. Y. and MILLS, J. P., 2005a. A non-contact method of controlling videogrammetry in surface modelling applications. *Proceedings, Optical 3-D Measurement Techniques VII* (Eds. A. Gruen and H. Kahmen). Vienna, Austria. Volume II: 124-132.

LIN, S. Y. and MILLS, J. P., 2005b. Integration of videogrammetry and terrestrial laser scanning for dynamic surface modelling. *Videometrics VIII*, San Jose, California, USA, SPIE Vol. 5665: 243–251.

LINDENBERGH, R., and PFEIFER, N. 2005. A statistical deformation analysis of two epochs of terrestrial laser data of a lock. *Proceedings, Optical 3-D Measurement Techniques VII* (Eds. A. Gruen and H. Kahmen). Vienna, Austria. Volume II: 61-70.

LINDENBERGH, R., PFEIFER, N. and RABBANI, T., 2005. Accuracy analysis of the Leica HDS3000 and feasibility of tunnel deformation monitoring. *International Archives of Photogrammetry, Remote Sensing and Spatial Information Sciences*, 36(3/W3): 24-29.

LUTES, J. A., 2002. *Automated Dam Displacement Monitoring Using a Robotic Total Station*. M.Sc.E. Thesis, Department of Geodesy and Geomatics Engineering Technical Report No. 214, University of New Brunswick, Fredericton, New Brunswick, Canada: 138 pages.

MAAS, H.-G., 1992a. Complexity analysis for the establishment of image correspondences of dense spatial target fields. *International Archives of Photogrammetry and Remote Sensing*, 29(B5): 102-107.

MAAS, H.-G., 1992b. Robust automatic surface reconstruction with structured light. *International Archives of Photogrammetry and Remote Sensing*, 29(B5): 709-713.

MAAS, H.-G., 1998a. Image sequence based automatic multi-camera system calibration techniques. *International Archives of Photogrammetry and Remote Sensing*, 32(B5): 763-768.

MAAS, H.-G., 1998b. Photogrammetric techniques for deformation measurements on reservoir walls. *Proceedings, IAG SC4 Symposium on Geodesy for Geotechnical and Structural Engineering*, Eisenstadt, Austria: 319-324.

MAAS, H.-G. and HAMPEL, U., 2006. Photogrammetric techniques in civil engineering material testing and structure monitoring. *Photogrammetric Engineering & Remote Sensing*, 72(1): 39-46.

MAAS, H.-G. and KERSTEN, T. P., 1994. Experiences with a high resolution still video camera in digital photogrammetric applications on a shipyard. *International Archives of Photogrammetry and Remote Sensing*, 30(5): 250-255.

MAAS, H.-G. and NIEDEROST, M., 1997. The accuracy potential of large format stillvideo cameras. *Videometrics V*, San Diego, USA, SPIE Vol. 3714: 145-152.

MACHACEK, M., SAUTER, M. and ROSGEN, T., 2003. Two-step calibration of a stereo camera system for measurements in large volumes. *Measurement Science and Technology*, 14(2003): 1631-1639.

MARZAN, G. T. and KARARA, H. M., 1976. Rational design for close-range photogrammetry. *Civil Engineering Studies, Photogrammetry Series*, No. 43, University of Illinois, Illinois, USA.

MASON, S., 1995. Conceptual model of the convergent multistation network configuration task. *The Photogrammetric Record*, 15(86): 277-299.

MASUDA, T. and YOKOYA, N., 1995. A robust method for registration and segmentation of multiple range images. *Computer Vision and Image Understanding*, 61(3): 295-307.

MCCLENATHAN, R. V., NAKHLA, S. S., MCCOY, R. W. and CHOU, C. C., 2006. Use of photogrammetry in extracting 3D structural deformation/dummy occupant

movement time history during vehicle crashes. *SAE 2005 Transactions Journal of Passenger Cars: Mechanical Systems*. 3099 pages: 736-742.

MEGYESI, Z. and CHETVERIKOV, D., 2003. Affine dense matching for wide baseline stereo, *Proceedings, Grafika 2003*. Budapest, Hungary: 109-114.

MERKLE, W. and MYERS, J. J., 2004. Use of the total station for load testing of retrofitted bridges with limited access. *Smart Structures and Materials 2004: Sensors and Smart Structures Technologies for Civil, Mechanical, and Aerospace Systems*, San Diego, USA, SPIE Vol. 5391: 687-694.

MIKHAIL, E. M., BETHEL, J. S. and MCGLONE, J. C., 2001. *Introduction to modern photogrammetry*. John Wiley & Sons, Inc., New York, USA. 479 pages.

MILLER, P. E., MILLS, J. P., EDWARDS, S. J., BRYAN, P., MARSH, S. and HOBBS, P., 2006. Integrated remote monitoring for coastal geohazards and heritage sites. *Proceedings, the ASPRS 2006 Annual Conference*. Reno, USA: 11 pages.

MILLS, J. P., 1996. *The Implementation of a Digital Photogrammetric System and Its Application in Civil Engineering*. PhD thesis, University of Newcastle upon Tyne, Newcastle upon Tyne, UK (unpublished): 252 pages.

MILLS, J. P., BUCKLEY, S. J. and MITCHELL, H. L., 2003a. Synergistic fusion of GPS and photogrammetrically generated elevation models. *Photogrammetric Engineering and Remote Sensing*, 69(4): 341-349.

MILLS, J. P., BUCKLEY, S. J., MITCHELL, H. L., CLARKE, P. J. and EDWARDS, S. J., 2005. A geomatics data integration technique for coastal change monitoring. *Earth Surface Processes and Landforms*, 30(6): 651-664.

MILLS, J. P., SCHNEIDER, D., BARBER, D. M. and BRYAN, P. G., 2003b. Geometric assessment of the Kodak DCS Pro back. *The Photogrammetric Record*, 18(103): 193–208.

MITCHELL, H. L., 1994. A comprehensive system for automated body measurement. *International Archives of Photogrammetry and Remote Sensing*, 30(B5): 265-272.

MITCHELL, H. L. and CHADWICK, R. G., 1999. Digital photogrammetric concepts applied to surface deformation studies. *Geomatica*, 53(4): 405-414.

MOFFITT, F. H. and BOSSLER, J. D., 1998. *Surveying,* tenth edition. Addison-Wesley, Menlo Park, California, USA. 738 pages.

NATIONAL INSTRUMENTS, 2007. Choosing the right bus. http://zone.ni.com/devzone/cda/tut/p/id/5386 [accessed 3rd February 2007].

NAVIN, M., 2005. Reflectance and transmittance measurements of plastic samples. http://www.shef.ac.uk/physics/research/pppa/research/t2k/reflectivity.pdf [accessed 2nd March 2006].

NEWCOMEN, H. W., MURRAY, C. and SHWYDIUK, L., 2003. Monitoring pit wall deformation in real time at Highland Valley Copper. *Proceedings, the 4th International Conference on Computer Applications in the Minerals Industries*. Calgary, Canada. (on CD-ROM.)

NIGHTLY.NET, 2006. Montreal's Olympic Stadium. http://www.nightly.net/cgi-bin/ultimatebb.cgi?ubb=get_topic;f=36;t=003072;p=0 [accessed 5th April 2006].

OTEPKA, J., 2004. *Precision Target Mensuration in Vision Metrology*. PhD dissertation, Institute of Photogrammetry and Remote Sensing, Vienna University of Technology, Vienna, Austria: 86 pages.

OTTO, F., 1967.Pneumatic structures. *Tensile Structures*, volume 1 (Ed. F. Otto). The M.I.T. Press, Cambridge, Massachusetts, USA. 320 pages: 10-168.

OTTO, F., 1969. Basic concepts and survey of tensile structures. *Tensile Structures*, volume 2 (Ed. F. Otto). The M.I.T. Press, Cambridge, Massachusetts, USA. 171 pages: 9-96.

PALAZZO, D. R., FRIEDMANN, R. M. P., NADAL, C. A., FILHO, M. L. S., VEIGA, L. A. K. and FAGGION, P. L., 2006. Dynamic monitoring of structures using a robotic total station. *Proceedings, XXIII FIG Congress.* Munich, Germany: 10 pages.

PAPPA, R. S., BLACK, J. T., BLANDINO, J. R., JONES, T. W., DANEHY, P. M. and DORRINGTON, A. A., 2003. Dot-projection photogrammetry and videogrammetry of gossamer space structures. http://techreports.larc.nasa.gov/ltrs/PDF/2003/tm/NASA-2003-tm212146.pdf [accessed 21st November 2003].

PARKER, D., 1999a. Dome supplier faces Montreal compensation battle. *New Civil Engineer*, 28 January: 4.

PARKER, D., 1999b. Are giant tents domed? *New Civil Engineer*, 4 February: 16–19.

PCTECHGUIDE, 2003. Digital video format. http://www.pctechguide.com/24dvid3.htm#DV_format [accessed 14th December 2003].

PEIPE, J., 1999. High resolution digital cameras in architectural photogrammetry. http://cipa.icomos.org/fileadmin/papers/olinda/99c404.pdf?PHPSESSID=b035987a0d53f66d333513ca1b4e8b71 [accessed 8th December 2005].

PFEIFER, N., GORTE, B. and WINTERHALDER, D., 2004. Automatic reconstruction of single trees from terrestrial laser scanning data. *International Archives of Photogrammetry, Remote Sensing and Spatial Information Sciences*, 35(5B): 114-119.

PILGRIM, L. J., 1991. *Simultaneous three dimensional object matching and surface difference detection in a minimally restrained environment*. Research Report No. 066.08.1991, Department of Civil Engineering and Surveying, University of Newcastle, New South Wales. 215 pages.

PILGRIM, L. J., 1996. Robust estimation applied to surface matching. *ISPRS Journal of Photogrammetry & Remote Sensing*, 51(1996): 243-257.

POYNTON, C. A., 1996. *A Technical Introduction to Digital Video*. John Wiley & Sons, Inc., New York, USA. 352 pages.

PRATT, W. K., 2001. *Digital Image Processing*, third edition. John Wiley & Sons, Inc., New York, USA. 735 pages.

PSALTIS, C. and IOANNIDIS, C., 2006. An automatic technique for accurate non-contact structural deformation measurements. *International Archives of Photogrammetry, Remote Sensing and Spatial Information Sciences*, 36(5): 242-247.

PULNiX, 2004. Why progressive scan? http://www.pulnix.com/Imaging/i-techC.html [accessed 15th September 2004].

REMONDINO, F., 2002. Image sequence analysis for human body reconstruction. *International Archives of Photogrammetry and Remote Sensing*, 34(5): 363-368.

REMONDINO, F. and EL-HAKIM, S., 2006. Image-based 3D modelling: a review. *The Photogrammetric Record*, 21(115): 269-291.

ROBERTS, G. W., DODSON, A. H., MENG, X. and COSSER, E., 2004. A Remote Bridge Health Monitoring System Using Computational Simulation and GPS Sensor Data. http://www.nottingham.ac.uk/iessg/research/research_project/isgres43/res_project_43.html [accessed 2nd January 2007].

ROBSON, S. and SHORTIS, M. R., 2001. *VMS 7.6 On-line Help Documents*.

ROBSON, S., SHORTIS, M. R. and RAY, S., 1999. Vision metrology with super wide angle and fish-eye optics. *Videometrics VI*, San Jose, USA, SPIE Vol. 3641: 199-206.

RYALL, T. G. and FRASER, C. S., 2002. Determination of structural modes of vibration using digital photogrammetry. *AIAA Journal of Aircraft*, 39(1): 114-119.

SAKIMURA, R. and MARUYAMA, K., 2007. Development of a new generation imaging total station system. *Journal of Surveying. Engineering*, 133(1): 14-22.

SAVVAIDIS, P., IFADIS, I., LAKAKIS, K. and CHALIMOURDAS, S., 2005. Use of robotic total stations for landslide monitoring. *Proceedings, International Symposium on Modern Technologies, Education and professional Practice in Geodesy and Related Fields*. Sofia, Greece: 179-190.

SCAIONI, M. and FORLANI, G., 2003. Independent model triangulation of terrestrial laser scanner data. *International Archives of Photogrammetry, Remote Sensing and Spatial Information Sciences*, 34(5/W12): 308-313.

SCARAMUZZA, D., 2007. Omnidirectional camera calibration toolbox for Matlab. http://asl.epfl.ch/~scaramuz/research/Davide_Scaramuzza_files/Research/OcamCalib_Tutorial.htm [accessed 15th March 2007].

SCHAFER, T., WEBER, T., KYRINOVIC, P., and ZAMENCNIKOVA, M., 2004. Deformation measurement using terrestrial laser scanning at the hydropower station of Gabcikovo. *Proceedings, INGEO 2004 and FIG Regional Central and Eastern European Conference on Engineering Surveying*. Bratislava, Slovakia: 10 pages.

SCHENK, T., 1999. *Digital Photogrammetry*. Terrascience, Laurelville, Ohih, USA. 428 pages.

SCHEUERMANN, R. and BOXER, K., 1996. *Tensile Architecture in the Urban Context*. Butterworth Architecture, Oxford, UK. 217 pages.

SCHMIDT, T. and TYSON, J., 2003. Full-field dynamic displacement and strain measurement using advanced 3D image correlation photogrammetry. http://www.trilion.com/Ppr.ARAMIS.ExpTech.June2003.pdf [accessed 14th March 2004].

SCHULZ, T. and INGENSAND, H., 2004a. Influencing variables, precision and accuracy of terrestrial laser scanners. *Proceedings, INGEO 2004 and FIG Regional Central and Eastern European Conference on Engineering Surveying*. Bratislava, Slovakia: 8 pages.

SCHULZ, T. and INGENSAND, H., 2004b. Terrestrial laser scanning - investigation and applications for high precision scanning. *Proceedings, FIG Working Week 2004.* Athens, Greece: 15 pages.

SHARMA, J. S., HEFNY, A. M., ZHAO, J., and CHAN, C. W., 2001. Effect of large excavation on deformation of adjacent MRT tunnels. *Tunnelling and Underground Space Technology*, 16(2001): 93–98.

SHORT, T. M., 1994. *How to use CUBA, the City University Bundle Adjustment. CUBA User's Manual*. Department of Civil Engineering, City University, London (unpublished): 59 pages.

SHORTIS, M. R., 1986. Close range photogrammetric measurements for structural monitoring, deformation surveys and engineering surveillance. *Australian Journal of Geodesy, Photogrammetry and Surveying*, 45: 55-64.

SHORTIS, M. R. and BEYER, H. A., 2001. Sensor technology for digital photogrammetry and machine vision. *Close Range Photogrammetry and Machine Vision* (Ed. K. B. Atkinson). Whittles Publishing, Caithness, UK. 371 pages: 106-155.

SHORTIS, M. R., CLARKE, T. A. and SHORT, T., 1994a. A comparison of some techniques for the subpixel location of discrete target images. *Videometrics III*, Boston, USA, SPIE Vol. 2350: 239-250.

SHORTIS, M. R., HARVEY, E. S. and SEAGER, J., 2007. A review of the status and trends in underwater videometric measurement. Invited paper, *Videometrics IX*, San Jose, California, USA, SPIE Vol. 6491: 26 pages.

SHORTIS, M. R., THOMPSON, M. W. and HALL, C. J., 1994b. An application of digital close range photogrammetry to the monitoring of large scale engineering structures. International Archives of Photogrammetry and Remote Sensing, 30(5): 365-373.

SLEIGH, A. C., 1991. Machine vision for open world applications. *Computer Vision and Image processing* (Ed. A. Barrett). Chapman and Hall, London, UK. 304 pages: 1-24.

SMITH, M. J., MATHER, J. S. B., GIBSON, K. A. H. and JOWETT, S., 1998. Measuring dynamic response of a golf club during swing and impact. *The Photogrammetric Record*, 16(92): 249-257.

SOL DATA, 1993. CYCLOPS. http://www.soldatagroup.com/Soldata/soldata_uk.nsf/0/02972685E2724B47C1257203004FCB9F/$file/Cyclops-uk.pdf [accessed 2nd January 2007].

STAIGER, R., 2003. Terrestrial laser scanning technology, systems and applications. *Proceedings, the 2nd FIG Regional Conference*. Marrakech, Morocco: 10 pages.

STERNBERG, H., 2006. Deformation measurements at historical buildings with terrestrial laser scanners. *International Archives of Photogrammetry, Remote Sensing and Spatial Information Sciences*, 36(5): 6 pages.

STOYANOV, D., 2007. Camera calibration tools. http://ubimon.doc.ic.ac.uk/dvs/index.php_m_581 [accessed 15th March 2007].

STROBL, K., SEPP, W., FUCHS, S., PAREDES, C. and ARBTER, K., 2007. Camera Calibration Toolbox for Matlab. http://www.vision.caltech.edu/bouguetj/calib_doc/ [accessed 15th March 2007].

SUMI, Y., KAWAI, Y., YOSHIMI, T. and TOMITA, F., 2002. 3D object recognition in cluttered environments by segment-based stereo vision. *International Journal of Computer Vision*, 46(1): 5-23.

SUWANNAKANTHI, R., SRICHAIKUL, P. and TANPRASERT, C., 2006. 3D objects in Wat Makutkasattriyaram's e-Museum: progress, experiences, and. Applied technologies. http://pnclink.org:8080/pnc2006/Presentation%20material/D-Museum%20--%20Rochabodin%20Suwannakanthi.pdf [accessed 14th February 2007].

SVOBODA, T., MARTINEC, D. and PAJDLA, T., 2005. A convenient multicamera self-calibration for virtual environments. *Presence: Teleoperators & Virtual Environments*, 14(4): 407-422.

THE BRITISH CONSTRUCTIONAL STEELWORK ASSOCIATION LIMITED, 2002. *National Structural Steelwork Specification for Building Construction*, fourth edition. The British Constructional Steelwork Association Ltd., London, UK. 69 pages.

THE MATHWORKS, INC., 2004. *MATLAB 7.0 On-line Help Documents*.

THIES, M. and SPIECKER, H., 2004. Evaluation and future prospects of terrestrial laser scanning for standardized forest inventories. *International Archives of Photogrammetry, Remote Sensing and Spatial Information Sciences*, 36(8/W2): 192-197.

THOMPSON, E. H., 1962. Photogrammetry. *The Royal Engineers Journal*, 76(4): 432-444.

TORLEGARD, A. K. I., 1980. An introduction to close range photogrammetry. *Developments in close range photogrammetry*, volume I. (Ed. K. B. Atkinson). Elsevier Applied Science, London, UK. 222 pages: 1-14.

TRINDER, J. C., 1989. Precision of digital target location. *Photogrammetric Engineering & Remote Sensing*, 55(6): 883-886.

TSAI, R. Y., 1987. A versatile camera calibration technique for high-accuracy 3D machine vision metrology using off-the-shelf TV cameras and lenses. *IEEE Journal of Robotics and Automation*, RA–3(4): 323-344.

TSAKIRI, M., LEKIDIS, V., STEWART, M. and KARABELAS, J., 2003. Testing procedures for the monitoring of seismic induced vibrations on a cable-stayed highway bridge. *Proceedings, the 11th FIG Symposium on Deformation Measurements.* Santorini, Greece: 8 pages.

TUCKER, C., 2002. Testing and verification of the accuracy of 3D laser scanning data. *Proceedings, ISPRS Technical Commission IV Symposium 2002.* Ottawa, Canada: 6 pages.

UFFENKAMP, V., 1993. State of the art of high precision industrial photogrammetry. http://www.slac.stanford.edu/econf/C930928/papers/018.pdf [accessed 8th December 2005].

UREN, J. and PRICE, W. F., 2006. *Surveying for Engineers,* fourth edition. Palgrave Macmillan, Hampshire, UK. 824 pages.

VERNON, D., 1991. *Machine Vision*. Prentice Hall International Ltd., Hertfordshire, UK. 260 pages.

VISINTINI, D., CROSILLA, F. and SEPIC, F., 2006. Laser scanning survey of the Aquileia basilica (Italy) and automatic modelling of the volumetric primitives. *International Archives of Photogrammetry, Remote Sensing and Spatial Information Sciences*, 36(5): 6 pages.

VOSSELMAN, G., SESTER, M. and MAYER, H., 2004. Basic computer vision techniques. *Manual of Photogrammetry*, fifth edition (Eds. J. C. McGlone, E. M. Mikhail and J. Bethel). American Society for Photogrammetry and Remote Sensing, Maryland, USA. 1151 pages: 455-504.

WALDHAUSL, P., 1992. Defining the future of architectural photogrammetry. *International Archives of Photogrammetry and Remote Sensing*, 29(B5): 767-770.

WATSON, D. F., 1992. *Contouring: A Guide to the Analysis and Display of Spatial Data.* Pergamon Press Ltd.. Oxford, UK. 321 pages.

WATT, P. J. and DONOGHUE, D. N. M.. 2005. Measuring forest structure with terrestrial laser scanning. *International Journal of Remote Sensing*. 26(7): 1437-1446.

WHITEMAN, T., LICHTI, D. D. and CHANDLER, I., 2002. Measurement of deflections in concrete beams by close-range digital photogrammetry. *International Archives of Photogrammetry and Remote Sensing*, 34(4): 22-26.

WILBURN, B., JOSHI, N., VAISH, V., LEVOY, M. and HOROWITZ, M., 2004. High-speed videography using a dense camera array. *Proceedings, IEEE Computer Society Conference on. Computer Vision and Pattern Recognition.* Washington DC, USA. Volume 2: 294-301.

WILBURN, B., JOSHI, N., VAISH, V., TALVALA, E., ANTUNEZ, E., BARTH, A., ADAMS, A., LEVOY, M. and HOROWITZ, M., 2005. High performance imaging using large camera arrays. *Proceedings, SIGGRAPH 2005*. Los Angeles, USA: 765-776.

WILBURN, B., SMULSKI, M., LEE, H.-H. K. and HOROWITZ, M., 2002. The light field video camera. *Media Processors 2002*, San Jose, USA, SPIE Vol. 4674: 29-36.

WILLIAMS, J. and BENNAMOUN, M., 2001. Simultaneous registration of multiple corresponding point sets. *Computer Vision and Image Understanding*, 81(1): 117-142.

WIRTH, H. and MORIT, G., 1995. The most flexible instrumentation for surveying and alignment - a high precision total station controlled by modern software. *Proceedings, the 4th International Workshop on Accelerator Alignment.* Tsukuba, Japan: 8 pages.

WOLF, P. R. and DEWITT, B. A., 2000. *Elements of Photogrammetry: with Applications in GIS*, third edition. McGraw Hill, New York, USA. 624 pages.

WOLF, P. R. and GHILANI, C. D., 2002. *Elementary Surveying: An Introduction to Geomatics*, tenth edition. Prentice-Hall, Inc., New Jersey, USA. 900 pages.

WONG, K. W., LEW, M. and WILEY, A. G., 1988. 3-D metric vision for engineering construction. *International Archives of Photogrammetry and Remote Sensing,* 27(B5): 647-656.

WOODHOUSE, N. G., ROBSON, S. and EYRE, J. R., 1999. Vision metrology and three dimensional visualization in structural testing and monitoring. *The Photogrammetric Record*, 16(94): 625-641.

WUNDERLICH, T. A., 2004. Geodetic monitoring with prismless polar methods. *Proceedings, INGEO 2004 and FIG Regional Central and Eastern European Conference on Engineering Surveying.* Bratislava, Slovakia: 8 pages.

YANG, T. Y., 1986. *Finite Element Structural Analysis*. Prentice-Hall, Inc., New Jersey, USA. 543 pages.

ZHANG, Z., 2000. A flexible new technique for camera calibration. *IEEE Transactions on Pattern Analysis and Machine Intelligence*, 22(11):1330-1334.

ZHU, J., SUN, D., TSO, S.-K. and MILLS, J. K., 2002. Vision guidance for a climbing robot. *Mechatronics and Machine Vision 2002: Current Practice* (Eds. R. Bradbeer and J. Billingsley). Research Studies Press Ltd., Baldock, Hertfordshire, UK. 373 pages: 23-32.

ZIEMANN, H. and EL-HAKIM, S. F., 1982. System calibration versus self-calibration. *International Archives of Photogrammetry*, 24(1): 117-122.

ZUMBRUNN, R., 1995, Systematic pointing errors with retroreflective targets. *Optical Engineering*, 34(9): 2691-2695.